20TH MEETING BULLETIN

JOINT ARMY-NAVY-AIR FORCE-ARPA-NASA

PANEL ON PHYSICAL PROPERTIES

OF SOLID PROPELLANTS

Volume I

NOVEMBER 14-16, 1961

RIVERSIDE, CALIFORNIA

20TH MEETING BULLETIN

JOINT ARMY-NAVY-AIR FORCE-ARPA-NASA PANEL ON PHYSICAL PROPERTIES OF SOLID PROPELLANTS

Volume I

NOVEMBER 14-16, 1961

RIVERSIDE, CALIFORNIA

FOREWORD

This Bulletin constitutes a record of the papers presented at the 20th Meeting of the JANAF-ARPA-NASA Panel on the Physical Properties of Solid Propellants, held at the Mission Inn Hotel, in Riverside, California, with Grand Central Rocket Company as host facility.

The second conference on structural integrity is being held in conjunction with this meeting, with the intent of furthering the application of stress analysis techniques to the prediction of rocket motor failure.

In order to facilitate the dissemination and handling of solid propellant information, the Bulletin has been divided into an unclassified (Volume I) and a classified volume (Volume II).

Dr. K. H. Sweeny, of the Aerojet-General Corporation, Azusa, California, is Chairman of the Physical Properties Panel at the present time, and Dr. M. L. Williams, of the California Institute of Technology, is the Vice Chairman.

TABLE OF CONTENTS

VOLUME I

ENGINEERING ANALYSIS (Cont'd.)

SPECIAL TEST PROCEDURES

VOLUMETRIC EFFECTS

FAILURE CRITERIA

PHYSICO-CHEMICAL EFFECTS

TABLE OF CONTENTS

VOLUME II

A SURVEILLANCE VIEWPOINT

Norman Fishman
Propulsion Sciences Division
Stanford Research Institute
Menlo Park, California

ABSTRACT

This paper offers a discussion to the Physical Properties Panel which looks at the investigation of mechanical properties and structural analysis from a surveillance viewpoint. The problems associated with gaining an understanding of the mechanical behavior of solid propellants are common to surveillance people and mechanical properties people; establishment of failure criteria and achieving meaningful mechanical properties measurements are common goals.

INTRODUCTION

Though this paper is in response to a request for a report from the Surveillance Panel, I have chosen to take the role of private citizen, rather than that of Vice-Chairman of the Surveillance Panel or that of investigator of aging phenomena under U.S. Air Force contract. Surveillance is a very broad term and means many different things to different people, depending on their particular mission. Therefore, this paper is presented as being written from what I consider to be a surveillance viewpoint.

One possible definition of surveillance can be drawn from a classical definition of reliability. Reliability is the probability of a device performing its objective adequately for the period of time intended under the operating conditions encountered. Thus, surveillance provides assurance that the reliability of the device is maintained above a prescribed level for the period of time intended after it has been put into service. If the device happens to be a solid propellant motor, then surveillance encompasses all components of the motor, such as the ignition system, motor case, nozzle, liner, various sealants, and the grain.

If the mode of failure of the motor is related to the propellant, and if ballistic performance, ignitability, or chemical stability do not place limitations on serviceable life, then we become interested in the physical behavior of the grain. This paper hopefully places before the Physical Properties Panel those areas of investigation which are of particular importance in the study of propellant aging and in the surveillance of solid propellant motors.

DISCUSSION

In propellant development, the desire to improve storage stability may influence propellant composition and formulation procedures. Similarly, during manufacture, aging considerations might result in modification of processing methods and quality control limits. Unfortunately, storage capability is a low priority consideration in

design, development, and procurement; after the unit is operationally deployed, we have nothing more to do with it than to determine how long it will be serviceable. , Then we have to go back to determine such things as how marginal was the design, how long will it take for expected changes to result in malfunction, are quality control limits sufficiently tight to assure uniform storage histories, etc. In general, those aspects of physical behavior which are of interest to you for design criteria and quality control are of equal interest to the surveillance community who interjects the influence of time and environment.

There are many possible modes of failure which might be encountered; these include rupture on ignition, crack formation, liner-case or propellant-liner bond separation, slump, etc. Each mode of failure might be experienced when the unit is first manufactured or at some time after the motor has been stored in its operational environment. There is a limiting factor or combination of factors which determine a criterion for failure; i. e. , cracks may result in regions where the strain exceeds a certain value, or rupture on ignition may occur when the elongation is less than a certain limiting value. These failure criteria help establish safety margins from the design standpoint. These same criteria must be known to determine when the unit is no longer serviceable, or, if rates of change are known, to predict when the unit will fail to perform adequately. Thus the problems of mechanical property measurement and understanding of physical behavior are common to the motor designer and to the user.

Perhaps the key need for all concerned is the sensitive and meaningful representation of mechanical behavior. The stress analyst must have meaningful data to develop his analytical model for the grain. Both the designer and the aging investigator require failure criteria, to be supplied empirically or analytically. All are concerned with the mechanism of rupture. The effective measurement of mechanical properties and interpretation of data are thus fundamental to propellant development, grain design, and to surveillance.

The aging investigator must determine which property of the propellant, as it changes in storage, most rapidly approaches its limiting value, or, by what manifestation of propellant aging will the motor first malfunction. He can measure rates of aging represented by changes in such properties as cross-link density, time-to-rupture, modulus and elongation, hardness, creep compliance, stress relaxation modulus, etc. If sufficient data are collected and communication lines are open, correlation with motor firing experience might serve to establish the property value limits for reliable performance. Similar correlation with results of accelerated aging studies might even enable a degree of predictability of serviceable life. However, if the mode of failure is determined and a means is available for making a meaningful measurement of the property or properties most closely related to that failure mechanism, then the entire process of determination and predictability of serviceable life becomes better defined.

Using a simplified example, if failure is expected by propellant-liner bond separation resulting from propellant creep, we can test the propellant for changes in creep behavior and thus arrive at a meaningful

aging rate. When propellant-liner bond separation does in fact occur, an integrated function of creep compliance and time might yield an empirically determined failure criterion. However, if analytical methods can provide the failure criterion, and if extrapolation of test results from accelerating conditions is known to be valid, then prediction of serviceable life can be made.

Taking the same hypothetical case a step further, if a nondestructively measured property (such as electrical resistivity, capacitance, or sonic absorption) can be correlated with the occurrence of motor failure, we can calibrate the age-meter in a full-scale surveillance program. Calibration can also be achieved if this same property can be correlated with the integrated creep function, and the criterion for failure can be determined analytically. This then enables a red-flag to be raised by the age-meter when failure becomes imminent.

A greater understanding of the mechanical behavior of propellant is required to make the determination and predictability of serviceable life possible. Specific areas of interest are not new to the Physical Properties Panel; your meeting bulletins over the past few years show that considerable effort has already been expended toward solution of the problems, and the collection of papers at this meeting show that definite progress is being made. The areas described briefly below are not in order of importance.

Physical Measurements and Data Evaluation. Appropriate measurements and pertinent evaluation processes should be available for testing properties related to the various failure modes. Once the expected mode of failure is determined, only tests meaningful of that mechanism need be conducted. Conversely, in an aging or surveillance program, by making a series of specific evaluations, changes indicating degradation of properties should be interpretable in regard to identification of the mode of failure to be expected. Thus, we should be able to test for changes in binder properties alone, for changes in binder-oxidant bond, or for composite properties which relate most closely to the failure mode.

Quality Assurance. To assure uniform storage histories, whether or not a nondestructive monitoring device is available, sufficiently sensitive and meaningful quality control tests should be used. It is not adequate for quality control to insure production batches of propellant which fall between arbitrarily or semi-arbitrarily specified limits; we must also know that all batches will age in the same manner and at the same rate. The availability of such control of quality will not only result in the ability to maintain higher levels of reliability in the field, but will also reduce the maintenance costs.

Fundamental Studies. For both the above areas of providing adequate measurement means for surveillance and quality control, we recognize that much of a somewhat fundamental nature remains to be studied. Examples of such work which come to mind most readily are listed below:

1. Dewetting phenomena must be more fully explored. Since the binder-oxidant bond appears to be affected most by aging, at least in some propellants, we should be able to measure properties which most nearly describe the strength or condition of this bond and how it will perform during motor operation. Included here are such studies as volume change under various conditions of stress and strain in uniaxial or multiaxial modes and under varying environmental pressures.

2. For both surveillance testing and quality control, greater attention must be given to humidity conditions and moisture content of the propellant. As test methods become more sophisticated and sensitivity to small differences increases, the effects of moisture may outweigh basic differences of propellant properties. Recognition must be given to the possibility that propellant moisture may be different from test to test or that such moisture may change during the course of a test. Similarly, for more effective simulation of the motor storage environment and for the determination of realistic propellant properties, studies should be conducted to determine what the history of moisture content is in the grain from the time of manufacture and into the period of transport and storage.

3. Probably the most important of all the fundamental problems are those associated with failure criteria. The establishment of failure criteria, whether by analytical or empirical means, is being awaited by all concerned with solid propellant motors, from the grain designer to the field surveillance monitor. To assist analytical efforts, it is important that more meaningful data be obtained. Thus, increased sophistication in test methods and data evaluation is to be desired whether measurements are being made by a research rheologist, by a quality control chemist, or by a field sampling technician.

CONCLUSION

In rereading what I have written above, I fear that I have generalized too much. However, to become too specific in this case would be akin to carrying the proverbial coals to Newcastle. The problems associated with gaining an understanding of the mechanical behavior of solid propellants are common to surveillance people and mechanical properties people; establishment of failure criteria and achieving meaningful mechanical properties measurements are common goals. Recognizing that propellants do change with age, and that different propellants age by different mechanisms in different environments, we gain the realization that the investigation of mechanical properties is even more complex than we had originally thought. Now more sensitive measures are required to study aging rate, more meaningful tests must be conducted in quality control, and rheology takes on a fourth dimension.

The agenda of the forthcoming Surveillance Panel meeting lists a particularly well rounded group of presentations. Representatives of the three services will discuss problems encountered in their surveillance programs. R. and D. phases of surveillance will be covered in more detail by speakers well qualified in each of the three major large motor programs -- Minuteman, Polaris, and Pershing. In addition to these, several papers will be presented in each of two sessions on surveillance

techniques and the chemistry of aging. Of particular interest to the Physical Properties Panel will be the reports of the two committees on critical problem areas and preferred surveillance testing methods. For additional information relating to surveillance, I refer you to the bulletins of the above meeting and of the five previous meetings.

We who work in surveillance are generalists; if we can give to the mechanical properties investigators and to the structural analysts the surveillance viewpoint, we will undoubtedly gain more from the specialists in these fields.

RECENT DEVELOPMENTS IN STRESS ANALYSIS FOR VISCOELASTIC MATERIALS

E. H. Lee. Brown University, Providence, R. I.

ABSTRACT

Viscoelastic material behavior complicates stress analysis problems, because of the variation of stress distributions with time caused by the time dependent material characteristics. However, such variation exhibits a flexibility in the solutions for stress distributions which it may be possible to utilize to meet design requirements. As an example, the influence of maintained internal pressure in an elastically encased hollow cylinder is shown to lead to a residual stress field which incorporates hydrostatic compressive stress components which will inhibit the initiation and growth of fracture cracks in the viscoelastic cylinder. Such phenomena have mainly been assessed on the basis of solutions for simple viscoelastic materials represented by spring-dashpot models with few elements. A method of using measured creep or relaxation functions in stress analysis calculations is presented, which permits solution for general linear viscoelastic response. This consists of numerical integration of the integral equations which represent certain stress analysis problems, and in particular cases it has been found to be simple to carry out and to yield accurate results. Another extension of stress analysis theory has been to include the effect of boundary motion which is neglected in the usual infinitesimal displacement theory in which boundary conditions are satisfied on the undeformed boundaries. A perturbation scheme applicable for linear viscoelastic operators, although the problem itself becomes non-linear because of the boundary motion, is presented for a simple illustrative example.

INTRODUCTION

Viscoelastic material behavior introduces considerable complexity into problems of stress analysis. The resulting stress distributions can vary with time, even when the applied loads remain constant and the inertia forces associated with the deformation are negligible so that quasi-static analysis is suitable. In contrast, stress distributions for elastic bodies remain constant in such circumstances. However, this possibility of the variation of the stress distribution due to the viscoelastic characteristics of the material provides a flexibility which it may be possible to utilize to meet design requirements. Such an example is referred to below, where the residual stresses built up by maintained pressure in the cavity of an elastically encased grain are shown to comprise a stress field which will tend to inhibit the initiation and growth of fracture cracks in curing, storage and firing conditions. The possibility of the development of such a residual stress field is a concomitant of the stress variation mentioned above and would not arise in an elastic body subjected to maintained internal pressure.

Study of such situations has been mainly based on analyses for simple linear viscoelastic materials, but from these, qualitative features can be inferred which can be applied more generally. The residual hydrostatic compressive stress field associated with maintained internal pressure in an elastically encased cylinder is such a feature which will clearly also arise in the case of more general viscoelastic behavior. However, it is important

to extend the range of quantitative solutions for more general linear materials and for non-linear materials. A method of solving the stress analysis equations in which material properties are introduced as creep or relaxation functions is described in this paper. It is based on the numerical solution of the integral equations to which certain stress analysis problems reduce. Measured creep and relaxation functions can be included directly, which thus provides solutions for general linear visco-elastic material behavior. Moreover, such measurements over a finite time range provide complete information concerning the material's response for stress analyses overthe same time range, and certain mathematical simpli-fications arise such as avoidance of the need for separate consideration of initial conditions which can introduce considerable analytical complexity, as discussed in references (1) and (2), if the differential operator stress-strain relations, commonly associated with spring-dashpot models, are used. Another area in which generalization is needed is to remove the limitation of infinitesimal displacements, and an example exhibiting an approach to this problem is also presented below.

PRESSURIZED CAVITY EFFECT

The influence of residual stresses developed in a hollow viscoelastic cylinder encased in an elastic shell due to maintained pressure in the cavity has been discussed in (3). Figure 1 shows the variation, as a
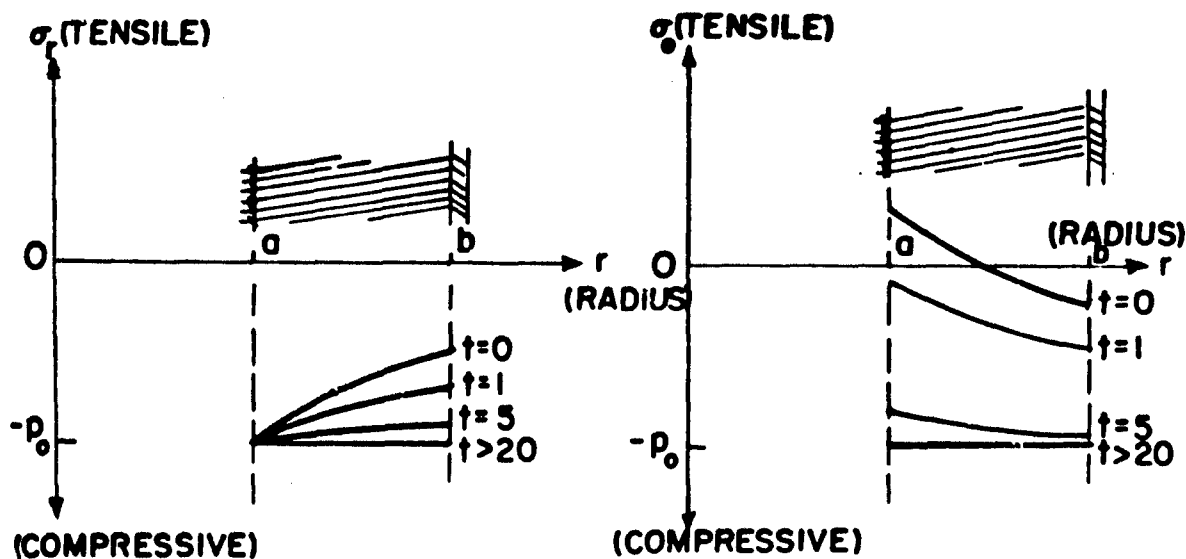
FIG. 1(a)
DISTRIBUTION OF RADIAL STRESS σ_r
UNDER SUDDENLY APPLIED AND MAINTAINED
INTERNAL PRESSURE

FIGURE 1(b)
DISTRIBUTION OF CIRCUMFERENTIAL STRESS
σ_θ UNDER SUDDENLY APPLIED AND
MAINTAINED INTERNAL PRESSURE

function of the time t, of the distribution of the radial stress σ_r and circumferential stress σ_θ for such a viscoelastic cylinder subjected to suddenly applied and maintained constant internal pressure p_o. These results were evaluated (4) for a circular cylinder with a concentric circular cavity and of material elastic in dilatation, and exhibiting Maxwell behavior in shear, represented by the model of Fig. 2. Thus in a relaxation test in shear such a material would relax to zero stress.
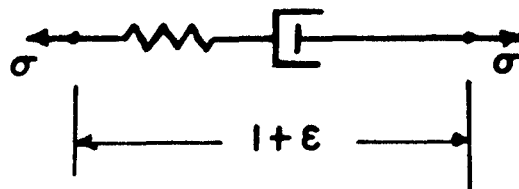
FIGURE 2. VISCOELASTIC MODEL REPRESENTING MAXWELL BEHAVIOR

Particular geometry and casing stiffness were assumed including a restraint against axial motion, but it is clear that qualitative aspects of the phenomenon to be discussed will apply for different cavity shapes and more general material behavior, and it is possible to make quantitative estimates of the factors involved. Fig. 1b shows that on loading appreciable hoop tensile stress occurs adjacent to the cavity. With maintained pressure the shear components of the stress relax and all direct stress components tend toward hydrostatic compression equal to the applied pressure. The time t is measured in units of the relaxation time of the viscoelastic response in shear, and for t > 20 the viscoelastic cylinder is virtually in a state of hydrostatic compression which transmits the full cavity pressure to the casing. Although detailed criteria for fracture are not known for viscoelastic materials, it is clear that hydrostatic compression will inhibit the initiation and growth of fracture cracks since under its influence no release of elastic energy occurs due to crack initiation or growth. Thus the state of stress developed through maintained loading will be most beneficial from this standpoint. The dangerous period during the history of stressing shown in Fig. 1 will be at the cavity surface immediately after load application due to the hoop tensile stresses. Superposition of the solution shown in Fig. 1 at different times yields the solution for gradual application of pressure, and it is found that sufficiently gradual build up of internal pressure completely eliminates the region of finite hoop tension, and hence the conditions which might lead to initiation of fracture.

If the internal pressure is released at time t_o, which occurs after the steady hydrostatic compression field has developed, the stress variation shown in Fig. 3 will occur subsequently. The hoop compression at the cavity surface increases on stress release, but this beneficial residual stress field gradually relaxes away. For the Maxwell behavior in shear the

stresses relax towards zero magnitude, but for a material exhibiting a finite limit stress in a relaxation test, some beneficial residual stress field would remain indefinitely.
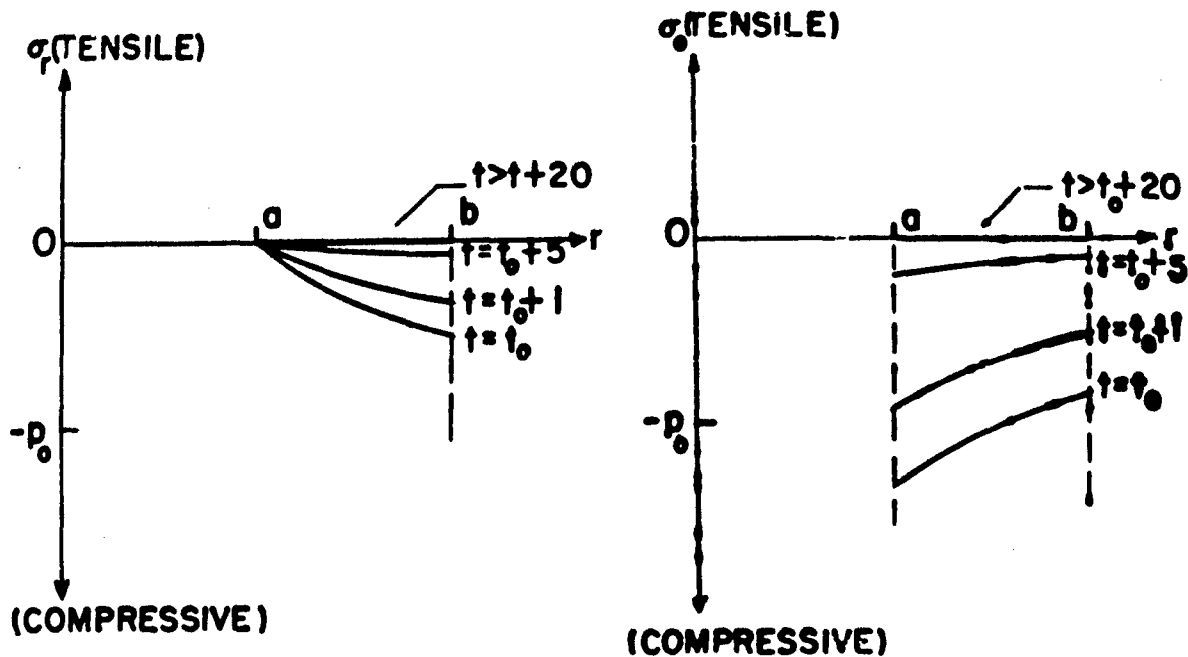
FIGURE 3. STRESS DISTRIBUTIONS AFTER REMOVAL OF INTERNAL PRESSURE

During rocket firing the pressure of the gaseous propellant acts within the cavity. For a linear viscoelastic propellant at the beginning of burning and subjected to prior pressurization, the stress distribution is given by superposition of the solution for internal pressure shown in Fig. 1 and the residual stress field shown in Fig. 3. If for simplicity of evaluation it is assumed that the full burning pressure is applied in advance and maintained up to the time of ignition, the steady hydrostatic compression stress field will continue into the burning phase until it is modified by the ablation of the cavity surface. This situation is shown by the broken lines in Fig. 4, contrasted with the full lines corresponding to the effect of burning gas pressure without prior pressurization, taken from Fig. 1. It is seen that the former comprises added compressive stress components which will provide a major influence for the inhibition of fracture. Such an effect will be maintained as burning proceeds. In view of the increased radial compressive stress at the outer radius, r=b, this benefit is offset by an increase in tension in the elastic casing. This effect during pre-pressurization could presumably be eliminated by additional support of the casing.

Although the quantitative results shown corresponds to a simple viscoelastic material and a simple geometry, it is clear that a similar effect will arise due to relaxation of shear stress for other cavity shapes and

σ_r(TENSILE)

σ_θ(TENSILE)
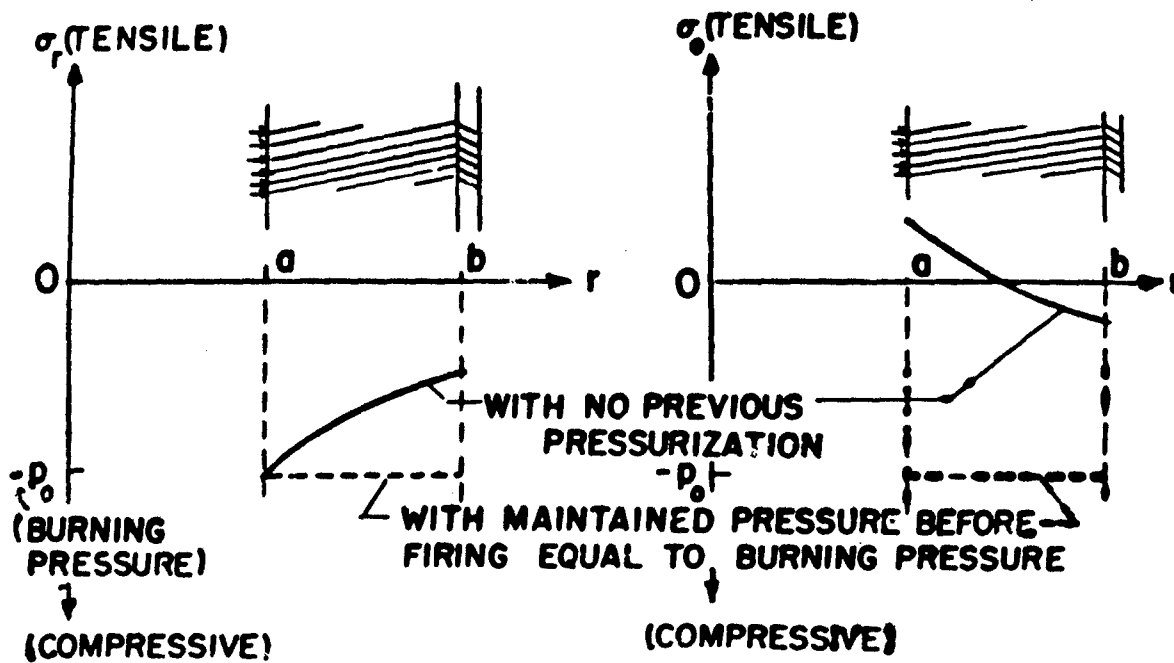
FIGURE 4.   STRESS DISTRIBUTIONS IMMEDIATELY AFTER FIRING

more general material behavior. A cruciform cavity will lead to stress concentrations which will increase the circumferential hoop tension on application of pressure, and the corresponding residual hoop compression on pressure release. For complete relaxation of shear stress no corresponding concentration of the steady hydrostatic compression will arise. Thus the influence of prior pressurization will be greater for a cruciform cavity. For a material which does not relax completely in shear, the state of hydrostatic compression would be approached but not completely realised as in the example cited.

It would be particularly beneficial to apply pressurization during curing when the modulus is low, since this will reduce the initial hoop tension, and shrinkage will occur in a hydrostatic compressive stress field which will inhibit crack formation. This environment would seem to be particularly valuable for composite material since the continuous hydrostatic compressive stress will prevent separation of the binder around the filler particles.

One way of looking at the suggestion presented above of utilizing the residual stress field due to maintained pressurization is that its action is equivalent to the effect of autofrettage in gun tubes. Autofrettage is a state of residual stress produced by plastic flow through the application of internal hydrostatic pressure during manufacture. Residual hoop compression occurs adjacent to the bore, with tension in the outer layers. The hoop compression in the grain shown in Fig. 3 and corresponding tension in the casing are the analogues of this distribution. On application of pressure in the bore when the gun is fired, the residual stress reduces the maximum hoop tension which is produced near the bore surface and thus inhibits failure. Because plastic flow is essentially rate independent, such beneficial residual stresses remain permanently. In a rocket with viscoelasticity replacing plasticity as the non-elastic effect which permits the residual stress system to be built up, these stresses are not permanent but must be maintained by retention of the pressure until some limited time before firing. Another way of visualizing the situation is that with a viscoelastic grain, gradual application of pressure produces less hoop tension than the same pressure applied suddenly. Thus to avoid the deleterious effect of the sudden rise in pressure on firing, this must be gradually applied beforehand. Such a design feature is only available because of the influence of the viscoelastic character of the grain material, and apart from the particular suggestion made in the paper, it is hoped that this example will focus attention on the more flexible design philosophy which components formed of viscoelastic materials permit. As demonstrated by the similarity of the present example to autofrettage, this general approach offers benefits analogous to those now being achieved by the application of plastic design methods for steel structures.

DIRECT USE OF RELAXATION AND CREEP MEASUREMENTS

Most stress analysis solutions for viscoelastic bodies in the literature assume simple material behavior corresponding to spring-dashpot models with few elements. This arises since the differential operator form of viscoelastic stress-strain relation is used:

$$\sum_{r=0}^{n_p} p_r \frac{\partial^r \sigma}{\partial t^r} = \sum_{r=0}^{n_q} q_r \frac{\partial^r \varepsilon}{\partial t^r} \qquad\qquad 1$$

where p_r and q_r are material constants, which leads to differential equations of order in t depending on n_p and n_q. If these orders are assumed to be small, solutions may be obtainable in convenient form, but an increase in the order of the differential equations, in general, greatly complicates the solutions. Moreover difficulties can arise in connection with initial conditions for the higher order equations as discussed in (1) and (2).

While materials exist with viscoelastic characteristics adequately represented by low order differential operator relations over several decades of time or frequency (5), most polymers exhibit a much more gradual change in their characteristic functions than is compatible with such a representation (6). The variation in the creep and relaxation functions between the short and long time asymptotes usually takes place over several decades of time, or equivalently the frequency spectrum is many decades wide in contrast to the narrow band or bands of rapid change corresponding to equation 1 with n_p and n_q small. For viscoelastic stress analysis problems in which the loading stimulates only a narrow frequency band of response, say one or two decades, satisfactory representation by, for example, a four-element model with $n_p = n_q = 2$ is possible (7), but a wider frequency range would demand more elements in the model and correspondingly higher order derivatives in the associated differential operators for satisfactory representation of material behavior. In effect a discrete frequency spectrum must be sufficiently dense to cause a smoothing of the influence of individual components, and this forces an increase in the orders n_p and n_q as the frequency band widens. However, the more gradually varying viscoelastic characteristics exhibited by many materials can be simply represented by the more general hereditary integral forms of linear viscoelastic operator relations:

$$\sigma(t) = \int_0^t G(t-\tau) \frac{d\varepsilon(\tau)}{d\tau} \, d\tau \qquad\qquad 2$$

where $G(t)$ is the relaxation modulus, or:

$$\varepsilon(t) = \int_0^t J(t-\tau) \frac{d\sigma(\tau)}{d\tau} \, d\tau \qquad\qquad 3$$

where $J(t)$ is the creep compliance. These relations arise directly by superposition of relaxation and creep responses respectively. Equations 2 and 3 include the assumptions that the material is undisturbed prior to zero time, which can usually be arranged in applications, and that if discontinuous changes in stress or strain are induced, appropriate interpretation in terms of delta functions is made. The former assumption gives the lower limit of integration zero in place of $-\infty$ for a material stressed for $t < 0$, and the latter removes separate initial value terms which would otherwise appear in addition to the integral.

Introduction of equations 2 and 3 into the stress analysis relations
can lead to representation of stress distributions in terms of the solutions
of integral equations for problems in which integration with respect to the
space variables can be carried out independently of the time operators.
Examples of such situations are given in reference (8) where it is shown
that simple numerical integration can yield accurate solutions with material
properties introduced as measured relaxation moduli. The numerical examples
treated in (8) concern thermal stresses in a slab and a sphere of visco-
elastic material with temperature varying with time and distance from the
surface in the former case, and with time and radius in the latter. A
temperature dependent shift of viscoelastic spectra on the log-frequency
scale was assumed, called thermo-rheologically simple behavior by Schwarzl
and Staverman (9). Such a problem involving a range of temperature in the
material stimulates a very broad equivalent frequency response, and use of
the integral operator forms 2 or 3 is needed for satisfactory representation
of material behavior rather than the differential form 1.

The resulting integral equations governing stress distributions are
Volterra type equations of the second kind of the form:

$$y(t) + \mu \int_0^t f'(t-\xi)y(\xi)d\xi = f(t) \qquad \qquad 4$$

where f is a normalized relaxation modulus. This can be approximated by
expressing the integral as a finite sum:

$$y(t_{n+1}) = f(t_{n+1})$$

$$+ \frac{\mu}{2} \sum_{i=1}^{n} [y(t_{i+1}) + y(t_i)][f(t_{n+1}-t_{i+1}) - f(t_{n+1}-t_i)] \qquad 5$$

by dividing the range of integration into finite intervals determined by
$t_1=0, t_2, t_3 \ldots t_i \ldots$, and using a mean value expression and the
trapezoidal rule for numerical integration. Equation 5 comprises a set of
simultaneous linear algebraic equations for the unknowns y_i. However,
taking n=0 gives y_1, and each successive equation determines y_{n+1} directly
in terms of previous values $y_1 \ldots y_n$. This sequential type of solution
arises since the integration limits 0,t lead to a triangular matrix for the
corresponding finite sum representation. The solution of 5 is thus simply
evaluated using an electronic computer, and in the examples detailed in (8)
remarkable accuracy was achieved. The finite difference form 5 permits
variation of the time step length, and this is a useful feature for the
extremely wide time range involved, 10^{-2} to 10^6 hrs., since the time step
can be increased with the time to provide approximately constant truncation
error over the range and so reduce the number of time intervals. After the
first step, a constant step in log t was used, since all functions became
smoother and approached zero with increasing time. For a particular example,
the change in the solution for

$$\Delta = \log_{10}t_{i+1} - \log_{10}t_i$$

increasing from 0.25 to 0.5 was only 0.7% of the maximum value, and even for a step length of $\Delta = 1$, which corresponds to a decade in t for each step, the change in the solution was only 1.5%. Thus viscoelastic stress analysis by numerical solution of the resulting integral equations provides a promising method of evaluation.

The direct use of measured material characteristics in a numerical procedure is a valuable feature. Certain stress analysis problems based on the laws 2 or 3 can be treated by application of the Laplace transform. For example, as discussed in (8), equation 2 becomes:

$$\bar{\sigma} = s\bar{G}\bar{\varepsilon} \qquad\qquad 6$$

where the bar represents the Laplace transform, and this form can be utilized to generate an associated elastic problem, from the solution of which the viscoelastic stress distribution can be determined by inversion of the resulting transform of the stress distribution. But in order to carry this out G must be approximated in analytical form for the determination of its Laplace transform. Muki and Sternberg (10) encountered difficulties in obtaining such an approximation over the wide time range involved, and in inversion of the resulting transform of the stress function as discussed in (8). Quite apart from this difficulty of evaluation, the Laplace transform being and integral to t $\rightarrow \infty$ can only be applied to problems in which the body does not change in form with time, and the boundary conditions remain of the same type at each surface point (11). For otherwise, in the former case, stress components at material points traversed by the boundary will only have meaning for a finite time, and in the latter, application of the transform to the boundary condition at a surface point would not generate a boundary condition on the transform of a dependent variable (traction or displacement) needed to prescribe the associated elastic problem. These restrictions rule out, for example, consideration of a cylinder with an ablating cavity. Such problems can be treated by the integral equation approach since no integration to t=∞ is involved.

Another advantage of the use of creep or relaxation measurements is that for any stress analysis problem concerned with the loading duration T, G(t) or J(t) measured for $0 \leq t \leq T$ completely prescribes the material behavior in so far as it influences the particular problem. This contrasts with the Laplace transform approach which utilizes properties for all t > 0, which must in part be assumed by extrapolation, although it is clear that the values for t > T cannot in fact affect the solution. If complex moduli are used a similar difficulty arises in connection with the infinite frequency range associated with the Fourier integral representation of a transient loading function. However for short times, high frequency oscillatory measurements are more easily obtained than creep and relaxation characteristics, and direct use of the latter may not be feasible.

Since arbitrary relaxation functions can be inserted in the numerical procedure, the complexity of the material behavior in terms of the spring-dashpot model, or the order of the corresponding differential operator representation (eqn. 1), does not affect the procedure for solution. This is in marked contrast to the added complexity associated with higher orders in the differential equation approach mentioned above. Moreover, as cited in (8), introduction of viscoelastic response in dilatation may only modify

the kernel in the integral equation, and so not introduce appreciable complexity.

FINITE DEFLECTION EFFECTS

Most viscoelastic stress and deformation analysis solutions in the literature have been based on the assumption of infinitesimal strains and deflections. Consistently with the latter assumption, boundary conditions have been satisfied on the undeformed boundary of the body under study. There is a range of situations in which small strain linear viscoelastic analysis adequately represents material response, but for which finite deflections must be considered with the consequent introduction of non-linearity into the analysis. This is commonly spoken of in elasticity theory as the introduction of geometrical non-linearity, and elastic instability problems fall in this category. In the analyses of such situations for elastic materials, the non-linearity causes the elastic modulus to become involved in the final solution in a complicated, non-linear manner. For example, in the finite bending of a beam or strut, commonly termed the elastica problem, the deflection can be represented in terms of elliptic integrals, with the square root of the Young's modulus occurring in a complicated functional form inside the argument of the elliptic integral. For the corresponding viscoelastic problem the elastic constant must be replaced by a viscoelastic operator, and interpretation of the solution in such cases has proved impossible. It is therefore necessary to modify the method of solution so that it can be appropriately interpreted when elastic constants are replaced by viscoelastic operators. In general the approach will differ from that most suitable for the corresponding elastic problem. The solution of such a problem for a viscoelastic cantilever beam with finite displacements, which is effectively the elastica problem with a modified boundary condition, has been presented in reference (12), and aspects of the solution are discussed below.

The usual approach to the corresponding elastic problem is to solve the non-linear differential equation obtained from the Bernoulli-Euler bending relation between curvature and bending moment. This can be written in the form:

$$\frac{\partial^2 \varphi}{\partial s^2} = - \lambda \cos \varphi \qquad 7$$

where

$$\lambda = \frac{L^2}{EI} R \qquad 8$$

and φ is the angle of deflection of a beam with arc length s along it, varying from 0 at the clamped end ($\varphi=0$) to L at the free end where the load R is applied. E is Young's modulus and I the quadratic section moment. In order to retain the elastic compliance 1/E in a linear form, double integration of eqn. 7 leads to the non-linear integral equation:

$$\varphi(s) = \lambda [\int_0^s u \cos \varphi(u)du + s \int_s^1 \cos \varphi(u)du] \qquad 9$$

This can be solved by iteration, according to

$$\varphi_n(s) = \lambda [\int_0^s u \cos \varphi_{n-1}(u)du + s \int_s^1 \cos \varphi_{n-1}(u)du] \qquad 10$$

and under certain conditions the required solution $\varphi(s)$ is given by the limit of $\varphi_n(s)$ as $n \rightarrow \infty$. Such an iterative scheme, or one modified by replacing φ_{n-1} by an average of previous iterates, has been shown in (12) to provide an accurate solution for large deflections. For each iteration λ occurs linearly.

For the corresponding viscoelastic problem $1/E$ in λ is replaced by the corresponding viscoelastic operator, and the resulting integral equation takes the form

$$\varphi(s,t) = \frac{L^2 J(0)}{I} [R(t)\Theta(s,t) + \int_0^t \frac{J'(t-\xi)}{J(0)} R(\xi)\Theta(s,\xi)d\xi] \qquad 11$$

where

$$\Theta(s,t) = \int_0^s u \cos \varphi(u,t)du + s \int_s^1 \cos \varphi(u,t)du \qquad 12$$

A similar iteration scheme applies to this double integral equation containing both space and time integrals. The viscoelastic operator occurs linearly in each iteration, so that the change from an elastic constant to a viscoelastic operator introduces no essential difficulty. Specific results based on this approach are given in (12). It is hoped that this example of a perturbation approach to finite deformation effects in a simple problem of viscoelastic stress and deformation analysis may suggest analogous methods for more involved problems.

BIBLIOGRAPHY

1. A. H. Corneliussen and E. H. Lee. Brown University Report DA-4750/2, 1960.
2. A. H. Corneliussen, E.F. Kamowitz, E.H. Lee and J.R.M. Radok. Brown University Report, Nord 18594/5, 1961.
3. E. H. Lee. Brown University Report, Nord 18594/4, 1961.
4. E. H. Lee, J.R.M. Radok and W. B. Woodward. Trans. Soc. Rheology 3, 41, 1959.
5. J. J. Benbow. Proc. Phys. Soc. B67, 120, 1954.
6. H. Kolsky and Y. Y. Shi. Brown University Report, Nonr 562(14)/5, 1958.
7. D. R. Bland and E. H. Lee, Jr. Appl. Mech. 23, 416, 1956.
8. E. H. Lee and T. G. Rogers. Brown University Report DA-G-54/1, 1961.
9. F. Schwarzl and A. J. Staverman. J. Appl. Phys., 23, 838, 1952.
10. R. Muki and E. Sternberg. J. Appl. Mech. 28, 193, 1961.
11. E. H. Lee. Proc. 1st Symp. Naval Struct. Mech., 456, Pergamon, 1960.
12. T. G. Rogers and E. H. Lee. Brown University Technical Report Nonr 562(30)/1, 1961.

ACKNOWLEDGMENT

ANALYTICAL METHODS

H. H. Hilton, Reporter

ANISOTROPIC, NONHOMOGENEOUS, LINEAR VISCOELASTIC ANALYSIS

By Harry H. Hilton,
Professor of Aeronautical and Astronautical Engineering
University of Illinois
Consultant to Aerojet-General Corporation

ABSTRACT

An analogy in terms of Fourier transforms is developed for anisotropic, nonhomogeneous viscoelasticity in terms of equivalent anisotropic elasticity. The special case of orthotropic viscoelasticity is discussed in detail, particularly the influence of orthotropy on the stress-strain relations for volume and deviatoric changes. Relations for anisotropic viscoelastic moduli, compliances, creep and relaxation functions, and differential operators are derived. Possible means of experimental determination of the anisotropic creep and relaxation functions are also discussed.

I. INTRODUCTION

Various forms of elastic-viscoelastic analogies for linear, isotropic, homogeneous or nonhomogeneous viscoelasticity have been discussed by Alfrey (1944, 1948) * Hilton et al (1953, 1961), Lee (1955, 1960) and Read (1950), to mention only a few. Detailed descriptions of these analogies have been given by Bland (1960), Lee (1955, 1960) and Hilton et al (1953, 1961). In general, except for the original analogy due to Alfrey (1944, 1948), which is restricted to only certain classes of boundary value problems, these correspondence principles are formulated in terms of either Fourier or Laplace transforms of the stresses and strains.

Anisotropic viscoelasticity, on the other hand has received little attention. Biot (1954) has derived linear anisotropic viscoelastic stress-strain equations in operator form, but such classical problems as those of anisotropic viscoelastic plates and shells appear not to have been treated in the literature.

Some of the fundamental aspects of anisotropic viscoelastic stress-strain relations for volumetric and deviatoric deformations are discussed in the present paper. These relations are first developed for orthotropic viscoelastic media and then extended to general anisotropic viscoelasticity. An analogy between anisotropic viscoelasticity and elasticity is formulated. Finally, some procedures for the experimental determination of anisotropic viscoelastic properties are also discussed.

II. ORTHOTROPIC LINEAR ELASTICITY

For the sake of simplicity it is advantageous to first discuss orthotropic viscoelasticity and then extend the results to the more general anisotropic case. Furthermore, since the aim of this paper is the formula-

* - References are listed by authors and presented in detail in the last section.

tion of an anisotropic elastic-viscoelastic analogy, it is of interest to first briefly examine the relations of orthotropic elasticity in a form which is convenient for subsequent viscoelastic interpretations.

Consider a Cartesian coordinate system $x = (x_k)$, $k = 1, 2, 3$, and an elastic solid of arbitrary shape with linear orthotropic elastic properties. The generalized Hooke's law for such an orthotropic system is (Sokolnikoff 1956):

$$
\begin{Bmatrix} \sigma_{11}^e \\ \sigma_{22}^e \\ \sigma_{33}^e \\ \sigma_{12}^e \\ \sigma_{13}^e \\ \sigma_{23}^e \end{Bmatrix} = \begin{bmatrix} C_{1111} & C_{2211} & C_{3311} & 0 & 0 & 0 \\ C_{1122} & C_{2222} & C_{3322} & 0 & 0 & 0 \\ C_{1133} & C_{2233} & C_{3333} & 0 & 0 & 0 \\ 0 & 0 & 0 & C_{1212} & 0 & 0 \\ 0 & 0 & 0 & 0 & C_{1313} & 0 \\ 0 & 0 & 0 & 0 & 0 & C_{2323} \end{bmatrix} \begin{Bmatrix} \epsilon_{11}^e \\ \epsilon_{22}^e \\ \epsilon_{33}^e \\ \epsilon_{12}^e \\ \epsilon_{13}^e \\ \epsilon_{23}^e \end{Bmatrix} \quad (2.1)
$$

and it can be inverted to read:

$$
\begin{Bmatrix} \epsilon_{11}^e \\ \epsilon_{22}^e \\ \epsilon_{33}^e \\ \epsilon_{12}^e \\ \epsilon_{13}^e \\ \epsilon_{23}^e \end{Bmatrix} = \begin{bmatrix} B_{1111} & B_{2211} & B_{3311} & 0 & 0 & 0 \\ B_{1122} & B_{2222} & B_{3322} & 0 & 0 & 0 \\ B_{1133} & B_{2233} & B_{3333} & 0 & 0 & 0 \\ 0 & 0 & 0 & B_{1212} & 0 & 0 \\ 0 & 0 & 0 & 0 & B_{1313} & 0 \\ 0 & 0 & 0 & 0 & 0 & B_{2323} \end{bmatrix} \begin{Bmatrix} \sigma_{11}^e \\ \sigma_{22}^e \\ \sigma_{33}^e \\ \sigma_{12}^e \\ \sigma_{13}^e \\ \sigma_{23}^e \end{Bmatrix} \quad (2.2)
$$

where the C matrix is the inverse of the B matrix and the superscript e denotes elastic quantities. In the unsymmetric case, there are 12 distinct constants, while in the symmetric case their number is reduced to nine. Equations (2.1) and (2.2) apply to either homogeneous or nonhomogeneous orthotropic elastic bodies.

In isotropic media it is convenient to discuss changes in volume and changes in shape separately, since each may involve a different stress-strain law. For small strains, volumetric changes in _isotropic_ media can be described in terms of relations between the mean stress σ and the mean strain ϵ where:

$$
\sigma = \frac{\sigma_{kk}}{3} \quad (2.3)
$$

$$
\epsilon = \frac{\epsilon_{kk}}{3} \quad (2.4)
$$

and where the repeated subscript indicates summation, but superscripts do not imply summation. The mean strain is a geometric property and remains the measure of strain components contributing to volume changes in <u>orthotropic</u> media as well. However, the mean stress is no longer a representation of the stress components contributing to the change in volume.

Consider an elastic orthotropic parallelepiped under hydrostatic compression. Since the mechanical properties in any three perpendicular directions are unequal, a pure change in volume cannot be produced by hydrostatic compression (or tension), but only if the stress components are:

$$\sigma_{11}^e = a_1 \sigma^{e*}$$ (2.5)

$$\sigma_{22}^e = a_2 \sigma^{e*}$$ (2.6)

$$\sigma_{33}^e = a_3 \sigma^{e*}$$ (2.7)

where:

$$3\sigma^{e*} = \frac{\sigma_{11}^e}{a_1} + \frac{\sigma_{22}^e}{a_2} + \frac{\sigma_{33}^e}{a_3}$$ (2.8)

and where the a_α are three distinct constants which are functions of the material property constants $C_{mnk\ell}$. In other words, under a hydrostatic compression p, only the stress components $a_1 p$, $a_2 p$ and $a_3 p$ contribute to a change in volume, while the remainder $(1 - a_1)p$, $(1 - a_2)p$, $(1 - a_3)p$ are the stress components causing changes in shape. The addition of the first three equations of (2.1) leads to:

$$3\sigma^e = K_1' \epsilon_{11}^e + K_2' \epsilon_{22}^e + K_3' \epsilon_{33}^e$$ (2.9)

where:

$$K_1' = C_{1111} + C_{1122} + C_{1133}$$ (2.10)

etc.

Similarly, from Equation (2.2) one can obtain by addition:

$$3\epsilon^e = \frac{\sigma_{11}^e}{K_1} + \frac{\sigma_{22}^e}{K_2} + \frac{\sigma_{33}^e}{K_3}$$ (2.11)

where:

$$\frac{1}{K_1} = B_{1111} + B_{1122} + B_{1133}$$ (2.12)

etc. It is seen that Equation (2.9) does not represent a stress-strain relation for changes in volume, while Equation (2.11) does. However, in an isotropic elastic medium, where $K_\alpha = K_\alpha' = K$ the bulk modulus, both Equations (2.9) and (2.11) reduce to the same usual volumetric relation.

The elastic orthotropic stress-strain relations for changes in shape may now be written as:

$$\sigma_{11}^e - a_1 \sigma^{e*} = 2G_1(\epsilon_{11}^e - \epsilon^e)$$ (2.13)

$$\sigma_{22}^e - a_2 \sigma^{e*} = 2G_2(\epsilon_{22}^e - \epsilon^e)$$ (2.14)

$$\sigma_{33}^{e} - a_3\sigma^{e*} = 2G_3(\epsilon_{33}^{e} - \epsilon^{e}) \tag{2.15}$$

$$\sigma_{12}^{e} = 2G_4\epsilon_{12}^{e} \tag{2.16}$$

$$\sigma_{13}^{e} = 2G_5\epsilon_{13}^{e} \tag{2.17}$$

$$\sigma_{23}^{e} = 2G_6\epsilon_{23}^{e} \tag{2.18}$$

and with ϵ^{e} given by Equation (2.11). The original 12 C_{mnkl} or B_{mnkl} constants have now been replaced by six G_β, three a_α and three K_α constants. In the isotropic case, these reduce to the usual two material properties, since then $G_\beta = G$ and $a_\alpha = 1$.

Substitution of Equation (2.11) into Equations (2.13) to (2.15) immediately leads to the system (2.2) with:

$$B_{1111} = \frac{1}{3G_1}\left(1 + \frac{G_1}{K_1}\right) \tag{2.19}$$

$$B_{2211} = \frac{1}{6G_1}\left(\frac{2G_1}{K_2} - \frac{a_1}{a_2}\right) \tag{2.20}$$

$$B_{1212} = \frac{1}{2G_4} \tag{2.21}$$

etc. Similarly, Equations (2.13) to (2.18) can be rearranged to obtain the system (2.1). The constants are related by expressions of the type:

$$C_{1111} = \frac{1}{D}\left[\frac{1}{9}\left(\frac{1}{G_2} + \frac{1}{K_2}\right)\left(\frac{1}{G_3} + \frac{1}{K_3}\right) - \frac{1}{36}\left(\frac{2}{K_3} - \frac{a_2}{a_3 G_2}\right)\left(\frac{2}{K_2} - \frac{a_3}{a_2 G_3}\right)\right] \tag{2.22}$$

$$C_{1212} = 2G_4 \tag{2.23}$$

etc., and where:

$$D = \begin{vmatrix} \frac{1}{3}\left(\frac{1}{K_1} + \frac{1}{G_1}\right) & \frac{1}{6}\left(\frac{2}{K_2} - \frac{a_1}{a_2 G_1}\right) & \frac{1}{6}\left(\frac{2}{K_3} - \frac{a_1}{a_3 G_1}\right) \\ \frac{1}{6}\left(\frac{2}{K_1} - \frac{a_2}{a_1 G_2}\right) & \frac{1}{3}\left(\frac{1}{K_2} + \frac{1}{G_2}\right) & \frac{1}{6}\left(\frac{2}{K_3} - \frac{a_2}{a_3 G_2}\right) \\ \frac{1}{6}\left(\frac{2}{K_1} - \frac{a_3}{a_1 G_3}\right) & \frac{1}{6}\left(\frac{2}{K_2} - \frac{a_3}{a_2 G_3}\right) & \frac{1}{3}\left(\frac{1}{K_3} + \frac{1}{G_3}\right) \end{vmatrix} \tag{2.24}$$

It is readily seen that for orthotropic elasticity the decomposition of deformations into deviatoric and volumetric ones leads to complex relations between material property constants. Furthermore, due to the fact that hydrostatic tension or compression no longer induces pure volumetric

deformations, the experimental determination of the three bulk moduli K_α, Equation (2.11), necessitates cumbersome experimentation, since the material must now be loaded in three orthogonal directions by unequal normal stresses.

III. ORTHOTROPIC LINEAR VISCOELASTICITY

The stress-strain relations given in Equations (2.11) and (2.13) to (2.18) for orthotropic elasticity can be constructed from equivalent mechanical models consisting of massless linear springs (one set for volumetric deformations and one set for deviatoric ones), and where each spring has a different spring constant. Similarly, viscoelastic mechanical models can be constructed from combinations of springs and dashpots. Anisotropic viscoelastic properties can be obtained in three ways:

(1) By varying values of spring constants and coefficients of viscosity (and hence material properties) in the various directions, but maintaining equal combinations of models in all directions.

(2) By varying types of models in different directions, but maintaining the same equivalent material properties constants in all directions.

(3) By combinations of (1) and (2).

The first approach yields differential time operators which are the same for all deviatoric stress-strain relations, but where the coefficients of these operators will have distinct values in different directions. (Another set of differential time operators may be used for the volumetric relations.) The second approach, which might be called an anisotropy in time, has all or some of the differential operators different, but corresponding coefficients in the various operators are equal in all directions. For instance, a three-element model might be used in the x_1 direction, while a five-element model is used in the x_2 direction and both models have equal initial conditions and corresponding relaxation time. Finally, the third representation combines the two above and gives the most general form of viscoelastic anisotropy.

The general orthotropic linear viscoelastic stress-strain relations can, therefore, be written in the form:

$$3Q'(\epsilon) = P_1'(\sigma_{11}) + P_2'(\sigma_{22}) + P_3'(\sigma_{33}) \tag{3.1}$$

$$P_1(\sigma_{11} - R_1[\sigma^*]) = 2Q_1(\epsilon_{11} - \epsilon) \tag{3.2}$$

$$P_2(\sigma_{22} - R_2[\sigma^*]) = 2Q_2(\epsilon_{22} - \epsilon) \tag{3.3}$$

$$P_3(\sigma_{33} - R_3[\sigma^*]) = 2Q_3(\epsilon_{33} - \epsilon) \tag{3.4}$$

$$P_4(\sigma_{12}) = 2Q_4(\epsilon_{12}) \tag{3.5}$$

$$P_5 \{\sigma_{13}\} = 2 Q_5 \{\epsilon_{13}\} \tag{3.6}$$

$$P_6 \{\sigma_{23}\} = 2 Q_6 \{\epsilon_{23}\} \tag{3.7}$$

where:

$$Q' = \sum_{j=0}^{q'} b'_j \frac{\partial^j}{\partial t^j} \qquad\qquad P'_\alpha = \sum_{j=0}^{p'_\alpha} a'_{j\alpha} \frac{\partial^j}{\partial t^j} \tag{3.8}$$

$$Q_\beta = \sum_{j=0}^{q_\beta} b_{j\beta} \frac{\partial^j}{\partial t^j} \qquad\qquad P_\beta = \sum_{j=0}^{p_\beta} a_{j\beta} \frac{\partial^j}{\partial t^j} \tag{3.9}$$

$$R_\alpha = \sum_{j=0}^{r_\alpha} c_{j\alpha} \frac{\partial^j}{\partial t^j} \tag{3.10}$$

where $\alpha =$ 1, 2, 3 and $\beta =$ 1, 2, 3, 4, 5, 6. The stress σ^* is now defined as:

$$3\sigma^* = R_1^{-1}\{\sigma_{11}\} + R_2^{-1}\{\sigma_{22}\} + R_3^{-1}\{\sigma_{33}\} \tag{3.11}$$

where R_α^{-1} indicates the inverse of the differential operator R_α. From Equations (3.1) to (3.7), it is seen that a maximum of 19 distinct ope. tors are needed to fully specify the volumetric and deviatoric behavior of orthotropic viscoelastic solids, as contrasted with only four operators necessary for isotropic viscoelasticity.

These differential stress-strain relations can be reduced to algebraic equations in the usual manner by introducing the Fourier transform technique, which has been previously applied in isotropic viscoelasticity (Read 1950, Hilton et al 1953, 1961). Let double bars denote Fourier transforms, such that:

$$\bar{\bar{\sigma}}_{k\ell}(x,\omega) = \frac{1}{2\pi} \int_{-\infty}^{\infty} \sigma_{k\ell}(x, t) e^{-i\omega t} dt \tag{3.12}$$

is the Fourier transform of $\sigma_{k\ell}(x, t)$. The conditions for the existence of the transforms are given by Sneddon (1951) and are generally met in viscoelastic problems.

Similarly, the transforms of the differential operators can be defined as:

$$\bar{\bar{P}}_\beta = \sum_{j=0}^{p_\beta} (i\omega)^j a_{j\beta}(x) \tag{3.13}$$

etc., provided the coefficients $a_{j\beta}$, $b_{j\beta}$, etc., are not functions of time. If these coefficients are functions of time, then they can be approximated piecewise by step functions in time as outlined by Hilton et al (1953, 1961). It is to be noted that the approach used by Morland and Lee (1960) of representing time variations of viscoelastic material

properties by thermorheologically simple models is restricted when applied to anisotropic media, since their analysis is predicated on the use of a single time shift parameter. In anisotropic viscoelastic media one would expect to find different time shift parameters for each of the directions and stresses in accordance with the multiplicity of differential operators indicated in Equations (3.1) to (3.7).

Application of the Fourier transform to Equations (3.1) to (3.7) now leads to:

$$3\bar{\bar{\epsilon}} = \frac{\bar{\bar{\sigma}}_{11}}{\bar{\bar{K}}_1} + \frac{\bar{\bar{\sigma}}_{22}}{\bar{\bar{K}}_2} + \frac{\bar{\bar{\sigma}}_{33}}{\bar{\bar{K}}_3} \qquad (3.14)$$

$$\bar{\bar{\sigma}}_{11} - \bar{\bar{R}}_1 \bar{\bar{\sigma}}^* = 2\bar{\bar{G}}_1 (\bar{\bar{\epsilon}}_{11} - \bar{\bar{\epsilon}}) \qquad (3.15)$$

$$\bar{\bar{\sigma}}_{12} = 2\bar{\bar{G}}_4 \bar{\bar{\epsilon}}_{12} \qquad (3.16)$$

etc., where:

$$\bar{\bar{K}}_\alpha = \bar{\bar{K}}_\alpha(x,\omega) = \frac{\bar{\bar{Q}}'}{\bar{\bar{P}}'_\alpha} \qquad (3.17)$$

$$\bar{\bar{G}}_\beta = \bar{\bar{G}}_\beta(x,\omega) = \frac{\bar{\bar{Q}}_\beta}{\bar{\bar{P}}_\beta} \qquad \text{(no summation)} \qquad (3.18)$$

$$\bar{\bar{\sigma}}^* = \bar{\bar{R}}_1^{-1}\bar{\bar{\sigma}}_{11} + \bar{\bar{R}}_2^{-1}\bar{\bar{\sigma}}_{22} + \bar{\bar{R}}_3^{-1}\bar{\bar{\sigma}}_{33} \qquad (3.19)$$

Equations (3.15) to (3.16) defining the Fourier transforms of orthotropic viscoelastic stresses and strains, are analogous to orthotropic elastic stress-strain relations of Equations (2.11) and (2.13) to (2.18), provided that the elastic moduli K_α, a_α and G_β are replaced by their equivalent complex moduli $\bar{\bar{K}}_\alpha$, $\bar{\bar{R}}_\alpha$ and $\bar{\bar{G}}_\beta$. Consequently, the analogy between orthotropic elasticity and orthotropic viscoelasticity consists of replacing in the elastic solution the elastic moduli by the complex moduli and inverting these equivalent elastic stresses and strains to obtain equivalent viscoelastic quantities. The boundary conditions of the equivalent elastic problem are the Fourier transforms of the viscoelastic boundary conditions. Therefore, if $\sigma^e_{kl}(x, w)$ is the equivalent elastic solution with proper complex moduli, then:

$$\sigma_{kl}(x, t) = \int_{-\infty}^{\infty} \sigma_{kl}(x\ \bar{\bar{K}}_\alpha\ \bar{\bar{R}}_\alpha\ \bar{\bar{G}}_\beta) e^{i\omega t}\ d\omega \qquad (3.20)$$

are the corresponding viscoelastic stresses. Similar expressions can also be written for the strains. Since the orthotropic elastic stresses and strains form the initial conditions of the corresponding viscoelastic problem, they must be known in any case.

For material properties which are time dependent, the piecewise analogy requires that equations of the type (3.20) be written for each time interval. The details of this procedure have been given by Hilton et al (1953, 1961) for isotropic nonhomogeneous viscoelasticity and may be readily

extended to anisotropic viscoelasticity by the proper definition of the complex moduli in Equation (3.20).

It has been seen in the orthotropic elastic formulation that stress-strain relations such as those of Equations (3.1) to (3.7) or (3.14) to (3.16) are awkward and a form of the type (2.1) or (2.2) is preferable. The latter set of relations can be obtained by algebraic manipulation of Equations (3.14) to (3.15), since Equation (3.16) is already in the desired form. The stress-strain relations in terms of Fourier transforms of the viscoelastic stresses and strains then are:

$$\bar{\bar{\sigma}}_{11} = \bar{\bar{C}}_{1111}\bar{\bar{\epsilon}}_{11} + \bar{\bar{C}}_{2211}\bar{\bar{\epsilon}}_{22} + \bar{\bar{C}}_{3311}\bar{\bar{\epsilon}}_{33} \qquad (3.21)$$

or:

$$\bar{\bar{\epsilon}}_{11} = \bar{\bar{B}}_{1111}\bar{\bar{\sigma}}_{11} + \bar{\bar{B}}_{2211}\bar{\bar{\sigma}}_{22} + \bar{\bar{B}}_{3311}\bar{\bar{\sigma}}_{33} \qquad (3.22)$$

etc., where $\bar{\bar{C}}_{mnkl} = \bar{\bar{C}}_{mnkl}(x, w)$ and $\bar{\bar{B}}_{mnkl} = \bar{\bar{B}}_{mnkl}(x, w)$. The relations between the C's and B's and the previously defined complex moduli are identical to those derived for orthotropic elasticity, Equations (2.19) to (2.23), except that double bars are placed over the appropriate quantities.

Time dependent stress-strain relations may also be written by applying the convolution theorem to Equations (3.21) and (3.22). These now result in the following integral stress-strain relations:

$$\sigma_{11}(x,t) = \int_{-\infty}^{\infty} \phi_{1111}(x,t'-t)\left[\frac{\partial}{\partial t'}\epsilon_{11}(x,t')\right]dt'$$

$$+ \int_{-\infty}^{\infty} \phi_{2211}(x,t'-t)\left[\frac{\partial}{\partial t'}\epsilon_2(x,t')\right]dt'$$

$$+ \int_{-\infty}^{\infty} \phi_{3311}(x,t'-t)\left[\frac{\partial}{\partial t'}\epsilon_{33}(x,t')\right]dt' \qquad (3.23)$$

etc., or:

$$\epsilon_{11}(x,t) = \int_{-\infty}^{\infty} \psi_{1111}(x,t'-t)\left[\frac{\partial}{\partial t'}\sigma_{11}(x,t')\right]dt'$$

$$+ \int_{-\infty}^{\infty} \psi_{2211}(x,t'-t)\left[\frac{\partial}{\partial t'}\sigma_{22}(x,t')\right]dt'$$

$$+ \int_{-\infty}^{\infty} \psi_{3311}(x, t'-t) \left[\frac{\partial}{\partial t'} \sigma_{33}(x, t')\right] dt' \qquad (3.24)$$

$$\epsilon_{12}(x, t) = \int_{-\infty}^{\infty} \psi_{1212}(x, t'-t) \left[\frac{\partial}{\partial t'} \sigma_{12}(x, t')\right] dt' \qquad (3.25)$$

etc., where ϕ_{mnkl} and ψ_{mnkl} are the orthotropic relaxation and creep functions (12 for the general case, or nine of each for symmetric cases), and are the inverse Fourier transforms of $C_{mnkl}/i\omega$ and $B_{mnkl}/i\omega$, respectively.

IV. ANISOTROPIC VISCOELASTICITY

In general linear anisotropic elasticity, the stress-strain relations (2.1) and (2.2) still hold, except that the C_{mnkl} and B_{mnkl} coefficients are now all nonzero and 36 in number (Sokolnikoff 1956). Under these general anisotropic conditions it is no longer useful to seek stress-strain relations for volumetric and deviatoric displacements. Consequently, one can pass directly to a discussion of anisotropic viscoelastic media. From the previous considerations of orthotropic media, one sees that the Fourier transform stress-strain relations can be written in tensor form as:

$$\bar{\bar{\sigma}}_{kl}(x, \omega) = \bar{C}_{mnkl}(x, \omega) \bar{\bar{\epsilon}}_{mn}(x, \omega) \qquad (4.1)$$

and:

$$\bar{\bar{\epsilon}}_{kl}(x, \omega) = \bar{B}_{mnkl}(x, \omega) \bar{\bar{\sigma}}_{mn}(x, \omega) \qquad (4.2)$$

which compare directly with the elastic relations of Equations (2.1) and (2.2) with no zero terms in the C and B matrices. Consequently, the analogy between the Fourier transforms of the anisotropic viscoelastic stresses and strains and the corresponding anisotropic elastic ones for complex moduli C_{mnkl} holds in the same manner as for the previously discussed orthotropic media.

For nonhomogeneous media, where the material properties are time as well as space dependent, Equations (4.1) and (4.2) also apply except that it is implied that the transforms are taken piecewise in various time intervals. The use of this approximate technique was discussed in Section 3.

Similarly, the inversion of Equations (4.1) and (4.2) leads to anisotropic integral stress-strain relations:

$$\sigma_{kl}(x, t) = \int_{-\infty}^{\infty} \phi_{mnkl}(x, t'-t) \left[\frac{\partial}{\partial t'} \epsilon_{mn}(x, t')\right] dt' \qquad (4.3)$$

$$\epsilon_{kl}(x,t) = \int_{-\infty}^{\infty} \psi_{mnkl}(x,t'-t)\left[\frac{\partial}{\partial t'}\sigma_{mn}(x,t')\right]dt' \tag{4.4}$$

where:

$$\phi_{mnkl}(x,t) = \int_{-\infty}^{\infty} (i\omega)^{-1}\overline{\overline{C}}_{mnkl}(x,\omega)e^{i\omega t}\,d\omega \tag{4.5}$$

$$\psi_{mnkl}(x,t) = \int_{-\infty}^{\infty} (i\omega)^{-1}\overline{\overline{B}}_{mnkl}(x,\omega)e^{i\omega t}\,d\omega \tag{4.6}$$

The ϕ and ψ are the anisotropic relaxation and creep functions. There are at most 36 of each while in the symmetric case they reduce to 21. It is also possible to define anisotropic viscoelastic stress-strain relations in terms of six P and 36 Q differential operators. These operators can be evaluated from Equation (4.3) by using the inverse properties of the Fourier transforms. The complex moduli will be polynomials in w of the type:

$$\overline{\overline{C}}_{mnkl} = \frac{\sum_{j=0}^{N^{mnkl}} d_j^{mnkl}(i\omega)^j}{\sum_{j=0}^{M^{mnkl}} f_j^{mnkl}(i\omega)^j} \tag{4.7}$$

and for each combination of k and l they can be reduced to a common denominator, so that Equation (4.1) may be written as:

$$\overline{\overline{\sigma}}_{kl} = \overline{\overline{Q}}_{mnkl}\frac{\overline{\overline{\epsilon}}_{mn}}{\overline{\overline{P}}_{kl}} \tag{4.8}$$

where the $\overline{\overline{Q}}$ and $\overline{\overline{P}}$ are polynomials in w. The inversion of Equation (4.8) then yields the differential equation of the anisotropic stress-strain relations and is in the form:

$$P^{kl}\{\sigma_{kl}\} = Q_{mnkl}\{\epsilon_{mn}\} \tag{4.9}$$

It would appear, however, that in this instance the integral representation of the stress-strain relations is less complicated.

In anisotropic viscoelastic media where dynamic loads are applied and where inertia terms are of importance, it can be readily shown that a similar analogy exists between the Fourier transforms of the viscoelastic stresses and strains and the Fourier transforms of elastic stresses and strains based on anisotropic viscoelastic complex moduli. This analogy is

essentially an extension and combination of the dynamic, isotropic visco-
elastic analogy of Bland (1960), the nonhomogeneous isotropic analogy of
Hilton et al (1953, 1961) and the present nonhomogeneous anisotropic analogy.

V.   EXPERIMENTAL DETERMINATION OF ANISOTROPIC CREEP AND RELAXATION FUNCTIONS

Since hydrostatic tension and compression of anisotropic materials
do not result in pure volumetric deformations, tests based on these types of
loading are no longer too useful in the determination of anisotropic material
properties. Instead, it is preferable to conduct static and dynamic experi-
ments to compute the complex moduli $\bar{C}_{mnkl}$ and compliances $\bar{B}_{mnkl}$ as functions
of frequency and temperature, and then use the Fourier inversions of Equations
(4.5) and (4.6) to obtain creep and relaxation functions ψ_{mnkl} and ϕ_{mnkl} .

The procedure for the determination of complex moduli and compliances
is as follows:

(1) Load anisotropic viscoelastic specimens with a simple harmonic
uniaxial stress $\sigma_{11} = \sigma_{11}^0 \, e^{i\omega t}$ (where σ_{11}^0 is a constant).

(2) Measure the strains at each frequency and temperature combina-
tion, $\epsilon_{mn} = \epsilon_{mn}^{011} \, e^{i\omega t}$.

(3) Repeat steps (1) and (2) for simple harmonic uniaxial stresses
σ_{22} and σ_{33} and single shear stress loadings.

(4) In a linear system, the strains will be simple harmonic for
simple harmonic loading. Therefore, Equations (4.1) become:

$$\text{for} \;\; \sigma_{11} = \sigma_{11}^0 e^{i\omega t}$$

$$\sigma_{11}^0 = \bar{C}_{mn11}(x,\omega) \epsilon_{mn}^{011} \tag{5.1}$$

$$0 = \bar{C}_{mnkl}(x,\omega)\epsilon_{mn}^{011}, \;\; k \neq l \neq 1 \tag{5.2}$$

$$\text{for} \;\; \sigma_{22} = \sigma_{22}^0 e^{i\omega t}$$

$$\sigma_{22}^0 = \bar{C}_{mn22}(x,\omega) \epsilon_{mn}^{022} \tag{5.3}$$

$$0 = \bar{C}_{mnkl}(x,\omega)\epsilon_{mn}^{022}, \;\; k \neq l \neq 2 \tag{5.4}$$

etc. Consequently, for each stress, six equations of the type (5.1) and (5.2)
have been formulated. For the six individual simple harmonic stresses a total
of 36 equations are obtained from which the 36 $\bar{C}_{mnkl}$ can be calculated for
each frequency and temperature combination.

(5) The same procedure as outlined in step (4) can be applied to Equations (4.2) to obtain the 36 compliances $\bar{B}_{mnk\ell}$. The same test data as above can be used here.

(6) The creep and relaxation functions can then be calculated from Equations (4.5) and (4.6).

(7) Static creep and relaxation data can also be used to obtain "static" values of creep and relaxation functions by using Equations (4.3) and (4.4) directly for the application of constant uniaxial stresses and strains.

If the material is linearly viscoelastic, then the $\bar{C}_{mnk\ell}$ and $\bar{B}_{mnk\ell}$ values will be independent of stress levels. If the material is not linear, then it may be approximated by a series of linear viscoelastic relations, each valid for a given stress or strain range.

REFERENCES

Alfrey, T.	1944	Quart. Appl. Math. 2, 113.
	1948	Mechanical Behavior of High Polymers, pp. 557 - 564 (Interscience, New York)
Biot, M. A.	1954	J. Appl. Physics, 25, 1385
Bland, D. R.	1960	The Theory of Linear Viscoelasticity, pp. 76 - 112 (Pergamon Press, New York)
Hilton, H. H. and Hassan, H. A. Russell, H. G.	1953	Wright Air Development Center Tech. Rep. 53-322
Hilton, H. H. and Russell, H. G.	1961	J. Mech. and Physics of Solids, 9, 152
Lee, E. H.	1955	Quart. Appl. Math., 13, 183.
	1960	Proc. 1st Symp. Naval Structural, p. 456.
Morland, L. W. and Lee, E. H.	1960	Trans. Soc. Rheol., 4, 223.
Read, W. T.	1950	J. Appl. Phys., 21, 671.
Sneddon, I. N.	1951	Fourier Transforms, p. 19 (McGraw-Hill, New York)
Sokolnikoff, I. S.	1956	Mathematical Theory of Elasticity, pp. 58 - 64 (McGraw-Hill, New York)

GENERAL SOLUTION OF CERTAIN INTEGRO-DIFFERENTIAL EQUATIONS OF LINEAR VISCOELASTICITY

Alexander S. Elder
Ballistic Research Laboratories

ABSTRACT

A stress function theory for linearly viscoelastic solids is developed in this paper. If body forces and inertial terms are neglected, the stresses may be expressed in terms of Maxwell stress functions, which in turn are given in terms of harmonic or biharmonic functions. The displacements are expressed directly in terms of harmonic functions through an extension of the Neuber-Papkovitch theory. Axially symmetric stresses and strains are given in terms of a single biharmonic function. The analysis does not involve boundary conditions and is valid for problems involving moving loads and moving boundaries. The theory may be used to formulate stress analysis problems in terms of Volterra integral equations using creep or relaxation functions as the kernel. The integral equations governing the stresses in a viscoelastic propellant grain subjected to the combined effects of internal pressure and erosion are derived.

INTRODUCTION

Solutions of static problems in elasticity have frequently been used in solving quasi-static problems in linear viscoelasticity. Alfrey combined separation of variables with superposition to solve problems in which the stresses were statically determinate (1). E. H. Lee removed the time dependence by using the Laplace transform on both the basic equations and the boundary conditions (2). The resulting equations for the transformed stresses and strains may frequently be solved by the methods of classical elasticity, provided the form of the body does not vary with time. J. R. M. Radok extended this method to certain problems in which the Laplace transform of the boundary conditions could not be obtained in explicit form (3). In all these problems rational functions representing the transformed stress-strain relations of the viscoelastic material were substituted for the elastic constants occurring in the associated elastic problem.

The early work of V. Volterra offers a more fundamental approach to problems of linear viscoelasticity (4). The mechanical properties are represented by creep functions or relaxation functions (5), which are obtained experimentally as the response to step functions of force or displacement. These functions are used as kernels in integrals of the hereditary type. V. Volterra formulated the integro-differential equations for the displacements of an anisotropic viscoelastic solid, using hereditary integrals in place of the elastic constants which occur in the classical theory of elasticity. The corresponding equations for an isotropic body may be formulated in terms of two time-dependent moduli, corresponding to the shear modulus and bulk modulus in elastic theory. In this paper, these integro-differential equations are solved in terms of arbitrary harmonic

functions. These solutions are obtained without reference to the boundary conditions, and are valid even when the boundary is being eroded (6).

BASIC EQUATIONS

If body forces and inertial forces are neglected, Navier's equations of equilibrium reduce to (7)

$$\frac{\partial \sigma_x}{\partial x} = \frac{\partial \tau_{xy}}{\partial y} + \frac{\partial \tau_{xz}}{\partial z} = 0$$

$$\frac{\partial \sigma_y}{\partial y} + \frac{\partial \tau_{xy}}{\partial x} + \frac{\partial \tau_{yz}}{\partial z} = 0 \qquad (1)$$

$$\frac{\partial \sigma_z}{\partial z} + \frac{\partial \tau_{xz}}{\partial x} + \frac{\partial \tau_{yz}}{\partial y} = 0$$

If the strains are sufficiently small, they may be obtained from the displacements by the formulas

$$\epsilon_x = \frac{\partial u}{\partial x} \qquad\qquad \gamma_{xy} = \frac{\partial u}{\partial y} + \frac{\partial v}{\partial x}$$

$$\epsilon_y = \frac{\partial v}{\partial y} \qquad\qquad \gamma_{xz} = \frac{\partial u}{\partial z} + \frac{\partial w}{\partial x} \qquad (2)$$

$$\epsilon_z = \frac{\partial w}{\partial z} \qquad\qquad \gamma_{yz} = \frac{\partial v}{\partial z} + \frac{\partial w}{\partial y}$$

Two stress-strain laws are required to express the mechanical behavior of an isotropic viscoelastic material. Let $G(t)$ be the response to a unit step function of shearing strain; then the response to an arbitrary strain is found from Boltzmann's superposition principle (8)

$$\tau_{xy} = \int_{-\infty}^{t} \frac{d\gamma_{xy}(t_1)}{dt_1} G(t - t_1) dt_1 .$$

The shear modulus also governs the relation between the stress differences and the strain differences.

$$\sigma_x - \sigma_y = 2 \int_{-\infty}^{t} \frac{d\left\{\epsilon_x(t_1) - \epsilon_y(t_1)\right\}}{dt_1} G(t - t_1) dt_1 .$$

Similarly, a time dependent bulk modulus is used to represent the behavior of a material when subjected to hydrostatic pressure.

$$\sigma_x + \sigma_y + \sigma_z = 3 \int_{-\infty}^{t} \frac{d\left\{\epsilon_x(t_1) + \epsilon_y(t_1) + \epsilon_z(t_1)\right\}}{dt_1} K(t - t_1) dt_1$$

If the stresses and strains are zero prior to $t = 0$, the stress-strain laws may be represented by Duhamel integrals (9).

$$\tau(t) = \gamma(t)\, G(0) + \int_0^t \gamma(t_1)\, G'(t - t_1)\, dt_1 \qquad (3)$$

The term $\gamma(t)\, G(0)$ represents the purely elastic response, while the hereditary integral represents the delayed response. A functional notation of Volterra will be used to abbreviate the right-hand side of Equation (3).

$$G\left[\gamma(t)\right] = \gamma(t)\, G(0) + \int_0^t \gamma(t_1)\, G'(t - t_1)\, dt_1 \qquad (4)$$

The stress-strain laws now take the form

$$\tau_{xy} = G\left[\gamma_{xy}(t)\right] \qquad (5)$$

$$\sigma_x - \sigma_y = G\left[\epsilon_x(t_1)\right] - G\left[\epsilon_y(t_1)\right] \qquad (6)$$

$$\Theta = 3K\left[e(t_1)\right] \qquad (7)$$

where

$$\Theta = \sigma_x + \sigma_y + \sigma_z \text{ and } e = \epsilon_x + \epsilon_y + \epsilon_z . \qquad (8)$$

The equations of equilibrium may now be written in terms of the displacements

$$\left.
\begin{aligned}
(3K + G)\left[\frac{\partial e(t)}{\partial x}\right] + 3G\left[\nabla^2 u(t)\right] &= 0 \\
(3K + G)\left[\frac{\partial e(t)}{\partial y}\right] + 3G\left[\nabla^2 v(t)\right] &= 0 \\
(3K + G)\left[\frac{\partial e(t)}{\partial z}\right] + 3G\left[\nabla^2 w(t)\right] &= 0
\end{aligned}
\right\} \qquad (9)$$

where

$$\nabla^2 u(x,\, y,\, z;\, t) = \frac{\partial^2 u}{\partial x^2} + \frac{\partial^2 u}{\partial y^2} + \frac{\partial^2 u}{\partial z^2} .$$

It is clear that

$$G\left[\nabla^2 u(t)\right] = \nabla^2 G\left[u(t)\right]$$

since the limits of integration in Equation (4) are independent of the space variables.

The strains satisfy compatability relations of the type (7)

$$\frac{\partial^2 \epsilon_x}{\partial y^2} + \frac{\partial^2 \epsilon_y}{\partial x^2} = \frac{\partial^2 \gamma_{xy}}{\partial x \partial y}$$

and

$$2 \frac{\partial^2 \epsilon_x}{\partial x \partial z} = \frac{\partial}{\partial x} \left(- \frac{\partial \gamma_{yz}}{\partial x} + \frac{\partial \gamma_{xz}}{\partial y} + \frac{\partial \gamma_{xy}}{\partial z} \right)$$

Four additional relations are obtained by cyclic permutation of the variables. If the strains are expressed in terms of the stresses, analogs of the Beltrami-Mitchell compatability equations are obtained.

$$9K \left[\nabla^2 \sigma_x(t) \right] + (6K + 2G) \left[\frac{\partial^2 \Theta(t)}{\partial x^2} - \nabla^2 \Theta(t) \right] = 0$$

$$9K \left[\nabla^2 \sigma_y(t) \right] + (6K + 2G) \left[\frac{\partial^2 \Theta(t)}{\partial y^2} - \nabla^2 \Theta(t) \right] = 0 \quad (10)$$

$$9K \left[\nabla^2 \sigma_z(t) \right] + (6K + 2G) \left[\frac{\partial^2 \Theta(t)}{\partial z^2} - \nabla^2 \Theta(t) \right] = 0$$

$$9K \left[\nabla^2 \tau_{xy}(t) \right] + (6K + 2G) \left[\frac{\partial^2 \Theta(t)}{\partial y \partial z} \right] = 0$$

$$9K \left[\nabla^2 \tau_{yz}(t) \right] + (6K + 2G) \left[\frac{\partial^2 \Theta(t)}{\partial x \partial z} \right] = 0 \quad (11)$$

$$9K \left[\nabla^2 \tau_{zx}(t) \right] + (6K + 2G) \left[\frac{\partial^2 \Theta(t)}{\partial z \partial x} \right] = 0$$

It will now be shown that the stresses and strains are biharmonic functions in the space variables. On adding Equations (10), it is seen that

$$(3K + 4G) \left[\nabla^2 \Theta(t) \right] = 0 \quad (12)$$

where

$$\Theta = \sigma_x + \sigma_y + \sigma_z .$$

Equation (12) represents the homogeneous Volterra integral equation

$$\left[3K(0) + 4G(0)\right] \nabla^2 \Theta(t) + \int_0^t \nabla^2 \Theta(t_1) \left\{3K'(t - t_1) + 4G'(t - t_1)\right\} dt_1 = 0 .$$

(13)

The only continuous solution of this equation is zero (Page 14, Ref. 10). Therefore

$$\nabla^2 \Theta = 0 .$$

(14)

Now set $\nabla^2 \Theta = 0$ in Equations 10. Equations of the types

$$9\nabla^2 \left\{K \left[\nabla^2 \sigma_x(t)\right]\right\} + \nabla^2 \left\{(6K + 2G)\left[\frac{\partial^2 \Theta(t)}{\partial x^2}\right]\right\} = 0$$

and

$$9\nabla^2 \left\{K \left[\nabla^2 \tau_{xy}(t)\right]\right\} + \nabla^2 \left\{(6K + 2G)\left[\frac{\partial^2 \Theta}{\partial y \partial x}\right]\right\} = 0$$

are obtained by differentiation. It is seen on interchanging the order of integration and differentiation, and then setting $\nabla^2 \Theta = 0$, that

$$\nabla^4 \sigma_x = 0, \quad \nabla^4 \sigma_y = 0, \quad \nabla^4 \sigma_z = 0$$

(15)

and similarly

$$\nabla^4 \tau_{yz} = 0, \quad \nabla^4 \tau_{zx} = 0, \quad \nabla^4 \tau_{xy} = 0 .$$

(16)

The corresponding results for the displacements are obtained from Equation 9. Differentiate the first equation with respect to x, the second with respect to y, and the third with respect to z, and add the resulting equations. The resulting equation

$$(3K + 4G) \left[\nabla^2 e(t)\right] = 0$$

represents a homogeneous Volterra integral equation, so that

$$\nabla^2 e = 0$$

(17)

where

$$e = e_x + e_y + e_z = \frac{\partial u}{\partial x} + \frac{\partial v}{\partial y} + \frac{\partial w}{\partial z} .$$

We also have from Equation (9)

$$\nabla^2 \left\{ (3K + G) \left[\frac{\partial e(t)}{\partial x} \right] \right\} + 3\nabla^2 G \left[\nabla^2 u(t) \right] = 0$$

so that

$$\nabla^4 u = 0, \quad \nabla^4 v = 0, \quad \nabla^4 w = 0 . \tag{18}$$

We see that harmonic and biharmonic functions have the same fundamental role in linear viscoelasticity as in the classical theory of elasticity.

STRESS FUNCTION THEORY

Maxwell (11) has shown that the equations of equilibrium have the general solution

$$\sigma_x = \frac{\partial^2 B}{\partial z^2} + \frac{\partial^2 C}{\partial y^2}, \quad \sigma_y = \frac{\partial^2 C}{\partial x^2} + \frac{\partial^2 A}{\partial z^2}, \quad \sigma_z = \frac{\partial^2 A}{\partial y^2} + \frac{\partial^2 B}{\partial x^2} \tag{19}$$

$$\tau_{yz} = - \frac{\partial^2 A}{\partial x \partial y}, \quad \tau_{zx} = - \frac{\partial^2 B}{\partial z \partial x}, \quad \tau_{yz} = - \frac{\partial^2 C}{\partial x \partial y} \tag{20}$$

$$\Theta = \nabla^2 (A + B + C) - \left(\frac{\partial^2 A}{\partial x^2} + \frac{\partial^2 B}{\partial y^2} + \frac{\partial^2 C}{\partial z^2} \right) \tag{21}$$

where

$$\nabla^2 \Theta = 0 .$$

Equations (10) and (11) are satisfied if

$$9K \left[\nabla^2 A \right] - (6K + 2G) \left[\Theta \right] = 0$$
$$9K \left[\nabla^2 A \right] - (6K + 2G) \left[\Theta \right] = 0 \tag{22}$$
$$9K \left[\nabla^2 A \right] - (6K + 2G) \left[\Theta \right] = 0$$

Langhaar and Stippes (12) have shown that Maxwell's stress functions for an elastic solid may be expressed in terms of harmonic functions. Assume that

$$\nabla^2 \phi_i = 0, \quad i = 0, 1, 2, 3 \tag{23}$$

$$F = \phi_0 + x \frac{\partial \phi_1}{\partial x} + y \frac{\partial \phi_2}{\partial y} + z \frac{\partial \phi_3}{\partial z} \tag{24}$$

$$\nabla^2 F = 2 \left(\frac{\partial^2 \phi_1}{\partial x^2} + \frac{\partial^2 \phi_2}{\partial y^2} + \frac{\partial^2 \phi_3}{\partial z^2} \right) \tag{25}$$

Then these authors show that

$$A = \frac{F}{2(1 - v)} - (\phi_2 + \phi_3)$$

$$B = \frac{F}{2(1 - v)} - (\phi_3 + \phi_1)$$

$$C = \frac{F}{2(1 - v)} - (\phi_1 + \phi_2)$$

Now $\frac{1}{2(1 - v)} = \frac{3K + G}{3K + 4G}$ since $v = \frac{3K - 2G}{6K + 2G}$ in an elastic solid. These results indicate that

$$A = (3K + G)\left[F\right] - (3K + 4G)\left[\phi_2 + \phi_3\right]$$
$$B = (3K + G)\left[F\right] - (3K + 4G)\left[\phi_3 + \phi_1\right] \qquad (26)$$
$$C = (3K + G)\left[F\right] - (3K + 4G)\left[\phi_1 + \phi_2\right]$$

should be appropriate stress functions for a linearly viscoelastic solid. We have

$$\nabla^2 A = \nabla^2 B = \nabla^2 C = (3K + G)\left[\nabla^2 F\right] \qquad (27)$$

and

$$\frac{\partial^2 A}{\partial x^2} + \frac{\partial^2 B}{\partial y^2} + \frac{\partial^2 C}{\partial z^2} = (3K + G)\ \nabla^2 F + (3K + 4G)\left[\frac{\partial^2 \phi_1}{\partial x^2} + \frac{\partial^2 \phi_2}{\partial y^2} + \frac{\partial^2 \phi_3}{\partial z^2}\right]$$

or

$$\frac{\partial^2 A}{\partial x^2} + \frac{\partial^2 B}{\partial y^2} + \frac{\partial^2 C}{\partial z^2} = (4\tfrac{1}{2} K + 3G)\left[\nabla^2 F\right]. \qquad (28)$$

The hydrostatic tension may be found by combining Equations (21), (27), and (28).

$$2\Theta = 9K\left[\nabla^2 F\right]$$

so that

$$(6K + 2G)\left[\Theta\right] = 9(3K + G)\left[K\left[\nabla^2 F\right]\right].$$

But

$$\nabla^2 A = (3K + G)\left[\nabla^2 F\right] \qquad (27)$$

so that

$$9K\left[\nabla^2 A\right] = 9K\left[(3K + G)\left[\nabla^2 F\right]\right].$$

The order of integration may be interchanged, so that

$$K\left[(3K + G)\left[\nabla^2 F(t)\right]\right] = (3K + G)\left[K\left[\nabla^2 F(t)\right]\right]$$

and therefore

$$9K\left[\nabla^2 A\right] - (3K + 2G)\left[2\Theta\right] = 0$$

in agreement with Equation (22). Equations involving $\nabla^2 B$ and $\nabla^2 C$ may be treated in the same manner. All the conditions of the problem are met, and therefore the functions A, B, and C of Equation (26) represent a set of Maxwell stress functions for a linearly viscoelastic solid.

The displacements may be obtained by integration with respect to the space variables in the manner indicated by Langhaar and Stippes. Displacements arising from motion as a rigid body are not included in these formulas.

$$G\left[u\right] = \frac{\partial}{\partial x}(A - B - C)$$

$$G\left[v\right] = \frac{\partial}{\partial y}(B - C - A) \qquad (29)$$

$$G\left[w\right] = \frac{\partial}{\partial z}(C - A - B)$$

Papkovitch (13) and Neuber (14) have given an alternate method of epxressing the displacements of an elastic solid in terms of harmonic functions.

$$u = 4(1 - v)\,\phi_1 - \frac{\partial H}{\partial x}$$

$$v = 4(1 - v)\,\phi_2 - \frac{\partial H}{\partial y} \qquad (30)$$

$$w = 4(1 - v)\,\phi_3 - \frac{\partial H}{\partial z}$$

where

$$\nabla^2 \phi_i = 0, \quad i = 0, 1, 2, 3 \qquad (31)$$

and

$$H = \phi_0 + x\phi_1 + y\phi_2 + z\phi_3 \qquad (32)$$

$$\nabla^2 H = 2\left(\frac{\partial \phi_1}{\partial x} + \frac{\partial \phi_2}{\partial y} + \frac{\partial \phi_3}{\partial z}\right) \qquad (33)$$

The corresponding displacements for a linearly viscoelastic solid are

$$u = (6K + 8G)\left[\phi_1\right] - (3K + G)\left[\frac{\partial H}{\partial x}\right]$$

$$v = (6K + 8G) \left[\phi_2 \right] - (3K + G) \left[\frac{\partial H}{\partial y} \right] \qquad (34)$$

$$w = (6K = 8G) \left[\phi_3 \right] - (3K + G) \left[\frac{\partial H}{\partial z} \right]$$

To verify this solution, first calculate e in terms of H.

$$e = \frac{\partial u}{\partial x} + \frac{\partial v}{\partial y} + \frac{\partial w}{\partial z}$$

or

$$e = (6K + 8G) \left[\frac{\partial \phi_1}{\partial x} + \frac{\partial \phi_2}{\partial y} + \frac{\partial \phi_3}{\partial z} \right]$$

$$- (3K + G) \left[\nabla^2 H \right]$$

which becomes

$$e = 3G \left[\nabla^2 H \right] \qquad (35)$$

in view of Equation (33).

We also have from Equation (34)

$$\nabla^2 u = - (3K + G) \left[\frac{\partial}{\partial x} \nabla^2 H \right]$$

$$\nabla^2 v = - (3K + G) \left[\frac{\partial}{\partial y} \nabla^2 H \right] \qquad (36)$$

$$\nabla^2 w = - (3K + G) \left[\frac{\partial}{\partial z} \nabla^2 H \right]$$

Now substitute these values of e and $\nabla^2 u$, $\nabla^2 v$, and $\nabla^2 w$ into the equilibrium equations (9). We find

$$(3K + G) \left[3G \left[\frac{\partial}{\partial x} \nabla^2 H \right] \right] - 3G \left[(3K + G) \left[\frac{\partial}{\partial x} \nabla^2 H \right] \right] = 0$$

plus two similar equations obtained by advancing the variables in cyclic order. Since

$$(3K + G) \left[3G \left[\nabla^2 H(t) \right] \right] = 3G \left[(3K + G) \left[\nabla^2 H(t) \right] \right]$$

equations (9) are satisfied; consequently Equations (34) represent a valid solution for the displacements. Formulas for the strains are obtained by differentiation; the stresses may then be calculated from Equations (5), (6), and (7).

If the stresses and strains are symmetric with respect to the axis, all derivatives with respect to the polar angle vanish, and the equations of equilibrium in cylindrical coordinates reduce to

$$\frac{\partial \sigma_r}{\partial r} + \frac{\partial \tau_{rz}}{\partial z} + \frac{\sigma_r - \sigma_\Theta}{r} = 0$$

$$\frac{\partial \tau_{rz}}{\partial r} + \frac{\partial \sigma_z}{\partial z} + \frac{\tau_{rz}}{r} = 0 \tag{37}$$

The strains are given by the formulas

$$\epsilon_r = \frac{\partial u}{\partial r}, \quad \epsilon_\Theta = \frac{u}{r}, \quad \epsilon_z = \frac{\partial w}{\partial z}, \quad \gamma_{rz} = \frac{\partial u}{\partial z} + \frac{\partial w}{\partial r}. \tag{38}$$

The stress-strain relations are

$$\left.\begin{aligned}
\sigma_r - \sigma_\Theta &= 2G\left[\epsilon_r - \epsilon_\Theta\right] \\
\sigma_r - \sigma_z &= 2G\left[\epsilon_r - \epsilon_z\right] \\
\tau_{rz} &= G\left[\gamma_{rz}\right]
\end{aligned}\right\} \tag{39}$$

$$\Theta = 3K\left[e\right]$$

The equilibrium equations may be expressed in terms of the displacements

$$(3K + G)\left[\frac{\partial e}{\partial r}\right] + 3G\left[\nabla^2 u - \frac{1}{r^2} u\right] = 0 \tag{40}$$

$$(3K + G)\left[\frac{\partial e}{\partial z}\right] + 3G\left[\nabla^2 w\right] = 0 \tag{41}$$

The stresses, strains, and displacements may be expressed in terms of a single biharmonic function (15). Assume that

$$\nabla^4 \psi = 0. \tag{42}$$

Then

$$\sigma_r = (3K - 2G)\left[\frac{\partial}{\partial z}\nabla^2 \psi\right] - (6K + 2G)\left[\frac{\partial^3 \psi}{\partial z \partial r^2}\right] \tag{43}$$

$$\sigma_\Theta = (3K - 2G)\left[\frac{\partial}{\partial z}\nabla^2 \psi\right] - (6K + 2G)\left[\frac{1}{r}\frac{\partial^2 \psi}{\partial r \partial z}\right] \tag{44}$$

$$\sigma_z = (9K + 6G)\left[\frac{\partial}{\partial z}\nabla^2 \psi\right] - (6K + 2G)\left[\frac{\partial^3 \psi}{\partial z^3}\right] \tag{45}$$

$$\tau_{rz} = (6K + 4G) \left[\frac{\partial}{\partial r} \nabla^2 \psi \right] - (6K + 2G) \left[\frac{\partial^3 \psi}{\partial r \partial z^2} \right] \qquad (46)$$

$$G \left[u \right] = - \frac{\partial^2 \psi}{\partial r \partial z} \qquad (47)$$

$$G \left[w \right] = 6G \left[\nabla^2 \psi \right] + (6K + 2G) \left[\frac{\partial^2 \psi}{\partial r^2} + \frac{1}{r} \frac{\partial \psi}{\partial r} \right] \qquad (48)$$

The brackets denote a linear functional of t as defined in Equation (4).

These stress functions are useful in formulating problems involving moving loads and moving boundaries. We will consider the stresses in a cylindrical rocket grain under the combined effects of erosion and internal pressure. The propellant is bonded to a thin elastic cover, so that the tangential strain and radial pressure are continuous at the interface. The propellant is considered to be linearly viscoelastic in shear, but purely elastic when subjected to hydrostatic pressure. It is assumed that the propellant and grain are in a condition of plane strain. The stress-strain laws become

$$\sigma_\theta + \sigma_r + \sigma_z = 3K(\epsilon_\theta + \epsilon_r) \quad \text{since} \quad \epsilon_z = 0$$

$$\sigma_\theta - \sigma_r = 2G \left[\epsilon_\theta - \epsilon_r \right]$$

$$\sigma_\theta - \sigma_z = 2G \left[\epsilon_\theta \right] \qquad (49)$$

The radial strain may be eliminated from the first two relations, giving

$$2G \left[\sigma_\theta + \sigma_r + \sigma_z \right] + 3K(\sigma_\theta - \sigma_r) = 12KG \left[\epsilon_\theta \right] . \qquad (50)$$

The pressure at the interface and the axial stress are the unknown variables in this analysis. The radial and tangential stresses are given by the usual Lamé formulas:

$$\sigma_r = \frac{a^2 p_a - b^2 p_b}{b^2 - a^2} - \frac{a^2 b^2 (p_a - p_b)}{r^2 (b^2 - a^2)}$$

$$\sigma_\theta = \frac{a^2 p_a - b^2 p_b}{b^2 - a^2} + \frac{a^2 b^2 (p_a - p_b)}{r^2 (b^2 - a^2)}$$

where

$$p_a = 0 \quad t < 0$$

$$p_a = p_a(t) \quad t > 0$$

$$\sigma_r = - p_a(t), \quad r = a(t), \quad t > 0$$

The inner boundary erodes during the burning of the rocket grain, so that

$$a = a(t), \quad t > 0 . \tag{50}$$

At the interface, $r = b$, and

$$\sigma_r = - p_b \tag{51}$$

$$\sigma_\Theta = \frac{2a^2 p_a - (a^2 + b^2) p_b}{b^2 - a^2} \tag{52}$$

Under conditions of plane strain, the tangential strain at the inner boundary of the case is given by

$$\epsilon_\Theta = q p_b \tag{53}$$

where

$$q = \frac{\nu + 1}{E} \left\{ \frac{(1 - \nu)(c^2 + b^2)}{c^2 - b^2} + \nu \right\}$$

and b is the inner radius of the case, c the outer radius. The results of the last three equations are substituted into Equations (49) and (50). A pair of simultaneous, linear integral equations for the determination of σ_z and p_b are obtained. It is believed that these equations can be solved by successive substitutions, using the purely elastic response as a first approximation.

$$\frac{2a^2 p_a - (a^2 + b^2) p_b}{b^2 - a^2} - \sigma_z = 2qG \left[p_b \right] \tag{54}$$

$$2G \left[\frac{2a^2 p_a - 2b^2 p_b}{b^2 - a^2} + \sigma_z \right] + 6K \left\{ \frac{a^2(p_a - p_b)}{b^2 - a^2} \right\} = 12qKG \left[p_b \right] \tag{55}$$

The stresses at intermediate radii can be calculated from the Lame formulas. The strains may then be determined from the stress-strain laws.

$$3K(\epsilon_\Theta + \epsilon_r) = \sigma_z + \frac{2a^2 p_a - 2b^2 p_b}{b^2 - a^2} \tag{56}$$

$$G \left[\epsilon_\Theta - \epsilon_r \right] = \frac{a^2 b^2 (p_a - p_b)}{r^2 (b^2 - a^2)} \tag{57}$$

The author has extended this analysis to rocket propellant grains subjected to the combined effects of internal pressure, tension in the axial direction, and erosion of the inner boundary (6).

REFERENCES

1. Turner, A., Jr. <u>Mechanical Behavior of High Polymers</u>. Interscience Publishers, New York, 1948.

2. Lee, E. H., Radok, J. R. M., and Woodward, W. B. <u>Stress Analysis for Linear Viscoelastic Materials</u>. Brown University, Sep 1959.

3. Radok, J. R. M. "Visco-Elastic Stress Analysis." Quarterly of <u>Applied Mathematics</u>, No. 1, Vol XV, Apr 1957, pp 198-202.

4. Volterra, V. <u>Theory of Functionals and of Integral and Integro-Differential Equations</u>. Dover Publications, New York, 1959.

5. Leadermann, H. "Proposed Nomenclature for Linear Viscoelastic Behavior." <u>Transactions of the Society of Rheology</u>, Vol 1, 1957.

6. Elder, A. S. "Derivation of Equations for the Stresses and Strains in a Cylindrical Viscoelastic Case-Bonded Grain." Aberdeen Proving Ground: BRL MR-1359, July 1961.

7. Timoshenko, S. and Goodier, J. N. <u>Theory of Elasticity</u>. McGraw-Hill Book Company, New York, 1951.

8. Tobolsky, A. V. <u>Properties and Structures of Polymers</u>. John Wiley and Sons, 1960, pp 103-106.

9. Mandel, J. "Sur Les Corps Viscoelastiques a Comportment Linineair." <u>IX Congres International de Mecanique Appliquee</u>, 1957, See Equation 2, p. 401, Tome V.

10. Tricomi, F. G. <u>Integral Equations</u>. Interscience Publishers, New York, 1959.

11. Maxwell, C. <u>The Scientific Papers of James Clerk Maxwell</u>. Vol 2, Dover Publications.

12. Langhaar, H. L. and Stippes, M. "Three Dimensional Stress Functions." <u>Journal of the Franklin Institute</u>, July 1954.

13. Papkovitch, P. F. <u>Comptes Rendus</u>. Vol. 195 (1932), pp. 513-515.

14. Neuber, H. <u>Theory of Notch Stresses: Principles for Exact Stress Calculation</u>. Washington, D. C.: The David W. Taylor Model Basin, Translation 74, Nov 45.

15. Love, A. E. H. <u>A Treatise on the Mathematical Theory of Elasticity</u>. Dover Publications, New York, 1944.

CYLINDRICAL ORTHOTROPY AND INHOMOGENEITY DUE TO
REINFORCEMENT OF PROPELLANT GRAINS

by

M. P. Bieniek, W. R. Spillers and A. M. Freudenthal
Columbia University, New York

In the analysis of cylindrical propellant grains with circumferential reinforcement of arbitrary nature and distribution throughout the thickness of the cylinder the dual effect of the reinforcement is to produce cylindrical orthotropy by increasing the rigidity in the direction of the reinforcement, and radial inhomogeneity by non-uniform distribution of the circumferential reinforcement. For short-time problems, such as internal pressurization the assumption of elasticity is tolerably accurate. For long-time processes, such as shrinkage, anisotropic inhomogeneous visco-elastic solutions have to be developed.

1. **Infinite Orthotropic Cylindrical Grain under Internal Pressure.**
The stress-strain relations for media with cylindrical orthotropy defined by 9 constants a_{ij} or c_{ij} have the form [1], [2], [3]

$$\varepsilon_{rr} = a_{11}\sigma_{rr} + a_{12}\sigma_{\theta\theta} + a_{13}\sigma_{zz} \;;\; 2\varepsilon_{\theta z} = a_{44}\sigma_{\theta z} \qquad (1.1)$$

and 4 equations of the same form for $\varepsilon_{\theta\theta}$, ε_{zz}, ε_{rz}, and $\varepsilon_{r\theta}$, or

$$\sigma_{rr} = c_{11}\varepsilon_{rr} + c_{12}\varepsilon_{\theta\theta} + c_{13}\varepsilon_{zz} \;;\; \sigma_{\theta z} = c_{44} 2\varepsilon_{\theta z} \qquad (1.2)$$

and 4 additional equations of the same form for $\sigma_{\theta\theta}$, σ_{zz}, σ_{rz}, $\sigma_{r\theta}$. The coefficients a_{ij} and c_{ij} are material constants and symmetrical $(a_{ij} = a_{ji}, c_{ij} = c_{ji})$. Their matrices are inversely related

$$[a_{ij}] = [c_{ij}]^{-1} \qquad (1.3)$$

Eq. (1.1) can be written in terms of the engineering constants of elasticity by introducing the identities

$$a_{11} = E_r^{-1}; \quad a_{12} = -\nu_{\theta r}E_\theta^{-1}; \quad a_{13} = -\nu_{zr}E_z^{-1}$$
$$a_{21} = -\nu_{r\theta}E_r^{-1}; \quad a_{22} = E_\theta^{-1}; \quad a_{23} = -\nu_{z\theta}E_z^{-1} \qquad (1.4)$$
$$a_{31} = -\nu_{rz}E_r^{-1}; \quad a_{32} = -\nu_{\theta z}E_\theta^{-1}; \quad a_{33} = E_z^{-1}$$

Of the 12 constants only 9 are independent, since the symmetry requirements (1.3) have to be satisfied.

The constants E_r, E_θ, E_z, $\nu_{r\theta}$, ν_{rz}, and $\nu_{\theta z}$ can be estimated by considering joint deformation of grain and reinforcement. Thus, for instance, for circumferential reinforcement of elastic modulus E_R and uniform percentage n

$$E_\theta = E_G\left[1 + n\left(\frac{E_R}{E_G} - 1\right)\right] \qquad (1.5)$$

where E_G denotes the modulus of the grain; the other two moduli $E_r \approx E_z \approx E_G$. The Poisson ratio $\nu_{r\theta}$ defining circumferential extension under radial stress is very small because of the restraint due to the reinforcement. Evaluating this restraint by assuming joint circumferential extension of grain and reinforcement the ratio

$$\nu_{r\theta} = \nu_G \left[\frac{n}{1-n} \frac{E_R}{E_G} + 1 \right]^{-1} \tag{1.6}$$

where ν_G is the Poisson ratio for the unreinforced grain. Thus, for instance, for $E_R/E_G = 10^3$ to 10^4 and $n = 0.01$ to 0.10 the ratios $E_\theta/E_G \approx 100$ and $\nu_{r\theta}/\nu_G \approx 0.01$ since it can be assumed that the higher the rigidity of the reinforcement the smaller will be the percentage used. Because of the symmetry conditions (1.3) therefore $\nu_{\theta r} = \nu_G$. The ratios ν_{rz} and ν_{zr} associated with the two non-reinforced directions are equal to ν_G while $\nu_{\theta z} \approx \nu_{\theta r}$.

Because of the assumed cylindrical symmetry of all relevant problems, the stress-components $\sigma_{rr} = \sigma_r$, $\sigma_{\theta\theta} = \sigma_\theta$, and $\sigma_{zz} = \sigma_z$ are the principal stresses, the strain components $\varepsilon_{rr} = \varepsilon_r$, $\varepsilon_{\theta\theta} = \varepsilon_\theta$ and $\varepsilon_{zz} = \varepsilon_z$ are the principal strains while all shear stresses and strains vanish.

In the case of plane stress $\sigma_{zz} = 0$ in Eqs. (1.1). In the case of plane strain $\varepsilon_{zz} = 0$; hence from the Eq. (1.1) for $\varepsilon_{zz} = \varepsilon_z = 0$:

$$\sigma_z = - \frac{1}{a_{33}} (a_{13}\sigma_r + a_{23}\sigma_\theta) \tag{1.7}$$

and therefore the Eqs. (1.1) for ε_r and ε_θ

$$\begin{aligned} \varepsilon_r &= \alpha_{11}\sigma_r + \alpha_{12}\sigma_\theta \\ \varepsilon_\theta &= \alpha_{12}\sigma_r + \alpha_{22}\sigma_\theta \end{aligned} \tag{1.8}$$

where

$$\alpha_{11} = a_{11} - a_{13}^2/a_{33} \; ; \; \alpha_{22} = a_{22} - a_{23}^2/a_{33}$$
$$\alpha_{12} = \alpha_{21} = a_{12} - a_{13}a_{23}/a_{33} \tag{1.9}$$

The single equilibrium equation

$$\frac{\partial \sigma_r}{\partial r} + \frac{\sigma_r - \sigma_\theta}{r} = 0 \tag{1.10}$$

the compatibility condition

$$\varepsilon_r - \frac{\partial}{\partial r}(r\varepsilon_\theta) = 0 \tag{1.11}$$

since $\varepsilon_r = \partial u_r/\partial r$ and $\varepsilon_\theta = u_r/r$.

Introducing the stress-function $f(r)$ defined by

$$\sigma_r = \frac{1}{r} \partial f(r)/\partial r , \quad \sigma_\theta = \partial^2 f(r)/\partial r^2 \tag{1.12}$$

so that Eq. (1.10) is automatically satisfied, into the compatibility condition (1.11), in which the strain components have been expressed in terms of the stresses with the aid of Eqs. (1.8) the following equation for $f(r)$ is

obtained:

$$\alpha_{11} \frac{1}{r} f' - \alpha_{22} f'' - \alpha_{22} r f''' = 0 \tag{1.13}$$

Its general solution is of the form

$$f'(r) = C_1 r^{-k} + C_2 r^k \tag{1.14}$$

where $k = \sqrt{\alpha_{11}/\alpha_{22}} = \sqrt{c_{22}/c_{11}}$, from which the stress and strain-components can be obtained with the aid of Eqs. (1.12) and (1.8).

An alternative solution of the plane strain problem can be obtained by expressing Eq. (1.10) in terms of the strains and displacement u_r, and solving the resulting differential equation for u_r. The solution has a form similar to Eq. (1.14)

$$u_r = A_1 r^k + A_2 r^{-k} \tag{1.15}$$

In Figs. 1, 2 and 3 the results of the analysis of a thick-walled cylindrical grain subject to internal pressure and contained by a thin elastic case are presented and compared to a corresponding isotropic problem. The material constants used are indicated on Fig. 1. The creation by the reinforcement of very high concentration of σ_θ at the inner surface is demonstrated in Fig. 2, the sharp reduction of the radial displacement in Fig. 3.

2. **Infinite Orthotropic Inhomogeneous Grain under Internal Pressure.** In order to eliminate or at least reduce the concentration of σ_θ without losing the advantage of the reinforcement, a non-uniform distribution of the reinforcement over the wall-thickness is necessary. In this case the parameters α_{ij} in Eqs. (1.8) are functions of the radius $\alpha_{ij}(r)$.

Introducing the expressions for ϵ_r and ϵ_θ with $\alpha_{ij}(r)$ into Eq. (1.11) and using a stress-function $f(r)$ as defined by Eq. (1.10) to satisfy the equilibrium condition, the differential equation for the stress function is obtained

$$f''' + \left(\frac{\alpha_{22}'}{\alpha_{22}} + \frac{1}{r}\right) f'' + \left(\frac{\alpha_{21}'}{\alpha_{22} r} - \frac{\alpha_{11}}{\alpha_{22} r^2}\right) f' = 0 \tag{2.1}$$

If the variation of α_{ij} is of the type

$$\alpha_{11} = \bar{\alpha}_{11} r^m ; \quad \alpha_{22} = \bar{\alpha}_{22} r^m ; \quad \alpha_{12} = \alpha_{21} = \alpha_{12} r^m$$

with real exponents m, Eq. (2.1) has the general solution

$$f'(r) = C_1 r^{n_1} + C_2 r^{n_2} \tag{2.2}$$

where C_1 and C_2 are integration constants and

$$n_{1,2} = \frac{1}{2}\left(-m \pm \sqrt{m^2 + 4(k^2 - mк)}\right) \tag{2.3}$$

with

$$k = \sqrt{\bar{\alpha}_{11}/\bar{\alpha}_{22}}, \quad \kappa = \bar{\alpha}_{12}/\bar{\alpha}_{22}$$

The constants C_1 and C_2 are determined from the boundary conditions $\sigma_r = -p$ at the inner surface and the displacement u_r at the outer surface is equal to the radial displacement of the containing shell.

The problem can now be solved of finding the percentage of reinforcement $n(r)$ which produces σ_θ = constant. In this case Eq. (1.10) can be directly integrated

$$\sigma_r = \sigma_\theta + c/r \tag{2.4}$$

where c is an integration constant, and introduced into the stress-strain relations Eqs. (1.2) for plane strain in which the strains are expressed by the displacement u_r. The resulting two simultaneous differential equations can be separated and integrated after introducing some simplifying assumptions and the function $n(r)$ obtained [4]. For certain assumed ratios of the material constants this function is shown in Fig. 4.

In order to determine the admissibility of the simplifications introduced, the tangential stresses have been determined in a cylindrical grain consisting of 10 orthotropic layers, the variation of the material parameters of which in radial direction approximates the distribution of n shown in Fig. 4. The method has been described in detail in reference [4]. The resulting stress distribution σ_θ shows an approximately constant stress at the center of each layer.

The same method has been used to analyze stresses during burning by removing consecutive layers from the inside and suitably adjusting the internal pressure under the implicit assumption that the rate of burning exceeds the rate of heat-transfer from the burning surface.

A program for the solution of this problem for the IBM 650 has been presented in reference [4].

3. <u>Viscoelastic Anisotropic Problems</u>. In the case of a viscoelastic anisotropic material, the stress-strain relations can be represented in the form of linear differential equations containing the components of stress and strain and their time derivatives. In symbolic notation they can be written as

$$\varepsilon_{ij} = a_{ij}(D)\sigma_{ij} \tag{3.1}$$

or

$$\sigma_{ij} = c_{ij}(D)\varepsilon_{ij} \tag{3.2}$$

where the differential operators $a_{ij}(D)$ and $c_{ij}(D)$ are certain rational functions of the operator $D = \partial/\partial t$. The operators $a_{ij}(D)$ can be most conveniently determined from the static tests in uniaxial stress or from wave propagation along a string or a thin bar. The operators $c_{ij}(D)$ can be

determined from static tests on confined specimens (uniaxial strain) or plane waves in a three-dimensional continuum. It is also possible to determine the operators $E_i(D)$, $\nu_{ij}(D)$, $G_i(D)$ corresponding to the "engineering" constants E_i, ν_{ij}, G_i, and then to calculate either $a_{ij}(D)$ or $c_{ij}(D)$. It should be noted that the operators $E_i(D)$, $a_{ij}(D)$, and $c_{ij}(D)$ are, in general, not of the same type. If, for instance, $E_i(D)$ corresponds to the behavior of a standard solid, $a_{ij}(D)$ and $c_{ij}(D)$ are usually of more complex structures since they can be expressed as certain combinations of the operators $E_i(D)$ and $\nu_{ij}(D)$. The converse is also true, i.e., even if, for instance, $c_{ij}(D)$ are relatively simple operators, $E_i(D)$ and $a_{ij}(D)$ may become much more complicated. With regard to the problems of stress and strain analysis, it is advisable to assume the operators which are actually used to be of possibly simple forms.

The application of the Laplace transformation to the relations (3.1) and (3.2) results in the algebraic relations

$$\bar{\varepsilon}_{ij} = \bar{a}_{ij}(s)\bar{\sigma}_{ij} \qquad (3.3)$$

and

$$\bar{\sigma}_{ij} = \bar{c}_{ij}(s)\bar{\varepsilon}_{ij} \qquad (3.4)$$

where $\bar{\varepsilon}_{ij}$ and $\bar{\sigma}_{ij}$ are the Laplace transforms of ε_{ij} and σ_{ij}, respectively while $\bar{a}_{ij}(s)$ and $\bar{c}_{ij}(s)$ are rational functions of the transformation parameter s. The equations of equilibrium, the relations between the components of strain and the displacement, and the compatibility equations, in terms of the Laplace transforms $\bar{\sigma}_{ij}$, $\bar{\varepsilon}_{ij}$, $\bar{u}_i$ are the same as in the case of an elastic material. Therefore, the solutions for $\bar{\sigma}_{ij}$, $\bar{\varepsilon}_{ij}$, and $\bar{u}_i$ are of the same type as the solutions for σ_{ij}, ε_{ij}, and u_i for an elastic material.

Considering the problem of an infinite cylinder in axially symmetrical state of stress, the general solution for the transformed radial displacement $\bar{u}_r$ will be of the form of Eq. (1..5), with

$$k = \sqrt{\bar{c}_{22}(s)/\bar{c}_{11}(s)} \qquad (3.5)$$

In a similar way, the transform of the stress function of this problem is of the form of Eq. (1.14) with k according to Eq. (3.5) and the components of stress

$$\bar{\sigma}_r = C_1 r^{-k-1} + C_2 r^{k-1} \qquad (3.6)$$

$$\bar{\sigma}_\theta = -C_1 k r^{-k-1} + C_2 k r^{k-1} \qquad (3.7)$$

The constants A_1, A_2 or C_1, C_2 are to be determined from the boundary conditions written also in the transformed version. The inversions of the expressions for $\bar{u}_r$ as well as of (3.6) and (3.7) become much more complicated than in the similar problems of viscoelastic isotropic media. It was possible, however, to obtain approximate inversions by certain series expansions [5]. In some types of viscoelastic anisotropic materials the expressions $\bar{c}_{11}(s)$ and $\bar{c}_{22}(s)$ are such that

$$k = \sqrt{\bar{c}_{22}(s)/\bar{c}_{11}(s)} \qquad = \text{constant},$$

and the inversions can be obtained in an elementary way.

In the case of elastically reinforced viscoelastic materials a specific problem of the interaction between the material and the reinforcing arises.

REFERENCES

1. S. G. Lekhnitskii, *Anizotropnye plastinki*, (Anisotropic plates), Moscow, 1957.

2. A.E.H. Love, *Theory of Elasticity*, Dover Publications.

3. A. E. Green and W. Zerna, *Theoretical Elasticity*, Oxford University Press, 1954.

4. A. M. Freudenthal and W. R. Spillers, "Analysis of an Anisotropic Non-homogeneous Hollow Cylinder," ONR Technical Report, Columbia University, 1961.

5. W. R. Spillers, Orthotropic Viscoelastic Thick-Walled Tube, ONR Technical Report, Columbia University, 1961.
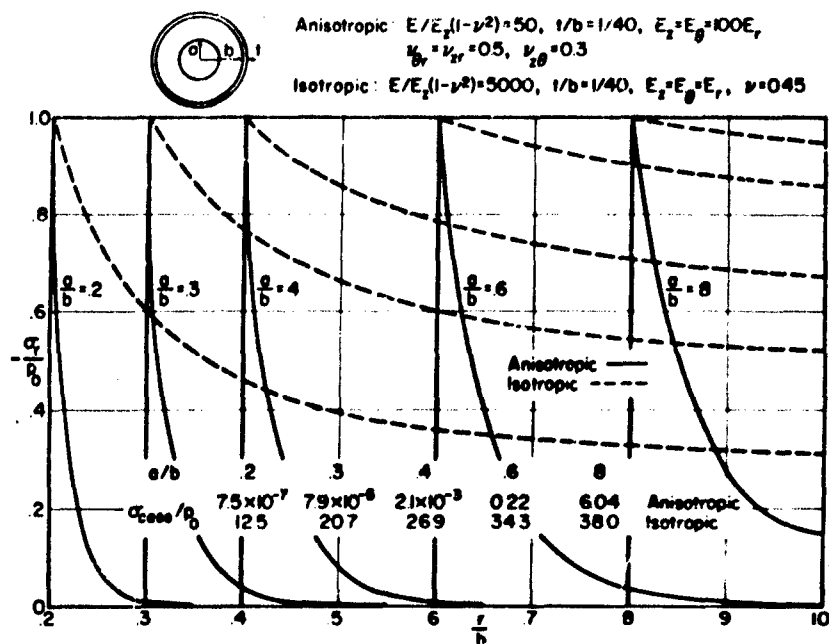
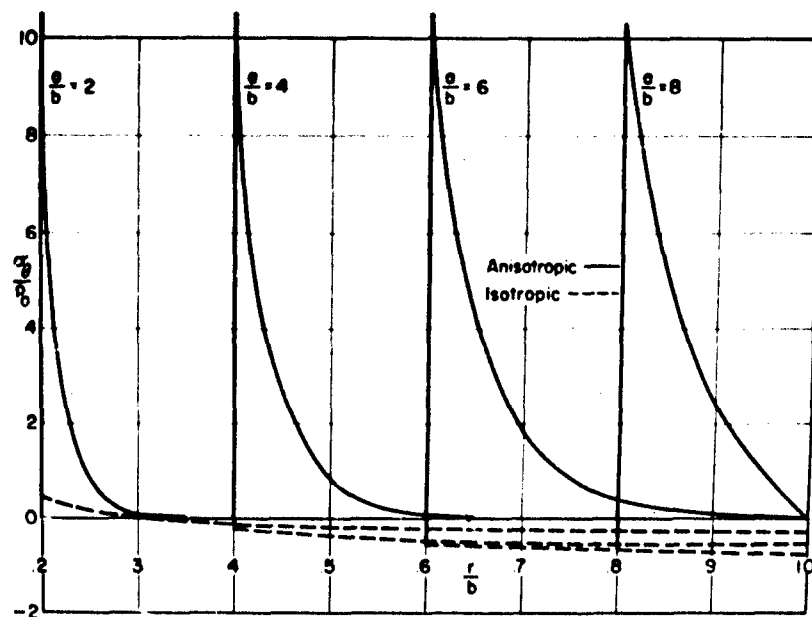FIGURE 1. RADIAL STRESS σ_r AND STRESS IN CASE
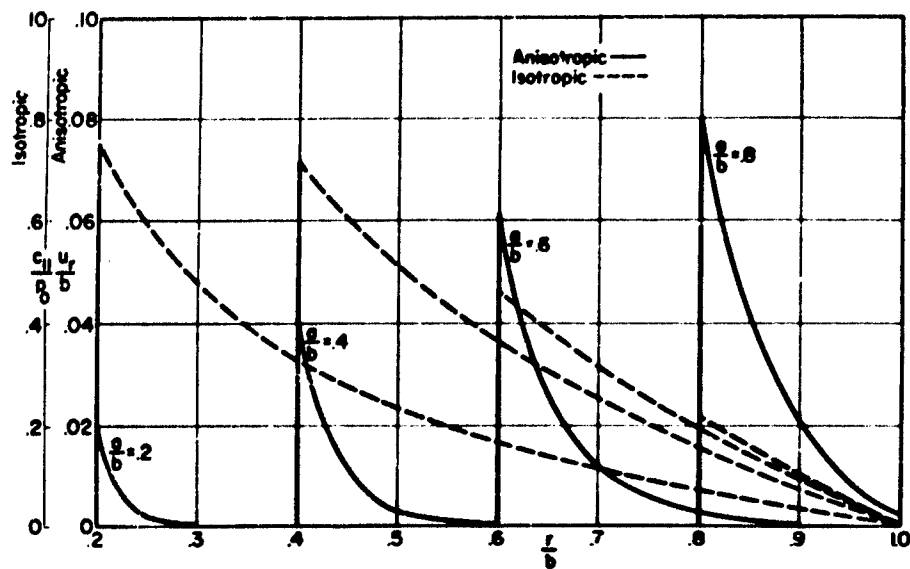

FIGURE 2. TANGENTIAL STRESS σ_θ

FIGURE 3. DISPLACEMENT u_r

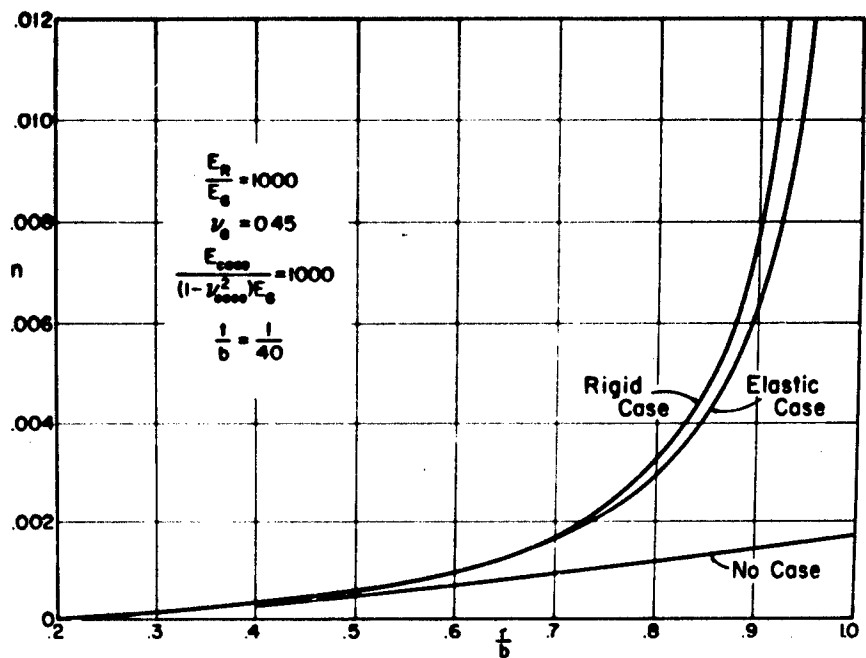
FIGURE 4. AMOUNT OF REINFORCEMENT n

STRESS ANALYSIS OF ANISOTROPIC ELASTIC AND VISCOELASTIC SOLIDS*

S. B. Dong
K. S. Pister

Department of Civil Engineering
University of California at Berkeley

ABSTRACT

A brief review is presented of the implications on stress analysis of anisotropy in elastic and viscoelastic materials. A general solution for axisymmetrically loaded elastic cylinders is given along with quantitative results for a pressurized cylinder comprised of a hexagonal material.

INTRODUCTION

The stress analysis of case-bonded cylindrical grains on the basis of isotropic linear elasticity and viscoelasticity has received considerable attention to date. An extensive body of information of this type has been reported by Williams, Blatz and Schapery [1]. It is well known, however, that filled propellants evince substantially different mechanical behavior in the presence of tensile stress fields than is found in compressive stress fields, as a result of the presence of voids and the pullaway effect of the binder from the filler particles. Accordingly, a type of stress-induced anisotropy is developed in the propellant, necessitating consideration of anisotropic constitutive equations. The general problem involves the solution of boundary value problems for each sub-domain of the body, defined by a particular state of stress, and the subsequent piecing-together of solutions at common interfaces. In each instance the solution required will be that appropriate to an anisotropic body. This paper is intended to review briefly the analysis of a class of problems associated with anisotropic cylinders. A more complete discussion of elastic and viscoelastic problems will be presented in a forthcoming report. The authors have drawn heavily from Lekhnitskii [2], who in addition to his own contributions, has summarized previous work in the field.

In view of the inherent viscoelastic behavior of propellants, attention is drawn to the correspondence principle, first proposed by Alfrey for

---

isotropic bodies [3] and later extended by Biot for anisotropic bodies [4]. Due to complexities arising in the use of the anisotropic correspondence principle, this method of solution is relegated to a minor role. Finally, as an example of the quantitative significance of anisotropy, curves of maximum tangential stress are presented for a pressurized thick-walled cylinder whose elastic properties are those of a hexagonal material.

SUMMARY OF THE FUNDAMENTAL EQUATIONS AND A GENERAL METHOD OF SOLUTION

Since many propellant configurations involve cylindrical geometries, the fundamental elastic field equations will be summarized in cylindrical coordinates. The equilibrium and compatibility equations, strain-displacement relations, and stress-strain laws are respectively:

$$\frac{\partial \sigma_r}{\partial r} + \frac{1}{r}\frac{\partial \tau_{r\theta}}{\partial \theta} + \frac{\partial \tau_{rz}}{\partial z} + \frac{\sigma_r - \sigma_\theta}{r} + R = 0 \tag{1a}$$

$$\frac{\partial \tau_{r\theta}}{\partial r} + \frac{1}{r}\frac{\partial \sigma_\theta}{\partial \theta} + \frac{\partial \tau_{\theta z}}{\partial z} + \frac{2\tau_{r\theta}}{r} + \boxed{H} = 0 \tag{1b}$$

$$\frac{\partial \tau_{rz}}{\partial r} + \frac{1}{r}\frac{\partial \tau_{\theta z}}{\partial z} + \frac{\partial \sigma_z}{\partial z} + \frac{\tau_{rz}}{r} + Z = 0 \tag{1c}$$

$$\left[\frac{1}{r^2}\frac{\partial^2}{\partial \theta^2} - \frac{1}{r}\frac{\partial}{\partial r}\right]\varepsilon_r + \left[\frac{\partial^2}{\partial r^2} + \frac{2}{r}\frac{\partial}{\partial r}\right]\varepsilon_\theta = \frac{1}{r}\frac{\partial}{\partial \theta}\left[\frac{\partial}{\partial r} + \frac{1}{r}\right]\gamma_{r\theta} \tag{2a}$$

$$\frac{\partial^2 \varepsilon_r}{\partial z^2} + \frac{\partial^2 \varepsilon_z}{\partial r^2} = \frac{\partial^2 \gamma_{rz}}{\partial r \partial z} \tag{2b}$$

$$\frac{\partial^2 \varepsilon_\theta}{\partial z^2} + \left[\frac{1}{r^2}\frac{\partial^2}{\partial \theta^2} + \frac{1}{r}\frac{\partial}{\partial r}\right]\varepsilon_z = \frac{1}{r}\frac{\partial^2 \gamma_{\theta z}}{\partial \theta \partial z} + \frac{1}{r}\frac{\partial \gamma_{rz}}{\partial z} \tag{2c}$$

$$\frac{2}{r}\frac{\partial^2 \varepsilon_r}{\partial \theta \partial z} = \left\{\frac{\partial}{\partial r} + \frac{2}{r}\right\}\left[\frac{\partial \gamma_{r\theta}}{\partial z} + \frac{1}{r}\frac{\partial \gamma_{rz}}{\partial \theta} - \left(\frac{\partial}{\partial r} + \frac{1}{r}\right)\gamma_{\theta z}\right]$$

$$+ \frac{2}{r}\left[\frac{\partial}{\partial r} + \frac{1}{r}\right]\gamma_{\theta z} - \frac{2}{r^2}\frac{\partial \gamma_{rz}}{\partial \theta} \tag{2d}$$

$$2\left[\frac{\partial^2 \varepsilon_\theta}{\partial r \partial z} + \frac{1}{r}\frac{\partial}{\partial z}(\varepsilon_\theta - \varepsilon_r)\right] = \frac{1}{r}\frac{\partial}{\partial \theta}\left[\frac{\partial \gamma_{r\theta}}{\partial z} - \frac{1}{r}\frac{\partial \gamma_{rz}}{\partial \theta} + \left(\frac{\partial}{\partial r} + \frac{1}{r}\right)\gamma_{\theta z}\right] \quad (2e)$$

$$\frac{2}{r}\frac{\partial}{\partial \theta}\left[\frac{\partial}{\partial r} - \frac{1}{r}\right]\varepsilon_z = \frac{\partial}{\partial z}\left[\left(\frac{\partial}{\partial r} - \frac{1}{r}\right)\gamma_{\theta z} + \frac{1}{r}\frac{\partial \gamma_{rz}}{\partial \theta} - \frac{\partial \gamma_{r\theta}}{\partial z}\right] \quad (2f)$$

$$\varepsilon_r = \frac{\partial u}{\partial r} \quad (3a)$$

$$\varepsilon_\theta = \frac{1}{r}\frac{\partial v}{\partial \theta} + \frac{u}{r} \quad (3b)$$

$$\varepsilon_z = \frac{\partial w}{\partial z} \quad (3c)$$

$$\gamma_{\theta z} = \frac{\partial v}{\partial z} + \frac{1}{r}\frac{\partial w}{\partial \theta} \quad (3d)$$

$$\gamma_{rz} = \frac{\partial w}{\partial r} + \frac{\partial u}{\partial z} \quad (3e)$$

$$\gamma_{r\theta} = \frac{1}{r}\frac{\partial u}{\partial \theta} + \frac{\partial v}{\partial r} - \frac{v}{r} \quad (3f)$$

$$
\begin{Bmatrix} \sigma_r \\ \sigma_\theta \\ \sigma_z \\ \tau_{\theta z} \\ \tau_{rz} \\ \tau_{r\theta} \end{Bmatrix}
=
\begin{bmatrix}
C_{11} & C_{12} & C_{13} & C_{14} & C_{15} & C_{16} \\
 & C_{22} & C_{23} & C_{24} & C_{25} & C_{26} \\
 & & C_{33} & C_{34} & C_{35} & C_{36} \\
 & & & C_{44} & C_{45} & C_{46} \\
 & & & & C_{55} & C_{56} \\
 & & & & & C_{66}
\end{bmatrix}
\begin{Bmatrix} \varepsilon_r \\ \varepsilon_\theta \\ \varepsilon_z \\ \gamma_{\theta z} \\ \gamma_{rz} \\ \gamma_{r\theta} \end{Bmatrix}
\quad (4)
$$

The symmetric C_{ij} matrix defines the elastic moduli of the material. There exist 21 independent coefficients for general anisotropy. It is sometimes convenient to work with a strain-stress law obtained by inverting Eq. (4):

$$\left[\varepsilon\right] = \left[S_{ij}\right]\left[\sigma\right] \quad (5)$$

In Eq. (5) the S_{ij} are called the elastic compliances of the material and are related to the C_{ij} by a matrix inverse

$$\left[S_{ij} \right] = \left[C_{ij} \right]^{-1} \tag{6}$$

Restricting ourselves in the sequel to problems of plane strain, the previous system of equations may be reduced to two equations involving two dependent variables $F(r,\theta)$, $\Psi(r,\theta)$, which are stress functions identically satisfying the equilibrium equations and defined by:

$$\sigma_r = \frac{1}{r}\frac{\partial F}{\partial r} + \frac{1}{r^2}\frac{\partial^2 F}{\partial \theta^2} + \overline{U} \quad ; \quad \sigma_\theta = \frac{\partial^2 F}{\partial r^2} + \overline{U} \quad ; \quad \tau_{r\theta} = -\frac{\partial^2}{\partial r \partial \theta}\left(\frac{F}{r}\right) \tag{7}$$

$$\tau_{rz} = \frac{1}{r}\frac{\partial \Psi}{\partial \theta} \quad ; \quad \tau_{\theta z} = -\frac{\partial \Psi}{\partial r} \tag{8}$$

In Eq. (7) $\overline{U}$ is a body force potential defined by

$$R = -\frac{\partial \overline{U}}{\partial r} \qquad \Theta = -\frac{1}{r}\frac{\partial \overline{U}}{\partial \theta} \tag{9}$$

Upon substituting Eq. (5) into the two non-vanishing compatibility equations using relations (7) and (8), a system of coupled differential equations in F and Ψ is obtained:

$$L_1 F + L_2 \Psi = 2\left[(S_{13}-S_{23})A - S_{36}B\right]\frac{\sin\theta}{r} + 2\left[S_{36}A + (S_{13}-S_{23})B\right]\frac{\cos\theta}{r}$$

$$- (\beta_{12}+\beta_{22})\frac{\partial^2 \overline{U}}{\partial r^2} + (\beta_{16}+\beta_{26})\frac{1}{r}\frac{\partial^2 \overline{U}}{\partial r \partial \theta} - (\beta_{11}+\beta_{22})\frac{1}{r^2}\frac{\partial^2 \overline{U}}{\partial \theta^2}$$

$$+ (\beta_{11}-2\beta_{22}-\beta_{12})\frac{1}{r}\frac{\partial \overline{U}}{\partial r} + (\beta_{16}+\beta_{26})\frac{1}{r}\frac{\partial \overline{U}}{\partial \theta} \tag{10}$$

$$L_3 F + L_4 \Psi = \left[-S_{35}A + 2S_{34}B\right]\cos\theta + \left[2S_{34}A + S_{35}B\right]\sin\theta$$

$$+ \frac{C}{r}S_{34} - 2\phi + (\beta_{14}+\beta_{24})\left(\frac{\partial \overline{U}}{\partial r} - \frac{\overline{U}}{r}\right) \tag{11}$$

$$- (\beta_{15}+\beta_{25})\frac{1}{r}\frac{\partial \overline{U}}{\partial \theta}$$

In Eqs. (10) and (11), $L_1 \ldots L_4$ are linear differential operators, A, B, and C are constants associated with σ_z, β_{ij} are composite elastic constants defined by $\beta_{ij} = S_{ij} - \frac{S_{i3}S_{j3}}{S_{33}}$ $(i,j=1,2,4,5,6)$, and ϕ denotes the

relative angle of twist of the cylinder. Explicit forms of the differential operators may be found in $\begin{bmatrix} 2 \end{bmatrix}$. Special forms of these operators will be given as they arise in the discussion of specific cylinder problems.

The stress boundary conditions on a cylindrical surface are:

$$\sigma_r \cos(n,r) + \tau_{r\theta} \cos(n,\theta) = R_n$$

$$\tau_{r\theta} \cos(n,r) + \sigma_\theta \cos(n,\theta) = \Theta_n \qquad (12)$$

$$\tau_{rz} \cos(n,n) + \tau_{\theta z} \cos(n,\theta) = 0$$

where n is the exterior normal. The boundary conditions on the ends of a cylinder are:

$$(A\eta + B\zeta + C)S - \frac{1}{S_{33}}\iint_S (S_{13}\sigma_r + S_{23}\sigma_\theta + S_{34}\tau_{\theta z} + S_{35}\tau_{rz} + S_{36}\tau_{r\theta})\,ds = P_z \qquad (13a)$$

$$AI_1 = \frac{1}{S_{33}}\iint_S (S_{13}\sigma_r + S_{23}\sigma_\theta + S_{34}\tau_{\theta z} + S_{35}\tau_{rz} + S_{36}\tau_{r\theta})(r\sin\theta - \eta)\,ds = M_1 \qquad (13b)$$

$$BI_2 - \frac{1}{S_{33}}\iint_S (S_{13}\sigma_r + S_{23}\sigma_\theta + S_{34}\tau_{\theta z} + S_{35}\tau_{rz} + S_{36}\tau_{r\theta})(r\cos\theta - \zeta)\,ds = M_2 \qquad (13c)$$

$$\iint_S \tau_{\theta z}\, r\, ds = T \qquad (13d)$$

where η, ζ are dummy variables, S, I_1, I_2 are cross-sectional area and moments of inertia, and P_z, M_1, M_2, T are the extensional force and bending and twisting moments, respectively.

AXISYMMETRICALLY LOADED THICK-WALLED CYLINDER

In the instance a thick-walled cylinder is loaded axisymmetrically, the stress functions F and Ψ are dependent on r only. In the absence of body forces the governing system of equations (10) and (11) reduces to:

$$\beta_{22}\left(\frac{d^4F}{dr^4} + \frac{2}{r}\frac{d^3F}{dr^3}\right) + \beta_{11}\left(-\frac{1}{r^2}\frac{d^2F}{dr^2} + \frac{1}{r^3}\frac{dF}{dr}\right) - \beta_{24}\frac{d^3\Psi}{dr^3} + \left(\beta_{14} - 2\beta_{24}\right)\frac{1}{r}\frac{d^2\Psi}{dr^2} = 0 \qquad (14)$$

$$-\beta_{24}\frac{d^3F}{dr^3} - \left(\beta_{14} + \beta_{24}\right)\frac{1}{r}\frac{d^2F}{dr^2} + \beta_{44}\left(\frac{d^2\Psi}{dr^2} + \frac{1}{r}\frac{d\Psi}{dr}\right) = \frac{CS_{34}}{r} - 2\phi \qquad (15)$$

The boundary conditions are:

on $r = a$ (inner radius) , $\sigma_r = -p$

$r = b$ (outer radius) , $\sigma_r = -q$. (16)

and at the ends

$$2\pi \int_a^b \sigma_z r\, dr = P \qquad\qquad 2\pi \int_a^b \tau_{\theta z} r^2\, dr = T \qquad (17)$$

The general solutions of Eqs. (14) and (15) are:

$$F(r) = C_0 \frac{\beta_{14}}{\beta_{11}} r + C_1 \frac{r^2}{2} + \frac{C_2}{1+k} r^{1+k} + \frac{C_3}{1-k} r^{1-k} + C_4 + \frac{\phi \mu_1 r^3}{3} \qquad (18)$$

$$\Psi(r) = C_0 \ln r + C \frac{S_{34}}{\beta_{44}} r + C_1 g_1 r + C_2 \frac{g_k r^k}{k} - C_3 \frac{g_{-k} r^{-k}}{k} + C_5 - \frac{\phi \mu_2 r^2}{2} \qquad (19)$$

where $C_0 \ldots C_5$ are constants of integration and k, g_1, g_k, g_{-k}, μ_1 , μ_2 are defined as:

$$k = \left[\frac{\beta_{11}\beta_{44} - \beta_{14}^2}{\beta_{22}\beta_{44} - \beta_{24}^2} \right]^{\frac{1}{2}}$$

$$g_1 = \frac{\beta_{14} + \beta_{24}}{\beta_{44}} \quad ; \quad g_k = \frac{\beta_{14} + k\beta_{24}}{\beta_{44}} \quad ; \quad g_{-k} = \frac{\beta_{14} - k\beta_{24}}{\beta_{44}} \qquad (20)$$

$$\mu_1 = \frac{\beta_{14} - 2\beta_{24}}{4(\beta_{22}\beta_{44} - \beta_{24}^2) - (\beta_{11}\beta_{44} - \beta_{14}^2)} \quad ; \quad \mu_2 = \frac{\beta_{11} - 4\beta_{22}}{4(\beta_{22}\beta_{44} - \beta_{24}^2) - (\beta_{11}\beta_{44} - \beta_{14}^2)}$$

From boundary conditions and the condition of single-valued displacements, the constants of integration can be evaluated.

Knowing F and Ψ , the stresses may be obtained from Eqs. (7) and (8). These expressions will be deferred until the discussion of a specific example. The appearance of the independent variable r raised to non-integral powers containing the elastic coefficients is noteworthy[*],

---

[*] This observation was also noted in [1] , p. 206.

particularly with reference to the dependence of the stress distribution on the elastic coefficients. This, of course, has additional implications with respect to the solution of anisotropic viscoelasticity problems.

CORRESPONDENCE PRINCIPLE FOR ANISOTROPIC VISCOELASTICITY

In linear isotropic viscoelasticity a useful analogy exists for the solution of boundary value problems. The correspondence principle has been repeatedly used for many isotropic problems. Following this principle an associated elastic problem with the proper boundary conditions in Laplace or Fourier transform space is inverted to obtain the viscoelastic response. This principle can be formally extended for anisotropic solids by replacing the elastic constitutive equations (4) by viscoelastic constitutive equations

$$\sigma_{ij} = Q_{ij}^{k\ell} \varepsilon_{k\ell} \quad \text{(summation on repeated indices)} \tag{21}$$

where Q_{ij}^{k1} is an operational tensor. Special forms of this tensor appear in $\begin{bmatrix} 4 \end{bmatrix}$ and $\begin{bmatrix} 5 \end{bmatrix}$.

The Laplace Transform of Eq. (21) along with similar transforms of the equilibrium and compatibility equations, strain-displacement relations and boundary conditions are necessary to complete the formal analogy.

Although this extension of the correspondence principle is straight forward, a cursory examination of a typical associated anisotropic elastic problem to be inverted reveals the difficulties involved. Recall from the solution of the cylinder problem in the previous section that the independent variable r appears raised to a fractional power containing elastic coefficients. Thus, the transforms of the viscoelastic operators appearing in the associated elastic problem will have the same form. A formidable task exists in reducing the associated elastic problem in general terms to a form which is readily invertable. Perhaps, for a specific problem, when numerical values of coefficients are inserted, it would be possible to simplify and invert with a reasonable amount of difficulty.

An alternative method of solution is to begin with the viscoelastic field equations and formulate a governing system of equations in both space and time. This system of partial differential equations may then by solved by any suitable means. The investigation of an orthotropic cylinder using a separation of variables technique has met with some success. Results of this study will be forthcoming.

EXAMPLE OF A THICK-WALLED CYLINDER OF HEXAGONAL MATERIAL

Stress analysis of a thick-walled cylinder with hexagonal material properties was conducted to assess the effect of this particular kind of anisotropy which is characteristic of stress-induced anisotropy for a pressurized propellant cylinder in plane strain. The term hexagonal refers to a special form of orthotropy in which two of the three elastic compliances, S_{11}, S_{22} and S_{33}, corresponding to radial, tangential, and axial directions, are identical. With this form of elastic symmetry, it is possible to reduce the number of independent elastic compliances from nine (for orthotropy) to five, viz.: S_{11}, S_{22}, S_{12}, S_{13}, S_{44}. The parameters S_{12}, S_{13} are associated with cross-effects while S_{44} is a shear compliance.

The values of the parameters adopted for the study are:

$$S_{11} = S_{33} = \frac{1}{540} \; ; \quad S_{22} = \frac{1}{300} \; ; \quad S_{13} = \frac{1}{1080}$$

$$S_{12} = S_{23} \tag{22}$$

$$k_1 = \frac{S_{11}}{S_{22}} = 0.556 \qquad k_2 = \frac{S_{13}}{S_{22}} = 0.278$$

$$k_3 = \frac{S_{12}}{S_{22}}$$

The parameter k_3 will be varied to obtain a family of curves. This parameter is essentially a measure of the cross-effect between the r and θ or the z and θ directions. No value was assigned to S_{44} since it does not appear in the expressions for the stresses. For an internally and externally pressurized cylinder, whose boundary conditions are given by Eq. (16), the expressions for the stresses σ_r and σ_θ are:

$$\sigma_r(r) = C_1 r^{-1-k} + C_2 r^{-1+k}$$

$$\sigma_\theta(r) = k\left[-C_1 r^{-1-k} + C_2 r^{-1+k}\right] \tag{23}$$

where

$$C_1 = \frac{qba^k - pab^k}{\left(\frac{b}{a}\right)^k - \left(\frac{a}{b}\right)^k}$$

$$C_2 = \frac{pab^{-k} - qba^{-k}}{\left(\frac{b}{a}\right)^k - \left(\frac{a}{b}\right)^k}$$

$$k = \sqrt{\frac{S_{11} - \frac{S_{12}^2}{S_{22}}}{S_{22} - \frac{S_{23}^2}{S_{33}}}}$$

(24)

A plot of $\sigma_\theta(a)$ versus b/a, the radii ratio, for internal pressure is shown in Figure 1. The close proximity of the family of curves with k_3 as a parameter discloses that the cross-effect has a negligible influence on the maximum stress for a particular value of k_1. Thus, it is seen that the major factor in the difference between the maximum stress in the isotropic and hexagonal cases is the parameter k_1, the ratio of the radial and tangential compliances. For solid propellants, which exhibit stress-induced orthotropy, k_1 is less than unity. Consequently, the maximum stress lies below that for an isotropic cylinder for all values of b/a. The upper curve in the figure, corresponding to $k_1 = 1.80$ and $k_2 = k_3 = .90$, is included to show the effect of interchanging the values of radial and tangential compliance.

ACKNOWLEDGMENT

REFERENCES

1. Williams, M. L., Blatz, P. J., Schapery, R. A., "Fundamental Studies Relating to System Analysis of Solid Propellants," Final Report-GALCIT 101, California Institute of Technology, February 1961.

2. Lekhnitskii, S. G., Theory of Elasticity of an Anisotropic Body, Gosudarstvennoe Izdatel'stvo Tekhniko-Teoreticheskoi Literaturi, Moscow-Leningrad, 1950 (in Russian).

3. Alfrey, T., "Non-Homogeneous Stresses in Visco-Elastic Media," _Quarterly of Applied Mathematics_, Vol. II, n. 1, pp. 113-119, April 1944.

4. Biot, M. A., "Dynamics of Viscoelastic Anisotropic Media," _Proceedings of the Second Midwestern Conference on Solid Mechanics_, pp. 94-108, 1955.

5. Hilton, H. H., "Anisotropic, Nonhomogeneous Linear Viscoelastic Analysis," _Report No. TD-16_, Solid Rocket Plant of Aerojet-General Corporation, Sacramento, California, July 1961.
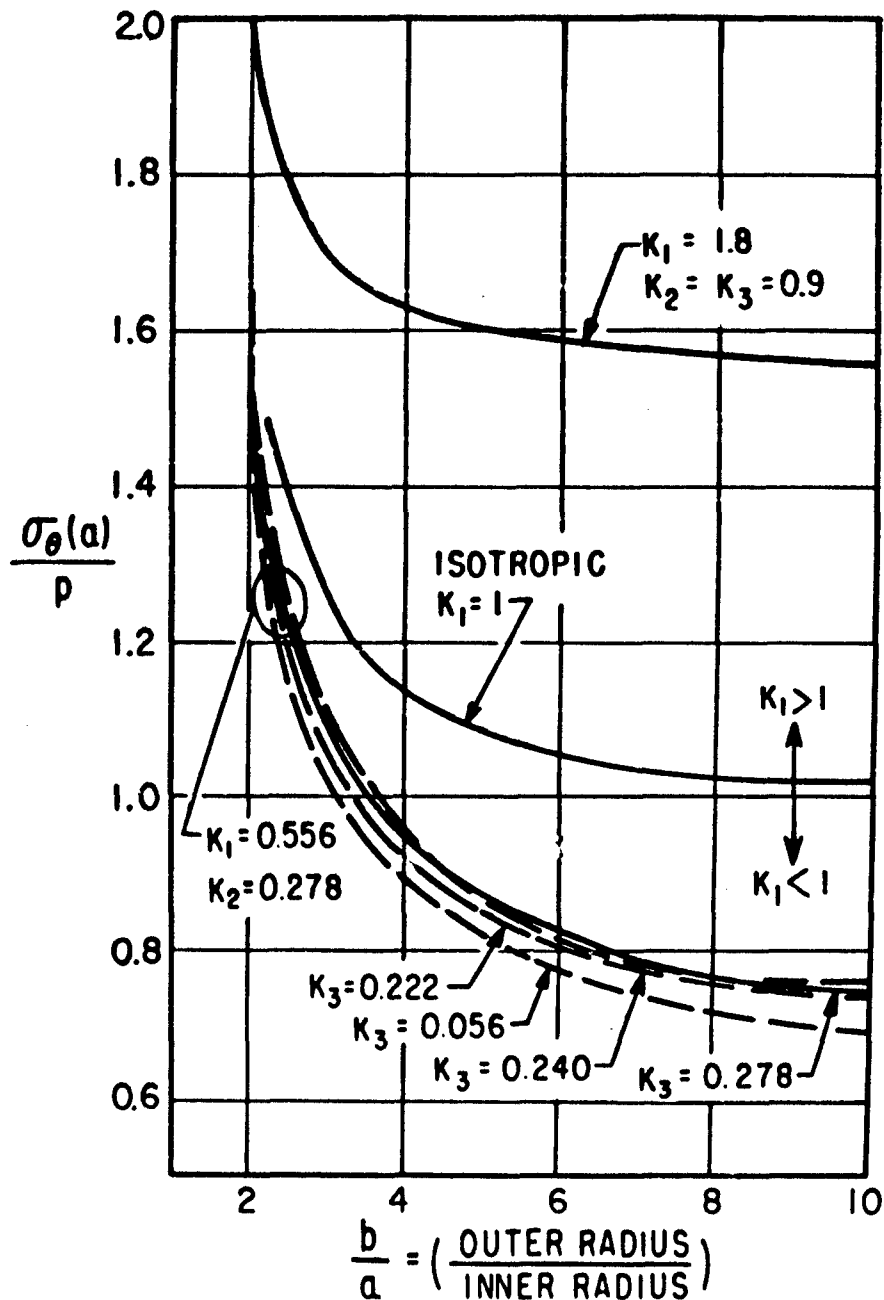
FIGURE 1. $\sigma_\theta(a)$ VS $\frac{a}{b}$ FOR INTERNAL PRESSURE

ON VISCOELASTIC SOLIDS WITH NOTCHES

by

J. E. Griffith, Assistant Professor
University of Florida
Gainesville, Florida

ABSTRACT

This paper represents a study of a linear viscoelastic solid molded into a body containing hyperbolic notches subjected to several types of applied stresses. The solid contains either shallow or deep notches. A viscoelastic cylinder whose inside surface is irregular and subjected to internal pressure is treated as a special case.

The stress and strain fields are determined by employing the elastic theory of Neuber (1) and the correspondence principle. Important parameters include notch depth, root radius, and other dimensions of the solid as well as viscoelastic material constants. The effect of grain size in limiting the macroscopic stress concentration is also considered. The determination of both stress and strain distribution on critical sections enables computation of fracture initiation as predicted by various criteria of failure.

REVIEW OF LINEAR VISCOELASTIC ANALYSIS

In the classical work of Neuber the stresses resulting from the presence of hyperbolic notches in elastic bodies are determined for various loading conditions. Among the special cases treated by Neuber three have been selected to exhibit the stress-strain behavior in a linear viscoelastic solid under a simple step load input. These cases are, (A) tension of a deeply notched bar, (B) tension of a bar with shallow notches, and (C) combined bending and tension of a bar with a deep notch on one side only. (See Figure 1). The latter case is then used as an approximation to the "star" propellant geometry.

Since only boundary forces are prescribed the elastic stresses are applicable for a linear viscoelastic body. Thus, the strains can be found as a function of time by using the correspondence principle provided the viscoelastic material operators are known. Once the stresses and strains are known various theories of failure and fracture may be considered.

The stress-strain behavior of a linear viscoelastic solid will be represented as

$$L \, S_{ij} = Q \, e_{ij} \tag{1}$$

where

$$L = a_m \frac{\partial^m}{\partial t^m} + a_{m-1}\frac{\partial^{m-1}}{\partial t^{m-1}} + \cdots a_0 \quad , \quad Q = b_n \frac{\partial^n}{\partial t^n} + b_{n-1}\frac{\partial^{n-1}}{\partial t^{n-1}} + \cdots b_0 \quad (2)$$

Assuming an incompressible material the strain tensor and strain deviator are the same, or

$$\epsilon_{ij} = e_{ij} \tag{3}$$

From Equations (1) and (3),

$$L\, S_{ij} = Q\, \epsilon_{ij} \tag{4}$$

In using the Neuber solutions for stresses the stress deviator S_{ij} is quickly found and the strain response determined from Equation (4) by various methods (2) depending on the material representation. For the purposes of simplification the three element model of Figure 1 will be used as well as the step load pattern

$$\text{Load} = 0 \qquad t < 0$$
$$\text{Load} = \text{Constant} \quad t \geq 0 \tag{5}$$

SPECIAL CASES

Case 1: Tension of a Viscoelastic Bar with Deep Notches. In Figure 1 (a) the dimensions of notch radius, bar width and thickness are shown. For the elastic case the curvilinear stress components are

$$\sigma_u = \frac{P \sin V_0}{(V_0 + \sin V_0 \cos V_0)\, h^2} \cosh u \cos v \left(2 + \frac{\cos^2 V_0 - \cos^2 v}{h^2} \right) = \sigma_{11}$$

$$\sigma_v = \frac{P \sin V_0}{(V_0 + \sin V_0 \cos V_0)\, h^2} \cosh u \cos v \left(\cos^2 v - \cos^2 V_0 \right) = \sigma_{22} \tag{6}$$

$$\tau_{uv} = \frac{P \sin V_0}{(V_0 + \sin V_0 \cos V_0)\, h^4} \sinh u \, \sin v \left(\cos^2 V_0 - \cos^2 v \right) = \sigma_{12}$$

By subtracting the hydrostatic component from the normal stress components the stress deviator components are found to be

$$S_{11} = \frac{P \sin V_0}{(V_0 + \sin V_0 \cos V_0)\, h^2} \cosh u \cos v \left(\frac{4}{3} + \frac{\cos^2 V_0 - \cos^2 v}{h^2} \right)$$

$$S_{12} = \frac{P \sin V_0}{(V_0 + \sin V_0 \cos V_0)\, h^4} \sinh u \, \sin v \left(\cos^2 V_0 - \cos^2 v \right) = S_{21}$$

$$S_{13} = S_{31} = S_{23} = S_{32} = 0 \, , \; S_{33} = -\frac{2}{3}\frac{P \sin V_0}{(V_0 + \sin V_0 \cos V_0)\, h^2} \cosh u \cos v$$

$$S_{22} = \frac{P \sin V_0}{(V_0 + \sin V_0 \cos V_0)\, h^2} \cosh u \cos v \left(\frac{\cos^2 v - \cos^2 V_0}{h^2} - \frac{2}{3} \right)$$

Using the stress deviator, eqs. (4) and (5), and the model in Figure 1(d) the strain components are

$$\epsilon_{11} = S_{11}\left[\frac{a_0}{b_0} - \left(\frac{a_0}{b_0} - \frac{1}{b_1}\right)e^{-\frac{b_0}{b_1}t}\right], \quad \epsilon_{12} = S_{12}\left[\frac{a_0}{b_0} - \left(\frac{a_0}{b_0} - \frac{1}{b_1}\right)e^{-\frac{b_0}{b_1}t}\right] \quad (7)$$

$$\epsilon_{22} = S_{22}\left[\frac{a_0}{b_0} - \left(\frac{a_0}{b_0} - \frac{1}{b_1}\right)e^{-\frac{b_0}{b_1}t}\right], \quad \epsilon_{33} = S_{33}\left[\frac{a_0}{b_0} - \left(\frac{a_0}{b_0} - \frac{1}{b_1}\right)e^{-\frac{b_0}{b_1}t}\right]$$

The material constants which appear in Equation (7) are defined for the three element model in Figure 1 (d). The variation of the strains with time across the narrowest section is shown in Figure 2 (a) where values for the material constants have been assumed. If the criterion of failure is maximum strain, the time for ϵ_{11} to reach a critical value at the root of the notch can be predicted. On the other hand, if maximum strain energy is the criterion, this energy can easily be determined at each material point according to the equation

$$U_{crit} = \sigma_{11}\epsilon_{11} + \sigma_{22}\epsilon_{22} + \sigma_{33}\epsilon_{33} + 2\sigma_{12}\epsilon_{12} \quad (8)$$

For incompressible materials the strain energy and distortion strain energy are alike. Other criterion, such as maximum shear strain, etc. can be found from Equations (5) and (7).

The effect of the notch curvature a/ρ can be found for both stresses and strains by noting that $\tan^2 v_0 = a/\rho$. In Figures 2 (a) and (b) a/ρ is 5 and 30, respectively.

Case 2. <u>Tension of a Viscoelastic Bar with Shallow Notches.</u> Again, using the stress solutions the strain field is determined in the same manner as in Case 1. The resultant strains are shown along the section through the notch normal to the tensile load. In Figures 2 (b) and (c) the notch curvature a/ρ is 5 and 30, respectively.

Case 3. <u>Combined Bending and Tension of a Viscoelastic Bar with a Deep Notch on One Side.</u> In Figure 1 (c) a bar is subjected to a tensile load P and bending moment M. The stress distribution across the critical narrow section is

$$\sigma_{11} = \frac{A_1}{h^2}\cos v\left(2 + \frac{\cos^2 v_0 - \cos^2 v}{h^2}\right) + \frac{A_2}{h^2}\left(-4 + \frac{\cos 2v - \cos 2v_0}{h^2}\right)\sin 2v$$

$$\sigma_{22} = \frac{A_1}{h^4}\cos v\left(\cos^2 v - \cos^2 v_0\right) + \frac{A_2}{h^4}\sin 2v\left(\cos 2v_0 - \cos 2v\right)$$

$$\sigma_{12} = 0 \quad (9)$$

The values of A_1 and A_2 are dependent on the loading P and M as well as the bar geometry, namely, the curvature ratio a/ρ. For the case $a/\rho = 5$,

$$A_1 = 1.42\,\sigma_T + .090\,\sigma_B$$

$$A_2 = .31\,\sigma_T + .081\,\sigma_B \tag{10}$$

where σ_T and σ_B are defined as the elementary elastic stresses of simple tension and bending, or

$$\sigma_T = \frac{P}{a\,d}$$

$$\sigma_B = \frac{6\,M}{a^2\,d} \tag{11}$$

Now consider an unsupported disk with periodic hyperbolic notches under internal radial stress, or pressure p, Figure 3(a). If the number of notches is n, then a representative segment of angle $2\pi/n$ may be used for analysis. As shown in figure 3(b) the moment and axial force for this segment are

$$P = p\,R_2\,d\,\cos \pi/n$$

$$M = p\,R_2\,d\,\cos \pi/n \left(R_0 - \frac{a}{2}\right) - \frac{p\,R_2\,d}{\cos \pi/n}(R_0 - x_0) \tag{12}$$

It is interesting to note the effect of the number of notch points for a particular geometry on the maximum stress σ_{11} at the notch root. Suppose the dimensions are related as

$$R_0 = 5a \qquad R_2 = 3a$$

$$R_1 = 4a \qquad x_0 = \left(5 - \frac{9}{2}\cos \pi/n\right) \tag{13}$$

where x_0 is approximated as

$$x_0 = R_0 - \left[\left(R_1 + \frac{R_0 - R_1}{2}\right)\cos \pi/n\right]$$

Combining equations (9) through (13),

$$\sigma_{11} = p\left[79\,p - 75\cos \pi/n\right] \tag{14}$$

The bracketed term in Equation (14) is shown in Figure 3(c) showing the reduction in root stress with increase in notches. There is little improvement in this stress-relief beyond eight notches. The applicability of Equation (14) depends on the approximation of the outer boundary of the disk as a straight line. The more notches the greater the accuracy in Figure 3(c). The stress distribution of σ_{11} across the web for the case n = 4 is shown in Figure 3 (d). The stress component σ_{22} is negligible compared to σ_{11} while σ_{33} is zero. From these stress components the strain components and their variation with time can be

predicted in the same manner as Case 1 and Case 2.

The effect of the curvature ratio a/ρ on maximum stress at the notch root can be determined for the preceeding values in Equation (13) and a reevaluation of A_1 and A_2. This dependency on a/ρ is plotted in Figure 3 (e). As the radius of curvature ρ approaches the average grain size D the stress will not increase at the root. According to Neuber's analysis for the elastic case an effective radius of curvature D/2 limits the stress magnitude. Suppose that a/ρ (effective) is 40. Then the curve in Figure 3 (e) terminates at $a/\rho = 40$ as indicated by the dashed line.

REFERENCES

(1) Neuber, H., Theory of Notch Stresses, Edwards Bros., 1946.

(2) Williams, M. L., Fundamental Studies Relating to Systems Analysis of Solid Propellants, Galcit Report SM 61-5, February, 1961.

LIST OF SYMBOLS

STRESS		STRAIN	
σ_{ij}	stress tensor	ϵ_{ij}	strain tensor
S_{ij}	stress deviator	e_{ij}	strain deviator

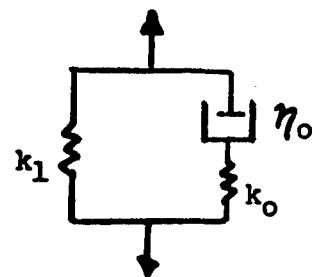|	
a_o, b_o, b_1	material constants
t	time
u,v	curvilinear coordinates
p1	average stress
$h^2 = \sinh^2 u + \cos^2 v$	
U_{crit}	strain energy
a	width of reduced section
ρ	radius of curvature
P	axial load
M	bending moment
x_o	center of force
p	pressure
n	number of star points
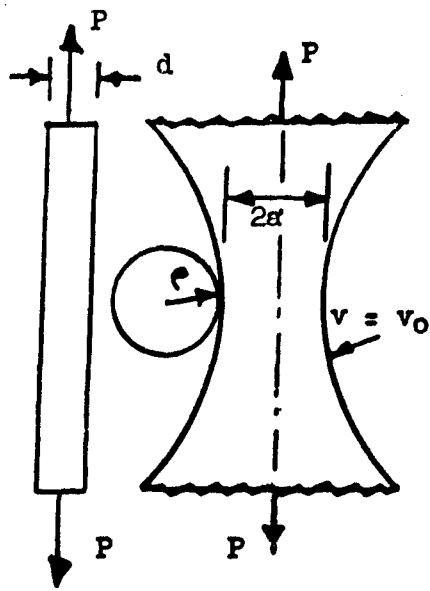
(a) deep notch
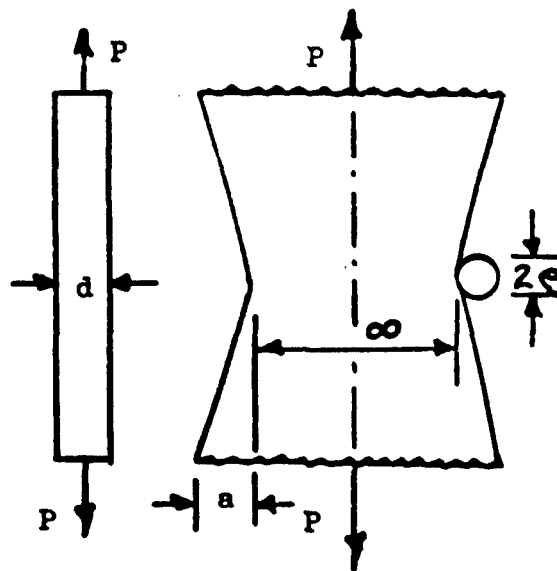
(b) shallow notch
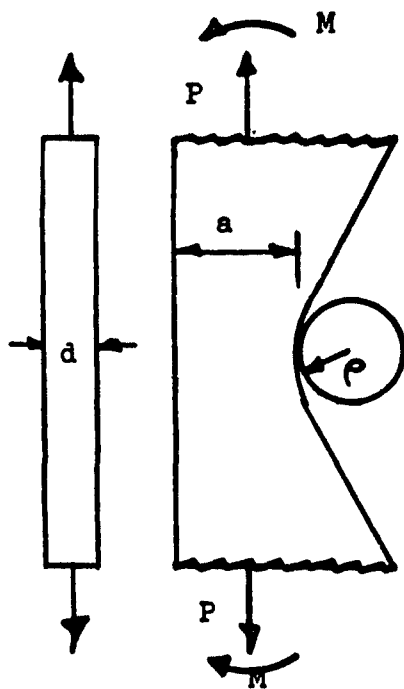
(c) deep notch on one side

(d) 3 element model

$$b_1 = k_1 + k_0$$
$$b_0 = k_1 k_0/\eta_0$$
$$a_0 = k_0/\eta_0$$

$$k_1 = 10, \quad k_0 = 5, \quad \eta_0 = 3.33$$

FIGURE 1. NOTCH GEOMETRY AND MODEL

(a) a/ρ = 5

(b) a/ρ = 30

(c) a/ρ = 5
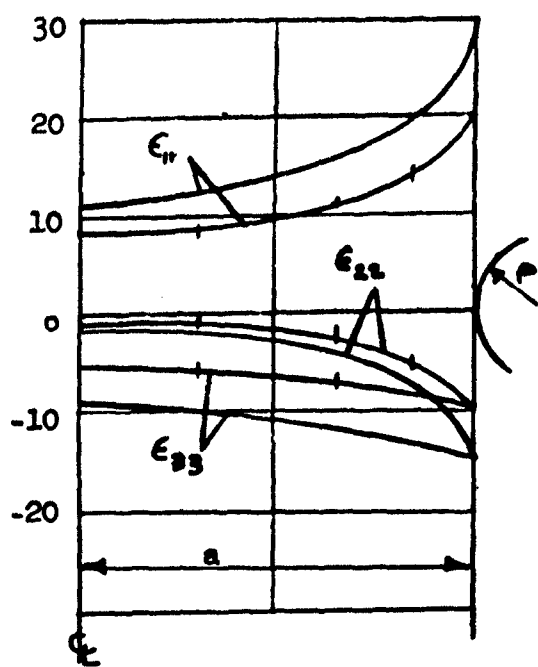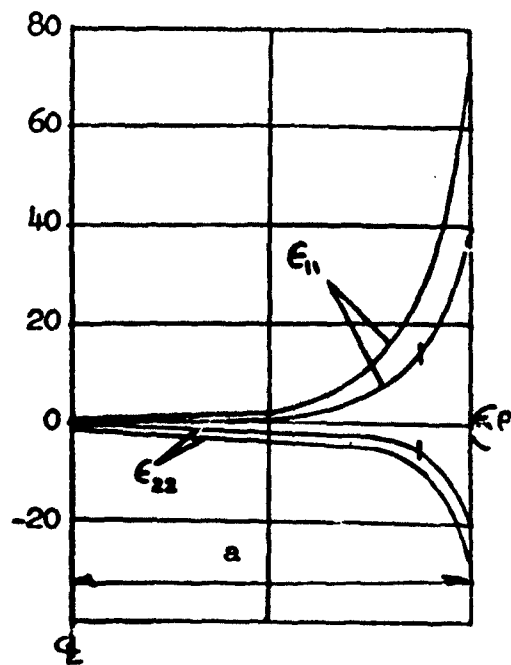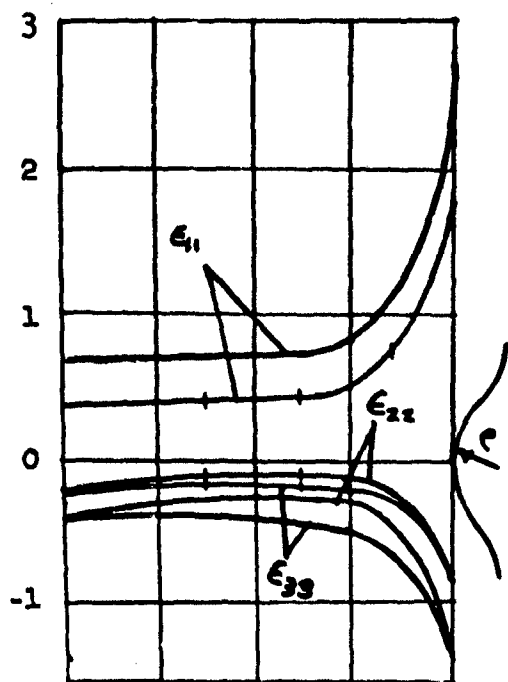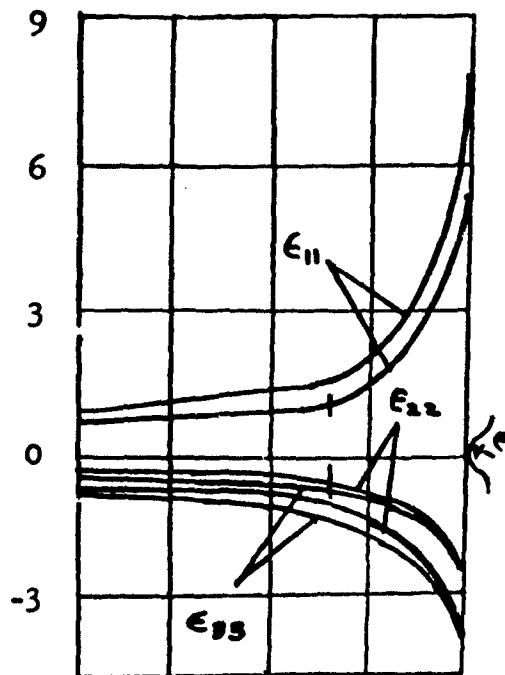
Legend
—+— time t = 0
——— time t = ∞

(d) a/ρ = 30

FIGURE 2. STRAIN DISTRIBUTION IN NOTCH SECTIONS
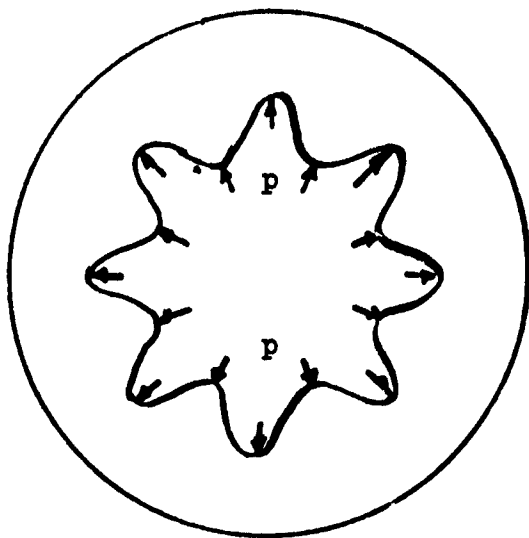
(a) n-star geometry

(b) representative segment
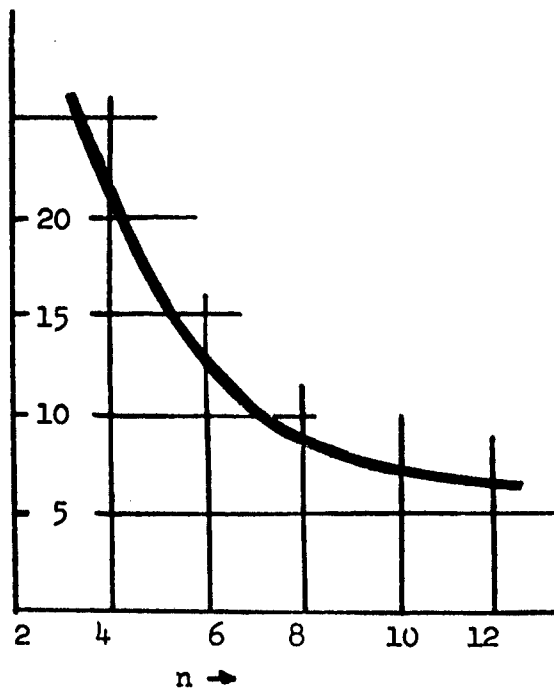
(d) $\sigma_{||}$ stress distribution

(c) notch number effect
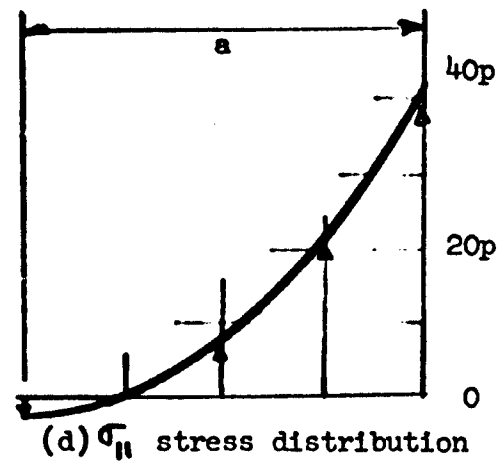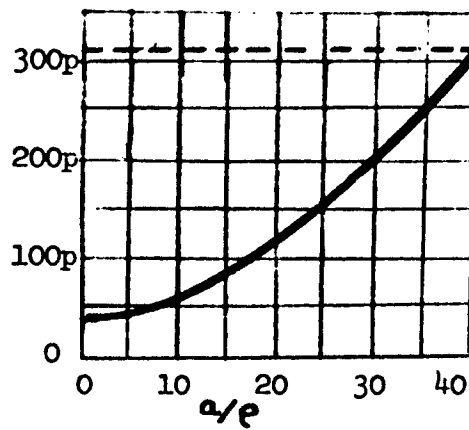
(e) a/ρ effect

FIGURE 3.   IRREGULAR CIRCULAR DISK UNDER RADIAL STRESS

END EFFECTS DUE TO SHRINKAGE IN SOLID PROPELLANT GRAINS[1]
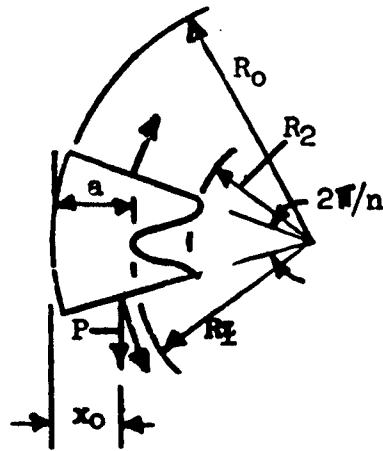
Charles H. Parr

Rohm & Haas Company
Redstone Arsenal Research Division
Huntsville, Alabama

ABSTRACT

A theoretical study of the end effect in case-bonded hollow circular propellant grains of finite length has been made for shrinkage loading due to curing and thermal shrinkage. The effects of radius ratio, length-to-diameter ratio, and Poisson's ratio on the stresses and displacements of the inside surface at the middle of the propellant grain are presented. It was concluded that estimations of stresses, strains, and the thermal expansion coefficients based on a plane strain analysis may be much in error due to the neglect of end effects.

INTRODUCTION

The current interest in profile measurements of propellant grains and in the use of case-bonded hollow circular propellant grains to evaluate the strain capability of propellants makes the prediction of actual stress and strain states and profiles of these configurations desirable. A method of numerical solution for the stresses, strains, and displacements in such cylinders has been devised. A hollow circular cylinder of finite length with flat ends was considered (Fig. 1) which was loaded by uniform linear shrinkage[2] of the cylinder material and which was bonded to a rigid case on the outer periphery and unloaded on the other surfaces. The assumptions of linearity, elastic response, homogenity, and isotropy were made. Details of the analysis for pressure, shrinkage, and acceleration loads will be presented in a forthcoming report (1) . Only the results of the analysis pertaining to shrinkage loading are presented here.

For the shrinkage loading, the strains and displacements in the cylinder were found to be directly proportional to the linear shrinkage, $-\delta$, and to be non-linear functions of the outer-to-inner radius ratio K, length-to-diameter ratio λ, and Poisson's ratio ν. The ratio of each stress to the elastic modulus was found to be similarly dependent on the same parameters. Thus, the strains and displacements depend on only two material parameters, the amount of shrinkage and Poisson's ratio. The stresses depend on the elastic modulus as well.

---

[2]In keeping with usual conventions, the shrinkage is expressed in terms of an expansion factor for which negative values indicate shrinkage. The linear expansion factor includes length changes due to both cure and thermal expansion. For thermal effects alone the expansion is simply the product of the linear coefficient of thermal expansion and the temperature change.

It was determined that the numerical solution for an elastic solid corresponds to the solution for a viscoelastic solid for long times if the equilibrium values of the relaxation modulus and Poisson's ratio are used in the elastic solution. Thus, the solution should correspond to equilibrium conditions in the propellant grain and should predict the profile of propellant grains when the actual profile has reached an equilibrium position.

RESULTS

Fig. 2 shows the theroretical radial displacement of the inner radius for a grain 32 in. in length having an outer radius of 3 in. and an inner radius of 1 in. for four sets of Poisson's ratio and linear expansion factor. Superposed are measured displacements due to thermal and cure shrinkage from a motor one inch longer, a 6C2-33 static test motor ($a = 1$, $b = 3$, $l = 33$) made with 112$_{bw}$ plastisol propellant. The profile had reached an equilibrium position. Neither of the properties ν or δ is known accurately for this propellant. The computed displacements are directly proportional to δ, and therefore for a given ν it was possible to select a value of δ which would fit the experimental data in the middle of the motor.

Accordingly displacement curves for $\nu = 0.49$ and $\nu = 0.50$ were fitted to the actual displacements at the middle of the motor to predict values of δ of -0.0050 and -0.0043 respectively. (For this motor the deflection at the center for $\nu = 0.5$ is 98.5% of the plane strain solution.)

It can be seen that any value of Poisson's ratio from 0.50 to 0.49 (and perhaps lower) when combined with a suitable value of δ will give a reasonable fit for the experimental data. This obviously suggests a method of determining Poisson's ratio if the unconstrained value of the shrinkage is known. The converse, however, would not apply since small errors in the value of Poisson's ratio would lead to large errors in the shrinkage. This demonstrates the dependence of the apparent shrinkage when the material is in a stressed state on the dilatancy (or compressibility).

Figs. 3 to 7 demonstrate the effect of the parameters λ, κ, and ν on the deviation of the radial displacement at the middle of various cylinders from the displacement in a cylinder of infinite length. The ratio of the radial displacement at the inside radius to the inside radius, u/a, in a cylinder of infinite length is given (2) by

$$\frac{u}{a} = \frac{-(1+\nu)\delta}{1+(1-2\nu)\kappa^2} [\kappa^2 - 1] . \tag{1}$$

From Figs. 3 to 7 it can be seen that the end effects are most severe for $\nu = 0.5$ and decrease rapidly with decreasing ν. End effects become less severe with decreasing radius ratio κ (decreasing web fraction). Most pronounced is the effect of cylinder length-to-diameter ratio λ.

Figs. 3 to 7 were constructed on the basis of computations completed at this time. Consequently, the data in some areas is insufficient so that cross plotting was used to produce the curves with the data at hand. The points actually calculated are shown on the figures.

Figs. 8 and 9 show the normal stresses in dimensionless form at the inside surface in the center of the cylinder as functions of κ and λ for Poisson's ratio of 0.5. The curves approach the plane strain solution asymptotically as λ increases.

CONCLUSIONS

It was determined that within the range of allowable strains in which the analysis is valid, say 10% or less, the end effects, expressed in dimensionless form are functions of only Poisson's ratio ν, the ratio of outer-to-inner radius κ, and the length-to-diameter ratio λ. All three parameters affect the nature of the end effects significantly in their ranges of interest.

Only a few profiles are presented in this paper; however, comparison of the many profiles which have been calculated showed that the apparent flatness of the deflection curve in the center section of the cylinder is not a reliable indication of the degree of approach to the plane strain condition. In actual measurements the apparent flatness is further clouded by normal scatter of data.

Consideration of these factors indicates that the use of case-bonded propellant cylinders for obtaining values of the thermal coefficient of expansion and of stress and strain failure at rupture is not at all straightforward and may lead to large errors if a plane strain analysis is used. For instance, suppose a motor with $\kappa = 6$ and $\lambda = 4$ is used to predict the thermal coefficient of expansion. For $\nu = 0.50$ the deflection expected can be seen from Fig. 3 to be only 65% of the plane strain deflection. If the prediction is based on a plane strain solution, the apparent coefficient of thermal expansion would be only 65% of the true coefficient of thermal expansion. If however, ν is known to be 0.49, the apparent coefficient of thermal expansion would be only 84% of the true value. But if ν is actually 0.49 for the propellant and is assumed to be 0.50, the apparent coefficient of thermal expansion using Eq. 1 would be

$$84\% \times \frac{\text{(Plane strain displacement for } \nu = 0.49)}{\text{(Plane strain displacement for } \nu = 0.50)}$$

or 48.5% of the true value. Errors of a similar type could occur in the prediction of stresses and axial strains.

REFERENCES

1. Rohm & Haas Company, Quarterly Progress Report on Engineering Research, No. P-61-17, September, 1961 (in press).

2. Rohm & Haas Company, Quarterly Progress Report on Weapons Research, No. P-57-5, April, 1957.
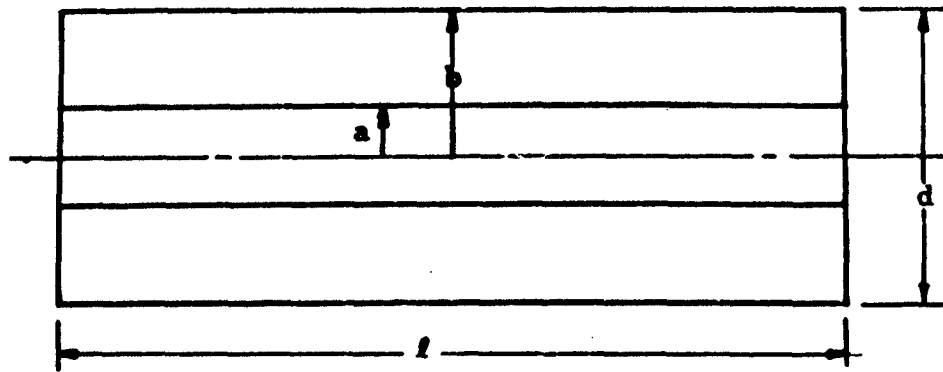
FIGURE 1. CYLINDER CONFIGURATION

Distance from End of Motor, in.
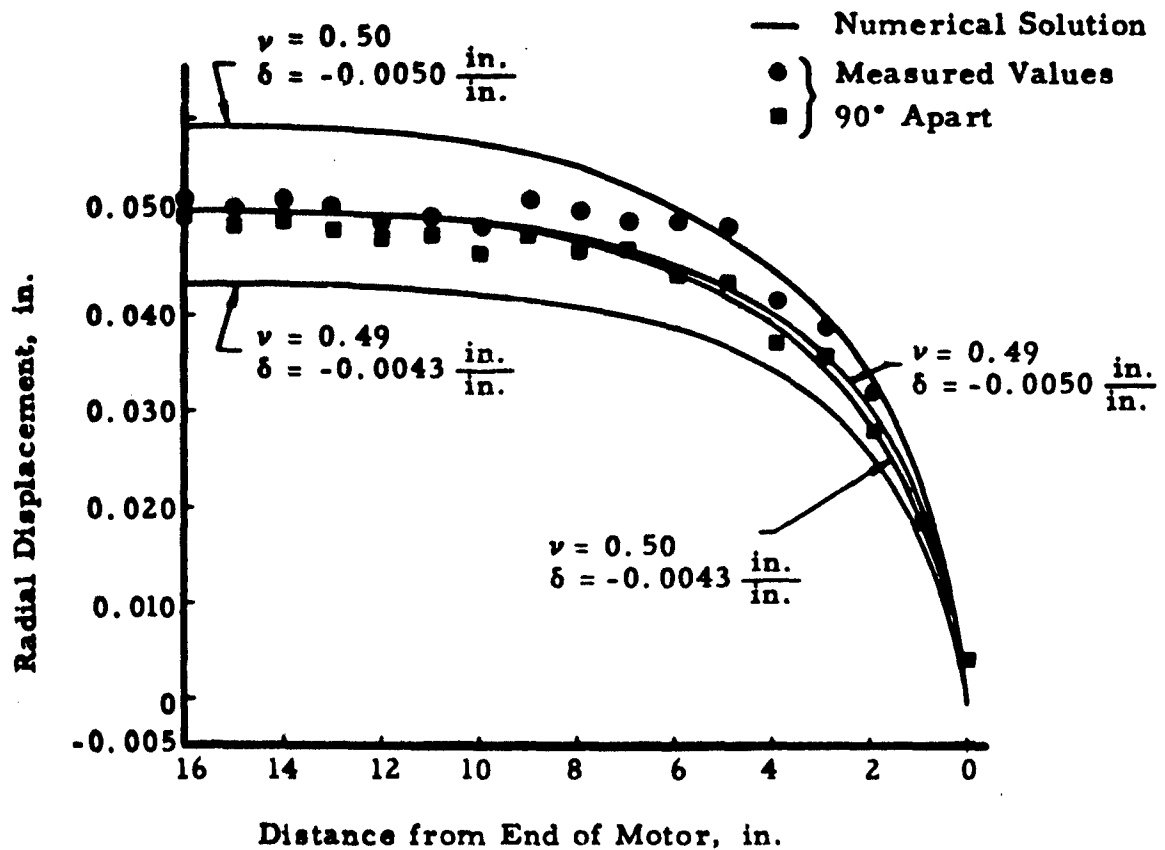
FIGURE 2.
RADIAL DISPLACEMENT OF INNER PROPELLANT SURFACE,
6C2-33 STM WITH 112$_{bw}$ PROPELLANT
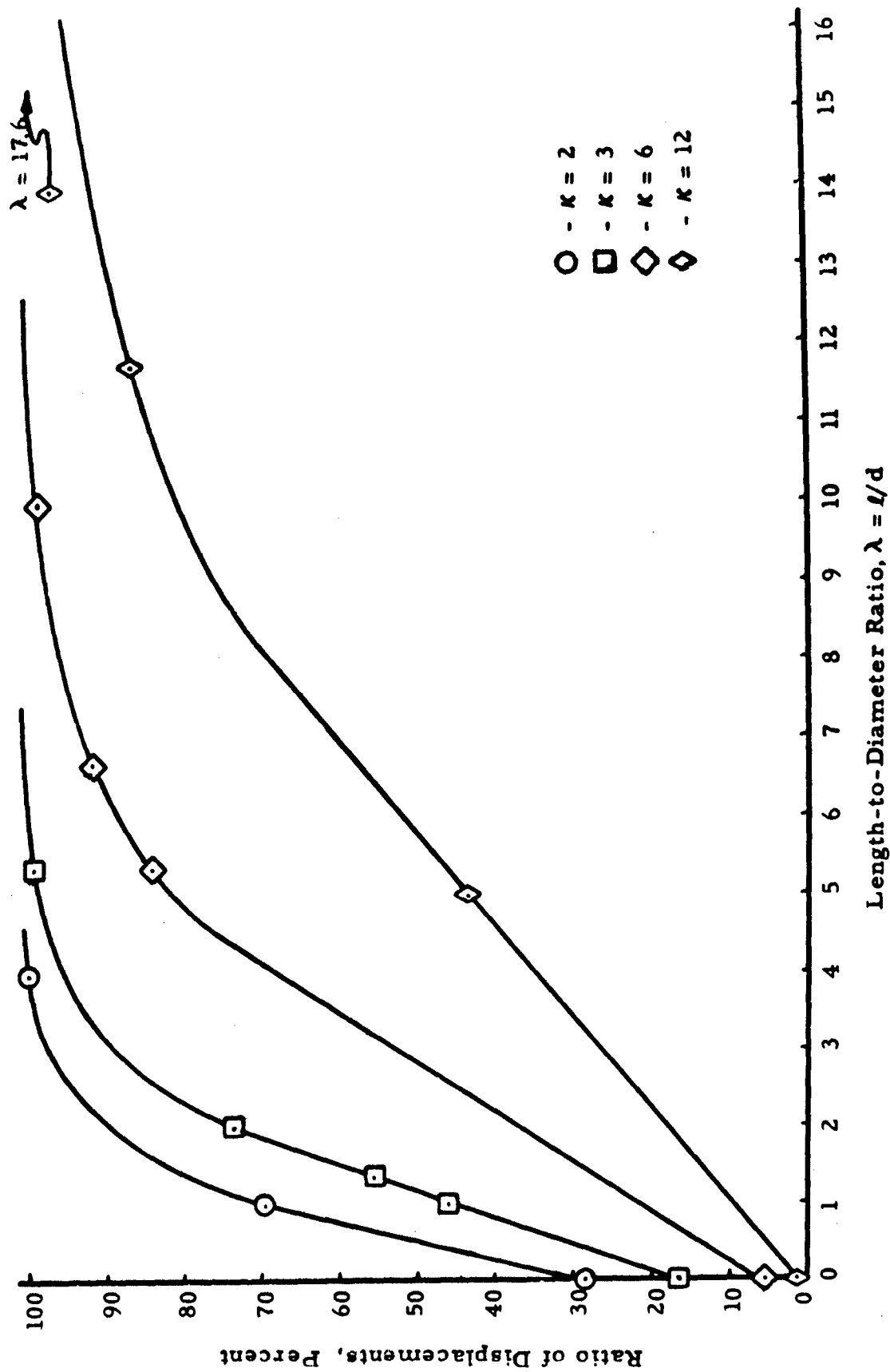
FIGURE 3.
RADIAL DISPLACEMENT AT INNER RADIUS IN MIDDLE OF CYLINDER OF FINITE LENGTH AS PERCENTAGE OF
RADIAL DISPLACEMENT IN EQUIVALENT CYLINDER OF INFINITE LENGTH $\nu = 0.50$.
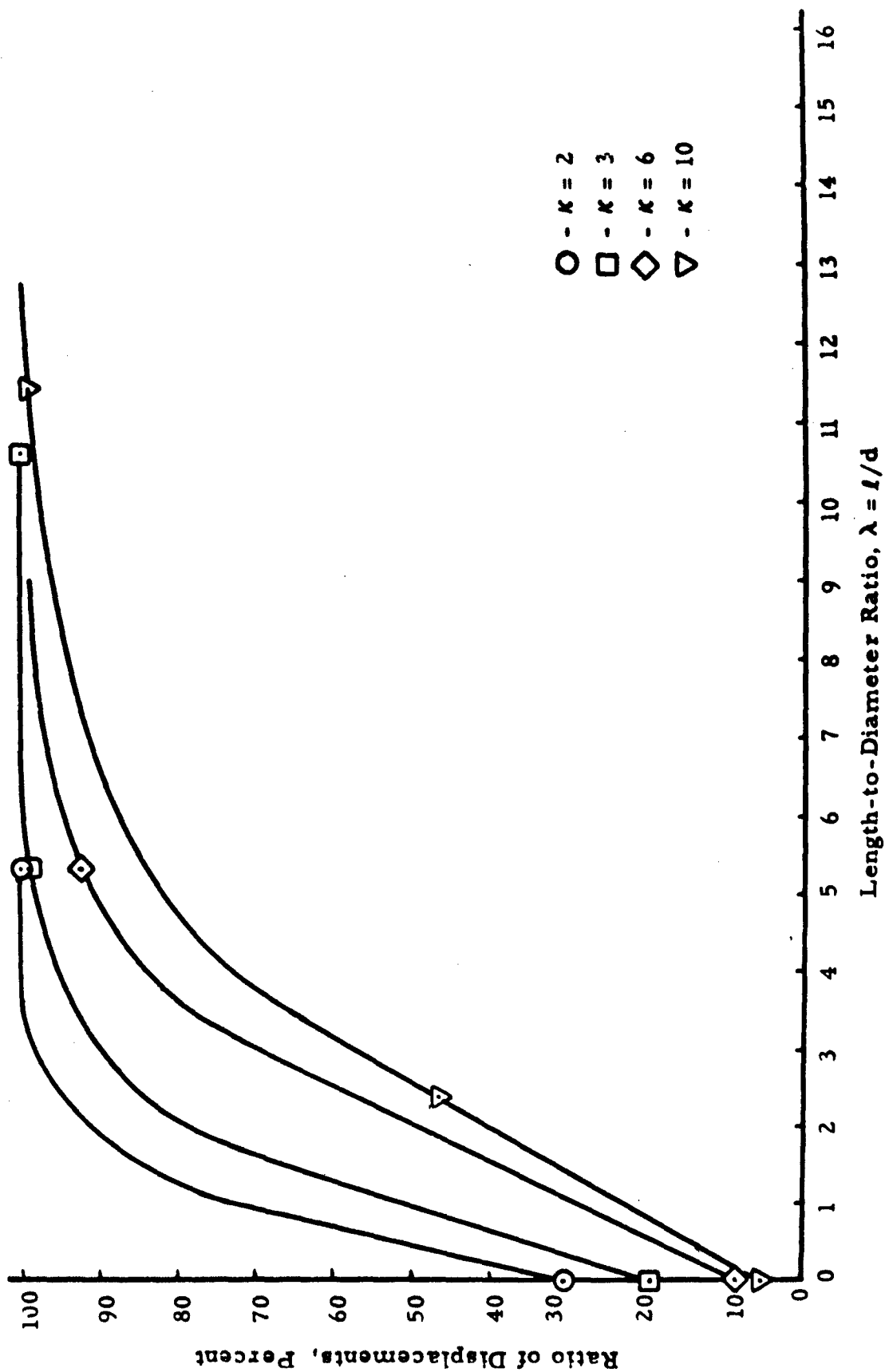
FIGURE 4.
RADIAL DISPLACEMENT AT INNER RADIUS IN MIDDLE OF CYLINDER OF FINITE LENGTH AS PERCENTAGE OF
RADIAL DISPLACEMENT IN EQUIVALENT CYLINDER OF INFINITE LENGTH $v = 0.49$.
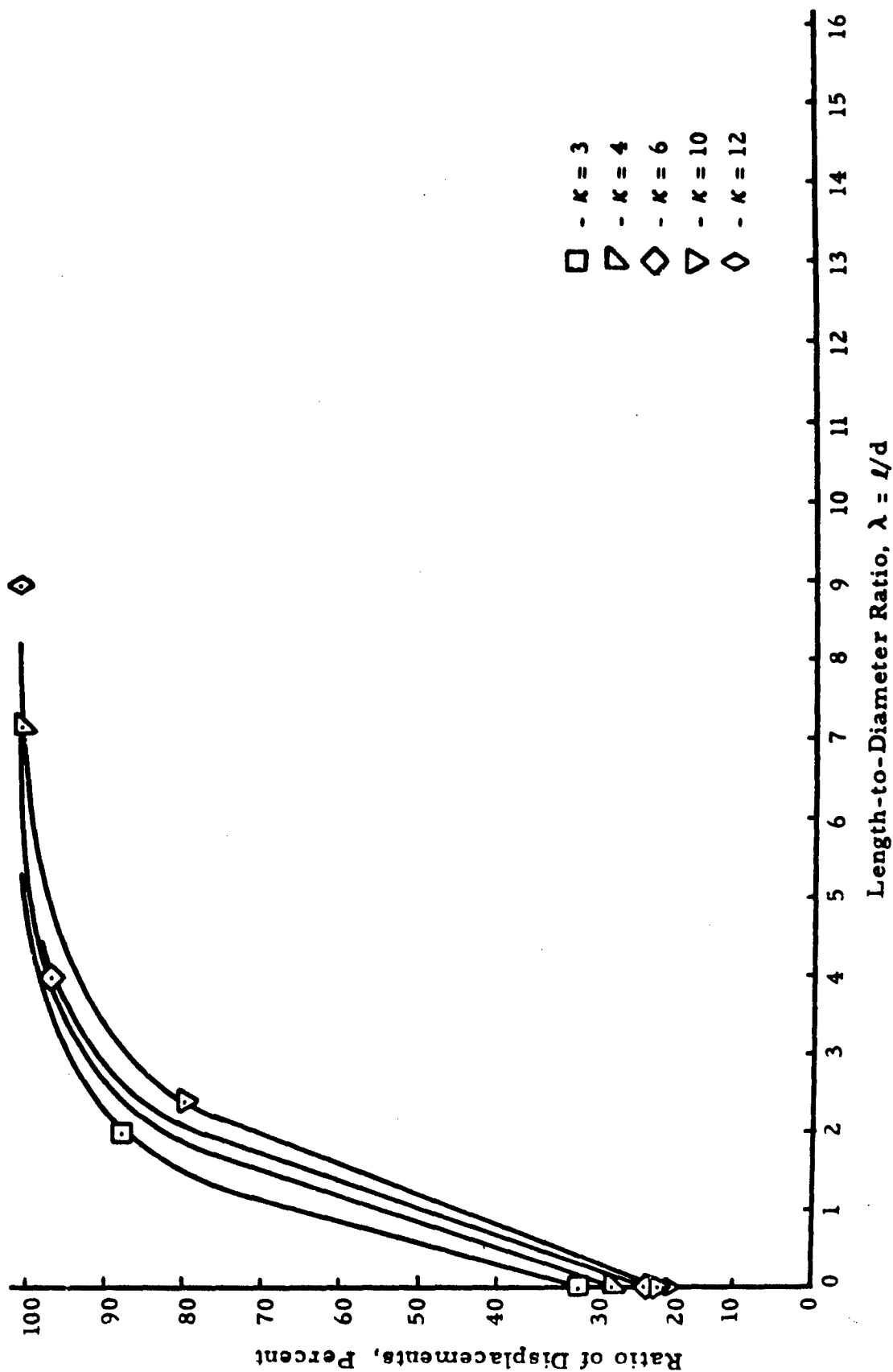
FIGURE 5.
RADIAL DISPLACEMENT AT INNER RADIUS IN MIDDLE OF CYLINDER OF FINITE LENGTH AS PERCENTAGE OF RADIAL DISPLACEMENT IN EQUIVALENT CYLINDER OF INFINITE LENGTH $\nu = 0.45$.
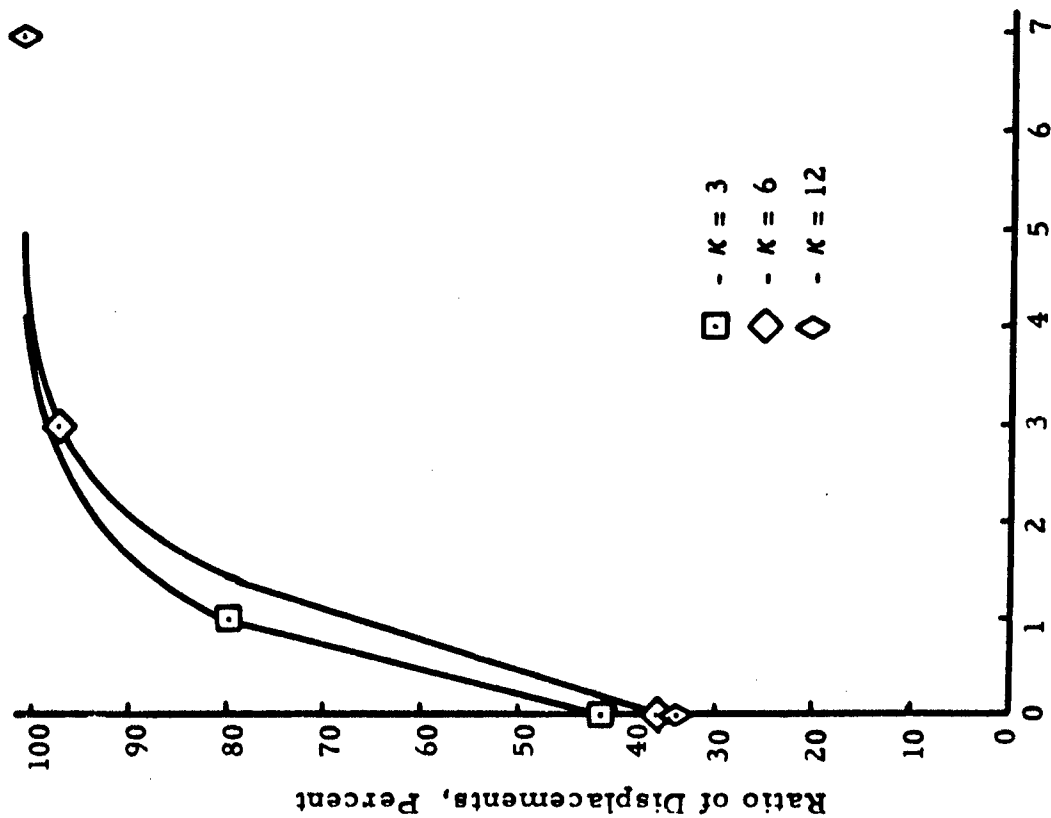
FIGURE 7. $\nu = 0.35$

FIGURE 6. $\nu = 0.40$
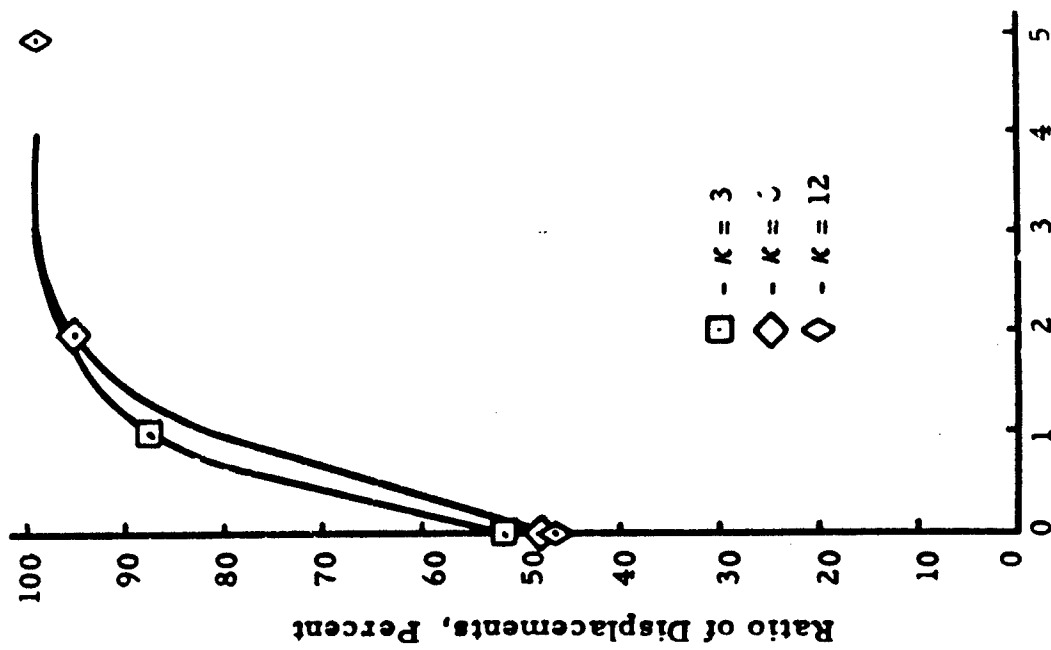
RADIAL DISPLACEMENT IN MIDDLE OF CYLINDER OF FINITE LENGTH AS PERCENTAGE OF RADIAL DISPLACEMENT IN EQUIVALENT CYLINDER OF INFINITE LENGTH.
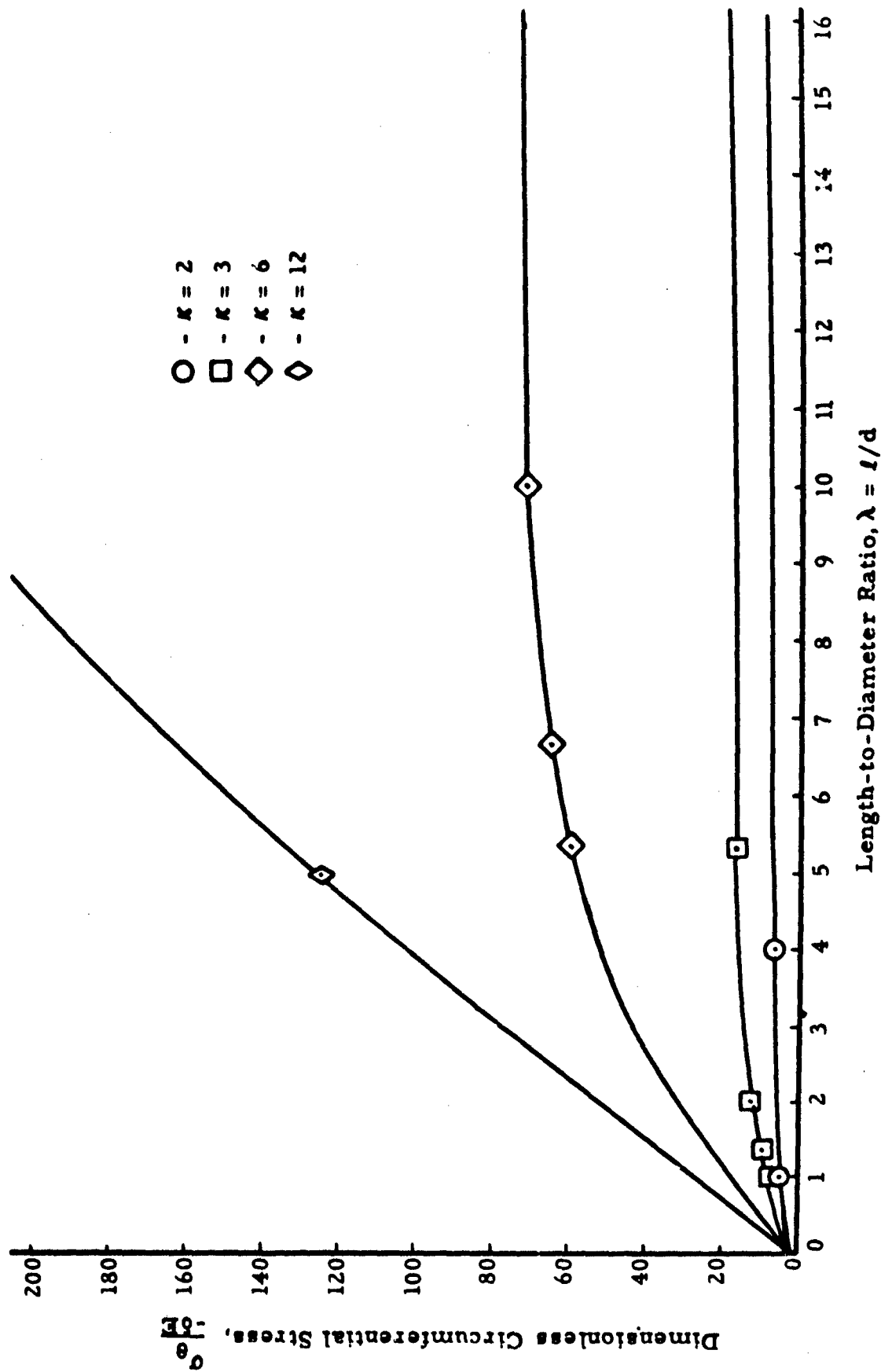
FIGURE 8.
RATIO OF CIRCUMFERENTIAL STRESS AT INNER RADIUS IN MIDDLE OF CYLINDER TO PRODUCT OF SHRINKAGE AND ELASTIC MODULUS, $\frac{\sigma_\theta}{-\delta E}$, AS A FUNCTION OF λ AND κ FOR $\nu = 0.50$.
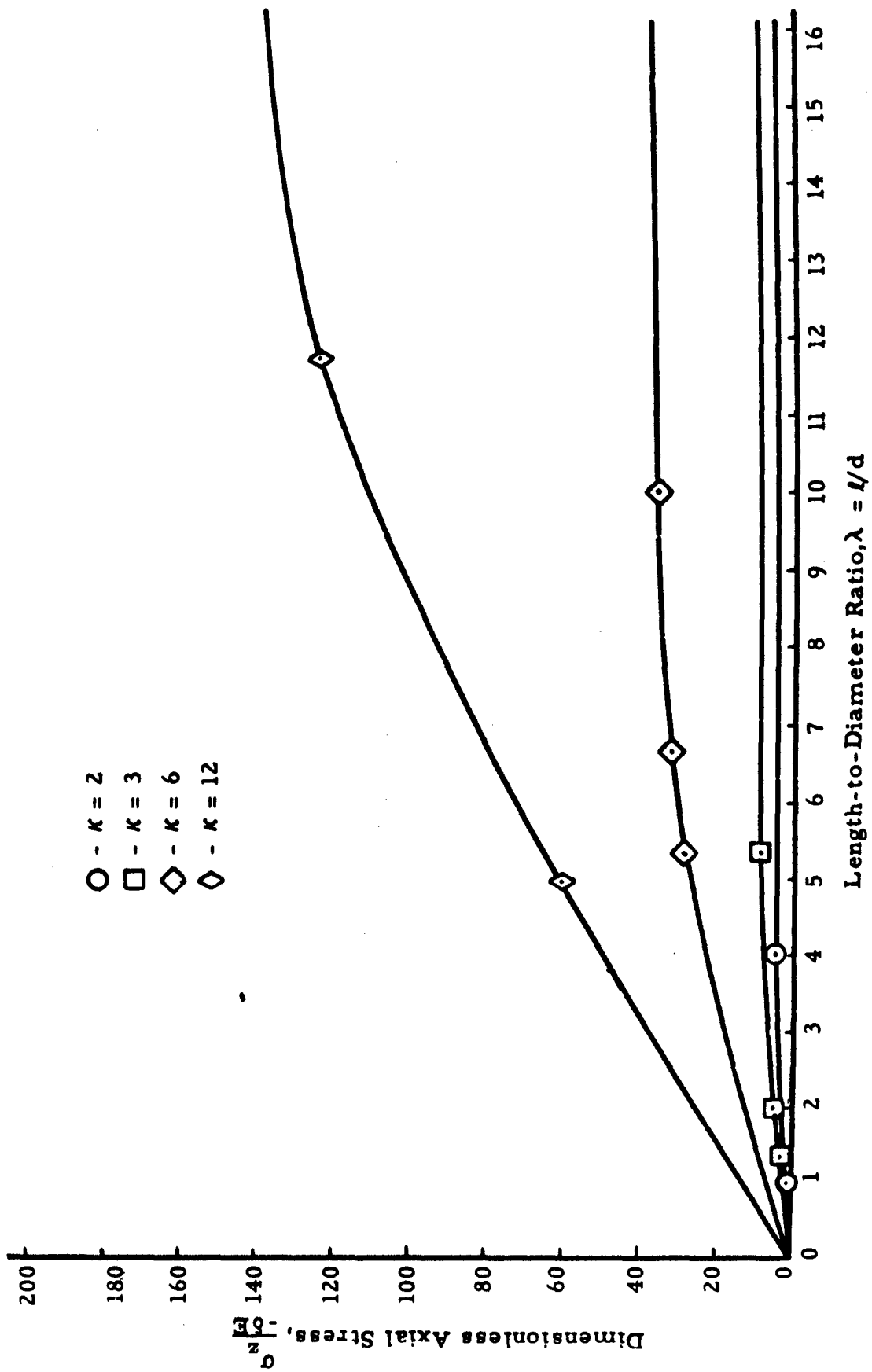
FIGURE 9.
RATIO OF AXIAL STRESS AT INNER RADIUS IN MIDDLE OF CYLINDER TO PRODUCT
OF SHRINKAGE AND ELASTIC MODULUS, $\frac{\sigma_z}{-\delta E}$, AS A FUNCTION OF λ AND κ FOR

Length-to-Diameter Ratio, $\lambda = \ell/d$

Dimensionless Axial Stress, $\frac{\sigma_z}{-\delta E}$

- $\kappa = 2$
- $\kappa = 3$
- $\kappa = 6$
- $\kappa = 12$

ENGINEERING ANALYSIS

K. L. Pister and J. S. Wise, Reporters

DEFORMATION OF CASE-BONDED PROPELLANTS UNDER AXIAL ACCELERATION

by
J. H. Thacher
Allegany Ballistics Laboratory
Rocket Center, West Virginia

ABSTRACT

An experimental method is described for determining deformations of casebonded propellant charges under axial accelerations similar to those encountered during flight. A twelve-inch diameter cylindrical steel case containing a fifteen inch long case-bonded charge with a six inch port was accelerated to approximately 40 "g" by means of the Allegany Ballistics Laboratory centrifuge. Measurements of deformations were made with linear potentiometers. Data from a base-restricted filled propellant (one containing metal fuel and solid oxidizer) and from a free-standing unfilled propellant approximating the binder composition of the filled propellant are presented. The results of these two tests cannot be directly compared to determine the effect of filler.

Experimental data are compared with the approximate linear viscoelastic theory of Williams and Knauss with respect to radial, axial, and time dependence of deformations. Limitations of both theory and experiment are discussed. Good agreement is obtained except at the bottom of the grain, where experimental measurements are larger than theoretical prediction.

INTRODUCTION

Large deformations of propellant induced by flight accelerations may be harmful to the ballistic performance of a rocket motor. Infinitesimal elastic and linear viscoelastic theories have been applied to the problem of slump in finite length, hollow, circular, case-bonded cylinders by Williams and Knauss.[2] An experiment to check this theory was conceived in collaboration with personnel from California Institute of Technology.[1] After a brief review of the theory, the experimental apparatus is described and the results reported and compared with theory.

THEORY

An approximate solution for the problem of slump in finite length hollow cylinders was obtained by the method of restricted variation of potential energy. The potential energy per unit volume was equated to the strain energy density minus the work done by the applied forces per unit volume. The strain energy was initially expressed in terms of the strain invariants. Product type functions were assumed for the radial displacement $u = R_1(r) g(z)$, and the axial displacement $w = R_2(r) f(z)$. Using these product type functions and the strain displacement relations for an axially symmetric body, the strain energy (and consequently the potential energy) was expressed in terms of R_1, R_2, f, g, and their derivatives. By performing the variation of the potential energy with respect to g and with respect to f and equating each variation equal to zero, and then combining these equations, the governing fourth order differential

equation yields a fourth order algebraic equation for the eigen values appearing in the hyperbolic functions of the general solution. Substituting the general solution in the variational equation gives the relationship between the arbitrary constants for the general solutions for f and g.

For the free standing grain, the requirement that the work on the end surfaces was zero was used as a boundary condition to evaluate the remaining constants. This means that forces are calculated on the free surfaces, but the calculated displacements are the best the assumptions will allow. For the base restricted grain, the condition is used that the displacement at the supported end is zero.

The following functions are assumed for R_1 and R_2

$$R_1 = \left(\frac{r}{b} - \frac{b}{r}\right),$$ the same as for a pressure type loading

$$R_2 = 1 - \left(\frac{r}{b}\right)^2 + 2 x^2 \ln \frac{r}{b},$$ the same as for slump in an infinitely long cylinder, where r = radius at any point within grain (inches)

$$x = a/b$$

a = inner radius of grain (inches)

b = outer radius of grain (inches)

Viscoelastic Solution

The elastic solution for radial and axial deformations is the product of a factor depending on Poisson's ratio and geometry Q, the number (n) times the acceleration of gravity multiplied by the density (ρ) and the reciprocal of the shear modulus (G)

$$w = \frac{Qn\rho}{G}$$

For a ramp type loading function (see Figure 3) using a 3-element model (a Maxwell model in parallel with a spring as in Figure 3) the force (F_0) displacement (δ) relationship is for $t \leq t_0$

$$\delta(t) = -\frac{F_0}{E_0} \frac{\tau_1}{t_0} \frac{E_1}{E_0} \left[1 - \exp\left(\frac{-E_0}{E_0 + E_1}\right)\frac{t}{\tau_1}\right] + \frac{F_0}{E_0}\frac{t}{t_0}$$

and $t \geq t_0$

$$\delta(t) = \frac{F_0}{E_0}\left\{1 + \left(\frac{\tau_1}{t_0}\right)\left(\frac{E_1}{E_0}\right)\left[1 - \exp\left(\frac{E_0}{E_0 + E_1}\right)\left(\frac{t_0}{\tau_1}\right)\right]\left[\exp\left(\frac{E_0}{E_0 + E_1}\right)\left(\frac{t}{\tau_1}\right)\right]\right\}$$

Where E_0, E_1 and τ_1 are model constants for the model shown in Figure 3 and t is the time, t_0 is the time required to reach maximum force, F_0.

In the viscoelastic solution $\frac{1}{G}$ is replaced by $\frac{3\delta(t)}{F}$, the three converting tensile to shear modulus. A viscoelastic solution using an integral operator to represent propellant response is available,[2] but sufficient data have not yet been obtained to use it.

EXPERIMENTAL

The experimental arrangement is presented in Figure 1. Propellants were cast in place using established case-bond systems. Measurements were made using linear potentiometers (Edcliffe 109079) to determine deformations. Ten, 1/2" x 1/2" x 1/32" brass tabs were bonded to the propellant grain to prevent direct contact of the potentiometers with propellant, a material which cannot withstand high bearing stress. The linear potentiometers measuring radial deformations were equipped with ball point pen attachments and the brass tabs were covered with paper to enable axial movement of the grain to be detected.

Procedure

The test assembly (Figure 1) was conditioned overnight at a temperature approximating the estimated temperature during the centrifuge test in order to minimize thermal stress. The test assembly was placed on the ABL centrifuge with its center of gravity 25 feet from the center of rotation. Axial acceleration was applied; the centrifuge was brought to the maximum "g" level as rapidly as possible and maintained at this acceleration for five minutes (several relaxation times of the propellant). From a typical acceleration vs. time curve (Figure 2) for the free standing unfilled propellant grain it is seen that a ramp type loading is a good approximation.

Propellant Properties

Two propellants were used in this program. One was a double base propellant with approximately 1:2 polymer to plasticizer ratio. The other used approximately the same binder matrix, but was filled with metal fuel (20 wt.%) and oxidizer (20 wt. %).

Poisson's Ratio

From extrapolation of deformed grid measurements of propellant samples to small strains, it is known that the correct value of Poisson's ratio to use in infinitesimal elasticity is approximately 0.5. However, the maximum value for which the theory is assumed to be valid is 0.46. Therefore a value for Poisson's ratio of 0.46 was used.

No quantitative estimate can be made of the error caused by the selection of Poisson's ratio = 0.46. Qualitatively, since the shear response is more important than the bulk response of the propellant in this problem, the exact value chosen for Poisson's ratio is not expected to be critical.

Shear Modulus

The time-dependent shear modulus is assumed to be 1/3 the time dependent tensile modulus as determined from tensile creep and recovery data. Sample creep and recovery data for the unfilled propellant at 90°F. are compared with the 3-element model data in Figure 3. The model constants giving the best fit were $E_1 = E_0 = 223$ psi., $T_1 = 71$ seconds. Constant load data were corrected to an effective value of stress by assuming constancy of volume of material. The strain was then related to the initial stress by multiplying by the ratio of initial and actual stresses. The

recovery of the sample is expressed as the maximum length minus the actual length at a later time divided by the initial length of the sample at the beginning of the creep and recovery experiments.

The shear modulus of the filled propellant at 40°F. is 1350 psi.

Density

Density of unfilled propellant 0.056 lb./in.^{3}
Density of filled propellant 0.065 lb./in.^{3}

Results and Discussions

Unfilled Free Standing Propellant Grain Centrifuged to 28 "g" at 90°F.

The deformed shape of the grain showing maximum deformations at experimentally recorded points together with the theoretical values at these same points is shown in Figure 4.

The deformations predicted for the above free standing grain are intermediate between those of an infinitely long grain and those of a 1.25:1 length:diameter ratio calculated by Williams and Knauss.[2] The observed radial deformations agree with the calculated values within an order of magnitude. The limited accuracy of linear potentiometers in this range of displacements prevents a more exact comparison of theory and experiment.

The experimentally measured axial deformations at the top of the grain are in very good agreement with the theory; the axial deformations at the bottom of the grain, however, are much larger than the theoretical values. No explanation for this discrepancy can be given at the present time, but it is interesting to note that Power observed the same effect in gelatin models.[3]

Time Dependence

Theoretical and experimental time dependence of the displacements is shown in Figure 5. The experimental data are scattered about the theoretical lines, but the general agreement with theory should be noted. Again no explanation is given for the extremely high values for deformations at potentiometer No. 9 (See Figure 4.)

Filled Base Restricted Propellant Grain Centrifuged to 40 "g" at 40°F.

The maximum radial deformation in a base-restricted propellant grain is given by Knauss as $\dfrac{0.015}{4} \dfrac{b^2}{G} \rho ng$

$$= \frac{0.015}{4} \frac{(36)\ (0.065)\ (40)}{1350} = 2.6 \times 10^{-4} \quad \text{inches}$$

Observed experimental readings were too small to measure which is consistent with the theory.

ASSUMPTIONS

Theoretical assumptions are those involved in the use of infinitesimal linear viscoelastic theory, the approximate nature of energy methods, 1 to 3 dimensional association, ramp type discontinuity, and the choice of Poisson's ratio.

Experimental errors occur in the conversion of constant load data to constant stress data, the use of linear potentiometers for small measurements, the restraining effect of the tabs on the propellant, and the bearing pressure of the potentiometer on the grain. Additional experiments showed these last two effects were small.[4]

REMARKS

Additional tests with a base-restricted unfilled propellant charge and with a free standing filled propellant charge were contemplated, but experimental difficulties prevented their completion. When such tests are completed, it should be possible to estimate the slump characteristics in actual rocket motors of propellants with various amounts of filler showing only Poisson's ratio and uniaxial creep and recovery properties. There is no a priori reason why filled and unfilled propellants should have different types of rheological responses.

The agreement between theory and experiment gives added confidence in the application of energy methods to problems of this type. The application of energy methods to more complex geometries should be considered.

CONCLUSIONS

An experimental check has been run on a theoretical analysis of a finite length case-bonded propellant charge under axial acceleration where it is possible to check with present equipment. Agreement is good except at the bottom of the propellant where deformations are much larger than theoretical. A base-restricted filled propellant also showed results consistent with theory.

BIBLIOGRAPHY

(1) Fourney, M. E., "Test Procedure for Determining Slump Characteristics of a Solid Propellant Rocket Engine Under Axial Acceleration," Southwest Engineers Technical Report 60-?, Pasadena, California, July 1960.

(2) Knauss, W. G., "Displacements in a Finite Hollow Cylinder Under Axial Acceleration," Galcit SM-59-9, Galcit SM-60-17 and Galcit 61-10, California Institute of Technology, July 1959, January 1961 and April 1961.

(3) Power, A. M., GCR Report No. P-0062-61 (CONFIDENTIAL), June 1961.

(4) Thacher, J. H., Research Progress Report, Code A2-52, July 3, 1961.
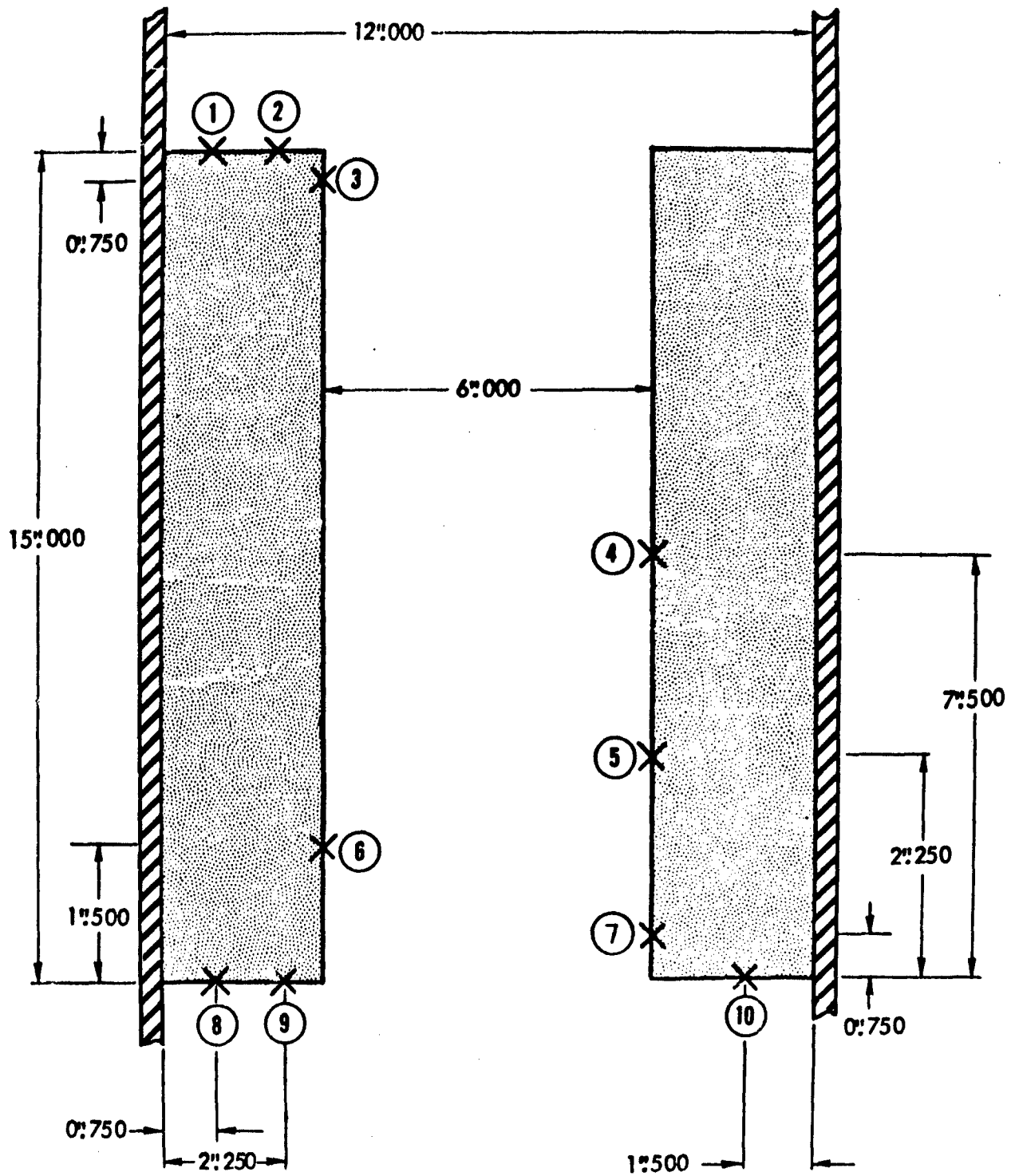
CIRCLED NUMBERS INDICATE LINEAR POTENTIOMETER LOCATIONS

FIGURE 1. CENTRIFUGE SLUMP TEST FREE STANDING UNFILLED PROPELLANT GRAIN
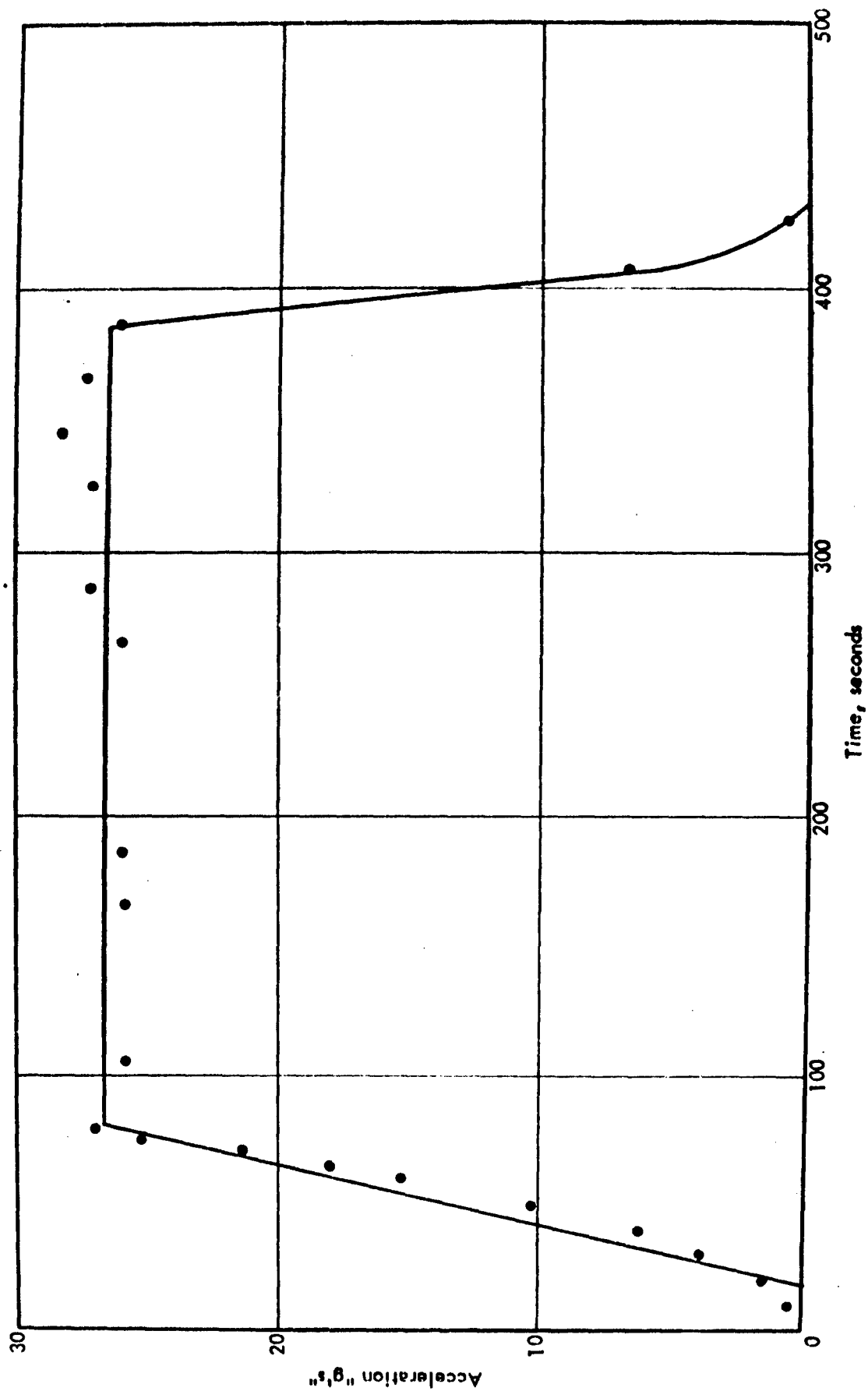
FIGURE 2. AXIAL ACCELERATION OF THE TEST ASSEMBLY APPLIED BY THE CENTRIFUGE VS TIME
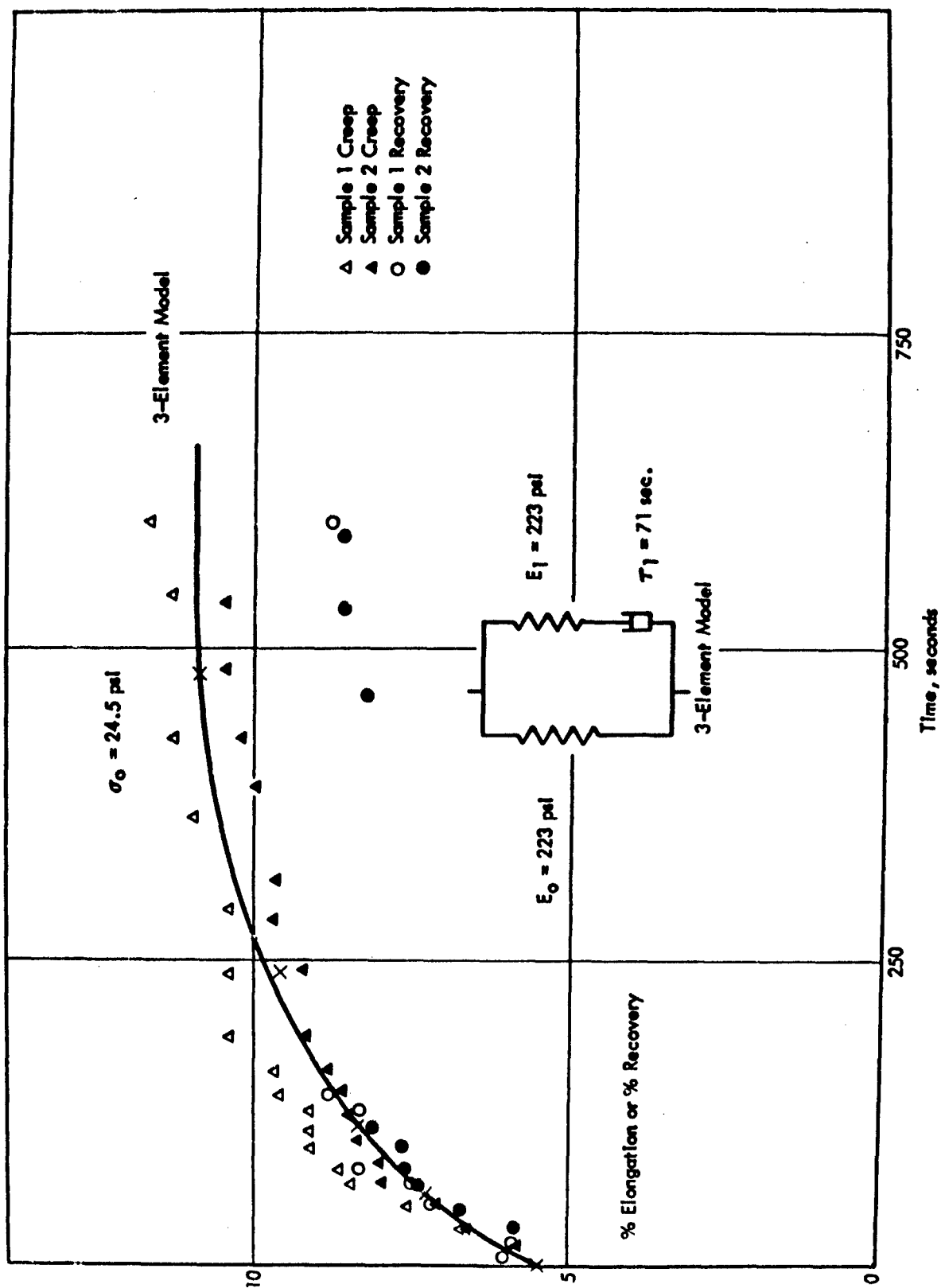
FIGURE 3. TENSILE CREEP UNFILLED PROPELLANT 90°F.

Axial Deformations at Ends

Radial Deformation at Inner Radius
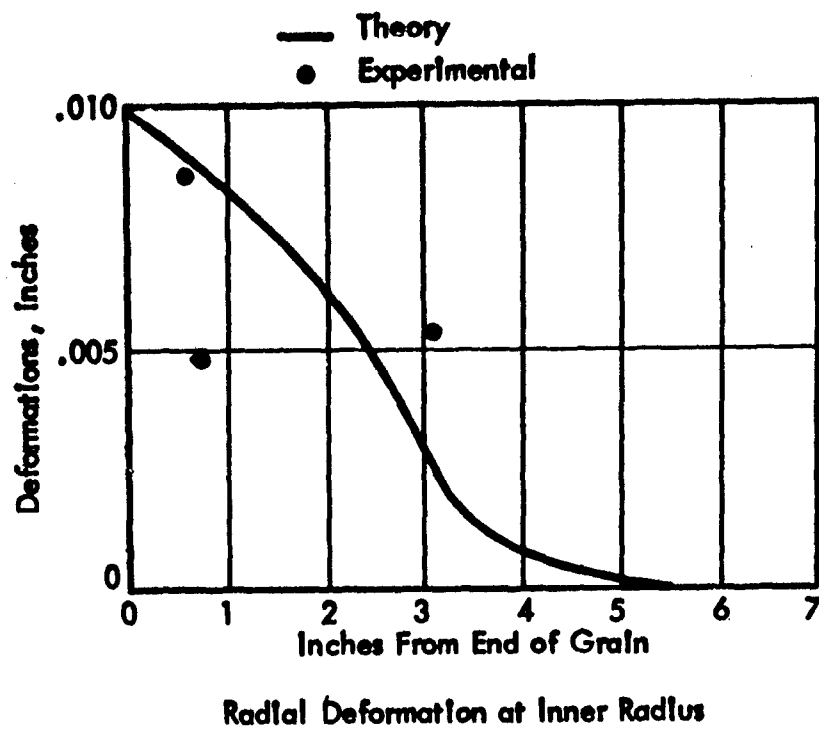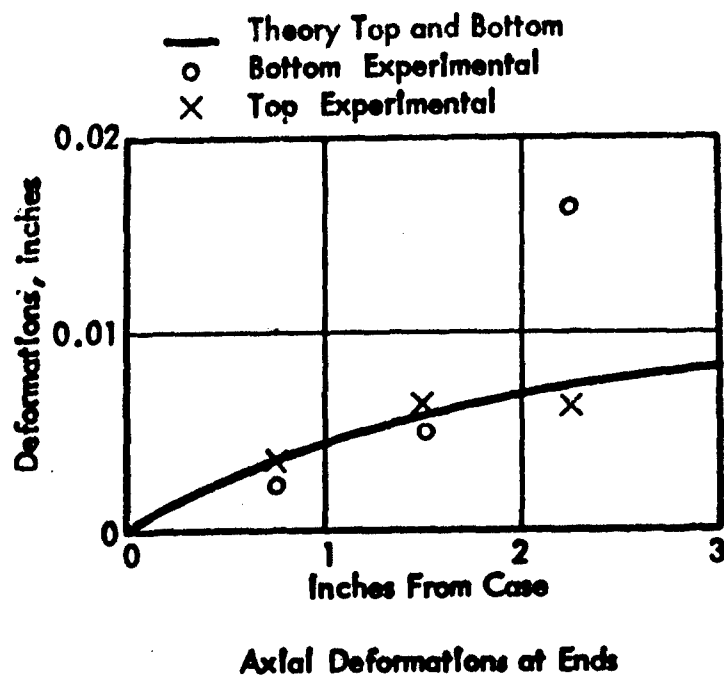
FIGURE 4. DEFORMED GRAIN SHAPE (NOTE SCALE)
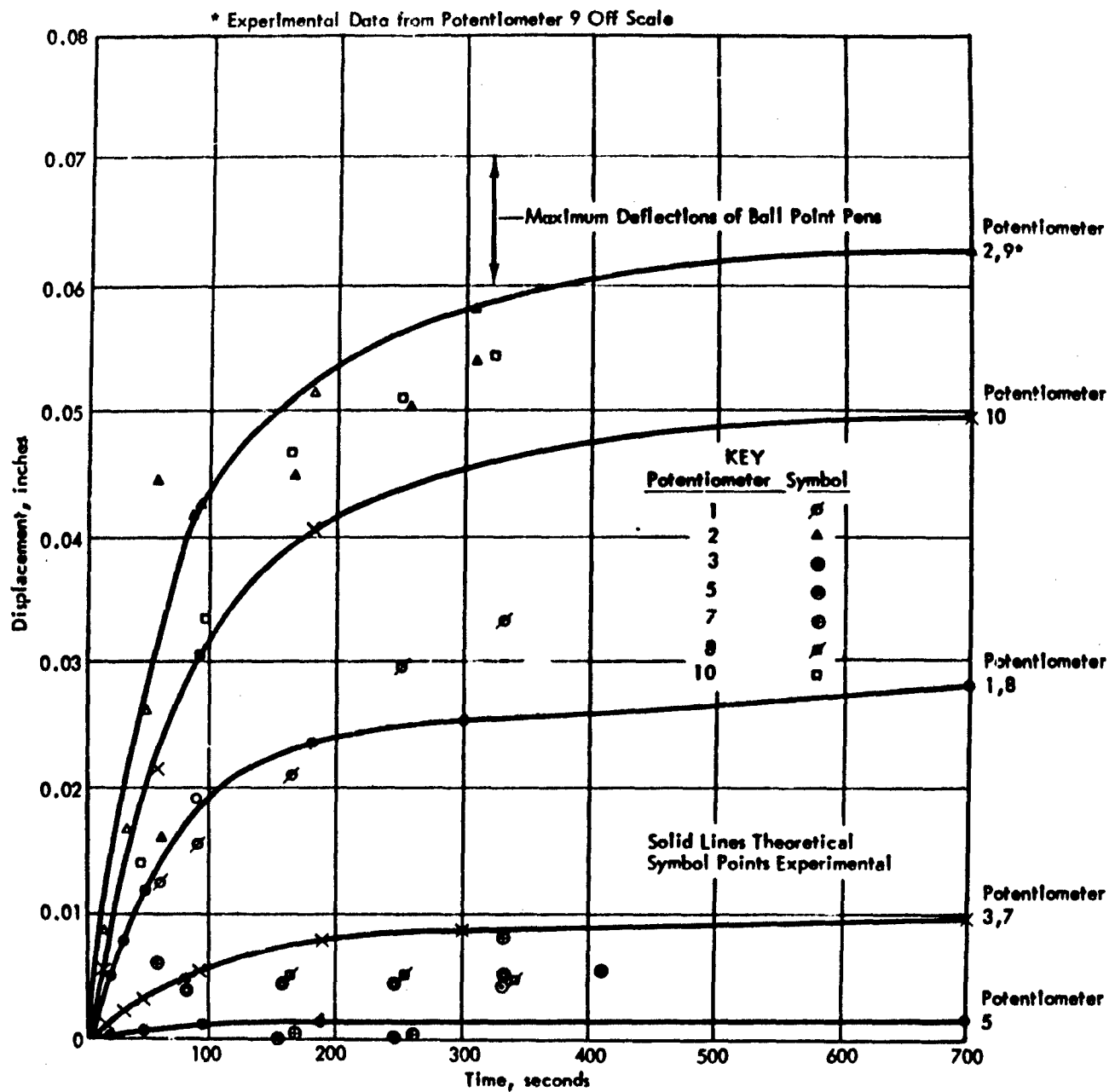
FIGURE 5.   TIME DEPENDENCE OF DEFORMATIONS

MOTOR STRAIN TESTING[1]

Clarke H. Lewis, Jr.
Research Engineer, Polymer Research Section

Jet Propulsion Laboratory
California Institute of Technology
Pasadena, California

ABSTRACT

A study at the Jet Propulsion Laboratory on the deflections of the inner surface of an internally-pressurized tubular-port propellant grain, case-bonded in a thin-walled chamber, is discussed. The effects of the $(b/a)^2$ ratio, pressurization rate, and pressure level are under investigation. The results of tests to date are presented and a comparison with a theoretical analysis based on small deformation elastic theory is made. The test apparatus is also described.

INTRODUCTION

One of the most difficult tasks in solid-propellant motor design is that of determining the suitability of a particular propellant-motor geometry combination with respect to anticipated thermal and pressure loadings. In every case, extensive experimental verification is required and, more often than not, modification of the design and even the propellant is necessary to produce a workable system.

Attempts have been made to correlate the behavior of a propellant grain under various loadings with uniaxial test data. None of these attempts have been particularly successful. Knowledge is very lacking of the manner in which strains are distributed in a grain configuration under thermal or pressure loading. Equally scanty is knowledge of the behavior of propellants in multiaxial stress-strain fields.

Increased effort is being expended in studying multiaxial problems, both experimentally and, theoretically. The program described below is itself designed to study the mechanical behavior of a composite solid propellant in situations more closely akin to operational environments. The initial part of the program has been a study of the effects of internal

---

pressurization. Subsequently an investigation of thermal cycling will be made in an effort to determine thermal loading and temperature history effects and to try to integrate these effects up to and including operational pressurization.

EXPERIMENTAL PROCEDURE

The test motor (Fig. 1) is a 7075-T6 aluminum chamber with a wall thickness of 0.040 in. at the center of the case test section. The propellant grain is trimmed back 3.75 in. from each end so that the grain lies wholly in the thin portion of the case. The ends of the case are tapered and threaded to accommodate heavy end caps. The inside diameter of the case is 2.646 in., and the web thickness is adjusted by the use of mandrels which vary from 1.000 to 0.265 in. in diameter to give $(b/a)^2$ ratios from 7 to 100.

A schematic diagram of the pressurization system is given in Fig. 2. Nitrogen at a constant pressure flows through an orifice into an accumulator whose volume can be adjusted. The nitrogen pressure, orifice diameter and free volume determine the rate of pressure rise. The accumulator pressure is amplified by a differential piston intensifier. Mineral oil is used downstream of the intensifier to pressurize the test motor at a rate that can be preset from 5 psi/sec to 50 psi/sec. By adjusting the parameters, it is possible to achieve pressurization rates that are linear over the pressure range and rate range of interest, to within 2%.

The pressure, circumferential strain, and axial strain of the outside of the case at its longitudinal center, and the change in inside radius of the grain at its longitudinal center are recorded during the test. The case strains are measured by SR-4 strain gages and the pressure is detected by the Statham pressure gage (Fig. 3). The change in inside radius is detected by a probe designed at JPL specifically for this test (Fig. 4). The probe consists of a pivoted beam with a steel ball on one end which rests against the propellant inner surface. The other end of the beam is attached to the movable core of a differential transformer set into the probe base. The base is located by pins in the end cap so that the movable core of the transformer is in the most linear region for each mandrel size, and, in addition, the beam pivot is placed so that the ball end of the beam contacts the propellant in the center of the longitudinal axis of the test chamber. The small spring holds the beam against the propellant surface with a force at the ball end that varies in the normal case from 2 to 4 grams.

Excitation of the transformer is done with a Wiancko system (Fig. 5). The sensitivity of this system is such that it is possible to detect movements of as little as 0.0002 in. over a range of 0.020 in. and yet still be able to monitor movements up to 0.250 in. Calibration

of the probe is done in a jig (Fig. 6) which is a replica of the end and inside geometry of the test chamber. The ball is positioned by a micrometer depth gage in a slot which is precisely located with respect to the center line of the chamber.

The accuracy figure stated above is true, strictly speaking, in one direction only as the probe has some mechanical hysterisis. For this reason calibration is done in the direction of increasing radius only. In use, the ball end of the beam is held off the propellant surface during assembly of the case and upper cap by a thin metal tube placed in the bore. After the cap is in place, the tube is withdrawn and the end of the beam is let down on the propellant surface. This method seems to be a satisfactory method of dealing with the hysteresis problem.

With the probe in place, the motor is placed in the test fixture (Fig. 3), evacuated, and filled with mineral oil. At this point, the operation becomes remote and the test is made.

DISCUSSION

Tests have been run and the data reduced on motors of $(b/a)^2$ ratio of 7 to 25 at a single rate of 20 psi/sec. The results of these tests are shown as points in Fig. 7, where the percentage change of the inner radius is plotted against $(b/a)^2$. Also shown in point form is the change of radius that would result if the inner surface deformed in a geometrically similar manner with respect to the case deformations and with no change in volume of the propellant. It is interesting to note that the agreement is quite good.

The curves in Fig. 7 are derived from small-deformation elastic theory for plane strain of an internally pressurized case-bonded propellant grain using a theoretical model (Ref. 1) fairly similar to the experimental configuration used in these tests. The difference is that the theoretical case assumes the propellant is cast completely up to the ends and bonded there, while the test motor grain is trimmed back and has the full bore pressure acting on it. The motor is made long to minimize this end effect within the midsection.

In the theoretical treatment, both the case and the propellant grain are considered elastic. Stresses are specified which match boundary conditions, and then the strains and displacements are determined within the requirement that at the bonded surfaces the stresses and displacements match between propellant and case. This development is most accurate for small strains, but should be useful in indicating trends for large strains. Experimentally and theoretically the effects of the axial strain are small, so that a considerable reduction in the complexity of the equations can be made with the assumption of plane

strain. The plane-strain hoop stresses and strains are quite close to those of the three-dimensional model, particularly in the incompressible region (Ref. 2).

The parameters used in the plane-strain equation in Fig. 7 were $E = 10^3$ psi and ν for the propellant of 0.5000 and 0.4995. The actual modulus of this propellant, using a JANAF uniaxial tensile test at the strain rates of this experiment, is of the order of 600 psi; however, using a larger tensile specimen and a photographic measurement of strains, the modulus tends to be closer to 10^3 psi. In any event the effect of modulus on inside strain should be small - below $E = 10^3$ psi for motors with $(b/a)^2 \leq 25$ and $\nu = 0.500$ (Ref. 3). The effect of hydrostatic pressure on the modulus in tension was not considered, but it would probably cause an increase (Ref. 4). The change in radius with pressure in these tests is linear within the accuracy of the measurements, so that the test results were normalized to a common pressure.

Based on the agreement of the data with the plane-strain treatment, the theory could be used to extrapolate these results to predict strains at higher $(b/a)^2$ ratios (Fig. 8). At $(b/a)^2 > 50$, it is predicted that strains in excess of 20% and even 30% are to be obtained during some part of the test. Thus it is to be expected that failures will occur and that the inside-diameter measuring probe will detect the development of cracks. A few tests have been run at $(b/a)^2$ ratios of 50, 75, and 100. Data reduction is not yet complete, but preliminary results indicate that the hoop strains are falling increasingly below the theoretical curve as the $(b/a)^2$ ratio increases. However, the case deformation is not decreasing rapidly enough to indicate that the effective modulus of the propellant is increasing. A probable explanation for this is that the end effects are becoming important and that compressive axial strain near the inner surface is reducing the radial movement of the propellant inner surface at the center.

SUMMARY AND CONCLUSIONS

The deflections of the midpoint of the inner surface of a tubular bore case-bonded propellant grain pressurized at a constant rate of 20 psi/sec have been measured over a range of $(b/a)^2$ ratio from 7 to 25. The data obtained agree very well with the equation for plane strain of a case-bonded grain using a modulus of the propellant equal to 10^3 psi and assuming that ν of the propellant = 0.5000. It is not possible to state conclusively here, but it appears, that the agreement will be less satisfactory at higher $(b/a)^2$ ratios.

REFERENCES

1. Williams, M. L., Blatz, P. J., and Schapery, R. A., Fundamental Studies Relating to Systems Analysis of Solid Propellants, GALCIT SM 61-5. Guggenheim Aeronautical Laboratory, California Institute of Technology, Pasadena, California.

2. Quarterly Summary Report No. 38-1. Jet Propulsion Laboratory, Pasadena, California, August 31, 1960 (Confidential)

3. Quarterly Summary Report No. 38-4. Jet Propulsion Laboratory, Pasadena, California, (Confidential)

4. Surland, C. C. and Jacobs, J. M., "Measurement of Triaxial Strains from Hydrostatic Stress", Bulletin of the 18th JANAF Meeting on Physical Properties of Propellants, Solid Propellant Information Agency, The Johns Hopkins University, Silver Spring, Maryland, June 1959.

MANDREL DIMENSIONS		
PART NO	A dia	(b/a)²
-6	1.000	7
-5	0.837	10
-4	0.529	25
-3	0.374	50
-2	0.306	75
-1	0.265	100

ALL DIMENSIONS IN INCHES
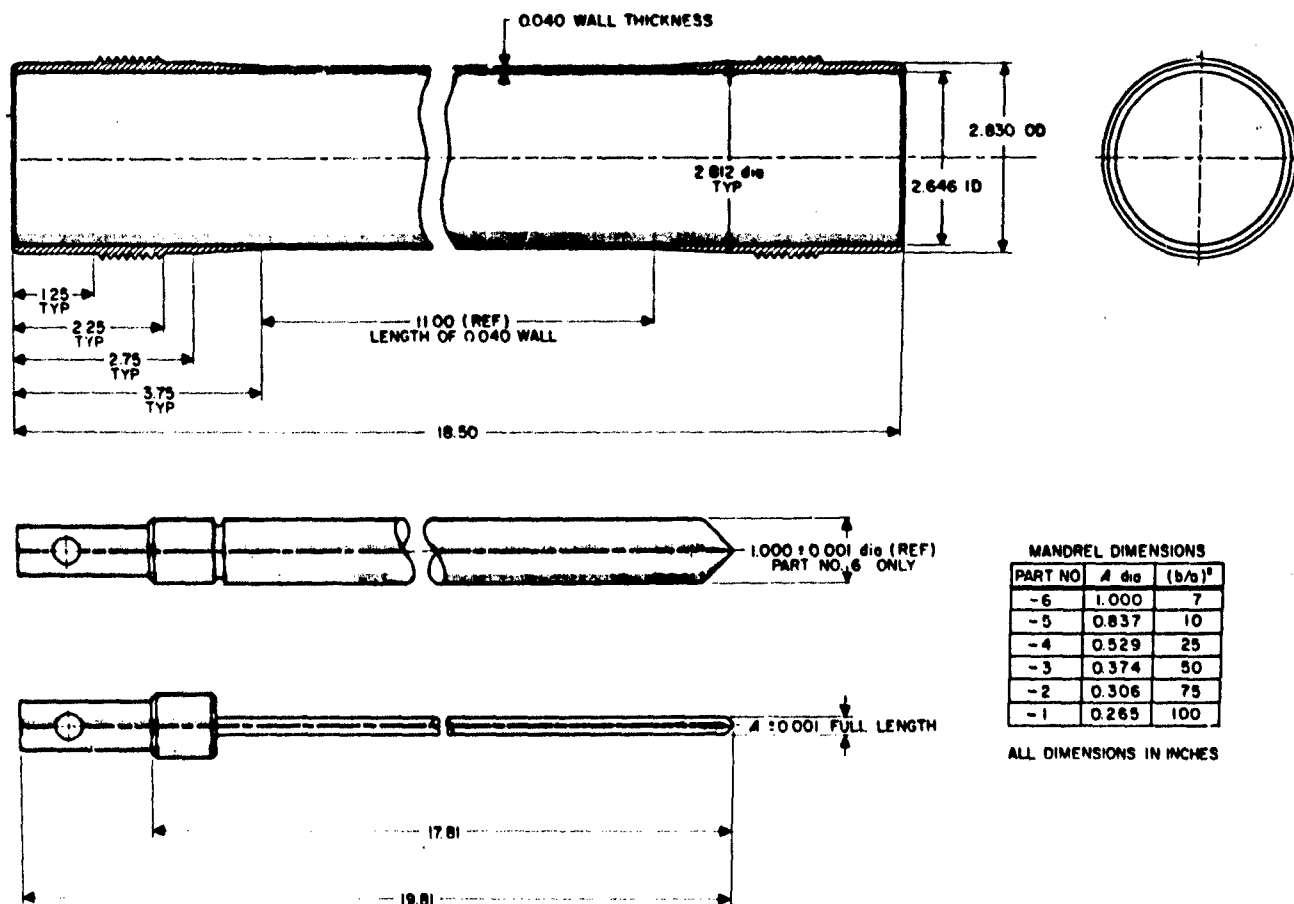
FIGURE 1. STRAIN-TEST MOTOR CASE AND MANDRELS
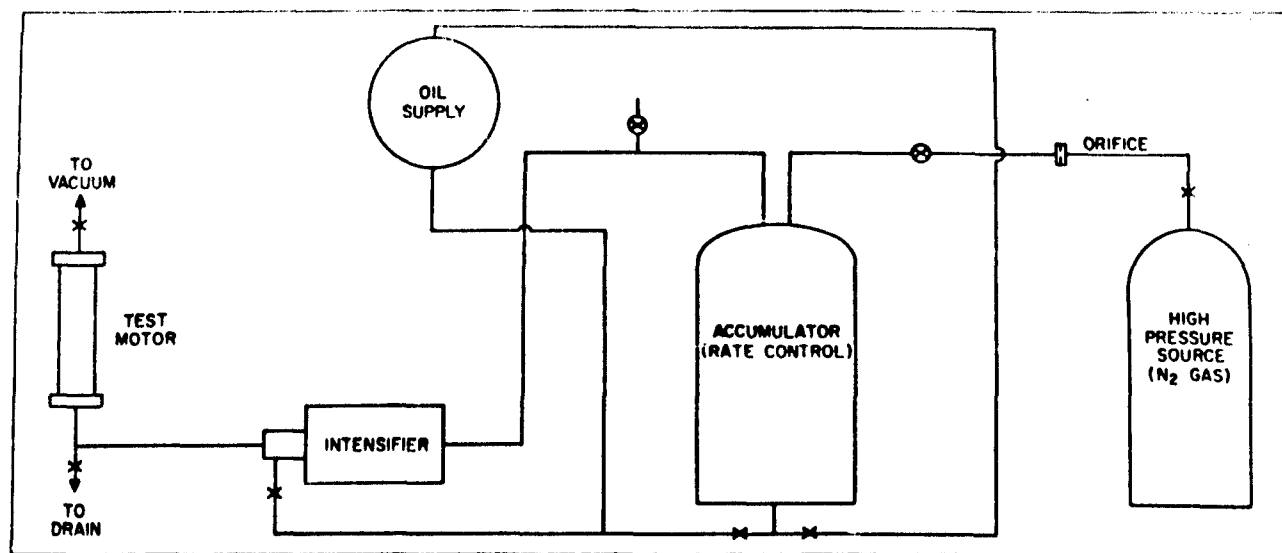
FIGURE 2. STRAIN-TEST MOTOR-PRESSURIZATION SYSTEM
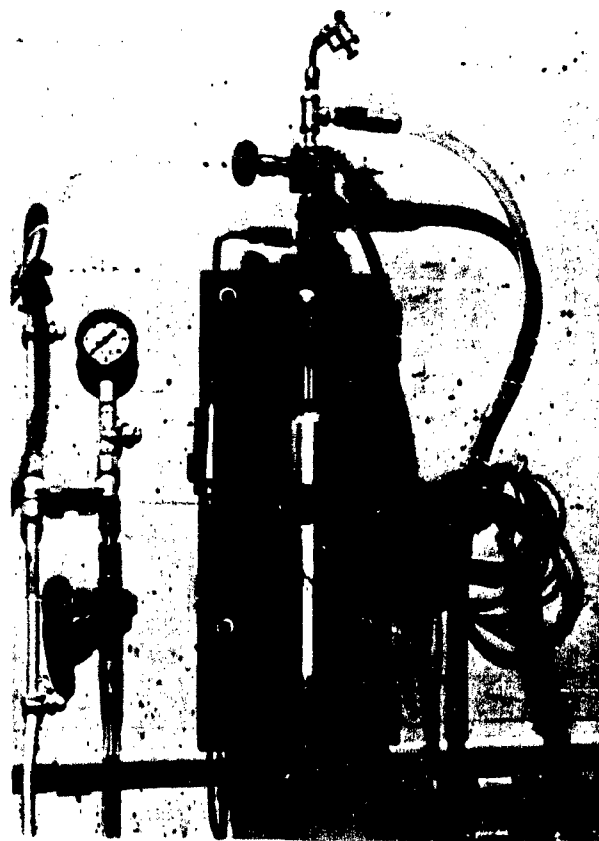
FIGURE 3.
DISPLACEMENT-MEASURING SETUP
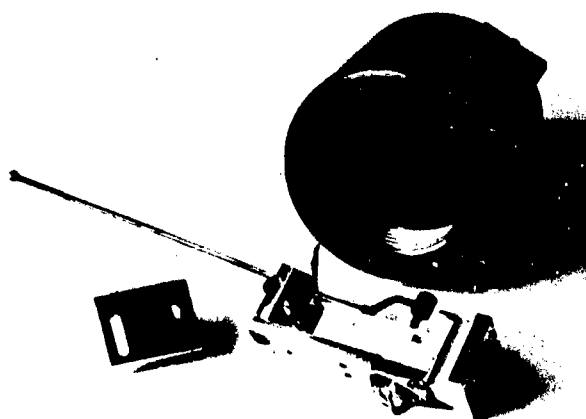
FIGURE 4.
PROBE FOR DETECTING INNER-SURFACE
RADIAL DISPLACEMENTS
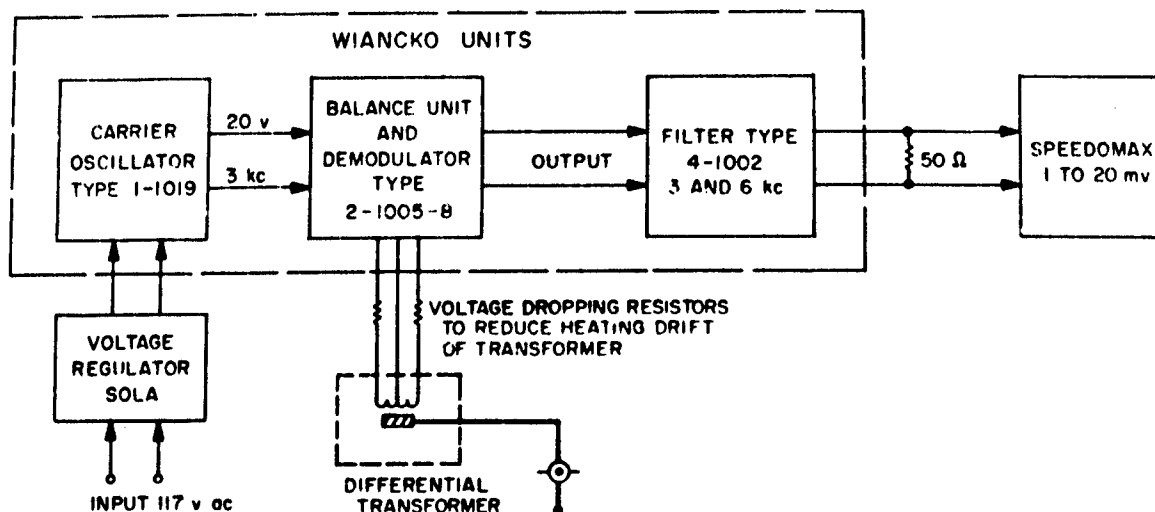
FIGURE 5. INSTRUMENTATION SYSTEM FOR PROBE

WIANCKO UNITS

CARRIER OSCILLATOR TYPE 1-1019 — 20 v, 3 kc → BALANCE UNIT AND DEMODULATOR TYPE 2-1005-8 — OUTPUT → FILTER TYPE 4-1002 3 AND 6 kc — 50 Ω → SPEEDOMAX 1 TO 20 mv

VOLTAGE REGULATOR SOLA

INPUT 117 v ac

VOLTAGE DROPPING RESISTORS TO REDUCE HEATING DRIFT OF TRANSFORMER

DIFFERENTIAL TRANSFORMER
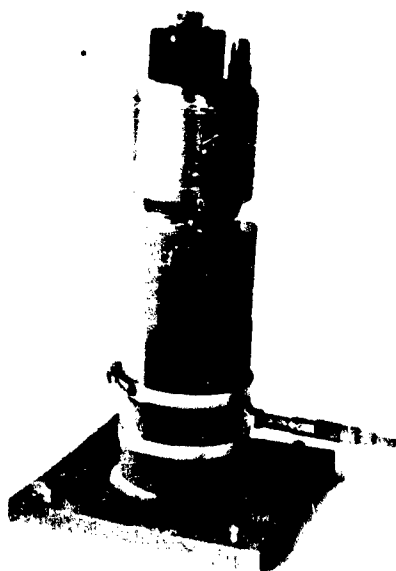
FIGURE 6. CALIBRATION JIG FOR PROBE

- RADIUS MEASUREMENT
- + CALCULATED FROM CASE ELONGATIONS, ASSUMING NO VOLUME CHANGE OF THE PROPELLENT

THEORETICAL EQUATION FOR PLANE STRAIN $E = 10^3$ psi
——— $\nu = 0.5000$
------- $\nu = 0.4995$
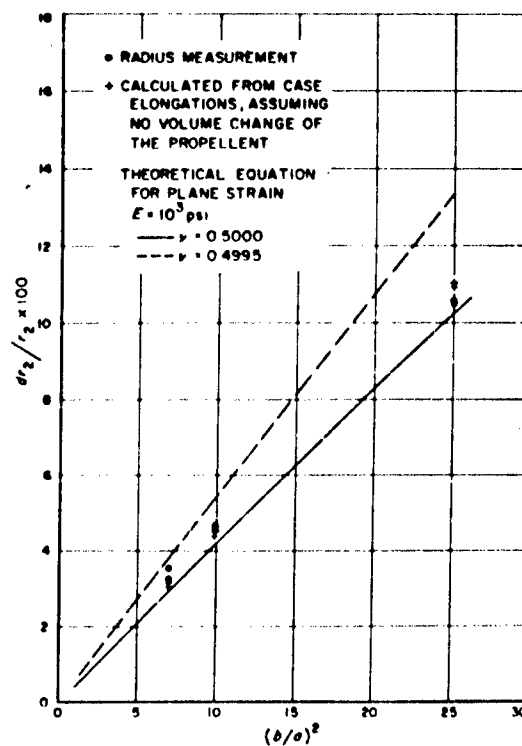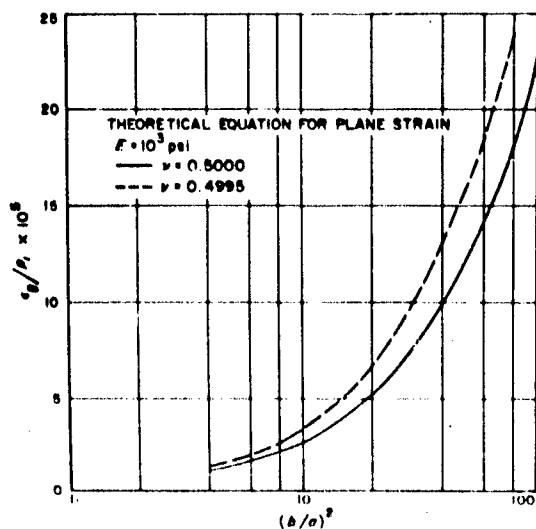
FIGURE 7.
TEST RESULTS NORMALIZED TO 1000 PSI

THEORETICAL EQUATION FOR PLANE STRAIN $E = 10^3$ psi
——— $\nu = 0.5000$
------- $\nu = 0.4995$

FIGURE 8.
TANGENTIAL STRAIN AT INNER PERIPHERY AS A FUNCTION OF WEB STRAIN

COMPUTATION OF THE THERMAL HISTORY OF A

SOLID PROPELLANT GRAIN DURING PROCESSING

Frank A. Graf, Jr.

Process Department

Wasatch Division

Thiokol Chemical Corporation

ABSTRACT

A two dimensional heat conduction problem, with associated heat generation for a large Polybutadiene Acrylic Acid (PBAA) propellant grain, was solved in the experimental program with which this paper deals. The equation was solved for a grain with a star-shaped cavity. The frequency factor, heat of reaction, and activation energy of the polymer binder system was evaluated by trial and error on the analog computer. The resulting values are influenced by the zero order reaction assumption. With the equation solved, various processing cycles were evaluated.

INTRODUCTION

This paper discusses the investigation of two dimensional heat conduction with associated heat generation for a large Polybutadiene Acrylic Acid (PBAA) propellant grain. The grain was cast with a star-shaped core. Other authors have found solutions to annular or solid cylindrical grain configurations, but these solutions were one dimensional and academic. (See Bibliography 1, 2, 3, and 4)

The heat generation term in the heat transfer equation was assumed to follow the Arrhenius expression, but no method of evaluating the activation energy and frequency factor was described.

Large solid PBAA propellant grains have exhibited an appreciable exothermic heat of reaction during cure. This phenomenon was not detected with smaller masses due to heat losses. Laboratory determinations of exothermic heat were not successful due to the slow reaction rate of the PBAA propellant curing system.

The temperature distribution encountered in a large PBAA propellant grain during different processing cycles was investigated. When the thermal gradients during the curing process were fully calculable, improved processing cycles could be evaluated.

An analog computer was used to simulate the curing reaction, since installation of thermocouples through a large live propellant grain was not possible. An engine case which was to be cast with inert propellant was available for a processing study.

The inert propellant grain was extensively thermocoupled so that the temperature profiles could be studied. The propellant had the same polymeric binder system, except that a different percentage of polymer was used than is normally compounded in live propellant.

EVALUATION OF PHYSICAL PROPERTIES FOR COMPUTER STUDY

The heat of reaction could not be successfully determined by using small samples in the laboratory. The maximum temperature increase experienced in the inert propellant was corrected for heat losses. The calculated heat of reaction determined from this experiment was initially used in the heat transfer equation. It was assumed that the heat of reaction would be constant over the temperature range studied.

The activation energy was calculated from curing data determined for the propellant system at various temperatures. The reaction rates were not known. The average reaction rate was assumed to be inversely proportional to the elapsed time necessary to partially cure the propellant. By using the equation:

$$E = \frac{RT_1 T_2}{T_2 - T_1} \ln \frac{t_1}{t_2}$$

a value was obtained for the activation energy. The propellant binder system curing reaction was composed of several complex reactions. This procedure yielded the activation energy in terms which was believed to suffice for the computer study.

There was no apparent way of pre-calculating the frequency factor in the Arrhenius expression. Various values for the frequency factor could be successively evaluated with the computer to match the experimental data, however.

The thermal conductivity was determined as a function of time during the curing reaction. Figure 1 indicates the relationship obtained. Note that the conductivity continued to drop after exceeding the normal cure time. This was one of the unexpected results of the program. The thermal conductivity of the propellant at time zero was somewhat indefinite due to the inherent difficulty found in determining it at that point.

COMPUTER SIMULATION OF THE HEAT TRANSFER EQUATION

The specific area in the grain chosen for investigation with the computer simulation is shown in Figure 2. Temperature stations were established at points radiating from the aluminum core (mandrel), as indicated, in order to study local hot zones between the flutes. The Analog Simulation Department of Thiokol Chemical Corporation's Wasatch Division employed a Pace 231-R Analog Computer for this work.

The curing reaction was assumed to follow a zero-order reaction for simplicity. The heat generation term was represented by the Arrhenius expression and the steel case was thermally thin. The Analog Simulation Department employed the following equation to describe the system:

$$\frac{\delta T}{\delta t} = \alpha \left(\frac{\delta^2 T}{\delta r^2} + \frac{1}{r} \frac{\delta T}{\delta r} + \frac{1}{r^2} \frac{\delta^2 T}{\delta \theta^2} \right) + \frac{Q}{C_p} \left(\frac{dn}{dt} \right)$$

where $\frac{dn}{dt} = - kn$ and $k = Be^{-A/RT}$ (Arrhenius Equation)

The variable thermal conductivity or thermal diffusivity was taken into account during the curing cycle. The value 10^{13} hr^{-1} was initially chosen for the frequency factor and the experimentally determined value for the activation energy used. Reasonable values for the frequency factor, the previously calculated heat of reaction, and the activation energy could not be matched with the experimental data. It was realized that the zero order reaction assumption was not correct. The three values were each substituted by trial and error on the Analog Computer until a match between the computed and experimental data was reached.

The unreacted polymer fraction was assumed to be 1.00 when the problem was initiated. The center cross section of the engine was chosen for the study. A plot of the unreacted polymer fraction versus time was made after the acceptable match was reached. See Figure 3. A correction of 1.00 to .90 for initial condition was necessary to allow for the time delay since the cure reaction actually commences in the propellant mixer and continues in the casting can. Because of the unreacted polymer fraction correction the heat of reaction and frequency factor had to be slightly rematched.

Once an acceptable correlation of the experimental data was acquired, (See Figure 4), it was only a matter of correcting the heat of reaction term to the live propellant problem to determine its thermal history. The heat of reaction varied linearly with the polymer percentage in the propellant since the polymer binder system was common to both. The activation energy and the frequency factor remained the same.

COMPUTER STUDY RESULTS

The major portion of the propellant mass is relatively insensitive to the environment outside of the case due to the low thermal conductivity, the large mass of the propellant, and the generated heat during cure. Extremely slow cool-down rates were, therefore, not unexpected. To cure such large propellant masses at a lower temperature, the propellant has to be cast at the lower temperature. The thermal history of a large propellant grain under normal curing conditions is shown in Figure 5. The exothermic heat of reaction results in a temperature gradient across the grain which persisted throughout processing.

The computer simulation evaluated various cure cycles. The cure cycle could not be optimized academically because there was a lower practical limit for the casting or curing temperature.

Adiabatic curing was investigated, but it permitted the entire exothermic heat of reaction to be retained. This phenomenon raised the temperature excessively. A system was suggested which would control the core temperature during curing by using a fluid for the temperature control medium. A lower-cure temperature was also evaluated using the core temperature control system suggested. See Figure 6. Thermal gradients were lower, but the apparent cure time was longer.

Since the propellant is exposed to a curing environment during the cool-down, it was postulated that the normal cure could be reduced. Processing cycles involving two and three days of cure, rather than the present four-day cure, were also evaluated.

PRACTICAL APPLICATION TO OTHER PROPELLANT SYSTEMS

The same frequency factor and activation energy calculated for one propellant system cannot be applied to other propellant systems which have different polymer binders. It is impractical to install thermocouples in a full scale engine each time a new propellant is to be evaluated. Instead, a small sphere can be thermocoupled radially out from the center of the wall, cast with propellant, and cured. The sphere would then serve as an adequate means of evaluating the heat of reaction, frequency factor, and activation energy.

CONCLUSIONS

A. The thermal histories of solid propellant grains can be calculated by means of an analog computer. The heat conduction with associated heat generation problem was solved two-dimensionally for a grain with a star-shaped configuration. By assuming a zero order of reaction, the frequency factor and activation energy obtained are influenced. When the thermal experimental data is matched to the computer data proper values for the frequency factor, heat of reaction, and activation energy will be obtained for the equation. Once known, the thermal history of any sized propellant grain for any processing cycle can be calculated.

B.   The PBAA propellant grain is relatively insensitive to the environment and acts as an excellent insulator. Temperature control of the core during processing results in lower thermal gradients. A combination of the lower temperature cure and the core temperature control system proved to be most effective.

BIBLIOGRAPHY

1.   Quarterly Progress Report on Engineering Research (Report No. P-59-17), Redstone Arsenal Research Division, Rohm and Haas Company.

2.   Quarterly Progress Report on Engineering Research (Report No. P-58-17), Redstone Arsenal Research Division, Rohm and Haas Company.

3.   Heat Conduction is an Infinite Cylindrical Medium with Heat Generated by a Chemical Reaction, by Peter L. Nichols, Jr., and Arthur G. Presson, an article in the Journal of Applied Physics, Vol. 26, No. 12, dated December 1954.

4.   Aeroplex Propellant Evaluation and Curing Studies, Report No. 498, by W. R. Kirchner, R. W. Lawrence, and F. R. Hepner, dated 9 March 1951, published by Aerojet Engineering Corporation.

SYMBOLS GLOSSARY

A = activation energy
B = frequency factor
C_p = average specific heat of the propellant
n = unreacted polymer fraction
R = gas constant
r = radial distance
Q = heat of reaction of propellant
T = temperature, absolute
t = time
α = thermal diffusivity
θ = angle in radians
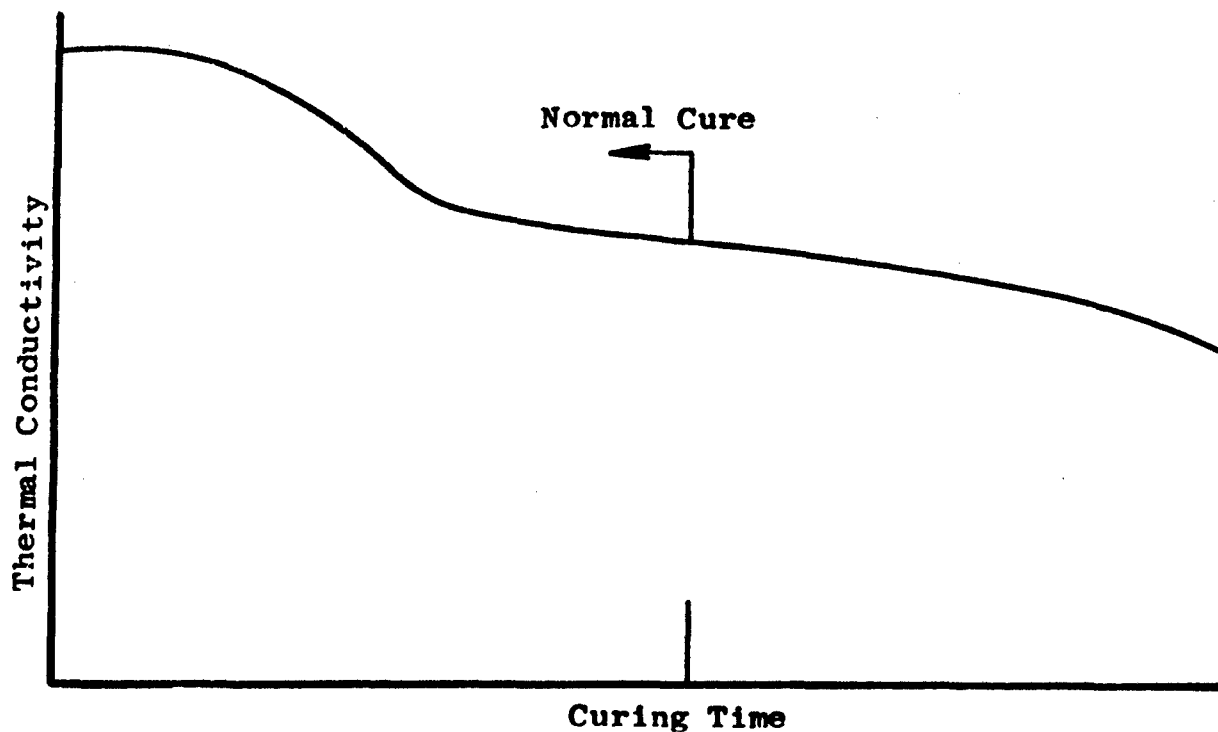
FIGURE 1. THERMAL CONDUCTIVITY OF FLAA PROPELLANT AS A FUNCTION OF CURING TIME
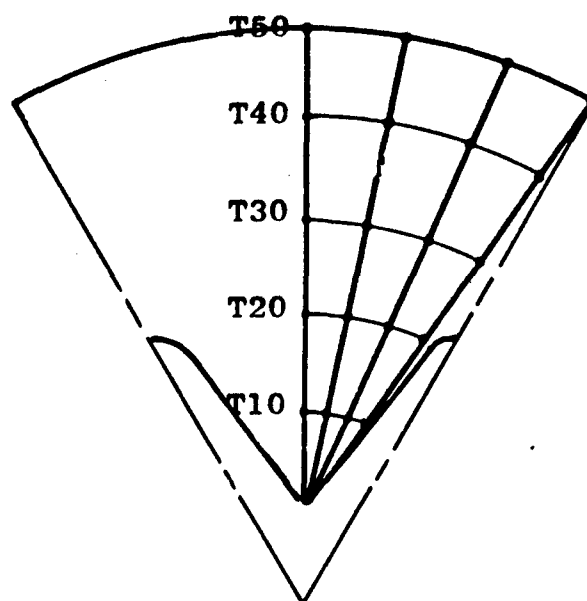
FIGURE 2. LOCATION OF TEMPERATURE STATIONS IN PROPELLANT GRAIN
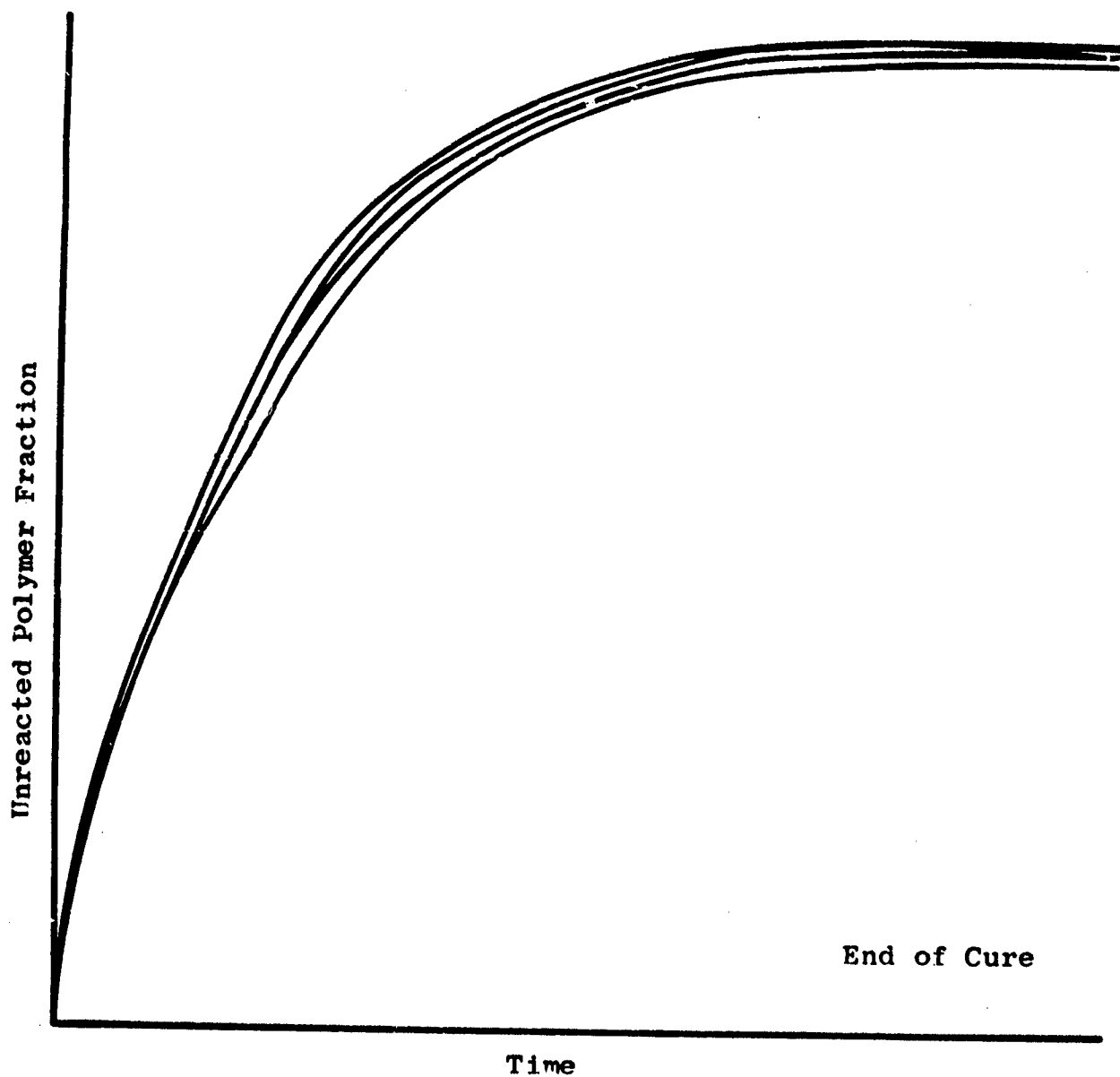
FIGURE 3. UNREACTED POLYMER FRACTION AS A FUNCTION OF TIME
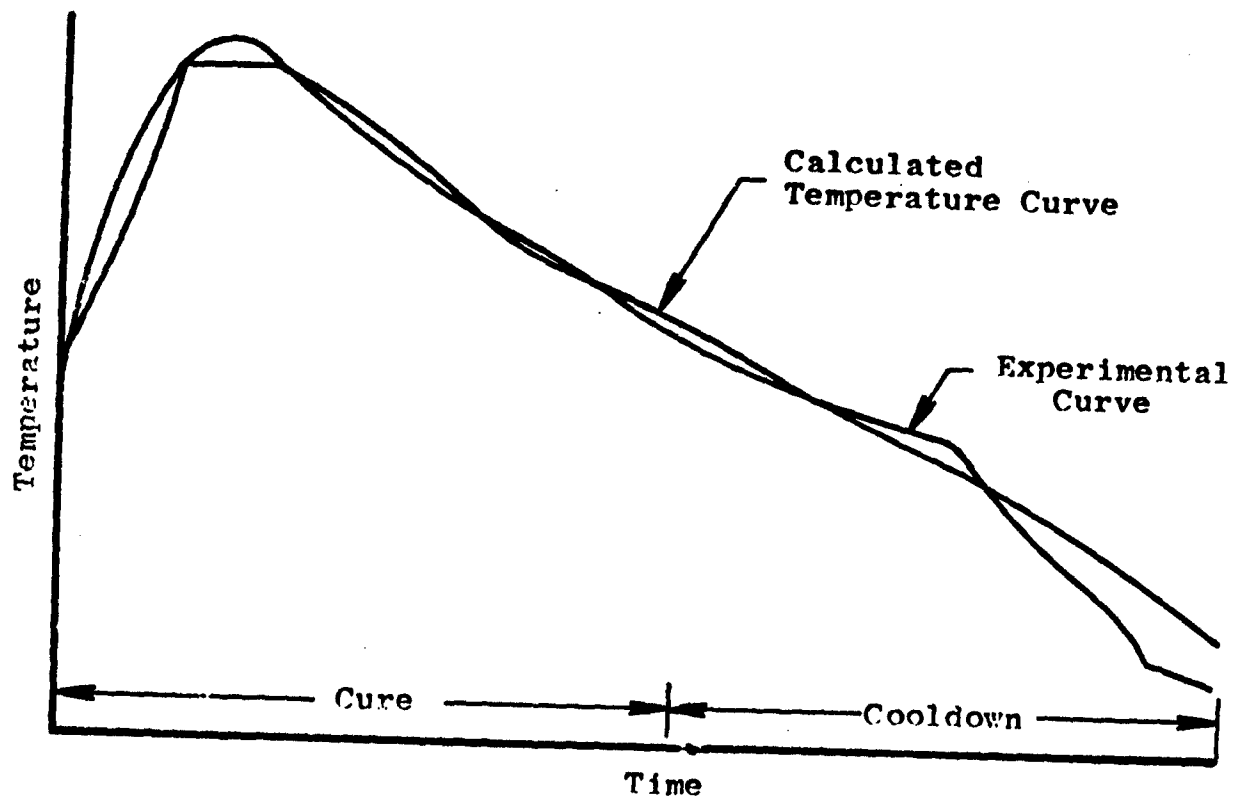
FIGURE 4. MATCH OF ANALOG CURVE VERSUS ACTUAL EXPERIMENTAL DATA
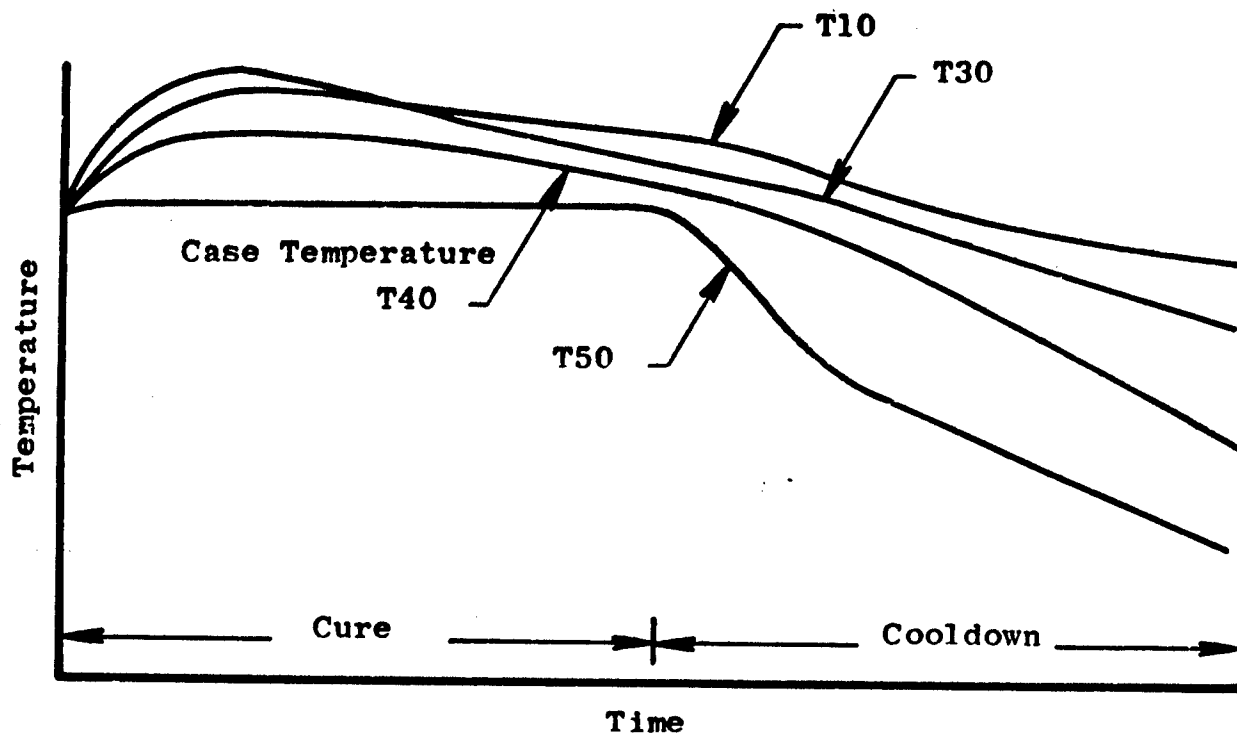
FIGURE 5.
TEMPERATURE PROFILES FOR A LARGE PBAA PROPELLANT
GRAIN UNDER NORMAL CURE CYCLE

Temperature

High Temperature Cure

T30

T2)

T10

T50

Cure ⟷ ⟷ Cooldown

Note: Core temperature
controlled to same
temperature as core.

T30

T40

Low Temperature Cure

T50

T10

Cure ⟷ Cooldown

Time
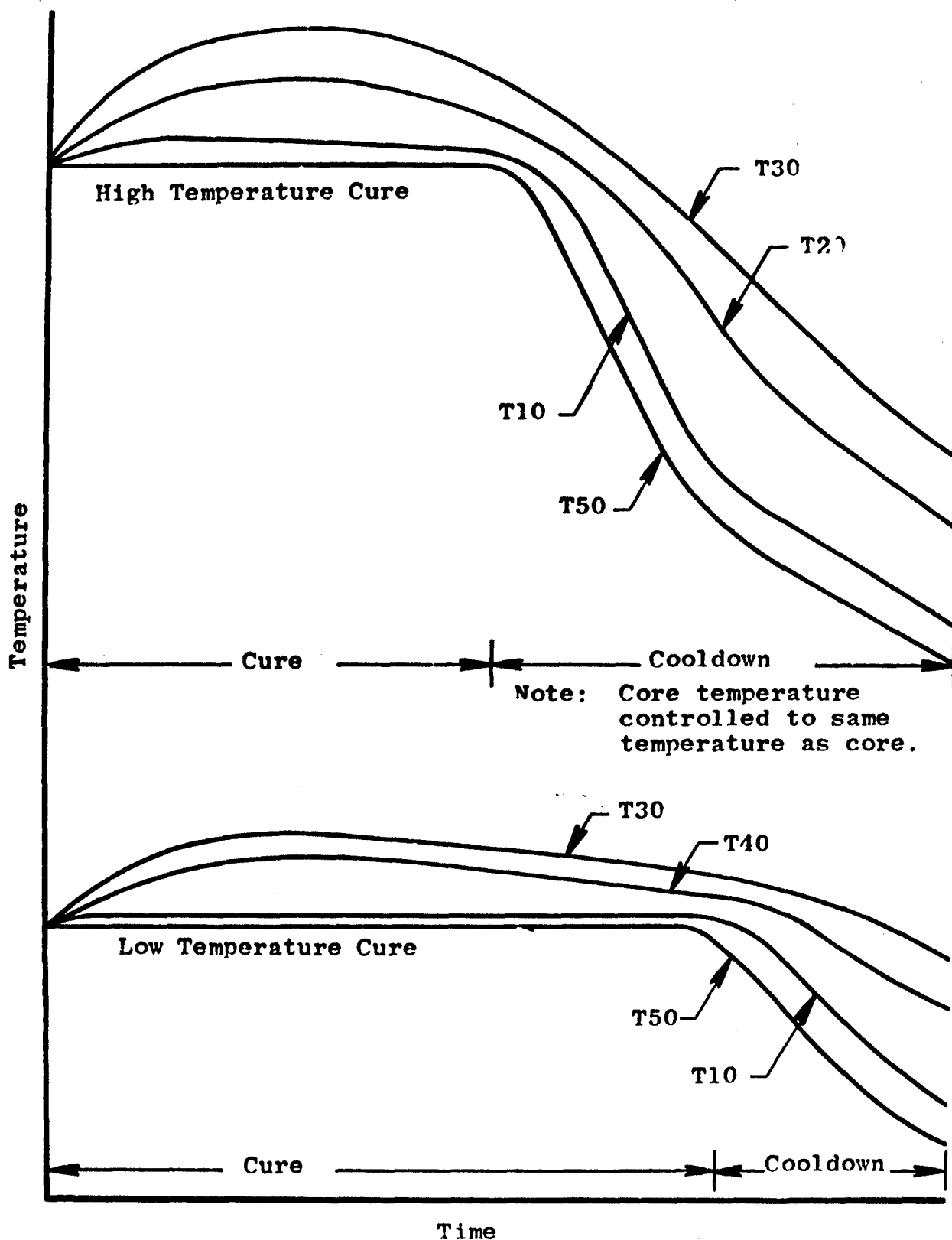
FIGURE 6. IMPROVED PROCESS CYCLES FOR A LARGE PBAA PROPELLANT GRAIN

FORCED TRANSVERSE VIBRATIONS OF A SOLID, ELASTIC CORE CASE-BONDED TO AN INFINITELY-LONG, RIGID CYLINDER [1]

By
J. H. Baltrukonis
Professor of Civil Engineering
THE CATHOLIC UNIVERSITY OF AMERICA
Washington 17, D. C.

ABSTRACT

The problem is solved of the forced, transverse vibrations of a solid, compressible, elastic core case-bonded to an infinitely-long, rigid cylinder. It is shown that the ratio of the amplitude response of the core axis to the amplitude of the casing depends on both the frequency of the forced vibration and Poisson's ratio for the core material. By plotting amplitude ratio versus frequency curves for different values of Poisson's ratio it is demonstrated that the amplitude ratio versus frequency plot for an incompressible, elastic core is a simple line spectrum. On the basis of this result it is concluded that considerable care must be exercised when interpreting the results of solutions of problems wherein the assumption of incompressible material is involved.

INTRODUCTION

The problem of the free, transverse vibrations of a solid, compressible, elastic core case-bonded to an infinitely-long, rigid, circular-cylindrical tank has been previously treated,[2] and the following frequency equations among other things were derived.

$$J_{n-1}(\Omega)\, J_{n+1}(k\Omega) + J_{n+1}(\Omega)\, J_{n-1}(k\Omega) = 0, \quad (n = 1, 2, \ldots) \quad (1)$$

These transcendental frequency equations define a doubly infinite set of natural circular frequency coefficients Ω_{nm}. The mode of vibration is identified by the subscript n while the subscript m identifies the frequency number within a given mode. In Eq. (1) k^2 denotes the ratio of the square of the shear wave velocity c_s to the square of the dilatational wave velocity c_c; i. e.,

$$c_s^2 = \frac{G}{\rho} \quad (2a)$$

2. Baltrukonis, J. H., "Free Transverse Vibrations of a Solid Elastic Mass in an Infinitely-Long, Rigid, Circular-Cylindrical Tank" J. Appl. Mechanics **27** 663 (December 1960)

$$c_c^2 = \frac{2(1-\nu)}{1-2\nu}\left(\frac{G}{\rho}\right) \tag{2b}$$

$$k^2 = \frac{c_s^2}{c_c^2} = \frac{1-2\nu}{2(1-\nu)} \tag{2c}$$

Since k depends only on Poisson's ratio, it is clear that the natural frequencies of free vibrations, as defined by Eq. (1), also depend only on Poisson's ratio. Figure 1 has been reproduced from the previous paper[2] in order to demonstrate this dependency for the first-order (n = 1) natural frequency coefficients Ω_{1m}. These curves exhibit very peculiar and interesting shapes but we wish to make the point here that as k tends to zero, the curves tend to finite real values of the natural frequency coefficients. The zero value for k corresponds to a value of 1/2 for Poisson's ratio ν which value defines incompressible material. Thus, Fig. 1 demonstrates that natural frequencies <u>do</u> exist for incompressible material.

We recall the problem under consideration. In the previous paper the question was posed: "Can natural frequencies exist?" The answer was affirmative even for incompressible material. The question immediately arises: "How can natural frequencies exist for incompressible material when it occupies the entire internal volume of the tank?" The vibration under consideration is one of plane strain in which there can be no displacement out of the plane of a cross-section; it has been shown, however, that free vibrations can exist in the modes under discussion. In the present report we are concerned with the explanation of this apparent contradiction.

We shall consider the problem of transverse vibrations of the solid, compressible, elastic core when the infinitely-long, rigid casing is oscillated by some external means with simple harmonic motion. The response of the core at a generic point r will be calculated. This result will be specialized to obtain the amplitude response of the core axis. The ratio of the amplitude response of the core axis to the amplitude of the casing will then be plotted as a function of the forcing frequency for various values of Poisson's ratio tending to 1/2. It will be seen that as Poisson's ratio tends to 1/2, that is, as the core material tends to become incompressible, the amplitude ratio-forcing frequency plots tend to a simple line spectrum. Clearly, this type of frequency response is physically impossible. That this should be the case is not surprising since incompressible material is an hypothetical material which cannot exist in nature. Nevertheless, the assumption of such a material is quite regularly used in practice. The present report

2.   Baltrukonis, J. H., "Free Transverse Vibrations of a Solid Elastic Mass in an Infinitely-Long, Rigid, Circular-Cylindrical Tank" J. Appl. Mechanics <u>27</u> 663 (December 1960)

presents one difficulty arising from the use of such an hypothetical material.

NOTATION

r, θ z	radial, circumferential and axial coordinate variables of polar cylindrical coordinates
t	time
u_r, u_θ u_z	radial, circumferential and axial components of displacement
ϕ ψ χ	displacement of potentials
k	ratio of shear wave velocity to dilatational wave velocity
c_c	dilatational wave velocity
c_s	shear wave velocity
ν	Poisson's ratio
G	shear modulus
ρ	mass density
e	mean normal strain $= \dfrac{1}{3}\left(\dfrac{\partial u_r}{\partial r} + \dfrac{u_r}{r} + \dfrac{1}{r}\dfrac{\partial u_\theta}{\partial \theta} + \dfrac{\partial u_z}{\partial z}\right)$
∇^2	Laplacian operator $= \dfrac{\partial^2}{\partial r^2} + \dfrac{1}{r}\dfrac{\partial}{\partial r} + \dfrac{1}{r^2}\dfrac{\partial^2}{\partial \theta^2} + \dfrac{\partial^2}{\partial z^2}$
ω	natural circular frequency
Ω	natural circular frequency coefficient
p	forcing circular frequency
λ	forcing circular frequency coefficient
b	radius of interface between elastic core and rigid tank
n	order number of vibration mode
m	frequency number within a given mode
J_n	Bessel function of the first kind of order n
C_1, C_2	Constants
W	Amplitude of vibration of the rigid casing

A prime over a quantity denotes the ordinary derivative of the quantity with respect to its argument.

STATEMENT AND SOLUTION OF THE PROBLEM

The general theory of vibrations of elastic continua in polar, cylindrical coordinates has been previously outlined[2]. In accord with this general theory we define the components of displacement as follows in terms of two displacement potentials ϕ and χ

$$u_r = \frac{\partial \phi}{\partial r} + \frac{1}{r} \frac{\partial \chi}{\partial \theta} \tag{3a}$$

$$u_\theta = \frac{1}{r} \frac{\partial \phi}{\partial \theta} - \frac{\partial \chi}{\partial r} \tag{3b}$$

$$u_z = 0 \tag{3c}$$

It was demonstrated[2] that the displacement equations of motion will be identically satisfied provided that the displacement potentials are taken as solutions of the following differential equations:

$$\frac{\partial^2 \phi}{\partial r^2} + \frac{1}{r} \frac{\partial \phi}{\partial r} + \frac{1}{r^2} \frac{\partial^2 \phi}{\partial \theta^2} = \frac{1}{c_c^2} \frac{\partial^2 \phi}{\partial t^2} \tag{4a}$$

$$\frac{\partial^2 \chi}{\partial r^2} + \frac{1}{r} \frac{\partial \chi}{\partial r} + \frac{1}{r^2} \frac{\partial^2 \chi}{\partial \theta} = \frac{1}{c_s^2} \frac{\partial^2 \chi}{\partial t^2} \tag{4b}$$

We now apply this general theory to the problem under consideration for which the boundary conditions are:

$$u_r \Big|_{r=b} = W e^{ipt} \cos \theta \tag{5a}$$

$$u_\theta \Big|_{r=b} = -W e^{ipt} \sin \theta \tag{5b}$$

We take a solution for the displacement potentials of the following form:

$$\phi = C_1 J_1 \left(k \lambda \frac{r}{b} \right) e^{ipt} \cos \theta \tag{6a}$$

---

2. Baltrukonis, J.H. "Free, Transverse Vibrations of a Solid Elastic Mass in an Infinitely-Long Rigid, Circular-Cylindrical Tank", J. Appl. Mech. <u>27</u> 663 (December 1960)

$$\chi = C_2 J_1 \left(\lambda \frac{r}{b} \right) e^{ipt} \sin \Theta \qquad (6b)$$

It may be verified by direct substitution that these potentials are solutions of Eqs. (4) provided we take

$$\lambda^2 = \frac{\rho \, p^2 b^2}{G} \qquad (6c)$$

Because of its relation to the forcing frequency p, λ will be referred to as the forcing frequency coefficient.

Substitution from Eqs. (6) into Eqs. (3) results in the following expressions for the displacements:

$$u_r = \left[C_1 \frac{k\lambda}{b} J_1' \left(k\lambda \frac{r}{b} \right) + \frac{C_2}{r} J_1 \left(\lambda \frac{r}{b} \right) \right] e^{ipt} \cos \Theta \qquad (7a)$$

$$u_\Theta = - \left[\frac{C_1}{r} J_1 \left(k\lambda \frac{r}{b} \right) + C_2 \frac{\lambda}{b} J_1' \left(\lambda \frac{r}{b} \right) \right] e^{ipt} \sin \Theta \qquad (7b)$$

We must now evaluate the constants involved in the solution given above. To this end we substitute from Eqs. (7) into the boundary conditions given by Eqs. (5) to obtain the following non-homogeneous system of two linear algebraic equations in the unknown constants:

$$\begin{vmatrix} (k\lambda) \, J_1'(k\lambda) & J_1(\lambda) \\[2mm] J_1(k\lambda) & \lambda \, J_1'(\lambda) \end{vmatrix} \begin{vmatrix} C_1 \\[2mm] C_2 \end{vmatrix} = \begin{vmatrix} Wb \\[2mm] Wb \end{vmatrix} \qquad (8a)$$

Such a system can have a consistent solution only if the determinant of the coefficients of the unknowns does not vanish. On expansion of this determinant we obtain

$$\Delta(\lambda) = - \frac{1}{2} k \lambda^2 \left[J_0(\lambda) \, J_2(k\lambda) + J_2(\lambda) \, J_0(k\lambda) \right] \qquad (8b)$$

On comparison of this result with Eq. (1) we find that Eq. (8b) has identically the same form as the frequency equation given by Eq. (1) except that the natural circular frequency coefficient Ω is replaced by the forcing frequency coefficient λ; i.e.,

$$\Delta(\Omega_{1m}) = 0 \ , \quad (m = 1, 2, 3, \ldots) \qquad (8c)$$

Thus, the determinant of the coefficients of the unknowns in Eq. (8a) will vanish whenever the forcing frequency coefficient λ is equal to the first-order natural circular frequency coefficient Ω_{1m}. As a result, we cannot expect to obtain a consistent solution of Eq.(8a) whenever $\lambda = \Omega_{1m}$. With this restriction in mind we proceed to

obtain the solution for the arbitrary constants, and substitution into Eqs. (7) finally results in

$$u_r = \frac{1}{2} W k \lambda^2 \Delta^{-1}(\lambda) \left[J_2(\lambda) J_2(k\lambda \tfrac{r}{b}) - J_2(k\lambda) J_2(\lambda \tfrac{r}{b}) \right.$$

$$\left. - J_0(\lambda \tfrac{r}{b}) J_2(k\lambda) - J_2(\lambda) J_0(k\lambda \tfrac{r}{b}) \right] e^{ipt} \cos\theta \qquad (9a)$$

$$u_\theta = \frac{1}{2} W k \lambda^2 \Delta^{-1}(\lambda) \left[J_2(\lambda) J_2(k\lambda \tfrac{r}{b}) - J_2(k\lambda) J_2(\lambda \tfrac{r}{b}) \right.$$

$$\left. + J_0(\lambda \tfrac{r}{b}) J_2(k\lambda) + J_2(\lambda) J_0(k\lambda \tfrac{r}{b}) \right] e^{ipt} \sin\theta \qquad (9b)$$

To obtain some insight into the physics of the problem let us investigate further the response of the axis. From Eqs. (9) it follows that

$$u_x \Big|_{\theta=0} = u_r \Big|_{\theta=0} = \frac{1}{2} W k \lambda^2 \Delta^{-1}(\lambda) \left[J_2(\lambda) J_2(k\lambda \tfrac{r}{b}) - J_2(k\lambda) J_2(\lambda \tfrac{r}{b}) \right.$$

$$\left. - J_0(\lambda \tfrac{r}{b}) J_2(k\lambda) - J_2(\lambda) J_0(k\lambda \tfrac{r}{b}) \right] e^{ipt}$$

$$u_x \Big|_{\substack{r=0 \\ \theta=0}} \equiv \overline{W} e^{ipt} = -\frac{1}{2} W k \lambda^2 \Delta^{-1}(\lambda) \left[J_2(k\lambda) + J_2(\lambda) \right] e^{ipt}$$

Finally, therefore, if we make use of Eq. (8b),

$$\frac{\overline{W}}{W} = \left[J_2(\lambda) + J_2(k\lambda) \right] \left[J_0(\lambda) J_2(k\lambda) + J_2(\lambda) J_0(k\lambda) \right]^{-1} \qquad (10)$$

This result defines an amplification factor for the axis of the core. We observe that this amplification factor depends not only on the forcing frequency but also on Poisson's ratio, since k depends on Poisson's ratio only.

ANALYSIS OF RESULTS AND CONCLUSIONS

Figure 1 shows velocity ratio k in function of the first-order circular frequency coefficients for free, transverse vibrations of a solid, compressible elastic core case-bonded to an infinitely-long

rigid, circular cylindrical tank. These plots demonstrate that natural modes of vibration exist even for an incompressible core when k = 0. This fact seems rather curious on closer consideration since the mode of vibration under investigation is one of plane strain and there appears to be no way in which an incompressible core can be deformed. In an attempt to provide at least a partial explanation of this apparent anomaly, Fig. 2 has been plotted to demonstrate variation with Poisson's ratio of the amplitude ratio-frequency characteristics of the core axis making use of Eq. (10). Since we are mainly interested in amplitude response in the neighborhood of the natural frequencies, the forcing frequency was normalized with the fundamental first-mode frequency in Fig. 2(a), and with the second first-mode frequency in Fig. 2(b). We observe that, as Poisson's ratio approaches 1/2 resonance peaks tend to become sharper and sharper until, finally, for an incompressible material (ν = 1/2) the frequency response is a simple impulse function and the entire characteristic curve is a discrete line spectrum as shown in Fig. 3.

It is clear that such a response characteristic is physically impossible for a real material. That this should be the case ought not to be surprising inasmuch as an incompressible material is an ideal material which, a priori, would not be expected to behave physically, exactly and entirely, as a real, nearly incompressible material. Although many physical characteristics of incompressible materials have counterparts in compressible materials, other properties of incompressible materials as e.g., frequency response, cannot be physically realized. This observation is important since many analytical studies are being carried out based on this assumption. In most cases, assumption of an incompressible material simplifies analysis considerably but we must be aware of its limitations.

Another interesting and important observation concerning Figs. 2 is the tremendous sensitivity to Poisson's ratio exhibited by the response curves. Very small changes in Poisson's ratio in the neighborhood of 1/2 produce considerable changes in the shape of the curves. This is important since many materials are very nearly incompressible, notably many high polymers including solid propellant materials.

The foregoing points up the necessity for considerable care when analyses are performed on the assumption of an ideally incompressible material. In many respects such material exhibits the properties of real materials but it sometimes displays characteristics that cannot be reproduced in nature. Furthermore, when the material under study is nearly incompressible, analysis must be performed with considerable care and precision since they are very sensitive to small changes in Poisson's ratio. It is clear that we must take great care in conducting experimental measurements of Poisson's ratio for these nearly incompressible materials.
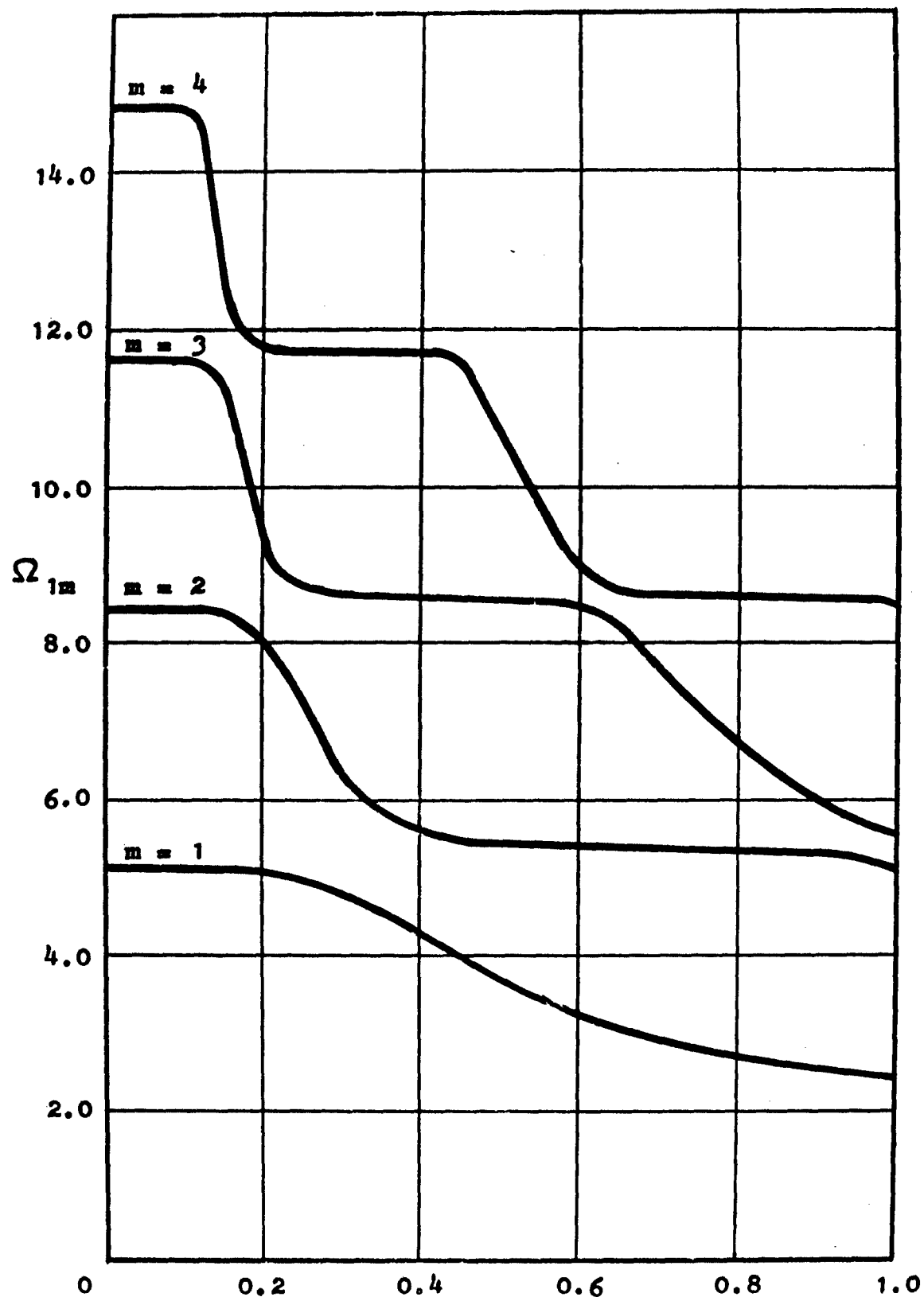
FIGURE 1.
FIRST-ORDER CIRCULAR FREQUENCY COEFFICIENTS AS FUNCTIONS OF POISSON'S RATIO
FOR TRANSVERSE VIBRATIONS OF A SOLID ELASTIC CORE CASE-BONDED TO AN INFINITELY-
LONG, RIGID, CIRCULAR-CYLINDIRCAL TANK
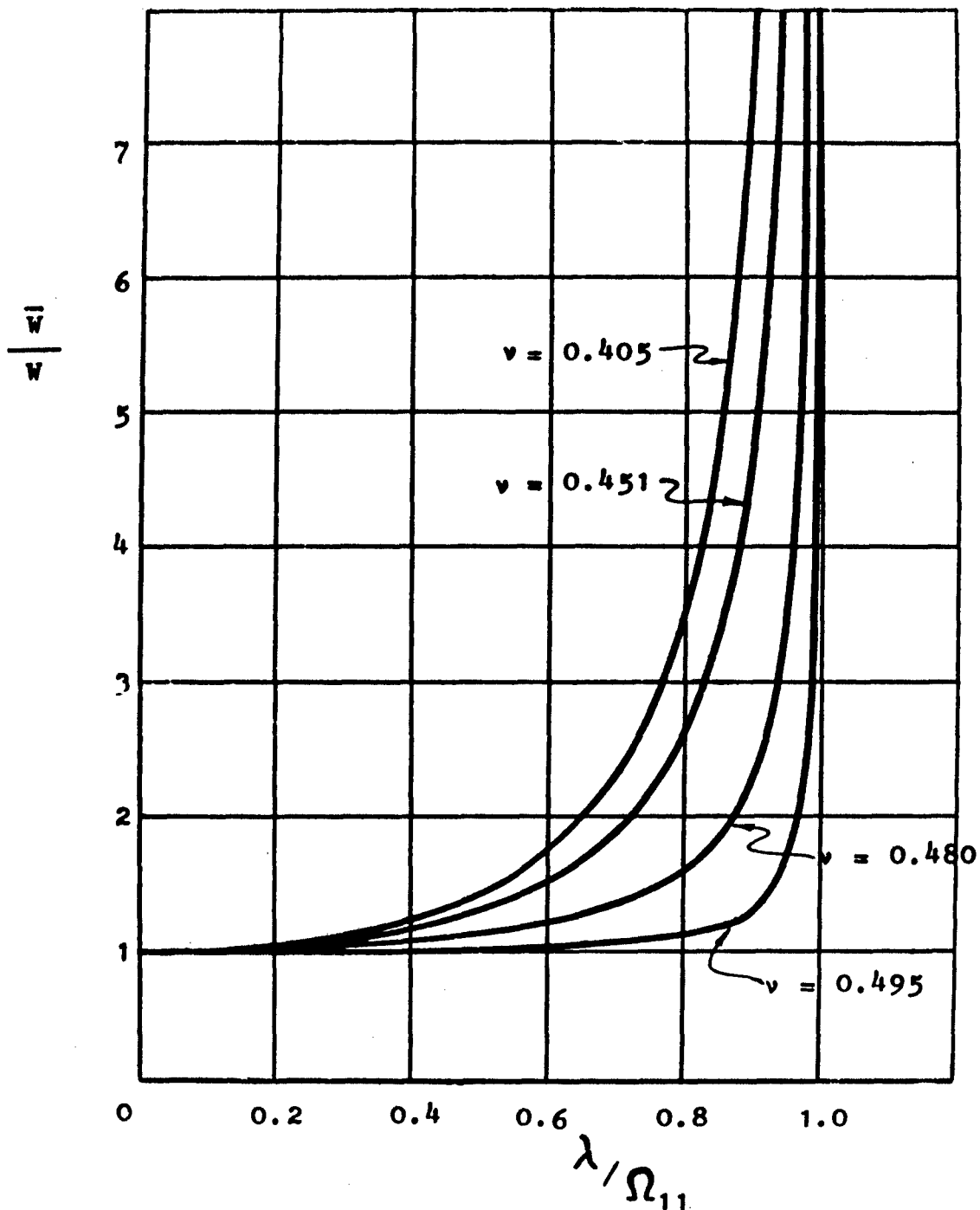
FIGURE 2. (a)
AMPLITUDE RATIO-FREQUENCY PLOTS IN THE NEIGHBORHOOD OF THE FUNDAMENTAL
RESONANCE OF A SOLID, ELASTIC CORE CASE-BONDED TO AN INFINITELY-LONG,
RIGID CYLINDER

FIGURE 2. (b)
AMPLITUDE RATIO-FREQUENCY PLOTS IN THE NEIGHBORHOOD OF THE SECOND RESONANCE
FOR FORCED TRANSVERSE VIBRATIONS OF A SOLID, ELASTIC CORE CASE-BONDED TO AN
INFINITELY-LONG RIGID CYLINDER

FIGURE 3.
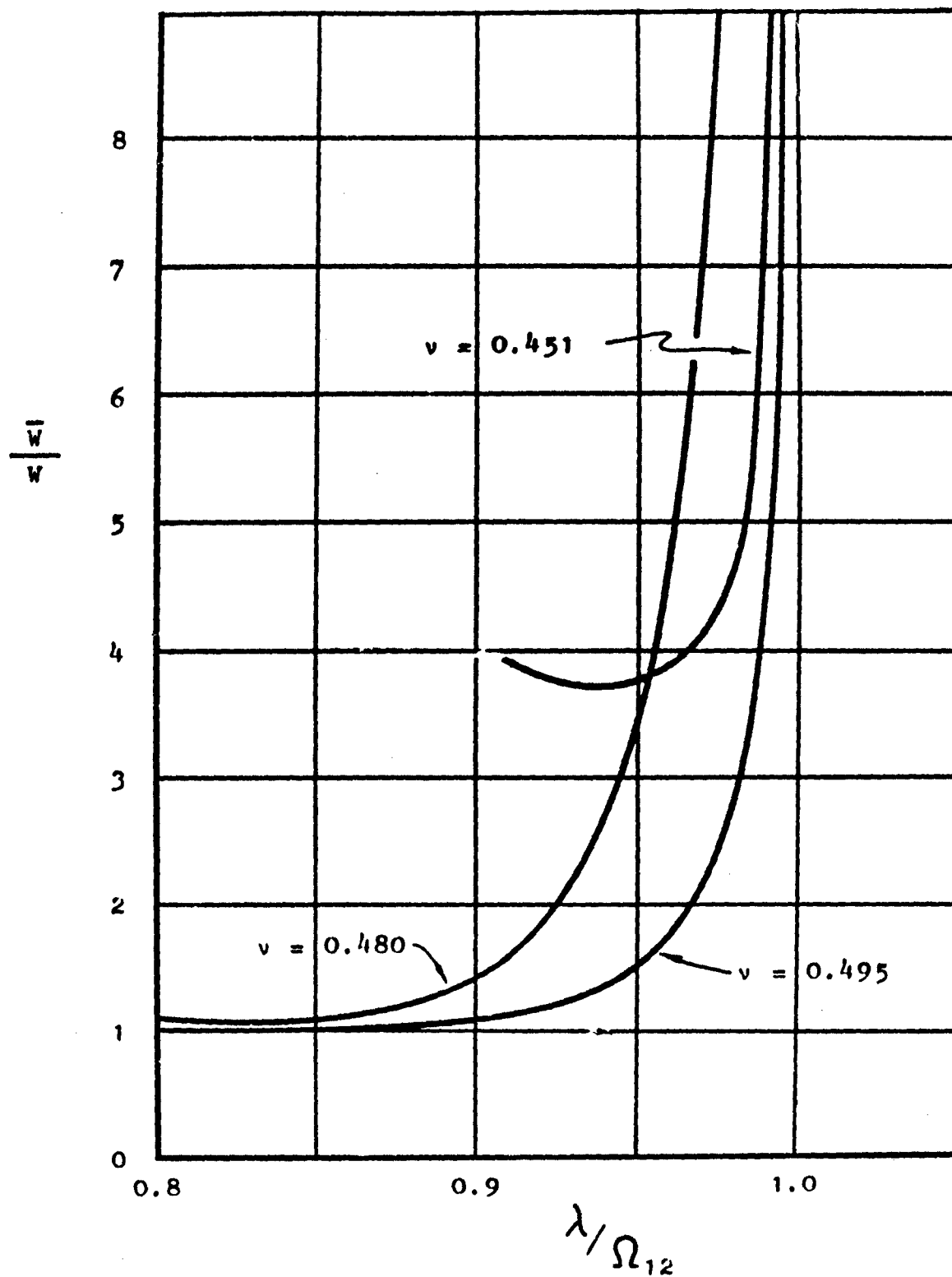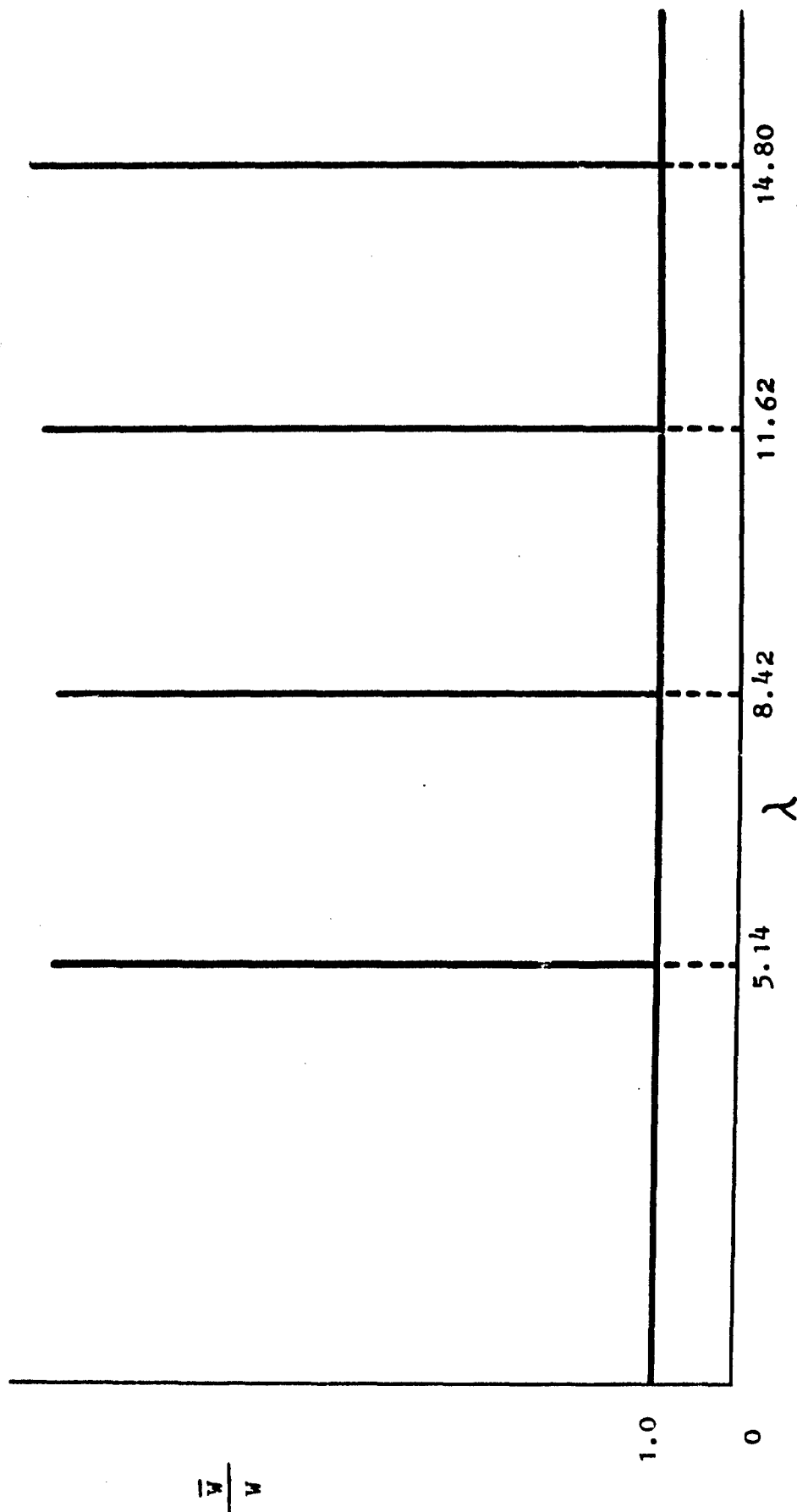AMPLITUDE RATIO-FREQUENCY PLOT FOR FORCED TRANSVERSE VIBRATIONS OF A SOLID INCOMPRESSIBLE
ELASTIC CORE CASE-BONDED TO AN INFINITELY-LONG, RIGID CYLINDER

PROPELLANT SLUMP IN LARGE SOLID ROCKET MOTORS
DURING LONG-TERM VERTICAL STORAGE

Robert A. Chase and Bernard L. Iwanciow
United Technology Corporation
A Subsidiary of United Aircraft Corporation
Sunnyvale, California

ABSTRACT

Propellant slump becomes an important design consideration as the size of solid rocket motors increases. Thus, study was conducted to develop a method of predicting propellant slump in large solid motors due to long-term vertical storage.

Creep tests of propellant samples under constant shear showed a linear stress-strain behavior with a logarithmic time variation. Similar tests involving constant tensile stress displayed similar behavior. These creep data serve as basic material properties information for the prediction of grain slump.

Maximum slump deformation is predicted for tubular perforation, cylindrical grains for a typical PBAA propellant.

Due to propellant slump, large tensile stresses are generated near to the free end at the liner-propellant interface. When combined with stresses due to propellant shrinkage resulting from polymerization and post-cure cool down, the propellant to liner bond becomes highly loaded.

INTRODUCTION

Propellant slump becomes an important design consideration as the size of solid rocket motors increases. Long-term vertical storage of large solid rocket motors can result in significant grain deformations which must be taken into consideration in motor design. Stresses induced by gravity forces during storage in combination with stresses due to propellant shrinkage as a result of polymerization and post-cure cool down can cause liner to propellant separation at upward facing free ends. Such a separation in a model test employing a Lucite case and binder to simulate the propellant is shown in Photograph 1. Thus, it is important that consideration be given to propellant slump resulting from vertical storage of larger solid rocket motors.

Photograph 1 - Simulated Liner-to-Propellant Bond Failure
in a Model Slump Test Motor

TRANSIENT DEFORMATION OF A TUBULAR GRAIN DURING VERTICAL STORAGE

A tubular grain configuration with burning of the free surfaces offers certain advantages in large segmented solid rocket motors. Thus, study of this particular grain configuration, shown in Figure 1, is quite appropriate.

Saint-Venant's principle[1], which we presume can be carried over to viscoelastic or plastic materials, tells us that sufficiently far removed from the free surfaces the grain is unaware of the existence of the free surfaces and the problem becomes one-dimensional spacewise. Tests indicate that two to three web thicknesses away from the free surfaces is sufficient to satisfy this condition.[2] As a first step we will consider grain deformations and stresses at points sufficiently far from free surfaces to be uninfluenced by the free surfaces, or equivalently, grain deformations and stresses of an infinitely long tubular grain.
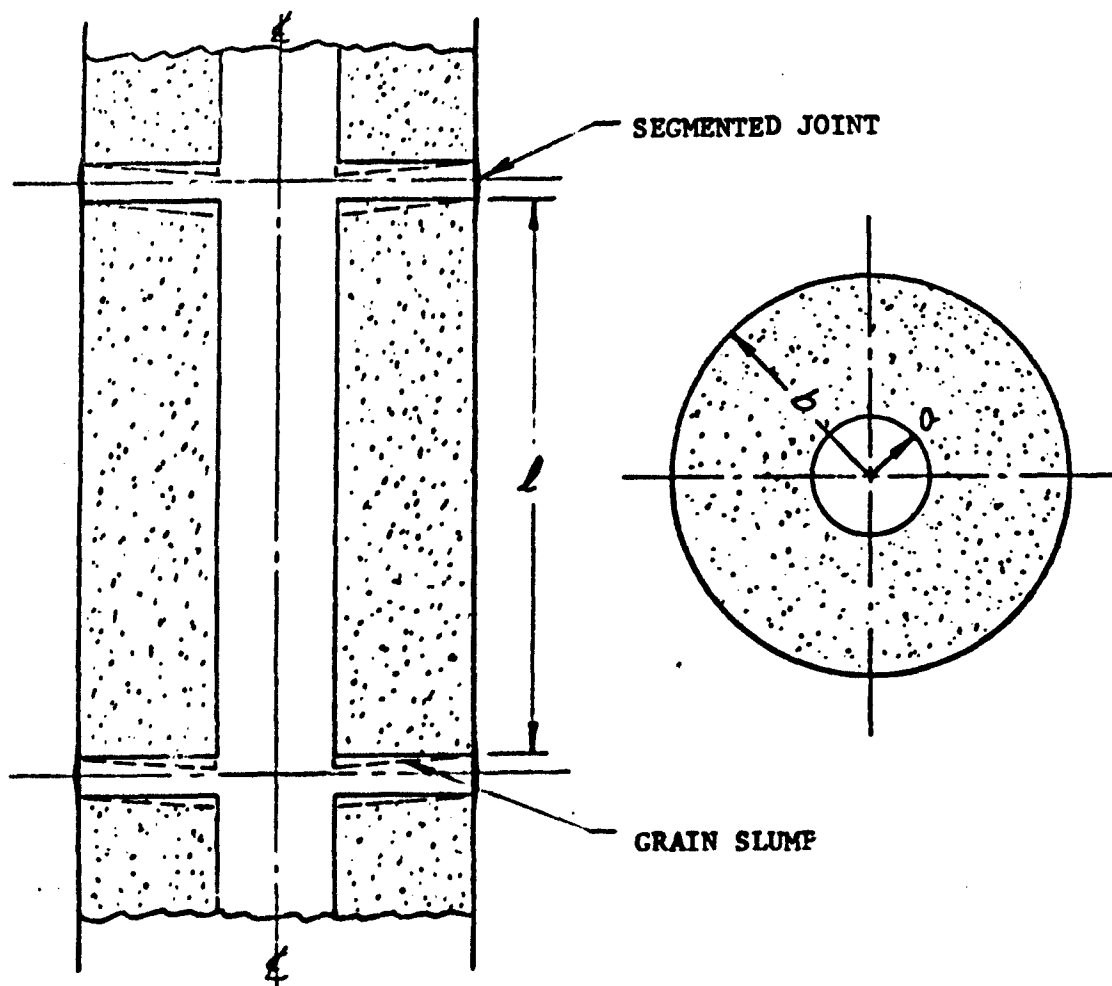
FIGURE 1.   FREE ENDED TUBULAR GRAIN CONFIGURATION

The Infinitely Long Tubular Grain - The tubular grain configuration shown in Figure 2 is considered to consist of a viscoelastic, or plastic, isotropic propellant and the motor case is considered to be rigid compared to the grain. Transient deformation of the grain is sufficiently slow so that inertial forces can be neglected. Therefore, the equations of equilibrium are

$$\frac{\partial \sigma_r}{\partial r} + \frac{\sigma_r - \sigma_\theta}{r} = 0 \tag{1}$$

$$\frac{\partial \tau_{rx}}{\partial r} + \frac{\tau_{rx}}{r} - \omega_p = 0 \tag{2}$$

where ω_p = Weight density of the propellant

and the stress boundary conditions are
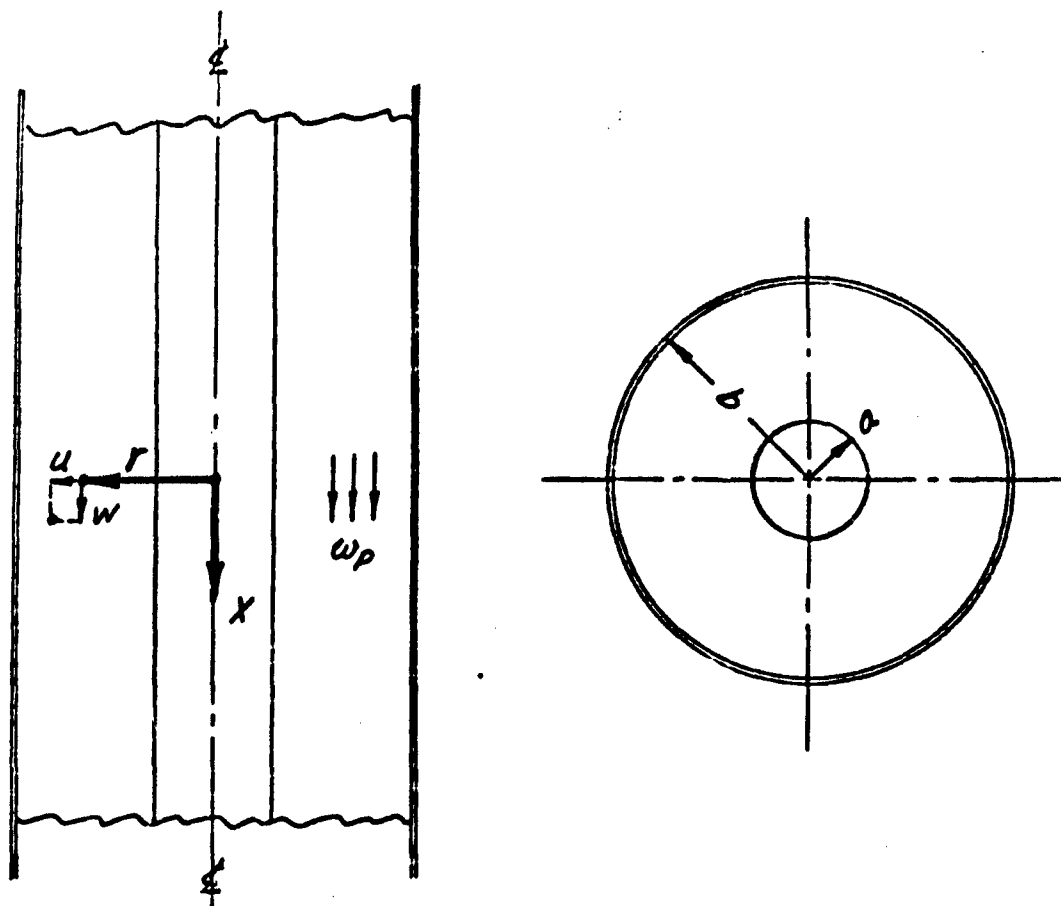
FIGURE 2. INFINITELY LONG TUBULAR GRAIN CONFIGURATION

$$\tau_{rx}(a,t) = 0 \tag{3}$$

$$\sigma_r(a,t) = 0 \tag{4}$$

$$\sigma_\theta(b,t) = 0 \tag{5}$$

Equation (2) can be integrated directly and applying the boundary condition (3), the shear stress distribution is found to be

$$\tau_{rx} = \frac{1}{2}\omega_p r\left[1-\left(\frac{a}{r}\right)^2\right], \tag{6}$$

a well known result.[3] It is noted that the shear stresses are constant with respect to time and that the maximum shear stress,

$$\tau_{rx_{MAX}} = \tau_{rx}(b) = \frac{1}{2}\omega_p b\left[1-\left(\frac{a}{b}\right)^2\right], \tag{7}$$

is proportional to the diameter of the grain.

The strain-deformation relations are

$$\epsilon_r = \frac{\partial u}{\partial r} \qquad (8)$$

$$\epsilon_\theta = \frac{u}{r} \qquad (9)$$

$$\gamma_{rx} = \frac{\partial w}{\partial r} \qquad (10)$$

The boundary conditions on these deformations are

$$u(b,t) = 0 \qquad (11)$$

$$w(b,t) = 0 \qquad (12)$$

Integrating equation (10) and applying the boundary condition (12),

$$w(r,t) = \int_r^b \gamma_{rx}(r,t)\,dr \qquad (13)$$

To evaluate the integral, the functional relationship between the time and space dependent shear strain, $\gamma_{rx}(r,t)$, and the space dependent shear stress, $\tau_{rx}(r)$, must be determined. This functional relationship is expressed by

$$\gamma_{rx} = \gamma_{rx}(\tau_{rx}, t) \qquad (14)$$

Long-Term Shear Stress-Strain Relation - Constant shear stress tests were conducted on a typical PBAA aluminized propellant to determine the functional relationship, equation (14). The test setup is shown in Photograph 2. Thin slabs of propellant were cast between steel plates which loaded the propellant in shear. The length to thickness ratio of the propellant slabs was made as large as practical to minimize the end effects. The shear strain was measured by means of a cathetometer, Cenco model 1164-A, far enough from the free end to be uninfluenced by the end effect. The temperature was maintained at $75^\circ F$.

The results of the test are plotted in Figure 3. Linearity of the data on a semilog plot was established following over one thousand hours of testing. It became apparent early in time that the shear strain was proportional to the shear stress at any instant of time. The functional relationship

$$\gamma(t, \tau) = 1.37 \times 10^{-3} \tau \log_e (1 + 8.7 \times 10^4 t) \qquad (15)$$

is a reasonably good fit of the data and satisfies the initial condition that $\gamma(0, \tau) = 0$

Propellant Transient Deformation - Since the functional relationship between shear stress and strain has been established to be of the form,

$$\gamma(t, \tau) = C_1 \tau \log_e (1 + C_2 t) \qquad (16)$$

the integral of equation (13) now can be evaluated. Substituting
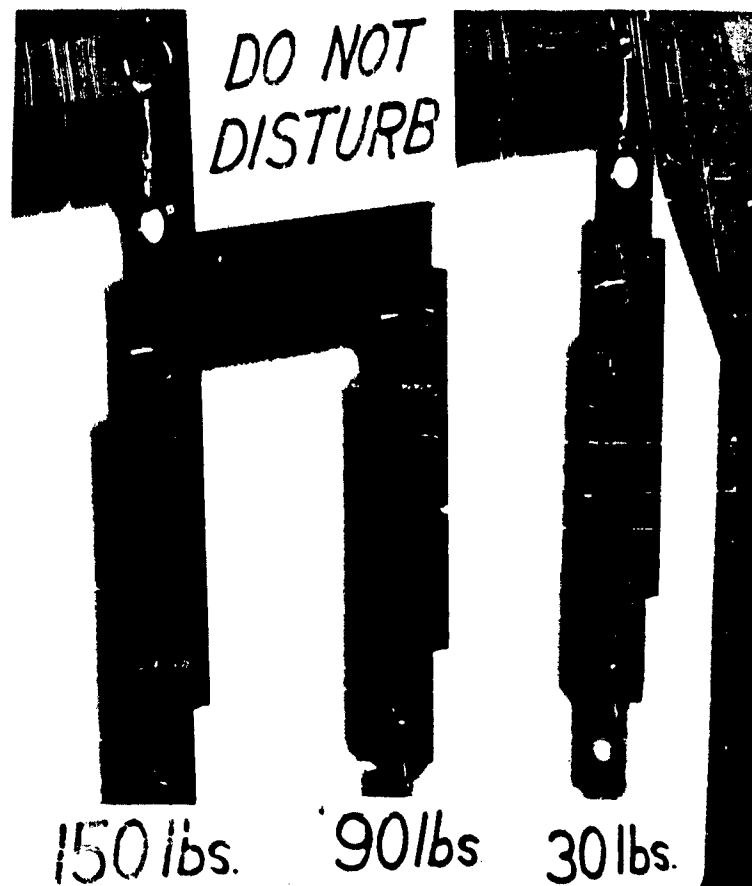
Photograph 2 - Test Setup for Establishment
of Shear Stress-Strain Relation

$$\gamma(t,\tau) = 1.37 \times 10^{-3} \tau \, log_e(1 + 8.7 \times 10^4 t)$$
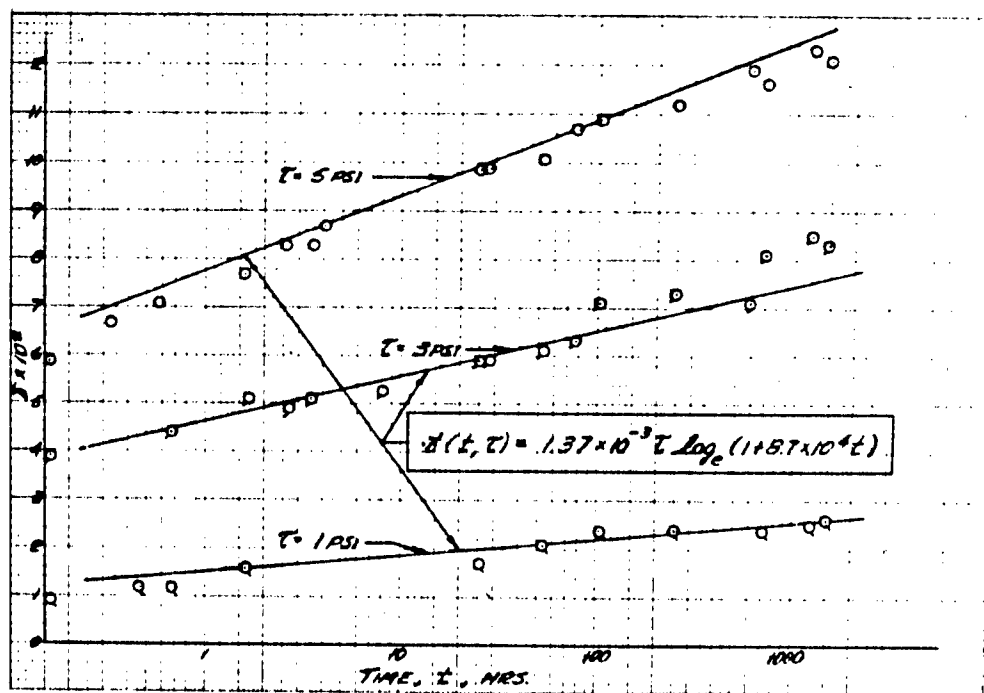
FIGURE 3.   RESULTS OF THE CONSTANT SHEAR STRESS TESTS PBAA PROPELLANT

equation (6) into equation (15) and integrating, the transient longitudinal deformation becomes

$$W(r,t) = \frac{b^2}{4} \omega_p C_1 \log_e (1 + C_2 t) \left[1 - \left(\frac{r}{b}\right)^2 - 2\left(\frac{a}{b}\right)^2 \log_e \frac{b}{r} \right] \qquad (17)$$

The maximum longitudinal deformation becomes

$$W_{MAX}(t) = W(a,t) = \frac{b^2}{4} \omega_p C_1 \log_e (1 + C_2 t) \left[1 - \left(\frac{a}{b}\right)^2 - 2\left(\frac{a}{b}\right)^2 \log_e \frac{b}{a} \right] \qquad (18)$$

where it is noted that the <u>deformation</u> is proportional to the <u>square</u> of the <u>diameter</u>.

As an example, we will substitute into equation (18) physical properties of a typical PBAA propellant and determine the magnitude of slump deformations which is possible in big motors. Substituting

$$C_1 = 1.365 \times 10^{-3} \text{ in}^2/\text{lb}$$
$$C_2 = 8.7 \times 10^4 \text{ 1/hrs}$$
$$\omega_p = 0.063 \text{ lbs/in}^3$$

and determining the maximum deformation as a function of time and b/a ratio, the result is plotted in general in Figure 4. The grain slump to be expected in a typical large solid rocket motor where

$$b = 80 \text{ inches}$$
$$b/a = 3$$

for a typical PBAA propellant after 10,000 hours vertical storage is seen to be

$$W_{max} = 1.83 \text{ inches}$$

<u>Determination of the Normal Stresses</u> - The compatibility equation can be written

$$\mathcal{E}_r = \frac{\partial}{\partial r} (r \mathcal{E}_\theta) \qquad (19)$$

We make the assumptions that the normal stress-strain relation is of the form

$$\mathcal{E} = C_3 \sigma \log_e (1 + C_2 t), \qquad (20)$$

similar to the shear stress-strain relation, and that the normal stresses are constant with time, assumptions which will be validated subsequently. Further, the propellant is considered incompressible so that $\nu = \frac{1}{2}$ Thus,

$$\mathcal{E}_r = \frac{3}{4} C_3 \log_e (1 + C_2 t) [\sigma_r - \sigma_\theta] \qquad (21)$$

$$\mathcal{E}_\theta = -\mathcal{E}_r \qquad (22)$$
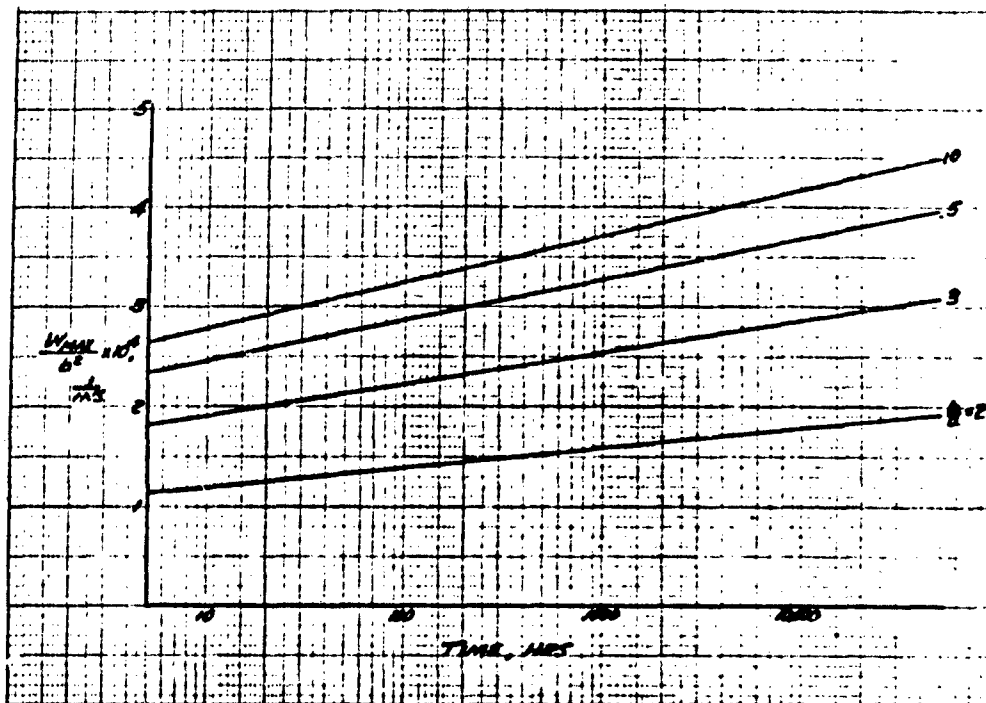
FIGURE 4.
GRAIN MAXIMUM SLUMP VERSUS TIME FOR
VARIOUS b/a RATIOS - PBAA PROPELLANT

Substituting (21) and (22) into the compatibility condition (19), we find

$$\sigma_r - \sigma_\theta = \frac{\partial}{\partial r}\left[r(\sigma_\theta - \sigma_r)\right] \tag{23}$$

Solving for σ_θ and σ_r simultaneously in equations (1) and (23) and
satisfying the boundary conditions (4) and (5), we find that

$$\sigma_\theta(r,t) = \sigma_r(r,t) = 0 \tag{24}$$

Thus, the normal stresses are found to be zero, satisfying the previous
assumption that the normal stresses are time independent.

Establishment of the Stress-Strain Relation - Tests were conducted to
establish the creep properties of a typical PBAA propellant under constant
stress. The test setup is shown in Photograph 3. The specimens were
standard JANAF tensile coupons and the transient strain was determined
optically by means of a cathetometer. The results of the test are plotted
in Figure 5. Linearity of the function on a semilog plot was evident until
tiny transverse cracks began to form at the higher stress levels late in
time. The functional relationship

$$\varepsilon(t,\sigma) = 3.46 \times 10^{-4} \sigma \log_e (1 + 8.7 \times 10^{-4} t) \tag{25}$$

fits the actual data quite well, thus, establishing the validity of
equation (20) with

$$C_3 = 3.46 \times 10^{-4} \frac{IN^2}{LB} \tag{26}$$
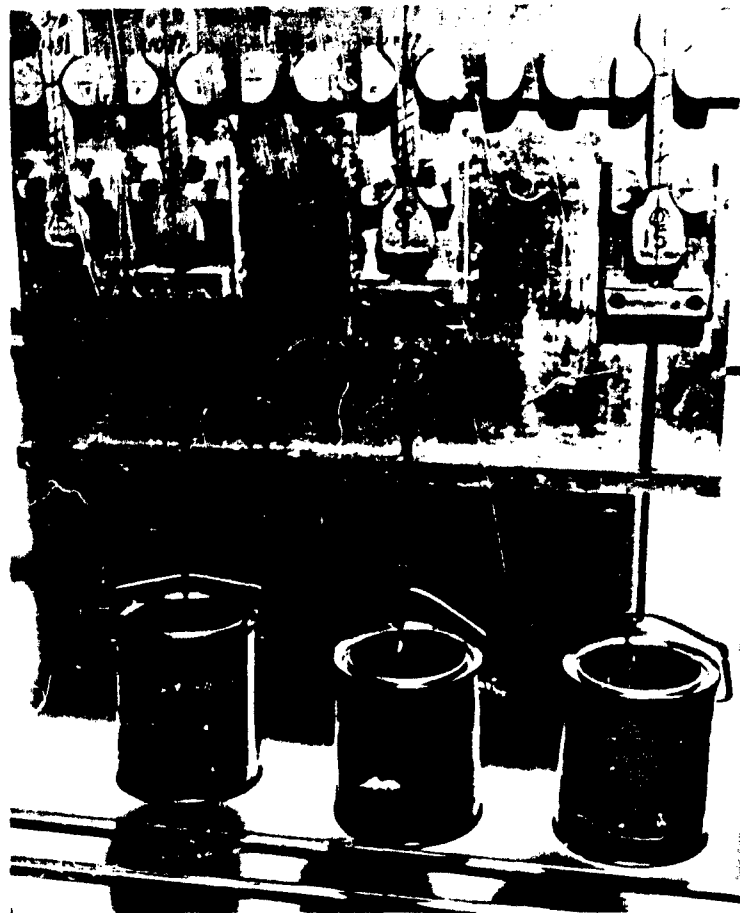
Photograph 3 - Test Setup for Establishment
of Tensile Stress-Strain Relations

$$\epsilon (t,\sigma) = 3.46 \times 10^{-2} \sigma \log_e (1 + 8.7 \times 10^{-2} t)$$
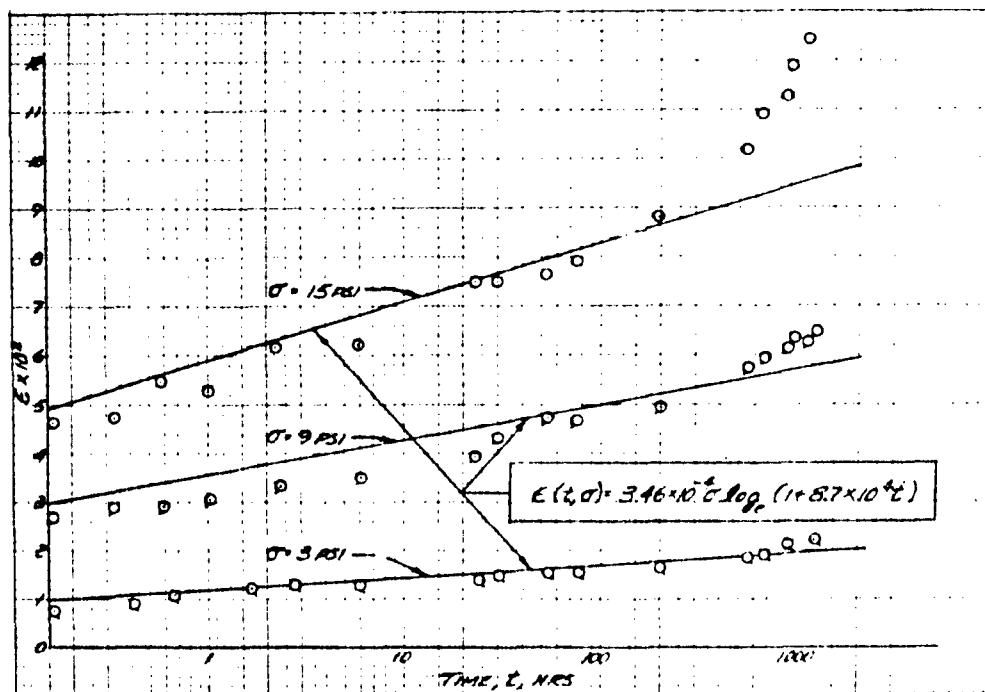
FIGURE 5. RESULTS OF THE CONSTANT TENSILE STRESS TESTS FBAA PROPELLANT

<u>The Finite Length Tubular Grain</u> - Gelatin tests have shown that the maximum longitudinal deformation at the lower free surface is increased by as much as 46% and at the upper free surface is reduced by as much as 46%.[4]

Thus, equation (18) is corrected to account for end effects by a multiplication factor, K, or

$$W_{MAX}(t) = \frac{1}{4} K b^2 \omega_p C_1 \log_e (1 + C_2 t)\left[1 - \left(\frac{a}{b}\right)^2 - 2\left(\frac{a}{b}\right)^2 \log_e \frac{b}{a}\right] \quad (27)$$

where

K = 1.46 at $X = \ell$

= 0.54 at $X = 0$

= 1.0 at $X = \frac{\ell}{2}$ if $\frac{\ell}{c} \geq 3(b-a)$

If the assumption is made that during slump the complete stress field is time independent, then the stresses and deformations can be determined by the elastic solution with time dependent modulus of elasticity. This is possible because of the linearity of strain with stress at any instant of time. It is seen from equation (20) that the instantaneous "effective modulus of elasticity" is

$$E(t) = \frac{1}{C_3 \log_e (1 + C_2 t)} \quad (28)$$

Since the uniform body forces are constant with time, it is quite plausible that the stress field also will be constant with time.

The free ends tend to promote high normal stresses at the propellant to liner bond. This can be seen by considering the elastic solution as the superposition of two solutions. The previously obtained solution for the infinite tubular grain satisfies all boundary conditions for the finite length grain except that the free surfaces have distributed shear stresses equal to

$$\tau_{rx}(0, r, t) = \frac{1}{2} \omega_p r \left[1 - \left(\frac{a}{r}\right)^2\right] \quad (29)$$

If we add to this solution the elastic solution free from body forces with equal but opposite sign surface shear stresses as shown in Figure 6, then the solution with free ends will be obtained. These surface shears are reacted locally to the ends by normal stresses in the liner to propellant bond, tension at the top and compression at the bottom. Numerical procedure currently is being set up to obtain the approximate solution of the latter problem.

CONCLUSIONS

Propellant slump in large solid rocket motors is sufficiently large to warrant consideration in grain design. The normal stresses induced in the liner to propellant bond are high and can promote liner to propellant bond failure. Further study to evaluate the magnitude of these stresses is mandatory.
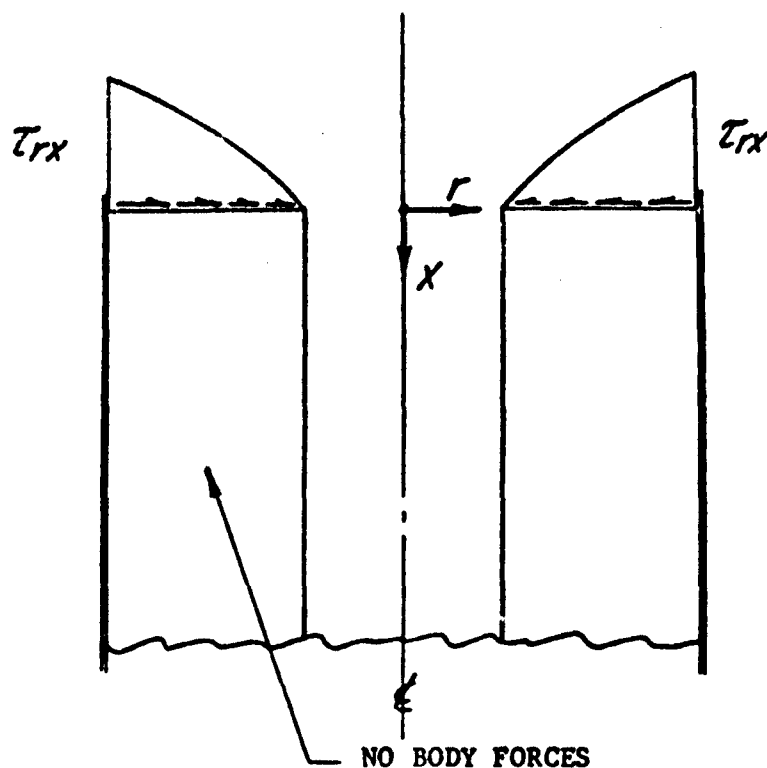
FIGURE 6.
REDUCED PROBLEM FOR DETERMINATION OF NORMAL
STRESSES AT THE LINER-TO-PROPELLANT BOND

REFERENCES

1. Timoshenko, S., "Theory of Elasticity". McGraw-Hill Book Co., Inc.,
    New York (1934).

2. Knauss, W. G., "Displacements in a Tubular Rocket Grain Under Axial
    Acceleration". GALCIT SM 61-10, California Institute of Technology,
    (April, 1961).

3. Williams, M. L.; Blatz, P. J.; and Schapery, R. A., "Fundamental
    Studies Relating to Systems Analysis of Solid Propellants".
    GALCIT SM 61-5, California Institute of Technology, (February, 1961).

4. "Research and Development for Advancing the State-of-the-Art of
    Segmented Solid Propellant Rocketry". GCR report No. P-0062-61,
    Quarterly Progress Report No. 3 (Confidential) (1961).

GRAIN FAILURE CRITERIA THROUGH MODEL TESTS

by

Robert A. Chase
and
Bernard L. Iwanciow

United Technology Corporation
A Subsidiary of United Aircraft Corporation
Sunnyvale, California

ABSTRACT

The feasibility of using stress models of larger prototype systems to obtain a failure criteria was tested. This technique differs from others[1] which have been reported in two important respects; first, the case material and stiffness was preserved through use of case model fabricated of steel to duplicate the case material of a larger prototype. Accurate simulation of the thermal stressing was thereby permitted in addition to stressing caused by case stretching during pressurization. Second, the rate of strain during pressurization duplicated that characteristic of large prototype engines. Strain rates of the order of 200 per cent per second were attained. Preliminary results appear encouraging, but suffer from lack of prolonged storage before the pressurization tests. Future tests, which will include longer storage periods will undoubtedly cause the region of successful performance to shrink considerably.

INTRODUCTION

The demonstrated success of large solid propulsion systems is a prelude to the use of still larger systems for important propulsion requirements of the future. Tests to develop a grain failure criteria utilizing only small amounts of propellant must be devised to permit economic large engine development without the need of resorting to unusually conservative grain designs.

Through the use of subscale model tests, it is anticipated that a satisfactory grain failure criteria will evolve. These tests avoid the difficulties associated with stress analysis of viscoelastic materials and the ambiguities associated with interpretation of results of uniaxial tensile tests.

The authors are indebted to John B. Baldwin and Johann Mertens for preparation and performance of the tests.

MODEL TESTS

Model tests make use of a small scale stress model of a prototype rocket engine. An identical geometric model of the grain is cast into a thin-wall case, carefully following processing procedures which are observed in the production of the prototype. After cooling, the subscale engine is subjected to any of a variety of conditions which duplicate those anticipated for the prototype. Long term storage at selected temperatures and thermal cycling are the two conditions of principal interest. Upon successful survival of

environment tests, the model is hydraulically pressurized at rates simulating the ignition transient. The grains are inspected and monitored for failure during each phase of the tests.

REQUIREMENTS FOR STRAIN SIMULATION

Straining conditions which must be simulated for successful application of model tests are:

1. Shrinkage and thermal strains during cure.

2. Thermal strains from differential contraction between the grain and the case, especially upon cooling from cure temperature.

3. Thermal strains from normal temperature fluctuations.

4. Pressurization upon ignition and steady-state burning.

The use of stress models of prototype systems permits accurate simulation of the above strain producing conditions. It is necessary to use identical materials, both for the propellant and the case and to design the cases to the same stiffness to preserve the grain strains in the model.

Through the use of identical propellant formulations and careful duplication of processing techniques, the grain strains resulting from cure shrinkage will be preserved for corresponding geometrics since cure shrinkage is an extensive property. One difficulty which arises in practice is due to the lack of a measureable exotherm during cure of the model as compared to the prototype engines. Measurements of exotherms in large grains indicate a 5 to 10°F temperature rise. If necessary this difference can be compensated for by adjusting the model cure temperature to reflect the difference in exotherms.

Thermal strains will be greater in large engines because of the nature of the heat transfer phenomena and the insulating characteristics of propellant. However, accepted operating procedures during cool down of large grains make use of gradual temperature changes to minimize large gradients. Fortunately, the cooling procedure for large grains will result in smaller differences in the thermal gradient in models and prototypes than might be realized. Thus no great differences in strains from thermal cycling will occur. Moreover, large grains are stored in temperature controlled facilities, further tending to minimize gradients and producing better simulation of temperature straining between model and prototype.

Ignition transients are the most difficult strain producing condition to simulate. Generally, the ignition transients are sigmoid curves which can be conveniently approximated by a ramp function. The slope of the ramp functions can be converted to constant strain rates which are necessary for quantitative description of the conditions leading to grain failure. The grain geometry and case rigidity must be preserved to obtain accurate strain simulation during ignition.

The use of identical grain and case materials in the model and prototype cannot be overemphasized. Inaccurate simulation of grain strains will result from attempts to substitute other materials. For example, substitution of a thicker walled aluminum case for a thin walled steel case will permit simulation of straining conditions during ignition and steady state pressurization, but will not permit proper straining to be realized during cure and thermal cycling.

Thus, by preserving propellant and case materials, grain geometry, case rigidity, grain processing conditions, ignition transient and operating pressure, complete simulation of the structural behavior of the prototype grain can be achieved through subscale testing. The mode of grain failure will become evident - whether it is during cure, post-cure temperature reduction, ignition or quasi-steady state pressurization.

DISCUSSION

The grain failure envelope for many propellants as determined by uniaxial tests has the characteristic shape (curve A-B) illustrated in Figure 1.[2] This envelope is defined by the terminal points of stress-strain curves obtained during uniaxial testing of the propellants over a wide range of temperatures and strain rates. The grain failure pattern during triaxial test may not necessarily follow the identical behavior as for uniaxial test, however, a general correspondence between temperature, strain rate and grain failure should exist.

It is instructive to describe the anticipated behavior of the failure pattern from model tests in a qualitative manner through the use of the uniaxial failure envelope. Superposed upon the stress-strain space are the initial stress-strain states of the free grain surface of the propellant grain (open symbols) as determined by the cure and thermal shrinkage together with grain geometry. (For cylindrical geometries, the important parameter is the b/a ratio; the case to perforation diameter). Upon pressurization the case expands and the bonded grains follow the case expansion, the total volumetric expansion of the case must be accommodated by a corresponding increase in volume of the perforation. The case strain is independent of the grain geometry and is determined solely by the operating pressure, however, the grain strain at the free surface will be determined by the geometry of the grain together with the magnitude of the case strain. Increasing the b/a ratio will result in a higher final circumferential strain. The vertical lines (Figure 1) terminated by solid symbols corresponding to the initial stress-strain states represent the corresponding circumferential strains of the grain upon reaching operating pressure.

For each initial state (b/a ratio) consider two stress-strain trajectories; xy corresponding to pressurization at low rates or at high grain temperatures, and xz corresponding to pressurization at high rates or at low grain temperatures. Whenever these trajectories cross the failure envelope, (AB), the grain will fail. Conservative grain geometries (b/a_1) survive all combination of ignition rate or grain temperature. High performance grain geometry (b/a_2) survive high temperature or slow ignition, but fail upon fast ignition or low temperature. The configuration (b/a_3) illustrates a poor grain design which survives storage, but fails upon ignition for all conditions.

.The model tests in progress consist of determination of the failure envelope of the grain by examination of a series of geometries (b/a ratios) over wide pressurization rates and a wide temperature range. Establishment of this envelope for any grain configuration will aid the development engineer to select grain designs with greater confidence.

PRELIMINARY TESTS AND RESULTS

A polybutadiene-acrylic acid based propellant was cast into three identical thin-wall cases. The b/a ratios were 3, 4.5, and 6.0. After curing, these grains were stored under ambient conditions for two weeks. Periodic visual inspection for grain failure was made but none was observed. The grains were tested for failure by thermal straining induced by cooling to 40, 20, 0, and -20°F. Inspection again indicated no cracking of the grains. Time did not permit extended storage at any of the test temperatures but this extended storage condition will be included in future studies.

The grains were brought to room temperature and pressurization tests were initiated. In order to obtain preliminary data to demonstrate the feasibility of this proposed method of strain simulation through model testing, it was necessary to carry out these initial dynamic tests without the benefit of a transducer to monitor the grain perforation diameter. The test procedure was modified to operate without a transducer to detect grain strain and grain failure by stepwise pressurization of about 200 psi intervals. After each cycle the case was depressurized, dismantled and the grains inspected for failure. In this way it was possible to obtain the failure pressure to within only ± 100 psi. The maximum test pressure was limited to about 800 psi to prevent damage to the case.

When the grain strain transducer is available these tests will be carried to maximum test pressure in one cycle. The failure point will be recorded as a discontinuity in the tracking of the grain strain transducer trace as compared to the case pressure transducer trace without requiring dismantling the grains during a test.

All tests were run at a nominal pressurization rate of 5000 psi/sec. The measured rates of pressurization usually fell within ± 200 psi/second of this value. This particular rate was selected as it is characteristic of the transient pressure rise to be expected in large booster systems. Subsequent testing will include a range of rates from 1000 psi/second to the maximum attainable by the system. By substitution of larger valves, it will be possible to attain rates two to five times greater than are presently available.

Tests at transient ignition rates were run at (75°F), 40, 20, and 0°F. Again, only short time conditioning at each test temperature was used (about one hour after steady-state temperature was reached.) No failures were observed in any of these tests except at a b/a = 6, and here only at 0°F. This failure occurred between 400 and 600 psi. Based upon these results, the failure envelope at a pressurization rate of 5000 psi/second (200 per cent per second) for the PBAA propellant selected at b/a ratio of six is presented in Figure 6.

DESCRIPTION OF EQUIPMENT AND OPERATION

1. Thin-walled case.

A sketch of the case used to simulate the prototype is shown in Figure 2. The case is constructed of 4130 steel heat treated to 180,000 psi stress. The inside diameter was accurately maintained by a honeing operation, the threads were cut into the end and the piece was heat treated. An expandable mandrel was used to support the case during the subsequent grinding operation to produce a uniform thin wall specified to be 0.0087" thick. These walls proved to be slightly thicker (about 0.0090"). However, systematic measurements showed the thickness to be uniform within 3 per cent. Strain gauges both circumferential and axial are mounted at 90° intervals at the outside center of the case. The case was hydrostatically tested to 950 psi and inspection proved that the elastic region was not exceeded during these tests. The end pieces are slightly concave to allow easy removal of entrained gas during filling with hydraulic fluid. A photograph of the loaded case with strain gauges attached is shown in Figure 3. Figure 4 shows the model mounted on the hydraulic system.

2. Pressurization System.

A block diagram of the pressurization system is shown in Figure 5. Figure 4 is a photo of the pressurization except for the high pressure pump. Referencing to the callouts in Figure 5, the operation of the system follows.

Hand valve (5) is closed and the high pressure pump is adjusted to deliver 500 psi greater than test pressure. Valves (10) and (14) are opened and hydraulic fluid (13) is metered into the subscale model (11) and the flow lines. The ballast tank (3) is filled about half full. Evidence of complete purging of trapped air is obtained by smooth flow of liquid from high point bleed (10). Valves (10) and (14) are closed, valve 8 is adjusted to select the correct pressurization rate. High pressure nitrogen (1) is metered into the ballast tank (3) by use of the regulator valve (2) until the desired test cutoff pressure is reached. The check valve (6) prevents pressurization of the system during this operation. The system is now ready for pressurization. The high speed solenoid valve (7) is opened and the high pressure fluid is throttled into the test system at a controlled rate until the preset test cutoff pressure is reached. At this point the check valve (6) opens and diverts the flow into the ballast tank. The solenoid valve (7) is closed. The system is maintained at the test pressure until the hydraulic fluid return valve (5) is opened to allow the excess fluid to return to the pump reservoir. During the pressurization cycle the strain and pressure transducer outputs are recorded on a high speed oscillograph.

SUMMARY

The description of the failure process presented in the discussion was validated by the preliminary test results. In order to define completely the failure envelope, longer conditioning times at test temperatures are required to duplicate the effects of stress relaxation and delayed failure. These tests focus attention on the need for specifying propellant mechanical property requirements only after the interaction with the case design, rate of ignition transient and effect of quasi-steady state pressurization are considered.
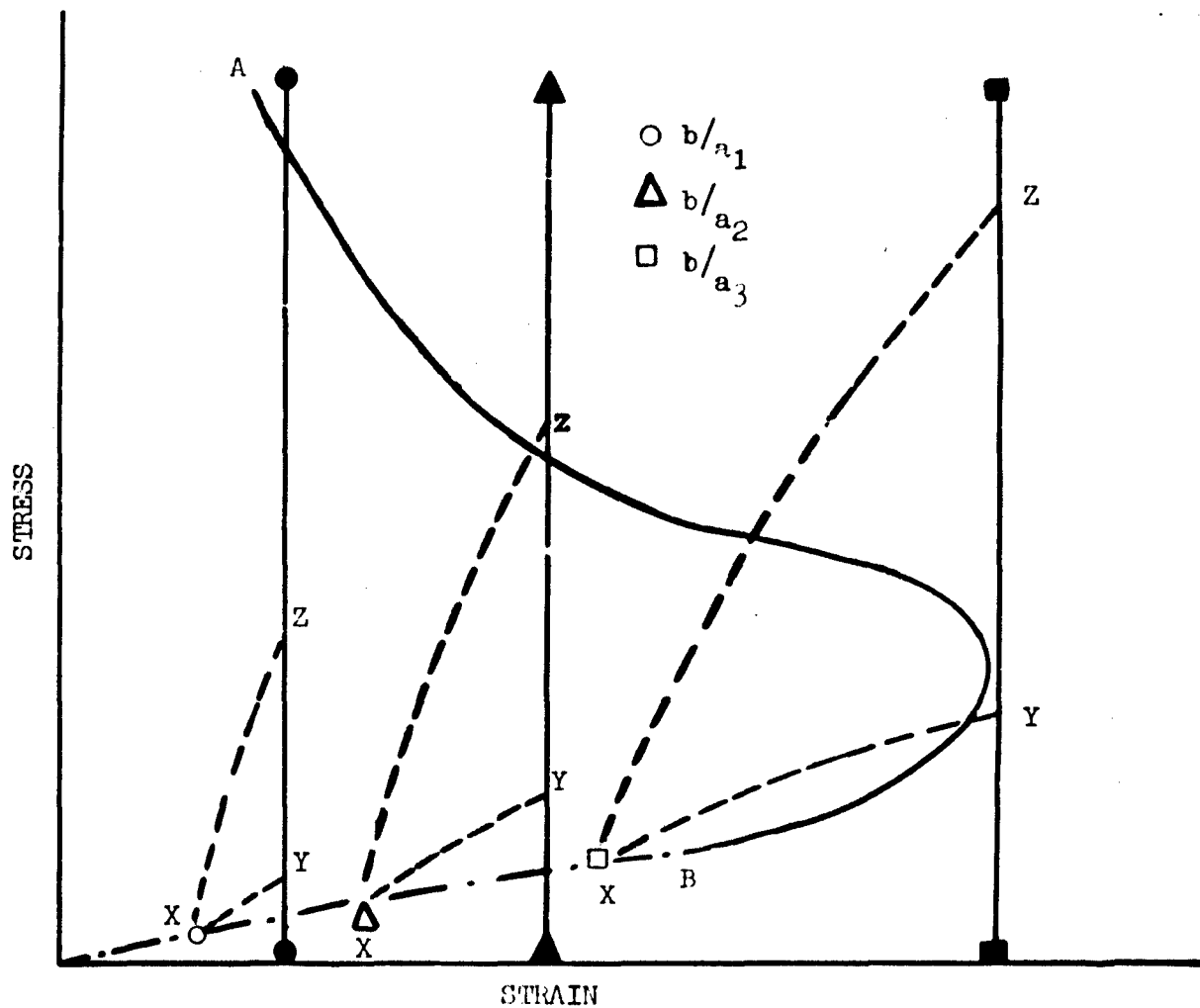
FIGURE 1.
RELATIONSHIP OF GRAIN FAILURE ENVELOPE TO
IGNITION TRAJECTORY AND GRAIN GEOMETRY
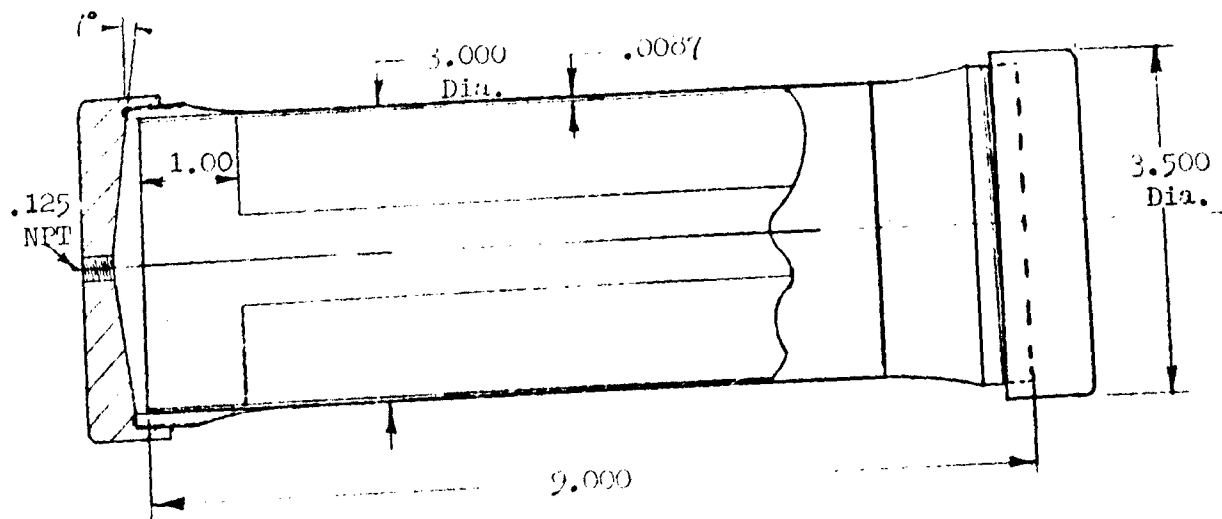
FIGURE 2. STRAIN SIMULATOR CASE
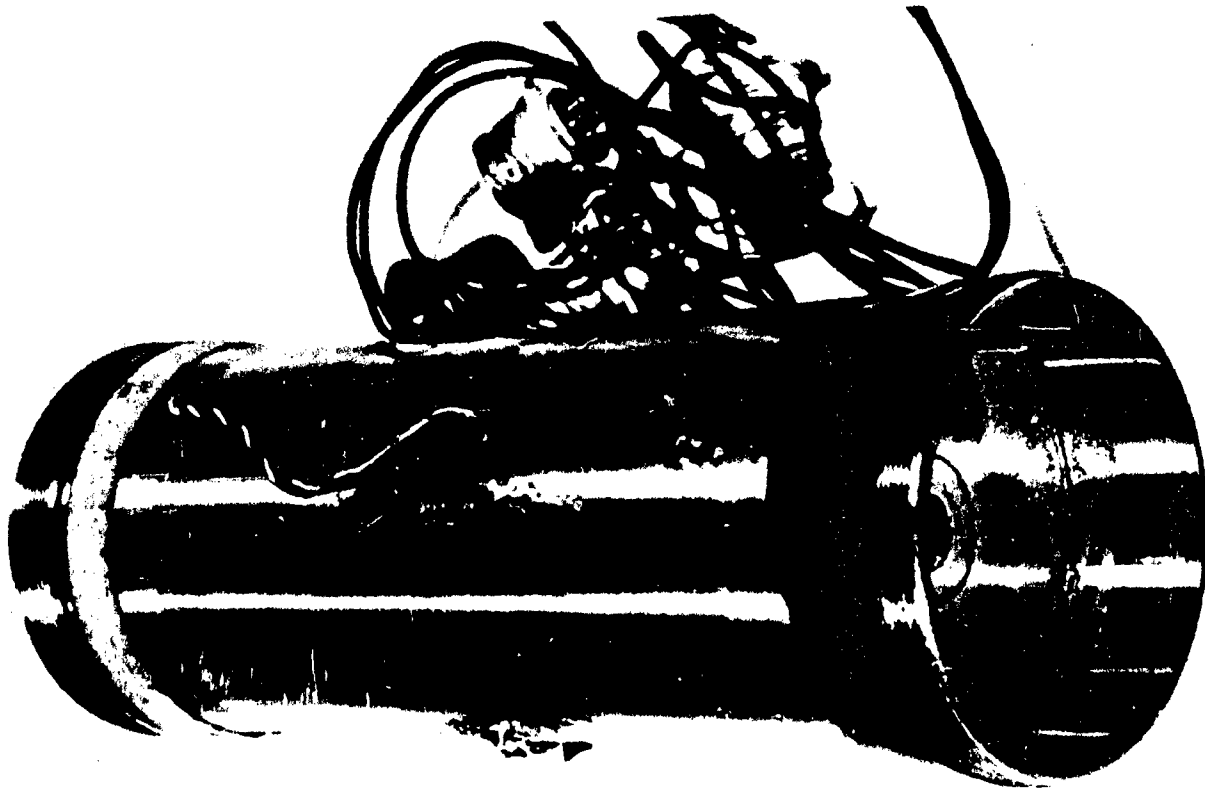
FIGURE 3. LOADED CASE $\left(\dfrac{b}{a}\right) = 6$
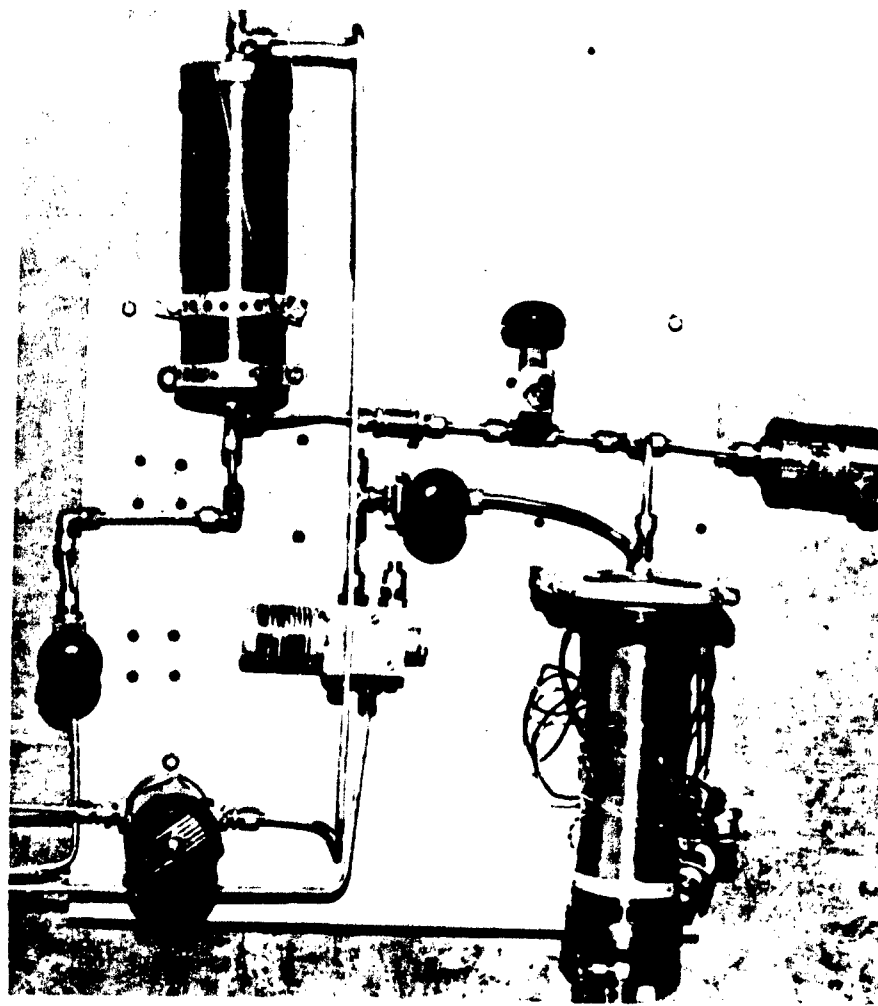
FIGURE 4. PRESSURIZATION SYSTEM
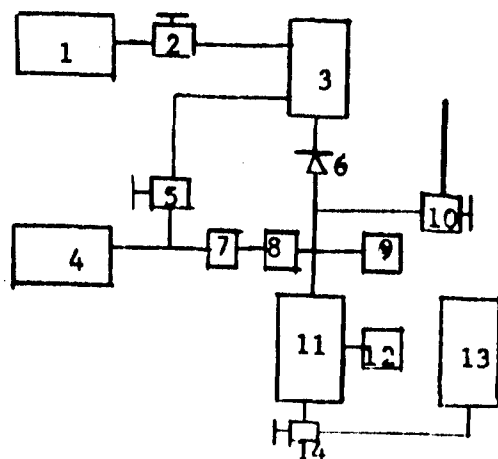
1. High Pressure Nitrogen
2. Grove Regulator
3. Ballast Tank
4. Hydraulic Pump
5. Return Flow Valve
6. Check Valve
7. Solenoid Valve
8. Metering Valve
9. Pressure Transducer
10. High Point Bleed
11. Subscale Model
12. Strain Transducers
13. Hydraulic Fluid Reservoir
14. Hand Valve

FIGURE 5. BLOCK DIAGRAM OF PRESSURIZING SYSTEM

Pressure (psig)

1000

500

0

-20   0   20   40   60   80

Grain Failure
Envelope
Estimated
Measured

Case Failure Pressure

Maximum Test Pressure

Failure
Point

Non-Failure
Test Points
(Open Circles)

$b/a = 6$

$\frac{dp}{dt} = 5000$ psi/sec

FIGURE 6. EXPERIMENTAL FAILURE ENVELOPE

REFERENCES

1. Jet Propulsion Laboratory, Quarterly Summary Report 38-4, pp. 2-4, April 1, 1961 to June 31, 1961.

2. Smith, T. L., S.P.E. Journal, Volume 16, No. 11, November 1960.

THE STRESSES IN AN ELASTICALLY REINFORCED PRESSURIZED VISCOELASTIC SPHERE WITH AN ERODING BOUNDARY

R. J. Arenz and M. L. Williams
California Institute of Technology
Pasadena, California

ABSTRACT

The stress distribution has been determined for a hollow viscoelastic sphere having a thin elastic reinforcing shell and subject to internal time-dependent pressure. The treatment includes the more general problem of an eroding internal boundary. The solution is discussed in detail for an incompressible Voigt material and the results compared with the analogous cylindrical situation.

INTRODUCTION

The viscoelastic stress distribution in an elastically reinforced viscoelastic cylinder under internal pressure has been discussed by Radok and Lee (1). The purpose of the present investigation is to study the analogous situation for a hollow sphere and hence examine the effect of equal biaxial hoop stresses. It may then prove desirable to return to a study of the cylinder except that one could now impose arbitrary biaxial stress ratios by subjecting the tube to axial tension or compression.
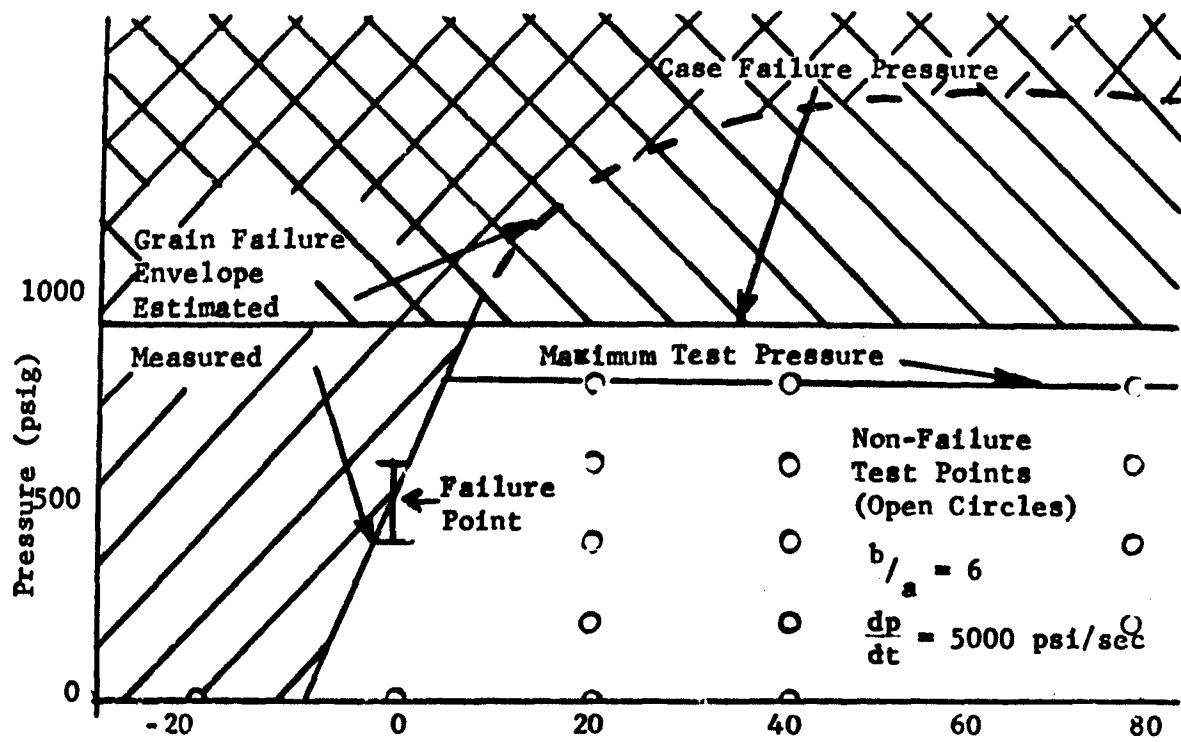
First of all, there is no particular difficulty in determining the stresses for small strains in even a viscoelastic pressurized sphere if it is not reinforced and has a constant internal boundary. For such a situation, it can be easily demonstrated that the elastic and viscoelastic distributions are identical, although the deformations in the latter case are of course time-dependent.

Next, the situation for an elastic reinforcing case can also be simply found, and within a knowledge of the appropriate material representation, e. g. Kelvin, Voigt, etc., the linear viscoelastic stresses can also be determined. Finally, and as an interesting and novel extension, the situation can, following the work of Radok and Lee, be treated for the case when the internal boundary of the reinforced sphere is eroding.

Following this outline then, the above problems will now be presented.

MATHEMATICAL FORMULATION

Consider a hollow sphere of concentric internal and external boundaries a and b, respectively, subjected to an internal pressure p_i. The external surface is reinforced and bonded to a thin elastic spherical container of outside radius c with properties E_c, G_c and ν_c, i.e., Young's modulus, shear modulus, and Poisson's ratio, respectively. For such geometry and loading conditions, considerations of spherical symmetry lead to the reduction of the usual three equations of equilibrium to one, viz.,

$$\frac{d\sigma_r}{dr} + \frac{2(\sigma_r - \sigma_\theta)}{r} = 0 \tag{1}$$

and only one non-zero displacement, u in the radial direction, through which the related strains and stresses are

$$\epsilon_r = \frac{du}{dr} = \frac{1}{E}\left[\sigma_r - 2\nu\sigma_\theta\right] \tag{2}$$

$$\epsilon_\theta = \frac{u}{r} = \frac{1}{E}\left[(1-\nu)\sigma_\theta - \nu\sigma_r\right] \tag{3}$$

where the material properties without subscripts apply to the sphere itself.

Equations (1)-(3) are three equations in three unknowns σ_r, σ_θ and u which are readily solved to give

$$\sigma_r = A - \frac{2}{3}\frac{B}{r^3} \tag{4}$$

$$\sigma_\theta = A + \frac{1}{3}\frac{B}{r^3} \tag{5}$$

$$u = \frac{r}{E}\left[(1-2\nu)A + \frac{(1+\nu)}{3}\frac{B}{r^3}\right] \tag{6}$$

<u>Boundary Conditions.</u>-For the problem under consideration, one has as the boundary condition at the internal radius

$$\sigma_r(a) = -p_i \tag{7}$$

and at the interface, the conditions that

$$\sigma_r^-(b) = \sigma_r^+(b) \tag{8}$$

$$u^-(b) = u^+(b) \tag{9}$$

while outside the sphere and reinforcing container

$$\sigma_r(c) = 0 \tag{10}$$

Using these conditions and the considerations of membrane theory for the thin reinforcing shell, the pressure $\sigma_r(b)$ is related to the tangential stress as follows:

$$\sigma_r(b) = \frac{1-\nu}{\nu - \frac{1-\nu_c}{2}\frac{Eb}{E_c h_c}}\sigma_\theta(b) \equiv \beta\sigma_\theta(b) \tag{11}$$

Proceeding with the determination of the constants A and B in (4) and (5), using (7) and (11), one has

$$A - \frac{2}{3}\frac{B}{a^3} = -p_i \tag{12}$$

$$A - \frac{2}{3}\frac{B}{b^3} = \beta[A + \frac{1}{3}\frac{B}{b^3}] \tag{13}$$

from which B can be eliminated in (13) using (12) to give

$$\frac{B}{b^3} = \frac{3}{2}(\frac{a}{b})^3 (A + p_i) \tag{14}$$

so that

$$\beta[1 + \frac{1}{2}(\frac{a}{b})^3]A - [1 - (\frac{a}{b})^3] A = - (\frac{\beta}{2} + 1)(\frac{a}{b})^3 p_i \tag{15}$$

from which A can be determined.

ELASTIC SOLUTION

First, in the case of a purely elastic material, the solution for the constants is immediate:

$$A = \frac{[1 + \frac{\beta}{2}] (\frac{a}{b})^3 p_i}{1 - (\frac{a}{b})^3 - \beta[1 + \frac{1}{2}(\frac{a}{b})^3]} \tag{16}$$

$$\frac{B}{b^3} = \frac{3}{2} \frac{(1-\beta)(\frac{a}{b})^3 p_i}{1 - (\frac{a}{b})^3 - \beta[1 + \frac{1}{2}(\frac{a}{b})^3]} \tag{17}$$

Since A and B depend on β which in turn is a function of the material properties of the sphere and case, both the stresses (equations (4) and (5)) and deformations (equation (6)) are affected by the relative rigidities of the materials involved.

If no reinforcing shell is present, $\beta = 0$ and the stresses are independent of the material properties of the sphere.

TIME DEPENDENT BEHAVIOR

Suppose now that we have a viscoelastic situation wherein the material properties depend upon time. Thus β becomes a time dependent differential operator, and as pointed out by Radok and Lee, it is important to retain the order of the terms in (15) which now becomes a differential equation in A(t).

As an example one can proceed to analyze the same case as Radok and Lee, namely an incompressible Voigt or Maxwell material. Recalling the definition of β in (11),

$$\beta = \frac{1-\nu}{\nu - [\frac{(1-\nu_c)b}{E_c h_c}]\frac{E}{2}} = \frac{1-\nu}{\nu - \frac{E}{2}\gamma} = \frac{1-\nu}{\nu - \gamma(1+\nu)G} \tag{18}$$

where $\gamma = b(1-\nu_c)/(E_c h_c)$ is time-independent, one has for the special case of an incompressible material, $\nu = 1/2$,

$$\beta = \frac{1}{1 - 3\gamma G} \tag{19}$$

From the stress-strain relations we have the viscoelastic formulation

$$P^p s_{ij} = Q^q e_{ij}, \qquad R^r \sigma_{ij} = S^s \epsilon_{ij} \tag{20}$$

where

$$\epsilon_{ij} = \tfrac{1}{2}(u_{i,j} + u_{j,i}), \quad s_{ij} = \sigma_{ij} - \tfrac{1}{3}\delta_{ij}\sigma_{kk},$$

$$e_{ij} = \epsilon_{ij} - \tfrac{1}{3}\delta_{ij}\epsilon_{kk} \tag{21}$$

and the operators are defined as

$$P^p = \sum_0^p p_n \, \partial^n/\partial t^n, \quad Q^q = \sum_0^q q_n \, \partial^n/\partial t^n,$$

$$R^r = \sum_0^r r_n \, \partial^n/\partial t^n, \quad S^s = \sum_0^s s_n \, \partial^n/\partial t^n \tag{22}$$

Thus the shear modulus is, in operator form,

$$2G = 2\mu = \frac{Q^q}{P^p} \tag{23}$$

and so

$$\beta = \frac{1}{1 - \frac{3\gamma}{2}\frac{Q^q}{P^p}} = \frac{P^p}{P^p - (\frac{3\gamma}{2})Q^q} \tag{24}$$

Writing

$$[a(t)/b]^3 = m(t) \tag{25}$$

equation (15) thus becomes

$$\frac{P^p}{P^p - (\frac{3\gamma}{2})Q^q}\left[1 + \frac{m}{2}\right]A - (1-m)A = -\left[\frac{P^p}{2(P^p - (\frac{3\gamma}{2})Q^q)} + 1\right]mp_i \tag{26}$$

and clearing, we find

$$P^p[mA] + \gamma Q^q[(1-m)A] = -[P^p - \gamma Q^q]\,mp_i \tag{27}$$

For the special two-element model operators

$$P^p = p_0 + p_1\,d/dt, \quad Q^q = q_0 + q_1\,d/dt \tag{28}$$

where the values $p_0 = 1$, $p_1 = 0$, $q_0 \neq 0$, $q_1 \neq 0$ imply an incompressible Voigt material, and $p_0 \neq 0$, $p_1 \neq 0$, $q_0 = 0$, and $q_1 = 1$ imply the incompres-

sible Maxwell model, (27) becomes

$$[(p_0 + p_1 \frac{d}{dt})m + \gamma(q_0 + q_1 \frac{d}{dt})(1-m)] A(t) = -[(p_0 - \gamma q_0) + (p_1 - \gamma q_1)\frac{d}{dt}] m(t) p_i(t) \quad (29)$$

which first order equation can be solved using an integrating factor.

CONSTANT INTERNAL BOUNDARY

In this case, specializing to $m \neq f(t)$, the equation (29) has the integrating factor

$$F(t) = \exp\left[-\frac{mp_0 + \gamma(1-m)q_0}{mp_1 + \gamma(1-m)q_1} t\right] \quad (30)$$

so that the solution is easily written down as

$$A(t) = \frac{me^{-Kt}}{p_1 m + \gamma(1-m)q_1} \int e^{Kt}[-p_0 + \gamma q_0 + (-p_1 + \gamma q_1)\frac{d}{dt}] p_i \, dt + Ce^{-Kt} \quad (31)$$

where

$$K = \frac{p_0 m + \gamma(1-m)q_0}{p_1 m + \gamma(1-m)q_1} \quad (32)$$

and the constant is to be determined by initial conditions.

THE BURNING BOUNDARY

When the boundary is eroding and $m = m(t)$, the calculations, as expected, become more complicated. The equation, however, can again be solved using an integrating factor $G(t)$ after first writing (29) in the form

$$[p_1 m + \gamma q_1(1-m)]\frac{dA}{dt} + [mp_0 + \gamma q_0(1-m) + (p_1 - \gamma q_1)\frac{dm}{dt}] A$$

$$= [(-p_0 + \gamma q_0) + (-p_1 + \gamma q_1)\frac{d}{dt}] (mp_i)$$

Thus

$$G(t) = \exp \int [-\frac{mp_0 + \gamma q_0(1-m) + (p_1 - \gamma q_1)(dm/dt)}{p_1 m + \gamma q_1(1-m)}] \, dt \quad (33)$$

$$= \frac{H(t)}{p_1 m + \gamma q_1(1-m)} \quad (34)$$

where as a result of division, integration, and simplification,

$$H(t) = \exp\left[-\frac{p_0 - \gamma q_0}{p_1 - \gamma q_1} t + \frac{\gamma(p_0 q_1 - p_1 q_0)}{p_1 - \gamma q_1} \int \frac{dt}{p_1 m + \gamma q_1(1-m)}\right] \quad (35)$$

Hence, for zero initial conditions the solution (after performing the indicated operations) becomes

$$A(t) = -G(t) \left\{ \frac{(p_1 - \gamma q_1)(mp_i)}{H(t)} + \gamma(p_0 q_1 - p_1 q_0) \int_0^t \frac{mp_i \, d\tau}{H(\tau)[p_1 m + \gamma q_1(1-m)]} \right\} \quad (36)$$

Equations (34), (35), and (36) depend upon the materials involved. If the particular constants are specified, the expressions may be evaluated, numerically if necessary, to give the time dependent stresses for an internally pressurized elastically reinforced sphere of incompressible Maxwell or Voigt type material characteristics.

APPLICATION TO INCOMPRESSIBLE VOIGT MATERIAL

The particular case of an incompressible Voigt material will now be considered. The viscoelastic coefficients in (28) are

$$p_0 = 1, \quad p_1 = 0, \quad q_0 \neq 0, \quad q_1 \neq 0 \quad (37)$$

Equations (34) to (36) correspondingly simplify to

$$G(t) = \frac{H(t)}{\gamma q_1(1-m)} \quad (38)$$

$$H(t) = \exp\left[\frac{1 - \gamma q_0}{\gamma q_1} t - \frac{1}{\gamma q_1} \int \frac{dt}{1-m} \right] \quad (39)$$

$$A(t) = -G(t) \left[\frac{-\gamma q_1(mp_i)}{H(t)} + \int_0^t \frac{mp_i \, d\tau}{(1-m)H(\tau)} \right] \quad (40)$$

A burning time function for annihilation of the viscoelastic interior can be approximated as

$$a(t) = \frac{a_0}{(1-kt)^{1/3}} \quad (41)$$

where a_0 is the initial radius. Analogously to the function used by Radok and Lee for the cylinder, this function leads to simple integrals for evaluation of the stresses. The annihilation time t_0 for the whole interior to be burned out will be given by

$$b = \frac{a_0}{(1-kt_0)^{1/3}} \quad (42)$$

and (41) may now be written

$$\frac{a(t)}{a_0} = \left[1 - \left(1 - \frac{a_0^3}{b^3}\right) \frac{t}{t_0} \right]^{-\frac{1}{3}} \quad (43)$$

Compared to these, the cylindrical relations of Radok and Lee involve a_0^2/b^2 and the square root instead of the cube root. The annihilation function (43) for various ratios b/a_0 is shown in Fig. 1. While these curves are slightly more non-linear than those indicated by Radok and Lee for the cylinder, still an approximately constant burning rate is exhibited if the

ratio b/a_0 is not too large.

For this function, (39) gives

$$H(t) = e^{-t/\tau_1} (t-t_0)^{t_0/\tau_0} \tag{44}$$

where τ_1 is defined as

$$\tau_1 = \frac{q_1}{q_0} , \tag{45}$$

that is, the delay time of the viscoelastic material, and

$$\tau_0 = \gamma q_1 (\frac{b^3}{a_0^3} - 1) = \gamma q_1 (\frac{kt_0}{1-kt_0}) \tag{46}$$

has the dimension of a time; it involves, besides the geometrical quantities b and a_0, the viscosity q_1 of the internal material and the elastic property γ of the reinforcement. Hence it can be thought of as a sort of delay time for the elastic casing when it is associated with the viscosity of the inner material.

Denoting the ratio of the annihilation time t_0 and τ_0 by

$$T = \frac{t_0}{\tau_0} , \tag{47}$$

equation (40) now becomes

$$A(t) = - \frac{1-kt_0}{k} \frac{p_i}{t-t_0} - \frac{1-kt}{k} T \; e^{-\frac{t}{\tau_1}} (t-t_0)^{T-1}$$
$$\int_0^t e^{\frac{\tau'}{\tau_1}} (\tau'-t_0)^{-(T+1)} p_i \, d\tau' \tag{48}$$

where the notation τ' is used for the variable of integration. This result may now be used to evaluate the radial and tangential stresses in the viscoelastic material. For example, using (4) and (14), the radial stress is given by

$$\sigma_r (r,t) = A - \frac{2}{3} \frac{B}{r^3} = A(1 - \frac{a^3}{r^3}) - \frac{a^3}{r^3} p_i \tag{49}$$

In particular, for $r = b$, the pressure on the casing is found to be

$$\sigma_r(b,t) = T(t-t_0)^T \; e^{\frac{-t}{\tau_1}} \int_0^t e^{\frac{\tau'}{\tau_1}} (\tau'-t_0)^{-(T+1)} p_i(\tau')d\tau' \tag{50}$$

By equation (11), this pressure is directly proportional to the hoop stress produced in the casing, the ratio of biaxial hoop stress to pressure being given by the factor $(b/2h_c)$.

At this point, it may be noted that (50) for the pressure on the casing is of essentially the same form as the comparable solution given by Radok and Lee for the case of cylindrical symmetry. The reason is apparent from a comparison of the operator form (27) of the differential equation and the stress equation (49) with the corresponding expressions on pages 8 and 11 of Radok and Lee's paper. Furthermore, the similarity is dependent on choosing the burning function (41) which, as was noted above, defines a different burning rate for the sphere than the comparable function for a cylinder. Hence direct equivalence of the type noted for equation (50) does not in general hold good for radii other than the boundaries of the viscoelastic material. This latter feature is valuable however, as certain non-dimensionalized results derived by Radok and Lee for the cylinder can be used for the sphere, keeping in mind the appropriate sign conventions and definitions of parameters.

Specifically, they consider the case of a step function pressure variation in which

$$p_i(t) = \begin{cases} 0 & \text{for } t \leq 0 \\ p_0 & \text{for } t > 0 \end{cases} \tag{51}$$

and the ratio T is an integer. Integration of (50) by parts T times results in

$$\sigma_r(b,t) = -\frac{p_0}{(T-1)!}\left[(1-\tau)^T e^{-\frac{\tau}{n}} \sum_{l=0}^{T-1} \frac{(-1)^{l+1}(T-l-1)!}{n^l}\right.$$

$$-\sum_{l=0}^{T-1} \left(\frac{1-\tau}{n}\right)^l (-1)^{l+1}(T-l-1)!$$

$$\left. + (-1)^T \left(\frac{1-\tau}{n}\right)^T e^{\frac{1-\tau}{n}} \int_{1-\tau}^{1} \frac{e^{-\frac{\sigma}{n}}}{\sigma} d\sigma \right] \tag{52}$$

where

$$n = \frac{\tau_1}{t_0} \quad \text{and} \quad \tau = \frac{t}{t_0} \tag{53}$$

As noted by Radok and Lee, the integral of (52) may be expressed in terms of the exponential integral

$$Ei(-x) = -\int_x^{\infty} \frac{e^{-y}}{y} dy \tag{54}$$

which is tabulated in Jahnke (2). In fact,

$$\int_{1-\tau}^{1} \frac{e^{-\frac{\sigma}{n}}}{\sigma} d\sigma = \int_{\frac{1-\tau}{n}}^{\frac{1}{n}} \frac{e^{-y}}{y} dy = Ei(-\frac{1}{n}) - Ei\left(\frac{\tau-1}{n}\right) \tag{55}$$

A plot of the stress $\sigma_r(b,\tau)$ at the interface against $\tau = t/t_0$ is shown

in Fig. 2 for the particular case when

$$\tau_0 = \tau_1 \tag{56}$$

which implies by (45) and (46) that

$$\gamma q_0 = \frac{1}{\dfrac{b^3}{a_0^3} - 1} \tag{57}$$

which indicates a fixed relationship between the elastic properties of the internal and reinforcing materials.

The plot of Fig. 2 is obtained directly from the corresponding graph of Radok and Lee in accordance with the statement above regarding the equivalence of this non-dimensional presentation at $r = b$. The parameters, however, must be taken as defined herein for the spherical geometry. Since T is the ratio between the annihilation and casing retardation times, the curves illustrate the time histories of the stress in the reinforcement (since it is directly proportional to the radial stress in the inner material) for different annihilation times for a given sphere and casing. The curve corresponding to $T = \infty$, that is, for very slow burning rate relative to delay time, may be deduced from the elastic results since in this case the elastic solution corresponding to the spring element of the Voigt model applies except for a duration of the delay time order of magnitude immediately after application of the pressure. In this quasi-steady region, putting $2G = q_0$, this stress is

$$\sigma_r (b, \tau) = \frac{-P_0}{2 - \tau} \tag{58}$$

During the initial period of the order of the delay time, the pressure on the casing increases from zero along the line 0A due to the viscoelastic stress. For $T \to \infty$ this appears as a vertical line with $\tau = 0$ as abscissa.

As the inner material disappears, the pressure on the casing increases until the casing carries the full gas pressure at time t_0, as indicated by the point B in Fig. 2. For longer times than t_0, the casing stress remains constant if the gas pressure is maintained.

As the parameter T decreases to the order unity, the pressure rise on the casing becomes more gradual. For the limit $T = 0$, annihilation is completed in a time short compared with the delay time, and viscoelastic deformation does not have time to take place to transmit the gas pressure to the casing. Thus the casing stress curve approaches OCB, the gas pressure being carried by the casing only when the inner material has been burned away.

Analogous curves may be calculated for cases in which τ_0 is a multiple of τ_1 or vice versa. The quasi-steady solution in each individual case will establish the proportionality factor and give the limiting curve for the time history of the radial stress.

DISCUSSION

A comparison can be made on the basis of Fig. 2 between the stress build-up in the spherical geometry and that in the cylinder treated by Radok and Lee. It will be assumed that the viscoelastic and reinforcing materials in each geometry have the same set of material properties (q_0, q_1, ν_c, etc.). Inasmuch as Fig. 2 is drawn for the case of $\tau_0 = \tau_1$, (57) immediately requires the satisfaction of the following condition:

$$\gamma_3 \left[\left(\frac{b_3}{a_{0_3}} \right)^3 - 1 \right] = \gamma_2 \left[\left(\frac{b_2}{a_{0_2}} \right)^2 - 1 \right] \tag{59}$$

where the subscripts 3 and 2 refer to the sphere and cylinder, respectively.

Assuming the reinforcement to be made of steel ($\nu_c = 0.3$) and taking standard rocket design practice of a roughly constant ratio of reinforcement thickness (h_c) to radius (b), the differing boundary conditions of the two geometries require that

$$\gamma_2 = 1.3\gamma_3 \tag{60}$$

As noted earlier, the radial burning rate is considered to be approximately constant, which permits the approximate relation of burning times to be written as

$$\frac{t_{0_3}}{t_{0_2}} = \frac{b_3 - a_{0_3}}{b_2 - a_{0_2}} \tag{61}$$

Consider now for a specific comparison a cylinder with $b_2/a_{0_2} = 2$, for which (59) and (60) give $b_3/a_{0_3} = 1.7$ as the corresponding sphere. To give the same initial conditions, set a_{0_3} equal to a_{0_2}. These results, combined with (61), (47) and the fact that the casing retardation time τ_0 must be the same for the two configurations, give

$$\frac{T_3}{T_2} = 0.7 \tag{62}$$

Since T_3 is less than T_2, Fig. 2 indicates a more gradual pressure rise on the casing as a function of τ for the spherical geometry. However, since the actual burning time t_{0_3} for the sphere is only 70% of that for the comparable cylinder, the stress rise at the reinforcement is in fact more rapid time-wise for the sphere throughout the complete burning time t_{0_3}. This is illustrated in Fig. 3. Similar results occur for other T ratios.

While a direct comparison for the same b/a_0 ratio would require the calculation of a new graph comparable to Fig. 2 for another τ_0/τ_1 ratio, the indication from the present work is that the pressure rise in the sphere is at a faster rate than in the cylinder.

REFERENCES

1. Radok, J. R. M., and Lee, E. H.: Stresses in Elastically Reinforced, Visco-elastic Tubes with Internal Pressure. Brown University T.R. No. 15 (Appl. Math. Div.) April 1956.

2. Jahnke, E., and Emde, F.: Tables of Functions. Dover Publications, New York, 1945.
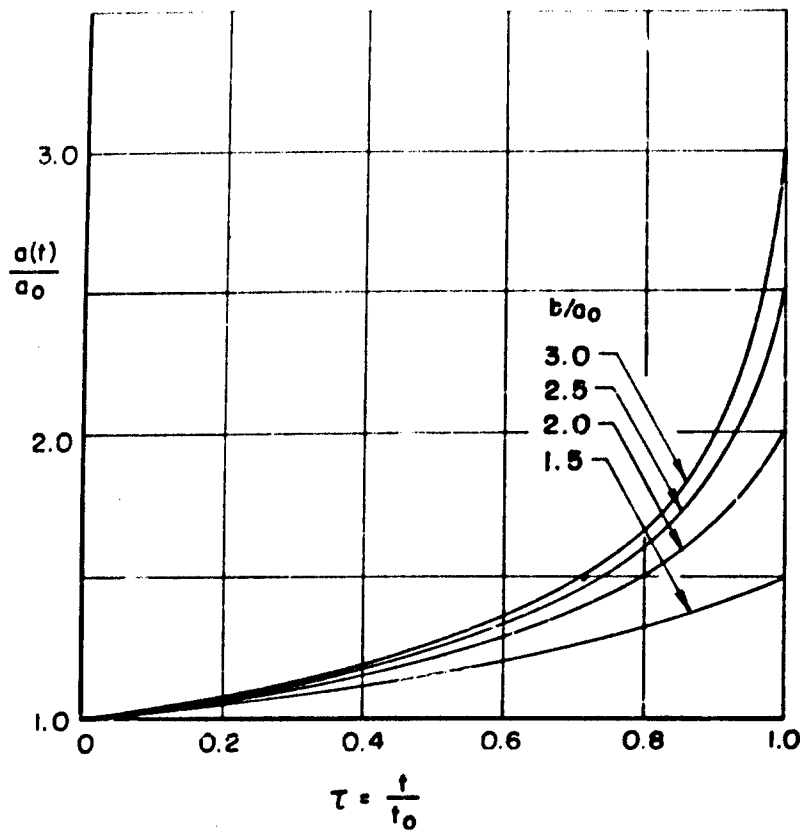
FIGURE 1.
ANNIHILATION FUNCTION
(43) FOR VARIOUS VALUES
OF b/a_o

a_o = Original Internal Radius

b = External Radius Of Visco-Elastic Material

t_o = Total Burning Time

FIGURE 2.
RADIAL STRESS AT REINFORCEMENT
(r = b)
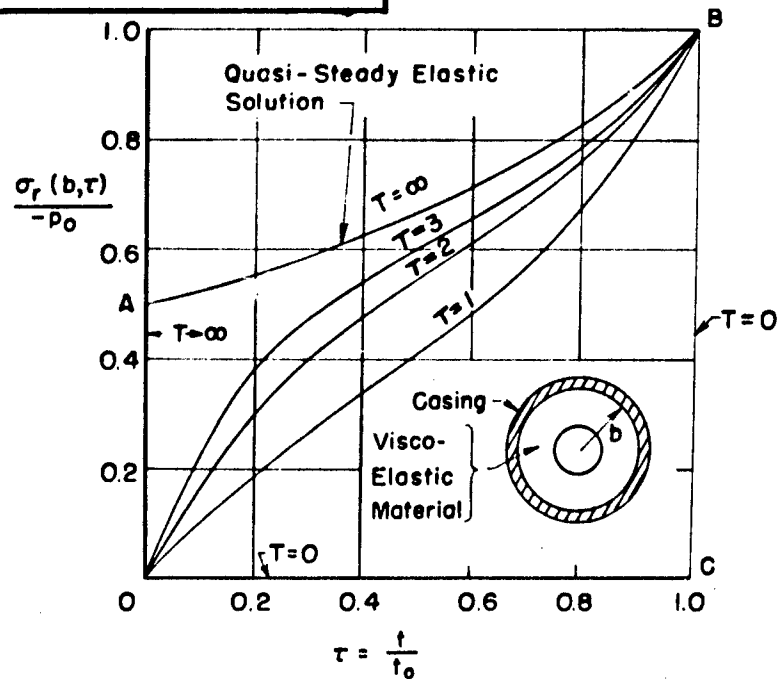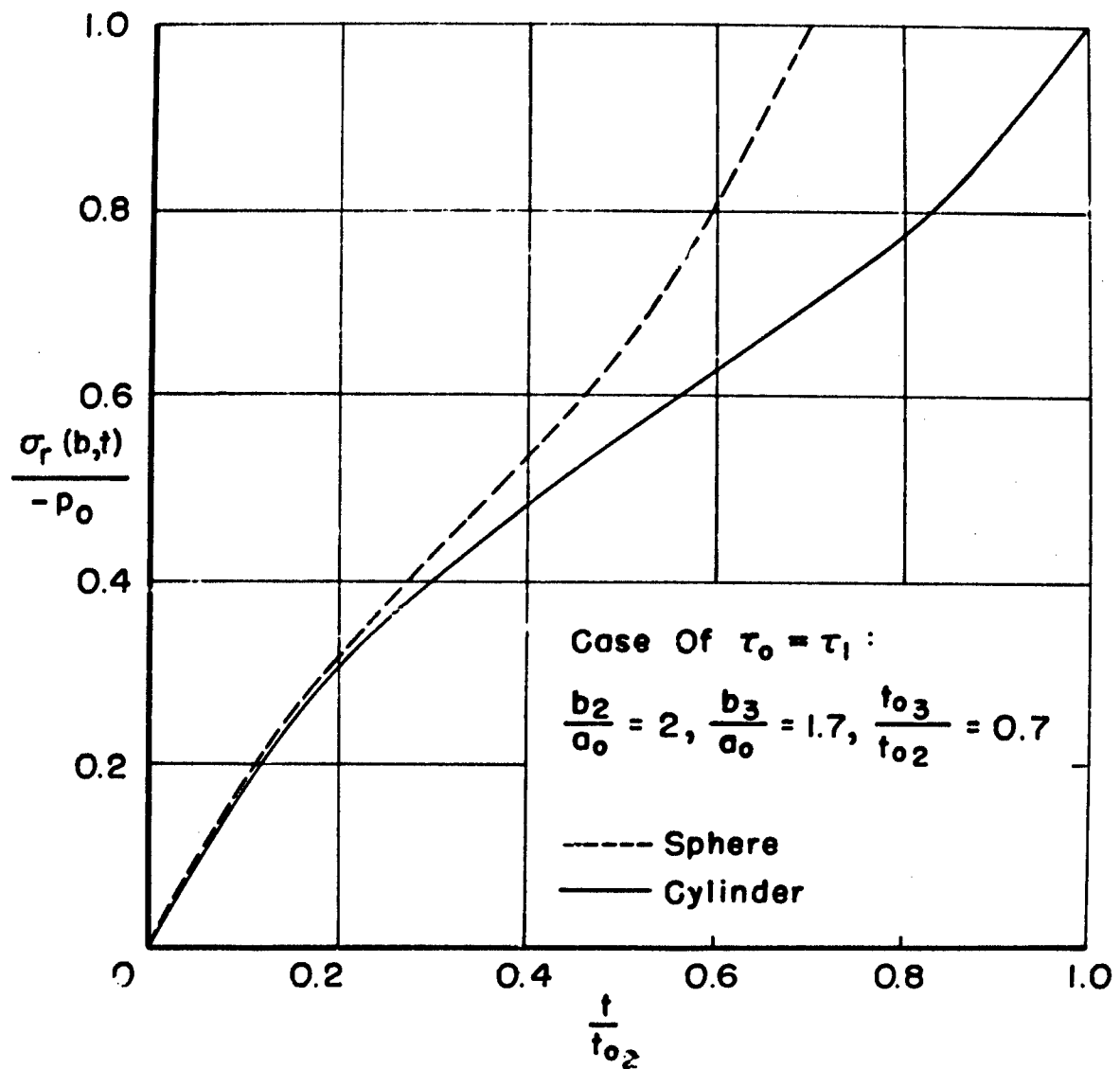
$T = \dfrac{t_o}{\tau_o} = \dfrac{\text{Annihilation Time}}{\text{Casing Retardation Time}}$

Curves For Case In Which $\tau_o = \tau_1$ = Visco-Elastic
Material Delay Time

FIGURE 3.
COMPARISON OF RADIAL STRESS RISE AT REINFORCEMENT IN
CYLINDER AND SPHERE FOR CASE IN WHICH $\tau_0 = \tau_1$

AXIAL SLUMP OF A CIRCULAR PORT GRAIN[1]

J. Edmund Fitzgerald, Associate Director
T. Harrison, Research Engineer
E. Francis, Research Engineer
Propulsion Engineering Division
Grand Central Rocket Co.
Redlands, California

ABSTRACT

Vertical slump tests were carried out for a 50 percent web fraction, 1.5 L/D circular port grain segment. One test was conducted using a 10-inch long gelatin grain and the other test was conducted using a 54-inch long Polycarbutene grain. Propellant properties were determined in the laboratory and described by a fourth order linear differential operator. Scaling relations between the gelatin model and the propellant model were confirmed. A consistent 35 percent deviation from the predictions of Knauss' theory was found. A prediction for a ramp function acceleration setback using the finite linear viscoelastic operator is given.

INTRODUCTION

The problem of accurately predicting axial slump in solid propellant grains has become quite acute with the advent of large solid propellant grains. This paper will briefly set forth the results of the following steps in the investigation.

(1) Creep and stress relaxation experiments on constant cross-section tab end samples carried out in order to determine the coefficients a_i, b_i in,

(2) The finite linear differential operation stress-strain law

$$\left[a_n \frac{\partial^n}{\partial t^n} + a_{n-1} \frac{\partial^{n-1}}{\partial t^{n-1}} + \cdots + a_1 \frac{\partial}{\partial t} + a_0 \right] \sigma(t)$$

$$= \left[b_n \frac{\partial^n}{\partial t^n} + b_{n-1} \frac{\partial^{n-1}}{\partial t^{n-1}} + \cdots + b_1 \frac{\partial}{\partial t} + b_0 \right] \epsilon(t)$$

used to characterize the gelatin and the propellant,

---

(3) The axial slump equation derived by Knauss and given in these proceedings, yielding the slump at the inner periphery of the port as

$$\omega(t) = \frac{3}{4} \rho g a^2 \left(\lambda^2 - 2 \ln \lambda - 1 \right) \frac{f(t)}{E}$$

where ρ = density, g = standard gravity, a = inner port radius, b = outer grain radius, $\lambda = b/a$, E = elastic modulus, and $f(t)$ is the time-dependent g-loading function.

(4) Use of the viscoelastic analogy wherein (writing the stress-strain law of step (2), as $P\sigma(t) = Q\epsilon(t)$ where P and Q are the differential operators), one substitutes the value of E in the equation of step (3) with $\frac{Q}{P}$ and solves the resulting differential equation.

(5) Slump tests on a 50 percent web fraction ($\lambda = 2.0$) gelatin model with L/D = 1.5 where D = 2b and the length L = 10 inches.

(6) Slump tests on a 50 percent web fraction Polycarbutene propellant model 36 inches in diameter by 54 inches long (L/D = 1.5) containing 2,500 lb of live propellant.

(7) Comparison of experiment with predicted theory.

PROPELLANT CHARACTERIZATION

Creep and stress relaxation experiments provided values for the stress-strain law referred to such that it becomes

$$\left[1.339 \frac{\partial^4}{\partial t^4} + 44.7 \frac{\partial^3}{\partial t^3} + 147.4 \frac{\partial^2}{\partial t^2} + 46.76 \frac{\partial}{\partial t} + 1.0 \right] \sigma(t)$$

$$= \left[2811 \frac{\partial^4}{\partial t^4} + 34,924 \frac{\partial^3}{\partial t^3} + 62,287 \frac{\partial^2}{\partial t^2} + 13,994 \frac{\partial}{\partial t} + 222.7 \right] \epsilon(t)$$

or $P\sigma(t) = Q\epsilon(t)$

ANALYTICAL SOLUTION

Rewriting Knauss' solution as

$$\omega(t) = A \frac{P}{Q} f(t)$$

where $A = \frac{3}{4} \rho g a^2 (\lambda^2 - 2 \ln \lambda - 1)$

and $f(t)$ is the ramp acceleration function

$$f(t) = Rt - R(t - t_1) u(t - t_1)$$

yields upon Laplace transformation

$$\omega(s) = \frac{AR(a_4 s^4 + a_3 s^3 + a_2 s^2 + a_1 s + a_0)(1 - e^{-t_1 s})}{s^2 (b_4 s^4 + b_3 s^3 + b_2 s^2 + b_1 s + b_0)}$$

Letting the four roots of the polynomial in the denominator be $-\beta_1, -\beta_2, -\beta_3$ and $-\beta_4$ (after normalizing b_4) and considering the two zero poles $-\beta_5 = -\beta_6 = 0$ given by S^2 then yields the six residues K_1, through K_6. The solution in the time space is then readily written as

$$\frac{\omega(t)}{AR} = K_1 e^{-\beta_1 t} + K_2 e^{-\beta_2 t} + K_3 e^{-\beta_3 t} + K_4 e^{-\beta_4 t} + K_5 + K_6 t$$

$$- \left[K_1 e^{-\beta_1 (t-t_1)} + K_2 e^{-\beta_2 (t-t_1)} + K_3 e^{-\beta_3 (t-t_1)} \right.$$

$$\left. + K_4 e^{-\beta_4 (t-t_1)} + K_5 + K_6 (t-t_1) \right] u(t-t_1)$$

TESTS

A 10-inch by approximately 6.6-inch gelatin model was first used to check the theory. The relaxation times were such as to cause the solution to degenerate to an elastic solution with a relaxation modulus $E = b_0/a_0$ of about 4.5 psi in a few minutes. The resultant experimental slump exceeded the predicted slump by 1.35 times.

A 36-inch diameter evaluation grain of polycarbutene propellant was tested for long-term slump wherein t_1 was several seconds. The theoretical curve, as well as the 1.35 factor curve, are plotted in Figure 1. Again it can be seen that the 1.35 factor applies here. Figure 2 shows the gelatin test setup and Figure 3 shows the propellant evaluation grain test. Figure 4 shows the prediction for a 120-inch diameter 1.5 L/D grain with a 6-g acceleration setback and a ramp time, t_1, of 0.1 seconds.

CONCLUSION

Utilizing a modification of Knauss' theory such that

$$\omega(t) = \rho g a^2 \left(\lambda^2 - 2 \ln \lambda - 1 \right) \frac{f(t)}{E}$$

yields vertical slump predictions that have been confirmed by approximately 6-inch diameter gelatin models and by 36-inch diameter propellant models. The use of the finite linear differential operator characterization of the propellant appears to be fully justified for slump predictions when a fourth order or higher operator is used. The use of uniaxially determined operators appears to be valid in predicting slump deflections in full-scale grain analogs.
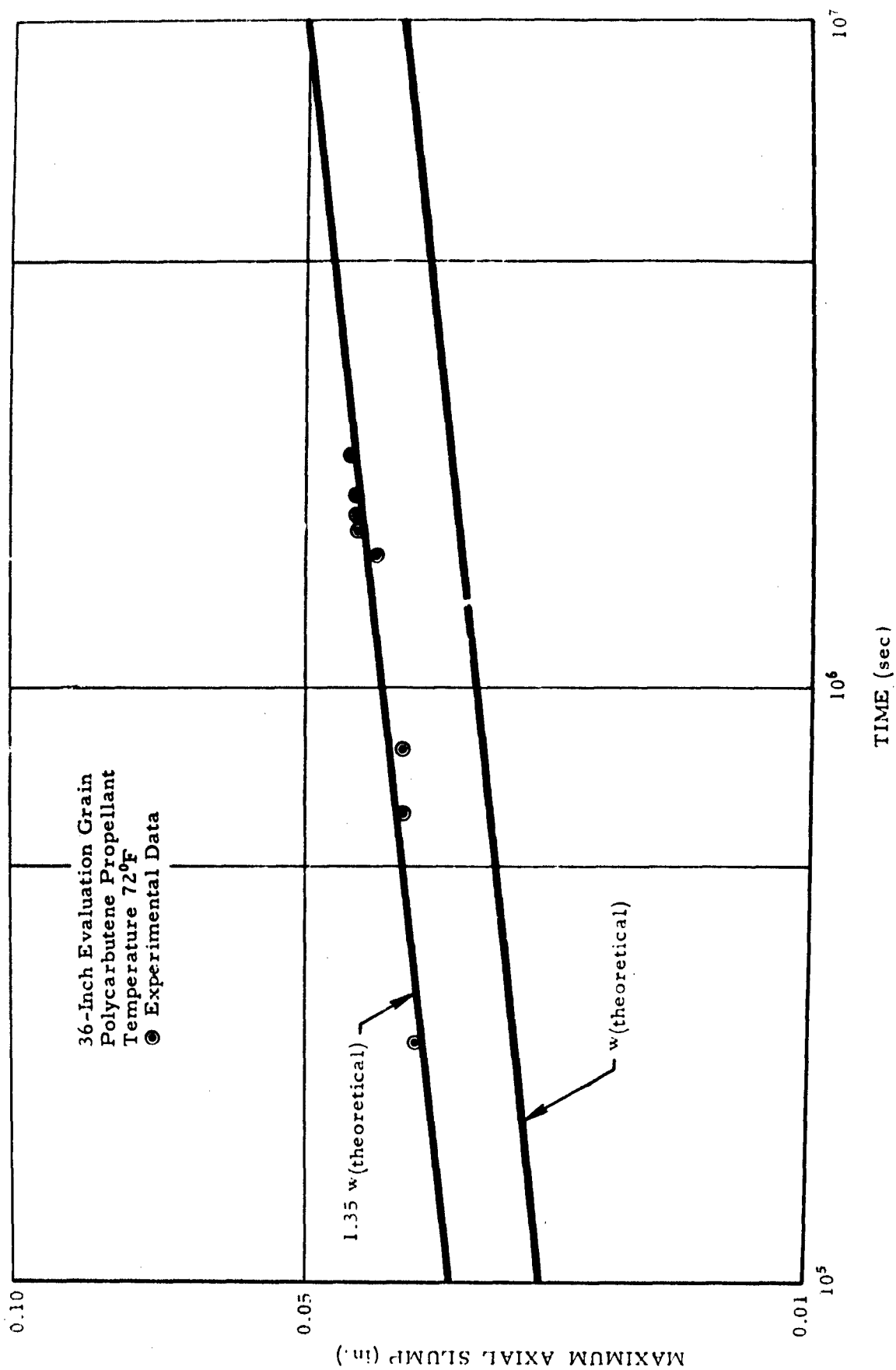
FIGURE 1. AXIAL SLUMP VERSUS TIME

FIGURE 2.
GELATIN SLUMP TEST APPARATUS

FIGURE 3.
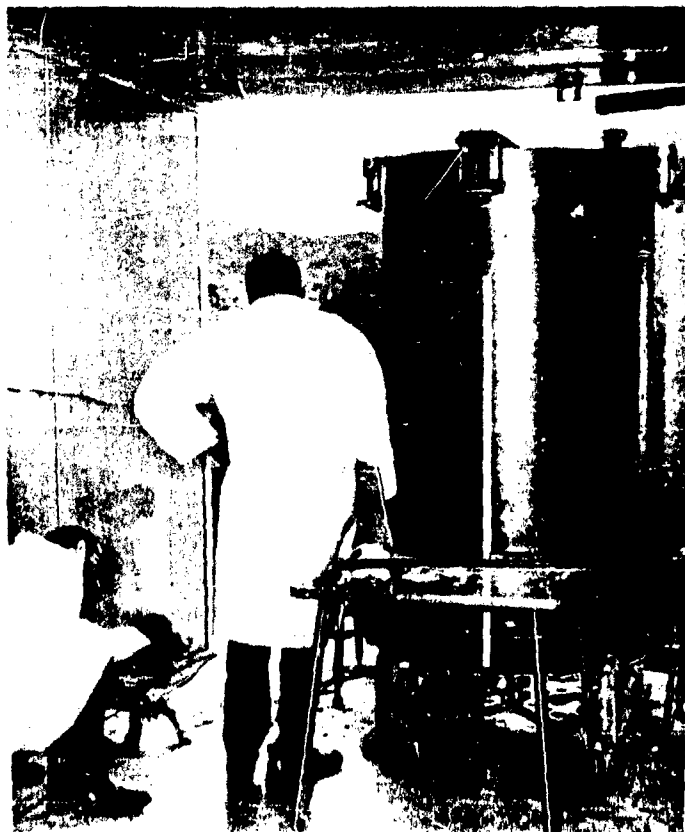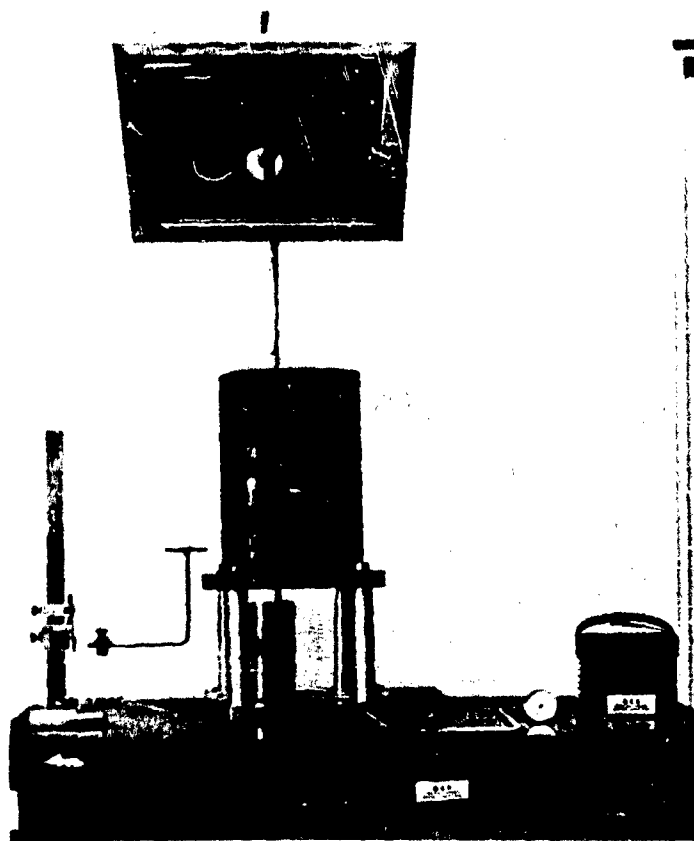EVALUATION GRAIN SLUMP TEST

FIGURE 4. SLUMP VERSUS TIME, LAUNCH ACCELERATION

120-Inch Diameter, 1.5 L/D
50 percent Web
Polycarbutene Propellant
Temperature 72°F

SLUMP DEFLECTION

ACCELERATION

TIME (sec)

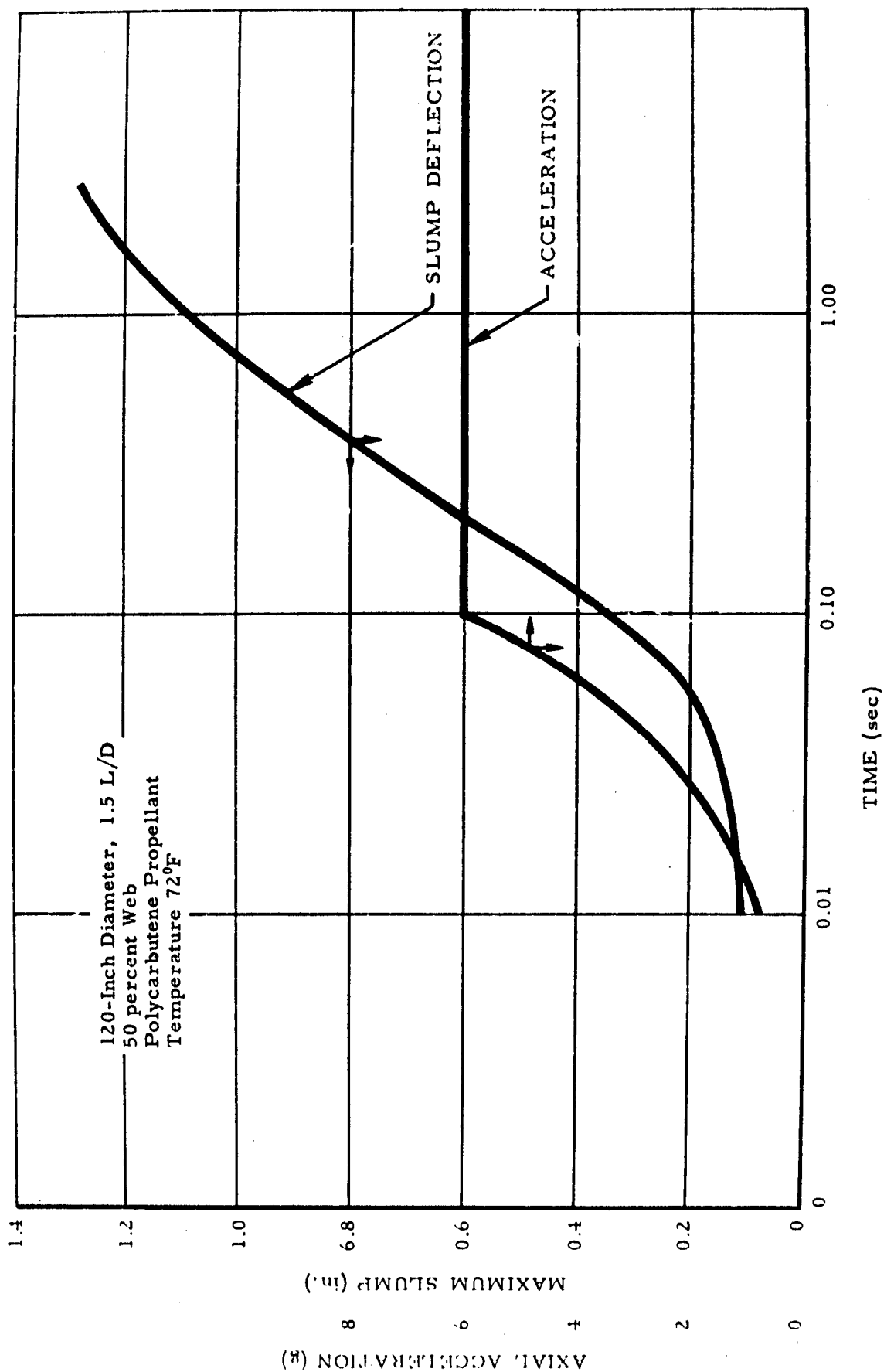MAXIMUM SLUMP (in.)

AXIAL ACCELERATION (g)

PROPELLANT STRAIN ANALYSIS BY THE PHOTOELASTIC COATING TECHNIQUE[a]

Anthony San Miguel
Research Engineer, Polymer Research Section

Jet Propulsion Laboratory
California Institute of Technology
Pasadena, California

ABSTRACT

The magnitude and direction of principal strains on the surface of propellants may be measured by using the photoelastic coating technique. Classical photoelasticity theory is found to define the stress-optic properties of a low-modulus birefringent resin used to coat propellant structures. A beam structure of propellant is examined. A method to separate the principal stresses in the resin coating is illustrated. The technique is then applied to four internally pressurized motors. Two six-pointed grains and two tubular grains are examined and found to exhibit smaller strains than would be predicted by contemporary theory.

INTRODUCTION

Failure of any material may be defined as a strain limit. When an environment causes a material to deform, it may eventually not satisfy design requirements. The problem of predicting strains is usually resolved by assuming stress conditions in a material and essentially relating strains to stresses via material parameters. The structures problem is then solved, at least for the first approximation, if two of the three unknowns are known. Usually the material parameters are the "catch all" in stress analyses.

The photoelastic coating technique represents one method of measuring the two-dimensional strain field. Ideally, the method corresponds to an infinite array of strain gages in two dimensions with the subsequent feature of point analysis. The object of this paper is to present an engineering technique that will enable the investigator to formulate more correct hypotheses regarding propellant-grain stress analysis.

The theory of the photoelastic coating technique is derived from classical photoelasticity (1, 2, and 3), which is based on an experimentally observed stress-optic relationship. It has been found that the relative retardations of normal polarized light, as it passes through a birefringent material, is proportional to the thickness of the birefringent material and to the difference of principal stresses (1).

$$\delta_1 - \delta_2 = 2Ct (\sigma_1 - \sigma_2) \tag{1}$$

where

$\delta_1 - \delta_2$ = relative retardation of light in wavelengths (λ)
C = stress-optic constant
$\sigma_1 - \sigma_2$ = principal stresses difference, $\sigma_1 > \sigma_2$
t = thickness of coating, in.

The photoelastic coating technique has existed for some time (4, 5, 6, and 7) and is analogous to the classical method. Its application to propellant work has been made feasible by the development of low-elastic-modulus (500 lb/in.^{2} or less), linear stress-optic, birefringent coating materials.

The experimental procedure is to bond the linear model (coating) to the structure. Upon stressing the structure, the strains are transmitted to the linear model. The strains in the linear model are measured by the same techniques available to the classical method.

The mechanical-optical system used for this study is a crossed polariscope (Figure 1). Essentially, this system consists of a light source and two polarizers, two $\lambda/4$ birefringent plates, the coated propellant under investigation, and a camera. Polychromatic light is plane polarized as it passes through the first polarizer. The first $\lambda/4$ plate transforms this plane polarized light to circularly polarized light, which then enters the birefringent coating, is reflected at the coating-structure interface, passes through the second $\lambda/4$ plate, and finally transmits through the second polarizer (analyzer) to the camera.

If polychromatic light is used as a source and the structure is loaded, the observer (camera) will see through the analyzer a repeating color spectrum over the entire surface area of the birefringent model. Each repetitive cycle (fringe) represents a linear increase in differences of principal stresses as indicated by Equation 1. Any specific colored curve describes a region in which the difference in magnitude of principal stresses is constant. These lines are called "isochromatics". Superimposed on the above curves are other regions of extinguished light. These "black" curves are called "isoclinics" and have the property of mapping out regions where the directions of principal stresses are the same. By rotating the polarizer-analyzer, the entire directional map

associated with the stresses may be plotted. These isoclinics may be effectively removed by inserting the $\lambda/4$ wave plates into the system.

To separate the principal stresses, a second equation must be introduced to solve for the second unknown; this may be done by applying the equilibrium equation to arbitrarily chosen cuts through the model-- the principal stresses may be graphically reduced by application of the boundary conditions (8 and 9). It should be noted that other methods may be used to separate the principal stresses.

EXPERIMENTAL PROCEDURE

The optic constant C in Equation 1 was obtained by taking a rectangular sample of the coating material and subjecting it to a tensile test. By applying a relatively uniform tensile stress, $\sigma_1 = P$, $\sigma_2 = 0$, a linear stress-birefringent relationship was observed. Average longitudinal and lateral strains were measured by recording displacements using a photographic technique. C was evaluated to have a value of 0.512×10^{-5} lb/in^2; the modulus of the material, E, was approximately 530 lb/in^2; and the average Poisson's ratio based on Cauchy strains was found to be about 0.44.

Defining the strain-optic constant

$$K = \frac{CE}{1 + \nu}$$

where ν is Poisson's ratio, Equation 1 may be transformed to relate the relative retardation to the difference in magnitude of the principal strains:

$$\delta_1 - \delta_2 = 2Kt (\epsilon_1 - \epsilon_2) \tag{2}$$

This relationship is based on the assumption that the principal strains coincide with the direction of the principal stresses, and that the modulus and Poisson's ratio remain constant. The optic-constant calibration is based on the stress-optic relationship (Equation 1) insofar as the principal strains cannot be measured precisely. However, the strain-optic relationship (Equation 2) is applicable to the coating because the strain-fringe and the stress-strain relationships are linear. K is found to have a value of 0.0019. Table I summarizes the correlation between principal stress and relative retardation.

To illustrate the applicability of the photoelastic coating method to the basic study of propellant stress analysis, a simple beam of inert propellant was studied. The birefringent coating was bonded to the surface of the beam. This specimen was subjected to a symmetrical three-point load applied by means of the hydraulic-pneumatic system. Figure 2 shows the loading system, the shear diagram, and the moment distribution. A

camera polariscope was used to obtain the photoelastic data which was in turn reduced by graphical superposition to Figure 3. The isochromatic fringe values correspond to those values shown in Table I. After the iso-clinics and isochromatics had been plotted, the principal stresses were separated graphically.

A section of the beam surface (A-A) was arbitrarily chosen to be examined for strain distributions. For the beam it is noted that the coating material exhibited the same stress-optic properties in compression as it did in tension. Figure 4 is self-explanatory and demonstrates the graphical procedure employed to separate the stresses in the coating. Figure 5 compares the photoelastic measurements in the coating to the theoretical stress distribution in the propellant.

The basic equipment and procedure were extended to a more useful and practical strain measurement. Two motor geometries were chosen for study: a simple tubular and a typical star propellant grain (Figure 6). The material tested was of the same inert formulations used in the beam and had physical properties very similar to those of an operational poly-urethane composite propellant. Both configurations were studied as external radially restricted and as free-standing grains, mounted vertic-ally in a test fixture. The contained grain consisted of the free grain inserted in a greased cylinder, permitting axial extension and minimizing any shear stresses.

Loading in all cases was applied internally by a nitrogen pressur-ized contoured latex bag, sealed to a shaft at both ends. The longitudinal expansion of the bag was controlled by means of adjustable end plates machined with a conical taper; the taper was required to compensate the specimen's internal radial expansion due to pressurization. A two-dimensional loading was assured by constant adjustment of the axial positions of the end plates during pressurization so that the bag could just be seen between the grain and tapered end plate.

A large sheet of birefringent coating resin was calibrated and cut to the desired shape, then bonded to the end of the grain so that neither the end plate nor the metal cylinder would touch the coating.

The pressure applied to the grains was 60 psi for the free standing grain and 150 psi for the contained grain. The isoclinic data are shown in Figure 7 for the two different grain configurations. Both geometries were traced from projected enlargements of color negatives; six photographs were used to give a sufficient isoclinic distribution.

The principal strains were determined at arbitrarily chosen cuts. Figure 8 illustrates the graphical representation of the isochromatics for their corresponding geometry and loading. In Figure 8 a plot in Cartesian coordinates of constant shear contours is superimposed upon the

isochromatic plot. These shear contours are referenced with respect to the direction of the arbitrarily chosen cuts and polarizing angles.

DISCUSSION AND CONCLUSION

For purposes of comparison and prediction, the strain distribution across the web of the tubular grain has been computed from small deformation elastic theory. Because of its geometric complexity, no attempt was made to treat the star shaped configuration analytically. The strain equations for a tubular grain are as follows:

Free tubular grain, plane stress conditions

$$\epsilon_r = \frac{a^2 p_i}{(b^2 - a^2)E} \left[(1 - \nu) - (1 + \nu) \frac{b^2}{r^2} \right]$$

$$\tag{3}$$

$$\epsilon_\theta = \frac{a^2 p_i}{(b^2 - a^2)E} \left[(1 - \nu) + (1 + \nu) \frac{b^2}{r^2} \right]$$

where

ϵ_r = radial strain, in./in.
ϵ_θ = circumferential strain, in./in.
a = inner radius of tubular grain = 1.25 in.
b = outer radius of tubular grain = 2.50 in.
p_i = internal pressure = 60 psi
E = tensile modulus = 730 psi
ν = Poisson's ratio = 0.50 (assumed)
r = radial distance to point in tubular grain, in.

r	1.25	1.50	1.75	2.00	2.25	2.50
ϵ_θ	0.178	0.128	0.0097	0.078	0.064	0.055
ϵ_r	-0.151	-0.100	-0.070	-0.050	-0.037	-0.027

Contained tubular grain, plane stress conditions

$$\epsilon_r = \frac{1}{(b^2 - a^2)E} \left[(1 + \nu)a^2 b^2 (p' - p_i) \frac{1}{r^2} + (1 - \nu)(p_i a^2 - p' b^2) \right]$$

$$\epsilon_\theta = \frac{1}{(b^2 - a^2)E} \left[-(1 + \nu)a^2 b^2 (p' - p_i) \frac{1}{r^2} + (1 - \nu)(p_i a^2 - p' b^2) \right]$$

where

$$p' = \frac{2 a^2 p_i}{\left[(1 + \nu)a^2 + (1 - \nu)b^2\right] + \dfrac{(b^2 - a^2)E}{(c^2 - b^2)E_c}\left[(1 + \nu_c)C^2 + (1 - \nu_c)b^2\right]}$$

(4)

All symbols are the same except:

p' = pressure at interface between grain and metal container, psi
E_c = tensile modulus of metal containers = 30×10^6 psi
ν_c = Poisson's ratio of metal container = 0.33
C = outside radius of metal container = 2.75 in.

r	1.25	1.50	1.75	2.00	2.25	2.50
ϵ_θ	0.132	0.078	0.046	0.023	0.010	0.000
ϵ_r	-0.220	-0.166	-0.134	-0.113	-0.098	-0.090

The applicability of photoelastic coating technique for the determination of propellant deformations is demonstrated by comparing standard beam theory with the experimental results (Figure 5). Note that, although the beam exhibited large rigid motion and rotation, the maximum strain at Section A-A was only about 7%. The close agreement between measurements and theory indicate that the experimental error (both recording and reduction) is relatively small. The discrepancies between small deformation elastic theory and experimental observations for the strain distribution corresponding to internal pressurization of a tubular grain are illustrated in Figure 9. It is noted that the theoretical prediction of strains would require that the specimen begin to blanch on the interior surface. This was not confirmed by visual inspection. Thus, for a free standing tubular grain at test pressure, it is shown that the theoretical prediction (Equation 3) is conservative by about 100%. For the contained tubular grain the circumferential strain agreed rather well; however, the radial strain prediction by theory (Equation 4) was about 1000% conservative. In the experiment, direct contact between the grain and metal cylinder was prevented by a film of grease. This film was intended to create an experimental plane-stress condition which may have contributed part of the radial discrepancy.

Figure 10 illustrates the radial and circumferential strain distributions across a star tooth (Section B-B) and across the web (Section A-A). For Section B-B the point of interest is at Cut 5 located in the interior of the grain. This point exhibited the largest strain. The high strain concentrations at the star fillets are not examined in this paper. It is noted that these areas contain the largest strains of the grain. On comparing Figure 10 to Figure 9 for web strains, it is noted that the corresponding circumferential strains have about the same maximum magnitude but that

the star grain has a much steeper gradient for 150 psi. The maximum radial strains for the star configuration are somewhat higher than for the corresponding tubular configuration; again a steeper gradient is observed.

These examples illustrate how the photoelastic coating technique may be used to study strain distributions on the surface of a propellant for any changing boundary condition. With this information, the general stress-distribution problem can be studied by use of the semi-inverse method of solution.

REFERENCES

1. Frocht, M. M., Photoelasticity, Vols. I and II, J. Wiley and Sons, New York, 1941 and 1948.

2. Coker, E. G., and Filon, L. N. G., Treatise on Photoelasticity, (Contains complete bibliography up to 1930), Cambridge University Press, London, England, 1931.

3. Mindlin, R. D., "A Review of the Photoelastic Method of Stress Analysis, Part II", (Contains complete bibliography from 1930-1939), Journal of Applied Physics, Vol 10, No. 5, May 1939.

4. Zandmann, F., and Wood, M. R., "Photostress, a New Technique for Photoelastic Stress Analysis for Observing and Measuring Surface Strains on Actual Structures and Parts", Product Engineering, Vol 27, No. 9, September, 1956.

5. McMaster, R. C., Editor, Nondestructive Testing Handbook, Vol 2, Sec 53, Society for Nondestructive Testing, Ronald Press Co., New York, 1959.

6. Jones, H. G., A Research Study to Advance the State-of-the-Art of Solid Propellant Grain Design, Quarterly Progress Report 4, R-E 132-60, Thiokol Chemical Corp., Elkton Div., Elkton, Maryland, July 18, 1960.

7. Bills, K. W., McCurdy, O. L., and Farnham, R. B., "The Development and Use of Birefringent Polymers for Determining Strain Distribution in Solid Propellants," Bulletin of the Fifth Meeting, JANAF Solid Propellant Information Agency, The Johns Hopkins University, Silver Spring, Maryland, September, 1960.

8. San Miguel, A., "Viscoelastic Strain Analysis by Photoelastic Coating Technique", Quarterly Summary Report No. 38-3, Jet Propulsion Laboratory, Pasadena, California, April 15, 1961.

9. San Miguel, A., "Viscoelastic Strain Analysis by Photoelastic Coating Technique, II", Quarterly Summary Report No. 38-4, Jet Propulsion Laboratory, Pasadena, California, July 15, 1961.

TABLE I. OPTICAL PROPERTIES OF COATING MATERIAL

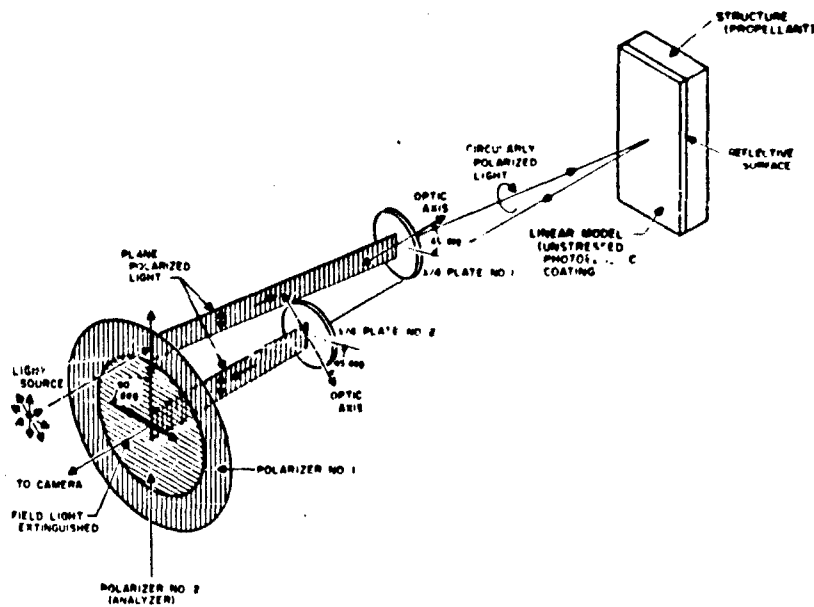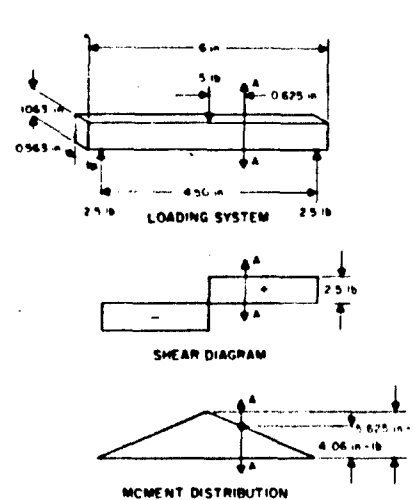| Color		True principal stress $(\sigma_1 - \sigma_2)$, $\sigma_1 - \sigma_2$; lb/in.	Relative retardation $(\delta_1 - \delta_2)$, 10^4 mm	Fringe value $\left(\dfrac{\delta_1 - \delta_2}{57.5}\right)$	Color		True principal stress $(\sigma_1 - \sigma_2)$, $\sigma_1 - \sigma_2$; lb/in.	Relative retardation $(\delta_1 - \delta_2)$, 10^4 mm	Fringe value $\left(\dfrac{\delta_1 - \delta_2}{57.5}\right)$
Crossed system	Parallel system				Crossed system	Parallel system			
Black	White	0	0	0	—	Tint of passage N	—	84.2	1.50
Gray	Yellowish-white	1.7	10.0	0.18	Greenish-yellow	Violet	28.0	87.0	1.52
White	Light red	4.5	26.0	0.45	Pure yellow	Indigo	30.9	91.0	1.60
Very pale yellow	Dark red brown	8.0	27.5	0.48	Orange	Greenish-blue	32.5	100.0	1.74
—	Tint of Passage N₁	—	28.7	0.50	Dark red	Green	35.9	110.0	1.92
Light-yellow	Indigo	10.3	30.0	0.52	Tint of passage N	38.9	115.0	2.00
Brown yellow	Gray blue	13.3	43.0	0.75	Indigo	Gray yellow	42.1	116.0	2.02
Reddish-orange	Bluish green	16.0	50.5	0.88	Green	Brown red	45.2	133.0	2.32
Red	Pale green	17.9	54.0	0.93	—	Tint of passage N	—	143.7	2.50
Tint of passage N₁	—	19.4	57.5	1.00	Greenish-yellow	Grayish indigo	48.4	145.0	2.52
Indigo	Gold Yellow	20.1	59.0	1.03	Carmen red	Green	59.0	153.0	2.57
Blue	Orange	22.8	66.0	1.14	Tint of passage N	—	60.7	172.0	3.00
Green	Red	25.5	75.0	1.30					

FIGURE 1. MECHANICAL-OPTICAL SYSTEM

FIGURE 2.
BEAM-LOADING SCHEMATIC
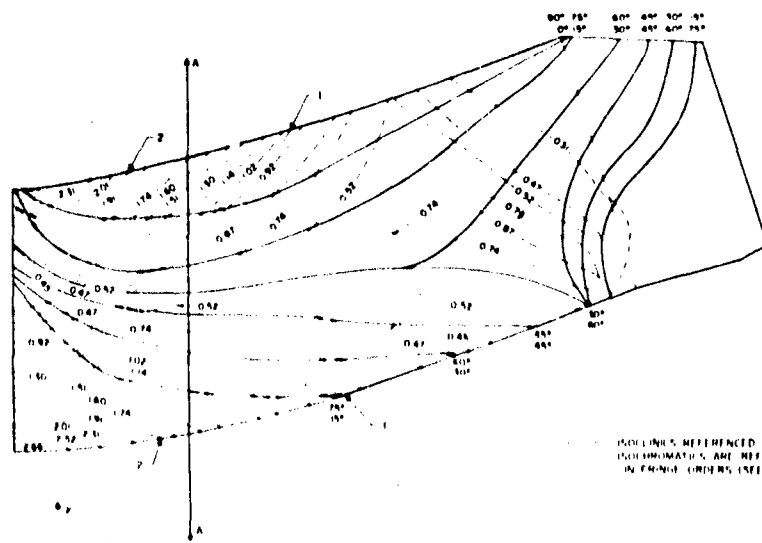
FIGURE 3.
ISOCLINIC-ISOCHROMATIC
PLOT

ISOCLINICS REFERENCED TO x-y AXES
ISOCHROMATICS ARE REFERENCED
IN FRINGE ORDERS (SEE TABLE I)

(a) τ_{xy} vs y AT SECTION A-A

(b) LINES OF EQUAL SHEAR

(c) GRAPHICAL MAGNITUDE OF $\frac{\partial \tau_{xy}}{\partial x}$ FOR CUTS 1 THROUGH 9

(d) τ_{xy} vs x USED TO DETERMINE $\frac{\partial \tau_{xy}}{\partial x}$ AT SECTION A-A

(e) σ_y vs y OBTAINED GRAPHICALLY FROM FIG (c) IN VIEW OF EQUILIBRIUM EQUATION $\frac{\partial \tau_{xy}}{\partial x} + \frac{\partial \sigma_y}{\partial y} = 0$
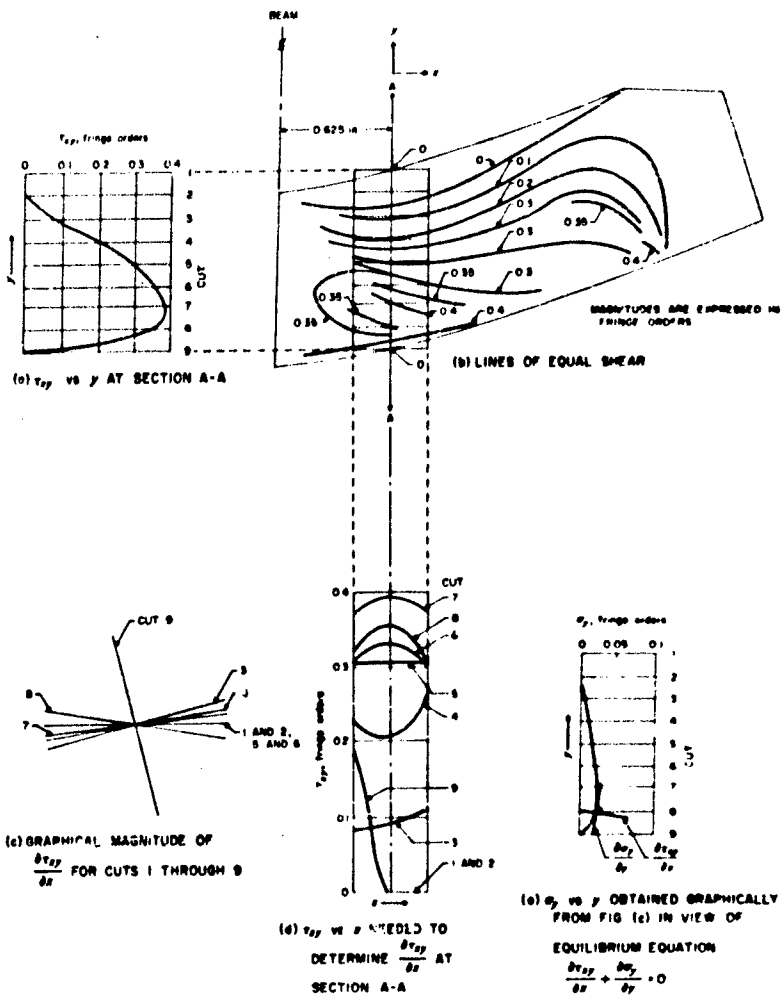
FIGURE 4. SEPARATION OF PRINCIPAL STRESSES IN COATING

FIGURE 5.
MEASURED VS THEORETICAL
STRESSES IN BEAM

FIGURE 6.
TUBULAR AND STAR
PROPELLANT GRAINS

FIGURE 7. ISOCLINIC PLOT

FIGURE 8. SECTIONS INVESTIGATED FOR STRAIN

FIGURE 9.   MEASURED VS THEORETICAL STRAINS IN TUBULAR GRAIN
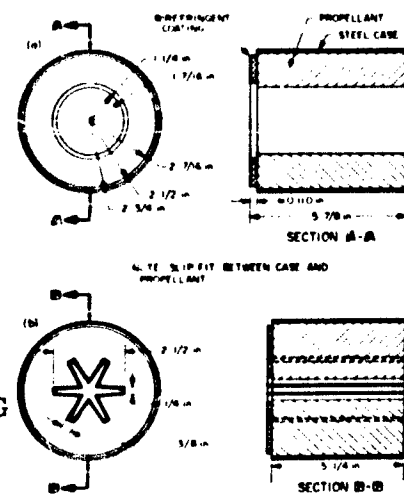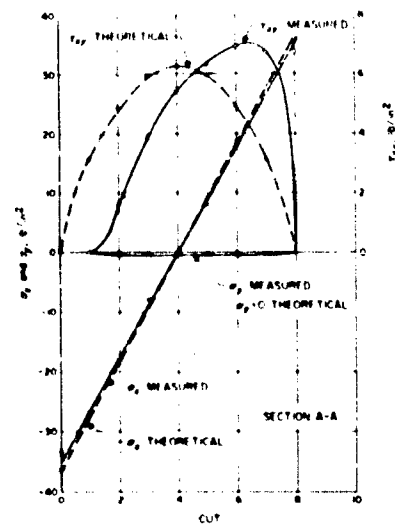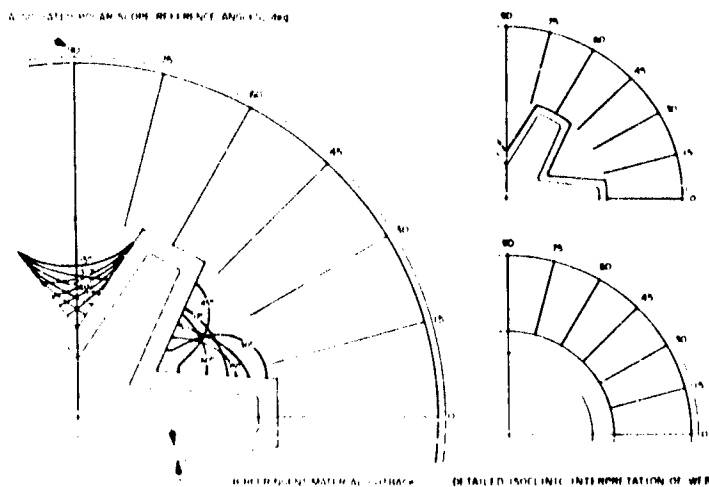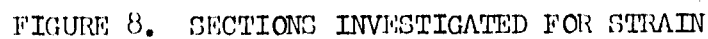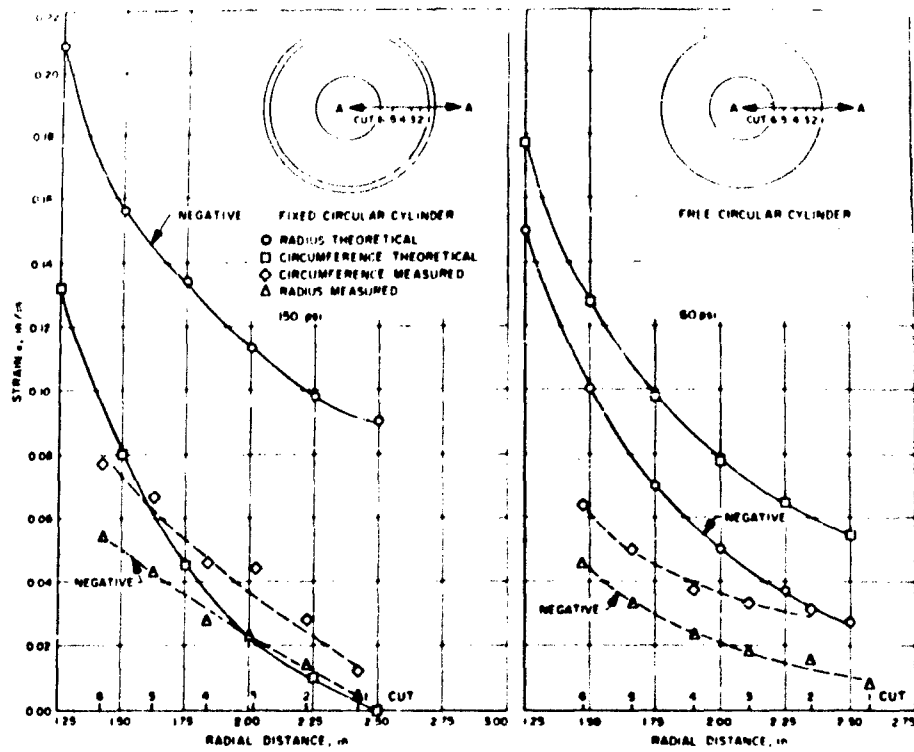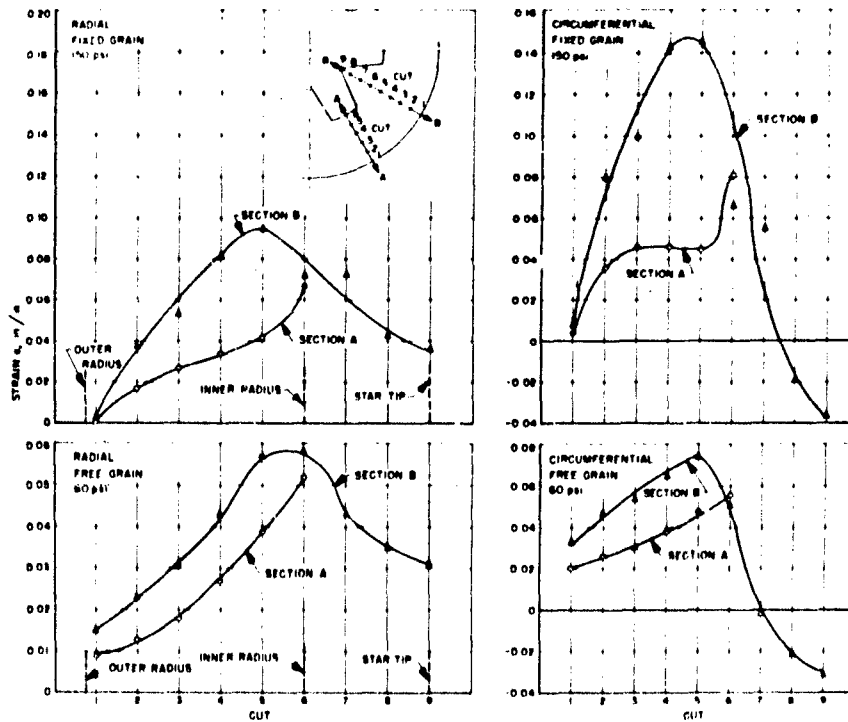

FIGURE 10.   STAR-GRAIN STRAIN DISTRIBUTION

DISPLACEMENTS IN AN AXIALLY ACCELERATED SOLID PROPELLANT ROCKET GRAIN*

Wolfgang G. Knauss
California Institute of Technology
Pasadena, California

ABSTRACT

Approximate deformations of a case bonded tubular rocket grain of finite length have been calculated by the minimum energy principle of infinitesimal elasticity. In order to estimate the accuracy of this method two solutions of different complexity have been compared with deformations in a gelatin model and fair agreement is found with respect to the deformation pattern.

The extension of the elastic solution to the time dependent case is accomplished only after some simplifying assumptions which are consistent with the approximate nature of the elastic solution. Sufficient information is presented to estimate the usefulness of the method in preliminary design and to aid in the analysis of similar problems.

INTRODUCTION

In the development of solid rocket motors the designer meets three major problem areas, namely the analysis of stress, of deformation and of temperature influence on both. While the analysis of stress is closely related to failure by rupture, deformation analysis concurs itself with failure due to excessive deformations, and in particular with the problem of slump. Slump may occur in short time-high acceleration flights of multistage rockets due to high inertial loading or in storage under gravity loading of one "g".**Although there are propellants available today which reduce this problem to a minimum in a moderate temperature environment, the trend to large solid propellant boosters emphasizes the importance of slump analysis. Because of the high cost of large booster grains, testing for slump becomes impractical and analytical means of predicting slump are needed. The analysis which we shall make is approximate; but it is hoped that it will provide a useful step in slump analysis and related problems.

In order to keep the analysis tractable the usual complex grain perforation is replaced by a circular port area and the propellant is considered to be bonded to an infinitely rigid case. Two cases will be considered. In one case the annular end surfaces are free to deform (FIGURE 1a) and in the other, the lower end surface is restrained from any motion (FIGURE 1b); these cases will be referred to as unsupported and supported cylinders, respectively. Although slump may be associated with large deformations we shall assume, as a matter of expediency, that the cylinder material is isotropic and linearly viscoelastic, and further that strains remain small so that the infinitesimal theory of elasticity applies. The time dependent solution is then obtained by first finding the solution for the case of time

---

* This work was supported in part by the Thiokol Chemical Corporation, Huntsville, Alabama.

** The problem of horizontal grain storage has been considered by G. Lianis (1).
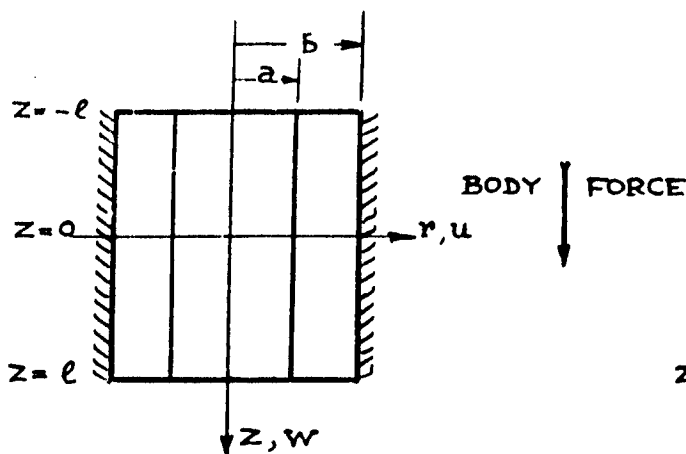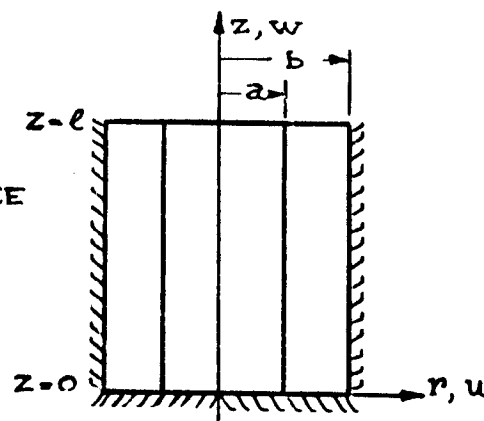
FIGURE 1a - UNSUPPORTED CYLINDER   FIGURE 1b - SUPPORTED CYLINDER

independent material properties, and by then extending this elastic solution
to the case of time dependent material properties through the method given
by Lee (2).

In the following γ, μ, ν, and λ represent, respectively, the body
force (density times acceleration), the shear modulus, Poisson's ratio, and
the Lame constant $2\mu/(1-2\nu)$.

An exact solution of the present problem could be attempted through
a method given by Pickett (3). However, this method is indeed very complex
and non-convergence of the solution is expected at points where end surfaces
and case meet; therefore the less time consuming Kantorovich restricted
variation energy method is chosen at some expense in accuracy. Because
displacements are sought in the solution, the potential energy theorem is
used: the mathematical foundation of this theorem is given in detail else-
where (4, 5, 6) but it will be useful to recall here its essential features and
requirements as they relate to the mechanics of this solution.

The theorem states that the potential energy, to be defined below, is
an absolute minimum for displacements satisfying boundary conditions and the
equations of equilibrium; an approximate solution results if the potential
energy is minimized without satisfying the equilibrium equations. The
theorem thus requires the selection of displacement functions which satisfy
the given displacement boundary conditions of the problem but contain some
arbitrariness which allows the variational procedure to minimize the
potential energy.

In the present problem the displacements vanish at the external
radius and for the supported cylinder also at one end surface; stresses are
prescribed at the remaining surfaces. The requirements of the theorem are
satisfied by choosing displacement functions u_i (i = 1, 2, 3) as a sum of
products

$$u_i = \sum_{n=1}^{N} \phi_n^i \, g_n^i \tag{1}$$

where the ϕ_n^i are, for convenience, functions of the radius only which
vanish at the outer radius, and the g_n^i are arbitrary functions of z. The
selection of the functions ϕ_n^i requires for best results some intuition or other

guiding principle, because some functions obviously will bring the potential energy closer to its absolute minimum than others and thus lead to a better approximation. Having chosen the displacement representations u_i one proceeds to calculate the potential energy V which is defined as the difference of the strain energy and the work done by the body forces F_j and the surface tractions T_j in moving through the displacements u_j.

$$V = \int_{VOL}\left\{(\lambda+2\mu)\vartheta^2 - 4\mu\vartheta_2\right\}d(vol) - \int_{VOL}F_j u_j d(vol) - \int_{\Sigma_\sigma}T_j u_j d\Sigma . \tag{2}$$

Here ϑ and ϑ_2 are the first and second strain invariants,

$$\vartheta = \frac{\partial u_i}{\partial x_i} = u_{i,i} \tag{3}$$

$$\vartheta_2 = \frac{1}{2}\left[\vartheta^2 - \frac{1}{4}\left(\frac{\partial u_i}{\partial x_j}+\frac{\partial u_j}{\partial x_i}\right)\left(\frac{\partial u_i}{\partial x_j}+\frac{\partial u_j}{\partial x_i}\right)\right] = \frac{1}{2}\left[\vartheta^2 - \frac{1}{4}(u_{i,j}+u_{j,i})(u_{i,j}+u_{j,i})\right]$$

repeated subscripts indicate summation and Σ_σ indicates that the third integral is to be taken only over that part of the boundary where the stresses are prescribed. The potential energy, V, is then minimized by setting its first variation equal to zero* when the functions g_n^i are varied. This procedure will yield (Nxi) second order differential equations for the determination of the functions g_n^i, often called Euler equations, as well as the appropriate boundary conditions for the functions g_n^i.

ANALYSIS OF THE PROBLEM

In order to apply this method to the problem of the accelerated cylinder one first notes that the radially symmetric loading makes the radial and axial displacement, u and w, dependent on the radial and axial coordinates r and z, only, and implies zero circumferential displacement. Choosing two-term displacement representations

$$\begin{aligned} u &= R_1(r)\,g_1(z) + R_2(r)\,g_2(z)\\ v &= 0\\ w &= \rho_1(r)\,f_1(z) + \rho_2(r)\,f_2(z) \end{aligned} \tag{4}$$

and selecting the functions **

$$R_1 = -\frac{1}{2}\left(1-\frac{r}{b}\right)^2 \qquad R_2 = \left(\frac{r}{b}\right)^2 \ln\frac{r}{b} \tag{5}$$

$$\rho_1 = 1 - \left(\frac{r}{b}\right)^2 \qquad \rho_2 = \ln\frac{r}{b}$$

one proceeds to calculate the potential energy V, EQUATION (2); because the body force acts only in the axial direction and surface tractions are zero where they are prescribed, the expression reduces to

$$V = \int_{VOL}\left\{(\lambda+2\mu)\vartheta^2 - 4\mu\vartheta_2\right\}d(vol) - \gamma\int_{VOL}w\,d(vol) \tag{6}$$

Substitution of the displacement representations EQUATION (4) into EQUATION (6) and subsequent integration over the radial coordinate renders the final expression for the potential energy as ***

* For a treatment of calculus of variations see e.g. ref. (7).
** An explanation for the choice of these functions has been given in ref. (6).
*** Primes denote differentiation with respect to z.

$$V = \pi \int_{-\ell}^{\ell} \{ m_1 g_1^2 + m_2 g_2^2 + m_3 g_1 g_2 + m_4 (f_1^1)^2 + m_5 (f_2^1)^2 + m_6 f_1^1 f_2^1$$

$$+ m_7 g_1 f_1^1 + m_8 g_1 f_2^1 + m_9 g_2 f_1^1 + m_{10} g_2 f_2^1 + n_1 (g_1^1)^2$$

$$+ n_2 (g_2^1)^2 + n_3 g_1^1 g_2^1 + n_4 f_1^2 + n_5 f_2^2 + n_6 f_1 f_2 + n_7 g_1^1 f_1$$

$$+ n_8 g_1^1 f_2 + n_9 g_2^1 f_1 + n_{10} g_2^1 f_2 - \Gamma_1 f_1 - \Gamma_2 f_2 \} \, dz \qquad (7)$$

where the constants m_i, n_i and Γ_i, are defined in the appendix. The variation of the potential energy with respect to the independent functions g_1, g_2, f_1 and f_2 leads to four differential equations

$$2 n_1 g_1^{11} + n_3 g_2^{11} + (n_7 - m_7) f_1^1 + (n_8 - m_8) f_2^1 - 2 m_1 g_1 - m_3 g_2 = 0 \qquad (8a)$$

$$n_3 g_1^{11} + 2 n_2 g_2^{11} + (n_8 - m_8) f_1^1 + (n_{10} - m_{10}) f_2^1 - m_3 g_1 - 2 m_2 g_2 = 0 \qquad (8b)$$

$$2 m_4 f_1^{11} + m_6 f_2^{11} + (m_7 - n_7) g_1^1 + (m_8 - n_8) g_2^1 - 2 n_4 f_1 - n_6 f_2 = -\Gamma_1 \qquad (8c)$$

$$m_6 f_1^{11} + 2 m_5 f_2^{11} + (m_8 - n_8) g_1^1 + (m_{10} - n_{10}) g_2^1 - n_6 f_1 - 2 n_5 f_2 = -\Gamma_2 \qquad (8d)$$

and to the boundary conditions for the functions g_i and f_i

$$2 n_1 g_1^1 + n_3 g_2^1 + n_7 f_1 + n_8 f_2 = 0 \quad \text{or } g_1 \text{ prescribed at } z = \pm \ell, \, 0 \qquad (9a)$$

$$2 n_2 g_2^1 + n_3 g_1^1 + n_8 f_1 + n_{10} f_2 = 0 \quad \text{or } g_2 \text{ prescribed at } z = \pm \ell, \, 0 \qquad (9b)$$

$$2 m_4 f_1^1 + m_6 f_2^1 + m_7 g_1 + m_9 g_2 = 0 \text{ or } f_1 \text{ prescribed at } z = \pm \ell, \, 0 \qquad (9c)$$

$$2 m_5 f_2^1 + m_6 f_1^1 + m_8 g_1 + m_{10} g_2 = 0 \text{ or } f_2 \text{ prescribed at } z = \pm \ell, \, 0 . \qquad (9d)$$

The solutions to the differential EQUATIONS (8a-d) are obtained by standard methods* as

$$g_1 = \sum_{k=1}^{8} c_k e^{\bar{\lambda}_k z} \qquad , \qquad g_2 = \sum_{k=1}^{8} \alpha_1^k c_k e^{\bar{\lambda}_k z} \qquad (10a)$$

$$f_1 = \sum_{k=1}^{8} \alpha_2^k c_k e^{\bar{\lambda}_k z} - \frac{\Gamma_2 n_6 - 2 n_5 \Gamma_1}{4 n_4 n_5 - n_6^2} \quad , \quad f_2 = \sum_{k=1}^{8} \alpha_3^k c_k e^{\bar{\lambda}_k z} - \frac{\Gamma_1 n_6 - 2 n_4 \Gamma_2}{4 n_4 n_5 - n_6^2} \qquad (10b)$$

Where the constants α_j^k are determined by substituting expressions (10a-b) into the differential equations 8, and the eight constants of integration c_k are determined from the boundary conditions EQUATION (9). Because displacements are not prescribed at $z = \pm \ell$ for the unsupported cylinder, the boundary conditions represented by the set of four equations in EQUATION (9) must be satisfied; but for the supported cylinder the displacements vanish at the supported end ($z = 0$) and hence the boundary conditions at $z = 0$ become

$$g_1 = g_2 = f_1 = f_2 = 0 ,$$

---

* See, e.g. reference (8) or any other textbook on differential equations.

At z = ℓ the displacements are again unspecified and therefore the set of EQUATIONS (9) applies. Thus the displacements satisfy the displacement boundary conditions where displacements are prescribed and the requirements of the potential energy theorem are met.

It should be recalled here that these boundary conditions arise in the minimization of the potential energy and that satisfaction of these "natural" boundary conditions is required if the potential energy is to be a minimum.

CALCULATIONS

The further solution of the problem is not readily cast into a closed form and requires therefore the numerical analysis for a particular cylinder configuration. Inasmuch as this paper intends to convey a feeling of the quality of the solution and not only a numerical result, solutions have been found for the two term displacement expansions given in EQUATION (1) as well as for one term displacements for which the radial functions are chosen as

$$R_1 = \frac{r}{b} \, \rho_1 ; \qquad R_2 = 0 \qquad\qquad (11)$$

$$\rho_1 = 1 - \left(\frac{r}{b}\right)^2 + 2\left(\frac{a}{b}\right)^2 \ln\frac{r}{b} ; \quad \rho_2 = 0$$

Calculations have been carried out for the following cylinder geometry

$$b = 2a$$
$$\ell = 1.25\, b \quad \text{(unsupported cylinder)}$$
$$\ell = 2.5\, b \quad \text{(supported cylinder)}$$
$$\nu = 0.45$$

and the resulting radial displacement patterns of the internal boundary are shown in FIGURE 2 for the one and two term solutions.
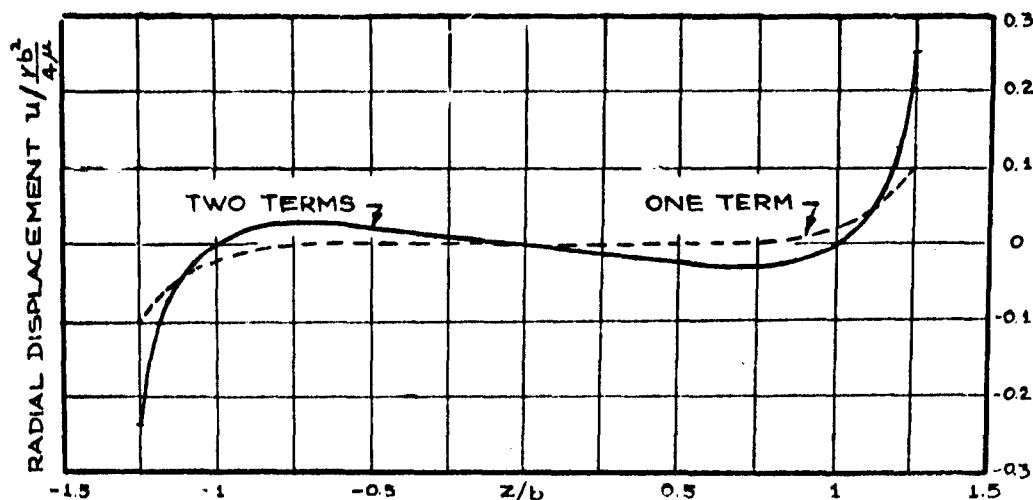

FIGURE 2. RADIAL DISPLACEMENT OF THE INTERNAL BOUNDARY FOR THE ONE TERM AND TWO TERM SOLUTIONS (UNSUPPORTED CYLINDER)

It was not possible to obtain a two term solution for the supported cylinder as this solution involved differences of very large numbers (of the

order 10^{20}) to obtain numbers smaller tnan unity; but a one term solution could be calculated and this is shown in FIGURE 8.*

A limit check of the solutions for an incompressible material ($\nu = 1/2$) shows that as Poisson's ratio approaches 1/2 the unsupported cylinder tends to deform like the infinite, unsupported cylinder and that the deformations of the supported cylinder tend to zero. This result is not physically reasonable because shear deformations, do exist in spite of the fact that volume changes do not occur. This limit behavior is a direct consequence of the approximate nature of the solution inasmuch as incompressibility requires the dilatation $= e_{11} + e_{22} + e_{33}$ to vanish, which in turn requires, under the assumed form of the displacements, that the displacements vanish. For this reason the solutions are very sensitive to Poisson's ratio, in the neighborhood of $\nu = 1/2$, yet for a Poisson's ratio smaller than about 0.46 this sensitivity is not any greater than one should normally expect; we therefore somewhat arbitrarily, restrict the approximate solutions to be valid for Poisson's ratio smaller than 0.46.

The fact that the solution is approximate could be simply illustrated by calculating the stresses from the displacements and substituting them into the equilibrium equations. Further, the boundary stresses do not vanish as prescribed in the exact solution: the radial stress σ_r as calculated for the one and two-term solution is shown in FIGURE 3. It is interesting to note that near the point ($r = a$, $z = L$) the one term solution renders a tensile stress, whereas the two term solution exhibits a compressive stress. (The radial displacement at this point is positive, i.e., outward.) If stresses are superposed on the stresses calculated from the approximate displacements to render zero boundary stresses, a compressive stress would be required for the one term solution, and a tensile stress for the two term solution; these stresses would cause the displacement to increase for the one term and to decrease for the two term solution. One is thus justified in claiming cautiously that the exact displacement (at the corner) lies between that given by the one and two term solutions. To predict a smaller bound on the maximum radial displacement on the basis of the absolute values of the maximal stresses does not appear to be justified.

COMPARISON WITH A MODEL

For the purpose of qualitative comparison, a model was made of commercial Jell-O having a length to diameter ratio of 1.25 and a radius ratio $a/b = 1/3$. The mold consisted of a clear thin walled lucite cylinder, a central brass mandrel and brass bottom. By pouring hot water through the hollow mandrel it was removed without destroying the internal surface; a similar procedure allowed removal of the bottom**

---

* For more details on the calculations see REFERENCE (6).
** In the process of removing mandrel and bottom, the corner formed by the end surfaces and the internal boundary was not preserved perfectly. The apparent displacements in the immediate vicinity of the corners are therefore not true displacements. Oval shaped and round objects in the photographs are bubbles caused in the removal of the mandrel.

Because the model exhibits large deformations, a comparison with an infinitesimal displacement solution as given here is perforce of a qualitative nature. Furthermore, no mechanical properties of the model material have been determined, so that agreement should be expected to be qualitative only. Quantative comparison thus showed differences of approximately 100 percent even after accounting for different radius ratios used in the calculations and in the model.

FIGURE 5 shows the model cylinder supported by the outside wall hanging under axial gravity forces. A close-up of the lower end, FIGURE 4, shows that the bottom surface is concave downward and not concave upward as the analytical result indicates in FIGURE 6. It is readily understandable that the one-term solution should exhibit this behavior because it is imposed by the choice of the radial function ρ; the fact that in the two-term solution one of the functions f_1 or f_2 is not such as to produce the downward-concave bottom surface can be explained by noting that this solution, too, makes use only of the same functions and does not introduce anything essentially new.* In view of this statement it is almost surprising that the two solutions differ as much as they do.

Agreement for the deformation of the internal cylindrical surface is fairly good, as can be seen by comparing FIGURES 5 and 6 for the unsupported cylinder, and FIGURES 7 and 8 for the supported cylinder.**

TIME DEPENDENCE OF THE DISPLACEMENT

Having obtained an approximate elastic solution, we shall now consider the effects of time dependent material properties. Because the numerical nature of the two term solution does not lend itself easily to the following considerations, we shall restrict ourselves to the one term solution which can be written in closed form, yet exhibits essentially the same time dependent behavior as the two term solution.

The one term displacement solutions are of the form

$$u = \frac{Yb^2}{4\mu} R(r)\left[a_1 \sinh \bar\lambda_1 \frac{z}{b} + a_2 \cosh \bar\lambda_1 \frac{z}{b} + a_3 \sinh \bar\lambda_2 \frac{z}{b} + a_4 \cosh \bar\lambda_2 \frac{z}{b}\right]$$

$$w = \frac{Yb^2}{4\mu} \rho_1(r)\left[1 + A_1 \sinh \bar\lambda_1 \frac{z}{b} + A_2 \cosh \bar\lambda_1 \frac{z}{b} + A_3 \sinh \bar\lambda_2 \frac{z}{b} + A_4 \cosh \bar\lambda_2 \frac{z}{b}\right]$$

(12)

where $\bar\lambda_{1,2}$ are the solutions of the equation

$$\bar\lambda^4 - \left[\frac{m_1}{4n_1} + \frac{4n_4}{m_4} - \frac{(4n_7 - m_7)^2}{16 n_1 m_4}\right]\bar\lambda^2 + \frac{m_1 n_4}{m_4 n_1} = 0$$

(13)

It will be useful to recall for later reference that the constants m_i and n_i depend on the shear modulus and the Lame constant and that the constants of integration a_i and A_i are functions of $\bar\lambda$.

---

* Note that ρ_1 for the one-term solution is equal to $\rho_1 + 2\left(\frac{a}{b}\right)^2 \rho_2$

   for the two-term solution.

** For more detailed comparison the reader is referred to REFERENCE (6).

We shall now describe the determination of the time-dependent deformations as outlined by Lee (2). According to this approach, the equations of elasticity and the boundary conditions are subjected to a Laplace transformation so that the time dependent properties are replaced by functions of the transform parameter p. In this transformed state, the problem constitutes an associated elastic problem which can be solved by ordinary elastic analysis. The solution of this associated elastic problem must then be inverted, in general by contour integration, to obtain the time dependent solution of the physical problem.

In the present cylinder problem, the boundary conditions are not time dependent and therefore the solution to the associated elastic problem is given by the elastic solution, e.g. EQUATION (12), if one considers the material constants to be functions of the transform parameter p. If the material responds elastically in bulk and is represented in shear by a Wiechert model, then the transformed material constants take the form

$$\mu(p) = \mu_e + \sum_{i=1}^{n} \frac{\mu_i}{p + 1/\tau_i} \tag{14}$$

and

$$\lambda(p) = k - \frac{2}{3} \mu(p)$$

Here k is the constant bulk modulus and μ_e, μ_i, and τ_i are long time elastic modulus, the ith spring element and i^{th} relaxation time of the Wiechert model, respectively*. Upon substituting $\mu(p)$ and $\lambda(p)$ into the m_i and n_i, one obtains from EQUATION (13) the characteristic values $\bar{\lambda}_i(p)$ so that e.g. the associated elastic radial displacement becomes

$$u(r, z, t) = \frac{\mathcal{L}[\gamma(t)]}{\mu(p)} R_1(r) \frac{b^2}{4} \left[a_1(p) \sinh \bar{\lambda}_1(p) \frac{z}{b} + a_2(p) \cosh \bar{\lambda}_1(p) \frac{z}{b} + \right.$$
$$\left. + a_3(p) \sinh \bar{\lambda}_2(p) \frac{z}{b} + a_4(p) \cosh \bar{\lambda}_2(p) \frac{z}{b} \right] \tag{15}$$

where $\mathcal{L}[\ ]$ denotes the Laplace transform of the quantity contained in the bracket. In the following we shall deal only with the radial displacement u as an example; the analysis for the axial displacement w follows identical arguments.

Let for simplicity of notation

$$g_1(p, z) = a_1(p) \sinh \bar{\lambda}_1(p) \frac{z}{b} + a_2(p) \cosh \bar{\lambda}_1(p) \frac{z}{b}$$
$$+ a_3(p) \sinh \bar{\lambda}_2(p) \frac{z}{b} + a_4(p) \cosh \bar{\lambda}_2(p) \frac{z}{b} \tag{16}$$

So that the Laplace transform of the u-displacement becomes simply

$$U(r, z, p) = \frac{\mathcal{L}[\gamma(t)]}{\mu(p)} R_1(r) \frac{b^2}{4} g_1(p, z). \tag{17}$$

---

* For a more detailed explanation see REFERENCE (9).

The inversion of this function can be effected with the help of the convolution theorem: If $G_j(t, z)$ is the Laplace inverse of $g_1(p, z)$ and $L(t)$ is the inverse of $\mathcal{L}[\gamma(t)]/\mu(p)$ then the convolution theorem renders the radial displacement

$$u(v, z, t) = \frac{b^2}{4} R_1(r) \int_0^t L(t-r) G_1(\tau, z) \, d\tau \qquad (18)$$

The Laplace inversion of $g_1(p, z)$ presents a formidable if not insurmountable task as is quickly realized by considering the complex dependence of the characteristic values λ_1 on the parameter p. However, the long time dependence of $G_1(t, z)$ may be checked by replacing p by $1/t$. It is then found that increasing time implies that Poisson's ratio approaches 1/2, a result which was rejected earlier on the ground that the approximate nature of the solution does not permit the limit case $\nu \to 1/2$. One is thus forced to obtain an approximate solution which also avoids the complex time dependence of the function $G_1(t, z)$.

We shall assume on physical grounds that the function $G_1(t, z)$ does not depend strongly on time and may be replaced by its value at zero time, with the result that the radial displacement becomes approximately

$$u(r, z, t) \approx \frac{b^2}{4} R_1(r) G_1(o, z) L(t) * \qquad (19)$$

The physical implications of this assumption are as follows: First note that the space dependence of the displacement is separated from the time dependence, which means that the shape of the deformed body does not change with time. Although one would not expect this to be true for an exact analysis one would nevertheless expect that the shape does not change very much as time increases, and hence that the approximation is fair in this respect. Further note that the time dependence of the displacement is the same as exhibited by the material in a simple shear test under the same type of loading. If, for instance, a constant body force is suddenly applied to the cylinder the displacements will increase at the same rate at which the shear strain increases in a shear test under a suddenly applied constant shear stress; the same is true, of course, for more general loading conditions. This again is not an unreasonable result because most of the deformation is expected to be due to shear.

The response to a suddenly applied unit shear stress, which is usually referred to as the shear compliance $J(t)$, is shown in FIGURE 9 for the propellant R_1 - 6x - $06p_1$ - 60F **. The quantity k which normalizes the time in that graph is the Tobolsky shift factor which determines the time scale of the response-to-load behavior at different temperatures. ***

* Note that for the step function $G_1(o, z)$ the convolution integral in EQUATION (18) becomes

$$G(o, z) \int_0^t \frac{d \ L(t - \tau)}{d \ (t - \tau)} \, d\tau \ .$$

** This data is from REFERENCE (9) and is actually the creep compliance in a tensile test; for lack of better data, however, the shear compliance $J(t)$ has been taken as three times the creep compliance.
*** For detailed information on the Tobolsky shift factor see Ref. (9).

For analytical calculations, it is convenient to approximate the compliance by the function

$$J(t) = J_e - \frac{J_e - J_g}{(1 + a\,t/k)^{\alpha}} \qquad (20)$$

where the constants a and α are determined in a curve fitting procedure. This function is also shown in FIGURE (9) for the same propellant.

In many cases, body force loads are not applied suddenly but in such a manner that a constant load is attained after some time. If such a loading is represented by the relation

$$\gamma(t) = \gamma_o \left[1 - \exp(-\beta t) \right] \qquad (21)$$

then the time response L(t) is found with the help of the convolution integral to be

$$L(t) = \gamma_o J_e \left[1 - e^{-\beta t} - \left(1 - \frac{J_g}{J_e} \right) e^{-\frac{\beta k}{a}\left(\frac{at}{k}+1\right)} \sum_{n=0}^{\infty} \left(\frac{\beta k}{a}\right)^{n+1} \frac{\left(\frac{at}{k}+1\right)^{n+1-\alpha} - 1}{n!\,(n+1-\alpha)} \right]_{\alpha \neq 1} \qquad (22)$$

The load EQUATION (21) and the corresponding time response $L(t)/\gamma_o J_e$ are plotted in FIGURE (10) as well as the step load and the response to a step load, J(t), as given by EQUATION (20). Initially the load $1 - \exp(-\beta t)$ is smaller than the step load, and hence the response is smaller than the response to a step load. After some time the step load and the exponentially rising load have the same constant value and the responses to the two different kinds of loading become more and more equal. If the exponential load-time curve rises to its limiting value faster than that shown in FIGURE (9), the response curve approaches the step load response at shorter times. If, for instance, the limiting constant value is reached within a few seconds, rather than in one minute, one would expect that the time response is essentially the same as the response to a step load.

From an engineering standpoint it now becomes important to determine the conditions under which one may treat a time dependent response behavior as a problem in response to a step load. The parameter that determines this is $\beta k/a$, which is equal to unity for the present calculations. Therefore, if $\beta k/a > 1$, the response becomes more like the response to a step load, and the converse is true if $\beta k/a < 1$. If, e.g. $1/\beta = 1/10$ min and $k = 1$ (T = 12°F), then $\beta k/a = 70$; one should thus expect that the time dependent displacements are well represented by EQUATION (20). In this case an elaborate analysis may be omitted because the time dependence of the displacements is given directly by the experimentally determined shear compliance. On the other hand if the temperature exceeds 40°F and the load-rise time $1/\beta$ is $1/5$ min = 12 sec, then $\beta k/a < 1$, and the response is expected to be poorly represented by the response to a step load, J(t).

To summarize the procedure of obtaining the time dependent displacements we restate the steps required to arrive at the result:

One first obtains the elastic displacement solution using the material properties for short times, usually referred to as the "glassy" properties. Then the ratio of the load to shear modulus is replaced by the appropriate

time function which is the inverse Laplace transform of the ratio of transformed load to the transformed modulus. The resulting expression will give an estimate of the displacements. Although this analysis was based on the one term solution the result is equally applicable to the two term solution because in either case the spatial dependence of the approximate time dependent displacements is the same as that for the purely elastic cylinder.

CONCLUSION

It has been shown that the Method of Restricted Variation leads to a reasonable elastic solution of a problem which is nearly impossible to solve exactly. In problems of similar nature, solutions of the accuracy as demonstrated here are often quite sufficient for some engineering applications; in such a case it would be economically poor to attempt a more accurate analysis, especially if some estimate of the quality (rather than accuracy) of the solution can be obtained by analyzing the approximate solution beyond the bare numbers which the mechanics of the solution produce.

The numerical results indicate that the maximum radial displacement lies probably between $0.1 \, \Upsilon b^2/4\mu$ and $0.25 \, \Upsilon b^2/4\mu$ for the elastic unsupported cylinder, and equals approximately $0.015 \, \Upsilon b^2/4\mu$ for the elastic supported cylinder. The large difference in the maximal displacements for the two cases is explained by the fact that in the supported cylinder the maximal displacement occurs near the support where the displacements are identically equal to zero, whereas no such restraint is placed on the radial deformation in the unsupported cylinder. Allowing for time dependent material properties of the type described in the body of the text, one should expect that a cylinder with an external radius of 12 inches and of specific gravity 1.5, exhibits a maximum radial displacement of about $3 \times 10^{-3} n$ inches and the supported cylinder $2.7 \times 10^{-4} n$ inches for long times; n is the number of "g"s to which the cylinder is subjected. Thus for an acceleration of 50"g" one should expect displacements on the order of 0.15 inches and 0.014 inches for the unsupported and supported cylinder, respectively.

The small size of the displacements is, of course, a result of the particular propellant used in the calculations. Although other propellants will allow larger deformations, a propellant of the type considered here justifies the use of infinitesimal elasticity for moderate values of acceleration if linear elastic methods are at all applicable to the analysis of solid propellant materials.

It is important to realize again that the preceding analysis is approximate. Although there is reason to believe that the time dependence of the solution is commensurate with the accuracy of the elastic solution there appears to be evidence that displacements calculated from uniaxial tensile test data lead to deformations much larger than found by experiment (10). It is therefore advisable to make and use calculations as presented here only with the full understanding of the approximations and assumptions that lead to the final result, lest it be used to predict slump behavior in a range of accuracy not warranted by the approximate nature of the analysis.

REFERENCES

1. Lianis, G.: "Stresses and Strains in Solid Propellant During Storage. American Rocket Society,"Paper No. 1592-61, February 1961.

2. Lee, E. H.: "Stress Analysis in Visco-Elastic Bodies." Brown University, Division of Applied Mathematics, Technical Report No. 8, June 1954.

3. Pickett, Gerald: "Application of the Fourier Method to the Solution of Certain Boundary Problems in the Theory of Elasticity." Journal of Applied Mechanics, September 1944.

4. Sokolnikoff, I. S.: Mathematical Theory of Elasticity. McGraw-Hill, 1956, second edition.

5. Timoshenko, S. and Goodier, J. N.: Theory of Electricity. McGraw-Hill, 1951, second edition.

6. Knauss, W. G.: "Displacements in a Tubular Rocket Grain Under Axial Acceleration." GALCIT SM 61-10, California Institute of Technology.

7. Crandall, S. S.: Engineering Analysis. McGraw-Hill, 1956.

8. Wayland, H.: Differential Equations Applied in Science and Engineering. Van Nostrand, 1957.

9. Williams, M. L.; Blatz, P. J.; and Schapery, R. A.: "Fundamental Studies Relating to Systems Analysis of Solid Propellants". GALCIT 101 Final Report GALCIT SM 61-5, California Institute of Technology, February 1961, p. 86, 87.

10. Thacher, J. H.: Research Progress Report A2-52 July 61; Allegany Ballistics Laboratory, Cumberland, Maryland.
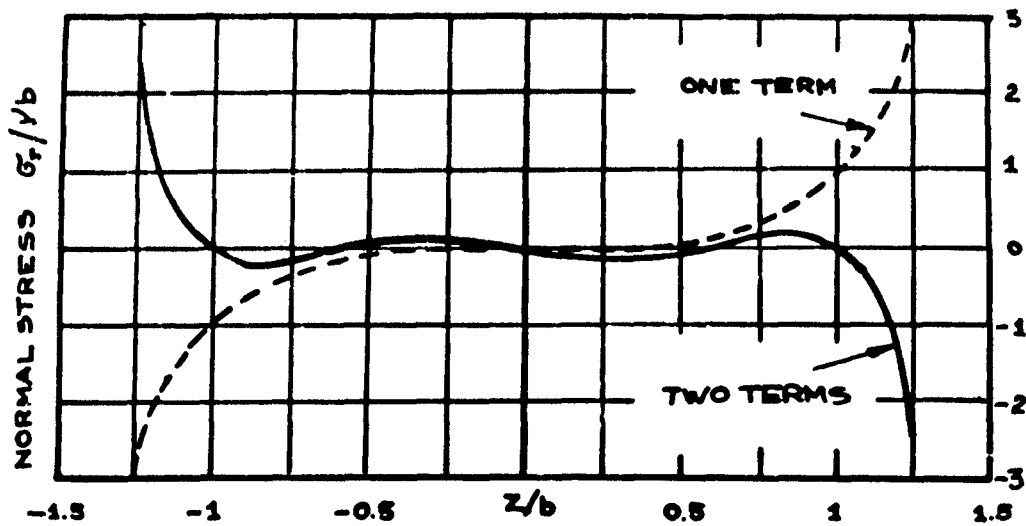
FIGURE 3.
RESIDUAL STRESS $\sigma_r/\gamma b$ ON THE INTERNAL BOUNDARY; THE EXACT
SOLUTION REQUIRES $\sigma_r = 0$ AT THE INTERNAL BOUNDARY
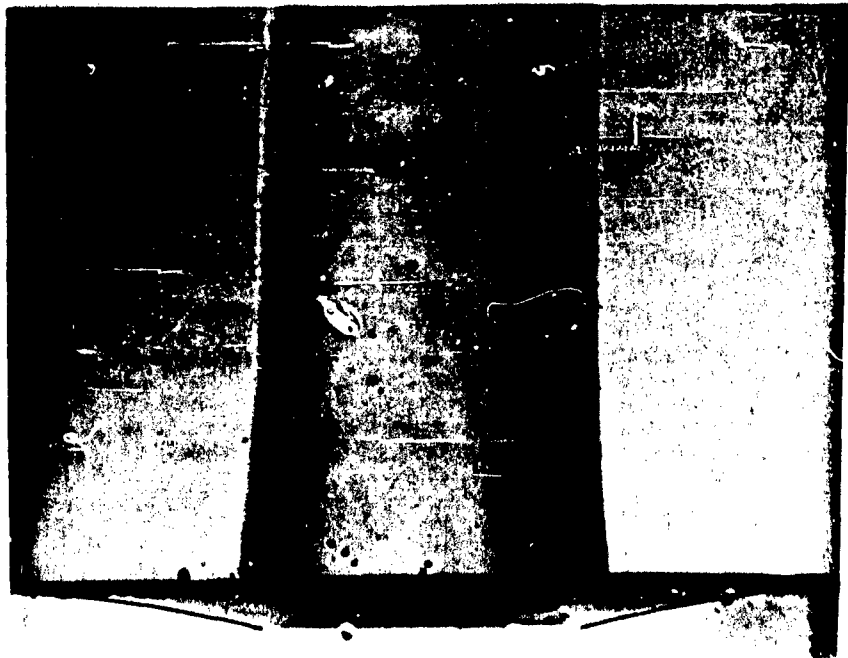

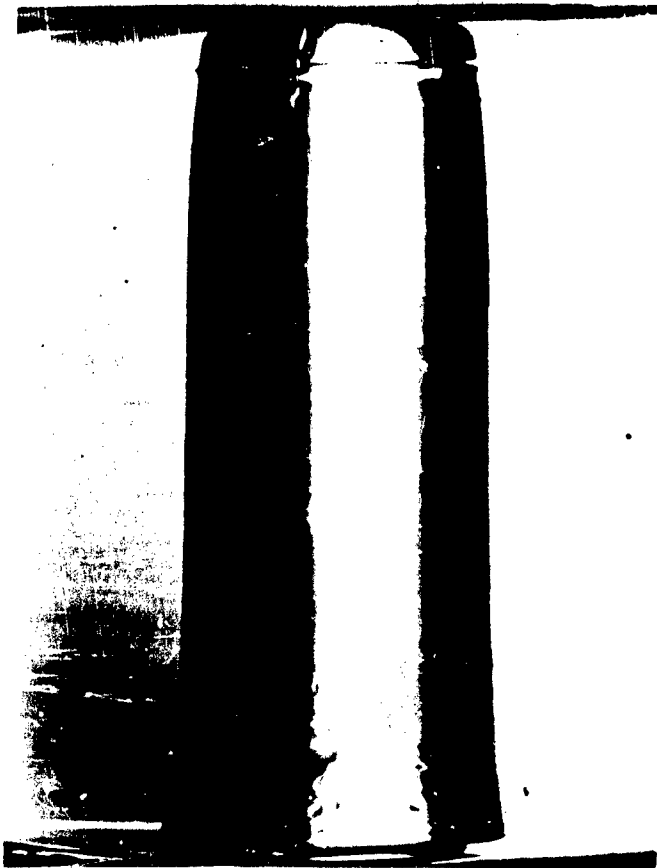FIGURE 4.   CLOSE UP VIEW OF AFT END OF UNSUPPORTED CYLINDER MODEL

FIGURE 5.
DEFORMATION OF THE INTERNAL BOUNDARY
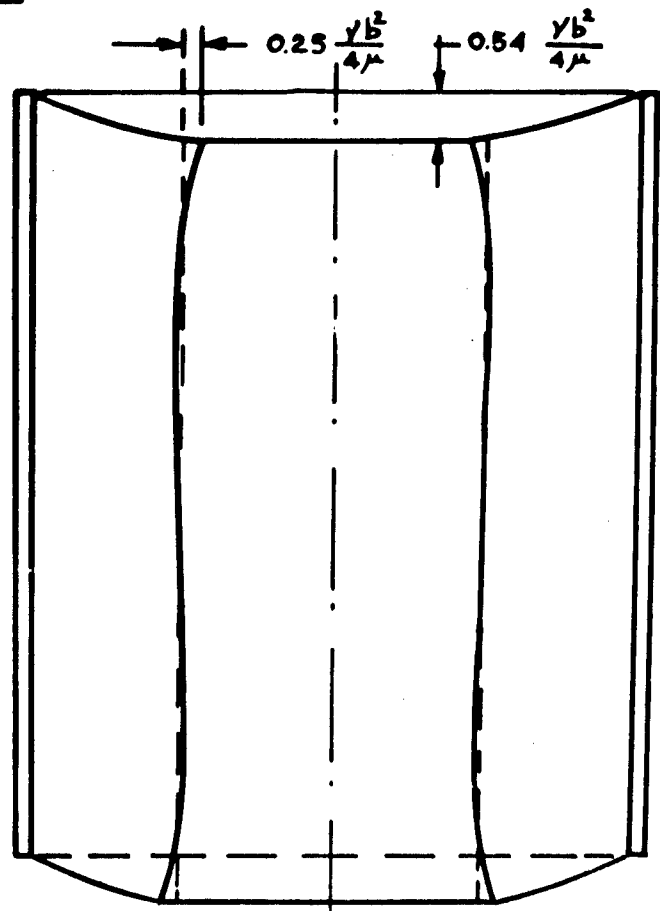IN THE UNSUPPORTED CYLINDER MODEL

FIGURE 6.
DEFORMATION OF THE INTERNAL BOUNDARY
IN THE UNSUPPORTED CYLINDER AS CAL-
CULATED FROM THE TWO TERM SOLUTION

FIGURE 7.
DEFORMATION OF THE INTERNAL BOUNDARY
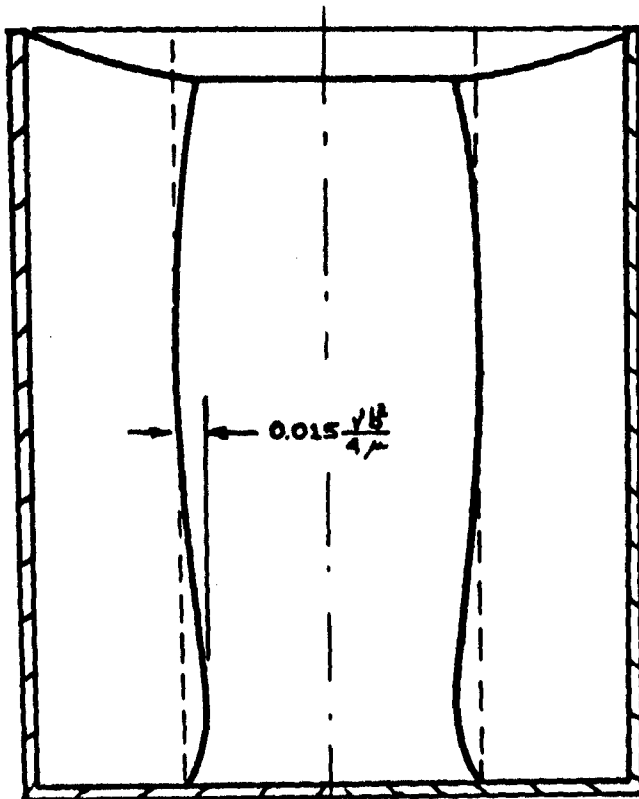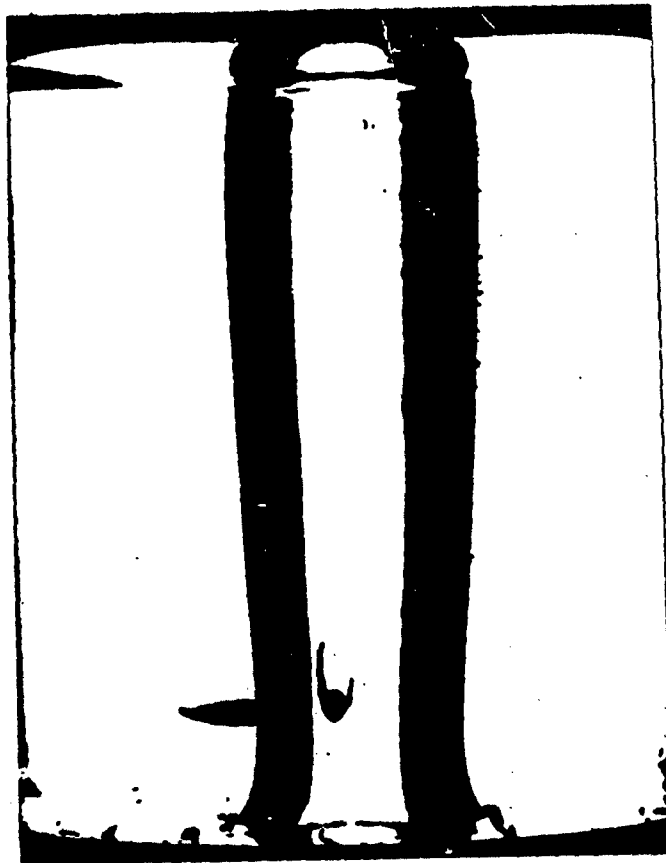IN THE SUPPORTED CYLINDER MODEL

$$0.015 \frac{\gamma l^4}{4r}$$

FIGURE 8.
DEFORMATION OF THE INTERNAL BOUNDARY
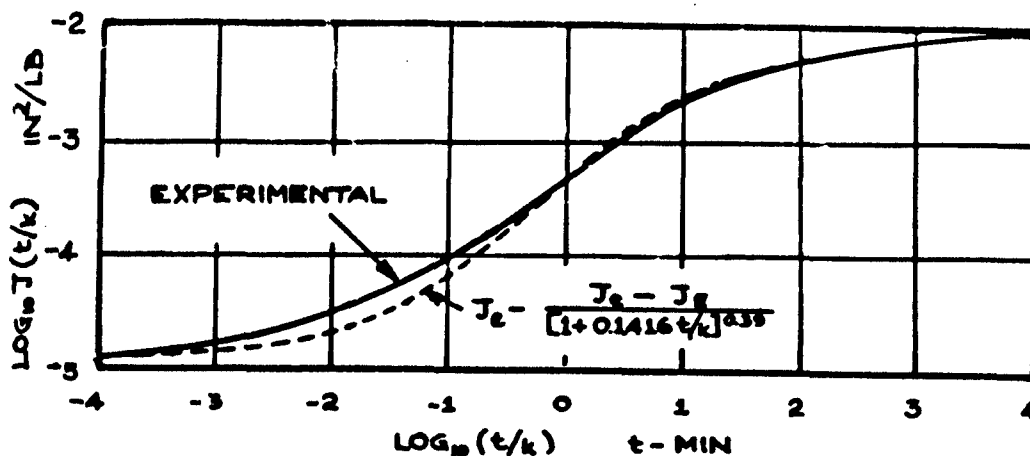IN THE SUPPORTED CYLINDER AS CAL-
CULATED FROM THE ONE TERM SOLUTION

FIGURE 9. SHEAR COMPLIANCE FOR R_1 - 6X-O. $6p_1$ - 6OF PROPELLANT
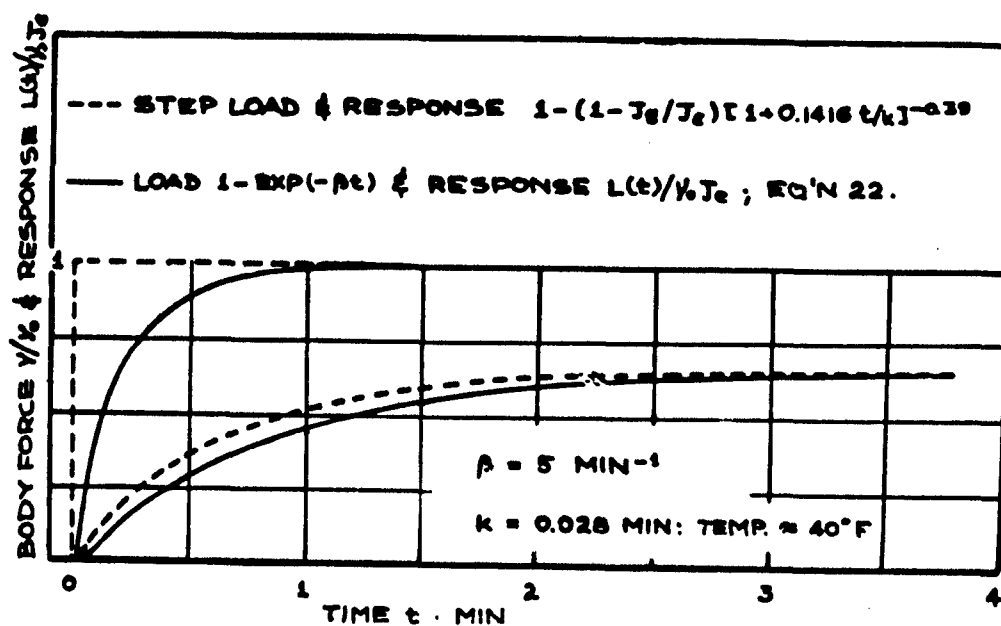

FIGURE 10.
TIME DEPENDENT BODY FORCE LOAD AND CORRESPONDING DISPLACEMENT
TIME RESPONSE FOR TWO DIFFERENT KINDS OF LOADING

APPENDIX

$$m_1 = \pi \int_a^b \left\{ (\lambda + 2\mu)\left(\frac{dQ_1}{dr} + \frac{R_1}{r}\right)^2 - 4\mu \frac{R_1}{r}\frac{dR_1}{dr} \right\} r \, dr$$

$$m_2 = \pi \int_a^b \left\{ (\lambda + 2\mu)\left(\frac{dR_2}{dr} + \frac{R_2}{r}\right)^2 - 4\mu \frac{R_2}{r}\frac{dR_2}{dr} \right\} r \, dr$$

$$m_3 = \pi \int_a^b \left\{ 2(\lambda + 2\mu)\left(\frac{dR_1}{dr} + \frac{R_1}{r}\right)\left(\frac{dR_2}{dr} + \frac{R_2}{r}\right) - 4\mu \frac{1}{r}\left(\frac{dR_1}{dr} R_2 + \frac{dR_2}{dr} R_1\right) \right\} r \, dr$$

$$m_4 = \pi \int_a^b (\lambda + 2\mu)\rho_1^2 \, r \, dr$$

$$m_5 = \pi \int_a^b (\lambda + 2\mu)\rho_2^2 \, r \, dr$$

$$m_6 = \pi \int_a^b 2(\lambda + 2\mu)\rho_1\rho_2 \, r \, dr$$

$$m_7 = \pi \int_a^b 2\rho_1\left(\frac{dR_1}{dr} + \frac{R_1}{r}\right) r \, dr$$

$$m_8 = \pi \int_a^b 2\rho_2\left(\frac{dR_1}{dr} + \frac{R_1}{r}\right) r \, dr$$

$$m_9 = \pi \int_a^b 2\rho_1\left(\frac{dR_2}{dr} + \frac{R_2}{r}\right) r \, dr$$

$$m_{10} = \pi \int_a^b 2\rho_2\left(\frac{dR_2}{dr} + \frac{R_2}{r}\right) r \, dr$$

$$n_1 = \pi \int_a^b \mu R_1^2 \, r \, dr \qquad\qquad \Gamma_1 = 2\pi \int_a^b \gamma \rho_1 \, r \, dr$$

$$n_2 = \pi \int_a^b \mu R_2^2 \, r \, dr \qquad\qquad \Gamma_2 = 2\pi \int_a^b \gamma \rho_2 \, r \, dr$$

$$n_3 = \pi \int_a^b 2\mu R_1 R_2 \, r \, dr$$

$$n_4 = \pi \int_a^b \mu \left(\frac{d\rho_1}{dr}\right)^2 r \, dr$$

$$n_5 = \pi \int_a^b \mu \left(\frac{d\rho_2}{dr}\right)^2 r \, dr$$

$$n_6 = \pi \int_a^b 2\mu \frac{d\rho_1}{dr}\frac{d\rho_2}{dr} r \, dr$$

$$n_7 = \pi \int_a^b 2\mu R_1 \frac{d\rho_1}{dr} r \, dr$$

$$n_8 = \pi \int_a^b 2\mu R_1 \frac{d\rho_2}{dr} r \, dr$$

$$n_9 = \pi \int_a^b 2\mu R_2 \frac{d\rho_1}{dr} r \, dr$$

$$n_{10} = \pi \int_a^b 2\mu R_2 \frac{d\rho_2}{dr} r \, dr$$

SPECIAL TEST PROCEDURES

K. W. Bills, Jr. and R. A. Chase, Reporters

PROPELLANT VISCOELASTIC CHARACTERIZATION IN CREEP AND STRESS RELAXATION TESTS[1]

J. W. Jones, Manager, Structural Integrity Department
D. Daniel, Research Engineer
D. A. Johnson, Research Engineer
Propulsion Engineering Division
Grand Central Rocket Co.
Redlands, California

ABSTRACT

The characterization of solid propellant viscoelastic properties in terms of linear differential operators by creep and stress relaxation test techniques is described. Test data illustrating the essential viscoelastic linearity of a Polycarbutene propellant are presented.

INTRODUCTION

The accurate determination of propellant physical properties in laboratory tests is a fundamental prerequisite to the engineering stress analysis of solid propellant rocket motor grains. Engineering analysis of rocket grains using the methods of linear viscoelastic analysis requires both specification of the propellant properties and definition of the time, temperature, stress and strain domain within which linear behavior of the propellant is obtained. Indeed, the definition of these domains can provide a first, conservative approximation to the critically important failure criteria for a propellant.

Propellant physical behavior within the linear behavior domain can be mathematically described by any of several equivalent methods. All such methods require exacting experimental data in order that the physical material descriptions will be of an order of accuracy useful in engineering analysis: The following paragraphs describe the analytical and experimental techniques used at the Grand Central Rocket Co. in the viscoelastic characterization of solid propellants in terms of linear differential operators.

DIFFERENTIAL OPERATOR MATERIAL PROPERTY SPECIFICATION

The majority of published solutions for stress distributions in linear viscoelastic bodies have been based on the linear differential operator specification of the relationship of time dependent stress $\sigma(t)$ to the corresponding strain $\epsilon(t)$

$$P\sigma(t) = Q\epsilon(t) \tag{1}$$

where

$$P = \sum_{i=0}^{n} a_i \frac{\partial^i}{\partial t^i} \qquad (2)$$

and

$$Q = \sum_{i=0}^{m} b_i \frac{\partial^i}{\partial t^i} \qquad (3)$$

in which n and m are not necessarily equal (1, 2). The constants a_i, b_i specify the stress strain law for a material at a constant temperature. The order of n with respect to m and the presence or absence of the constant a_0 define various aspects of the limiting behavior of the material (1). For example, when $a_0 = 0$ stress diminishes to zero at a constant strain as time increases.

The finite differential operator form of material property specification for propellants was selected in favor of, for example, integral property representation, because of the inherent ease in its mathematical manipulation through the use of Laplace transform techniques as well as because of the availability of published stress analysis solutions based on operators.

TEST MODE ANALYSIS

The two basic experimental methods used in laboratory determination of propellant viscoelastic properties were uniaxial creep and stress relaxation tests in which the test mode was a ramp function strain input.

Creep tests were initiated by elongation at a constant strain rate until a preselected stress level was obtained. The selected stress level was then held constant for the duration of the test. Stress relaxation tests were initiated by elongation at a constant strain rate to a preselected strain level that was maintained constant for the test duration. The analysis for the stress relaxation test is presented below as an illustration of the techniques used in determining the numerical values of the operator coefficients a_i and b_i

Consider a bar of a linearly viscoelastic material as defined by the finite linear differential operator stress-strain law

$$\left[\frac{\partial^n}{\partial t^n} + a_{n-1} \frac{\partial^{n-1}}{\partial t^{n-1}} + \cdots + a_1 \frac{\partial}{\partial t} + a_0 \right] \sigma(t)$$

$$= \left[b_n \frac{\partial^n}{\partial t^n} + b_{n-1} \frac{\partial^{n-1}}{\partial t^{n-1}} + \cdots + b_1 \frac{\partial}{\partial t} + b_0 \right] \epsilon(t) \qquad (4)$$

which is strained uniaxially at a constant strain rate R to a strain $e(t_1)=Rt_1$ and held at the strain level Rt_1. The input strain is, hence

$$e(t) = Rt - R(t-t_1)u(t-t_1).$$

(5)

Laplace transformation yields, in the transform parameter s,

$$\sigma(s) = \frac{R}{s^2}\left[\frac{b_n s^n + b_{n-1} s^{n-1} + \cdots + b_1 s + b_0}{s^n + a_{n-1} s^{n-1} + \cdots + a_1 s + a_0}\right]\left(1 - e^{-t_1 s}\right).$$

(6)

Expansion of the polynomial quotient in equation 6 by partial fractions to obtain

$$\frac{\sigma(s)}{R} = \left[\frac{A_{n+2}}{s^2} + \frac{A_{n+1}}{s} + \frac{A_1}{s+\alpha_1} + \cdots + \frac{A_n}{s+\alpha_n}\right]\left(1 - e^{-t_1 s}\right)$$

(7)

where the $-\alpha_i$ are the roots of the polynomial in the denominator of equation 6 and the A_i are the partial fraction residuals, is a convenient algebraic rearrangement leading directly to the Laplace inversion to obtain the solution for the time dependent stress

$$\sigma(t) = R\left[A_{n+2}t + A_{n+1} + A_1 e^{-\alpha_1 t} + \cdots + A_n e^{-\alpha_n t}\right]$$

$$- R\left[A_{n+2}(t-t_1) + A_{n+1} + A_1 e^{-\alpha_1(t-t_1)} + \cdots + A_n e^{-\alpha_n(t-t_1)}\right]u(t-t_1).$$

(8)

Experimental data for stress relaxation tests were fit to equation (8) to obtain numerical values for the A_i and α_i. The operator coefficients were then determined as following from the above derivations and defining K_i^n as the summation of the products formed by multiplying together the members of all possible combinations of n values taken i at a time,

$$a_{n-1} = K_1^n(\alpha)$$

$$a_{n-2} = K_2^n(\alpha)$$

$$\vdots$$

$$a_{n-k} = K_k^n(\alpha) \tag{9}$$

and

$$b_n = A_1 K_1'^n(\alpha_1 = 0) + A_2 K_1^n(\alpha_2 = 0) + \cdots$$

$$\cdots + A_n K_1^n(\alpha_n = 0) + A_{n+1} K_1^n(\alpha) + A_{n+2}$$

$$b_{n-k} = A_1 K_{k+1}^n(\alpha_1 = 0) + A_2 K_{k+1}^n(\alpha_2 = 0) + \cdots$$

$$\cdots + A_n K_{k+1}^n(\alpha_n = 0) + A_{n+1} K_{k+1}^n(\alpha) + A_{n+2} K_k^n(\alpha) \tag{10}$$

It is informative to note that the roots of the stress operator, $-\alpha_i$, can be interpreted directly from curve fit data as the reciprocal relaxation times of the material.

EXPERIMENTAL METHODS

Test specimens used in uniaxial material characterizations at GCR are metal or wooden tab end tensile specimens. Metal tab end specimens are prepared by bonding metal tabs, with grip attachments, to the ends of bars of propellant 3/8 by 3/8 by 5 inches in size, machined to tolerances of ± 0.002 inches. Wooden tab and specimens are prepared to the same size and tolerances by cutting and machining from blocks of propellant cast into lined wooden boxes to obtain "cast on" wooden gripping tabs. Figures 1, 2 and 3 show, respectively, the propellant box casting, the machining apparatus and a finished wooden tab end tensile specimen. A metal tab end tensile specimen can be seen in the apparatus illustrated in Figure 4.

Stress relaxation tests are presently made using the spring-actuated Stanford Research Institute Rapid Relaxometer (Figure 4). This device was used at its lowest straining speed in order to preserve the linearity of the ramp strain input to a relaxation test.

Creep tests are presently made using the Instron Universal Tester to unload a weight onto a tensile specimen (Figure 5). The stress in this test is maintained at a constant level through use of a tension spring connected in series with the weight. The spring is selected to cause a force decrease with specimen elongation in the proportion required to compensate for the Poisson effect, assuming a Poisson's ratio of 1/2 for the propellant.

Both the creep and stress relaxation test devices are instrumented for load and displacement measurement.

EXPERIMENTAL DATA

Creep and stress relaxation characterizations of a Polycarbutene propellant have been made at a temperature of $70° \pm 2°F$ for a time duration of 120 seconds. Data for these tests were curve fit, by computer, with an accuracy of ± 2 percent and the corresponding operator coefficients for a fourth order operator were determined. Stress levels of up to 50 psi and strain levels up to 12 percent were explored. Typical data, as determined from stress relaxation tests, in terms of the operator coefficients a_i and b_i are shown in Table I. The coefficients are shown normalized in terms of the lowest order coefficient of the stress operator, a_0 .

TABLE I

DIFFERENTIAL OPERATOR COEFFICIENTS
POLYCARBUTENE PROPELLANT*

$\epsilon(t_i)$	0.03	0.05	0.05	0.05	0.07	0.07	0.07	0.09	0.09	0.12	0.12
t_i (sec)	0.100	0.181	0.186	0.180	0.260	0.260	0.260	0.350	0.350	0.510	0.500
a_4	0.996	0.831	2.463	1.420	1.449	0.881	1.236	1.497	1.211	1.218	1.531
a_3	43.04	34.93	55.76	47.79	43.58	35.56	51.153	43.23	44.05	41.46	51.11
a_2	141.1	133.2	160.4	159.3	144.2	138.0	163.6	135.8	148.6	133.2	163.9
a_1	45.68	46.35	46.64	54.37	46.77	48.29	47.74	43.22	45.69	42.34	47.22
a_0	1.00	1.00	1.00	1.00	1.00	1.00	1.00	1.00	1.00	1.00	1.00
b_4	1,840	1,819	3,322	2,502	2,467	2,264	3,050	2,847	3,123	3,316	4,372
b_3	31,120	29,190	38,860	34,380	33,160	31,340	37,110	33,070	36,550	33,760	45,620
b_2	62,590	62,520	67,740	68,520	61,630	61,980	62,810	56,770	62,300	51,020	67,280
b_1	14,100	15,200	14,760	16,310	13,640	15,190	13,440	12,510	13,320	11,260	13,650
b_0	233.3	248.9	242.1	234.0	215.7	234.4	210.0	217.8	215.6	192.4	205.7

*84 percent solids loading. Test temperature $70 \pm 2°F$.

DISCUSSION

Perhaps the most important result of this research program thus far has been the demonstration that a highly filled propellant can be treated analytically as a linear viscoelastic solid at finite strain levels. The data shown in Table I show, for engineering purposes, excellent linearity. Without confirmation of the essential validity of assuming linear behavior in propellant grain stress analysis, the value of linear theory in engineering analysis would be small indeed. The data presented in Table I have been used successfully in engineering analysis of slump in a thirty-six inch diameter, fifty percent web fraction grain (Ref. 3). The excellent agreement between the observed and predicted slumps are a demonstration of the practical use of laboratory data in accurate prediction of the behavior of the full-scale propellant grains.

Although the experimental methods are not treated in minute detail in this paper, it is pertinent to remark on a few of the more vital points in this area. Precision test specimens are mandatory for viscoelastic propellant characterization. Propellant specimens degraded by die cutting, hand trimming and general abuse are unsatisfactory. While the tab end specimens do not exhibit a pure uniaxial stress and strain distribution, the perturbations are quite small, especially by comparison to the "JANAF" dumbbell specimen, which was found to be of qualitative value only. Clearly, it must be possible to conduct an accurate stress analysis of the test specimen if the data derived from a test of the specimen are to be used in grain analysis. Unfortunately, the "JANAF" specimen does not meet this requirement. Finally, the test apparatus must impose an accurately controlled test mode on a specimen if useful data are to be obtained. Initial conditions and transients produced during initiation of a test must be measured and dealt with; they cannot be disposed of by approximation. This problem is particularly acute in the interpretation of test data for the second and fractional second time domain. In all cases it was found to be mandatory to sacrifice speed for control in, for example, applying the initial strain in a stress relaxation test. Improved methods of maintaining precision test mode control in high speed tests are badly needed.

REFERENCES

(1) Alfrey, T., Mechanical Behavior of High Polymer, Interscience Publishers, N.Y., 1948

(2) Lee, E. H., and Rogers, T.G., "Solution of Viscoelastic Stress Analysis Problems Using Measured Creep or Relaxation Functions", Interim Tech. Rpt. No. 1, U. S. Army Research Office (Durham) Project No. 1892-E.

(3) Fitzgerald, J. Edmund, et al, "Axial Slump of a Circular Port Grain", 20th Meeting of the JANAF Physical Properties Panel, Riverside, California, 1961.

FIGURE 1.
BOX CASTING FOR WOODEN TAB END
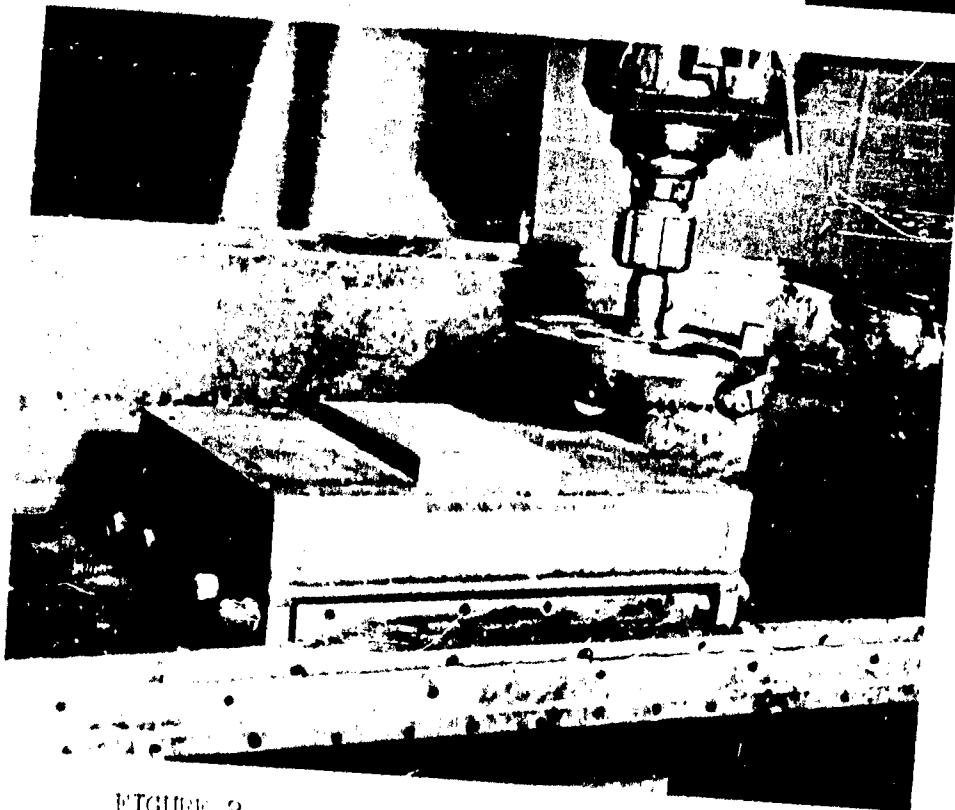TENSILE SAMPLE PREPARATION

FIGURE 2.
TAB END TENSILE SAMPLE PREPARATION
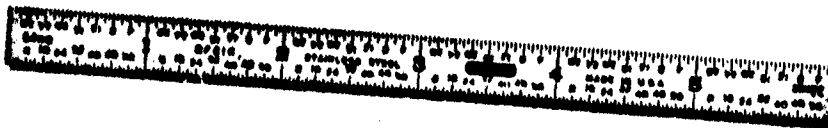MILLING CUT USING VACUUM BASE

FIGURE 3.   TAB END TENSILE SAMPLE
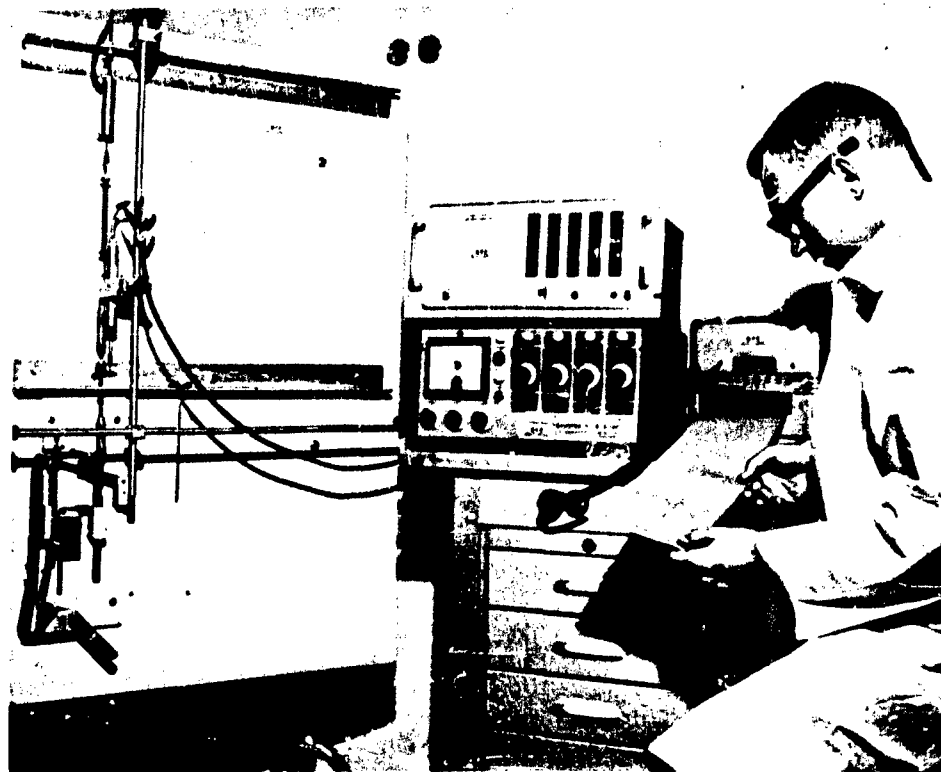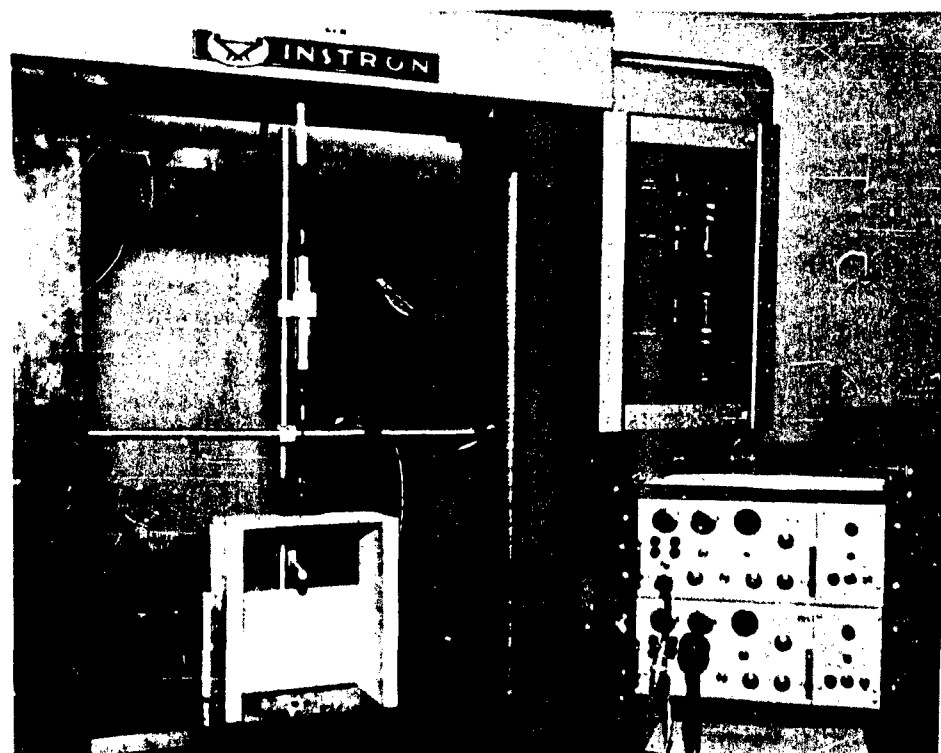
FIGURE 4. STRESS RELAXATION APPARATUS

FIGURE 5. CREEP APPARATUS

DEVELOPMENT OF A BONDED-END TENSILE SPECIMEN

M. H. Cooper and J. B. Baldwin*
Thiokol Chemical Corporation, Huntsville, Alabama

ABSTRACT

A tensile specimen assembly which consists of a rectangular bar of propellant bonded to two end-plates has been developed. Photographic strain measurements and studies with birefringent coatings have indicated that end effects are small; this conclusion is in agreement with a mathematical estimate. Tests with paired specimens revealed a level of precision for the bonded-end specimen comparable to that of the die-cut JANAF specimen.

INTRODUCTION

It is the purpose of this paper to summarize the experience gained with the bonded-end tensile specimen at the Redstone Division of Thiokol Chemical Corporation since the initial report (1) given at the preceding meeting of this Panel. Interest in this type of propellant specimen has increased greatly in the past year; its advantage -- lack of jaw flow -- over the conventional dumbbell specimen has encouraged the use of this specimen in other tests, e.g., stress relaxation, creep, high-speed tensile, and strain dilatation. A similarly growing interest in the study and application of the square flat-end specimen configuration at other laboratories has been noted (2, 3).

The investigations conducted at Redstone were mainly concerned with comparison of the accuracy and precision of the bonded-end specimen with that of conventional dumbbell specimens. A better knowledge was desired of the extent to which the rigidly bonded ends affected the strain field of the rest of the specimen; and since the preparation of the bonded-end specimen is considerably more involved than that of the die-cut flat dumbbells, an examination of test result variation would be of value.

EXPERIMENTAL PROCEDURE

The specimen assembly consisted of a 1/2"x1/2"x4" rectangular bar (cut from a propellant sample with a band saw) which was attached at the ends to two steel plates with an epoxy cement. This cement (Epon 828 and Shell curing agent "D", 5:1) was cured at 200°F. for 2 hours, with the bar and plates held in position by an alignment rig. The effective specimen length was taken as the distance along the propellant bar between the cured adhesive at the end-plates. Figure 1 shows a bonded-end specimen at three stages of a test. Low-temperature tests required the use of

Present address: United Technology Corporation, Sunnyvale, California.
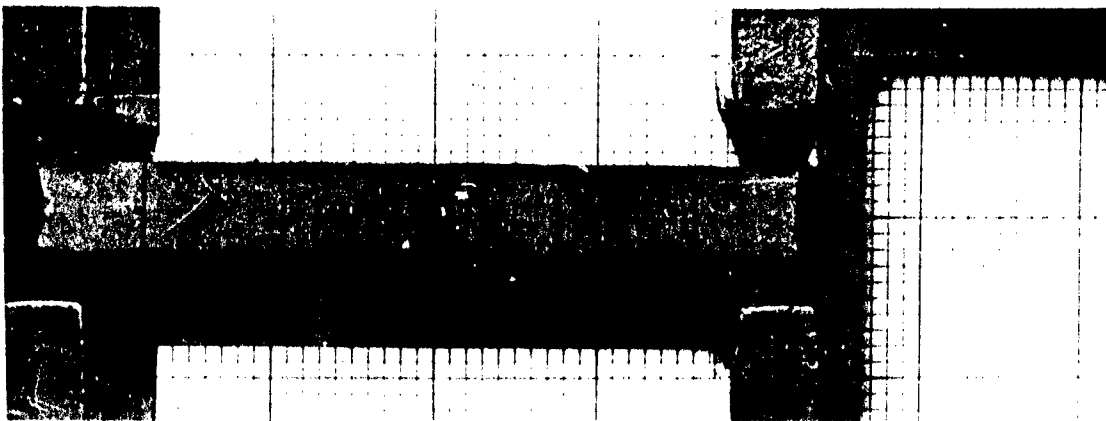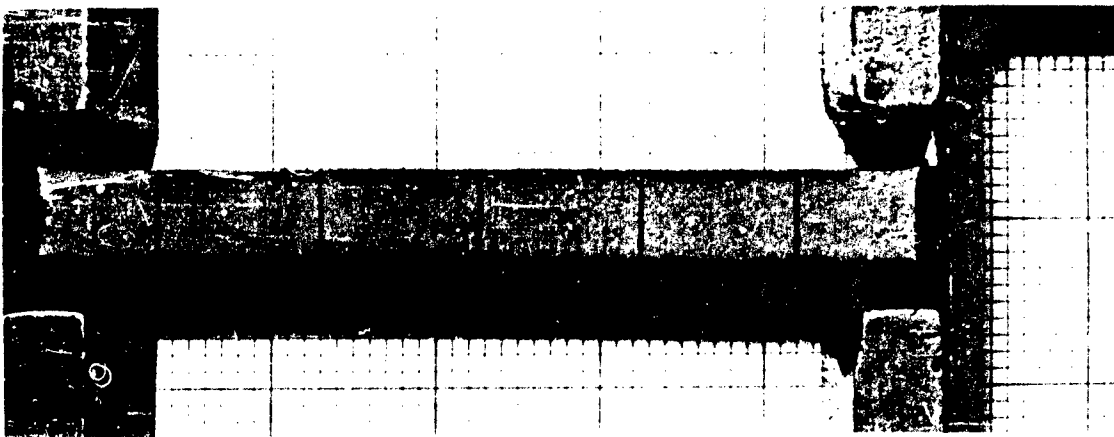
$\epsilon = 5\%$ $\epsilon = 15\%$ $\epsilon = 30\%$

FIGURE 1. BOILED-END TENSILE SPECIMEN AT VARIOUS LEVELS OF STRAIN
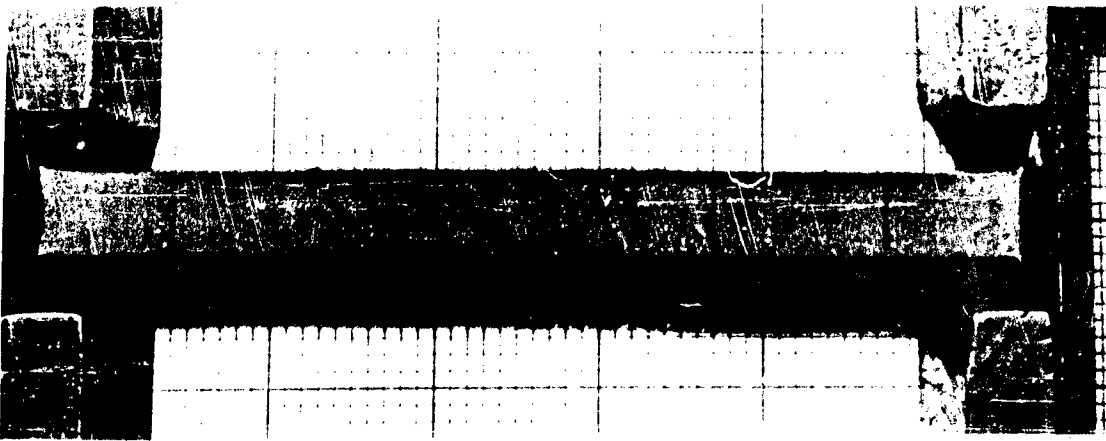
epoxy resin end-plates instead of steel, the latter producing frequent bond failures at temperatures below 20°F.

To achieve an unusually wide range of strain rates, one series of tests was run in which both crosshead speed and specimen length were varied. Birefringent coatings of a low-modulus polymer (castor oil-isocyanate) were applied to bonded-end and dumbbell-type specimens and color motion pictures were made of the stress patterns that appeared during the test. Photographic measurements of strain were made with a 35-mm. sequence camera and benchmarked specimens.

To compare the test reproducibility of the bonded-end specimen with that of the JANAF specimen, pairs of both types of specimen were prepared from the same mix of propellant. These pairs (23 bonded-end and 30 JANAF) were taken from adjacent positions in the propellant sample; this similarity of origin minimized the effect of heterogeneity within a propellant sample on the test results. All testing was done at a crosshead speed of 2 inches per minute and a temperature of 77°F. Nominal maximum stress and strain at break data were obtained from the load-elongation charts; an effective gage length of 2.6 inches was assigned to the JANAF specimen. The absolute difference or range was computed from the data of these parameters for each pair (4). The observed ranges of each group of similar data were arranged in ascending order and plotted to form a cumulative frequency distribution which was compared with the theoretical range distribution based on the estimated standard deviation and range factors (5).

DISCUSSION

The "necking-down" of the bonded-end specimen in Figure 1 gives a qualitative indication of the extent of the end effects. The TPH-8041 propellant specimen shown in the photographs was pulled at 2 inches per minute and the test temperature was 77°F. The major stress patterns present in the specimens used in the photoelastic studies are represented by the darkened areas in the sketches of Figure 2.
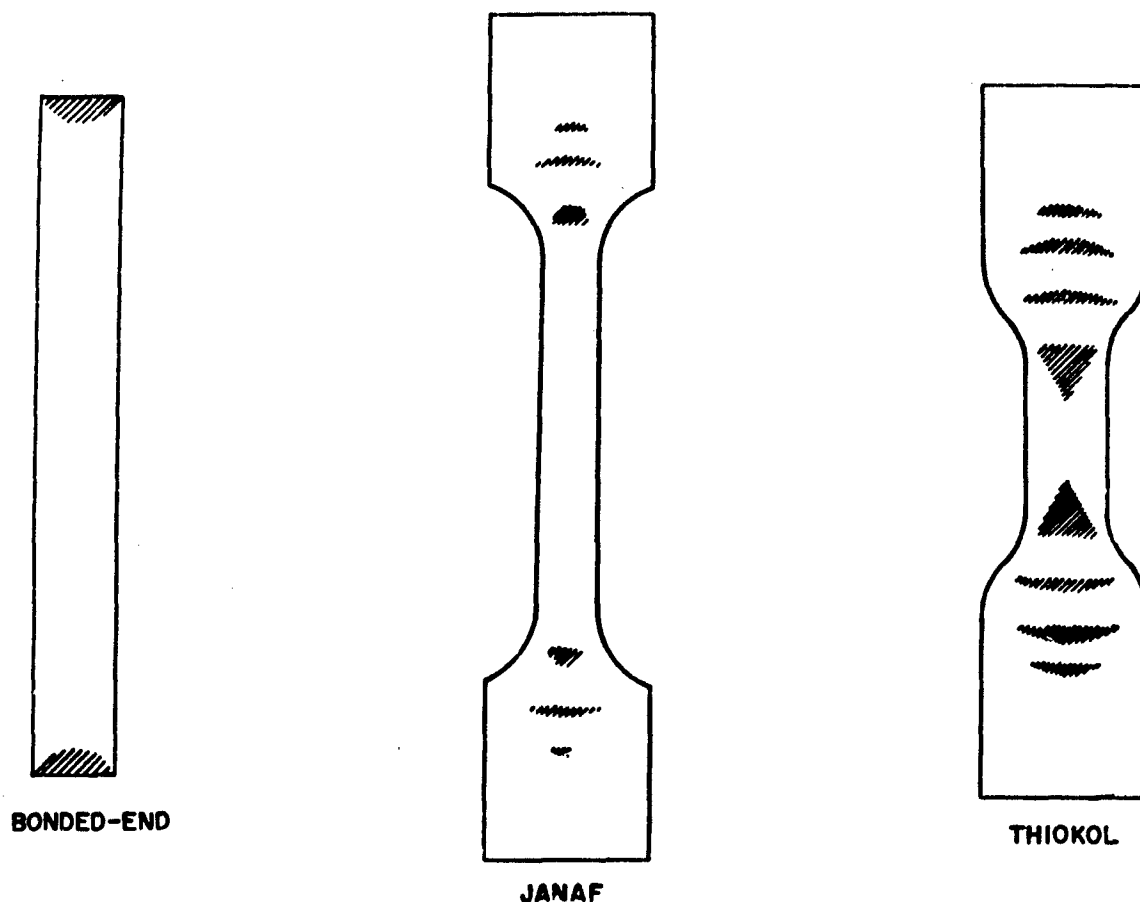
BONDED-END

JANAF

THIOKOL

FIGURE 2. TYPICAL STRESS PATTERNS AT 10% STRAIN

The characteristic patterns found in the jaw regions of the dumbbell types are strikingly evident in the case of the shorter and thicker Thiokol specimen; here, the straight test section is definitely involved. These two illustrations agree well with a mathematical estimate (6) based on a specimen of circular cross-section: the limit of significant end effects is about one-half the specimen's radius. The comparison of bonded-end specimen elongations from photographic measurement and those obtained from crosshead movement revealed differences of only a few per cent. The tests made at different strain rates (various specimen lengths at constant crosshead speed and vice versa) resulted in close agreement in elastic modulus values at the same strain rate by the two methods.

In the area of test precision, the sample standard deviations calculated from the ranges of pairs of the bonded-end and JANAF do not differ appreciably. Similarly, the comparisons of the observed range values with the theoretical curves in the maximum stress and strain at break plots of cumulative frequency distribution (Figures 3 and 4, respectively) indicate that the two methods of specimen preparation and testing have comparable levels of reproducibility.
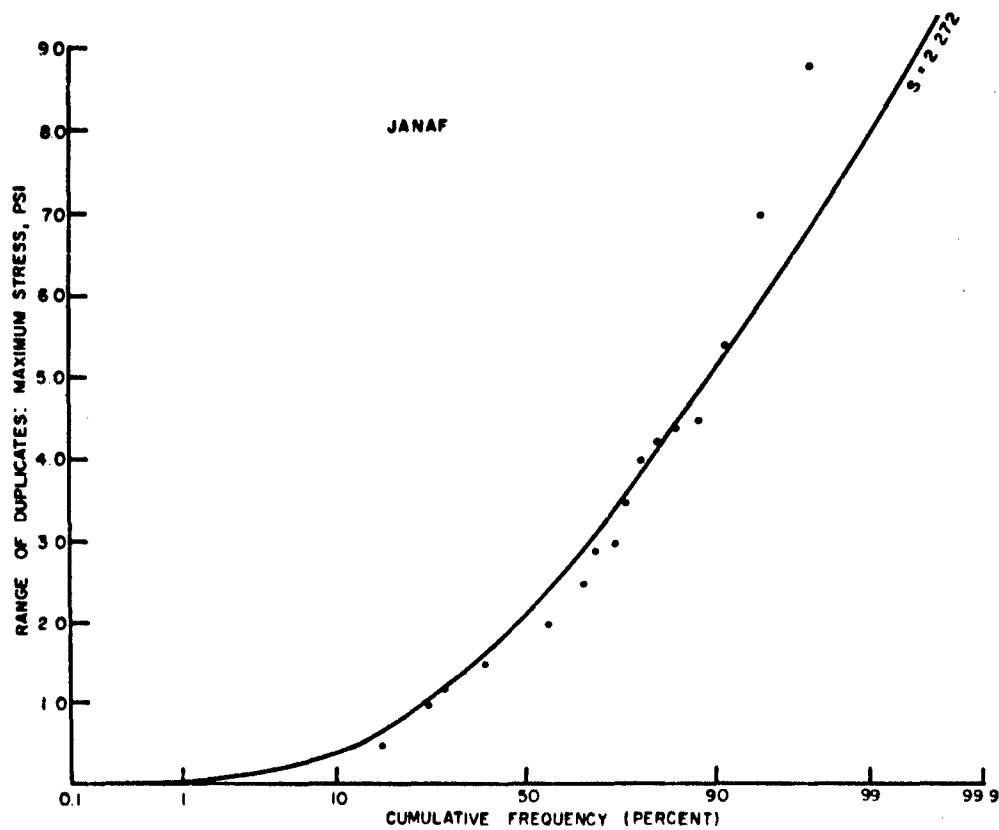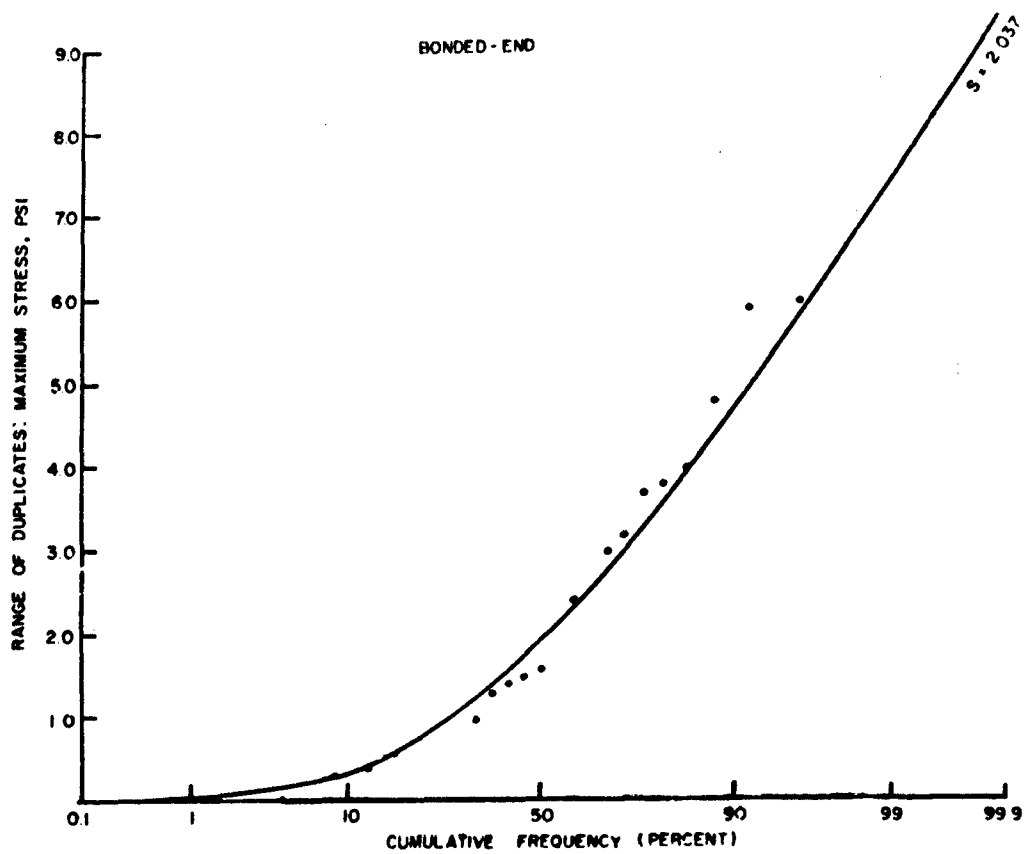
FIGURE 3. COMPARISON OF TENSILE SPECIMENS: MAXIMUM STRESS
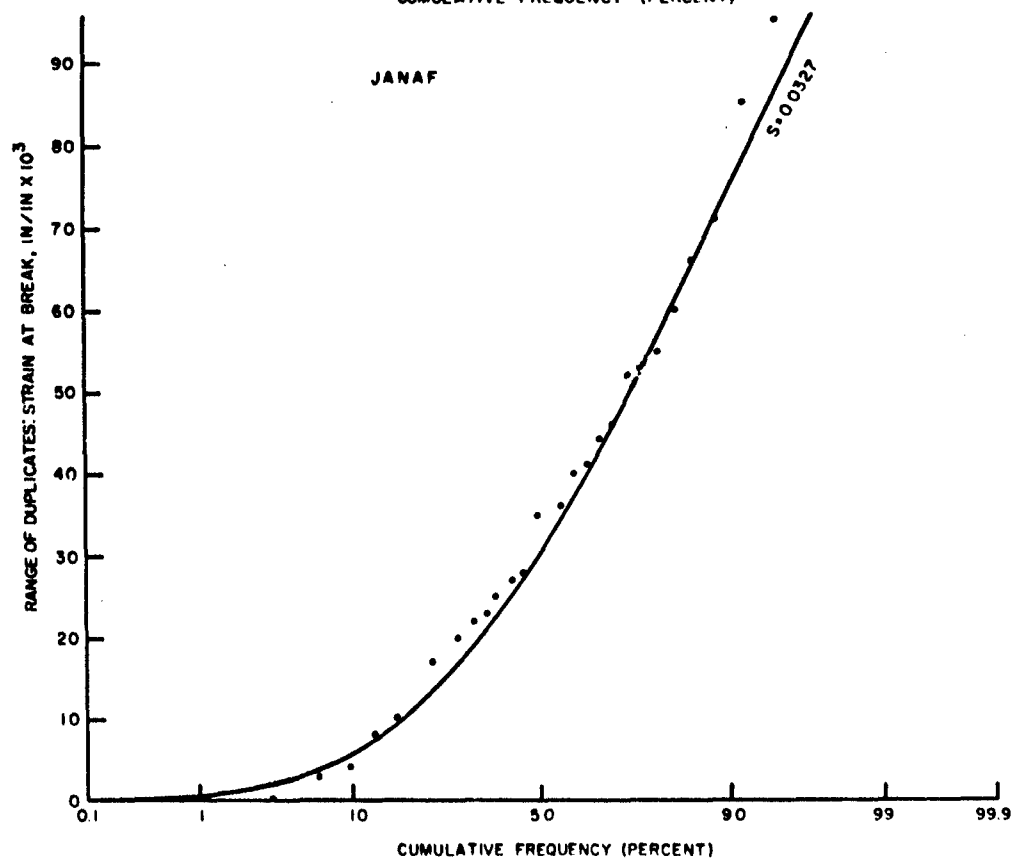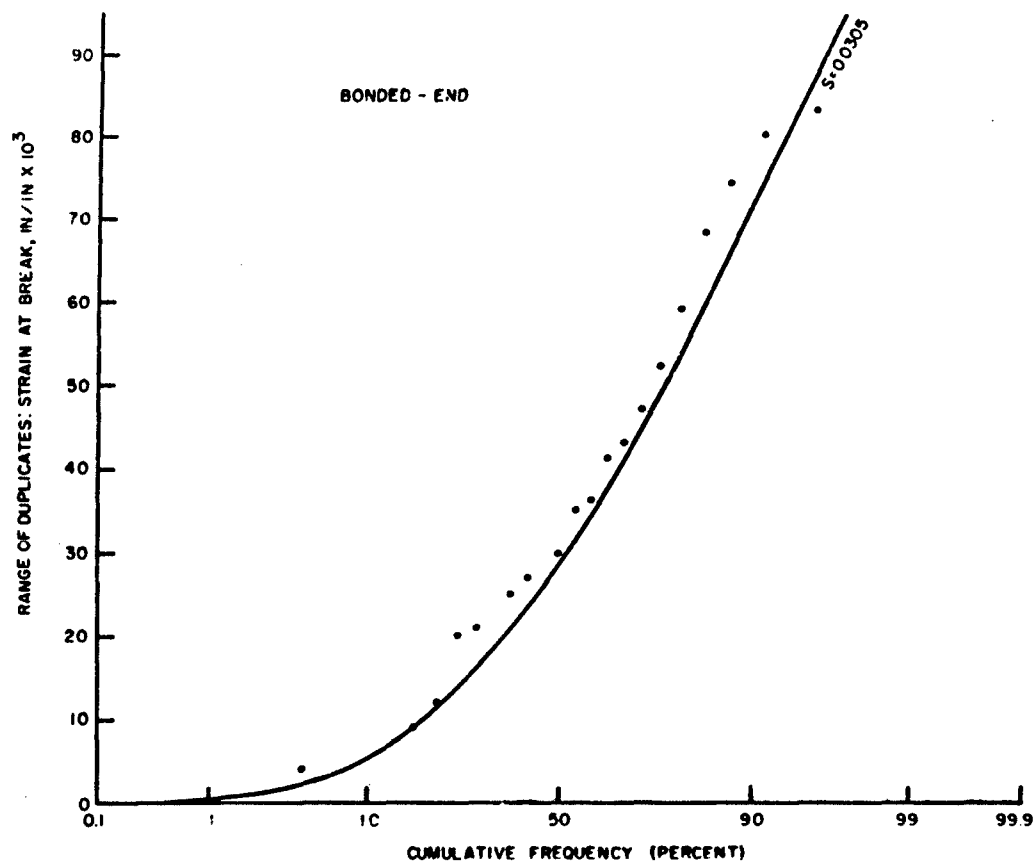
FIGURE 4. COMPARISON OF TENSILE SPECIMENS: STRAIN AT BREAK

CONCLUSIONS

The evidence presented here indicates that the bonded-end specimen yields tensile test data that are more realistic than those from the conventional dumbbell specimen. The end effects are slight, and the remainder of the specimen possesses a good degree of uniformity. From a test precision standpoint, the relatively unrefined bonded-end specimen studied here is equal to the routine JANAF specimen.

Future work will include the development of a suitable ambient cure, simplification and refinement of specimen fabricating, and investigation of cheap, disposable end-plate materials.

REFERENCES

1. Baldwin, J. B., and Cooper, M. H., Bulletin of the JANAF Physical Property and Surveillance Panels, PP-13/SPSP-8, p. 151 (1960).

2. Jones, J. W., Grand Central Rocket Co. Report No. P-0063-61, p. 8 (1961).

3. Yabuta, S., Rubber Chem. and Tech., 44, 342, (1961).

4. Youden, W. J., Ind. and Eng. Chem., 49, 79A (1957).

5. Hald, A., "Statistical Tables and Formulas," pp. 60-61, John Wiley and Sons, Inc., New York, 1952.

6. Williams, M. L., private communication.

THE DEVELOPMENT OF A SPECIMEN AND TEST METHOD TO PROVIDE ACCURATE UNIAXIAL TENSION MECHANICAL PROPERTIES*

By
John Southey Wise
Thiokol Chemical Corporation
Redstone Division
Huntsville, Alabama

ABSTRACT

This paper describes the course of a year's effort directed towards the development of a uniaxial tension test specimen, capable of providing physical property information suitable for use in engineering mechanical performance calculations. Details of the specimen, test method, and data reduction technique are presented.

INTRODUCTION AND BACKGROUND

Over the past several years, the Redstone Division of Thiokol Chemical Corporation has been working on advanced programs directed at resolving the outstanding problems of propellant mechanics. The work reported herein lies in the general area of propellant properties, and is primarily concerned with the development of a uniaxial test specimen which will provide property information suitable for engineering calculations. It has been generally thought for some years throughout the industry that the small dogbone specimens, particularly those having very short lengths of uniform cross-section, were inadequate insofar as their capability to yield uniaxial property data which could be reliably used in engineering mechanical performance calculations. With the increased demand for higher energy levels and the corresponding increase in solids content, the need for reliable property data has become acute. To meet this need, we have seen the trend from the very short length specimens, of the Thiokol type, to the JANAF specimen, then to benchmarked JANAF specimens with photographic strain measurements, and today development is proceeding on the small cross-section, end-bonded specimen and several other types such as to provide reliable uniaxial test information, suitable for engineering use at minimum time and cost.

The work covered in the present paper is spread over a one-year period extending up to the present time, and is concerned with the development of a uniaxial test specimen, test method, and data reduction technique,

to meet a set of quite well defined requirements. These requirements were as follows:

1. The strain field is to be macroscopically uniform, over a length of at least three inches, for all strain magnitudes up to and including fracture, over the temperature range of 160°F to -80°F, and at strain rates over the range .002 in/in/min. to 2 in/in/min.

2. Fracture will consistently occur in the region of uniform strain at all temperatures and strain rates of interest.

3. The cross-section area is to be sufficiently large that the microscopic defects and imperfections will not affect mechanical behavior. It is the intent to determine gross macroscopic behavior as contrasted with microscopic or sub-microscopic behavior.

4. The combination of specimen, experimental method, and data reduction technique, must be such as to provide uniaxial, constant or near constant strain rate, test data which will be suitable for engineering mechanical performance calculations.

It was reasonably well established at the outset that the primary problem areas were related to migration of material out of the jaws, high strain magnitude and sharp strain gradients in the region of the jaws, and the attainment of a uniform strain field. Furthermore, it was suspected that jaw flow could be minimized, but not eliminated. With these throughts in mind, a specimen was designed to investigate jaw flow. Inert propellant was used, and the specimens were marked with a cartesian grid in the region of the jaws. Through photographic means, the flow patterns were observed. On the basis of these tests, the necessary cross-section area and its variation in the region of the jaws was established. It was also observed from these tests that the satisfaction of the uniform strain field requirement at temperatures of 120°F and higher would require an excessively long specimen, due to increased migration through the jaws at such temperatures. This problem was resolved by incorporating what has come to be known as a "flow-reservoir". This device is in essence a "stopper" between the jaws and the length of uniform cross-section. It is designed to reduce jaw flow, to provide low strain levels in the region of the jaws, and to smooth the strain field in the region of the jaws. Several tests of this initial design, using inert propellant and liner formulations, were conducted at several strain rates at high and low temperatures. The strain field was observed to be essentially uniform, and fracture was consistently obtained within the region of uniform strain. Several minor safeguarding type modifications were made, and a tentative final design was established. The specimen resulting from these tests, which is in use at the present time, is shown in Figure 1 - this specimen is presently known as the "flow-reservoir" specimen.

EXPERIMENTAL PROCEDURE

The flow-reservoir specimens require considerable inspection and preparation prior to tensile testing. The specimens are X-ray inspected to insure that no voids, flaws, or other defects are present in critical regions. The specimen is then dimensionally inspected, with the cross-sectional area being determined by an average of caliper measurements taken at three stations located within the region of uniform cross-section. Acceptable specimens are then prepared for testing by inscribing inked benchmarks on the propellant surface. This operation is performed with extreme care. Fifteen benchmarks are inscribed in the length of uniform cross-section. This series of benchmarks consists of lateral dark lines arranged at regular intervals of approximately 1/4-inch. The areas between the dark lines are retouched with white coloring ink to produce the necessary contrast for the photographic records. The final preparation before testing is the bonding of the specimen ends to the test grips. The bonding technique reduces extrusion of the sample from the grips during testing and insures more uniform specimen contact with the grip surfaces. Extreme caution in the handling of the specimen is observed during all the inspection and preparation procedures such as to prevent damage to the specimen.

The specimen tensile tests are conducted on an Instron tester. As the grips are already bonded to the specimen ends, the specimen attachment to the Instron machine is accomplished by attaching the grips to the cross-head arms. One grip is attached initially to the top cross-head arm, and the tensile load of the deadweight specimen and remaining attachment grip is measured and recorded. The load indicator is then returned to zero, and the second grip is then attached to the lower cross-head arm, maintaining a zero load on the load indicator. A compressive load is then applied to the sample, which is one-half of the recorded deadweight tensile load. The compressive load is calculated to produce and maintain an essentially strain-free state in the specimen. At this point, a photograph of the specimen is taken to record this strain-free condition.

The test records consist of Instron load charts and photographic records. The Instron chart records a graph of load versus time. When the test begins, photographs of the specimen are taken for each approximate 5 per cent strain interval. In addition to the specimen, each photograph includes a vertical scale which provides a measurement of cross-head displacement and a clock which shows the time elapsed between photographs. Photographs are taken with a modified K-22 aerial camera, and the negative thereby produced is 9 in. x 9 in. in size.

DATA REDUCTION TECHNIQUE

The strain data are measured from the photographs taken with the modified K-22 aerial camera. The records consist of a sequence of photographs, beginning with the picture taken during the initial compressive loading technique and ending with the specimen failure. These photographs can be related to the test progression by either the time lapse or the cross-head displacement measurement.

Both axial and lateral strain measurements are possible by the photographic method. Axial strain is determined by the Fischer method, which consists of plotting the benchmark displacement versus the original or reference benchmark position. The slope of this plot determines axial strain. Lateral strain is determined in the same manner by using the average of specimen width displacements which are measured at five stations along the gage length. Additional plots of cross-head displacement versus time enables an accurate determination of the starting point for cross-head displacement, and correlates each photograph to the Instron load versus time chart.

At this point, it is now possible to calculate several valuable physical properties from the tensile test. Poisson's Ratio can now be determined from a plot of axial strain versus lateral strain. The instantaneous cross-section area can now be calculated, using the equation:

$$A = A_o (1 - \epsilon_1)^2$$

where:

A = instantaneous cross-section area (in^2)

A_o = initial cross-section area (in^2)

ϵ_1 = lateral strain (in/in)

The true stress can be determined by dividing the load by the corrected cross-sectional area. Volume dilatation can be calculated by the equation:

$$\frac{\Delta V}{V} = (1 - \epsilon_1)^2 (1 + \epsilon_3) - 1$$

where:

ϵ_1 = the lateral strain

ϵ_3 = the axial strain

RESULTS

Due to the necessity for brevity, a minimum of test results will be presented.

At this writing, constant strain rate tests, using the "flow-reservoir" specimen, have been conducted at several temperatures on two mixes of TP-H8041 propellant. Data reduction has not been completed on either mix; however, sufficient data are available to provide (1) impressions as to the smoothness and continuity of the results, and (2) a comparison with routine Thiokol and JANAF data. Figures 2, 3, and 4 show plots of modulus, maximum stress, and strain at fracture as functions of temperature for the three types of specimens. From these plots, the following may be observed:

1. The modulus as determined from the flow-reservoir specimen appears to be consistently higher than with the routine Thiokol and JANAF specimen.

2. Maximum stress as determined from the flow-reservoir specimen appears to be lower than either routine Thiokol or JANAF at temperatures above -40°F. At temperatures below -40°F, maximum stress with the flow-reservoir specimen appears to increase rapidly.

3. There appear to be strong qualitative and quantitative differences in strain at fracture data derived from the three types of specimens.

4. There is insufficient data to provide evidence of the test-to-test variation in properties at constant temperature and strain rate, as determined by the flow-reservoir specimen.

Stress, strain curves in the temperature parameter are shown in Figure 5. These curves serve to give some impression of the precision of the experimental data. The data is smooth and the trends are as expected. It is of interest to note the relatively small variation in strain at maximum true stress over the temperature range 140°F to -50°F.

Stress, strain curves for Thiokol, JANAF, and flow-reservoir specimens at 135°F, 77°F, and -40°F are shown in Figures 6, 7, and 8. The strong qualitative and quantitative differences, in data yielded by the three different types of specimens, is obvious.

Curves of volume dilatation versus axial strain are shown in Figures 9 and 10. These curves are extremely interesting in that they serve to shed light on a question that has been discussed at considerable length throughout the industry for several years - namely, the problem of volume change per unit volume in uniaxial tension. These volume dilatation data imply that for at least one solid propellant, the hypothesis of incompressibility in uniaxial tension is totally invalid. Furthermore, these findings support earlier work by Bills and Sweeney at Aerojet General in which it was implied that the dilatational characteristics were quite strongly

dependent on the stress, strain state.

DISCUSSION

The first year's effort on this program has seen the development of a
specimen, an experimental method, and a data reduction technique. These
three items have been used in several experiments on a typical Thiokol HA
solid propellant. The experiments which have been conducted to date
(approximately 40) strongly imply that the first three of the four previously
stated requirements have been met, i.e:

1. The strain field has been shown to be macroscopically uniform
   over the temperature range 140°F to -50°F.

2. In all tests conducted thus far (approximately 40 tests), fracture
   has occurred within the region of uniform strain and constant
   cross-section - moreover, the fractures have occurred within
   a 3-1/2" length within this region.

3. In all tests conducted to date, there has been no evidence of
   small defects or imperfections leading to premature fracture,
   or adversely affecting test results.

There is insufficient evidence at this time to provide implications as
to whether the fourth requirement is or is not satisfied. It is felt that the
satisfaction or non-satisfaction of this requirement will be established when
a number of tests at constant strain rate, and constant temperature, are
conducted at several temperatures. Such experiments will provide evi-
dence of consistency and repeatability.

There is one point of interest that may be gleaned from the present
results, and which possibly should be enlarged upon at this time. As
pointed out in the Discussion, there are gross differences in the three
types of data presented in Figures 6, 7, and 8. These data supposedly
represent stress, strain curves in uniaxial tension of TP-H8041 at several
temperatures. Supposedly, the stress, strain response in uniaxial tension
should represent a unique material property. These data clearly imply
that the response in uniaxial tension is other than unique. Based on these
results, we must admit that either the response is not unique, or the
response is strongly dependent on the type of specimen and test procedure.
At this time, I put forth the hypothesis that the response in uniaxial tension
is unique, provided a reasonable test specimen is used, reasonable test
conditions are satisfied, and reasonable laboratory test procedures are
adhered to. It is quite reasonable to consider the possibility that the
uniaxial test specimens and procedures which have been used throughout
the industry for the past ten years are totally incapable of providing
information which is representative of these materials in uniaxial tension

under uniform strain field conditions. Work at the Redstone Division, over the past eighteen months, has demonstrated, beyond reasonable doubt, that the strain field in Thiokol and JANAF specimens, over broad ranges of temperature, for typical composite solid propellants is in general macroscopically non-uniform. It has also been shown that the so-called "gage length", as used in calculating the strain for Thiokol and JANAF specimens, is a function of at least propellant, strain magnitude, and temperature. These findings should serve to raise serious questions as to the applicability of non-uniform strain field, uniaxial test data, in mechanical performance calculations.

In the course of our work during the past year, it has become increasingly obvious that two very real sources of difficulty in the area of physical properties are:

1. Crude experimental methods.

2. Crude data reduction methods.

Although the techniques used in the course of the present work are quite refined by some standards, they leave much to be desired in several respects - namely:

1. Temperature control.

2. Strain determination.

3. Time correlation.

During our further work on the development of this specimen, we shall study these three facets of the problem and attempt to demonstrate satisfaction of the fourth requirement. It is also planned, during the coming year, to investigate the various aspects of converting these experiments to routine test procedures.

The work thus far with the flow-reservoir specimen has been extremely encouraging. The completion of the successful development of this specimen will provide an extremely powerful tool in the following respects:

1. Those individuals working in the areas of mechanical performance and structural integrity will be able to obtain experimental data which they can have confidence in, which will be meaningful, and which will be subject to interpretation, correlation, and comparison.

2. Mechanical performance studies can be conducted wherein the effects of size and location of defects can be realistically

evaluated.

3. Studies can be conducted wherein both the qualitative and quantitative effects of storage time and temperature on mechanical performance can be realistically evaluated.

4. The qualitative and quantitative effects of humidity, radiation, and other environmental conditions can be determined with sufficient precision such as to permit engineering interpretation and meaningful use of test data in mechanical performance calculations.

5. The precise determination of endurance and recovery properties in uniaxial tension.

6. The fundamental aspects of the gross, macroscopic mechanics of solid propellants can be intelligently and meaningfully investigated.

These are but a few of the many possibilities that come within reach when we have the capability to measure and determine true mechanical properties. From this standpoint, the development of a specimen to provide such information will truly be an asset to the industry and a step forward for solid propellant rocket technology. From the standpoint of realism or essentiality, let it suffice to say that the industry has today, and has had in the past, its share of problems related to mechanical performance of propellant - there is little reason to suspect that the number or magnitude of these problems will decrease as we move into the era of big boosters using increased energy content propellants.

CONCLUSIONS

It would be inappropriate and premature to attempt to draw conclusions, at this time, as to the relative goodness, badness, validity, invalidity, or the applicability of the "flow-reservoir" specimen as a medium for developmental physical properties determination or as a possible medium for routine physical properties. The results to date are highly encouraging insofar as the use of this specimen in developmental, laboratory type, experiments are concerned. The work during the coming year will serve to point the way towards adaptation to routine testing, providing such adaptation is reasonable.

Several technical conclusions, based on test results, may be firmly drawn:

1. The strain field in this specimen, over approximately 4-1/2" of the length of uniform cross-section, is macroscopically uniform for strains up to 45% for a typical Thiokol HA propellant.

3. The experimental results consistently invalidate the hypothesis of zero dilatation in uniaxial tension.

SUMMARY

The "flow-reservoir" specimen has passed the first stage of developmental testing. In tests conducted to date, using a typical Thiokol HA propellant, this specimen has demonstrated its capability to provide a highly uniform strain field and to consistently fracture within this uniform strain field. The results of approximately forty tests are encouraging and imply that this specimen will be an extremely important tool for the industry in advanced work in mechanical properties testing.

ACKNOWLEDGEMENT

FIGURE 1. FLOW RESERVOIR SPECIMEN

Modulus versus Temperature
Propellant Type TP-H8041
Mix No. K-266
Binder/Curing Agent Ratio - 88.2/11.8
52.5% Ground

Flow-Reservoir Specimen

JANAF Routine Specimen

Thiokol Routine Specimen

Temperature, °F

Modulus, psi ÷ 1000

FIGURE 2.

FIGURE 3.

Strain at Fracture versus Temperature
Propellant Type TP-H8041

Mix No. K-266
Binder/Curing Agent Ratio- 88.2/11.8
52.5 % Ground

Thiokol Routine Specimen

JANAF Routine Specimen

Flow-Reservoir Specimen

Temperature, °F

Strain at Fracture, in./in.

FIGURE 4.

True Stress versus Axial Strain
Flow Reservoir Specimen
Photo-Uniform Strain Field
Average Initial Strain Rate: .285 in/in/min
Propellant Type TP-H8041
Mix No. K-266
Binder/Curing Agent Ratio- 88.2/11.8
52.5% Ground

FIGURE 5.

FIGURE 6.

Stress versus Axial Strain
Propellant Type TP-H8041
Mix No. K-266
Test Temperature: +135°F
Binder/Curing Agent Ratio - 88.2/11.8
52.5% Ground

Flow-Reservoir Specimen
JANAF Routine Specimen
Thiokol Routine Specimen

Axial Strain, in./in.

Stress, psi

Stress versus Axial Strain
Propellant Type TP-H8041
Mix No. K-266
Test Temperature: + 77°F
Binder/Curing Agent Ratio – 88.2/11.8
52.5% Ground

Flow-Reservoir Specimen

JANAF Routine Specimen

Thiokol Routine Specimen

Axial Strain, in/in

Stress, psi

FIGURE 7.

Stress versus Axial Strain
Propellant Type TP-H8041
Mix No. K-266
Test Temperature: -40 °F
Binder/Curing Agent Ratio-88.2/
11.8
52.5% Ground

Thiokol Specimen

Flow-
Reservoir Specimen

JANAF Routine Specimen

Axial Strain, in/in

Stress, psi

FIGURE 8.

Volume Dilation versus Axial Strain
Flow-Reservoir Specimen
Photo-Uniform Strain Field
Initial Strain Rate: .252 in/in/min.
Propellant Type TP-H8041
Mix No. K-266

Test Temperature: +140°F
Binder/Curing Agent Ratio- 88.2/11.8
52.5% Ground

Volume Dilation, in.³/in.³

Axial Strain, in./in.

FIGURE 9.

Volume Dilation versus Axial Strain
Flow-Reservoir Specimen
Photo-Uniform Strain Field
Initial Strain Rate: 0.355 in/in/min.
Propellant Type TP-H8041
Mix No. K-265
Test Temperature: -40°F
Binder/Curing Agent Ratio—88.2/11.8
52.5% Ground

Axial Strain in./in.

Volume Dilation, in³/in³
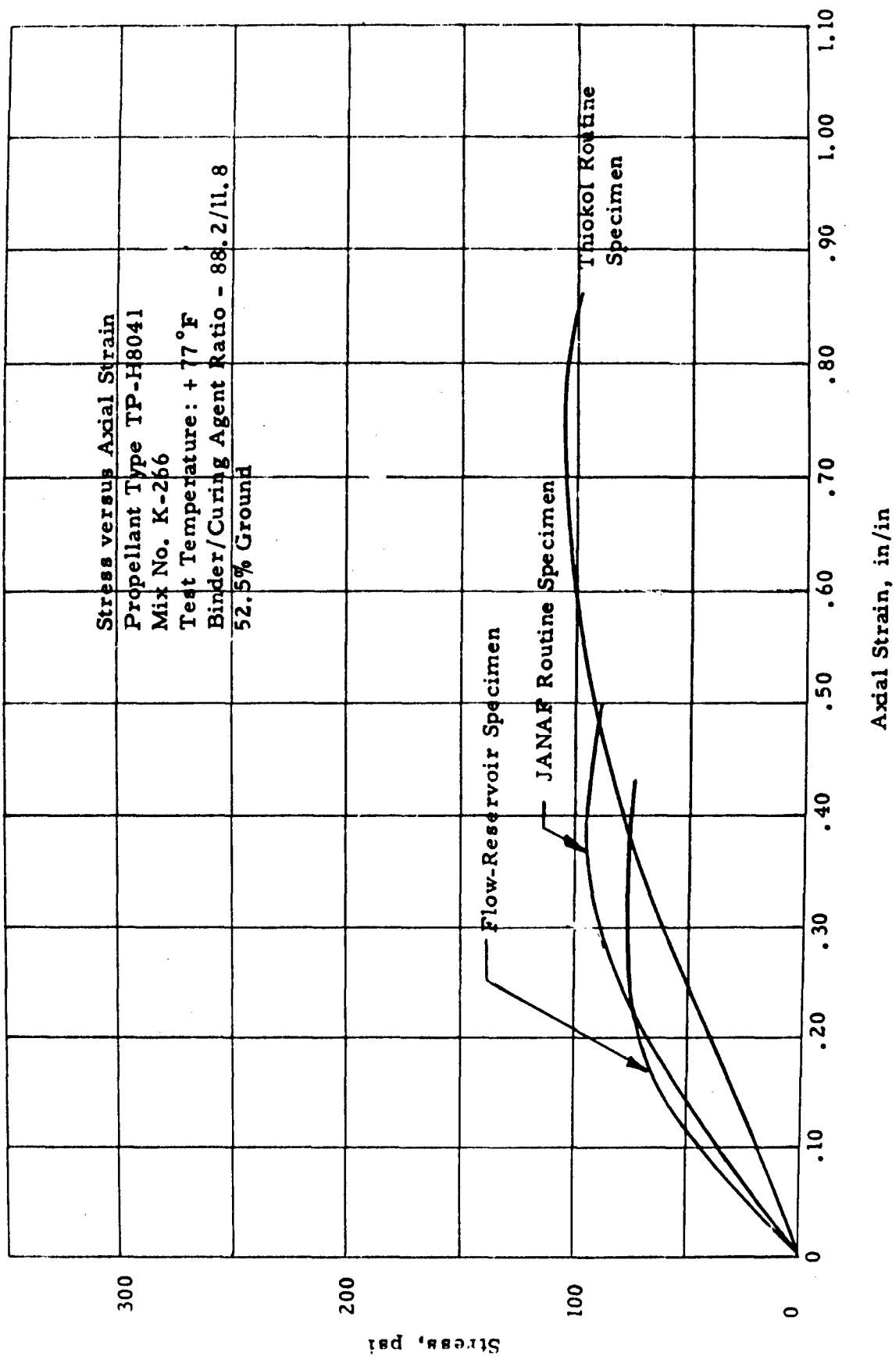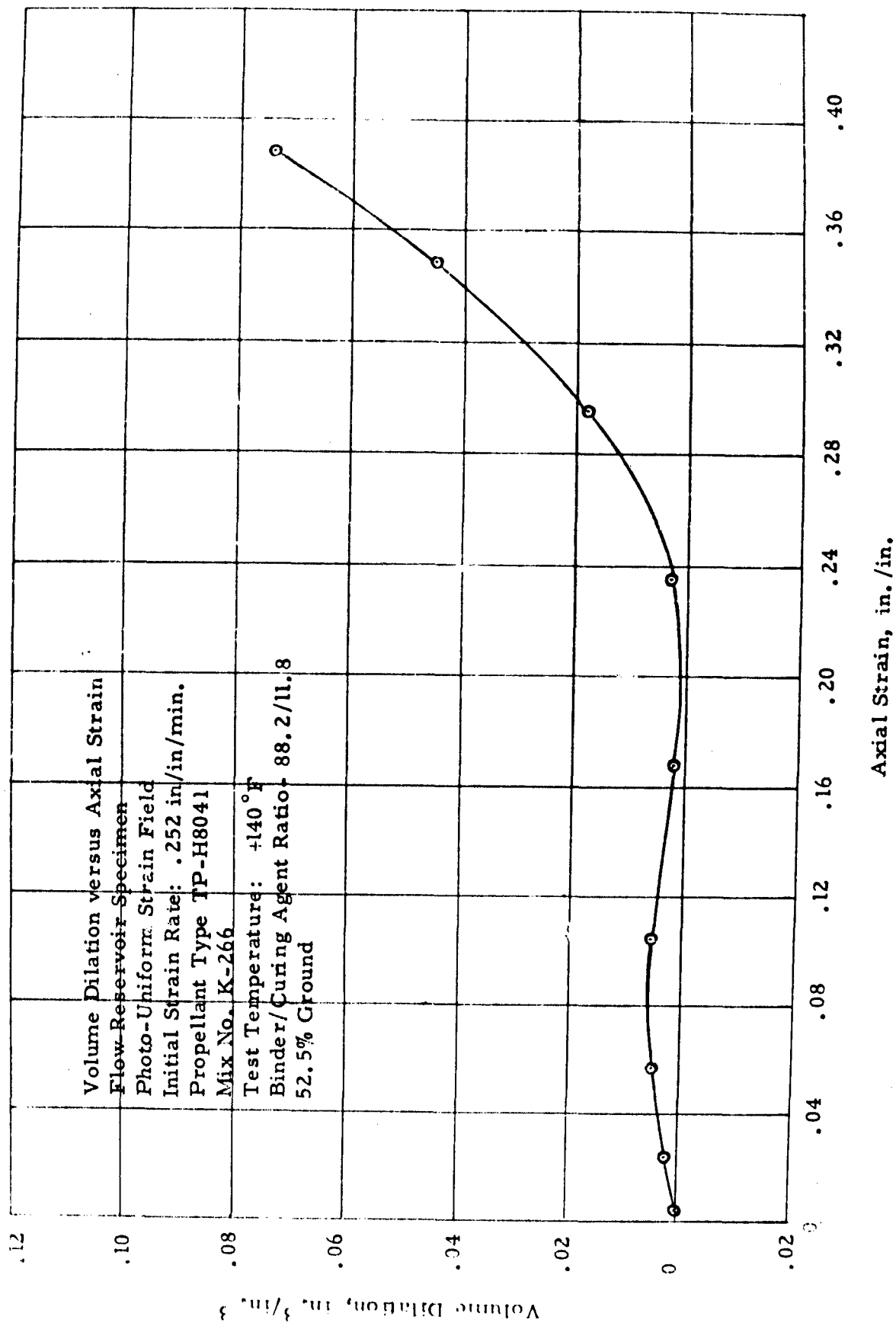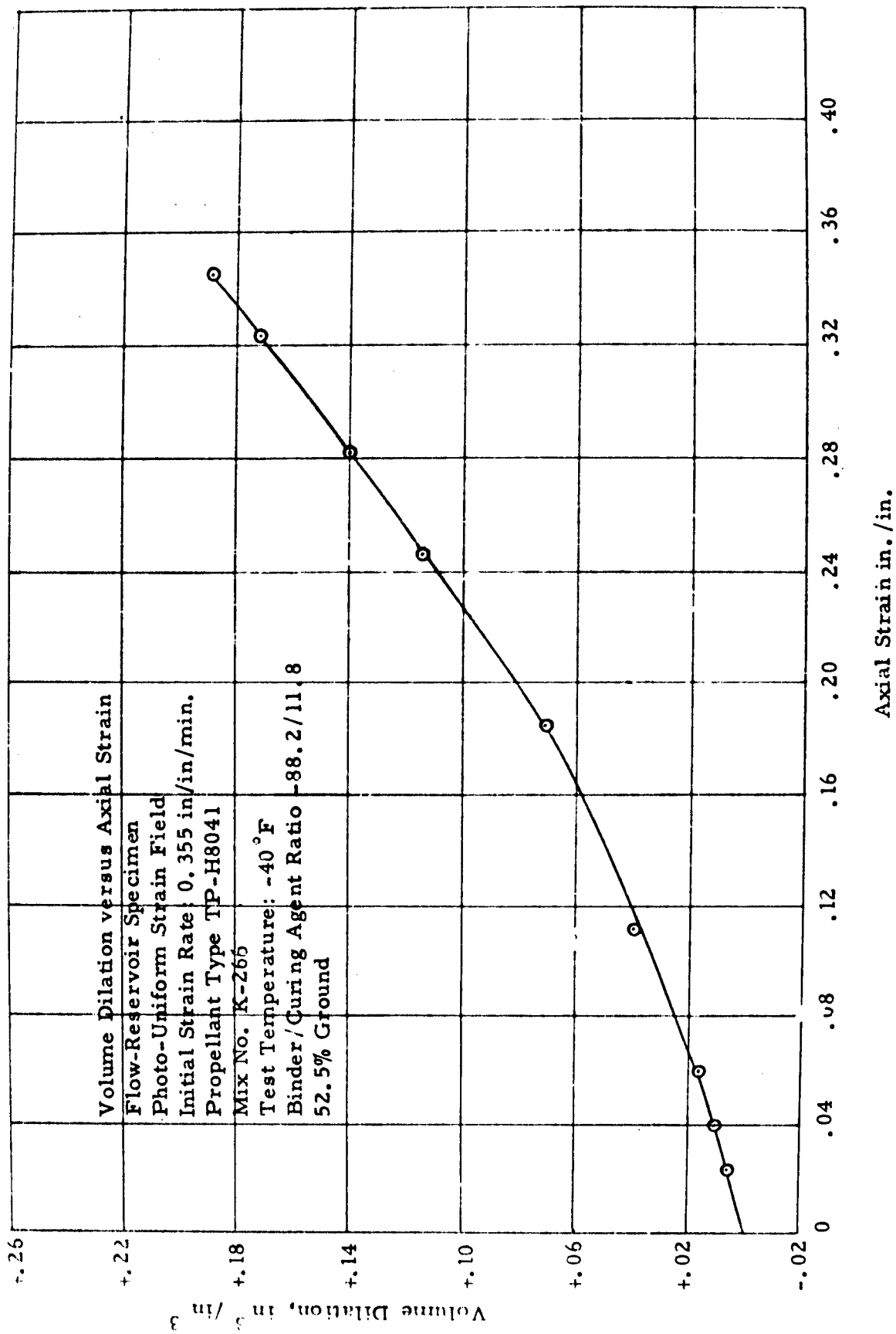
FIGURE 10.

JANAF TENSILE TEST SPECIMEN PREPARATION AND EVALUATION

R. J. Farris, H. P. Briar, F. H. Davidson, R. D. Steele

Aerojet-General Corporation

ABSTRACT

A method of precision machining of JANAF tensile test specimens has been developed using a vacuum holding fixture to retain a slab of propellant in place while a fly cutter produces the desired shape, and the gang slitting produces a group of up to 10 test specimens from this shaped slab.

Small spring clip strain gauges were used to compare the true strain with normally recorded crosshead strain on both milled and standard die cut tensile test specimens. The milled specimens showed a considerable improvement out to 30% strain levels.

Comparisons on the test variability of both milled and die cut tensile test specimens showed a reduced variability in the normally recorded stress values due probably to better precision in determining the width and thickness of the test specimens. The precision with which machined test specimens can be produced suggests that there would be no need for individual width and thickness measurements and that the testing machines could eventually record directly in PSI.

INTRODUCTION

There is need for improvement in the design and production of JANAF propellant tensile test specimens. The validity and accuracy of propellant tensile, stress relaxation, and creep test data are greatly enhanced when the test specimens are uniform.

A widely used method of sample preparation for the JANAF tensile sample involves band sawing slabs of propellant 1/2" in thickness and die cutting flat dumbbell bars from the slabs. This is a fast and simple method of sample preparation, but yields undesirable effects, such as: non-parallel faces in the gauge section with a trapezoidal cross section; the sample is subjected to compressive stresses while being die cut, and both the die cut surface and the bandsawed surface are rough and scarred as if torn rather than cut; the trapezoidal shape of the die cut specimen is difficult to measure with a variation below 3 to 5%; the shoulders of the specimen are not parallel and present seating problems, requiring time-consuming correction during data reduction, and the samples tend to bend in the fixtures introducing non-linearity in strain rate and producing a strain gradient across the specimen.

Low modulus values, poor strain readings, premature failure, and high variances are all effects observed with die cut specimens. For example, the initial portion of the stress-time curve appears linear with die cut samples, due to the non-linear strain rate. The increasing strain rate results in an increase in the force levels and produces a non-linear strain distribution

along the time axis of the curve. This effect can be greatly reduced with highly uniform JANAF specimens and it can be completely eliminated with end-bonded specimens or pressure gripped specimens such as the Stanford Research Institute rectangular specimen.

PRECISION MILL CUT SPECIMENS

Some of the advantages which will accrue to precision machined JANAF tensile specimens are; direct calibration of the testing machines in terms of PSI, since the sample size precision attainable should eliminate the need for individual width and thickness measurements; more accurate initial modulus data and improved strain measurements from the improved seating of the sample in the holding fixtures; and finally, less influence on the failure properties due to surface irregularities.

At Aerojet-General's Physical and Mechanical Properties Laboratory, techniques have been developed for production milling of precision JANAF tensile specimens.

A vacuum chuck was finally decided upon as the holding fixture. This appears the best system for precision milling since a slab of propellant being held down by one atmosphere of pressure would only be distorted about 1×10^{-5} inches per inch in height. A fixture shown on a vertical mill in Figures 1, 2, and 3 was designed and built to accomodate a band sawed slab on one side for the first milling operation (Figure 2) and with a fillet on the other side to accomodate the half milled slab for the second milling operation (Figure 3). A piece of aluminum plate was ported, relieved, valved, and manifolded such that any or all of the six sets of ports could be used at one time. A thin rubber liner was bonded to the face of the fixture. Blocks of the liner were cut away over each port and a screen the same thickness as the rubber was bonded in its place. The screen was of a type that allowed good horizontal as well as vertical flow of air. The screen serves two functions. It allows its total area to act as a chuck and yet gives support to the propellant. This results in high friction between the propellant-fixture interface preventing the propellant from moving.

The cutting tool for the JANAF specimen on a vertical mill is quite simple. It is designed with the half inch radius and an extended cutting arm to reduce the slab thickness to one inch and assure the proper depth of cut in the gauge section. Simple fly cutters such as these easily exhaust the cutting chips but do so in all directions, requiring a hood with high vacuum cleaning capacities. Mandril speeds from 1200 to 2000 RPM and feed rates 2 to 10 inches/minute function excellently. The vertical mill is probably preferred in this type of operation because the contact surface of the tool to the propellant can be minimized to about one inch.

The milling tool for a horizontal mill is a more complex and expensive tool. It is best made up of three pieces, a gauge profiler with a tab reducer on each side. Chip removal is the biggest problem with this type of tool and because of this a 4 bladed helical flute cutter was chosen. The advantages of a horizontal mill would be that the chip removal would all be in the same direction and evacuation would be quite simple. This type of tool would however have about 30 times as much contact with the propellant

presenting the possibility of safety hazard. Shown below is a simple profile cutter for a horizontal mill.

Horizontal Mill Tool
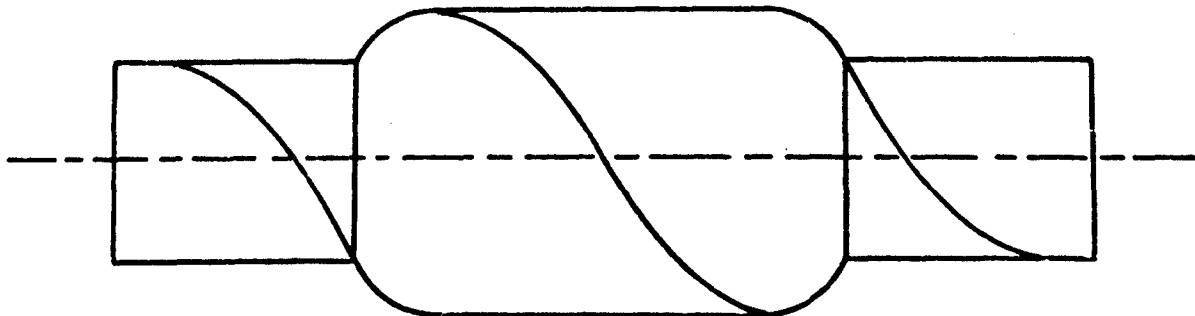
The gang slitting operation takes place on a horizontal mill. The mandril has 13 standard 5 inch carbide tipped slitting saws spaced 0.500" apart. A special fixture was made to hold the milled slab while the slitting operation took place. Mandril speeds of 150 to 500 RPMs function excellently.

All of these milling operations are performed remotely without the aid of coolants.

The milling operation is extremely simple. It requires that the milling tool be centered over the fillet and adjusted for the proper depth of cut. Both of these adjustments are then locked in place and the operation then consists of putting slabs on and turning them over.

STRAIN EVALUATION

A recent innovation which is becoming quite useful in the study of propellant tensile strains is the spring clip strain gauge. This type of strain gauge was introduced by C. C. Surland and T. Smith as a method for measuring axial and lateral strains on tensile specimens.

The gauge (Figure 4) consists of an 0.5 inch wide strip of 0.002 inch feeler gauge stock bent into a half circle of approximately 0.5 inch radius. Strain gauges are glued two on the inside and two on the outside of the curve of the clip to form the standard strain gauge bridge configuration of two gauges in compression and two in tension. The clip is designed so that the tips of the gauge will spring outwards from its centerline in order to follow the motion of a stretching specimen. When not in use the gauge is restrained by a safety clip and is also provided with a limiting wire to prevent overstraining.

In use the gauge was wired into a four prong plug and plugged directly into an Instron load cell plug. The Instron recorder was thus utilized to make extension recordings. Any other strain gauge or load cell measuring system might also be used.

The gauge is applied to the standard JANAF tensile specimen by gluing two small plastic blocks about 1 inch apart on the strain portion.

The gauge held its position by friction against the blocks (Figure 5).

To further illustrate the improvement in tensile properties attained with milled tensile specimens, stress and elongation tests were performed with the gauge mounted on both milled specimens and die cut specimens. Since the dimensions of a die cut bar are variable side to side, several tests were run with the gauge first mounted on the narrow side and several more with it mounted on the wide side. Initial gauge length was taken from the clip gauge reading at the start of the test. The data shown in Figures 6 and 7 was then plotted as true sample elongation from the clip gauge versus Instron chart time. The samples tested were standard JANAF propellant tensile specimens at $77°F$ and 2 inches/minute. The straight line at 0.74 min^{-1} represents the strain rate that should be observed with no error and a 2.7 inch effective gauge length.

Propellant tests are quite sensitive to strain rate, thus any deviation from the 0.74 min^{-1} line indicates a possible source of error. Figure 7 shows a marked difference in behavior depending on whether the wide or narrow side of a stamped bar is measured. The data suggest that no two parts of the tensile specimen are being strained at the same rate, and that photographic strain measurement on any sample other than a carefully prepared symmetrical sample would have a large inherent error.

The results of the milled bar strain measurements are somewhat improved out to about 30% strain. However, even here the results are not perfect. After 30% strain the results begin departing rapidly from a constant strain rate test. The propellant bars tested above have a nominal maximum stress of about 120 PSI and a strain at maximum stress of about 44%.

MILLED BARS VERSUS DIE CUT BARS

The original data obtained in a careful comparison of milled samples versus the standard die cut JANAF tensile specimens showed an improvement in the variability of nominal maximum tensile, S_{nm}, no change in the variability of strain at maximum stress, γ_m, and an improvement in the variability of the modulus, E. A further check of the variability was made on 5 lots of propellant just after the milling procedure was initiated as a routine procedure. The initial results were verified; however it would seem that a year later the stamping procedures were producing more uniform results.

The original results are tabulated below.

VARIANCE VALUES

	S_{nm}	γ_m	E	N
Stamped	50	3.3	5600	40
Stamped	65	2.1	18000	4
Milled	15	2.8	2200	10

The results of a check on 5 batches 1 year later, 4 tests/batch milled, 4 tests/batch die cut are tabulated below.

VARIANCE VALUES

	S_{nm}	Y_m	E	N
Between Batches	291	154	164000	5
Within Stamped Replicates	35	3.1	8860	20
Within Milled Replicates	16	3.2	1330	20

Variability of the quality of the milling operation is easily maintained within very tight limits. Of over 200 specimens prepared in succession, the sample width varied 0.6% from 0.375". Similar data illustrates the quality of the gang slitting operation.

S_{nm} = Nominal Maximum Stress

Y_m = Strain at S_{nm}

E = Initial Modulus

$$\text{Variance} = \frac{\sum_{i=1}^{n} (X_i - \bar{X})^2}{n - 1}$$

CONCLUSION

Advantages in the form of improved tensile test data have been shown for precision machined JANAF test specimens. Milling procedures with at least the same production efficiency and cost as the standard die cutting procedures have been developed. Improvements in the test data are in the form of reduced variability in the stress values observed on stress-strain curves due to improved accuracy in cross sectional area measurements, and in closer approximation of the initial portion of the true stress-strain curve through improved sample seating.
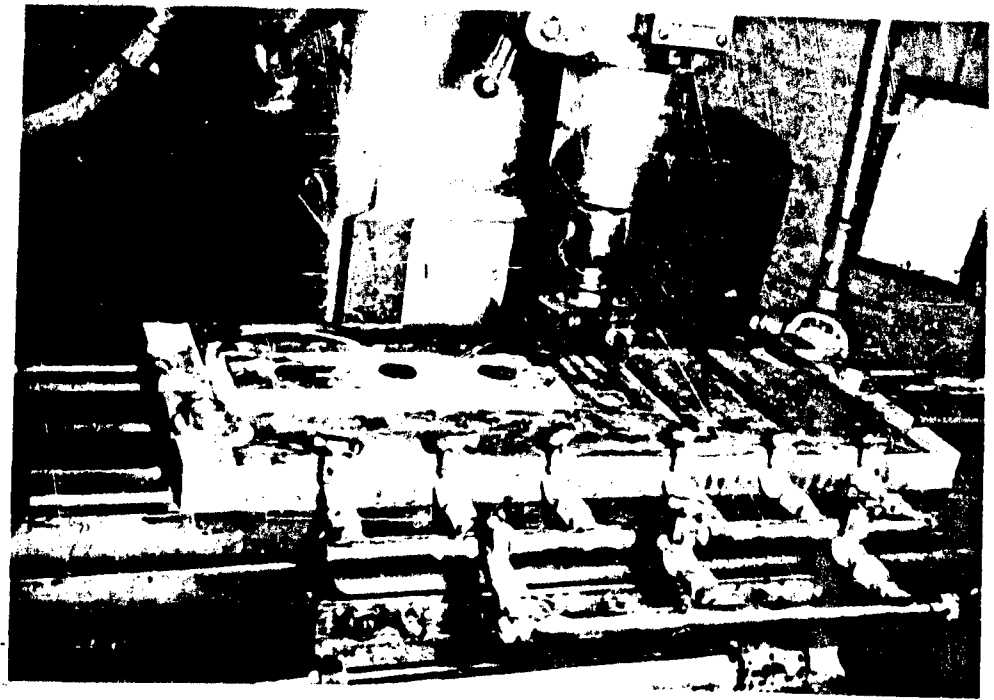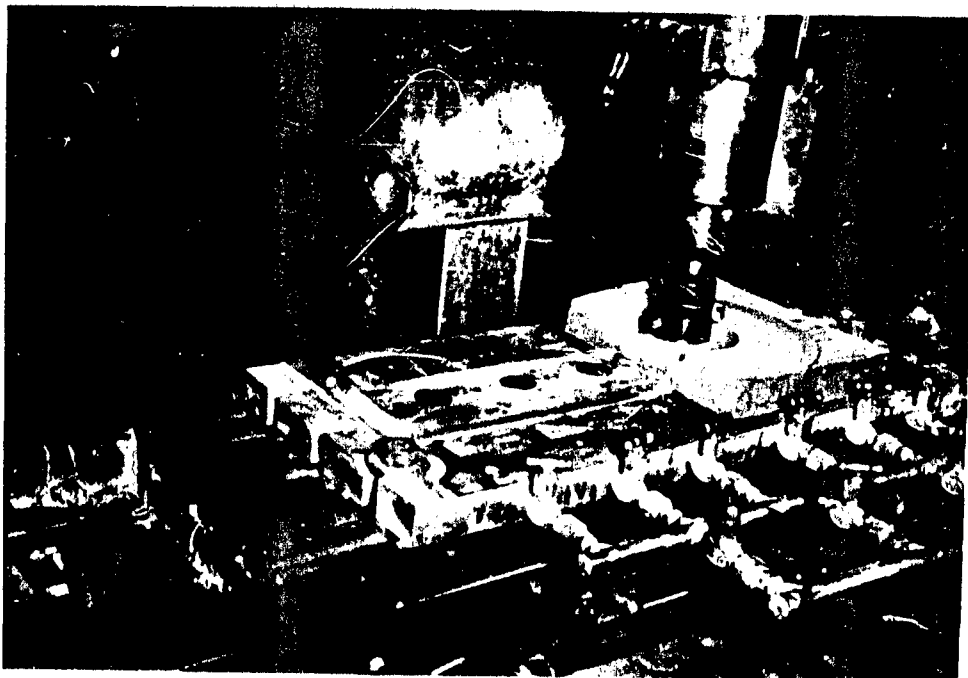
FIGURE 1. VACUUM HOLDING FIXTURE
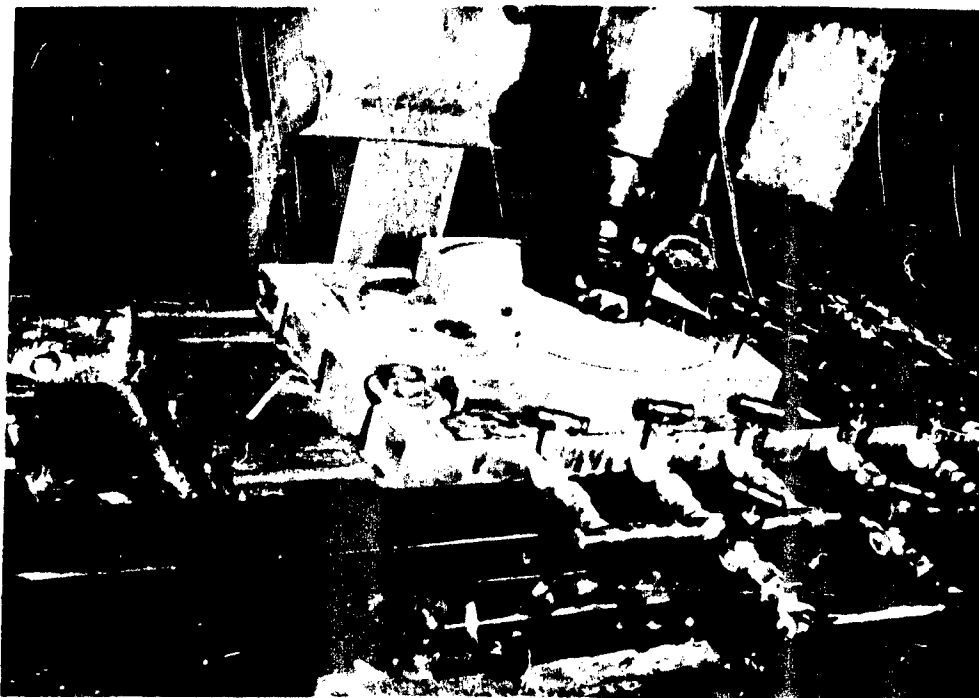

FIGURE 2. FIRST PROFILING OPERATION

FIGURE 3.   SECOND PROFILING OPERATION

FIGURE 4.
SPRING CLIP STRAIN GAUGE

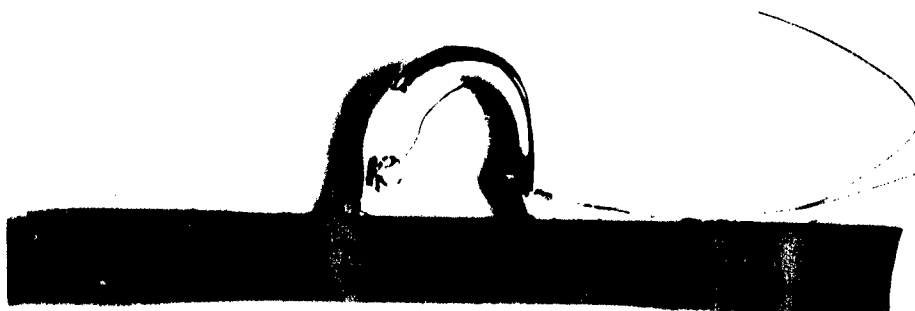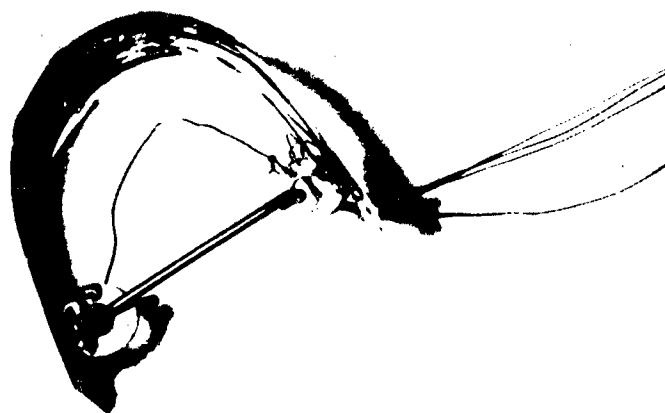FIGURE 5.   SPRING CLIP STRAIN GAUGE MOUNTED
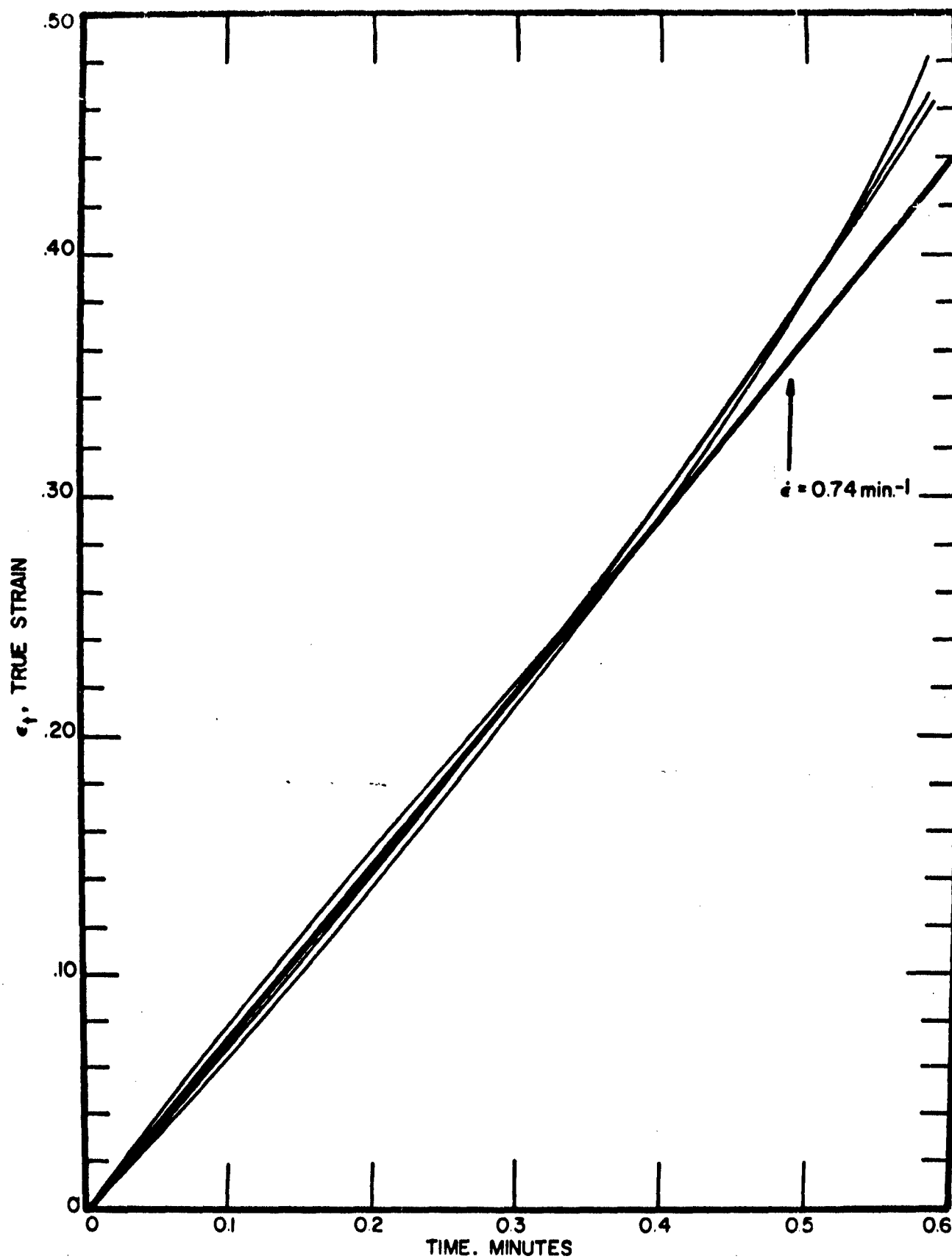   ON JANAF DUMBELL SPECIMEN

FIGURE 6.   TRUE STRAIN VS TIME FOR MILLED JANAF SAMPLES
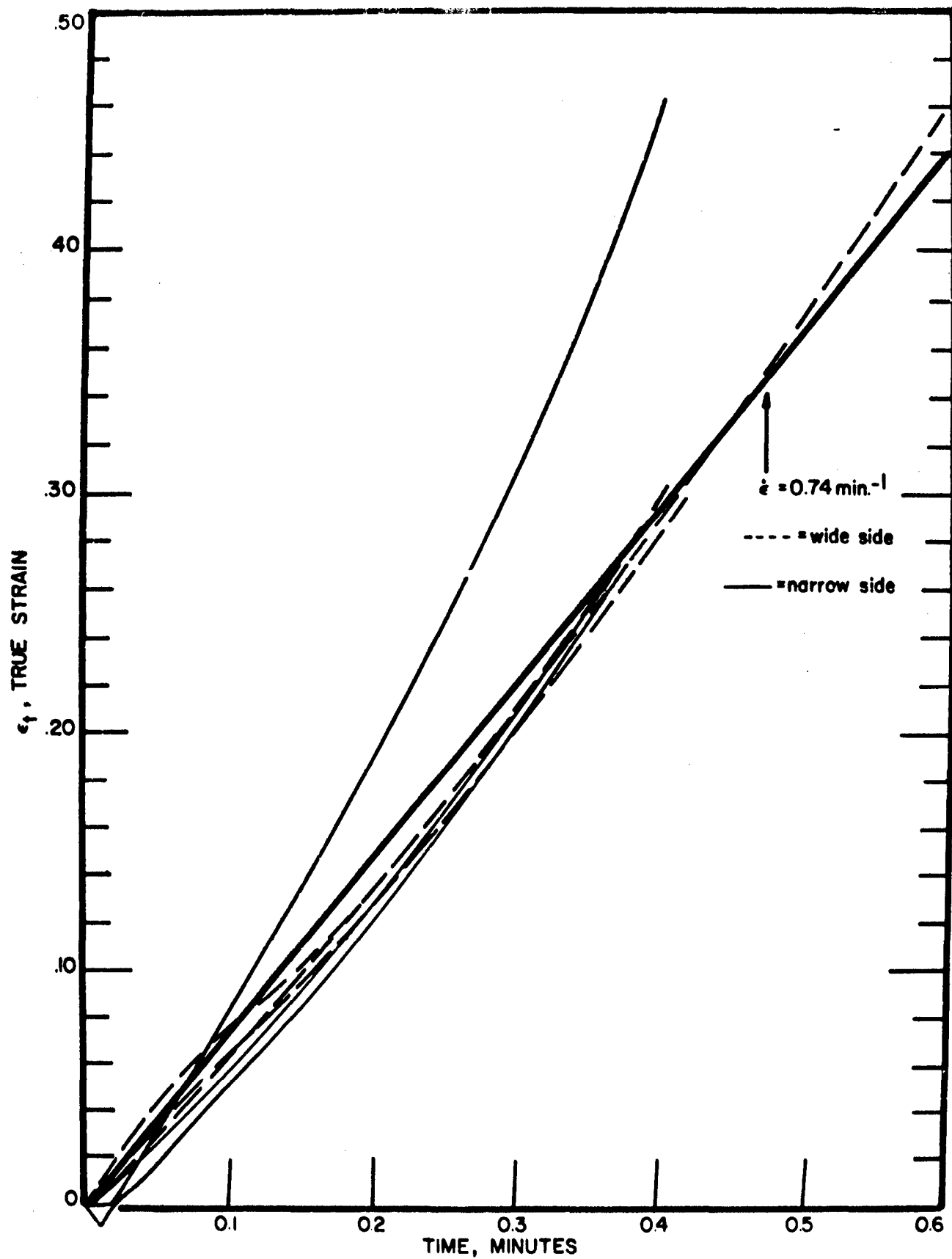
FIGURE 7. TRUE STRAIN VS TIME FOR DIE CUT JANAF SAMPLES

The figure shows a plot of ϵ_t, TRUE STRAIN (vertical axis, from 0 to .50) versus TIME, MINUTES (horizontal axis, from 0 to 0.6). Legend: $\dot{\epsilon} = 0.74\ min.^{-1}$; - - - - = wide side; —— = narrow side.

A METHOD OF STRAIN GAGE DATA REDUCTION
FOR LOW MODULUS MATERIALS (1)

R. E. Sennett III[2] and S. Shore[3]
Dyna/Structures, Inc.
Springfield, Pennsylvania

ABSTRACT

This investigation was undertaken to develop a method of calculating strains in a low-modulus material from data obtained with high modulus strain gages. The presence of a high modulus strain gage on the surface of a low modulus material (e.g., solid propellant) leads to the distortion of the strain field in the vicinity of the gage. Therefore, the fundamental objective of this report is to predict the value of the strain in the low modulus material in the gage area from the response of the strain gage. A solution to the problem was obtained by simulating the actual physical conditions with an idealized condition of an elastic inclusion in an elastic thin plate, with each material having different material properties.

The solution was obtained in two steps:

(1) The problem of the stress-distribution on the boundary of a rigid inclusion was solved.

(2) The stress-distribution from (1) was then imposed on the elastic inclusion and the stress-distribution in this body was obtained.

This method was found to compare favorably with the solution of an elastic inclusion in an elastic plate for a low-modulus plate. (See Appendix.)

From this solution, correlation between strain in the inclusion (gage) and strain in the surrounding material was obtained.

ANALYSIS

We first determine the stress-distribution around a small circular rigid inclusion of radius "b" contained in a large rectangular plate under uniform axial stress σ_x. (See Figure 1a.)

Since the inclusion is small, we assume that the stress-distribution on a circle of radius "a" inscribed in the plate is unaffected by the inclusion. Plane strain is also assumed.

Transforming the uniform stress-distribution to the boundary of the circle of radius "a," we obtain:

$$\sigma_r(a) = \frac{\sigma_x}{2} (1 + \cos 2\theta) \tag{1}$$

$$\sigma_{r\theta}(a) = -\frac{\sigma_x}{2} \sin 2\theta \tag{2}$$

(1) and (2), along with the conditions that u, the radial displacement, and v, the tangential displacement, are zero at r = b (inclusion is welded to the plate), form our set of boundary conditions. (See Figure 1b.)

From the strain-displacement and stress-strain relationships expressed in polar coordinates, we obtain the following stress-displacement equations:

$$\sigma_r = \frac{E}{(1-2\nu)(1+\nu)} \left[\nu\left(\frac{1}{r}\frac{\partial v}{\partial \theta} + \frac{u}{r}\right) + (1-\nu)\frac{\partial u}{\partial r} \right] \tag{3}$$

$$\sigma_\theta = \frac{E}{(1-2\nu)(1+\nu)} \left[\nu\frac{\partial u}{\partial r} + (1-\nu)\left(\frac{1}{r}\frac{\partial v}{\partial \theta} + \frac{u}{r}\right) \right] \tag{4}$$

$$\sigma_{r\theta} = \frac{E}{2(1+\nu)} \left[\frac{1}{r}\frac{\partial u}{\partial \theta} + \frac{\partial v}{\partial r} - \frac{v}{r} \right] \tag{5}$$

Substituting (3), (4), and (5) into the equilibrium equations, we obtain the following displacement equilibrium equations in polar coordinates:

$$\nabla^2 u - \frac{u}{r^2} + \frac{1}{2(1-\nu)}\left[\frac{1}{r}\frac{\partial^2 v}{\partial r \partial \theta} - \frac{1}{r^2}\frac{\partial^2 u}{\partial \theta^2} - \frac{(3-4\nu)}{r^2}\frac{\partial v}{\partial \theta} \right] = 0 \tag{6}$$

$$\nabla^2 v - \frac{v}{r^2} + \frac{1}{1-2\nu}\left[\frac{1}{r^2}\frac{\partial^2 v}{\partial \theta^2} + \frac{1}{r}\frac{\partial^2 u}{\partial r \partial \theta} + \frac{(3-4\nu)}{r^2}\frac{\partial u}{\partial \theta} \right] = 0 \tag{7}$$

Since u is an even function, v is an odd function.

$$\text{Letting } u = U_n(r) \cos n\theta \tag{8}$$

$$\text{and} \qquad v = V_n(r) \sin n\theta \tag{9}$$

we obtain, after substitution into (6) and (7),

$$U_n'' + \frac{1}{r} U_n' - \frac{(1+n^2)}{r^2} U_n$$

$$+ \frac{1}{2(1-\nu)}\left[\frac{n}{r} V_n' + \frac{n^2}{r^2} U_n - \frac{(3-4\nu)}{r^2}n V_n \right] = 0 \tag{10}$$

$$V_n'' + \frac{1}{r} V_n' - \frac{(1+n^2)}{r^2} V_n$$

$$+ \frac{1}{1-2\nu} \left[- \frac{n^2}{r^2} V_n - \frac{n}{r} U_n' - \frac{(3-4\nu)}{r^2} n U_n \right] = 0 \quad (11)$$

where differentiation with respect to r is indicated by primes.

Noting that (10) and (11) are coupled Euler equations, we let $r = e^z$. Performing this transformation and denoting derivatives with respect to z by $\cdot$, we have:

$$\ddot{U}_n - \left[1+n^2 - \frac{n^2}{2(1-\nu)} \right] U_n + \frac{n}{2(1-\nu)} \left[\dot{V}_n - (3-4\nu) V_n \right] = 0 \quad (12)$$

$$\ddot{V}_n - \left[1+n^2 + \frac{n^2}{1-2\nu} \right] V_n - \frac{n}{1-2\nu} \left[\dot{U}_n + (3-4\nu) U_n \right] = 0 \quad (13)$$

letting $U_n = \sum_{k=1}^{4} A_{kn} e^{\lambda kn z}$ \quad (14)

and $V_n = \sum_{k=1}^{4} B_{kn} e^{\lambda kn z}$ \quad (15)

we obtain:

$$A_{kn} \left[\lambda_{kn}^2 - \left\{ 1+n^2 - \frac{n^2}{2(1-\nu)} \right\} \right]$$

$$+ B_{kn} \frac{n}{2(1-\nu)} \left[\lambda_{kn} - (3-4\nu) \right] = 0 \quad (16)$$

$$A_{kn} \left(\frac{-n}{1-2\nu} \right) \left[\lambda_{kn} + (3-4\nu) \right]$$

$$+ B_{kn} \left[\lambda_{kn}^2 - \left\{ 1+n^2 + \frac{n^2}{1-2\nu} \right\} \right] = 0 \quad (17)$$

Since (16) and (17) are homogeneous equations, we require that the determinant of the coefficients vanish in order for a solution to exist. Thus, we obtain an equation from which we may solve for the λ_{kn}. We find:

$$\lambda_{1n} = 1 + n$$

$$\lambda_{2n} = -(1 + n)$$

$$\lambda_{3n} = (1 - n)$$

$$\lambda_{4n} = -(1 - n)$$

Note that λ_{kn} is \quad (18) independent of ν.

Solving (16) for B_{kn} in terms of A_{kn}, we obtain:

$$B_{kn} = A_{kn} \left[\frac{2(1-\nu)}{n} \right] \left[\frac{1+n^2 - \dfrac{n^2}{2(1-\nu)} - \lambda_{kn}^2}{\lambda_{kn} - (3-4\nu)} \right] \qquad (19)$$

Defining

$$p_{kn} = \left[\frac{2(1-\nu)}{n} \right] \left[\frac{1+n^2 - \dfrac{n^2}{2(1-\nu)} - \lambda_{kn}^2}{\lambda_{kn} - (3-4\nu)} \right] \qquad (20)$$

we write

$$B_{kn} = p_{kn} \, A_{kn} \qquad (21)$$

Substituting the four roots of λ_{kn} into the expression for p_{kn}, we find:

$$p_{1n} = \frac{-4+4\nu-n}{n-2+4\nu} \qquad p_{2n} = +1 \qquad p_{3n} = \frac{-n+4-4\nu}{-2-n+4\nu} \qquad p_{4n} = -1 \qquad (22)$$

From (14) and (15), we have:

$$U_n(r) = A_1 r^{1+n} + A_2 r^{-(1+n)} + A_3 r^{1-n} + A_4 r^{-(1-n)} \qquad (23)$$

$$V_n(r) = p_1 A_1 r^{1+n} + p_2 A_2 r^{-(1+n)} + p_3 A_3 r^{1-n} + p_4 A_4 r^{-(1-n)} \qquad (24)$$

Our boundary conditions become:

axially symmetric	non-axially symmetric
$_0\sigma_r(a) = \dfrac{\sigma_x}{2}$	$_2\sigma_r(a) = \dfrac{\sigma_x}{2} \cos 2\theta$
$_0\sigma_{r\theta}(a) = 0$	$_2\sigma_{r\theta}(a) = -\dfrac{\sigma_x}{2} \sin 2\theta$
$U_0(b) = 0$	$U_2(b) = 0$
$V_0(b) = 0$	$V_2(b) = 0$

$$(25) \qquad\qquad (26)$$

Substituting the form of the displacements (8), (9), into the stress-displacement relations (3), (4), (5), we have:

$$\frac{_n\sigma_r}{\cos n\theta} = \frac{E}{(1-2\nu)(1+\nu)} \left[\nu \left(\frac{n}{r} V_n + \frac{1}{r} U_n \right) + (1-\nu) U_n' \right] \qquad (27)$$

$$\frac{_n\sigma_\theta}{\cos n\theta} = \frac{E}{(1-2\nu)(1+\nu)} \left[\nu U_n' + (1-\nu) \left(\frac{n}{r} V_n + \frac{1}{r} U_n \right) \right] \qquad (28)$$

$$\frac{n\sigma_{r\theta}}{\sin n\theta} = \frac{E}{2(1+\nu)}\left[-\frac{n}{r}U_n + V_n' - \frac{1}{r}V_n\right] \tag{29}$$

We first consider the axially symmetric part of the solution $(n = 0)$.

Applying boundary conditions (25) to (23) and (27), we find:

$$U_0 = \frac{\sigma_x}{2}\frac{(1-2\nu)(1+\nu)}{E}\frac{1}{\left[1+\left(\frac{b}{a}\right)^2(1-2\nu)\right]}\left[r - \frac{b^2}{r}\right] \tag{30}$$

$$_0\sigma_r = \frac{\sigma_x}{2}\left[\frac{1 + (1-2\nu)\left(\frac{b}{r}\right)^2}{1 + \left(\frac{b}{a}\right)^2(1-2\nu)}\right] \tag{31}$$

$$_0\sigma_\theta = \frac{\sigma_x}{2}\left[\frac{1 + (2\nu-1)\frac{b^2}{r^2}}{1 + \left(\frac{b}{a}\right)^2(1-2\nu)}\right] \tag{32}$$

$$_0\sigma_{r\theta} = 0 \tag{33}$$

We now consider the non-axially symmetric part $(n = 2)$. From (23) and (24), we have:

$$U_2 = A_1 r^3 + A_2 r^{-3} + A_3 r^{-1} + A_4 r$$

$$V_2 = p_1 A_1 r^3 + p_2 A_2 r^{-3} + p_3 A_3 r^{-1} + p_4 A_4 r$$

$$U_2' = 3A_1 r^2 - 3A_2 r^{-4} - A_3 r^{-2} + A_4$$

$$V_2' = 3p_1 A_1 r^2 - 3p_2 A_2 r^{-4} - p_3 A_3 r^{-2} + p_4 A_4$$

Using these expressions in (27), (28), and (29), we obtain:

$$\frac{2\sigma_r}{\cos 2\theta} = \frac{E}{1+\nu}\left[-3A_2 r^{-4} - \frac{A_3}{1-\nu}r^{-2} + A_4\right] \tag{34}$$

$$\frac{2\sigma_\theta}{\cos 2\theta} = \frac{E}{1+\nu}\left[-\frac{3}{\nu}A_1 r^2 + 3A_2 r^{-4} - A_4\right] \tag{35}$$

$$\frac{2\sigma_{r\theta}}{\sin 2\theta} = \frac{E}{2(1+\nu)}\left[-\frac{3}{\nu}A_1 r^2 - 6A_2 r^{-4} - \frac{1}{1-\nu}A_3 r^{-2} - 2A_4\right] \tag{36}$$

Applying boundary conditions (26) and solving the resulting equations for A_1, A_2, A_3, and A_4, we find:

$$A_1 = \frac{\frac{k}{b^2}\frac{6}{1-\nu}(\beta^{-1}-\beta)}{\frac{1}{\nu(1-\nu)}\left[\frac{3}{2}(3-4\nu)\beta^{-3}+6\beta^{-2}-9\beta^{-1}+\frac{3}{2}(3-4\nu)\beta+6(4\nu^2-6\nu+3)\right]} \tag{37}$$

$$A_2 = \frac{kb^4\frac{3}{2\nu(1-\nu)}\left[\beta^{-3}-(4\nu-3)\beta^{-1}\right]}{\frac{1}{\nu(1-\nu)}\left[\frac{3}{2}(3-4\nu)\beta^{-3}+6\beta^{-2}-9\beta^{-1}+\frac{3}{2}(3-4\nu)\beta+6(4\nu^2-6\nu+3)\right]} \tag{38}$$

$$A_3 = \frac{kb^2\frac{6}{\nu}\left[-\beta^{-3}+(4\nu-3)\right]}{\frac{1}{\nu(1-\nu)}\left[\frac{3}{2}(3-4\nu)\beta^{-3}+6\beta^{-2}-9\beta^{-1}+\frac{3}{2}(3-4\nu)\beta+6(4\nu^2-6\nu+3)\right]} \tag{39}$$

$$A_4 = \frac{k\frac{3}{2\nu(1-\nu)}\left[(3-4\nu)\beta^{-3}-3\beta^{-1}+4(4\nu^2-6\nu+3)\right]}{\frac{1}{\nu(1-\nu)}\left[\frac{3}{2}(3-4\nu)\beta^{-3}+6\beta^{-2}-9\beta^{-1}+\frac{3}{2}(3-4\nu)\beta+6(4\nu^2-6\nu+3)\right]} \tag{40}$$

where $\beta = \left(\frac{b}{a}\right)^2$

$k = \frac{\sigma_x}{2}\frac{1+\nu}{E}$

As $\beta \longrightarrow 0$

$A_1 \longrightarrow 0$

$A_2 \longrightarrow \frac{kb^4}{3-4\nu}$

$A_3 \longrightarrow -\frac{4kb^2(1-\nu)}{3-4\nu}$

$A_4 \longrightarrow k$

Thus, (34), (35), and (36) become:

$$\frac{2\sigma_r}{\cos 2\theta} = \frac{\sigma_x}{2}\left[\frac{-3}{3-4\nu}\left(\frac{b}{r}\right)^4 + \frac{4}{3-4\nu}\left(\frac{b}{r}\right)^2 + 1\right] \tag{41}$$

$$\frac{2\sigma_0}{\cos 2\theta} = \frac{\sigma_x}{2}\left[\frac{3}{3-4\nu}\left(\frac{b}{r}\right)^4 - 1\right] \tag{42}$$

$$\frac{2\sigma_{r\theta}}{\sin 2\theta} = \frac{\sigma_x}{4}\left[\frac{-6}{3-4\nu}\left(\frac{b}{r}\right)^4 + \frac{4}{3-4\nu}\left(\frac{b}{r}\right)^2 - 2\right] \tag{43}$$

As $\frac{b}{a} \longrightarrow 0$, (31), (32), and (33) become:

$$_0\sigma_r = \frac{\sigma_x}{2}\left[1 + (1-2\nu)\left(\frac{b}{r}\right)^2\right] \tag{44}$$

$$_0\sigma_\theta = \frac{\sigma_x}{2}\left[1 - (1-2\nu)\left(\frac{b}{r}\right)^2\right] \tag{45}$$

$$_0\sigma_{r\theta} = 0 \tag{46}$$

Thus, the total solution for the stresses in a plate containing a small, rigid inclusion becomes:

$$\sigma_r = \frac{\sigma_x}{2}\left\{\left[1 + (1-2\nu)\left(\frac{b}{r}\right)^2\right] + \cos 2\theta\left[\frac{-3}{3-4\nu}\left(\frac{b}{r}\right)^4 + \frac{4}{3-4\nu}\left(\frac{b}{r}\right)^2 + 1\right]\right\} \tag{47}$$

$$\sigma_\theta = \frac{\sigma_x}{2}\left\{\left[1 - (1-2\nu)\left(\frac{b}{r}\right)^2\right] + \cos 2\theta\left[\frac{3}{3-4\nu}\left(\frac{b}{r}\right)^4 - 1\right]\right\} \tag{48}$$

$$\sigma_{r\theta} = \frac{\sigma_x}{4}\sin 2\theta\left[\frac{-6}{3-4\nu}\left(\frac{b}{r}\right)^4 + \frac{4}{3-4\nu}\left(\frac{b}{r}\right)^2 - 2\right] \tag{49}$$

At $r = b$ (boundary between inclusion and elastic material),

$$\sigma_r(b) = \frac{\sigma_x}{2}\left\{2(1-\nu) + \cos 2\theta\left[\frac{4(1-\nu)}{3-4\nu}\right]\right\} \tag{50}$$

$$\sigma_{r\theta}(b) = \frac{\sigma_x}{4}\sin 2\theta\left[\frac{8(\nu-1)}{3-4\nu}\right] \tag{51}$$

We now use (50) and (51) as applied stresses on a circular elastic region (core).

We define:

E = Young's modulus for the plate material

E_1 = Young's modulus for the inclusion

ν = Poisson's ratio for the plate material

ν_1 = Poisson's ratio for the inclusion

Our boundary conditions for the elastic core become:

$$_0\sigma_r(b) = \sigma_x(1-\nu) \qquad U_0 = 0$$
$$_0\sigma_{r\theta}(b) = 0 \qquad\qquad V_0 = 0 \tag{52}$$

$$2^{\sigma}r(b) = \sigma_x \left[\frac{2(1-\nu)}{3-4\nu}\right] \cos 2\theta \qquad U_2 = 0$$

$$2^{\sigma}r\theta(b) = \sigma_x \left[\frac{2(\nu-1)}{3-4\nu}\right] \qquad V_2 = 0 \qquad (53)$$

We first consider the axially symmetric part. Applying boundary conditions (52) to (23), (24), (27), and (29), we find:

$$U_o(r) = \frac{\sigma_x(1-\nu)(1-2\nu_1)(1+\nu_1)}{E_1}\, r \qquad (54)$$

$$V_o(r) = 0 \quad \text{(by virtue of axial symmetry)} \qquad (55)$$

$$_o\sigma_r = \sigma_x\,(1-\nu) \qquad (56)$$

$$_o\sigma_\theta = \sigma_x\,(1-\nu) \qquad (57)$$

$$_o\sigma_{r\theta} = 0 \qquad (58)$$

Now consider the non-axially symmetric part. Applying boundary conditions (53) to (23), (24), (34), and (36), we find:

$$U_2(r) = \sigma_x \left[\frac{2(1-\nu)}{3-4\nu}\right]\left(\frac{1+\nu_1}{E_1}\right) r \qquad (59)$$

$$V_2(r) = -\sigma_x \left[\frac{2(1-\nu)}{3-4\nu}\right]\left(\frac{1+\nu_1}{E_1}\right) r \qquad (60)$$

$$_2\sigma_r = \sigma_x \left[\frac{2(1-\nu)}{3-4\nu}\right] \cos 2\theta \qquad (61)$$

$$_2\sigma_{r\theta} = -\sigma_x \left[\frac{2(1-\nu)}{3-4\nu}\right] \sin 2\theta \qquad (62)$$

$$_2\sigma_\theta = -\sigma_x \left[\frac{2(1-\nu)}{3-4\nu}\right] \cos 2\theta \qquad (63)$$

Thus, the stresses in the circular elastic core are given by:

$$\sigma_r = \sigma_x \left[(1-\nu) + \frac{2(1-\nu)}{3-4\nu} \cos 2\theta\right] \qquad (64)$$

$$\sigma_{r\theta} = -\sigma_x \left[\frac{2(1-\nu)}{3-4\nu}\right] \sin 2\theta \qquad (65)$$

$$\sigma_\theta = \sigma_x \left[(1-\nu) - \frac{2(1-\nu)}{3-4\nu} \cos 2\theta\right] \qquad (66)$$

Since $u = U_o(r) + U_2(r) \cos 2\theta$ where U_o and U_2 are given by (54) and (59), respectively,

$$u = \frac{\sigma_x(1-\nu)(1-2\nu_1)(1+\nu_1)}{E_1} r + \sigma_x \left[\frac{2(1-\nu)}{3-4\nu}\right] \left(\frac{1+\nu_1}{E_1}\right) r \cos 2\theta \quad (67)$$

At $\theta = 0$

$$u = \sigma_x \left(\frac{1+\nu_1}{E_1}\right) \left[(1-\nu)(1-2\nu_1) + \frac{2(1-\nu)}{3-4\nu}\right] r \quad (68)$$

$$\therefore \epsilon_r = \frac{\partial u}{\partial r} = \sigma_x\left(\frac{1+\nu_1}{E_1}\right) \left[(1-\nu)(1-2\nu_1) + \frac{2(1-\nu)}{3-4\nu}\right]$$

$$\therefore \sigma_x = E_1\epsilon_r \frac{1}{(1+\nu_1)\left[(1-\nu)(1-2\nu_1) + \frac{2(1-\nu)}{3-4\nu}\right]} \quad (69)$$

where E_1 = Modulus of inclusion

ϵ_r = Strain in inclusion (constant throughout)

σ_x = Applied stress

If the inclusion were not present, then we have for the elastic plate

$$(1-\nu^2)\,\sigma_x = E\,\epsilon_x \qquad \therefore \epsilon_x = \frac{\sigma_x}{E}(1-\nu^2)$$

For $\nu_1 = .32$ $E_1 = 26\times10^6$, which are typical properties for metal foil gages, and
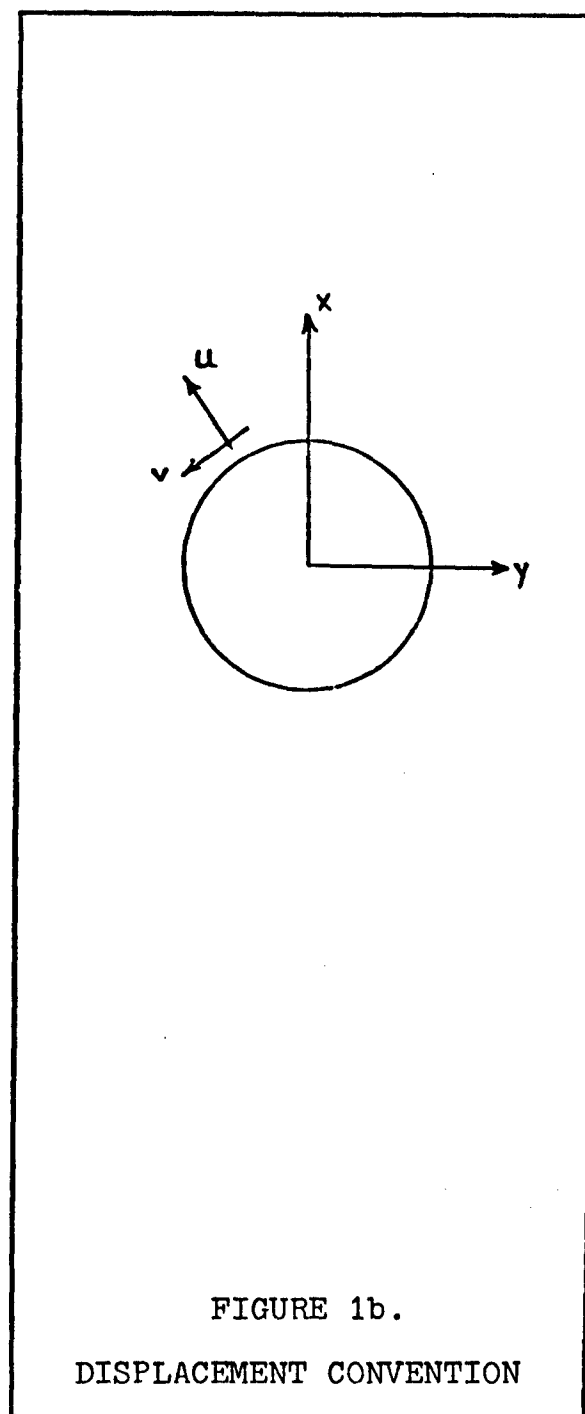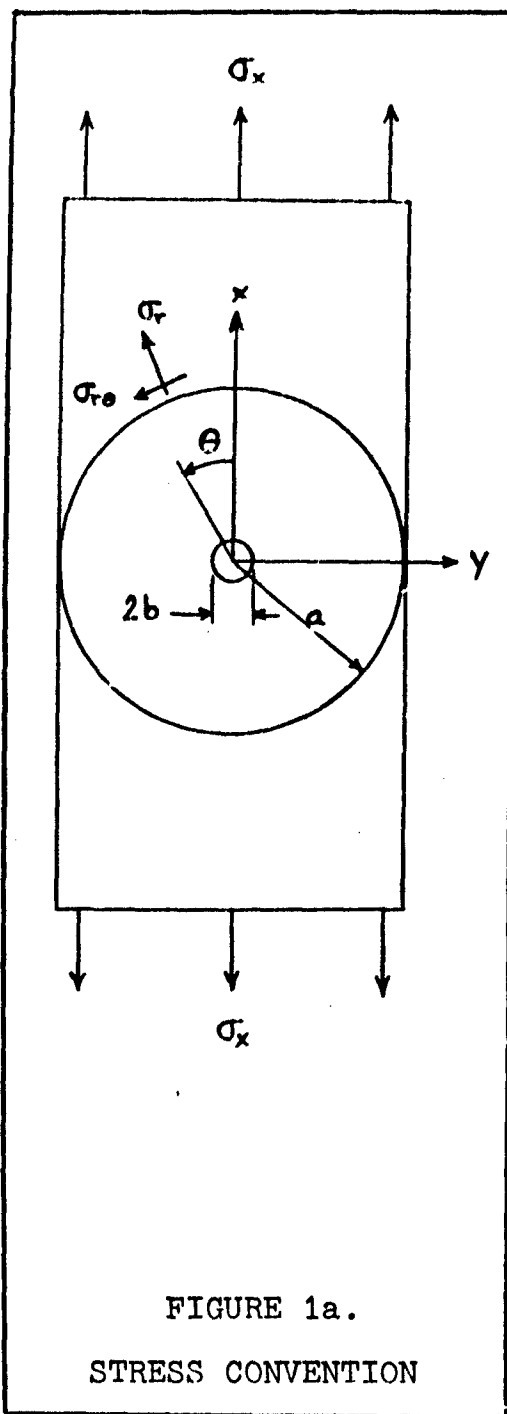
$$\nu = .5$$
$$\epsilon_r = \frac{\sigma_x}{.642E_1} \qquad\qquad \epsilon_x = 12.519\times10^6 \frac{\epsilon_r}{E} \quad (70)$$

$$\therefore \frac{\epsilon_x}{\epsilon_r} = .642 \frac{E_1}{E}(1-\nu^2)$$

CONCLUSIONS

We find that by knowing the material properties of each material and the strain in the inclusion (gage), the strain can be found in the propellant which would be present if the gage were absent.

FIGURE 1a.

STRESS CONVENTION

FIGURE 1b.

DISPLACEMENT CONVENTION

APPENDIX

Comparing numerically the solution presented in this report to the solution of the problem of an elastic inclusion in an elastic plate with $v_1 = .32$, $v = .5$, we find the results agree to four significant figures. That is,

$$\frac{\epsilon_x}{\epsilon_r} = .4815 \frac{E_1}{E}$$

Thus, it is seen that the assumption of the gage as a rigid inclusion gives excellent results with a very low modulus plate.

We next compute the effect of the inclusion at various multiples of the radius "b."

Using the solution obtained for the plate (region outside of the inclusion), we compute ϵ_r at $\theta = 0^\circ$ and compare with ϵ_r, which would be present if the inclusion were absent.

$$r = 4.6 \ b \qquad \%\text{error} = 11.70$$

$$r = 8.6 \ b \qquad \%\text{error} = 4.62$$

$$r = 14.6 \ b \qquad \%\text{error} = 1.47$$

$$r = 20.6 \ b \qquad \%\text{error} = 0.75$$

Thus, if a gage of 1/4-inch length is used, an error of less than 2% occurs at a distance of 1.75 inches.

A DEVICE TO MEASURE THE CHANGE IN WIDTH CONTINUOUSLY DURING UNIAXIAL TENSILE TESTS[1]

Clarke H. Lewis, Jr.
Research Engineer, Polymer Research Section

Jet Propulsion Laboratory
California Institute of Technology
Pasadena, California

ABSTRACT

A brief description is given of a device which measures the change in width of an elastomeric tensile specimen continuously during test. It can operate at temperatures of -65 to 160° F and with specimen widths of 1.000 to 0.375 in. It is actuated by the moving crosshead of the testing machine and returns to its starting point when the crosshead is returned. Width is measured at the center point of the specimen to an accuracy of ±0.0005 in.

INTRODUCTION

One of the commonest tests used in the characterization of physical properties of elastomeric materials such as solid propellants is the uniaxial tensile test conducted at constant crosshead speed of the testing machine. During the course of such a test, the specimen undergoes considerable axial elongation (20-50%) and lateral contraction (10-15% on each axis).

One of the principal difficulties associated with this test is that of determining the stress and strain in the specimen; usually, just the load exerted by the specimen on the stationary grip and the position of the moving grip are known.

Contributing to this problem is the fact that the grips customarily used allow the specimen to creep in the grips under load. This phenomenon has two effects: the amount of strain in the specimen is reduced, and the strain rate is decreased. To account for this, an effective gage length in excess of the actual specimen length is used to convert grip movement to strain in the specimen. This gage length is found by measuring the strains directly by such means as photography and then assuming this gage length to be constant for all strains and rates. The gage length depends on the point at which the strain and the crosshead movement are matched (Fig. 1). As a result of the gage-length variation, the strain rate varies during the test, although mainly at the beginning of the test and near maximum load (Fig. 2).

Similarly when determining the stress, the reduction of cross-sectional area must be considered. The assumptions used here vary from that of constant area to letting $A = A_0/(1 + \epsilon_z)$. The latter expression is derived assuming an incompressible material. While this expression is more reasonable than assuming the area is constant, experimentally Poisson's ratio falls below the incompressible case (Fig. 3). The uncertainty of the axial strain also affects this expression.

To deal with these difficulties, direct measurement of the strain is necessary. To some extent, this is now common practice. The means used have been either a visual measurement using a scale or micrometer, or photographing a pattern of circles or dots on the specimen. Both of these methods are inaccurate at low strains, and particularly with the photographic method the data reduction is very involved and lengthy.

In an effort to make the direct measurement of these strains easier and more accurate, the design and development of devices to measure continuously axial strain and lateral contraction of a uniaxial tensile specimen was undertaken. At this time, the axial-strain extensometer is still under development and will be discussed at a future date. The lateral-dimension measuring device has been developed and tested and is the subject of the following discussion.

DISCUSSION

The device consists of two parts: the width-measuring transducer, and the platform mechanism upon which the transducer is mounted. The transducer (Fig. 4) has two arms which touch either side of the specimen. One arm is fixed when in use but can be adjusted to accommodate specimen widths from 1.020 to 0.350 in. The other arm is spring-loaded to remain in contact with the specimen as it reduces in width. The position of the moving arm is measured by a linear potentiometer through a lever to the arm. The potentiometer is calibrated to read out width directly.

The transducer is mounted on three Teflon beads on the platform and positioned by pins (Fig. 5). It is free to move laterally so that as the specimen contracts, the spring-loaded arm causes this assembly to move enough to keep the fixed arm in contact with the specimen also. The other function of the platform is to position the arms at the desired point throughout the test. The platform moves vertically on two rods mounted on the moving crosshead of the machine. The platform is held up by counterweights and is moved downward by the pulley system at a rate equal to one-half of the crosshead speed. Thus, if the measuring arms are positioned vertically at the center of the specimen, they will follow this point as the crosshead moves. It is assumed here that the initial center of the specimen remains midway between the grips. This is not strictly true; however, the error has been seen to be small using photographs. Specimens are easily inserted

from the front, and of course ultimately will be engaged by the axial extensometer after being positioned as shown in Fig. 6.

Steps are being taken to further refine the transducer. At present the device will measure a width of 1.000 in. to an accuracy of ±0.0005 in. with a linearity of 1% over 0.100 in. of movement. Maximum deflection of the spring-loaded arm produces a 5-psi pressure on the specimen. It would be desirable to improve the linearity and to decrease the actuating force.

Figure 7 shows the effect of measuring strains directly as compared to using a predetermined gage length. The widths measured by the lateral dimension device compared very well with those determined by photographs, and were more consistent. The data-reduction time was reduced by 75%. Ultimately it will be possible to use this device and an extensometer with a test that could be run at constant strain rate over a measured gage length and would produce measured values of true average stress and strain on this element.
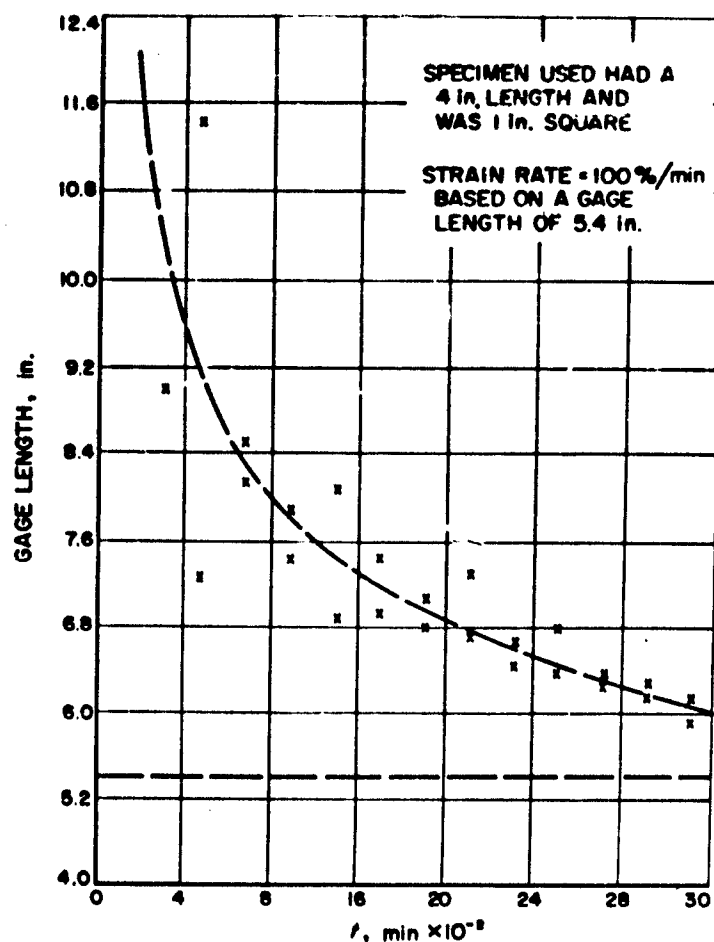

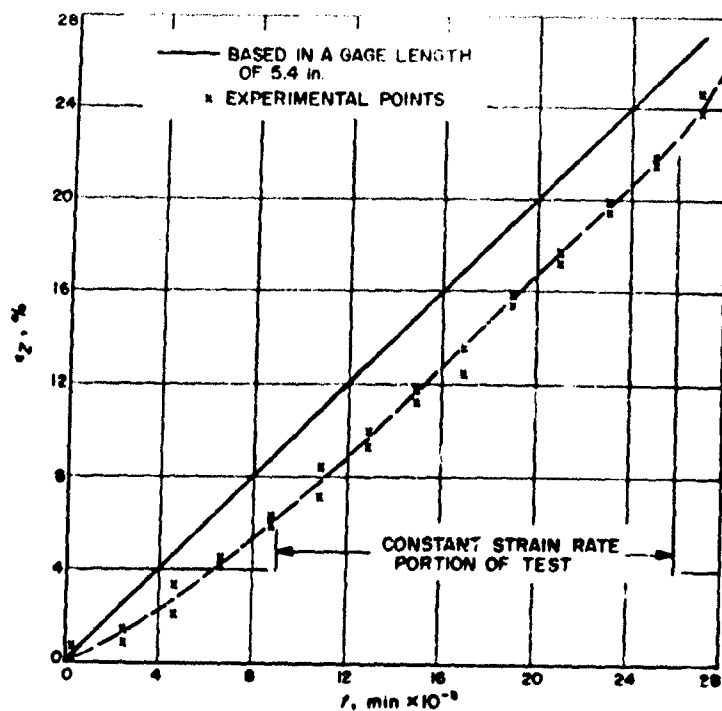FIGURE 1. VARIATION OF GAGE LENGTH DURING A UNIAXIAL TENSILE TEST

FIGURE 2.
COMPARISON OF MEASURED AXIAL
STRAIN WITH PROGRAMMED STRAIN

FIGURE 3.
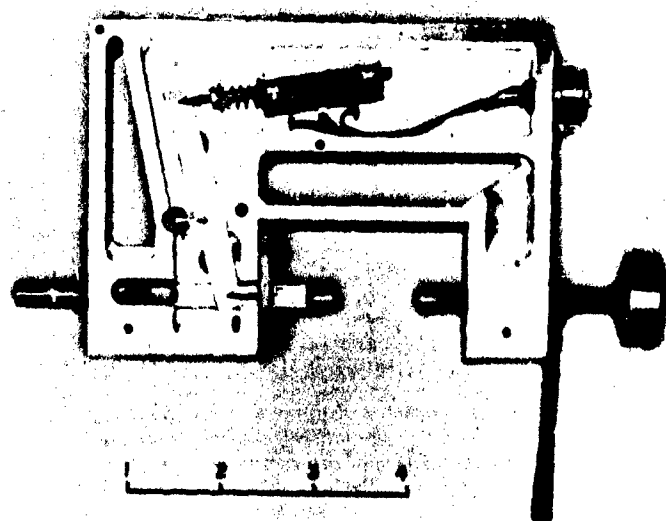POISSON'S RATIO AS A FUNCTION
OF AXIAL STRAIN

$$\eta = \frac{1}{e}\left[1 - \sqrt{\frac{1}{1+e}}\right]$$

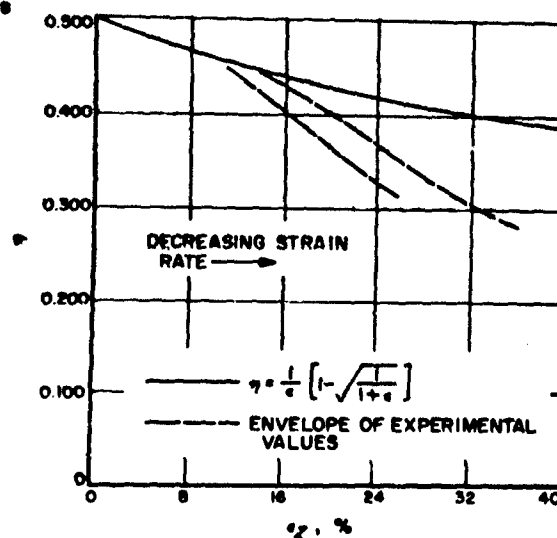ENVELOPE OF EXPERIMENTAL VALUES

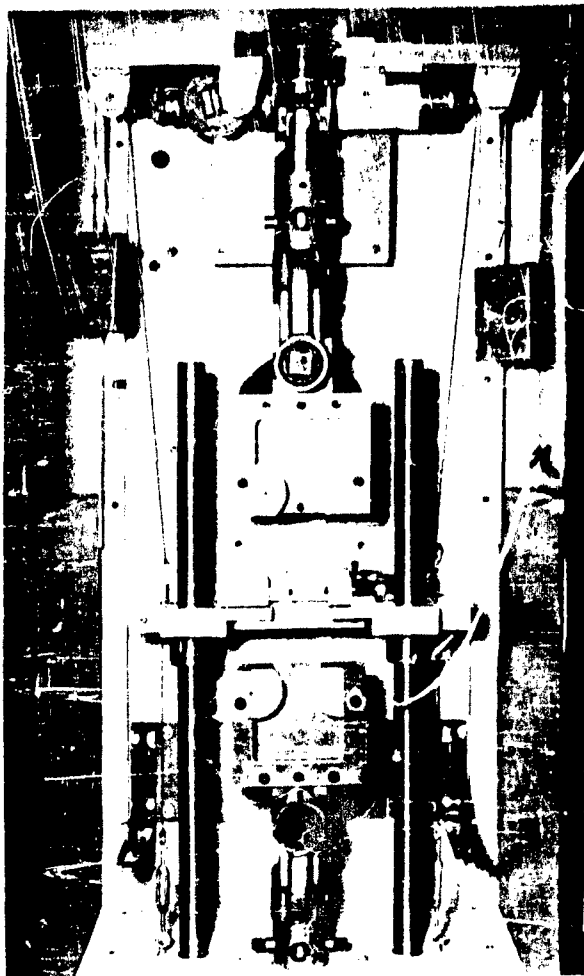
FIGURE 4.
WIDTH-MEASURING
TRANSDUCER

FIGURE 5.
TRANSDUCER MOUNTED ON
MOVING PLATFORM
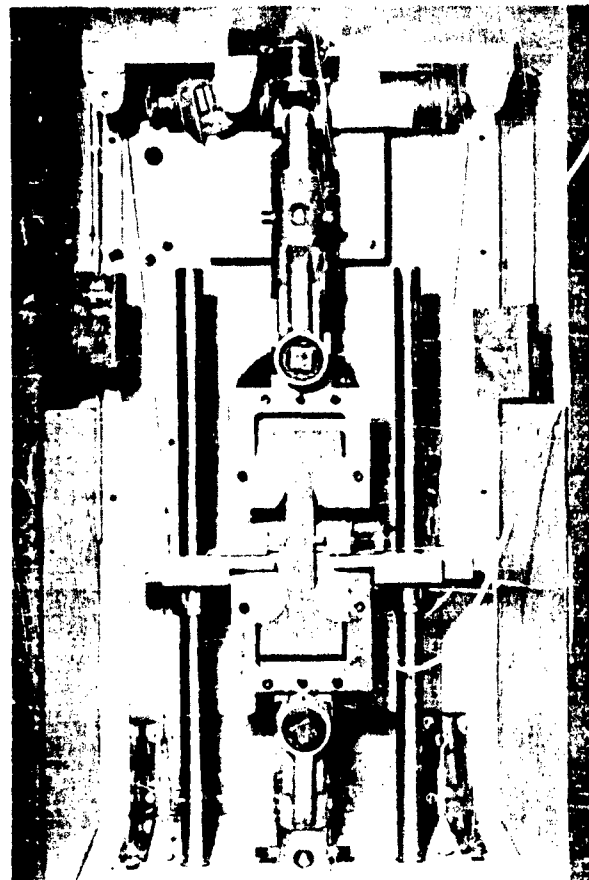
FIGURE 6.
LATERAL-DIMENSION MEASURING
DEVICE SET UP FOR TEST.

FIGURE 7.   STRESS AS A FUNCTION OF STRAIN

$$\bar{\sigma} = \frac{L}{A_0}(1 + \epsilon_T)$$

WHERE $\epsilon_T = \epsilon_Z'$
6.4 in. GAGE LENGTH

$$\bar{\sigma} = \frac{L(w_{x_0})^2}{A_0(w_x)}$$

w_x MEASURED BY
LATERAL DIMENSION
DEVICE
ϵ_Z DETERMINED FROM
PHOTOS OF DOTS ON
SPECIMEN
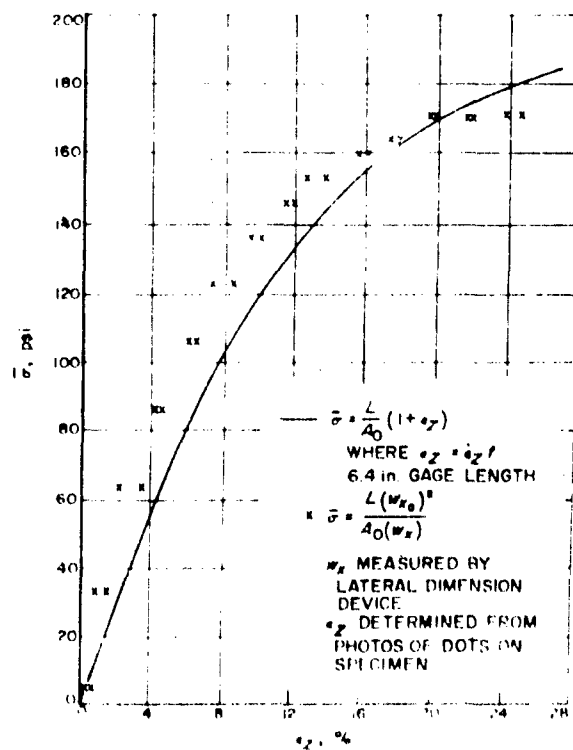
FURTHER DEVELOPMENT OF A BI-AXIAL STRESS TEST
FOR VISCOELASTIC MATERIALS[1]

John J. Brisbane

Rohm & Haas Company
Redstone Arsenal Research Division
Huntsville, Alabama

ABSTRACT

A method of testing solid propellants in a bi-axial stress field which consists of the diametrical compression of an elliptical disk between the platens of a testing machine has been proposed by J. E. Fitzgerald of the Grand Central Rocket Company. The typical fracture in this test is a tensile failure at the center of the disk where the stress field is bi-axial. Previous work on this test at Grand Central was performed on a circular disk for which only one ratio of the bi-axial stresses is obtainable at the center of the disk.

A stress analysis using classical small deformation elastic theory was made of an elliptical disk under diametrical compression by a concentrated load which showed that various ratios of bi-axial stresses at the center of the disk could be obtained if elliptical disks with different ratios of major to minor axes were used. To determine the effects of the large deformations which occur at the points of loading when a propellant is subjected to this test, a photoelastic investigation was made using an elastic material. When compared with the photoelastic results, the theoretical stress analysis was found to be inadequate for predicting the stresses when large deformations existed at the points of loading. The photoelastic investigation yielded empirical solutions for the stresses and the stress ratio at the centers of elliptical disks with ratios of major to minor axes equal to 1.0, 1.5, and 2.0 as a function of the percent decrease in major axis.

To extend the experimental solution for an elastic disk to a viscoelastic material, a non-rigorous method analogous to the method applied to the Hertz contact problem by Lee and Radok was used. This method utilizes the results from the photoelastic investigations of the elastic disk to predict the stresses at the center of a viscoelastic disk.

The results of a limited test program on propellants yielded a satisfactory correlation with the viscoelastic solution at small deformations, but correlation at large deformations was not as good as desired. However, there are several possible sources of experimental error that have not yet been investigated.

INTRODUCTION

The majority of physical property data for solid propellants has to this date been obtained by the use of the uni-axial tension test. While this test gives valuable information on propellants, it does not give data obtained under the combined stress conditions existing in a rocket motor. In order to obtain more realistic design information, considerable effort has been expended throughout the industry to develop a bi-axial stress test. The bi-axial stress test presents difficulty because the loading of the specimen and the analysis of the stress field are both troublesome.

The bi-axial test considered in this paper was first proposed by J.E. Fitzgerald of Grand Central Rocket Company (1)[1]. The test consisted of the diametrical compression of a circular disk between the platens of a testing machine. The typical failure resulting from this test is a tensile failure at the center of the disk where the stress field is bi-axial, being formed by a compressive stress in the direction of the load and a tensile stress perpendicular to the load. With a circular disk there is only one ratio of principal stresses available at the center of the disk (2). Thus, Fitzgerald proposed that further work might be done to determine if different stress ratios might be obtained by using elliptical disks with different ratios of major to minor axes.

This paper presents an extension of this test to elliptical disks with consideration being given to large deformations and viscoelastic effects. The purpose of the paper is to demonstrate the existence of a bi-axial stress field at the center of an elliptical disk and its dependence on the ratio of major to minor axes and to develop a method whereby the bi-axial stress at failure can be predicted.

ELASTIC ANALYSIS

A stress analysis based on classical small deformation elastic theory was made of an elliptical disk loaded along either the major or minor axes by a concentrated compressive load. This model was analyzed to determine approximately the range of stress ratios at the disk center which could be expected by varying the ratio of major to minor axes in actual tests.

The theoretical analysis is to lengthly for inclusion here. The complex variable method of Muskhelishvili (3) was used. Expressions for the principal stresses at the center of the disk were found in infinite series form. Fig. 1 shows the resulting ratio of principal stresses at the disk center. It can be seen that the ratio of the tensile to the compressive principal stresses for this type of test can be expected to lie between zero and about one third.

To determine the effects of the large deformations that can occur under the platens at the points of loading during the test, a photoelastic investigation was carried out. The photoelastic models were made from Hysol 8705 polyurethane rubber obtained in sheet from Hysol Corporation[2]. This

---

[1] Numbers in parentheses indicate references at the end of the paper.

[2] Hysol Corporation, Olean, New York.

material, which exhibited elastic properties throughout the range needed
for the investigation, possesses a very large stress-optic coefficient so
that a large number of fringes were available even at small deformations
and loads. The photoelastic study was carried out using standard methods
of stress separation such as the shear difference method and the numerical
integration of Filon's transformation of the Lamé-Maxwell equations for
sections of symmetry (4). Pictures of the isochromatic pattern for two
different values of the applied load are shown in Fig. 2 for an elliptical
disk having a 3-in. major axis, a 2-in. minor axis, and a 1/2-in thickness.

The photoelastic investigation indicated that the theoretical solution for
a concentrated load was not adequate when large deformations occurred at
the loading points. The results of the photoelastic investigation are shown
in Figs. 3 and 4. Fig. 3 is a plot of the absolute value of the principal
stresses at the center of the disk divided by the shear modulus as a func-
tion of the percent decrease in the major axis. It was found that the photo-
elastic analysis of the case where the load was placed along the major axis
was less difficult than the case where the load was placed along the minor
axis, and all experimental results are for a loading along the major axis.
Fig. 4 shows a graph of the applied load per unit thickness divided by the
minor semi-axis and the shear modulus as a function of the percent decrease
in major axis. The reason for the selection of these particular dimension-
less quantities for the graphs will be evident later in the paper.

VISCOELASTIC ANALYSIS

In viscoelastic stress analysis there exists a certain class of problems
in which the stress distribution is the same as for the equivalent elastic
problem. The elastic solution for this class of problem contains no
elastic constants, and the stresses are linearly related to the loads. For
a two-dimensional problem, a sufficient condition for the elastic stress
solution to be independent of elastic constants is that the boundary conditions
be expressed in terms of the applied stress alone. Generally in cases
where this condition is not met, the elastic and viscoelastic stress solutions
are not the same (5).

In the test that has been proposed the boundary conditions are not only
mixed, but the point separating the stress conditions and the displacement
conditions changes with load. Therefore, need for a viscoelastic stress
solution exists.

The same type of time dependent mixed boundary conditions exist in
the Hertz contact problem which has been solved for a viscoelastic material
by Lee and Radok (6) using assumptions later justified by experimental
verification of their solution. A method analogous to the Lee and Radok
method was used to attempt to predict the stresses that occur in the visco-
elastic disks by using the experimentally determined stresses in the
elastic disks described above.

For linear viscoelastic materials, the relation between stress and
strain can be written as

$$s_{ij}(t) = \int_0^t G(t-\tau) \frac{de_{ij}(\tau)}{d\tau} d\tau \tag{1}$$

where $s_{ij}(t)$ and $e_{ij}(t)$ are the time dependent deviatoric stress and strain components and $G(t)$ is the relaxation modulus (7). It is assumed that an analogous expression can be used to relate the load and the principal stresses at the center of the disk to the displacement of the loaded axis. Let the applied load and principal stresses at the center of the elastic disk be expressed as

$$\frac{P}{b} = G\phi_1\left(\frac{\alpha}{2a}\right) ,$$

$$\sigma_{x_o} = G\phi_2\left(\frac{\alpha}{2a}\right) , \text{ and} \tag{2}$$

$$\sigma_{y_o} = G\phi_3\left(\frac{\alpha}{2a}\right) ,$$

where

P = applied load per unit thickness,
σ_{x_o} = principal stress at disk center perpendicular to the load,

σ_{y_o} = principal stress at disk center parallel to load,

G = elastic shear modulus,
α = decrease in major axis,
a = undeformed major semi-axis, and
b = undeformed minor semi-axis.

For a constant crosshead speed

$$\alpha = At. \tag{3}$$

Hence Eq. 2 can be written

$$\frac{P}{b} = G\phi_1\left(\frac{A}{2a}t\right)$$

$$\sigma_{x_o} = G\phi_2\left(\frac{A}{2a}t\right) , \text{ and} \tag{4}$$

$$\sigma_{y_o} = G\phi_3\left(\frac{A}{2a}t\right) .$$

It is pointed out for emphasis that the ϕ functions are to be determined from the elastic experimental solutions (e.g., see Figs. 3 and 4).

The assumed analogy to Eq. 1 can then be written

$$\frac{P(t)}{b} = \int_0^t \frac{G(t-\tau)}{2} \frac{d\phi_1(\tau)}{d\tau} d\tau ,$$

$$\sigma_{x_o}(t) = \int_0^t \frac{G(t-\tau)}{2} \frac{d\phi_2(\tau)}{d\tau} d\tau , \text{ and} \tag{5}$$

$$\sigma_{y_o} = \int_0^t \frac{G(t-\tau)}{2} \frac{d\phi_3(\tau)}{d\tau} d\tau .$$

The factor of $1/2$ appears due to the fact that the relaxation modulus was determined for use with Cauchy strain components which are $1/2$ of the normally defined strain.

To eliminate the need for graphical integration, the functions $\phi_1(\frac{\alpha}{2a})$, $\phi_2(\frac{\alpha}{2a})$, and $\phi_3(\frac{\alpha}{2a})$ were expressed as polynomials of the third degree in $\frac{\alpha}{2a}$. Thus

$$\phi\left(\frac{\alpha}{2a}\right) = B'\left(\frac{\alpha}{2a}\right)^3 + C'\left(\frac{\alpha}{2a}\right)^2 + D'\left(\frac{\alpha}{2a}\right). \tag{6}$$

When Δt is substituted for α and the value of A is known, Eq. 6 becomes

$$\phi(t) = Bt^3 + Ct^2 + Dt, \tag{7}$$

where B, C, and D are constants. Now if the relaxation modulus is known for the material used in the test, the integration indicated in Eqs. 5 can be performed to find the load and the stresses at the center of the viscoelastic disk.

In order to check the validity of Eqs. 5, the applied load on a viscoelastic disk can be computed by the use of the relaxation modulus and the function ϕ_1 for a given rate of loading. This load can be compared with the applied load versus time plot recorded by the testing machine. If these two curves agree there is good reason to believe that the viscoelastic stresses can be predicted by the analogy used to obtain Eqs. 5.

TESTING

The limited testing that has been carried out to check this analogy was carried out on Thiokol[1] HC propellant. There were two reasons for using this propellant: (1) the relaxation modulus has been measured by Thiokol and (2) test results could be correlated with those obtained by Thiokol with their membrane test.

The specimens were cut from 1-in. thick disks sawed from 5-in. cylinders that had been cast in ice cream cartons. The cylinders were part of a special 5-gal. batch that was mixed especially for this testing.

Thiokol had earlier determined the relaxation modulus of this material from uni-axial constant strain data using the Blatz Modified Power Law (8). The relaxation modulus so determined is

$$G(t) = \frac{E_r - E_e}{\left[1 + \frac{t}{\tau_o}\right]^\beta} + E_e, \tag{8}$$

where at the reference temperature of 243°K

$$E_r = 1.48\,(10^4)\ \text{lbf-in.}^{-2},$$

---

[1]Thiokol Chemical Company, Redstone Division, Huntsville, Alabama.

$$E_e = 2.00 \, (10^2) \text{ lbf-in}^{-2} \, ,$$

$$\beta = 2.60 \, (10^{-1}) \, , \text{ and}$$

$$\tau_o = 0.57 \, (10^{-4}) \text{ min.}$$

Multiplication of τ_o by the shift factor allows the modulus to be determined at other temperatures. The shift factor can be determined for HC propellant from the WLF equation,

$$\text{Log}_{10} a_T = - \frac{8.86(T-243)}{101.6-(T-243)} \, , \tag{9}$$

where T is the temperature in degrees Kelvin.

For $T = 298°K(77°F)$, $a_T = a_{298} = 7.73(10^{-4})$. Thus for room temperature,

$$\tau_o = 1.21(10^{-7}) \, . \tag{10}$$

The check of the analogy was performed on elliptical disks of HC propellant having a 3-in. major axis, a 2-in. minor axis, and a 1-in. thickness. The test was run on a Baldwin testing machine at a crosshead speed of 1.92 in.-min^{-1}. For this speed and specimen, the ϕ function determined from the elastic experiments becomes

$$\phi_1(t) = 2.88t^3 + 1.95t^2 + 1.64t \, . \tag{11}$$

When this value of $\phi_1(t)$ along with the relaxation modulus at 298°K was substituted into the first of Eqs. 5 and the indicated integration performed, the following result was obtained.

$$\frac{P(t)}{b} = 116t^{0.74} \, [2.22 + 2.98t + 4.90t^2] + 288t^3 + 44.6t^2 + 164t \, . \tag{12}$$

The above relation along with the experimental curve determined from the test are shown in Fig. 5. The agreement of the curves in suprising when it is considered that errors due to batch-to-batch variation in propellant relaxation modulus and in the determinations of the relaxation modulus of the propellant and of the shear modulus of the elastic disk are present in the analysis. Such good agreement should be considered somewhat fortuitous until the results are substantiated by further tests.

Another method of checking the analogy is to determine the propellant relaxation modulus directly from the test at one strain rate and use it to predict the load-time curve at a faster strain rate. In doing this the shear modulus of the elastic material does not appear in the final results. This method of determining viscoelastic properties was mentioned by Lee and Radok in their paper on the Hertz contact problem. Start by using the first of Eqs. 5 for the load, namely

$$\frac{P(t)}{b} = \int_0^t \frac{G(t-\tau)}{2} \frac{d\phi_1(\tau)}{d\tau} \, d\tau \, . \tag{5}$$

The Laplace transform of this equation is

$$\frac{\bar{P}(p)}{b} = \frac{\bar{G}(p)}{2} \, p\bar{\phi}_1(p) \, , \tag{13}$$

where the bar over a function denotes its Laplace transform and p is the transform variable. Now defining the equivalent modulus as

$$G^{\#}(p) = p\overline{G}(p) \tag{14}$$

Eq. 13 can be written as

$$\frac{\overline{P}(p)}{b} = \frac{G^{\#}(p)}{2}\,\overline{\phi}_1(p) \tag{15}$$

By rearrangement of Eq. 15, the equivalent modulus can be expressed as

$$G^{\#}(p) = \frac{2\overline{P}(p)}{b\overline{\phi}_1(p)} \tag{16}$$

If for a specific test, the load-time curve that is recorded on the test machine is fitted by some function of t, and the Laplace transforms of it and of the function $\phi_1(t)$ from the equivalent elastic test are taken, then the equivalent modulus can be determined from Eq. 16. Since the function of t used to fit the recorded load-time curve is only good for the time interval of the test, the equivalent modulus is only good for the time interval of the test.

To check this method, a test was run on a disk of HC propellant having a major axis of 3 in., a minor axis of 2 in., and a thickness of 1 in. at a crosshead speed of 1.92 in.-min^{-1}. The equivalent modulus was determined from Eq. 16 and then used in Eq. 15 to predict the load-time curve at a crosshead speed of 4.87 in.-min^{-1}.

In order to take the Laplace transforms of $\frac{P(t)}{b}$ and $\phi_1(t)$ determined at the 1.92 in.-min^{-1} crosshead speed for this elliptic disk, these functions were fitted with the following approximations.

$$\frac{P(t)}{b} = 1030\,(t - 0.05) + 51.5\,e^{16.9t} \tag{17}$$

and

$$\phi_1(t) = 0.717\left[e^{1.88\frac{A}{a}t} - 1\right]. \tag{18}$$

For A = 1.92 in.-min^{-1} and 2a = 3 in., Eq. 17 becomes

$$\phi_1(t) = 0.717\left[e^{2.40t} - 1\right]. \tag{19}$$

For the same size specimen but for A = 4.87 in.-min^{-1},

$$\phi_1(t) = 0.717\left[e^{6.09t} - 1\right]. \tag{20}$$

The exponential form for the approximations has been used in place of the polynomial to make the mathematical work involved in the Laplace transforms easier. The equivalent modulus found from a test run at 1.92 in.-min^{-1} crosshead speed is found by substituting the transforms of Eqs. 17 and 18 into Eq. 16. This leads to

$$G^{\#}(p) = \frac{318(p + 109)(p-2.40)}{p(p + 16.9)(0.717)(2.40)} .$$ (21)

Eq. 21 is valid only for the time interval of the test at 1.92 in.-min^{-1} cross-head speed. Now for a check, the load-time curve for a specimen run at 4.87 in.-min^{-1} crosshead speed was calculated. Substituting the transform of Eq. 20 and Eq. 21 into Eq. 15 gives

$$\frac{\overline{P}(p)}{b} = \frac{159(p + 109)(p-2.40)(6.09)}{p^2(p + 16.9)(p-6.09)(2.40)} .$$ (22)

Taking the inverse transform of Eq. 22 leads to

$$\frac{P(t)}{b} = 405 \left[2.54t - 0.769 + 0.271e^{-16.9t} + 0.48e^{6.09t} \right] .$$ (23)

The plot of Eq. 23 is shown in Fig. 5 along with the experimental results of the test run at 4.87 in.-min^{-1}. The two curves give satisfactory agreement at small deformations, but the disagreement is quite large at the larger deformations.

The stresses at the center of the viscoelastic disk, which would be determined in the same manner as the applied load, can not be determined at this time, since the elastic stresses determined experimentally do not cover the full range of the test. An extension of the experimental measurement of the elastic stresses to larger deformations will be attempted using a grid method.

DISCUSSION

The test is not as simple as was originally thought. Two main factors contribute to the complications: (1) the stress ratio at the center of the disk changes as the loading points undergo large deformations and (2) the stresses in the viscoelastic disk are not the same as for the elastic disk due to the mixed boundary conditions and time dependent surface of contact.

In comparing the load-time curves calculated by use of the assumed analogy to the curves recorded during the test (Figs. 5 and 6), it can be seen that good agreement was obtained for small decreases in the major axis. However, for larger decreases in the major axis the theoretical curve increases faster than the experimental curve. This could possibly be caused by a slow gradual failure taking place which would cause the load in the test to be lower than the theoretical curve. So far this investigator has been able to detect failure by visual means only, since the recorded data gives no indication of when the failure occurs. This visual method makes the checking of the above source of error difficult. The techniques will be reviewed and improved in an attempt to reduce the error which still exist.

The experimental measurement of the stresses for the elastic disk has not yet been extended to cover the large deformations that occur during the testing of the viscoelastic disk. The existing curves are only valid for tests run fast enough or at low enough temperatures to produce failure in the viscoelastic disk within the range of the elastic stress solution.

Any future work that will be done on extending the elastic measurements to larger deformations will be done with a grid method analysis. Since the flat surfaces of the specimen are not parallel at large deformation of the loading points and the fringes become very numerous and difficult to count, the photoelastic technique would become very tedious.

REFERENCES

1. J. E. Fitzgerald, "A Bi-Axial Stress Test for Solid Propellants", Bulletin of the Joint Meeting JANAF Panels of Physical Properties and Surveillance of Solid Propellants, September, 1960.

2. S. Timoskenko and J. N. Goodier, "Theory of Elasticity" McGraw-Hill, New York, 1951, pp. 107-8.

3. N. I. Muskhelishvili, "Some Basic Problems of the Mathematical Theory of Elasticity", P. Noordhoff, Gronengen, Holland, 1953.

4. M. M. Frocht, "Photoelasticity", John Wiley & Sons, New York, 1957.

5. E. H. Lee, "Viscoelastic Stress Analysis", Proceedings of the First Symposium on Naval Structural Mechanics, Pergamon Press, New York, 1960.

6. E. H. Lee and J. R. M. Radok, "The Contact Problem for Viscoelastic Bodies", J. Appl. Mech., Setpember, 1960, pp. 438-44.

7. H. A. Stuart, "Die Physik der Hochpolymeren, Band IV, Theorie and Molekulare Deutung Technologischer Eigenshaften von Hochpolymeren Werkstoffen", Springer, Berlin, 1956.

8. M. L. Williams, P J. Blatz, and R. A. Schapery, "Fundamental Studies Relating to System Analysis of Solid Propellants", California Institute of Technology, GALCIT 101 Final Report, February, 1961.

Long Beam   Circular Disk   Long Column

Ratio of principal stresses, Tension/Compression

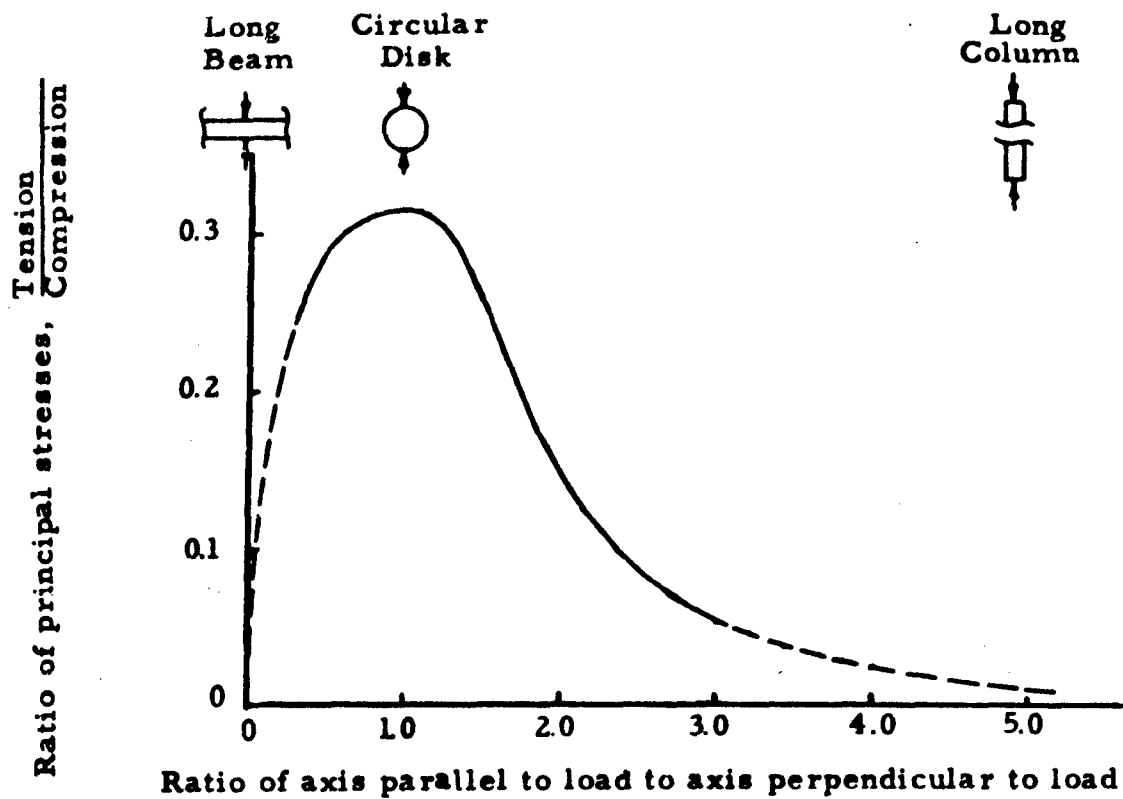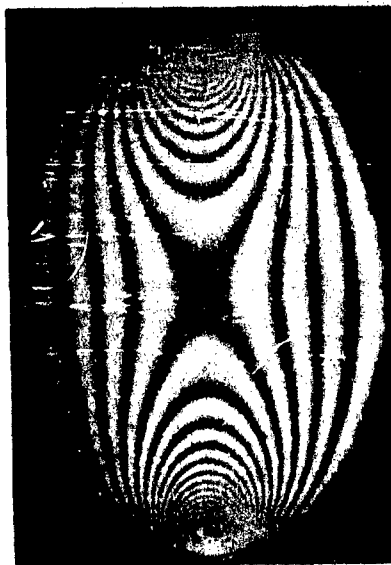Ratio of axis parallel to load to axis perpendicular to load

FIGURE 1. THEORETICAL RATIO OF PRINCIPAL STRESSES AT CENTER OF ELASTIC DISK

3.5% Decrease in Major Axis   10.9% Decrease in Major Axis
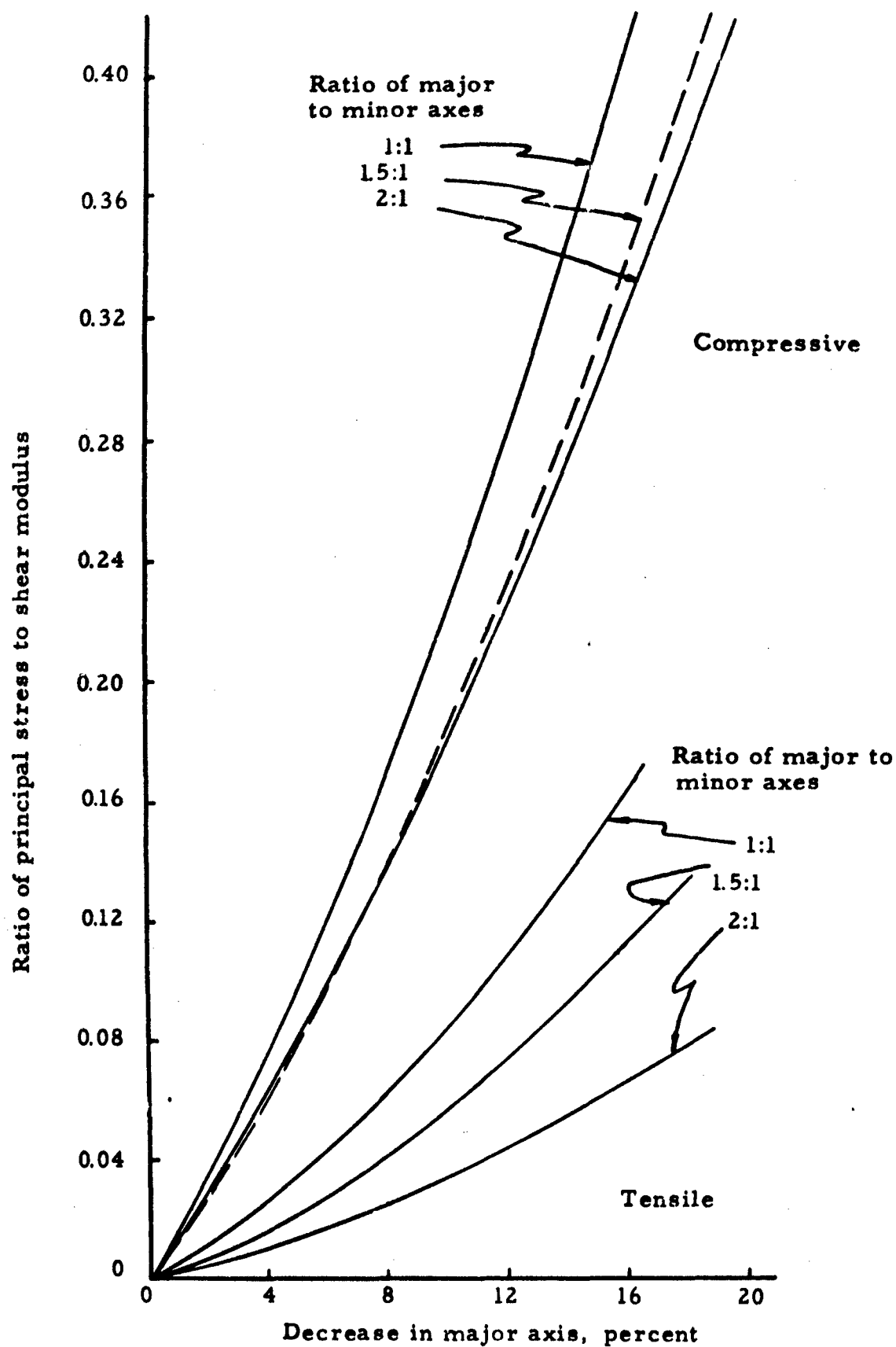
FIGURE 2. ISOCHROMATIC PATTERN FOR ELASTIC DISK

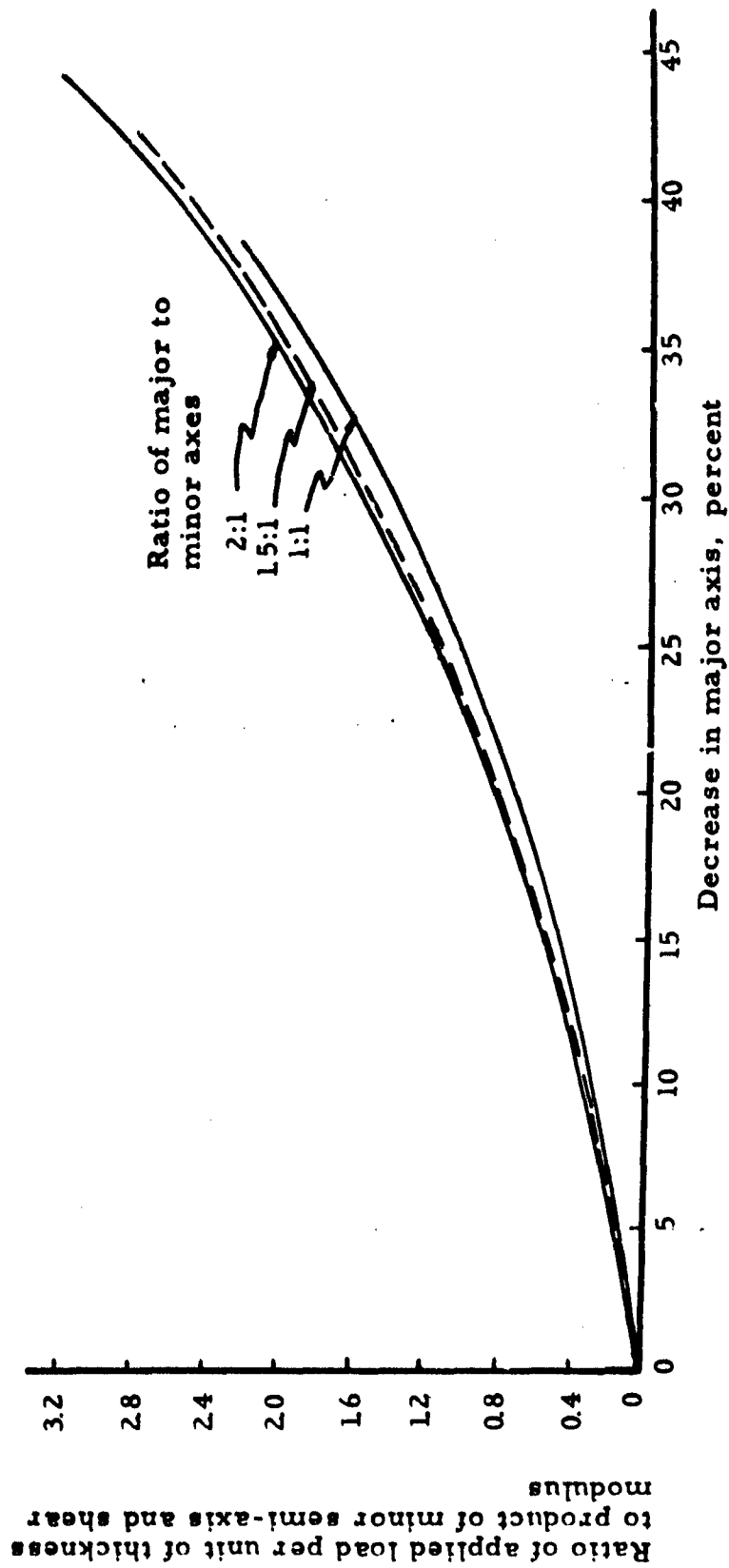FIGURE 3. EXPERIMENTAL PRINCIPAL STRESSES AT CENTER OF ELASTIC DISK

FIGURE 4.   EXPERIMENTAL LOADS REQUIRED TO PRODUCE GIVEN DISPLACEMENTS ALONG MAJOR AXIS OF ELASTIC DISK
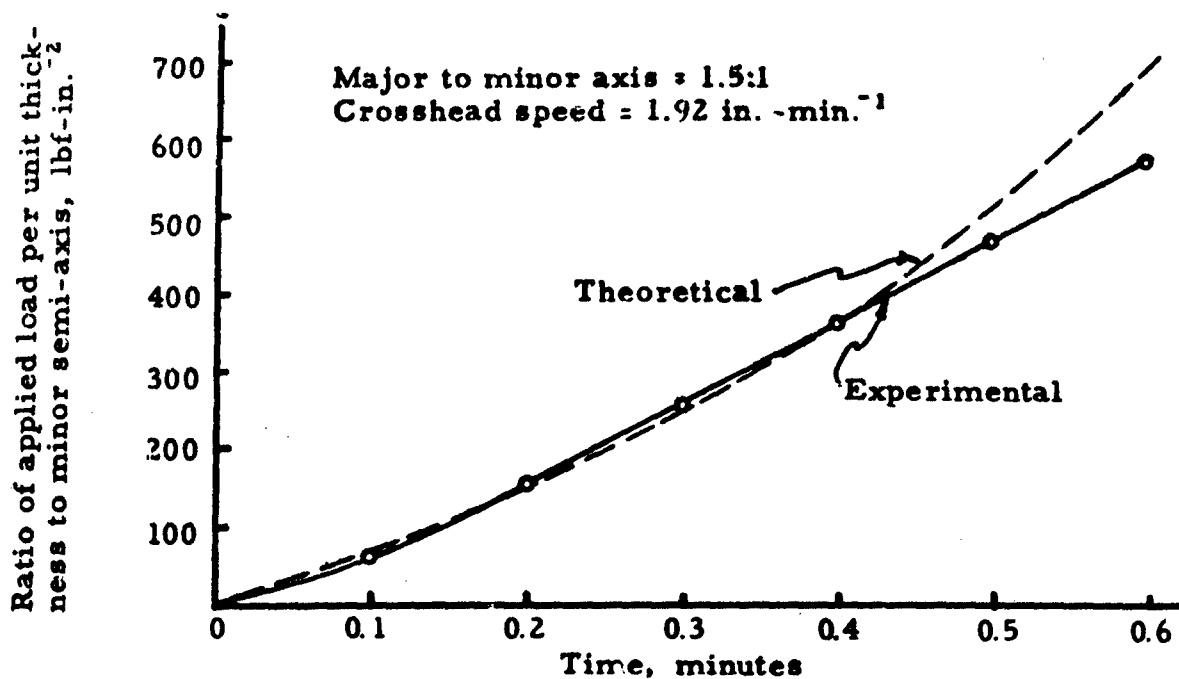
FIGURE 5.
COMPARISON OF LOAD-TIME CURVES FOR A VISCOELASTIC
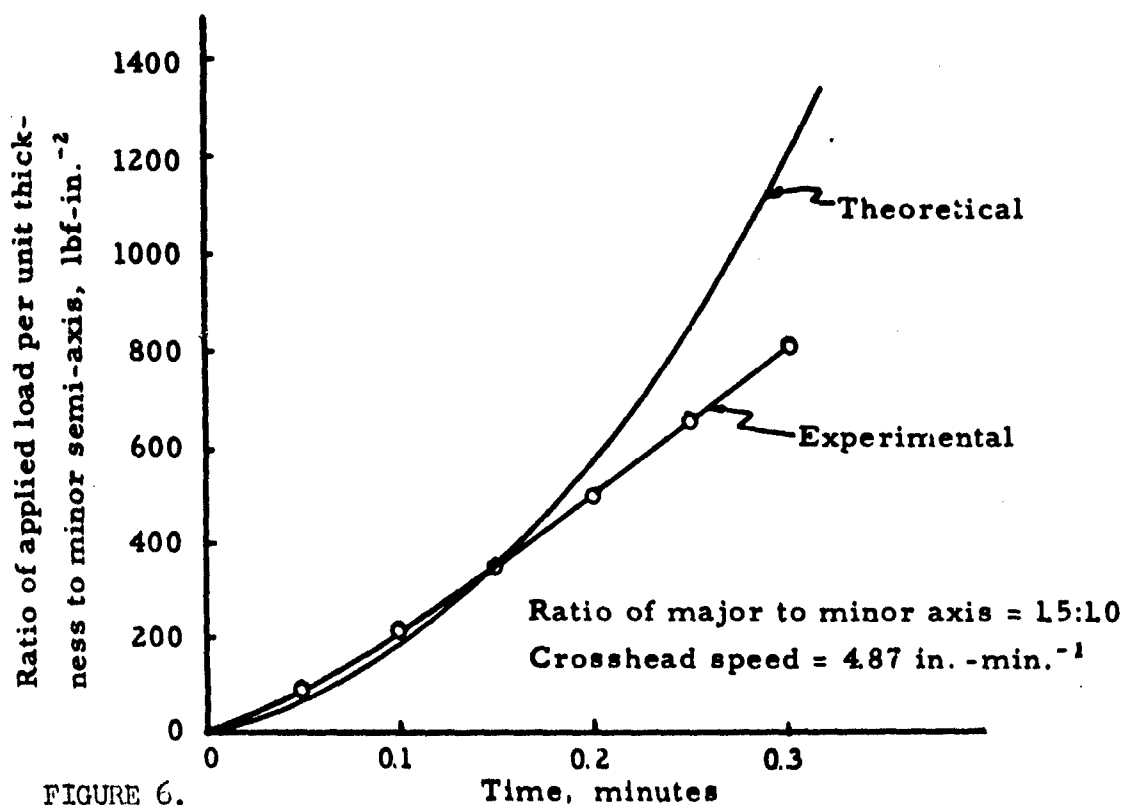DISK DETERMINED EXPERIMENTALLY AND BY INTEGRATION

FIGURE 6.
COMPARISON OF LOAD-TIME CURVES FOR A VISCOELASTIC DISK
DETERMINED EXPERIMENTALLY AND BY LAPLACE TRANSFORMS

AN EXPERIMENTAL TECHNIQUE FOR DETERMINING THE DYNAMIC TENSILE MODULUS OF VISCOELASTIC MATERIALS

D. E. Nicholson
D. S. Blomquist
R. H. Lemon

HERCULES POWDER COMPANY
Bacchus Plant
Magna, Utah

ABSTRACT

This paper describes a vibrating reed test for the determination of the dynamic tensile moduli of a solid propellant. The analysis used in reducing the experimental data to plot storage moduli and loss tangent vs frequency is that of Bland and Lee for linear viscoelastic materials.

An experimental technique is presented that is simple to conduct, yet provides valuable, analyzable information. The results presented were gathered at ambient temperature. Tests were conducted on various sample configurations to obtain the optimum length to width ratio.

The information obtained in this test provides the analyst with one of the basic properties required to determine the stress distribution to characterize a propellant within the bounds of the theory of linear viscoelasticity.

INTRODUCTION

Hercules Powder Company is conducting a program to characterize composite double base propellants. The application of the linear theory of viscoelasticity to this investigation requires that at least two of the four parameters of Lame's equations be measured. The test procedure presented is for one of these parameters: complex tensile modulus. The complex tensile modulus $(E^*(i\omega))$ is composed of two parts for a viscoelastic material, such as propellant. First, the storage modulus $(E'(\omega))$ is the stress in phase with the strain divided by the strain. A measure of the stress 90 degrees out of phase with strain divided by the strain is termed the loss modulus $(E''(\omega))$. The relationship of these parameters to the complex modulus is given by:

$$E^*(i\omega) = E'(\omega) + i\,E''(\omega) \qquad i = \sqrt{-1}$$

The ratio of loss to storage moduli $\dfrac{(E'')}{(E')}$ is by definition the loss tangent, which is a measure of the energy dissipated to the energy stored in cyclic deformation. The loss tangent determines such mechanical properties as damping of free vibrations, attenuation of propagated waves, and the frequency width of resonance response.

It is the ratio of the amplitudes, A, between the free and clamped ends and the phase lag, ϕ of the free end behind the clamped end that are significant. These are given by:

$$Ae^{-i\theta} = \frac{\cosh \psi + \cos \psi}{1 + \cosh \psi \cos \psi}$$

or more explicitly

$$A = \sqrt{\frac{C_1^2 + C_2^2}{C_3^2 + C_4^2}} \tag{3a}$$

$$\theta = - \text{Tan}^{-1}\left[\frac{C_1 C_4 + C_2 C_3}{C_1 C_4 - C_2 C_4}\right] \tag{3b}$$

where if $\psi = x + iy$

$C_1 = \cosh x \cos y + \cos x \cosh y$

$C_2 = \sinh x \sin y - \sin x \sinh y$

$C_3 = 1 + \cos x \cosh x \cos y \cosh y + \sin x \sinh x \sin y \sinh y$

$C_4 = \sin x \cosh x \cos y \sinh y - \cos x \sinh x \sin y \cosh y$

The real and imaginary components of the dimensionless compliance are obtained from equation (2) as follows:

$$R(\psi^4) = x^4 (1 - 6D^2 + D^4) \tag{4a}$$

$$I(\psi^4) = 4x^4 D (1 - D^2) \tag{4b}$$

where

$$D = \text{Tan}\left[\frac{\text{Tan}^{-1}(E''/E')}{4}\right]$$

and $\psi = x + iDx$

Equation (2) is needed in inverted form to solve for $E^* = E' + i E''$ in terms of ψ. This form is:

$$E' + i E'' = \frac{m \omega^2}{I} L^4 \psi^{-4} \tag{5}$$

For purely elastic materials the stress is in phase with the strain. However, as indicated in the above equation, there exists a component of stress which is out of phase with strain for viscoelastic materials. Therefore $E'(\omega)$ is associated with the elastic component of the modulus while $E''(\omega)$ is a function of the viscous component of the modulus.

Basic theory for the test is that derived by Bland and Lee[1]. However, this relatively complex theory has been reduced to an equation that can be solved by a laboratory technician. Herein lies a major asset of this test.

Test results are for CYH propellant, a composite double-base formulation. Future investigations will include investigation of other propellants.

The need for dynamic tensile modulus information by the stress analyst confronted with the problems of structural integrity has prompted the writing of this paper.

THEORY OF THE INVESTIGATION

This paper describes calculation of the complex modulus of a linear viscoelastic material from measurements of the steady forced oscillation of a vibrating reed of the material. The calculations described are based on the theory and results of Bland and Lee. These results are applied in devising an experimental method to measure the complex modulus of the linear viscoelastic material as a function of frequency.

The method is based on measurements of the relative amplitude and phase lag of the motion of the free and driven ends of the reed. The analysis is based on a general linear viscoelastic law, and takes into account the influence of the frequency dependent moduli of the material on the frequency and amplitude of the resonance peaks.

Bland and Lee show that the governing differential equation for the vibration of an elastic rod at angular frequency, ω, is:

$$\frac{\partial^4 y}{\partial x^4} - \frac{m\omega^2 y}{I E^*} = 0 \tag{1}$$

where m is the mass per unit length of the rod, I is the second moment of the cross-section, and E^* is the complex modulus of the material.

For the case of a reed clamped at the driven end and free at the other end, the solution of equation (1) at $x = L$ (where L is the length of the reed), is:

$$y = W \frac{\cosh \psi + \cos \psi}{1 + \cosh \psi \cos \psi} e^{i\omega t}$$

where

$$\psi^4 = \frac{m\omega^2}{I E^*} L^4 \tag{2}$$

and

W = the amplitude of the clamped end

Using these results, a graphical solution for the complex modulus is possible when a set of experimental data is given.

Equations (3) establish a one-to-one correspondence between the amplitude ratio and phase lag at a given frequency and the real part of the dimensionless compliance, $R (\psi)^4$, and the loss tangent, E''/E', of the viscoelastic material at the same frequency. With the mass density of the viscoelastic material, specimen dimensions, and frequency all known, the complex modulus is readily calculated from Equation (5) by using the dimensionless compliance ψ^4 found from the graph in Figure 1.*

An example of this correspondence is shown by the dotted lines in Figure 1. If for a given frequency $\omega = 15$ cps, the corresponding amplitude ratio and phase lag are found to be $A = 2.94, \theta = 1.10$, then the values $R (\psi)^4 = 8.80$ and $I (\psi)^4 = 4.60$, are read from the figure on the abscissa and ordinate, respectively. Putting these values into Equation (5), the complex modulus for that particular frequency is obtained.

EXPERIMENTAL PROCEDURE

The objective of this investigation was to obtain a continuous measurement of dynamic tensile modulus over a large frequency range. Previous investigators, (Nolle[2], Strella[3], and Newman[4]), have measured the complex tensile modulus at the resonant frequency with similar devices. This limitation is not inherent in the theory development by Bland and Lee, which was the basis for this investigation.

A propellant specimen, in the form of a cantilever beam, was suspended in a vertical position. Figure 2 is a photograph of a sample in place. The fixed end of the beam was held on an aluminum sample holder by means of a compatible epoxy adhesive. Suspension was vertical to minimize gravitation effects, thus avoiding slump in the traverse direction. Three different length to width (L/D) ratios were tested to determine minimum ratio of the specimen configuration under investigation. This search was initiated for two practical reasons: 1) the difficulties of machining specimens of the configuration used are proportional to the length; and 2) the force required to excite the specimen is reduced as L/D decreases. Both these factors had a pronounced effect in selecting the specimen configuration, which was 1/4 in. square with lengths ranging from 2-1/2 to 4 in.

A single test consisted of sinusoidally forcing the fixed end of a vertical cantilever beam (reed) of propellant at a constant double amplitude.

---

* This plot is but a portion of that required to find E* over the entire frequency range. A complete plot would be one in which $R (\psi)^4$ and $I (\psi)^4$ have magnitudes of 360 and 150 respectively.
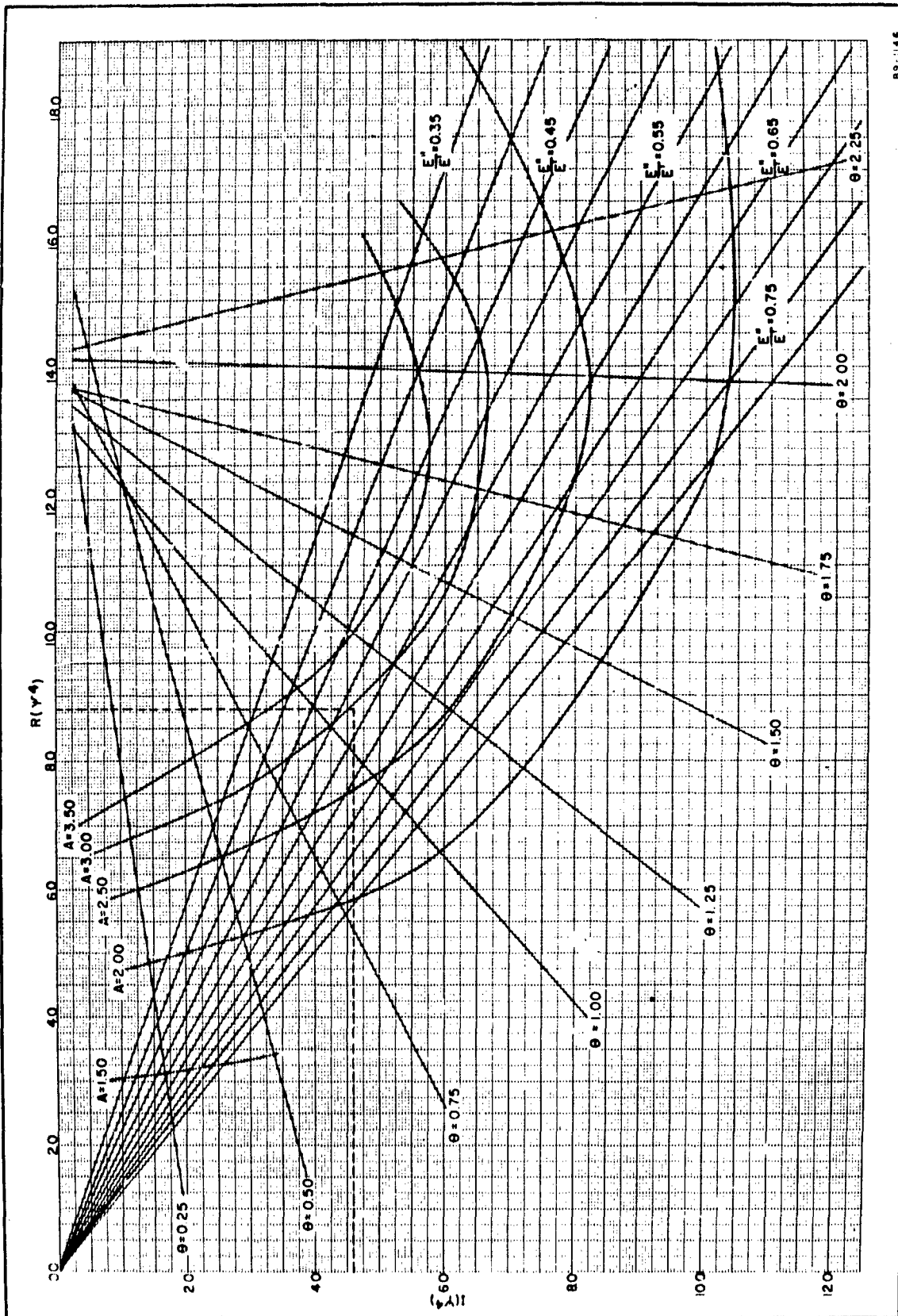
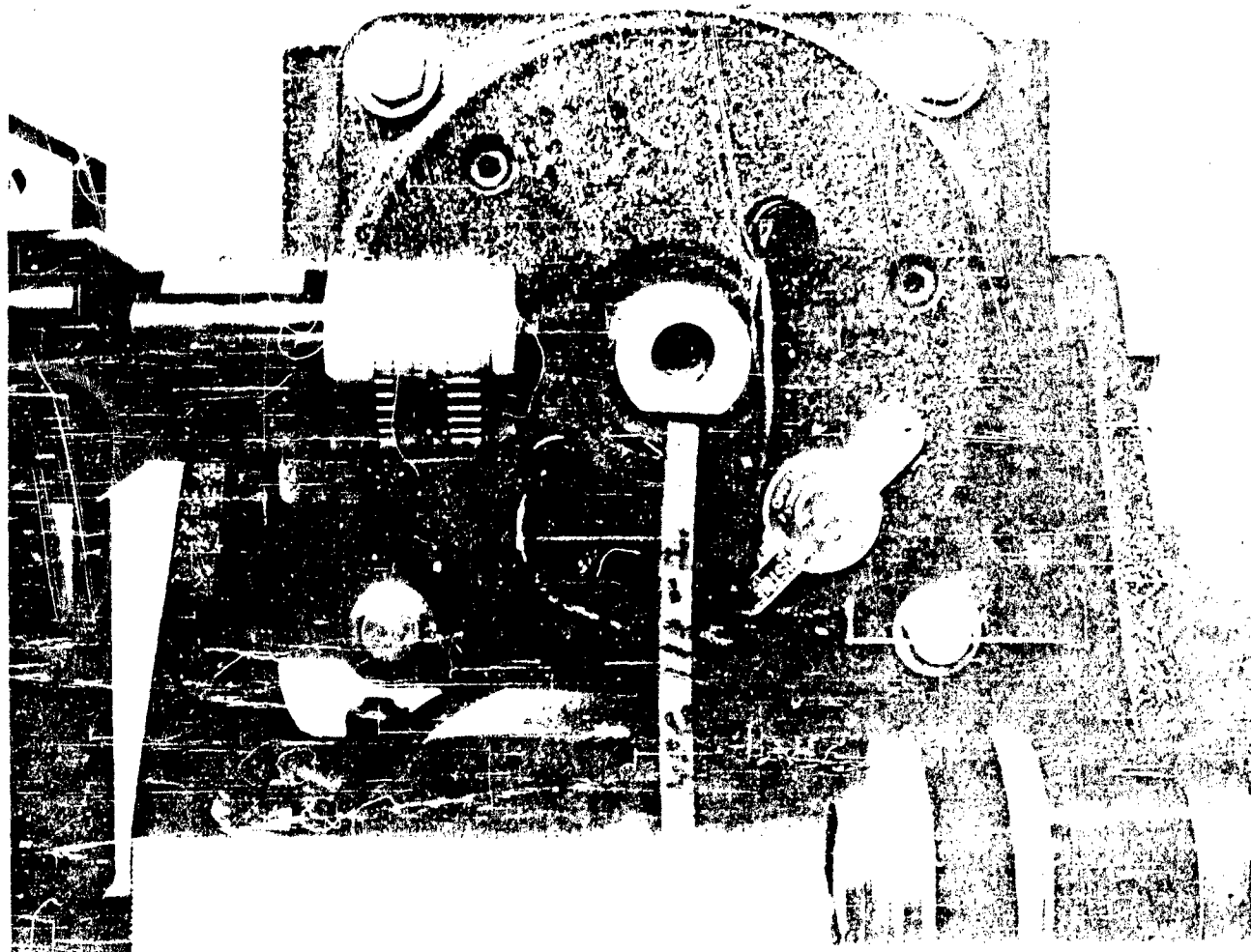FIGURE 1. GRAPHIC SOLUTION TO THEORY OF BLAND AND LEE

FIGURE 2. PROPELLANT SPECIMEN ON ELECTRODYNAMIC SHAKER

Frequency was limited to a range of 10 to 200 cps by the instrumentation. At discreet frequencies over the range investigated, the amplitude ratio (displacement of free end to displacement of fixed end), was recorded. Simultaneously, a measurement of the phase angle between the fixed and free ends was made by monitoring the output of two Optrons on an oscilloscope. (Optrons are optical displacement transducers with a photocell servo loop. A small light spot follows the motion of the beam, giving a voltage output directly proportional to the motion being measured.) A small aluminum target was mounted on the free end of the beam for efficient Optron tracking.

The voltage output of the Optrons was determined by a vacuum tube voltmeter (VTVM). To avoid the need for corrections due to different calibration factors between two meters, one VTVM was alternately used to measure both peak input and peak output voltages.

The phase angle was determined using an oscilliscope with a dual-channel plug in. The input and output signals were superimposed to allow complete monitoring of the signals and calculation of phase angle. The period was measured by expanding one complete cycle over the face of the oscilliscope. The trace was then expanded with a 5x magnifier, allowing the time interval to be measured. Phase angle (ϕ) may be calculated knowing that;

$$\theta = \frac{\text{Time Interval}}{\text{Period}} \times 360^0$$

where time interval is the time elapsed between a common point on two superimposed sine waves and period is the reciprocal of frequency.

A frequency sweep was made from 10 to 200 cps. A plot was made of the output analog voltage, allowing a direct correlation between frequency and amplification ratio. In order to avoid heating of the sample via the shaker, the tests were run as rapidly as possible consistent with obtaining accurate data. As a check for heating, fatigue, and instrumentation drift after each run, a return to low frequency was made, and amplification ratio and phase angle were again measured. Testing was in a 70 $\pm 2^{\circ}$ F temperature-controlled room.

A block diagram of the test setup is shown in Figure 3.

1. HEWLETT PACKARD 200J – OSCILLATOR
2. MCINTOSH MI-200AB – 200 WATT POWER AMPLIFIER
3. GOODMAN 390A – 25LB FORCE ELECTRODYNAMIC EXCITER
4. OPTRON 701-242 – OPTICAL DISPLACEMENT TRANSDUCER
5. BRUEL & KJAER 2409 – VACUUM TUBE VOLTMETER
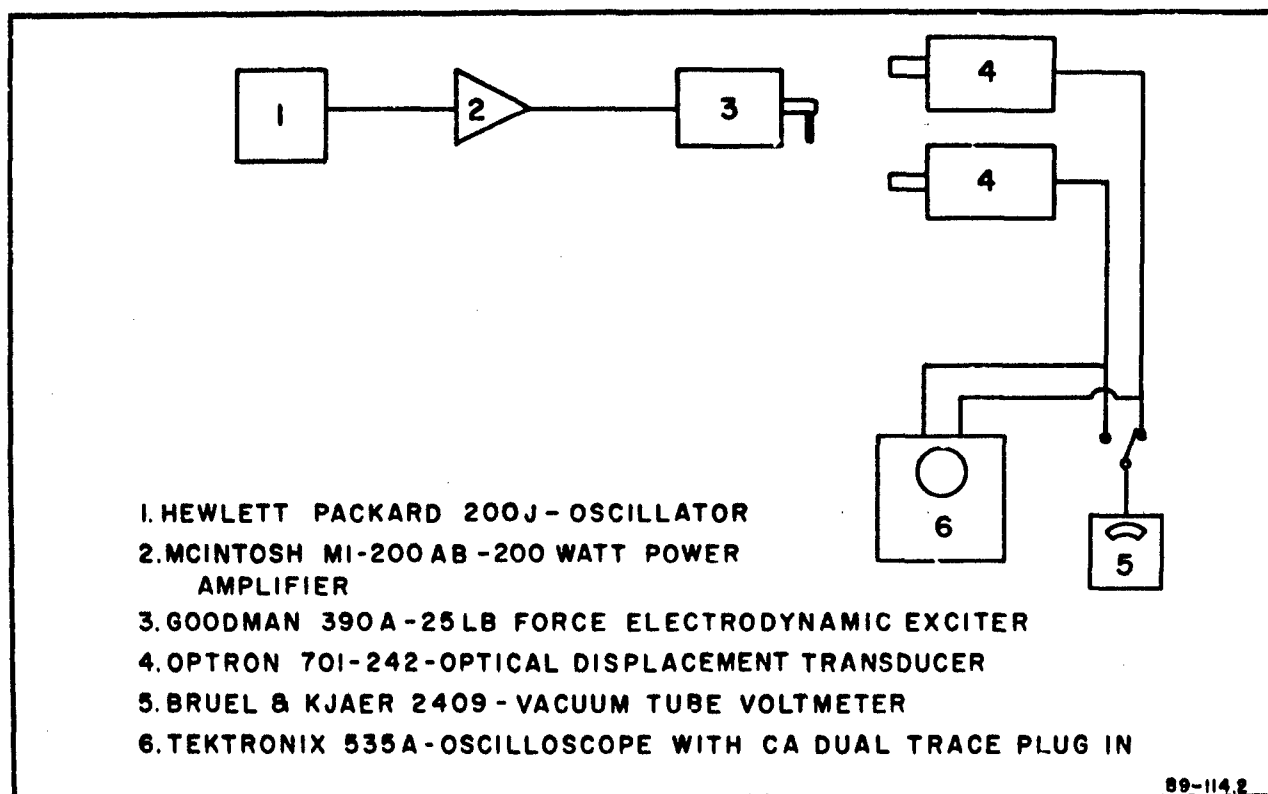6. TEKTRONIX 535A – OSCILLOSCOPE WITH CA DUAL TRACE PLUG IN

89-114.8

FIGURE 3. BLOCK DIAGRAM OF VIBRATING REED MECHANISM

RESULTS OF TESTS

The data presented is for three L/D ratios and three sinusoidal displacements. The L/D ratios and excitation amplitudes are 12, 14, and 16 and 0.003, 0.0045, and 0.006, in., respectively. Results of nine tests, one for each displacement at each of the three L/D ratios, are given in Table 1.

Tests were conducted in such a way that linearity of the forcing deformations could be checked. Table I is a comparison of amplitude ratios and phase angles for each L/D ratio over the frequency range of the investigation. Clearly, if the amplitude ratio and phase angle do not change with excitation amplitude, for a given L/D ratio

and frequency, it can be concluded that the material is linear; i.e., stress is proportional to strain. The average errors for the amplitude ratio data shown are 5.7, 5.5 and 7.0 percent respectively for L/D ratios of 12, 14, and 16. This percent error can easily be reduced to within engineering tolerances.

Figure 4 is a plot of amplification ratio and phase angle vs frequency. The data shown are test results for all three L/D ratios at 0.003 in. excitation amplitude. The figure illustrates the effect of L/D on the occurance of the first resonant frequency. For L/D ratios of 14 and 16 the second resonance is also apparent. This second resonance is very wide and flat because of the high damping of the CYH propellant.

Reduced data is plotted in figures 5 and 6. Figure 5 is a plot of the storage modulus as a function of frequency; Figure 6 is a plot of loss tangent vs frequency. From these plots it is obvious the L/D ratio of 12 is in disagreement with that for L/D vaves of 14 and 16. Comparison of storage modulus data with that obtained by Thacher[5] for L/D ratios of 14 and 16 is in good agreement, if test conditions and different propellant oxidizers are considered. Based on this comparison, and the results predicted by the theory of linear viscoelasticity, an L/D ratio of 14 was selected as the minimum. The differences between L/D ratios of 14 and 16 can be attributed to sample preparation, instrumentation drift, and slight temperature variations.
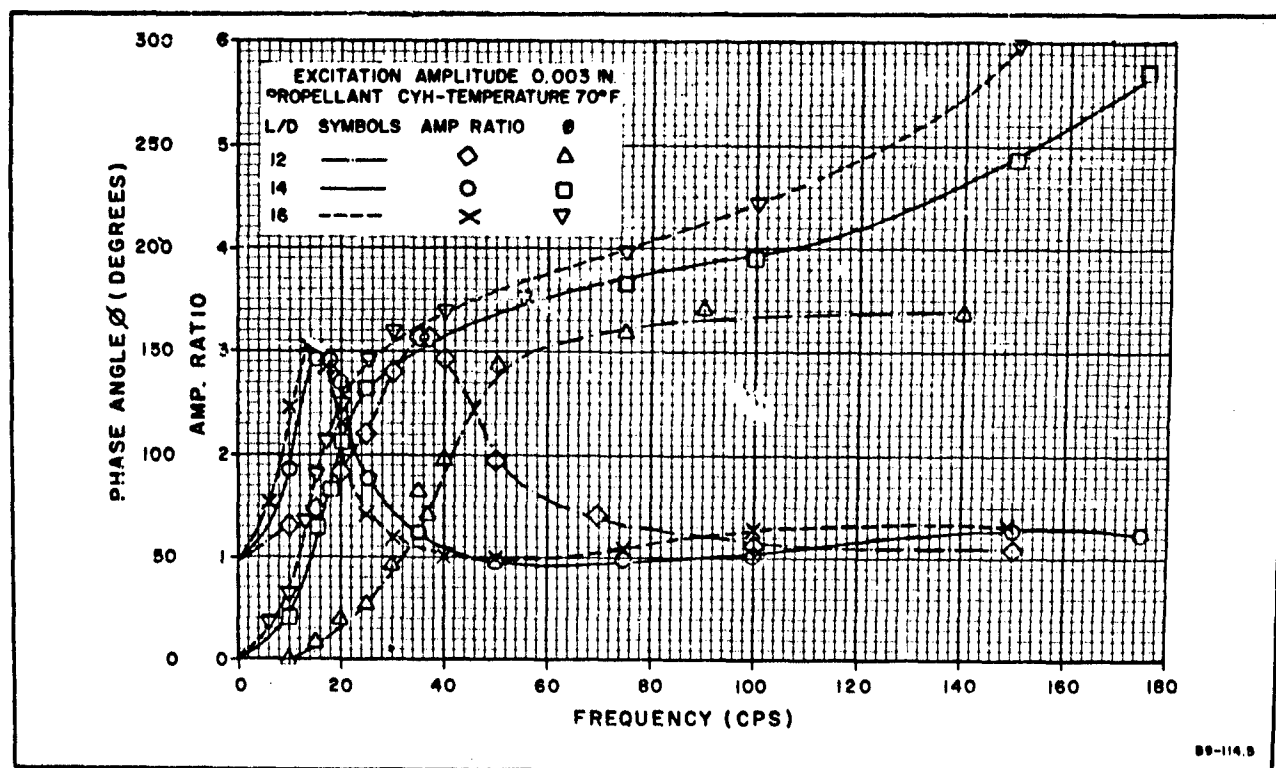

FIGURE 4. PHASE ANGLE AND AMPLITUDE VS FREQUENCY

L/D	FREQUENCY CPS	AMPLIFICATION RATIO Driving Displacement (in.)			PHASE ANGLE (DEGREES) Driving Displacement (in.)		
		0.003	0.0045	0.006	0.003	0.9945	0.006
12	10	1.28	1.27	1.37	0	0	0
	15	1.47	1.68	1.58	9.1	7.7	11
	20	1.83	1.89	1.89	20	20	19
	25	2.21	2.38	2.21	26	26	28
	30	2.84	2.80	2.84	47	50	52
	35	3.15	3.22	3.10	82	85	77
	37	3.13	3.21	3.05	72	85	77
	40	2.94	3.08	2.73	99	99	103
	50	1.97	2.09	2.05	144	144	148
	75	1.43	1.47	1.42	158	158	158
	100	1.11	1.11	1.16	171	175	176
	150	1.09	1.12	1.16	168	180	183
	200	1.20	1.20	1.31	188	176	176
	10	1.30	1.40	1.41	0	0	0
14	10	1.89	1.89	1.89	18	14	17
	15	2.94	2.94	3.26	63	61	61
	18	2.94	2.94	3.10	81	83	90
	20	2.73	2.73	2.64	107	101	107
	25	1.79	1.82	1.89	131	131	128
	35	1.26	1.26	1.31	151	147	149
	50	.96	.98	.95	180	180	180
	75	.95	.98	.89	183	180	174
	100	1.03		1.1	196	202	200
	150	1.28	1.40	1.37	242	260	255
	175	1.23	1.26	1.21	284	283	283
	200	.97	.98	1.00	306	306	306
	250	.71	.78		360	360	
	15	3.15	3.19	3.15	96	85	87
16	6	1.51	1.68	1.56	18	17	17
	10	2.48	2.38	2.42	32	32	32
	13	3.05	3.22	3.12	68	64	68
	15	3.05	3.15	3.05	91	88	91
	17	2.81	2.66	2.73	107	111	106
	20	2.31	2.38	2.31	125	125	125
	25	1.47	1.68	1.47	147	149	147
	30	1.20	1.22	1.37	160	160	160
	40	1.02	1.02	1.06	170	164	164
	50	1.00	1.00	1.05	176	170	167
	75	1.07	1.09	1.26	199	199	196
	100	1.26	1.27	1.36	222	228	228
	150	1.26	1.14	1.26	298	298	298
	10	2.75	2.52	2.57	41	39	37

TABLE I. TABULATION OF AMPLIFICATION
RATIO AND PHASE ANGLE FOR VIBRATING
REED TEST OF CYH PROPELLANT
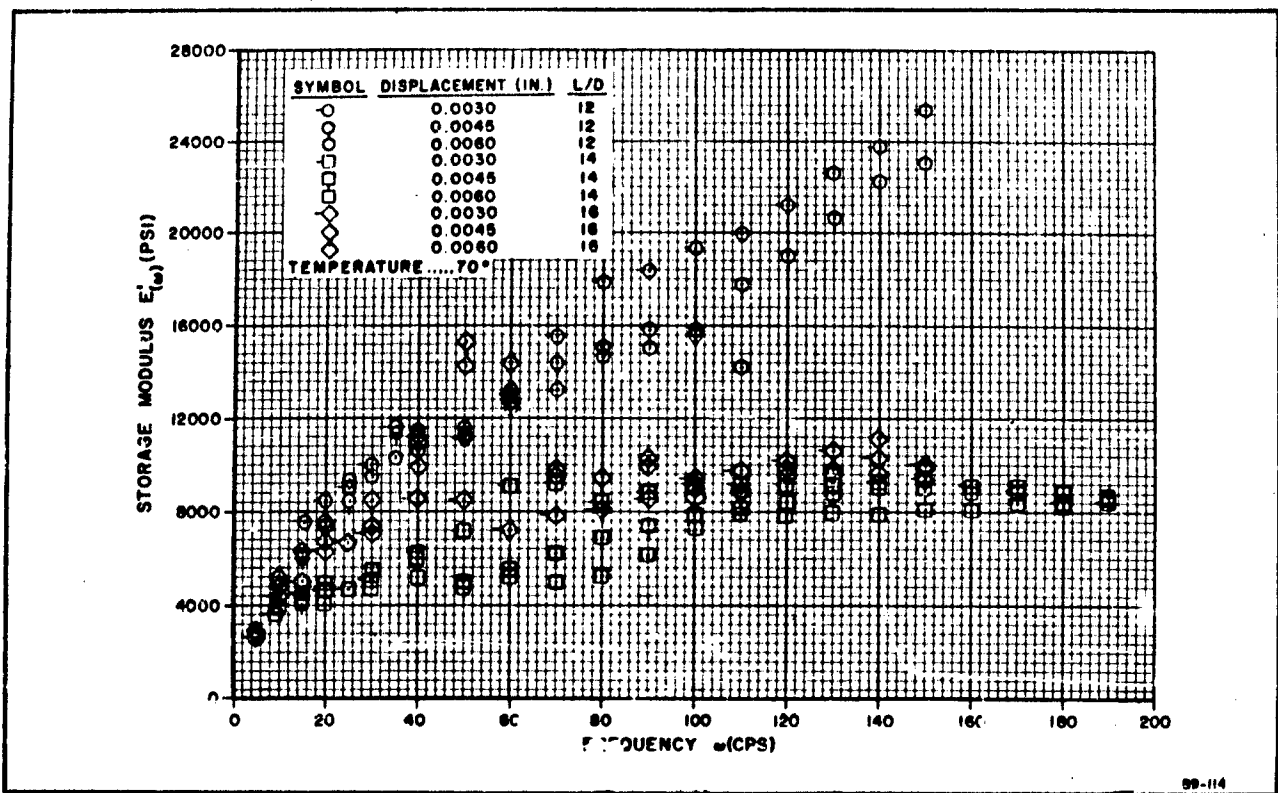TEST TEMP. 70° F ± 2° F
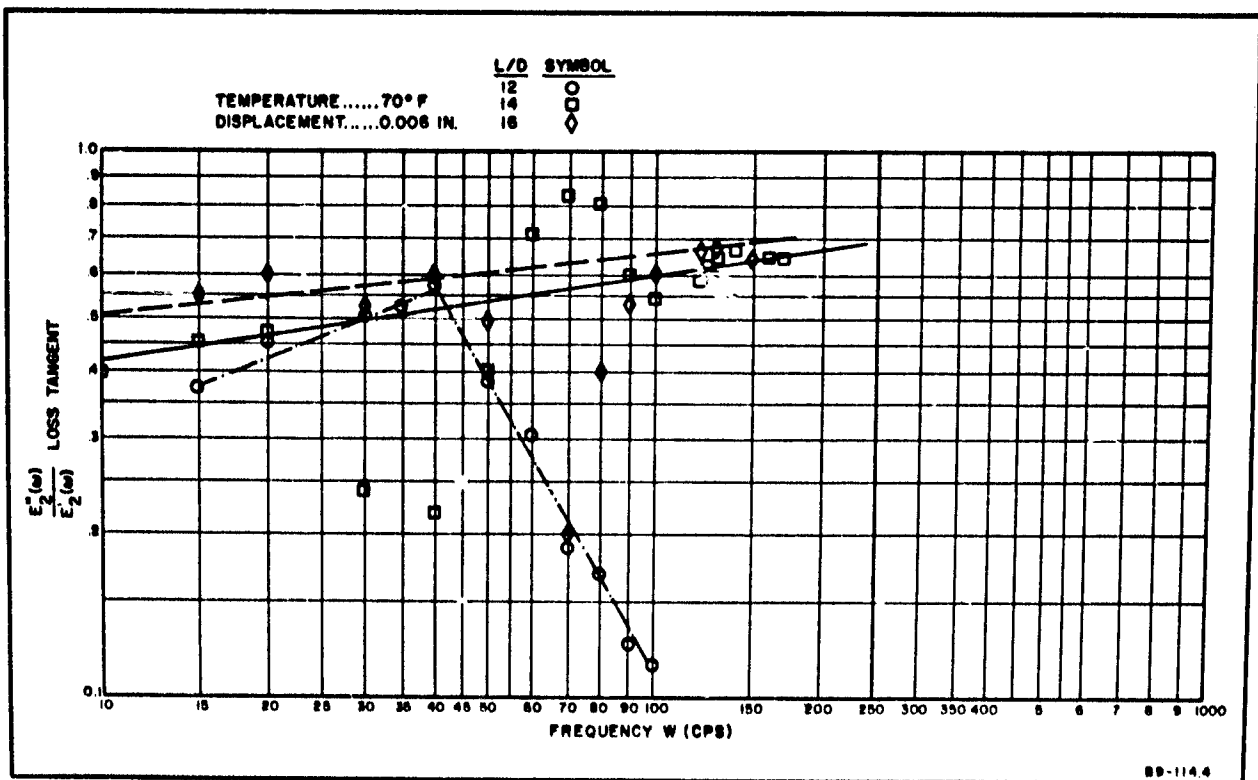
FIGURE 5.   STORAGE MODULUS VS FREQUENCY

FIGURE 6.   LOSS TANGENT VS FREQUENCY

Further examination of Figures 5 and 6 reveal a band of scatter in the data from 30 to 100 cps. This scatter can be explained by one of two phenomena. The first, and least likely, is 60 cps noise in the instrumentation. The second possible source is a lack of sensitivity in the region of antiresonance. The latter explanation is more sound, because the scatter of both Figures 5 and 6 occurs in the region of antiresonance, (see Figure 4). Similar results have been noted by other investigators in this region. No attempt is made to explain this point without further investigation.

The tests described in this paper have three adverse features: 1) expensive equipment must be used, 2) the instrumentation is complicated, and 3) the tests require long times to run. Proximity reluctance transducers are now available that cost less than 5 percent of the Optrons, thus appreciably reducing the cost. To simplify the test the instrumentation could be designed to print out results automatically. The accuracy of the test is a function of instrumentation; therefore, this should be kept in mind when selecting equipment. The required time for testing is also directly related to instrumentation. By using a sweep oscillator with servo control the time of one test could be reduced to a minute or less. This would minimize effects of fatigue, heating of sample, variation of ambient temperature and instrumentation drift. Effects of fatigue and internal heating are not well defined at this writing; therefore, it may be desirable to use this kind of test for investigation of these parameters.

CONCLUSIONS

The objectives of this test were to perfect an experimental technique for determining the dynamic tensile modulus of solid propellants over a wide frequency range. This capability has been demonstrated over a limited frequency range. Furthermore, a method for reducing the data has been demonstrated which can be handled by laboratory technicians.

Investigation has shown that the optimum L/D ratio is 14. This value represents a specimen which provides accurate data, is simple to machine and requires a minimum excitation energy.

Instrumentation of the test as conducted is expensive and imposes limitations on its capabilities. Suggestions are made as to how these limitations can be eliminated, thus providing the expermenter with an efficient, simple method for determining the dynamic tensile modulus.

Use of the results from this test, coupled with one other complex parameter, dynamic shear modulus, will allow the analyst to solve the field equations for the general theory of linear viscoelasticity. The availability of this solution should be a major step toward the solution of many problems associated with the structural integrity of large solid propellant motors.

REFERENCES

1. "The Calculation of the Complex Modulus of Linear Viscoelastic Materials From Vibrating Reed Measurements," Bland, D. R. and Lee E. H. Journal of Applied Physics, Vol. 26, pg 1947 - 1503 (Dec 1955).

2. "Methods for Measuring Dynamic Mechanical Properties of Rubber Like Materials", Nolle, A. W., Journal of Applied Physics, Vol. 19.

3. Development of Vibrating Reed Technique for Measuring Properties of Polymers, S. Strella, Pictinny Arsenal, TR 2143 March 1955.

4. "A Vibrating Reed Apparatus for Measuring the Dynamic Mechanical Properties of Polymers," S. Newman, Journal of Applied Polymer Science, Vol II; pg 333 - 3 6 (1959).

5. Research Progress Report by J. H. Thacher, Allegany Ballistics Laboratory, Feb. 1961.

6. ASTM Bulletin No. 215, Maxwell, B., July 1956.

GAUGE LENGTH IN UNIAXIAL TESTING

A. J. Ignatowski
Rohm & Haas Company
Redstone Research Division
Redstone Arsenal, Alabama

The guage length of a uniaxial tensile specimen may be deduced in a number of ways. Basically, however, all of these ways must examine the strain by some independent, external means as a function of the crosshead displacement. A frequently used method is the photographic method in which fiducial marks placed on the specimen are photographed while the specimen is elongated.

If one writes for the strain rate

$$\dot{\epsilon} = \frac{R}{L_o}$$

where R is the crosshead rate, and Lo is the effective gauge length, no assumptions are inherently included that Lo is truly a constant. That is, Lo may or may not be a function of R. On the other hand, a straight line relationship between $\dot{\epsilon}$ and R indicates that Lo is a constant. Figure 1 is a plot of photographically determined strain rates as a function of the crosshead rate. A straight line relationship exists within experimental error with a slope of unity. The intercept at R equals one inch per minute, give the effective gauge length. For the propellant examined at $77^{\circ}F$, Lo equals 3.32 inches.

Some additional data would seem to show the gauge length is temperature sensitive (therefore, probably, also, modulus sensitive). Figure 2 shows the variation of observed strain rates versus temperature at constant crosshead rate for a particular propellant. This can only be accounted for on the basis of a temperature variable gauge length.
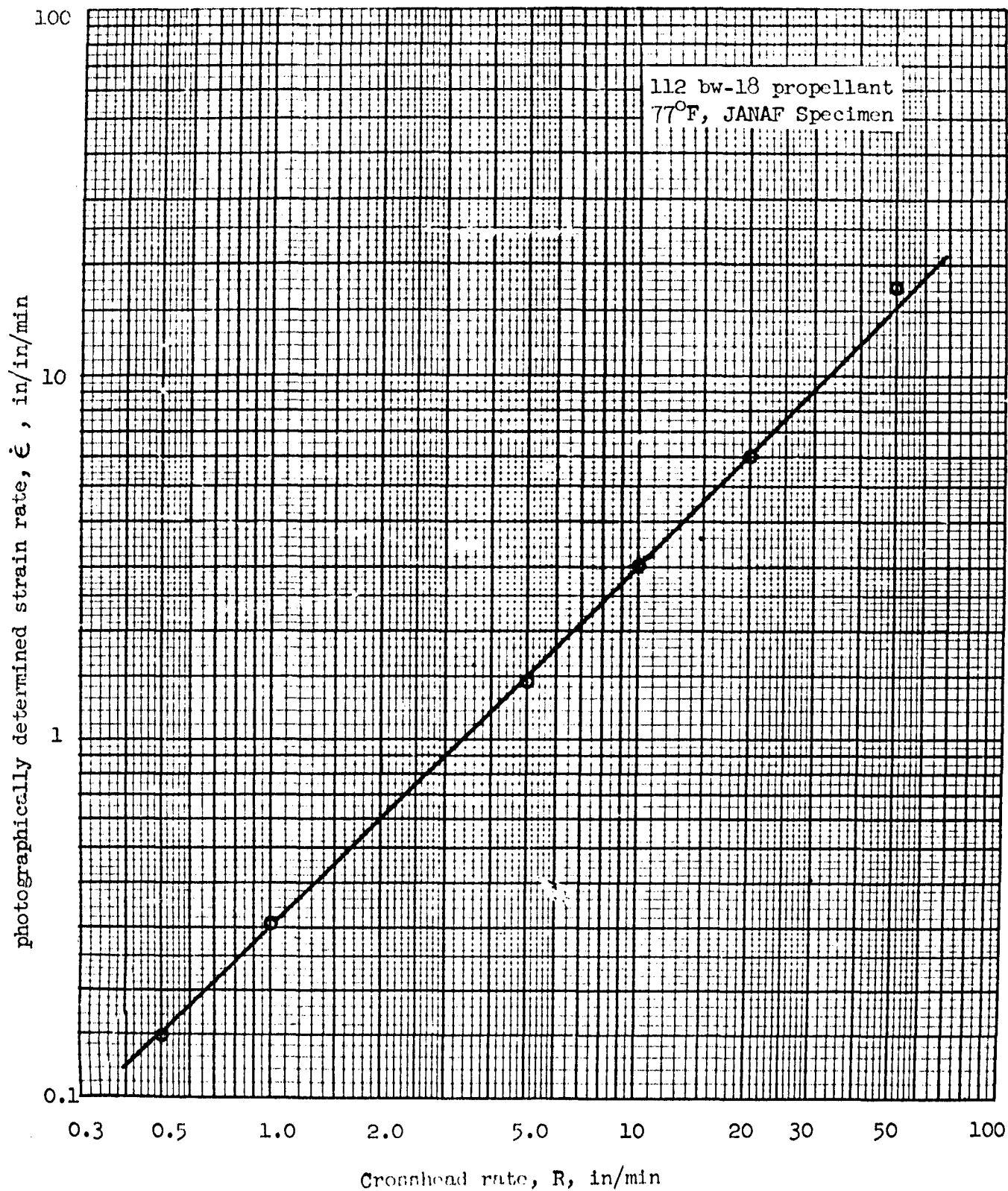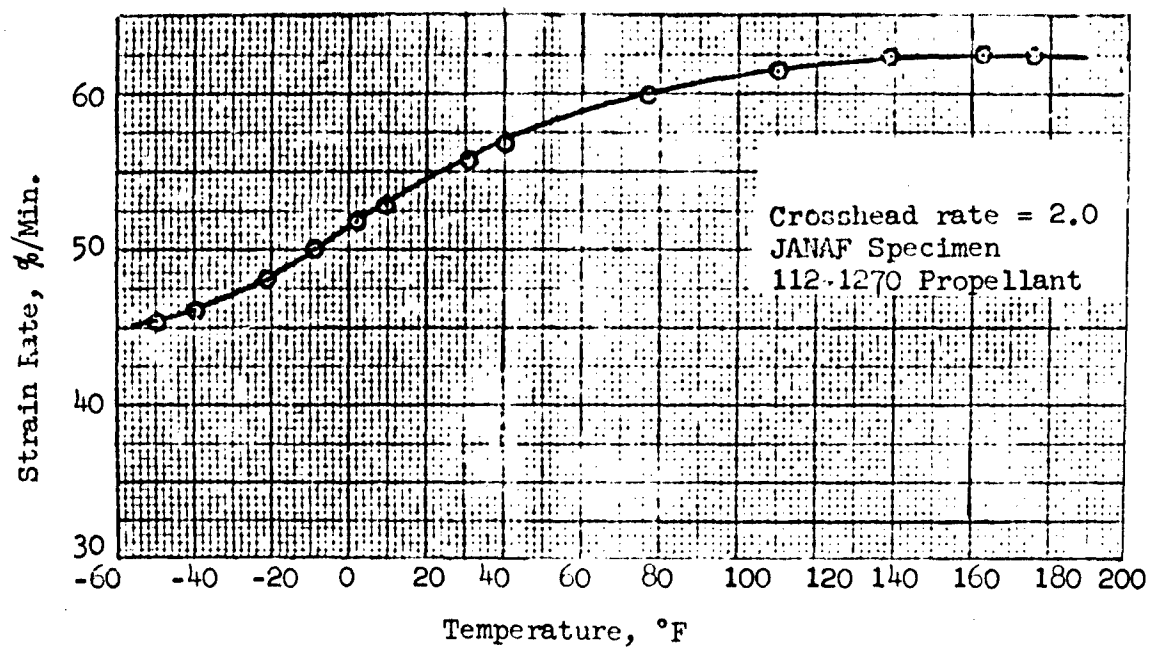
FIGURE 1.

FIGURE 2.

EFFECTIVE GAGE LENGTH MEASUREMENTS IN PROPELLANTS

T. H. Duerr

Propulsion Laboratory, ARGMA
Redstone Arsenal, Alabama

At the present time the concept of effective gage length for propellant uniaxial strain measurements should be of only historic and academic interest. The bonded end tab specimen for everything but strictly routine quality control work appears to be a major advancement in propellant mechanical property testing. However, because of the large amount of data already accumulated with JANAF specimens and the traditional reluctance toward change further examination of test data may be warranted in an effort to reach mutual agreement on the question of effective gage length.

Tests in the ARGMA Propulsion Laboratory have all been performed with JANAF die cut specimens with a thickness of approximately .30 inch. Two ink dots .020 - .030 inch diameter were placed along the center inch of the gage length section. These were photographed with a 70 mm Varitron Pulse camera during the constant cross head displacement rate tests. The film data was reduced on a Telereadex machine. Each frame was read ten times to minimize the operator error.

The effect of specimen thickness on stress-strain behavior for one type of plastisol propellant is indicated in Figure 1. These data represent three tests at each thickness except .50 inch, where only two tests are shown. It appears that the thickness has some effect on the stress, but only minor effect on the strain. Indeed, the strain effect seems in large measure the result of normal data scatter for this combination of specimen and propellant. Consequently the thickness of the specimen was not considered significant over the range of .20 - .50 inch in effecting the results of gage length determinations.

The test temperature of the specimen is likely to change the effective gage length (Le) - Figure 2 presents Le data on eleven propellant compositions as a function of temperature. Each symbol represents an average of at least five constant crosshead displacement rate tests where Le was determined at maximum nominal stress. There is no consistent trend for all propellants, however, the data appears to strongly imply that regardless of the temperature Le is in excess of 3.0 for almost any conceivable propellant of current interest. Temperature changes also result in small but definite changes in Le for a given propellant.

Time or rate of strain is the other obvious variable which could have a pronounced effect on Le determined at maximum nominal stress. For the plastisol propellant referred to previously, Figure 3 indicates the effect of reduced time on Le. These data are referred to 296 K and represent the average of three specimens tested at each condition. Although, the scatter of the data leaves small confidence in any definite trend, it is pertinent to note that over approximately 14 decades of reduced time Le is always in excess of 3.2 with only one exception.

The strain level in the test specimen has perhaps the greatest effect on Le as is shown in Figure 4. Each type symbol represents data points from one test specimen. Even well beyond the strain at maximum nominal stress, that is, close to the rupture strain, Le is always greater than 3.0. The tendency of Le in Figure 4 to approach and exceed 5.0, (the overall length of the test specimen) is somewhat fictious since the accuracy of the data reduction method is limited to about 2-3% strain.

Figure 5 shows the strain rate variation in the center inch section of a die cut JANAF specimen tested at 2.0 inch per minute crosshead displacement rate. The different symbols represent different test specimens. The dotted line represents .74 inch per minute per inch or 2.7 inches effective gage length. The experimental strain rate is always less than .74 inch per minute per inch, but does closely approach this value just prior to specimen rupture. This observation merely substantiates Figure 4. Although, the strain rate is continuously changing during the test because of jaw extrusion and seating this variability would not seem important as regards Le in light of Figure 3.

The conclusions of this study are:

a. Use of 2.7 inches for effective gage length as is commonly done results in uniaxial strain values at maximum nominal stress that are normally 15-20% higher than actually occurs in the specimen.

b. The actual effective gage length is so strain, temperature, and composition dependant in the standard JANAF (die cut) specimen that its use be discontinued in favor of some type of end bonded specimen except for the most preliminary compositional screening tests and production quality control tests.
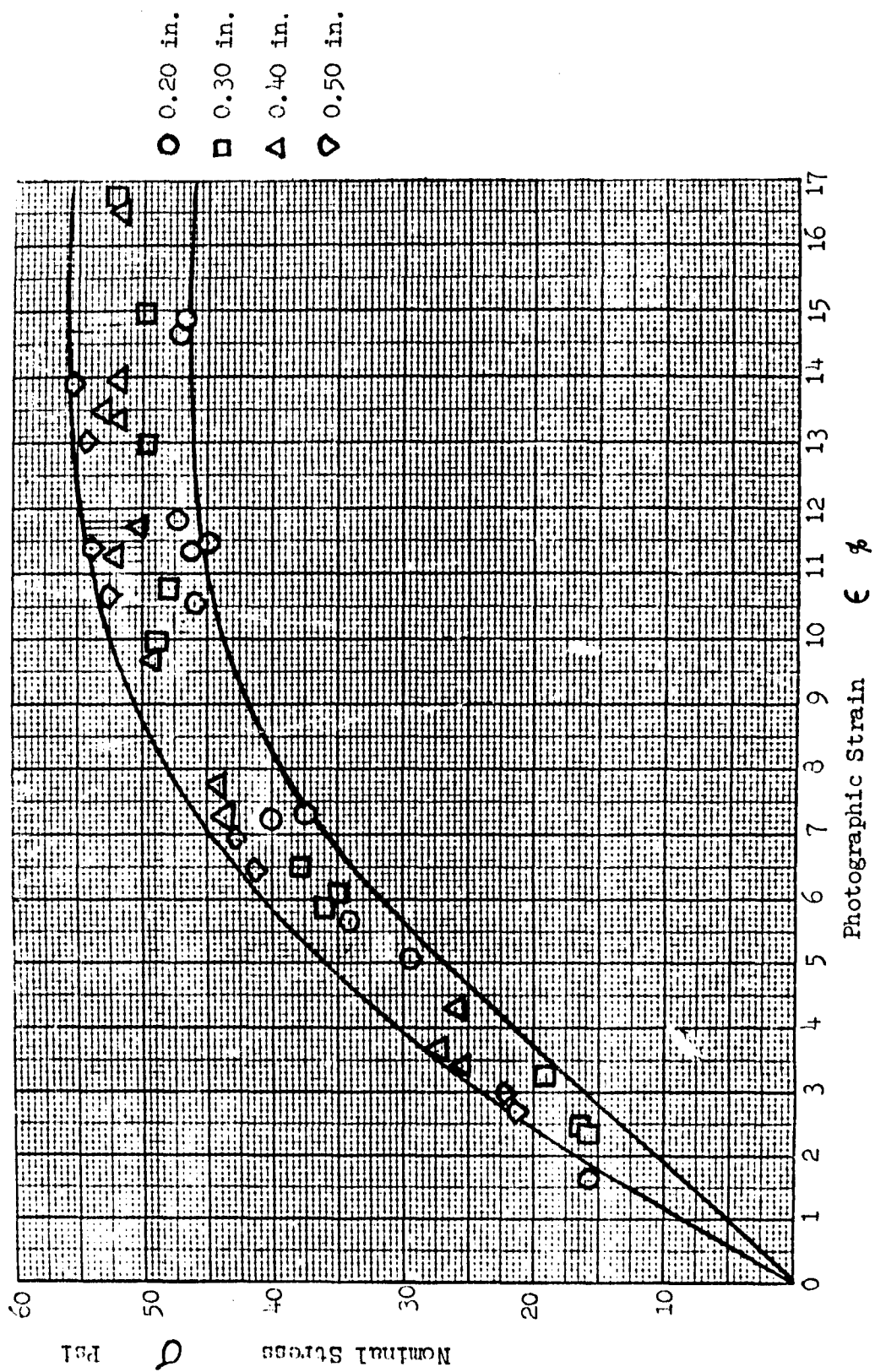
FIGURE 1.   THICKNESS EFFECT ON STRESS-STRAIN CURVE - JANAF SPECIMEN
77°F - 2.0 In/Min

Die Cut JANAF Specimens
2.0 In/Min

PBAA H 8126
CBAN
P.A. QB C55-16
PLASTISOL 102BN-55
ANP X-3 4516
P.A. QZC-67-10
PLASTISOL OMAX S-2E
NITROSOL N-6045
DMM-EX
RDS-229
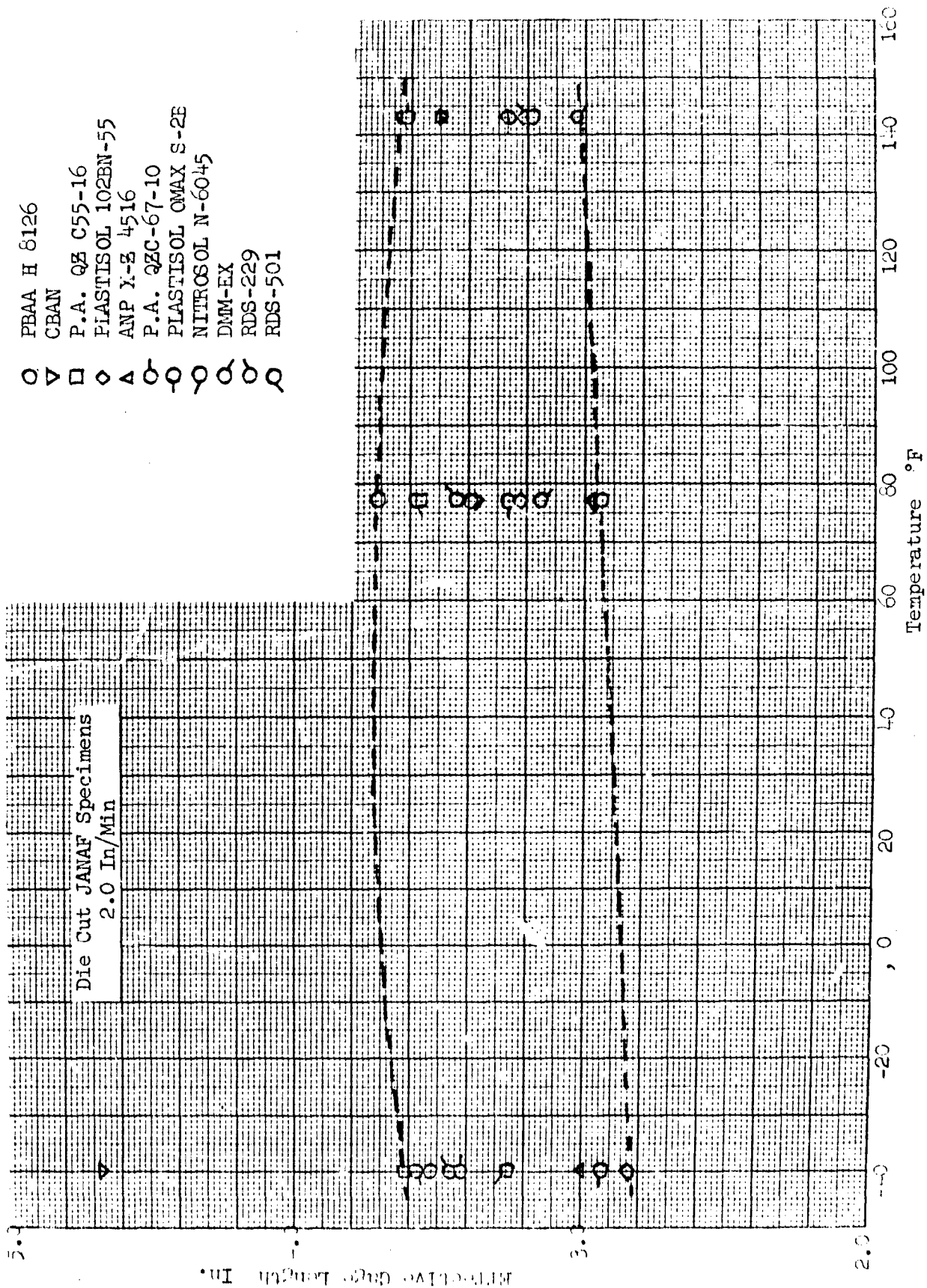RDS-501

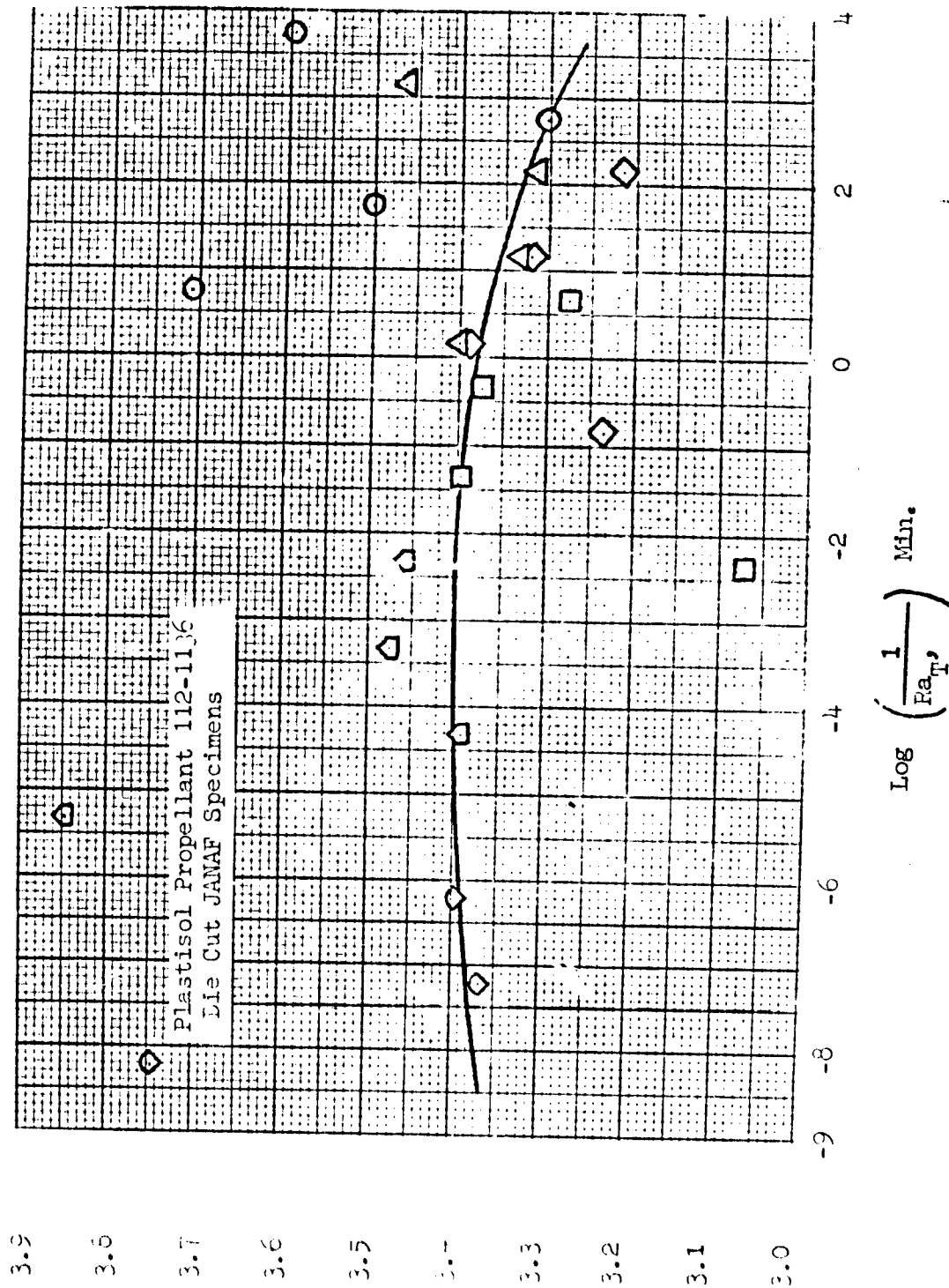Temperature °F

Effective Grip Length, In.

FIGURE 2. E.C.L. VS TEMPERATURE

FIGURE 3. EFFECTIVE GAGE LENGTH VS REDUCED TIME
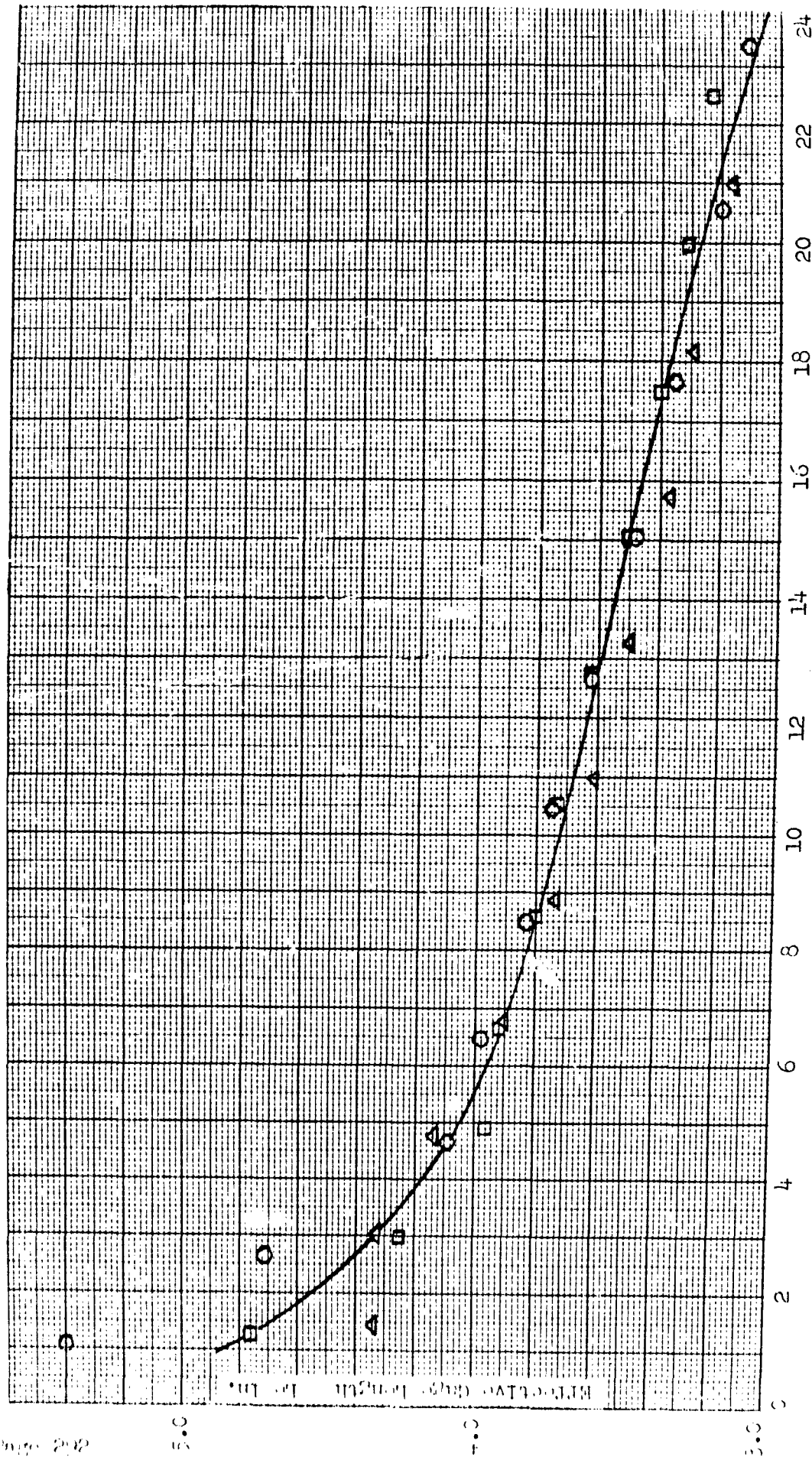
FIGURE 4. E.G.L. VS STRAIN
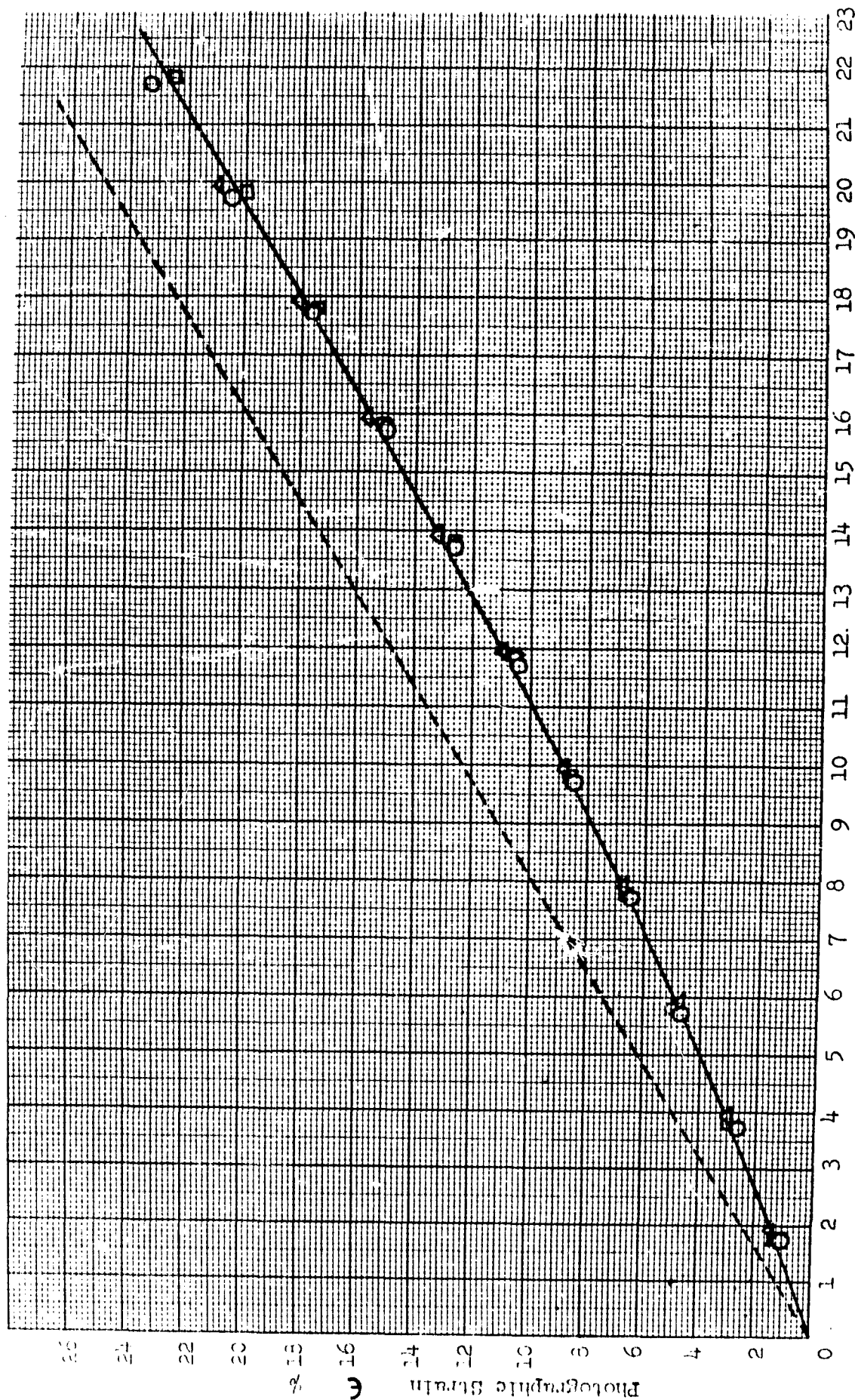Plastisol Propellant 112-1136A
73°F; 2.0 In/Min
Die Cut JANAF Specimens

Strain ε %

Effective Gage Length, L, In.

FIGURE 5. STRAIN VS TIME
Plastisol Propellant 112-1136A
73°F; 2.0 In/Min
Die Cut JANAF Specimens

VOLUMETRIC EFFECTS

S. C. Britton, Reporter

VOLUME CHANGES IN POLYURETHANE PROPELLANTS SUBJECTED TO SMALL STRAINS

G. J. Svob, P. C. Colodny, L. A. Waddle, and T. B. Lefferdink

Aerojet-General Corporation

ABSTRACT

A technique has been developed for the measurement of small volume changes in polyurethane propellants, such as those produced by thermal expansion or by strains. A small end-bonded sample is mounted in a fixture, suspended from an analytical balance, and weighed in a liquid of known density. Successive measurements can be made as the sample is strained by the fixture in small increments. Volume changes with strain and the calculated value of Poisson's Ratio have been determined for several propellants as a function of temperature, humidity and aging.

The apparatus has been also used for following the volume changes in unstrained binders and propellants as a function of temperature. From these measurements the coefficients of thermal expansion and the second order transition temperatures of both propellants and binders have been obtained.

INTRODUCTION

The application of a tensile deformation to a propellant specimen results in an increase in volume of the specimen due to the rupturing of adhesive bonds between the binder and oxidizer with the subsequent formation of voids. A knowledge of the extent of volume increase and the strain at which it begins is important to the understanding of the stress-strain behavior of the propellant in question.

In the past volume change measurements have been made using a dilatometer (1) or a modified hydrometer device (2). In addition to requiring an elaborate apparatus, these techniques are susceptible to errors produced by small temperature fluctuations and are limited in their sensitivity.

The method described here was developed with the aim of circumventing these difficulties and providing a simple, accurate technique for the routine measurement of volume changes as a function of strain.

EXPERIMENTAL TECHNIQUE

The test specimen consists of a small propellant sample (1/4" x 1/2" x 2") coated with a thin layer of polyurethane rubber and bonded endwise between rectangular shaped pieces of acrylic plastic, one of which has been drilled and tapped in two places to accept 1/8" calibrated screws (Figure 1). The specimen is suspended from the pan of an analytical balance by a thin nylon monofilament into a liquid of known temperature and density contained in a Dewar flask. A strain is applied stepwise by turning the calibrated screws a given number of revolutions thus forcing

the end pieces apart. The immersed weight is measured at strain intervals of about 0.5% until failure. For a sample having an initial volume of 5 cc a volume change of 0.004% can be detected.

TREATMENT OF DATA

The volume changes are calculated from the following relationship:

$$\Delta V = \Delta W/d_1$$

where

ΔV = volume, V, at extension, l, minus initial volume, V_o.

ΔW = initial immersed weight, minus immersed weight at extension, l.

d_1 = liquid density at temperature of measurement.

The ratio of the deformed volume can be expressed by the product of the three principal extension ratios. If we assume that the strain is isotropic the volume ratio can be given by the product of the linear extension ratio and the square of the lateral extension ratio. If we express this in terms of logarithmic strain and differentiate with respect to the logarithmic extension ratio the following relationship is obtained: (1)

$$\frac{d \ln V/V_o}{d \ln \lambda_1} = 1 + 2 \frac{d \ln \lambda_2}{d \ln \lambda_1}$$

It is sometimes convenient to define Poisson's Ratio ν, as follows:

$$\nu = - \frac{d \ln \lambda_2}{d \ln \lambda_1}$$

So that the slope of a plot of $\ln V/V_o$ versus $\ln \lambda_1$ is equal to $1 - 2\nu$ and ν is easily obtained.

It should be noted that the above method of calculation of ΔV assumes that the volume change occurs uniformly throughout the sample. This is not always the case. Some propellants have a tendency to yield in very localized bands. Since practically all of the volume change occurs in these yielded areas the number of bands formed and thus the sample size become extremely important. We are presently working on methods for determining the proportion of sample involved in the dewetting process.

INTERPRETATION OF DATA

Figure 2 shows a plot of ΔV versus strain for ANP-2639AF propellant. It is obvious that the volume begins to increase immediately upon the application of strain. Up to about 15% strain the volume changes slowly. However, above 15% strain the rate of volume change increases markedly. Figure 3 shows uniaxial tensile curves obtained from samples of this same propellant tested at the standard rate of 0.74 min^{-1} in air and while submerged in water. It can be seen that the initial moduli are identical,

but at about 15% strain the curve representing the sample tested under water departs from the standard test curve and the sample fails at lower values of stress and elongation. A similar test performed with the sample submerged in silicone oil gave results identical to those obtained from the standard test in air. Tests were also performed in which samples were cycled to continuously higher strain levels while in the contact with air, water and silicone oil. In the air and silicone oil tests the curves obtained from each cycle up to strains approaching γ_m were practically identical to the original except for a small amount of relaxation. In the case of the test under water, however, after a strain of 15% was exceeded, succeeding cycles exhibited a drastic decrease in modulus. Tensile tests performed approximately two weeks after cycling in air to strains well past γ_m have shown that the original properties were almost completely recovered. This is perhaps indicative that little or no tearing occurs within the binder during repeated straining in air.

A so called "Water Drop Test" has been developed in which tensile specimens are extended and held at various strain levels after which a drop of water is placed anywhere along the gauge section and the time to failure recorded. At strain levels above the critical strain the water reduces the time to failure by a factor of several thousand. At strain levels below the critical strain the water has little effect immediately but produces blanching after several hours.

From an examination of these data a possible mechanism for the de-wetting process emerges. In the first portion of the ΔV versus extension curve (Figure 2) the volume change is the result of the enlargement of existing voids and the formation of a small number of additional voids in areas where no bond exists between the binder and oxidizer. As the strain approaches some critical level (15% in the sample cited) the stress exerted on the binder-oxidizer bonds in the vicinity of the vacuoles formed in-itially becomes sufficient to cause rupture of these bonds. As these bonds break the stress on neighboring particles is increased and further dewetting occurs. This process continues until complete dewetting or failure is the result. When a sample in contact with water is extended beyond the critical strain, the water is sucked into the voids formed near the pro-pellant surface and, because of its solvating effect, weakens the binder between oxidizer particles thus initiating tearing with an accompanying reduction in retractive force and early failure.

EFFECT OF SPECIAL TREATMENTS

Effect of Various Fillers

Since the volume increase noted when a propellant specimen is extended is due to the formation of vacuoles as a result of the rupturing of binder-oxidizer bonds, it follows that these measurements give a good indication of the relative bond strength between the binder and various fillers.

Samples of a polyurethane binder were prepared containing the follow-ing filler loadings:

Filler	Weight Percent
NH_4ClO_4	70
NH_4ClO_4 (epoxy coated)	70
$KClO_4$	70
$KCl + NH_4ClO_4$	69 + 1
Al	80

The volume change was measured as a function of strain for each of these composites. The data are plotted in the form Log V/V_o versus Log L/L_o in Figure 4. These data indicate that aluminum forms the strongest bond followed in order by $KClO_4$, epoxy coated NH_4ClO_4, NH_4ClO_4 and KCl.

Effect of Aging

Figure 5 presents a plot of Log V/V_o versus Log L/L_o for unaged ANP-512 propellant and ANP-512 aged 4 1/2 years at 60° and 150°F. For the sample aged at 60°F the difference in dilatation can be almost entirely explained on the basis of binder-oxidizer bond degradation since both swelling data and physical properties measurements indicated very little binder degradation. The binder of the 150°F sample, on the other hand, was found to be severely degraded to the point where the small amount of binder-oxidizer interaction remaining is the principle factor in maintaining the physical form of the propellant.

Effect of Previous History

Figure 6 is a plot of Log V/V_o versus Log L/L_o for a sample of poly-urethane binder containing 50% by volume of glass beads. The sample was strained stepwise to about 11% and then the strain was released stepwise back to 0%. This cycle was then repeated twice. It can be seen that the volume recovery is practically complete as the strain is released but on succeeding cycles the slope of the curve representing the application of strain increases and approaches that of the recovery curve. Thus the necessity for stating the conditions and previous history of a sample for physical measurements such as Poisson's Ratio is quite obvious.

Figure 7 is a similar plot for a sample containing 40 volume percent glass beads cycled to increasingly higher strains. The path of the volume change retraced itself up to a critical strain of about 6%. At that point a sharp change in slope was observed and the recovery curve followed a different path. The immediate and complete reversibility noted in the first portion of the curve reinforces the belief that this initial volume change is due to inherent voids and small unbonded areas.

Effect of Humidity

From some earlier work concerned with the effect of high humidity treatment upon propellant properties (3) it was inferred that the absorbed moisture adversely affected the tensile properties by weakening the binder-

oxidizer bond. However, at that time no direct measurement of the effect was made.

Figure 8 presents a plot of volume change versus strain for a polyurethane potassium chloride composite prior conditioned at 77°F and relative humidities of approximately 0 and 60%. The dried samples did not show an appreciable volume increase until the strain level reached 10%, while the samples conditioned at 80% R.H. began to increase in volume at about 3% indicating that the binder-oxidizer bonds in the latter samples had been considerably weakened.

Similar measurements at 0° and 77°F on samples of ANP-2913 CD are represented in Figures 9 and 10. It is interesting to note that the shape of the curve obtained from the high humidity treated sample tested at 0°F is quite different from that obtained at 77°F and the volume change is an order of magnitude greater. The change in curve shape may be due to a concurrent shrinkage taking place analagous to that observed in many propellants upon storage at 0°F. The greater volume change may be due to a weakening of the binder oxidizer bond and/or a stiffening of the binder at the low temperature.

VOLUME CHANGES ON UNSTRAINED SAMPLES AS A FUNCTION OF TEMPERATURE

The buoyancy technique described earlier has been extended to the measurement of volume changes as a function of temperature with the aim of determining the second order transition temperatures and thermal coefficients of expansion of binders and propellants.

The unstrained sample is suspended from the analytical balance and submerged in the liquid in the Dewar (Ethanol) which has been previously cooled to about -160°F by the use of dry ice and liquid nitrogen. The sample is allowed to come to thermal equilibrium and its weight in the liquid and temperature are recorded. The temperature of the liquid and sample is then increased by 5 to 10°F by use of an immersion heater and another measurement made. This process is continued until the required temperature range has been covered. The density of the liquid is monitored concurrently by measuring the change in weight in the liquid, with temperature, of a piece of inval of known weight and density.

Some typical plots of specific volume versus temperature for a polyurethane binder and the corresponding propellant are presented in Figures 11 and 12, respectively. Measurements on a number of different systems have shown that in some cases the second order transition temperature of the propellant is somewhat higher than that of the binder, while in some instances the two are the same. The reason for this is not completely understood at this time.

SUMMARY AND CONCLUSIONS

A modified direct buoyancy technique has been developed for the measurement of volume changes as a function of strain in filled polymers. The method has three distinct advantages:

1. Simplicity - Only an analytical balance is required.

2. High degree of sensitivity - For a sample volume of 5 cc a volume change of 0.004% is detectable.

3. Partial self-compensation of thermal effects - The samples and buoyant liquid have similar coefficients of expansion thus tending to cancel the effects of small thermal fluctuations.

Data obtained indicate that the volume of a propellant begins to change immediately upon the application of strain, probably due to the enlargement of voids initially present and vacuoles formed adjacent to unbonded areas. However, extensive dewetting does not begin until some critical strain level, characteristic of the propellant, has been reached.

It was found that mechanical cycling, aging and high humidity treatment tend to weaken the binder-oxidizer bonds in polyurethane composites.

The buoyancy technique has also been used for measuring volume as a function of temperature and the subsequent determination of the second order transition temperatures and thermal expansion coefficients of binders and propellants.

Work is now in progress to extend this technique to the measurement of volume changes with strain at different temperatures, under biaxial strain conditions and under constant strain as a function of time.

ACKNOWLEDGEMENTS

REFERENCES

1. Smith, T. L., Transactions of the Society of Rheology, III, 113-136 (1959)

2. Rainbird, R. W. and Vernon, J. H. C., "An Instrument for the Measurement of Volume Changes Occurring in Tensile Testing", Bulletin Joint Meeting, JANAF Physical Properties and Surveillance Panels, pp.39-44 (1960)(Confidential)

3. Stedry, P. J. and Landel, R. F., "Effects of Humidity on the Mechanical Properties of Selected Polysulfide and Polyurethane Propellants", Bulletin Joint Meeting, JANAF Physical Properties and Surveillance Panels, pp. 393-417 (1960)(Confidential)

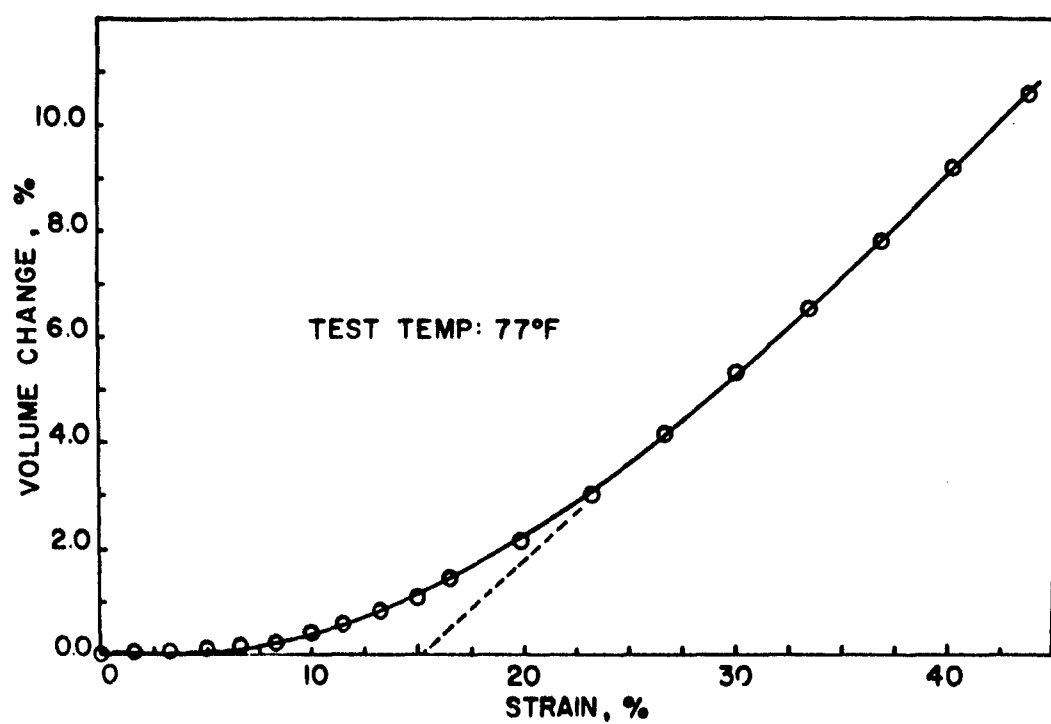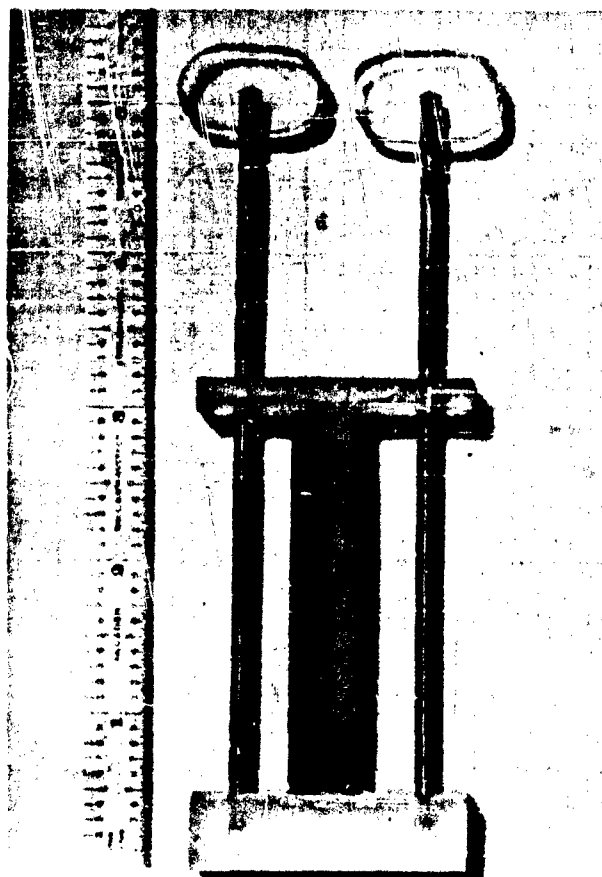FIGURE 1.
DILATATION TEST SPECIMEN
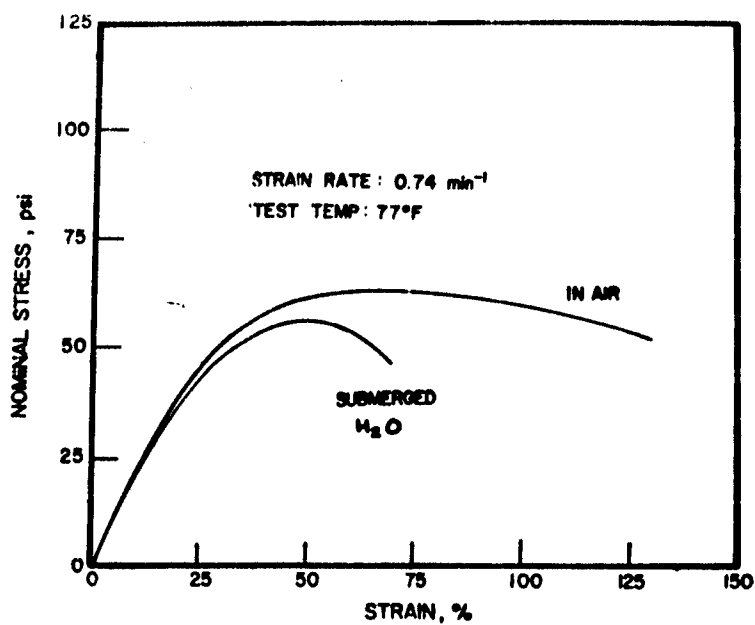

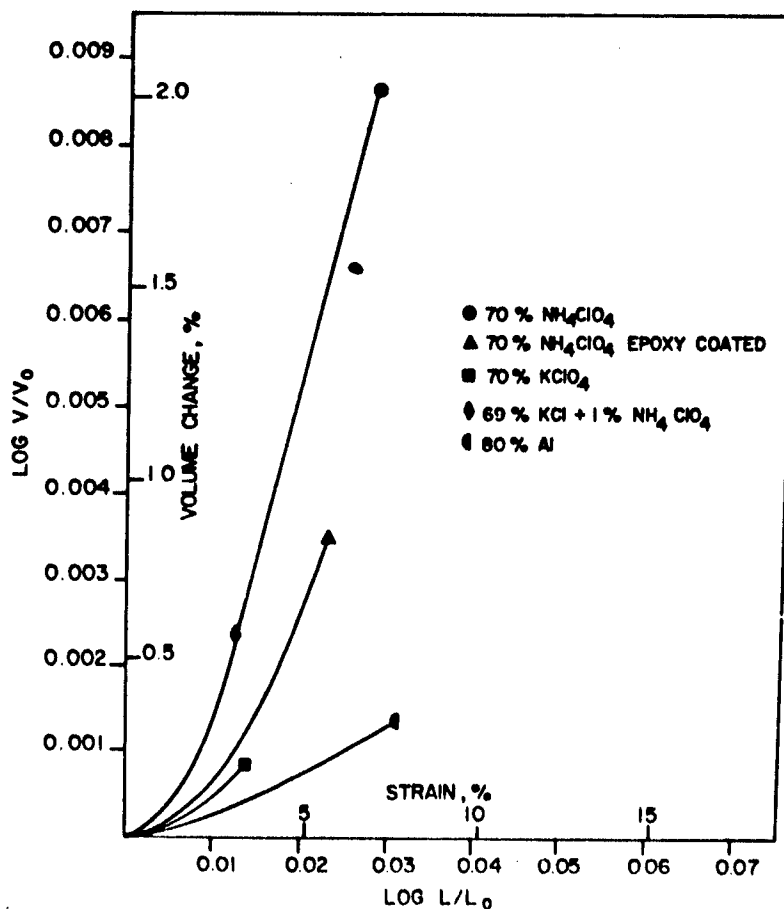
FIGURE 2. VOLUME CHANGE VS STRAIN FOR ANP-2639 AF

FIGURE 3.
STRESS-STRAIN CURVES FOR ANP-2639AF TESTED IN AIR AND WATER

FIGURE 4.
LOG VOLUME CHANGE VS LOG EXTENSION RATIO FOR POLYURETHANE BINDER CONTAINING VARIOUS FILLERS (77°F) (Filled ANP-512 Binder)
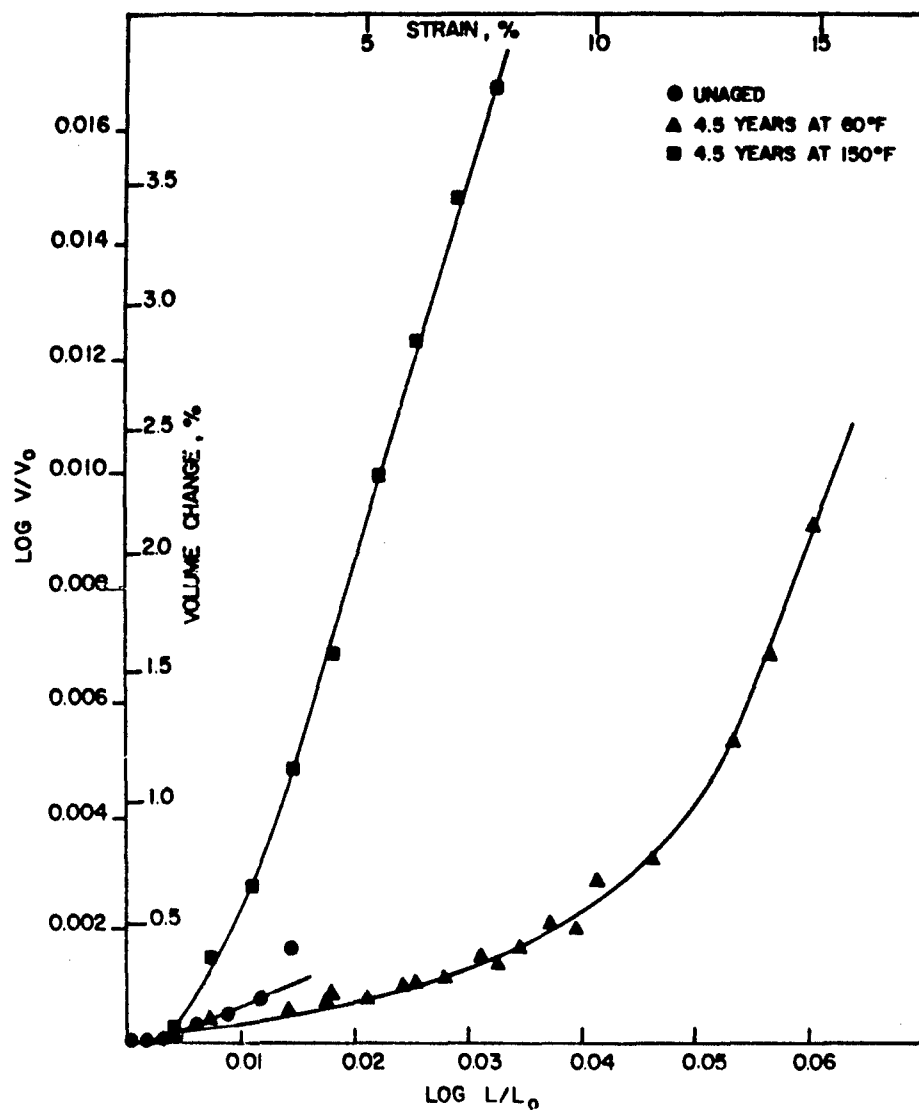
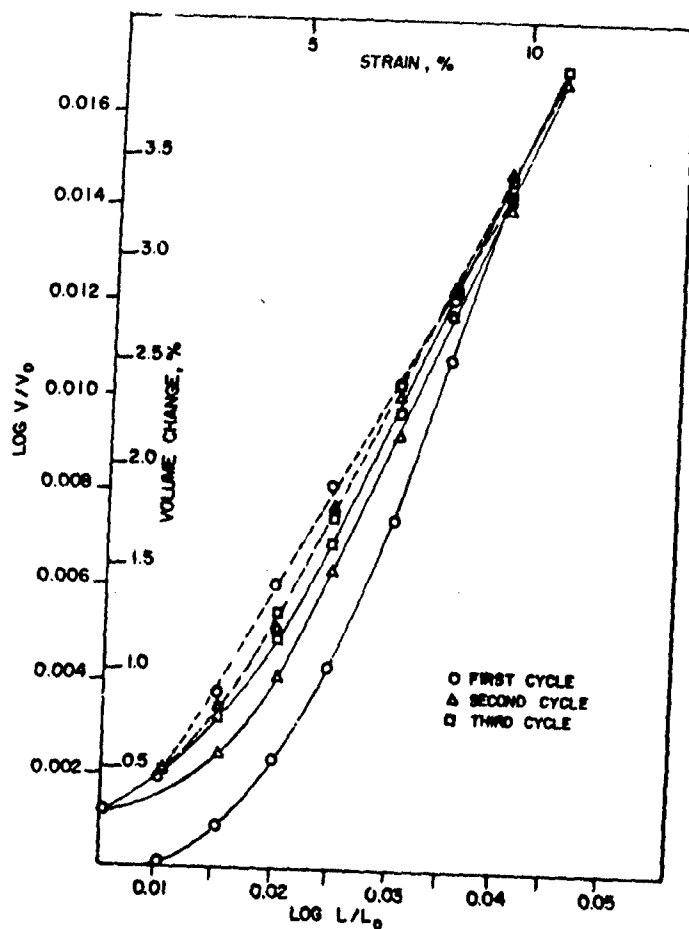FIGURE 5. EFFECT OF AGING UPON THE DILATATION OF ANP-512DS (77°F)

FIGURE 6.
EFFECT OF REPEATED STRAINING UPON
THE DILATATION OF A 50 VOLUME
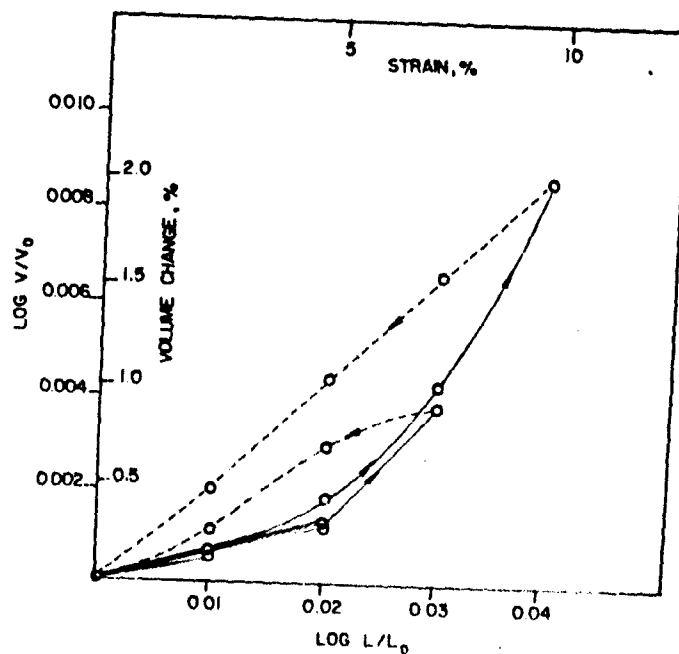PERCENT GLASS BEAD-POLYURETHANE
COMPOSITE (77°F)

FIGURE 7.
EFFECT OF CYCLING TO INCREASING
STRAIN UPON THE DILATATION OF A
40 VOLUME PERCENT GLASS BEAD-
POLYURETHANE COMPOSITE (77°F)

FIGURE 8.
EFFECT OF PRIOR HUMIDITY TREAT-
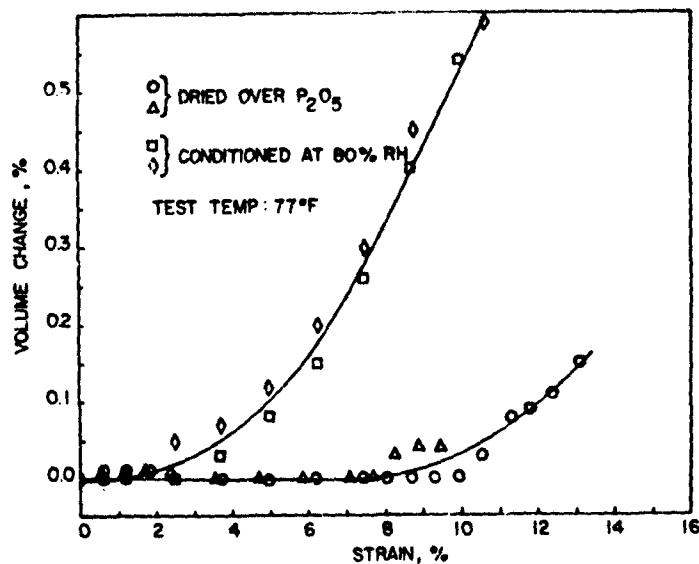MENT UPON THE DILATATION OF
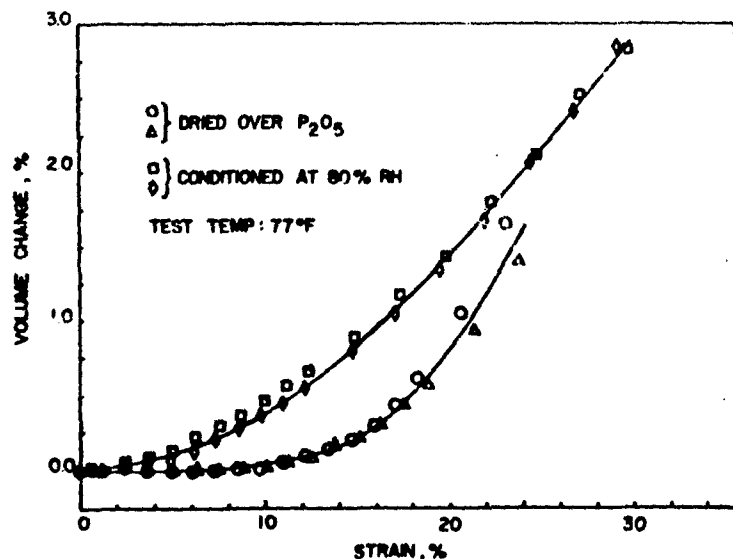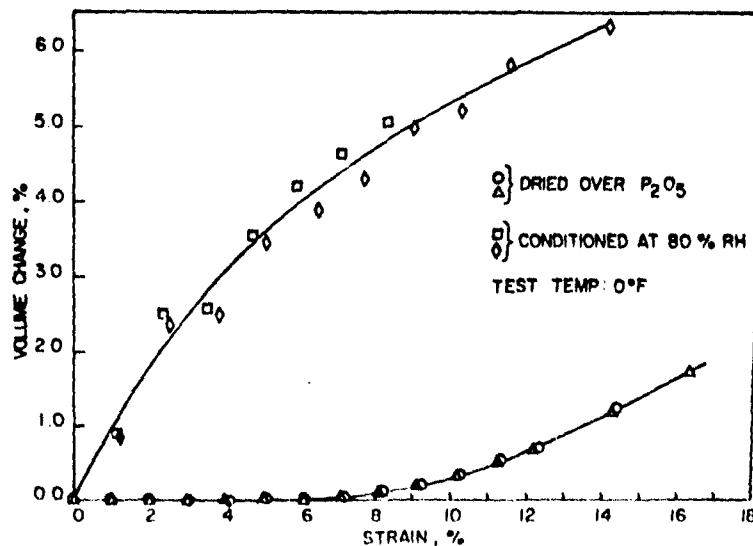DP-31 INERT PROPELLANT (77°F)

FIGURE 9.
EFFECT OF PRIOR HUMIDITY TREAT-
MENT UPON THE DILATATION OF
ANP-2913CD (77°F)

FIGURE 10.
EFFECT OF PRIOR HUMIDITY TREAT-
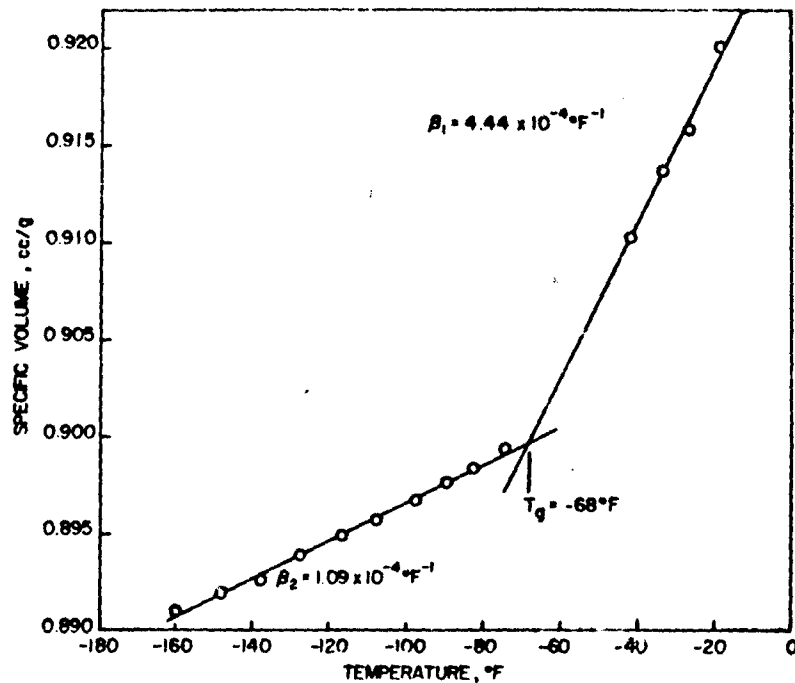MENT UPON THE DILATATION OF
ANP-2913CD (0°F)

FIGURE 11. SPECIFIC VOLUME VS TEMPERATURE FOR ANP-2639AF BINDER
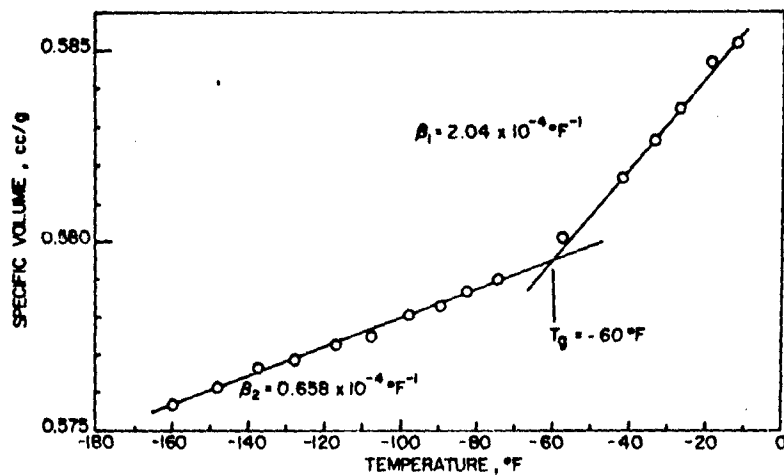

FIGURE 12. VOLUME VS TEMPERATURE FOR ANP-2639AF PROPELLANT (Unaged)

DILATOMETRIC BEHAVIOUR OF COMPOSITE SOLID PROPELLANTS UNDER UNIAXIAL TENSION

R. B. Kruse, Thiokol Chemical Corporation,
Redstone Division, Huntsville, Alabama

ABSTRACT

A volumetric method is described for the measurement of Poisson's ratio as a function of strain for composite solid propellants. This method is quite precise, the standard error of estimate being approximately 0.002, or about 0.4 per cent. The technique makes use of a bonded-tab-end specimen which is strained at a constant rate in a dilatometer.

A study has been initiated into the rate and temperature dependence of Poisson's ratio as a function of strain, with a view towards time-temperature superposition of the results. Preliminary results do not show a consistent dependence upon strain rate, but the strain-functionality of Poisson's ratio clearly varies with temperature.

INTRODUCTION

Elastic and viscoelastic materials, when subjected to strains either in tension or compression, may, if the strains are finite, undergo a change in volume. This is particularly true of heterogeneous materials which are capable of large strains, such as composite solid propellants. The extent of the volume change, if any, and its relationship to the imposed strain are of extreme importance in the engineering analysis of such materials. In order to solve the stress-strain problem of a solid propellant grain of given geometry, it is necessary to know to a considerable degree of confidence the dilatational behaviour of the material making up the propellant charge under the prevailing conditions. Poisson's ratio, which is a measure of dilatational behaviour, was the parameter studied in the experiments described in this paper. It is a relatively simple matter to obtain values of Poisson's ratio in hydrostatic compression, since it may be directly related to the hydrostatic compressibility, a parameter which has for some time been measured on a routine basis at the Redstone Division. At finite strains, however, Poisson's ratio in tension would not be expected to be the same as in compression. In point of fact, the elastic limit is defined as the level of strain below which Poisson's ratio and the modulus of elasticity are the same in tension as in compression[1]. It would be expected that the Poisson's ratio of composite propellant would, above the elastic limit, be a function of strain.

DISCUSSION

The following brief discussion is intended to clarify the terms used in this paper. We will define Poisson's ratio in tension as follows: Suppose that a tensile specimen of uniform square cross-section is extended in uniaxial tension from its original length (L) to a new length (L+ΔL). This elongation will be accompanied by a strain along the axes normal to the direction of applied stress. These strains will be negative; in other words, the specimen will contract or "neck down." If the original width is W, the width corresponding to (L+ΔL) may be represented as (W+ΔW). Poisson's ratio may then be defined as the ratio of the normal strains, i.e.,

$$\mu' = -\frac{\frac{\Delta W}{W}}{\frac{\Delta L}{L}} \tag{1}$$

This ratio is referred to throughout the remainder of this paper as Poisson's ratio by the normal strain ratio definition, and designated by μ'.

The use of normal strain, $\Delta L/L$, as a measure of elongation is unsatisfactory, however, for any but infinitesimal strains.[2] A consistent definition of strain will result, however, from relating a differential increase in length to the instantaneous length. We will therefore replace ΔL with dL and the original length L with the instantaneous length L_i. Defining a "natural" strain e_n, we write:

$$e_n = \int_{L_o}^{L_i} \frac{dL}{L}$$

which, upon integration, yields the simple result:

$$e_n(L) = \ln \frac{L_i}{L_o} = \ln\left(\frac{L_o + \Delta L}{L_o}\right) = \ln\left(1 + \frac{\Delta L}{L_o}\right) \tag{2}$$

For finite strains, then, equation (1) is not satisfactory, despite its simplicity, and must be replaced by the ratio of the natural strains:

$$\nu = -\frac{e_n(W)}{e_n(L)} = -\frac{\ln\left(1 + \frac{\Delta W}{W}\right)}{\ln\left(1 + \frac{\Delta L}{L}\right)} = -\frac{\log\left(1 + \frac{\Delta W}{W}\right)}{\log\left(1 + \frac{\Delta L}{L}\right)} \tag{3}$$

Poisson's ratio as defined by equation (3) will be referred to as Poisson's ratio by the natural strain ratio definition and will be designated by ν

A further advantage of the definition expressed by equation (3) is that the natural strains correspond to the volume strain and hence to the bulk modulus in hydrostatic tension. For an infinite bulk modulus in hydrostatic tension (corresponding to a totally incompressible material in the opposite stress octant), ν must be equal to 0.5, independent of strain.

To prove this, we may return to the tensile specimen of uniform square cross-section. (The following argument may be generalized to a specimen of any cross-section.) The volume of such a specimen, before strain is applied, is simply $V_0 = L \times W^2$. The volume at some finite strain is $V_i = (L+\Delta L)(W+\Delta W)^2$. If the volume of the specimen does not change with strain, then:

$$(L + \Delta L)(W + \Delta W)^2 = LW^2$$

$$\frac{L + \Delta L}{L} = \frac{W^2}{(W + \Delta W)^2} \tag{4}$$

$$\ln\left(1 + \frac{\Delta L}{L}\right) = -2 \ln\left(1 + \frac{\Delta W}{W}\right)$$

combining with equation (3):

$$-\frac{\ln\left(1 + \frac{\Delta W}{W}\right)}{\ln\left(1 + \frac{\Delta L}{L}\right)} = \frac{1}{2} = \nu \tag{5}$$

If the normal strain ratio definition is used, however, ν' will be found to vary with strain even if the volume of the specimen remains constant. The relationship of ν' to strain if volume is constant may be shown by proceeding from equation (4) to:

$$\left(\frac{W + \Delta W}{W}\right)^2 = \frac{1}{\frac{L + \Delta L}{L}}$$

$$1 + \frac{\Delta W}{W} = \sqrt{\frac{1}{1 + \frac{\Delta L}{L}}} \tag{6}$$

$$-\frac{\Delta W}{W} = 1 - \sqrt{\frac{1}{1 + \frac{\Delta L}{L}}}$$

combining with equation (1):

$$\frac{-\frac{\Delta W}{W}}{\frac{\Delta L}{L}} = \nu' = \frac{1}{\frac{\Delta L}{L}}\left(1 - \sqrt{\frac{1}{1 + \frac{\Delta L}{L}}}\right) \tag{7}$$

EXPERIMENTAL PROCEDURE

Because of its importance as an engineering parameter, there have been many attempts in the past to measure Poisson's ratio of composite propellants as a function of strain. These attempts have included measurement of ellipticity of circles inscribed on the faces of tensile specimens, direct measurement of change in width of specimens being strained, and, at the Redstone Division, measurement of change in area of a face of tensile specimens with strain. None of these methods yielded precise Poisson's ratio values, mainly because of the difficulty of measuring small changes in length and area. In fact, the Poisson's ratio values were so scattered as to have little, if any, engineering value.

The methods utilized in the experiments described in this paper combine the recently developed bonded-tab-end specimen[3] with dilatometric techniques such as those described by Rainbird and Vernon[4]. The bonded-tab-end tensile specimen offers two advantages which make possible precise measurements of Poisson's ratio in tension: (1) The gauge length is fixed, so that on a tensile testing device which imposes a constant strain rate, it is not necessary to measure small strains by photographing or other methods. They can be related directly to time elapsed from the beginning of the test. (2) Tab ends, in which the strain fields are virtually impossible to determine, are eliminated, so that when the specimen is immersed in a fluid and subjected to uniaxial tension, the entire specimen is in a state of strain which can be accurately determined.

In the experiments described in this paper, Poisson's ratio is calculated from change in volume of the tensile specimen as a function of strain. A device to accomplish direct measurement of this volume change as the specimen is being strained is shown diagrammatically in Figure 1. Several candidate working fluids for this device were tested, and that which showed the least penetration of the propellant for extended periods of time at high temperatures was selected. This was Dow Corning DC-550 silicone oil. The specimens are placed in a dilatometer and elongated at various constant rates. The change in height of the fluid in the capillary column is then followed photographically.

SUMMARY OF RESULTS

The initial evaluation of the test procedure consisted of three replicate tests, which were carried out on samples from the same mix of propellant (TP-H8126). Several factors combined to make these tests somewhat uncertain as to reproducibility, and more replicate tests are consequently planned. However, the standard error of estimate of these tests is at least one order of magnitude less than could be obtained by any other technique attempted at this Division. The indivual test results are shown in Figures 2 and 3. The average values, along with the 2σ limits, are shown in Figures 4 and 5. The standard error of estimate for both ν and ν' is ±0.0019; hence, the 2σ limits are at 0.0038. The original estimate of accuracy in the Poisson's ratio values, when the strain dilatometer was designed, was ±0.005. It is expected that future standardization tests, which will incorporate refinements of test technique, will show an even greater degree of accuracy in the determination of Poisson's ratio.

Figure 6 shows ν for two mixes of a propellant made with the HA fuel binder system based upon the TP-H8041 formulation. The ingredients of these mixes were first thoroughly dried, and then a known amount of moisture was added to the ingredients of one mix, designated F-255, while the other, designated F-256, was made with the dried ingredients. The addition of moisture evidently had an adverse effect upon the binder-filler

bond strength of F-255, as reflected by the more abrupt decrease of Poisson's ratio with strain. It should be stressed at this point, however, that de-wetting of the solids may not necessarily be undesirable from the standpoint of motor performance.

A study was initiated to determine the effect of temperature and strain rate upon the variation of Poisson's ratio with strain. One possibility which suggested itself was that the variations of Poisson's ratio with strain might be superposable on a reduced strain rate basis, as uniaxial tensile properties appear to be. From the data gathered thus far, however, the effect of strain rate, if any, upon the variation of Poisson's ratio with strain is not clear.

CONCLUSIONS

An examination of Figure 7, which is a plot of Poisson's ratio of TP-H7003 propellant as a function of strain at 135°F and strain rates of 0.05, 0.5 and 5.0/min., shows that no consistent variation of Poisson's ratio as a function of strain with strain rate was observed. The same lack of a consistent variation of the strain dependence of Poisson's ratio with strain rate is shown in Figure 8, which represents Poisson's ratio measured as a function of strain at the same three strain rates as in the previous figures, and at a test temperature of 77°F. A consistent temperature dependence of the relationship between Poisson's ratio and strain has been obtained, however, as can be seen from Figure 9, which shows the Poisson's ratio curves for the same propellant, measured at a single strain and several temperatures. In view of the fact that many curves of tensile stress vs. strain, generated at the Redstone Division, involve stresses and strains at maximum stresses, for which corrections in cross-sectional area were made on the basis of constant volume, it was of considerable interest to compare the results of this assumption with plots of true stress vs. strain which could now be calculated from the Poisson's ratio values. The results have shown that the assumption of constant volume resulted in a much more accurate stress-strain curve than the use of a constant cross-sectional area. The true stresses are much nearer to the corrected stresses than to the nominal stresses calculated upon the basis of the initial cross-sectional area. Strain at maximum stress remains virtually unchanged when corrected stress values are replaced by the true stress values.

REFERENCES

1. S. Timoshenko and J. N. Goodier, "Theory of Elasticity," McGraw-Hill Book Co., New York (1951).

2. M. Reiner, "Deformation and Flow," H. K. Lewis and Co., London (1949).

3. J. B. Baldwin and M. H. Cooper, JANAF Publication No.
PP-13/SPSP-8, 151, 1960 (Confidential).

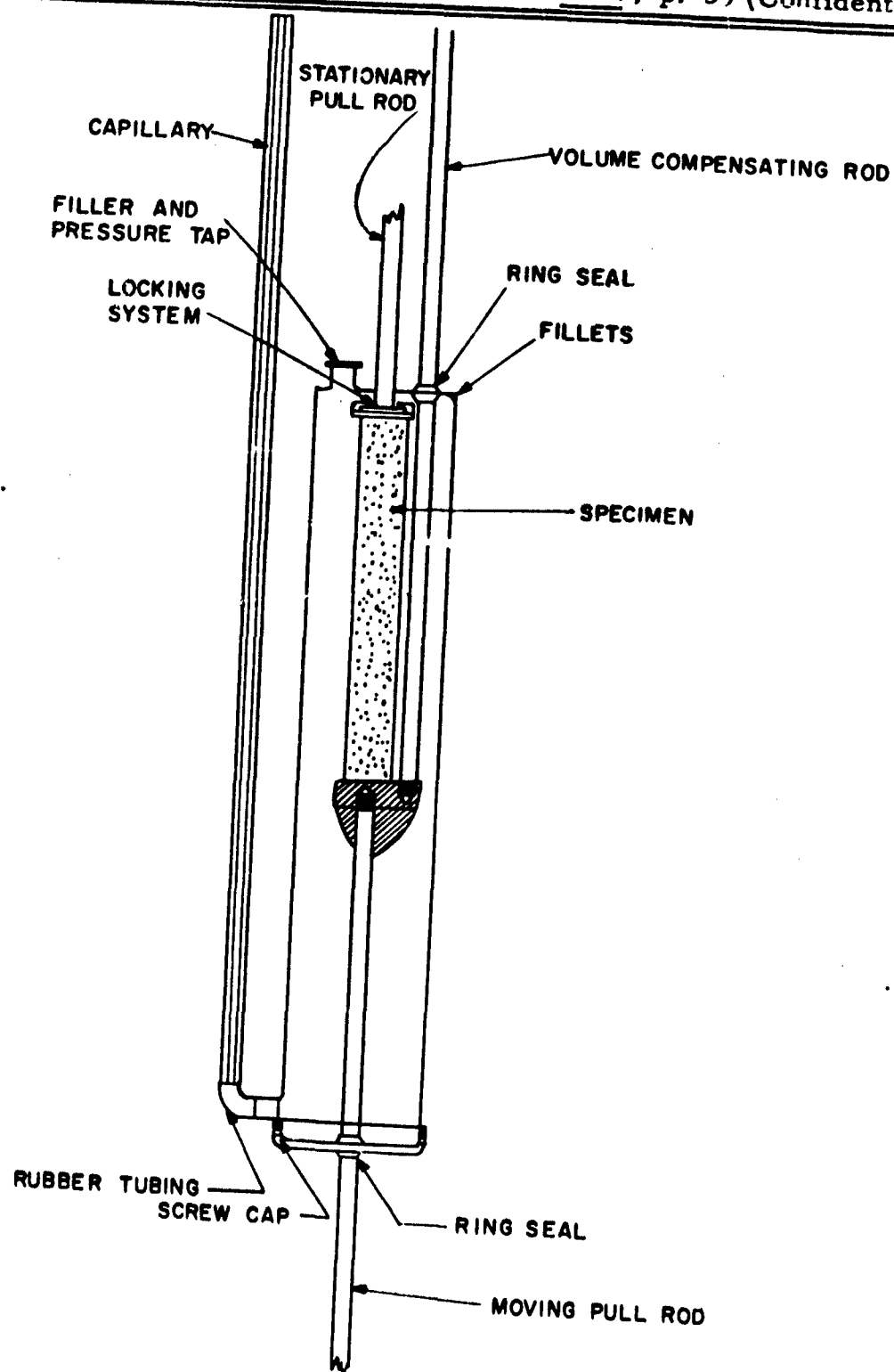4. R. W. Rainbird and J. H. C. Vernon, Ibid., p. 39 (Confidential).

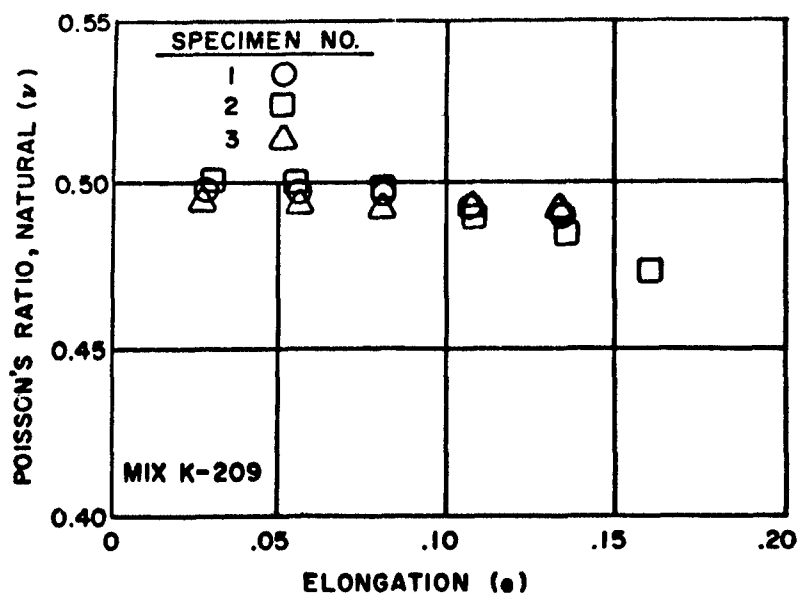FIGURE 1.   STRAIN DILATOMETER

FIGURE 2.
NATURAL STRAIN RATIO VERSUS
ELONGATION (INDIVIDUAL
TESTS)

FIGURE 3.
NORMAL STRAIN RATIO VERSUS
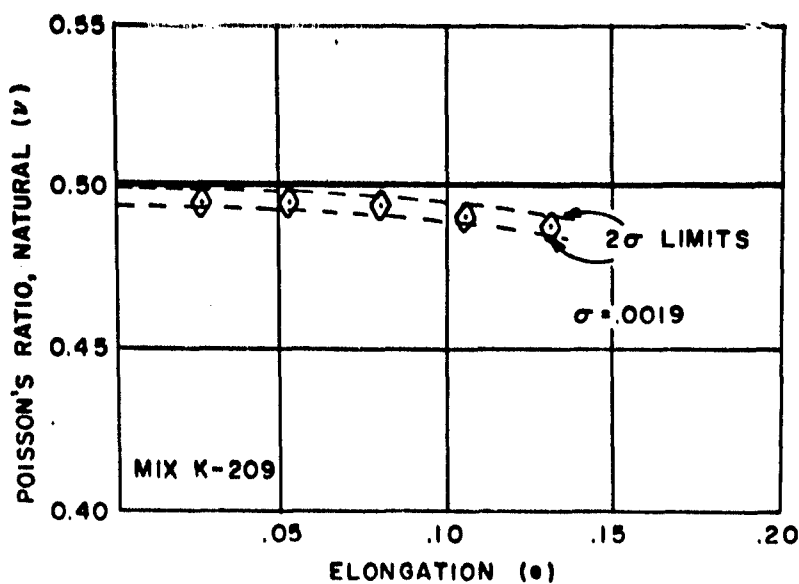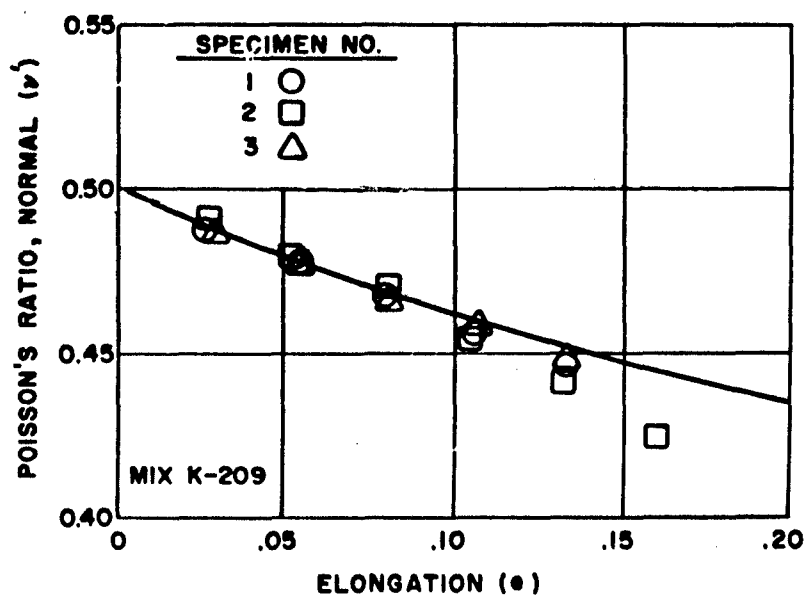ELONGATION (INDIVIDUAL TESTS)

FIGURE 4.
NATURAL STRAIN RATIO VERSUS
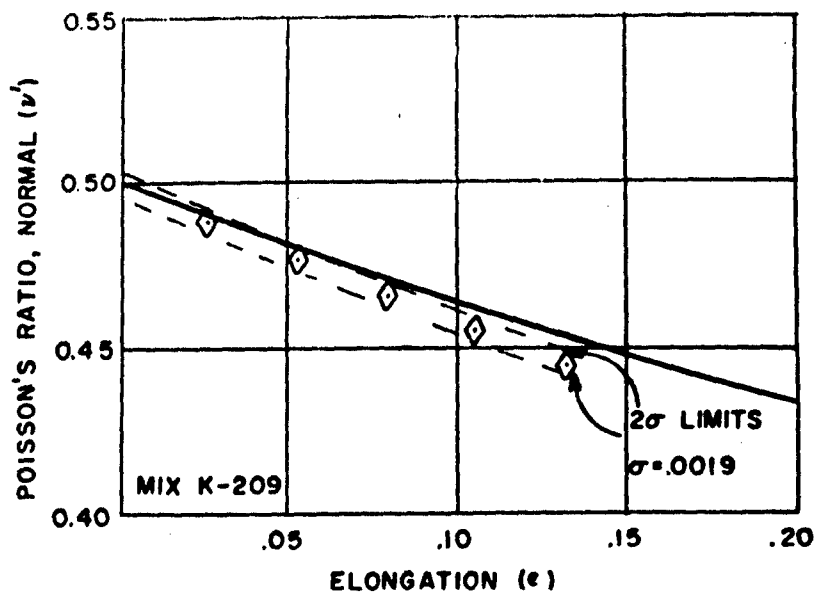ELONGATION (AVERAGES AND
CONFIDENCE LIMITS)

FIGURE 5.
NORMAL STRAIN RATIO VERSUS
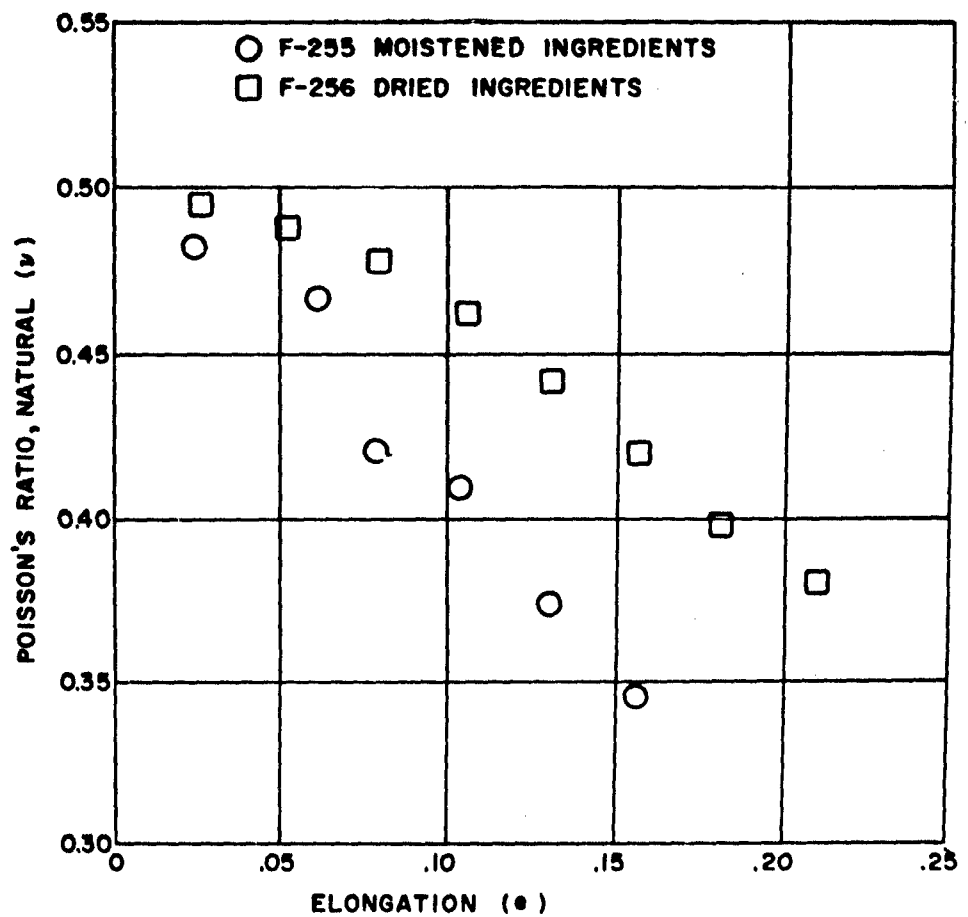ELONGATION (AVERAGES AND
CONFIDENCE LIMITS)

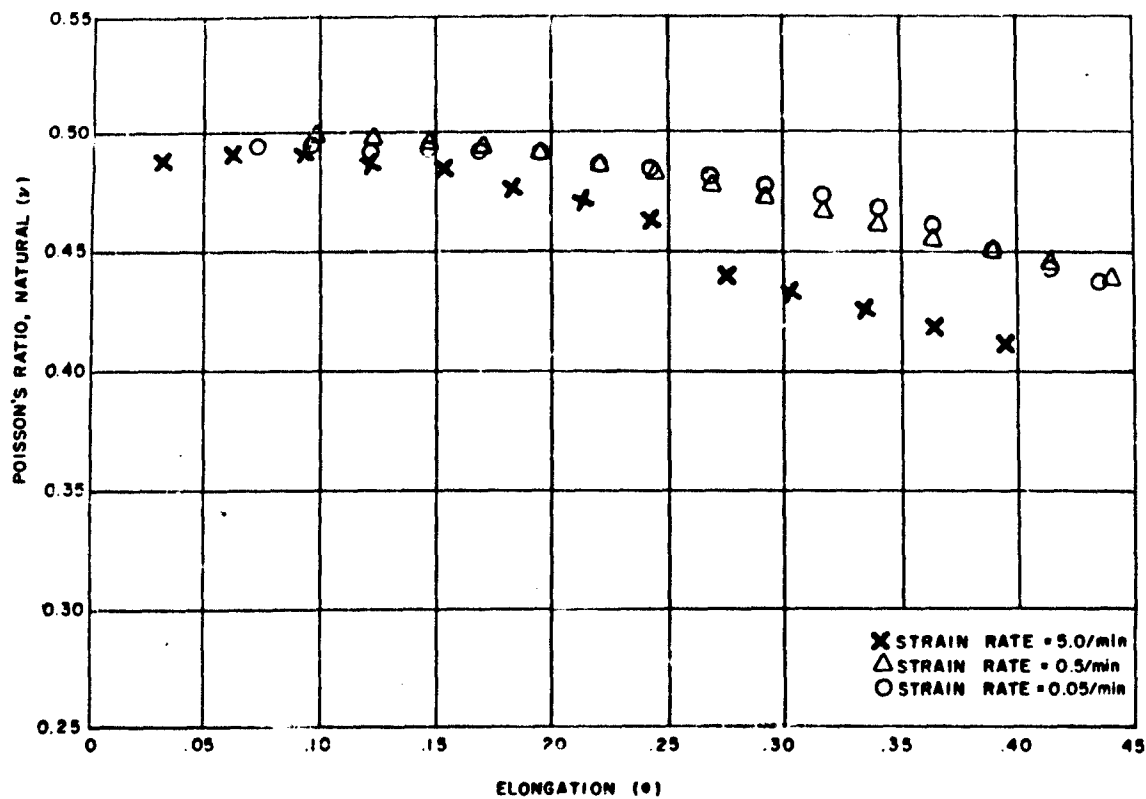FIGURE 6. EFFECT OF MOISTURE ON POISSON'S RATIO

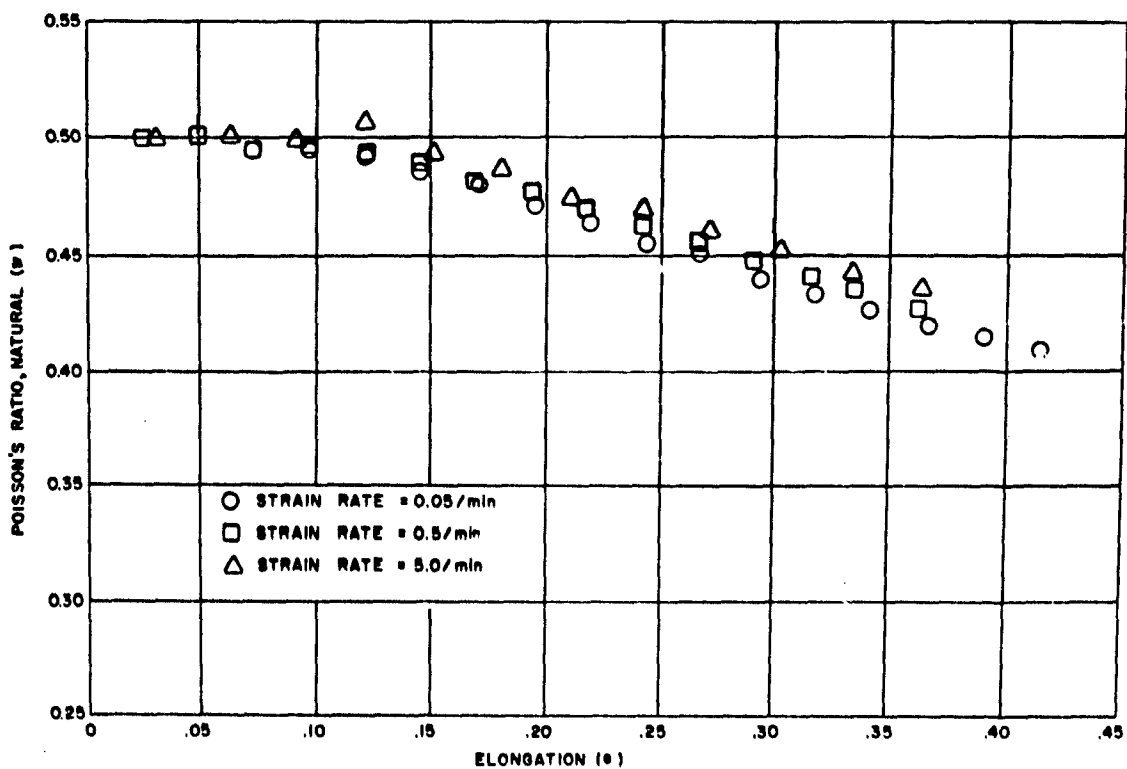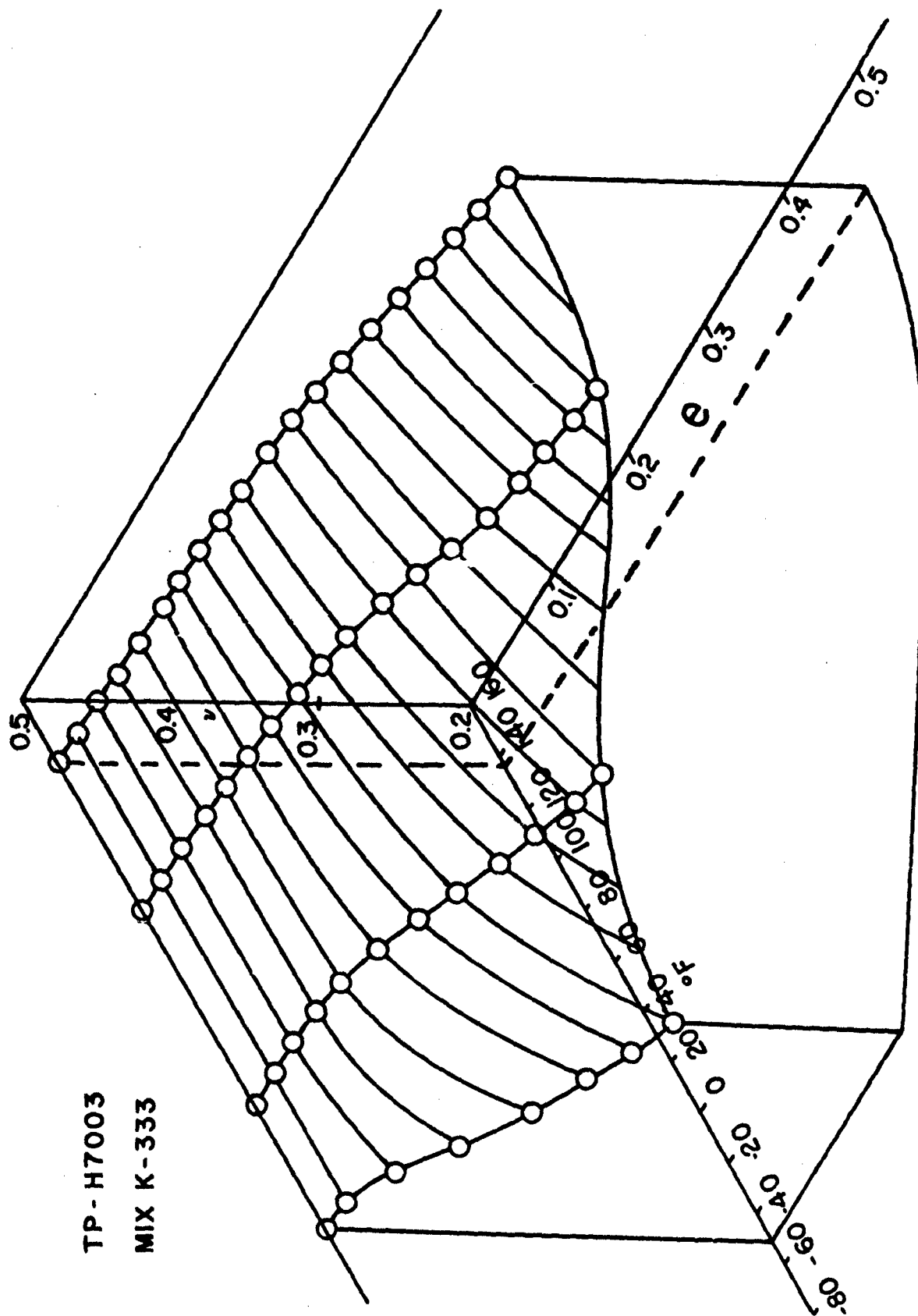FIGURE 7. EFFECT OF STRAIN RATE ON POISSON'S RATIO AT 135°F.

FIGURE 8. EFFECT OF STRAIN RATE ON POISSON'S RATIO AT 77°F.

TP-H7003

MIX K-333

FIGURE 9. POISSON'S RATIO VERSUS TEMPERATURE AND STRAIN

AN APPARATUS FOR MEASURING THE BULK MODULUS
OF SOLID PROPELLANTS

Neal C. Wogsland
Ballistic Research Laboratories

ABSTRACT

An apparatus has been developed to measure the bulk modulus of solid propellants and other viscoelastic materials in the 0 - 2500 psi pressure range. The pressure-volume-temperature data recorded during calibration of the apparatus using steel samples of various sizes was used to determine the expansion characteristics of the pressure chamber and to calculate the equilibrium bulk modulus of the transmitting fluid. A knowledge of these parameters permits calculation of the corresponding modulus of a propellant sample tested in a similar manner. These isothermal measurements are sufficiently accurate for use in the stress analysis of solid-propellant rocket motors. The apparatus can be used to determine, approximately, the adiabatic bulk modulus of the transmitting fluid and to estimate this modulus for a test specimen. This apparatus also can be used to obtain data on the effects of voids on the bulk properties of porous propellants.

INTRODUCTION

The mechanical behavior of solid propellants is of considerable importance to the designers of solid-propellant rocket motors. The propellant must be sufficiently stiff to minimize creep during storage and yet must not be brittle enough to crack under the pressures at which it burns.

The basic methods of solving problems in stress analysis are well established for elastic materials. If a material is homogeneous and isotropic, its mechanical behavior can be described by two elastic constants. If, for example, the shear modulus of elasticity, G, and the bulk modulus, K, are determined, then Young's modulus, E, and Poisson's ratio, ν, can be calculated from the relations

$$E = \frac{9KG}{3K + G} \qquad \text{and} \qquad \nu = \frac{3K - 2G}{6K + 2G}$$

which are given by Alfrey in a different notation (1).

For viscoelastic materials, problems of stress analysis frequently can be formulated in terms of Volterra integral equations if the moduli are known (2). The current theory of linear viscoelasticity makes no distinction between moduli measured under adiabotic and isothermal conditions. This assumption, while sufficiently correct for the shear modulus (3), is not entirely correct for the bulk modulus for which thermodynamic effects are important. Only the equilibrium bulk modulus measured under isothermal conditions can be measured accurately with the apparatus described in this paper, as it is hard to distinguish between thermodynamic and viscoelastic effects if the application of pressure produces a significant change of temperature.

At the Ballistic Research Laboratories, a study is being conducted to determine to what extent the theory of linear viscoelasticity can be applied to the stress analysis of solid propellants (4). To correlate theory with

experimental results, experiments are being devised to measure the bulk
modulus and the shear modulus, which have been chosen as the principal
independent variables to be studied. As the bulk modulus is only slightly
time-dependent, and is generally much larger than the shear modulus, the
equilibrium bulk modulus is sufficiently accurate for stress problems in
which isothermal conditions prevail. However, for dynamic problems, the
increase in modulus occurring under adiabatic conditions must be considered.
Little compressibility information is available for solid propellants except
for the equilibrium measurements at Aerojet-General Corporation (5).

EXPERIMENTAL PROCEDURE

The apparatus described in this paper was designed primarily to measure
the equilibrium bulk modulus of solid propellants and other viscoelastic
solids by measuring the change of volume produced by a change of pressure.
The intensifier principle was used to obtain a large magnification of the
volume change during pressurization. A chamber size of approximately 1 cu.
in. was selected so that small specimens could be tested effectively. This
is especially important in development programs when only small samples of
newly-synthesized propellants are available. The system was designed for
operation in the 0 - 2500 psi pressure range (all pressures referred to in
this paper are gage pressures). The intensifier principle could be used
for much higher pressures with appropriate design. This is a relatively
safe apparatus since any sudden surge of pressure would result in failure
of the pressure transducer. It also avoids the danger of poisoning associ-
ated with a mercury apparatus.

The apparatus consists of a pressure intensifier and auxiliary equip-
ment and instrumentation including hydraulic pumps, valves, pressure trans-
ducer and dial gage, strain indicator, sight glass, thermocouple, microvolt-
amplifier, and strip-chart recorder. Photographs of the system are shown
in Figures 1 and 2 and a schematic diagram in Figure 3.

The test sample is placed directly in the intensifier chamber to mini-
mize the volume of fluid required and therefore minimize the influence of
the fluid on the test data. If necessary, the test sample may be given an
impermeable coating to prevent penetration of hydraulic fluid into the
pores or to prevent a possible chemical reaction. Hercoflex 600 hydraulic
fluid has been used with solid propellants at the BRL but Hercolube A,
Dow-Corning DC-200, or several other fluids probably should be equally
satisfactory. During the initial setup of the apparatus, a vacuum pump
is used to evacuate each chamber as it is filled with the fluid. When a
sample is prepared for testing, the test chamber is filled to overflowing
before installing the closure so that no air will be entrapped.

The calibration of volume change in the test chamber vs. sight-glass
reading was obtained by measurement and calculation. The pressure transducer
was calibrated in conjunction with the strain-indicator and a standard dead-
weight tester. The chromel-alumel thermocouple was set up to measure
temperature change by placing the reference junctions under ambient labora-
tory temperatures of $77^\circ - 1^\circ F$. The temperature scale of the recorder
chart was established from thermocouple data sheets since they provided
sufficient accuracy for this test.

FIGURE 1.
COMPRESSIBILITY APPARATUS AND
AUXILIARY EQUIPMENT

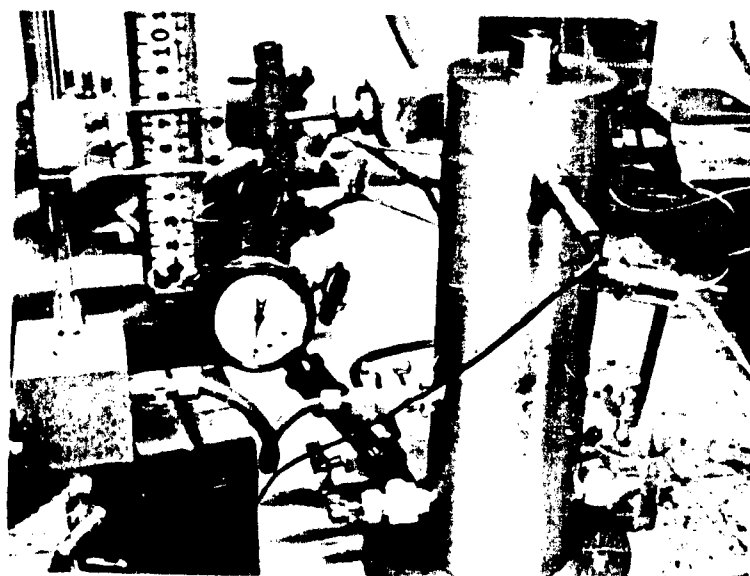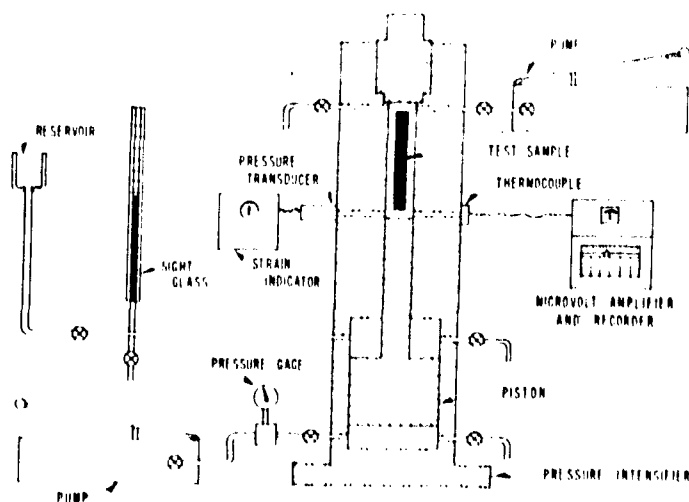

FIGURE 2.
COMPRESSIBILITY APPARATUS

FIGURE 3.
SCHEMATIC DIAGRAM OF
COMPRESSIBILITY APPARATUS

The apparatus was calibrated by measuring the pressure-volume-temperature changes while conducting tests using steel samples of different sizes. Accepting handbook values for the compressibility of steel, the expansion characteristics of the pressure chamber and the equilibrium (isothermal) bulk modulus of the transmitting fluid were calculated from the P-V-T data observed. For each pressure step, an interval of 10 minutes was allowed prior to recording the data so that temperature equilibrium would be reached. This same procedure is followed for isothermal testing of propellant samples.

An approximate value for the adiabatic bulk modulus of the transmitting fluid is obtained by quickly pressurizing the system from 0 psi to a desired pressure level and immediately recording the P-V-T data. The pressure is then dropped to 0 psi, the system is allowed to reach equilibrium temperature, and the cycle of operations is repeated for each additional pressure level that is needed. An estimate of the adiabatic bulk modulus of a test sample can be made in a similar manner. The results are influenced considerably by the thermodynamic properties of the fluid.

DISCUSSION

This apparatus has been used to measure the equilibrium bulk modulus of several solid propellants and other viscoelastic materials. The bulk modulus is defined by the secant formula

$$K = V_o \frac{\Delta p}{\Delta V}$$

where

K is the equilibrium bulk modulus,

V_o is the original volume,

Δp is the change in pressure,

ΔV is the change in volume.

The sight-glass reading gives only the apparent change of volume and must be corrected for the expansion of the chamber and compression of the fluid (6). These corrections are incorporated in the formula

$$K = \frac{V_o}{\frac{\Delta V}{\Delta p} - C - \frac{V_f}{K_f}}$$

and are determined by calibrating the apparatus.

C accounts for the expansion of the test chamber,

V_f is the initial volume of the transmitting fluid,

K_f is the isothermal bulk modulus of the fluid.

Values obtained for several materials are tabulated in Table I, which includes the average moduli for both the 0 - 2500 psi and the 500 - 2500 psi pressure ranges. The compressibility curves of these materials are not quite linear and the bulk modulus increases as the pressure increases. The third figure, although not significant, is included in the tabulated results to illustrate this increase in modulus.

TABLE I. EQUILIBRIUM BULK MODULI, IN PSI, OF
SEVERAL VISCOELASTIC MATERIALS AT $77^\circ \pm 1^\circ$F

Pressure Range, psi (gage)	0 - 2500	500 - 2500
Hercoflex 600 Fluid	249,000	252,000
Polystyrene (commercial rod)	472,000	476,000
Polytetrafluoroethylene (commercial teflon rod)	363,000	367,000
Polyurethane (pluracol base)	258,000	267,000
Propellant No. 1 (cast double base)	432,000	438,000
Propellant No. 2 (composite double base)	583,000	621,000
Propellant No. 3 (composite)	834,000	882,000

The compressibility effects of voids can be observed closely with this apparatus because the slippery teflon piston seals permit the piston to creep at levels somewhat below the preload on the seals. Porous materials show large differences between their average moduli over these two pressure ranges because the voids undergo considerable compression at low pressures. With soft propellant compositions, their effects can be ignored above approximately 100 psi. The tabulated results for propellants Nos. 2 and 3 are from the second compression cycle for each material because the initial cycles were strongly non-linear while the voids were being compacted. Figure 4 illustrates these effects for a composite double-base propellant with a porosity of approximately 1/3%.
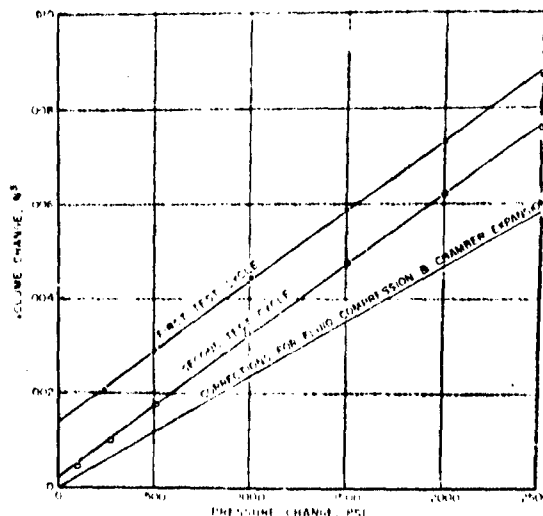

FIGURE 4. SUCCESSIVE COMPRESSIBILITY CURVES FOR PROPELLANT OF 1/3% POROSITY

SUMMARY AND CONCLUSIONS

This apparatus provides a satisfactory means for measuring the isothermal bulk modulus and compressibility of solid propellants and other viscoelastic materials in the 0 - 2500 psi pressure range. The isothermal measurements are sufficiently accurate for use in the stress analysis of solid-propellant rocket motors. This tester also can be used to obtain information on voids in porous propellants and on their effects on the bulk properties. The principal weakness of this apparatus is the masking of test data for the test sample by the relatively large volume of transmitting fluid (37% minimum). This is especially true when adiabatic data is desired. However, greater accuracy could be obtained with a larger test chamber. In its present form, accepting samples up to 1/2 in. diameter and 3 in. long, it is especially applicable to the testing and screening of the small samples normally available with newly-synthesized experimental propellants.

REFERENCES

1. Alfrey, T., Jr. Mechanical Behavior of High Polymers: Table I, p. 15. New York: Interscience Publishers, 1948.

2. Lee, E. H. and Rogers, T. G. Solution of Viscoelastic Stress Analysis Problems Using Measured Creep or Relaxation Functions. Providence, R. I.: Brown University, Aug 1961.

3. Ferry, J. D. Viscoelastic Properties of Polymers: 101. New York: John Wiley & Sons, 1961.

4. Elder, A. S. Stress Function Theory for Linearly Viscoelastic Solids. Aberdeen Proving Ground: BRL MR-1282, June 1960.

5. Sweeny, K. H. and Bills, K. W., Jr. Poisson's Ratio Determination; Compressibility Measurement. Bulletin of the Seventeenth Meeting of the Joint Army-Navy-Air Force Panel on Physical Properties of Solid Propellants, 111-112. Silver Spring, Md.: Johns Hopkins Univ., SPIA/PP 11, May 1958. (Confidential report)

6. Bridgeman, P. W. The Physics of High Pressure: 102. London: G. Bell and Sons, 1949.

FAILURE CRITERIA

K. H. Sweeny, Reporter

FAILURE CRITERIA FOR SOME POLYURETHANE PROPELLANTS

Warren T. Milloway and James H. Wiegand

Aerojet-General Corporation

ABSTRACT

Experimental and theoretical studies are being carried on at Aerojet-General Corporation, to establish failure criteria applicable to simple case bonded hollow cylindrical grains. For uniaxial tension, where the rate of elongation and temperature are controlled variables, the test results vary from specimen-to-specimen and from batch-to-batch, and a study of batch variability of the uniaxial test was made. Forty batches of a 65% NH_4ClO_4 17% Al polyurethane propellant showed a high correlation between elongation at break at 77°F and elongation at break for 180°, 40°, 0°, and -40°F, indicating that a test at any one of these test temperatures could be used to characterize population. The coefficient of variation between batches was found to vary with temperature and varied from 26% at -75°F to 51% at 180°F for one formulation of polyurethane propellant. The coefficient of variation between replicates for the same propellant formulations was 15% at -75°F and 7% at 180°F. The variation between cartons varied from small to insignificant.

The correlation of breaking strain at different rates and temperatures using the WLF technique on one batch was found to be improved if an addition vertical shift factor was added to account for the lowering of the maximum failure at lower temperatures. However, by using a shift for rate on a temperature correlation the variability was lower and the data appear to be in good agreement with two straight lines.

The minimum strain at break at -75°F for uniaxial tensile test was found to be at least twice the hoop strain of a thermal cycled (110° to -75°F) case bonded hollow cylinder of propellant when no failures were observed. When the minimum strain at break was less than the hoop strain of the cycled cylinder, the grain always cracked. The region between one and two is an expected area of doubt caused by the wide distribution of propellant properties.

INTRODUCTION

The objective of this paper is to describe the experimental and theoretical studies carried on at Aerojet-General Corporation to establish failure criteria applicable to simple case bonded hollow cylindrical grain and evaluate these criteria by cycling such cylinders to failure. The concept of failure necessarily includes a study of the behavior of those members of the population most likely to fail. The usual measurement of properties and correlation of data centers around consideration of mean behavior with estimates of variability being made to assess the measurement quality. Stress and strain calculations also focus on the use of mean values of the parameters and comparison with the mean of observed deflections. Failure, however, is concerned with the likelihood of a particular

stress or strain occurring at the point where the material properties are
least adequate. The formation of yield bands in propellants gives partic-
ular point to this problem. The data suggest that as the strains increase,
yield bands occur and change the distribution of strains to produce regions
in which failure will occur before further strain is produced in the un-
yielded regions. Thus, the usual elastic stress calculations and techniques
such as photoelasticity do not directly lead to predictions of failure.

This paper will cover (1) the results of studies on the batch-to-batch
variability of breaking strain, of uniaxial tensile test over a range of
temperatures, (2) the correlation of breaking strain of uniaxial tensile
test with rate and temperature and (3) the correlation of uniaxial tensile
elongation to break with failure by grain cracking as a result of the
thermal cycling of a case bonded hollow cylinder of propellant.

BATCH VARIABILITY OF FAILURE BEHAVIOR

The large variability associated with propellant properties suggests
that certain batches, and certain portions of these batches, will be more
susceptible to failure than others. A related hypothesis is immediately
suggested for experimental testing: the failure behavior under different
types of stress-strain environments are related such that those batches
with the highest incidence of failure in one environment will have the
highest incidence in another. It is clear that we lack the knowledge at
this time to define failure mechanisms in detail for different batches or
even different compositions. A possible procedure is to compare property
measurements with small-scale motors, and validate the results as full-
scale motor data become available. It is evident that during the validation
process, the small-scale motor data the the property data would become
increasingly firm as a basis for acceptance criteria.

The production of polyurethane propellant for several programs at the
Sacramento Solid Rocket Plant of the Aerojet-General Corporation offers the
possibility of taking data on different batches of propellant and deter-
mining the correlation between failure values of different mechanical
property tests. Instron data at one strain rate are taken from -75° to 180°F
in these several programs. A study has been completed of data taken on one
carton from each of 40 batches of a polyurethane propellant containing
65% NH_4ClO_4 and 17% Al. Figures 1 to 4 show correlation graphs of the
elongation at failure at 77°F versus the failure value at the other test
temperatures for each of the cartons studied. The data were also analyzed
numerically to give the correlation coefficient shown on each figure.
Except for -75°F, the data gave high correlations, and in particular, the
three cartons giving highest elongations and the two giving lowest elonga-
tions (except as shown in Figure 4 for -75°F) were the same in all cases.
This would indicate that a test at any one of the test temperatures would
have screened out the same extreme cartons of the population as any other
test temperature except -75°F. The -75°F data are in question at this time
because of a particularly strong effect of pre-test humidity exposure on
-75°F test results; these tests were run on specimens experiencing a fairly
wide range of humidity prior to being placed in -75°F conditioning for test.

The variability of this propellant was also statistically analyzed in
more detail for three cartons of each of three widely different batches.

It was found that the variability tended to decrease between batches and increase within cartons as the test temperature decreased. When the three batches were considered together, coefficients of variation between batches ranged from 51% at 180°F down to 26% at -75°F as contrasted with the between replicate variation which increased from 7% to 15% over the same temperature range. Table 1 contains the mean values for the 3-batch, 3-carton, 3-replicate analysis and the variability analysis data are tabulated in Table 2.

An additional analysis of two of the batches, 18-M-1 and 21-M-1, was made. In this case, test data from two additional cartons from each of these batches were available. The means of these two batches were more nearly alike at the middle temperatures and tended to diverge at the extremes, which would minimize variability at the middle temperatures. The between replicate values, however, followed patterns identical to those from the initial analysis of all three batches. Table 3 contains the results of the variance analysis in terms of coefficients of variation. All of the coefficients of variation listed had a significance level of 0.95 or greater.

Table I

MEAN VALUES OF BREAKING STRAIN FOR A THREE BATCHES OF A POLYURETHANE PROPELLANT
(Each value represents the average of 9 samples)

	1	2	3
Batch	15-M-2	18-M-1	21-M-1
180°F	19.9	98.0	73.0
77°F	28.1	93.6	93.3
0°F	35.7	113.3	104.0
-40°F	33.1	69.8	61.7
-75°F	18.2	26.6	23.3

Table II

COEFFICIENTS OF VARIATION FOR THREE BATCHES
THREE CARTONS, THREE REPLICATES OF A POLYURETHANE PROPELLANT

	Between Batches	Between Replicates
180°F	51%	7.1%
77°F	46%	9.8%
0°F	50%	8.8%
-40°F	35%	9.8%
-75°F	26.3%	14.9%

Table III

COEFFICIENTS OF VARIATION FOR TWO BATCHES, 18-M-1 AND 21-M-1
FIVE CARTONS, THREE REPLICATES OF A POLYURETHANE PROPELLANT

	Between Batches	Between Replicates
180°F	22%	4.3%
77°F	8.9%	7.1%
0°F	---	12%
-40°F	7.2%	10.5%
-75°F	21%	14%

CORRELATION OF FAILURE BEHAVIOR

WLF Rate Shift Factor Correlation

The correlation of mechanical property behavior at different rates
and temperatures has been performed on many polymers following the shift
factor technique of Williams, Landel, and Ferry (2)(WLF). Correlation of
failure behavior for a rubber was shown by Smith and Stedry.(1) Correlation
of failure in the highly filled polyurethane systems has not been reported
in the literature. From consideration of available test data on propellants,
it appeared that the maximum elongations at failure at any rate for different
temperatures were not the same, this maximum decreasing as the temperature
decreased. A test of the correlation is difficult since for only a few
temperatures and rates generally studied, do the elongations go through a
maximum, so only a portion of any set of data can provide data applicable
directly to the question. Uniaxial tensile failure data for one batch of
this propellant were available at temperatures from -75°F to 180°F and
strain rates from 0.074 to 1000 min^{-1}. The values are tabulated in Table 4,
each value being an average of five specimens. The analysis of the data
was performed graphically using the WLF technique by shifting the points,
plotted as ε_b versus log R for each temperature, horizontally and also
vertically as required to produce a continuous curve of ε_b versus log Ra$_T$.
Analysis started with the 180°F data and proceeded systematically down to
-75°F. The vertical shift, not required for elastomers without filler, was
done without regard to fitting a particular pattern and the results are
shown in Figure 5 where the experimental locations of the point $\varepsilon_b = 0$,
R = 1 min^{-1} are shown. The final reduced scale, log Ra$_T$, was selected for
a shift factor based on the WLF equation, as discussed below. The vertical
shift required, described by the term ε_T, was apparently zero for tempera-
tures of 80°F and above, but became increasingly large as the temperature
approached -75°F. The equation shown on Figure 5 describing the line
drawn for ε_T is

$$\varepsilon_T = 0.29 + 0.10 \log a_T \tag{1}$$

The same points used to define the line given by Equation (1) are
shown in a different way on Figure 6, e.g., the vertical shift ε_T versus

<center>**Table IV**</center>

<center>UNIAXIAL TENSILE FAILURE STRAINS, %, FOR A POLYURETHANE PROPELLANT</center>

Temp., °F	Strain Rate, min.$^{-1}$						
	0.074	0.74	7.4	100	500	1000	2000
180	46.4	52.4	65.0	81.8	92.5	92.2	90.1
140	50.8	56.9	66.5	85.4	88.6	100	92.7
110	55.8	67.8	71.4	84.9	88.6	91.4	107
80	66.4	66.1	81.4	92.2	95.3	98.8	99.9
40	71.1	76.4	79.6	98.1	91.8	90.0	88.1
0	70.6	84.2	79.2	76.0	65.8	62.5	68.1
-40	58.3	56.4	47.6	65.8	44.4	26.2	22.8
-60	50.2	53.0	48.4	———	23.9	15.5	14.8
-75	35.1	27.0	17.0	9.4	8.9	5.2	3.5

temperature, and the corresponding value of the shift factor, log a_T, versus temperature. The equations are

$$e_T = 0.24 - 0.004t \tag{2}$$

and

$$\log a_T = -0.5 - 0.04t \tag{3}$$

The selection of line positions was chosen to make the constants of Equations 1, 2, and 3 consistent among themselves, e.g., any two of the equations will define the third.

Considering now the usual WLF shift factor, the WLF equation can be rearranged to give

$$T = T_s - 101.6/(1 + \frac{8.86}{\log a_T}) = T_s - A_T \tag{4}$$

In this form, it can be seen that a graph of T versus A_T will be a straight line of unit slope. Such a graph is shown in Figure 7, with a graph of log a_T versus A_T shown at the right for convenience. Using the data of Figure 5, before T_s was selected and the data normalized, an arbitrary shift was made by assuming a value of log a_T at -75°F and thus determining the relative value of log a_T for all the other reference data points on Figure 5. Plotting these on Figure 7, the data gave a line of slope 0.89, and $T_s = 243$°K. Selection of a second estimate of log a_T at -75°F gave a second line of slope 1.10 and $T_s = 230$°K. Interpolation, which was found

to be non-linear, finally gave data which produced a line of slope 1.00 and $T_g = 235°K$ ($t_g = -36°F$).

If a WLF shift factor relation holds in this case for the low temperature data, then the straight line relation of Equation (3) would not be expected to apply. Comparison of the straight line with the WLF curve for $t_g = -36°F$ from Figure 7 is shown in Figure 6.

Temperature Shift Correlation

The scatter of the shift data for this propellant system led to an examination of the data when plotted versus temperature at each rate. It was discovered that the data could be superimposed to give a lower variability when an arbitrary origin was shifted both horizontally and vertically as shown in Figure 8. Not only do the data show good agreement with two straight line segments, but the shift points of the origin — selected at 0°F and zero strain — are remarkably consistent and show none of the scatter characteristic of the rate shift data of Figure 5. When plotted as log R versus the temperature shift required in Figure 9, a good straight line is obtained having the equation

$$\log R = 3.1 - 0.057t \tag{5}$$

Plotting the ε_R value at each point versus the temperature does not, however, give a straight line but rather a curve suggesting that ε_R does not increase above some limiting value even for very low rates of testing. This possibility may be evaluated by tests on the Very Low Rate Tester, but is already suggested by the values obtained in constant strain failure testing, equivalent to extremely low rates of loading.

The two straight line segments of Figure 8 give

$$\varepsilon_b + \varepsilon_R = 0.64 + 0.008t \text{ , } t < 50°F \text{ at } 1000 \text{ min.}^{-1} \tag{6}$$

$$= 1.14 - 0.0015t \text{ , } t > 50°F \text{ at } 1000 \text{ min.}^{-1} \tag{7}$$

It is of interest to note that the maximum occurs near 0°F for $R = 0.74 \text{ min}^{-1}$, a general characteristic of many polyurethane propellant systems.

A useful relation is obtained by taking the approximation relation from Figure 9

$$\varepsilon_R = 0.0043t \tag{8}$$

and substituting for t from Equation (5) gives

$$\varepsilon_R = 0.23 - 0.075 \log R \tag{9}$$

Substituting for ε_R from Equation (9) in Equations (6) and (7), we have

$$\varepsilon_b = 0.41 + 0.008t + 0.075 \log R \tag{10}$$

for temperatures below that giving the maximum ε_b and

$$\varepsilon_b = 0.91 - 0.0015t + 0.075 \log R \qquad (11)$$

for temperatures above. This maximum shifts with temperature, occurring at 53°F for 1000 min.$^{-1}$, 31°F for 100, 12°F for 7.4, -7°F for 0.74, and -18°F for 0.074 min.$^{-1}$.

The excellent correlation obtained by the temperature shift method will be tested on other systems. It would be expected that a difference would be observed in the basic constants of the relations, analogous to the rate shift produced by variations in the glass temperature for the WLF type of correlation.

CORRELATION OF FAILURE DATA WITH MOTOR FAILURES

Small motors with cast-in-case cylindrical grains have been used for studies of strain produced in motors and some of these motors have experienced failures. It appeared possible to test a failure hypotheses by study of these failures. A survey was made of 41 of these small case-bonded motors containing three different polyurethane propellants that had been thermally cycled to -75°F; b/a ratios from 4 to 12.5 were tested. Of these 41 motors, 15 failed by longitudinal cracking of the propellant grain. The strain in the motor, was compared at -75°F to the standard Instron data with the hope of establishing a correlation between the propellant failure strain under the condition as seen in the motor and the failure strain as encountered in uniaxial tensile tests.

The propellant property used was the lowest tensile strain at break reported from the two or three tensile tests taken at -75°F. Since some of the motors had been stored for various lengths of time at 0°F before cycling to -75°F an estimated correction for embrittlement was added to the strain at break as measured on unembrittled propellant. The strain at break corrected for embrittlement was divided by the measured strain in the motor on its first cycle to -75°F, to give a ratio called $\varepsilon_b/\varepsilon_{mm}$. The ratio of $\varepsilon_b/\varepsilon_{mm}$ is shown plotted against the percent of motors cracking at that ratio in Figure 10. When the ratio $\varepsilon_b/\varepsilon_{mm}$ was one or less all of the motors failed; when the ratio was two or more none of the motors failed. The region between one and two is the expected area of doubt caused by the wide distribution of propellant properties.

The embrittlement corrected value of strain at nominal maximum stresses was also divided by the measured strain of the motor on the first cycle to -75°F and plotted against the percent of motors failed as shown in Figure 11. As is evident by comparing Figure 11 with Figure 10, the strain at break would appear to be a much more discriminating value to use for predicting failure due to thermal cycling.

The correlation shown in Figure 10 using the relation $\varepsilon_b/\varepsilon_{mm}$ emphasizes the importance of adequate data on ε_b within and between batches, and the probable importance of measuring ε_b under environmental conditions closely approaching those in the motor. The success of the correlation with uniaxial data suggests that a concentration on uniaxial failure behavior is warranted for correlation with failure data on small charges having unrestrained ends. The data on yield bands also suggest that study on the number of yield bands produced in tubular grains is pertinent in this type

of correlation, as well as a general study of the production of yield bands at various temperatures; or more specifically, the formation of such bands in tensile specimens due to simultaneously straining and changing temperature.

GRAPHICAL REPRESENTATION OF FAILURE BEHAVIOR

The distribution of failure elongations at the various measurement temperatures can be combined with the expected strain in the motor as shown in Figure 12 to give a graphical representation of the expected failure behavior. This figure is drawn using the lower 3σ limit of individual failure values to describe the failure value expected in the poorest batch used in the motors. From the correlation of Figure 10, the intersection of the lower 3σ curve with the line corresponding to twice the maximum expected motor strain should be the highest temperature, T_f, at which failure could be expected. Similarly, the intersection with the calculated strain in the motor of the lowest failure elongation expected from the best batch of propellant, ε_{bm}, would give the lowest temperature, T_{uf}, to which any of the motors could be expected to cycle before failure.

ACKNOWLEDGEMENT

REFERENCES

1. Smith, T. L., and Stedry, P. J., "Time and Temperature Dependence of the Ultimate Properties of SBR Rubber at Constant Elongations", Journal of Applied Physics, 31, 1892-1898 (1960).

2. Williams, M. L., Landel, R. F., and Ferry, J. D., "The Temperature Dependence of Relaxation Mechanisms in Amorphous Polymers and Other Glassforming Liquids", Journal American Chemical Society, 77, 3701-37-7 (1955).
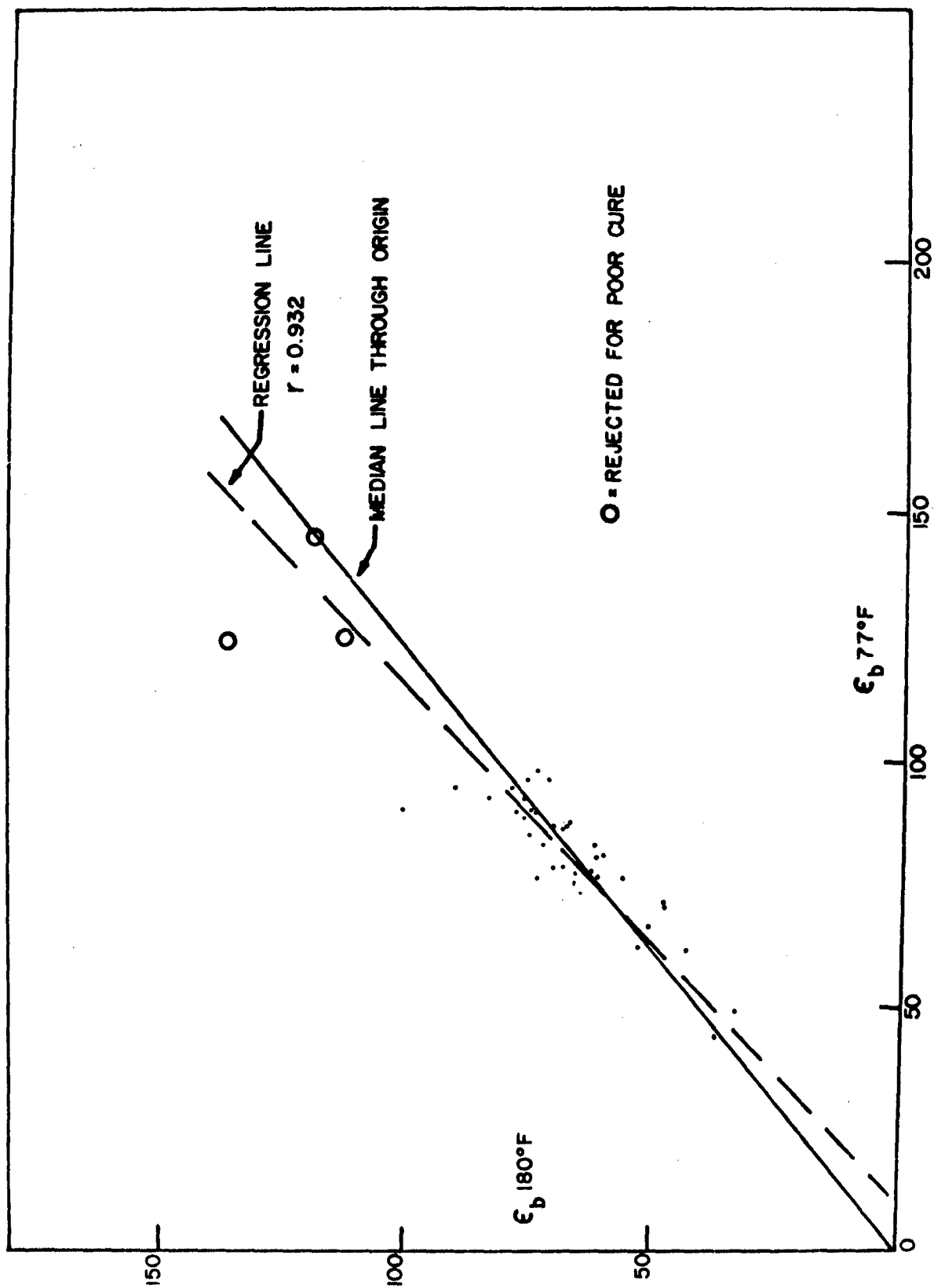
FIGURE 1. CORRELATION OF FAILURE STRAIN AT 180°F WITH THAT AT 77°F FOR SAME BATCH
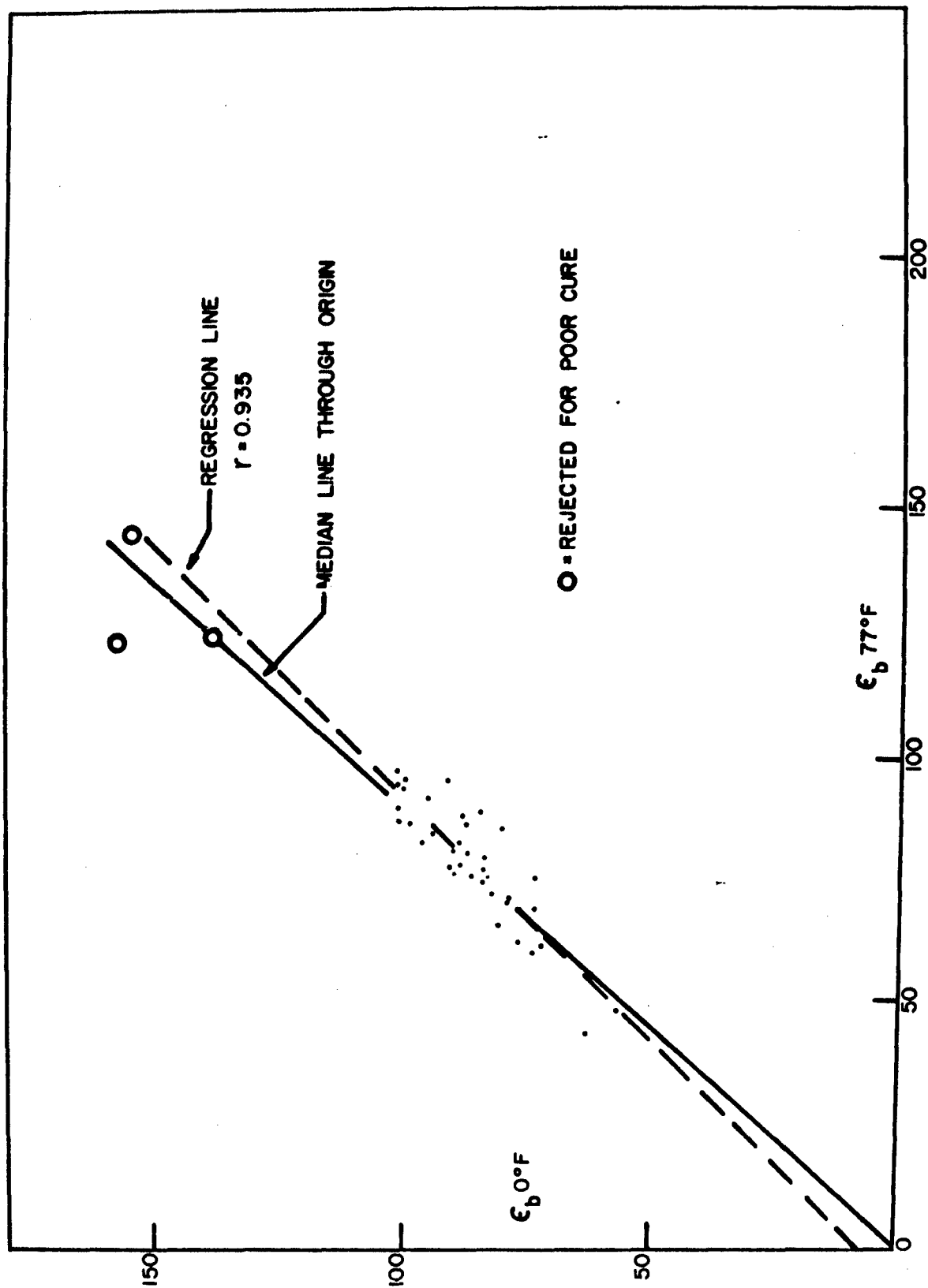
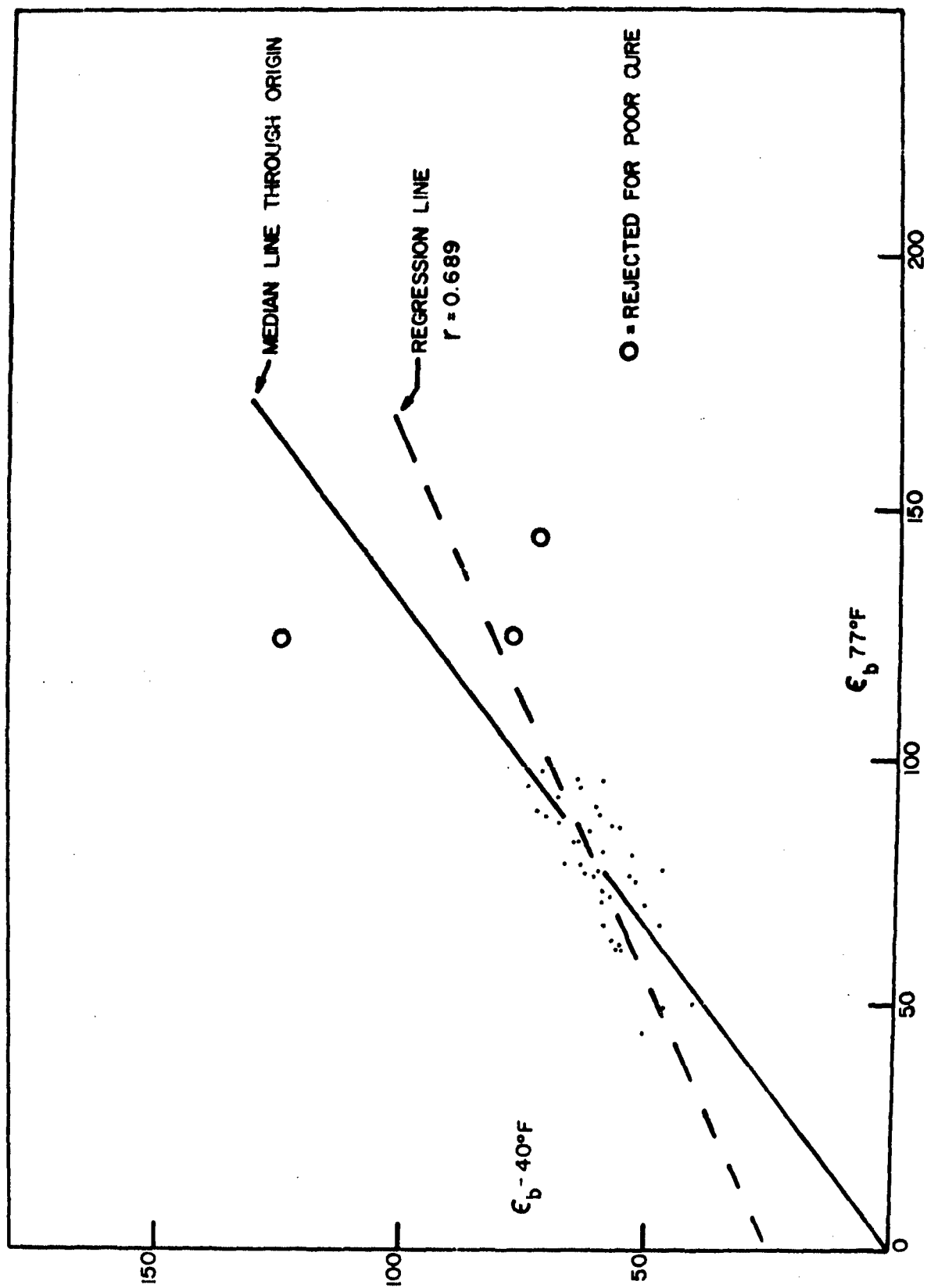FIGURE 2. CORRELATION OF FAILURE STRAIN AT 0°F WITH THAT AT 77°F FOR SAME BATCH

FIGURE 3. CORRELATION OF FAILURE STRAIN AT -40°F WITH THAT AT 77°F FOR SAME BATCH

MEDIAN LINE THROUGH ORIGIN

REGRESSION LINE
r = 0.689

O = REJECTED FOR POOR CURE

$\epsilon_{b\ 77°F}$

$\epsilon_{b\ -40°F}$
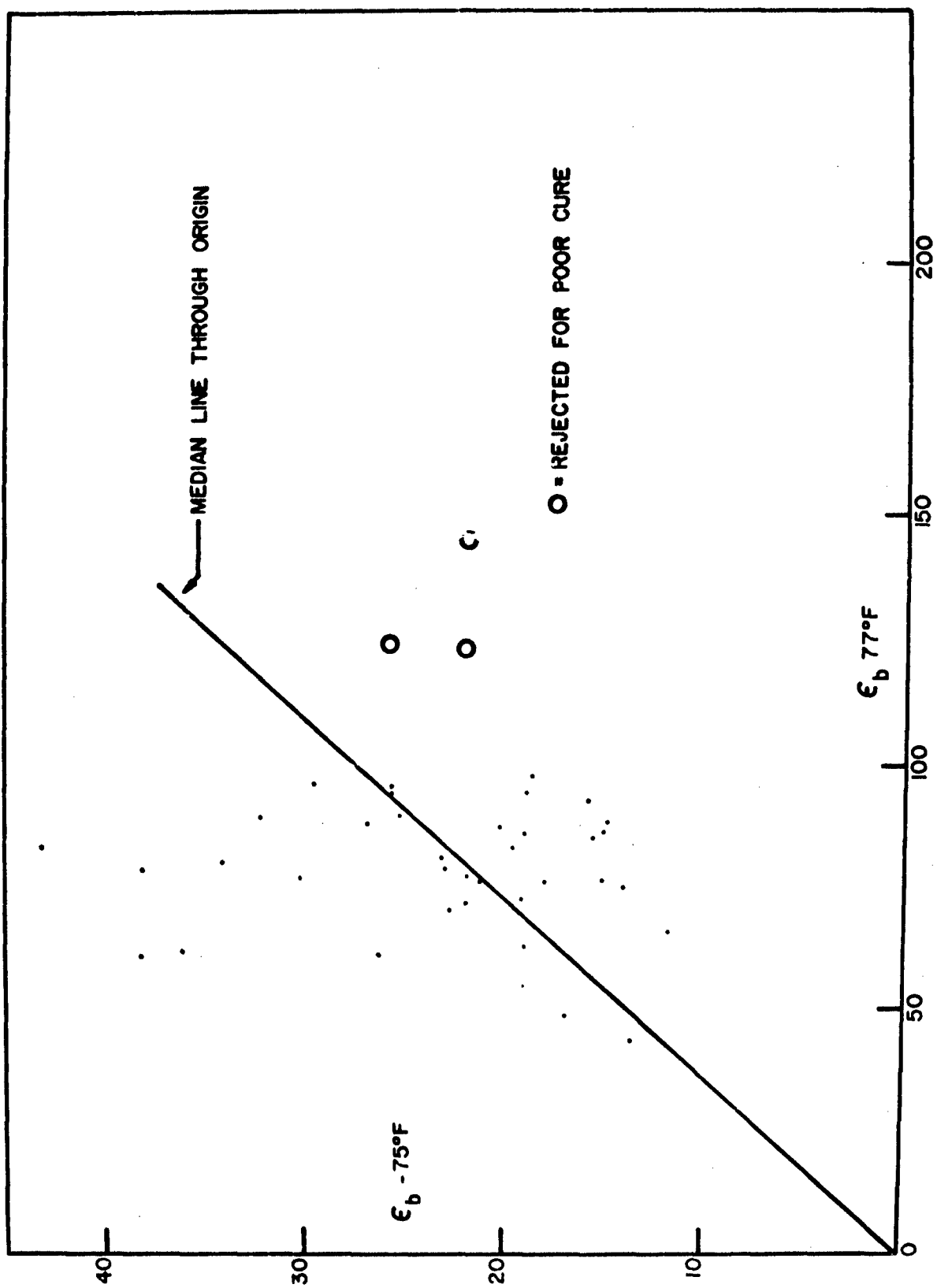
FIGURE 4. CORRELATION OF FAILURE STRAIN AT -75°F WITH THAT AT 77°F FOR SAME BATCH
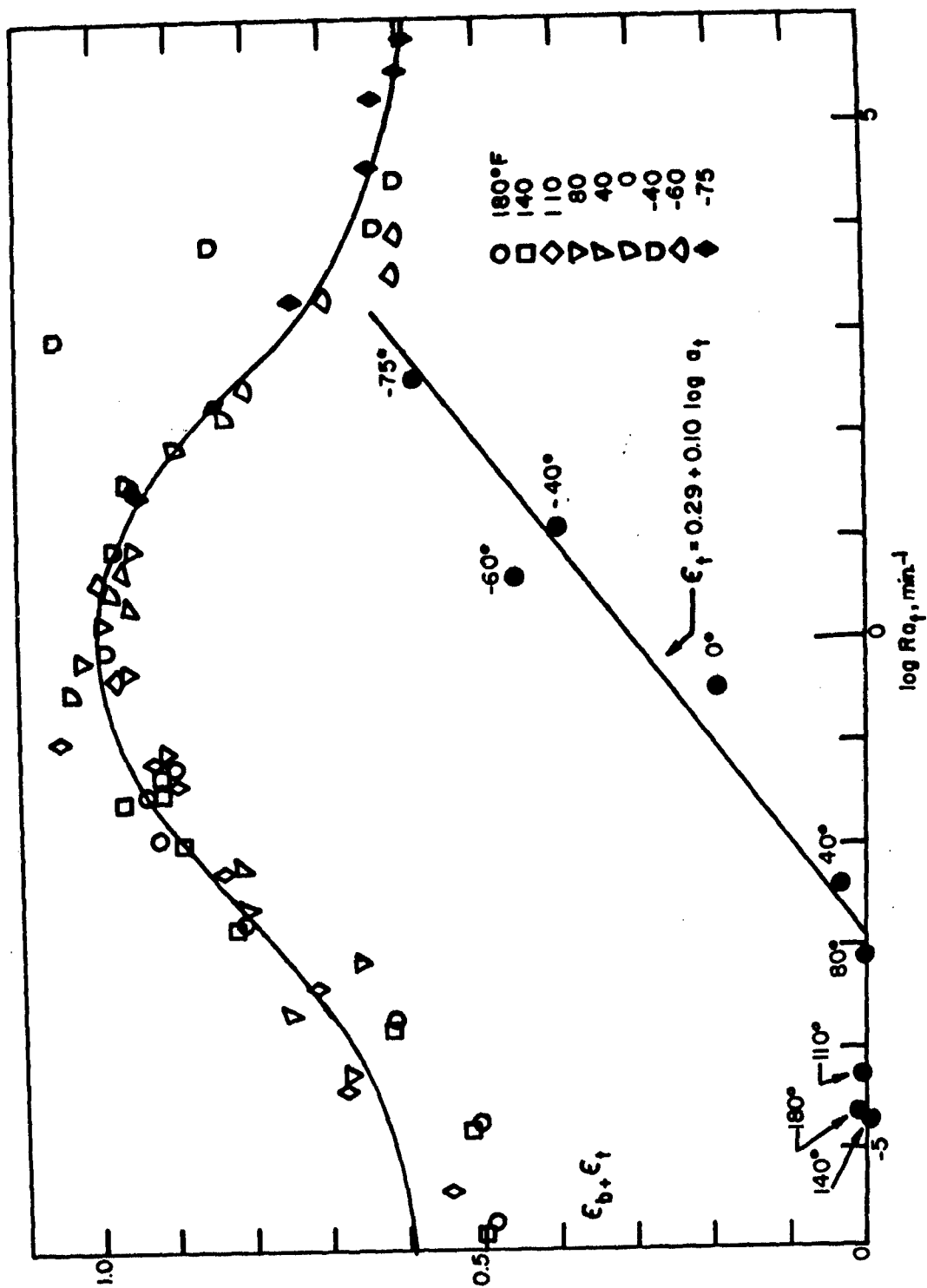
FIGURE 5.
FAILURE STRAIN OF A POLYURETHANE PROPELLANT WITH
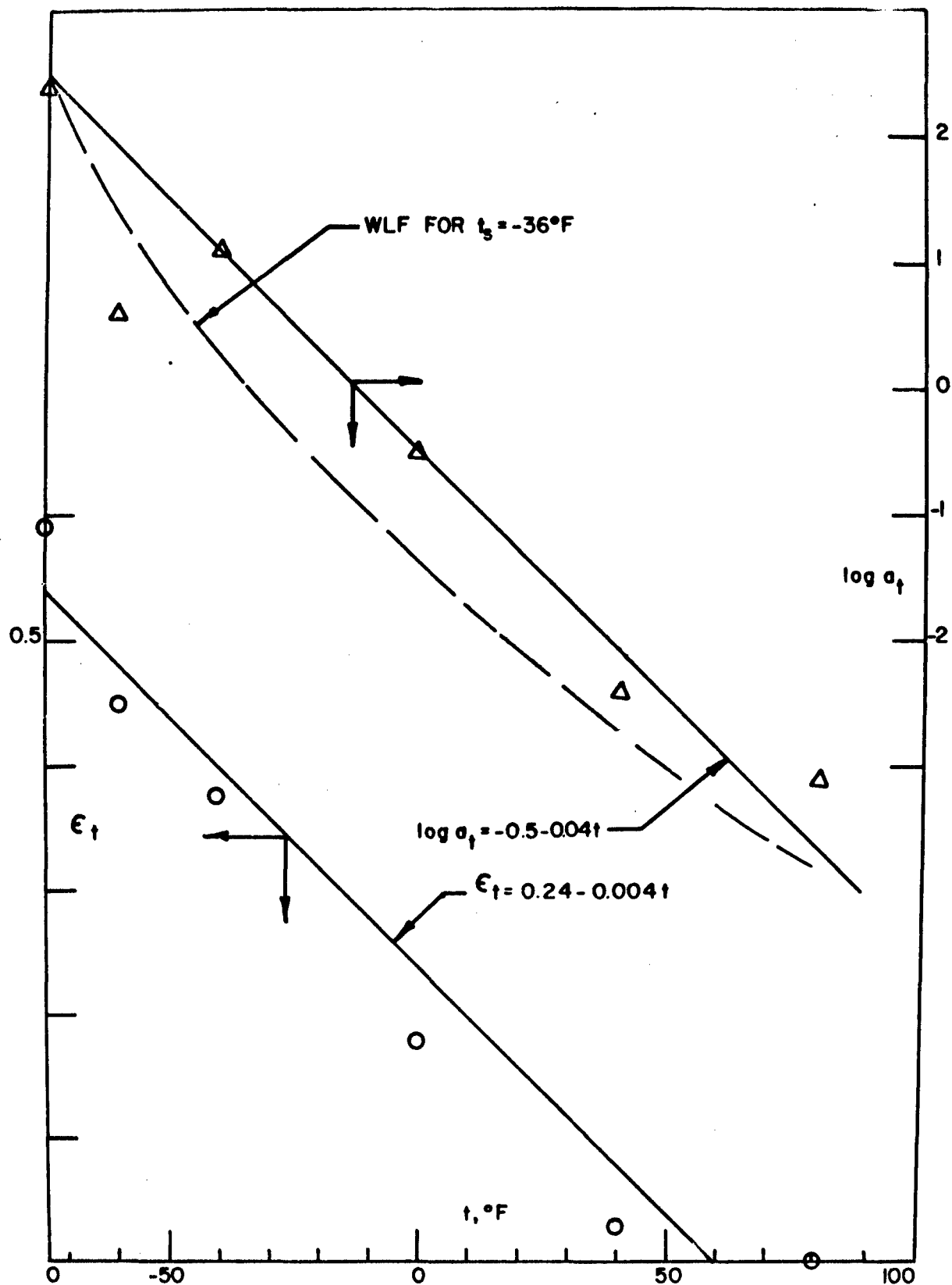REDUCED RATE OBTAINED WITH VERTICAL SHIFT FACTOR

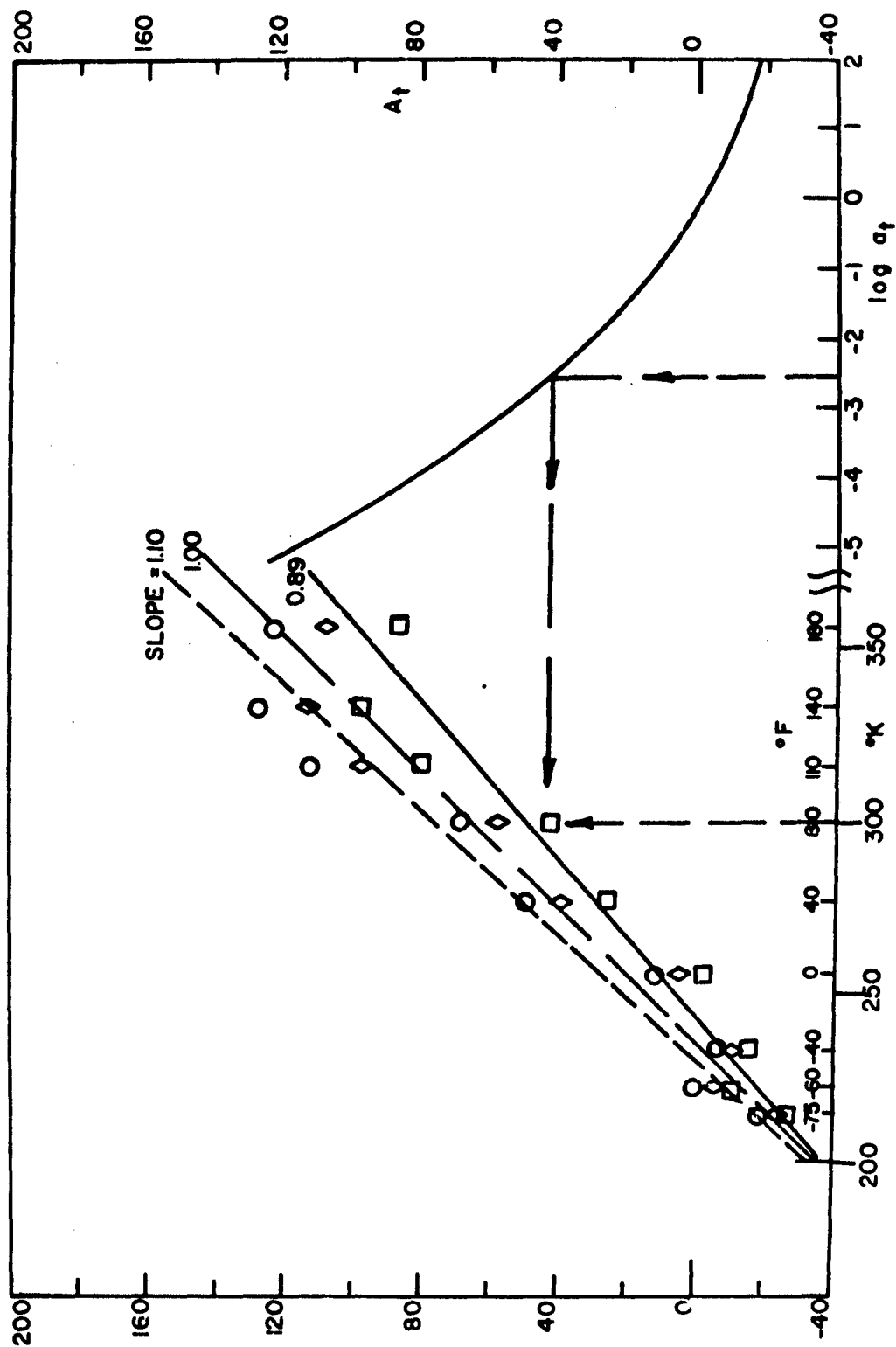FIGURE 6. RELATIONSHIPS OF SHIFT FACTOR AND TEMPERATURE

FIGURE 7.
DETERMINATION OF REFERENCE TEMPERATURE, T_s, USING
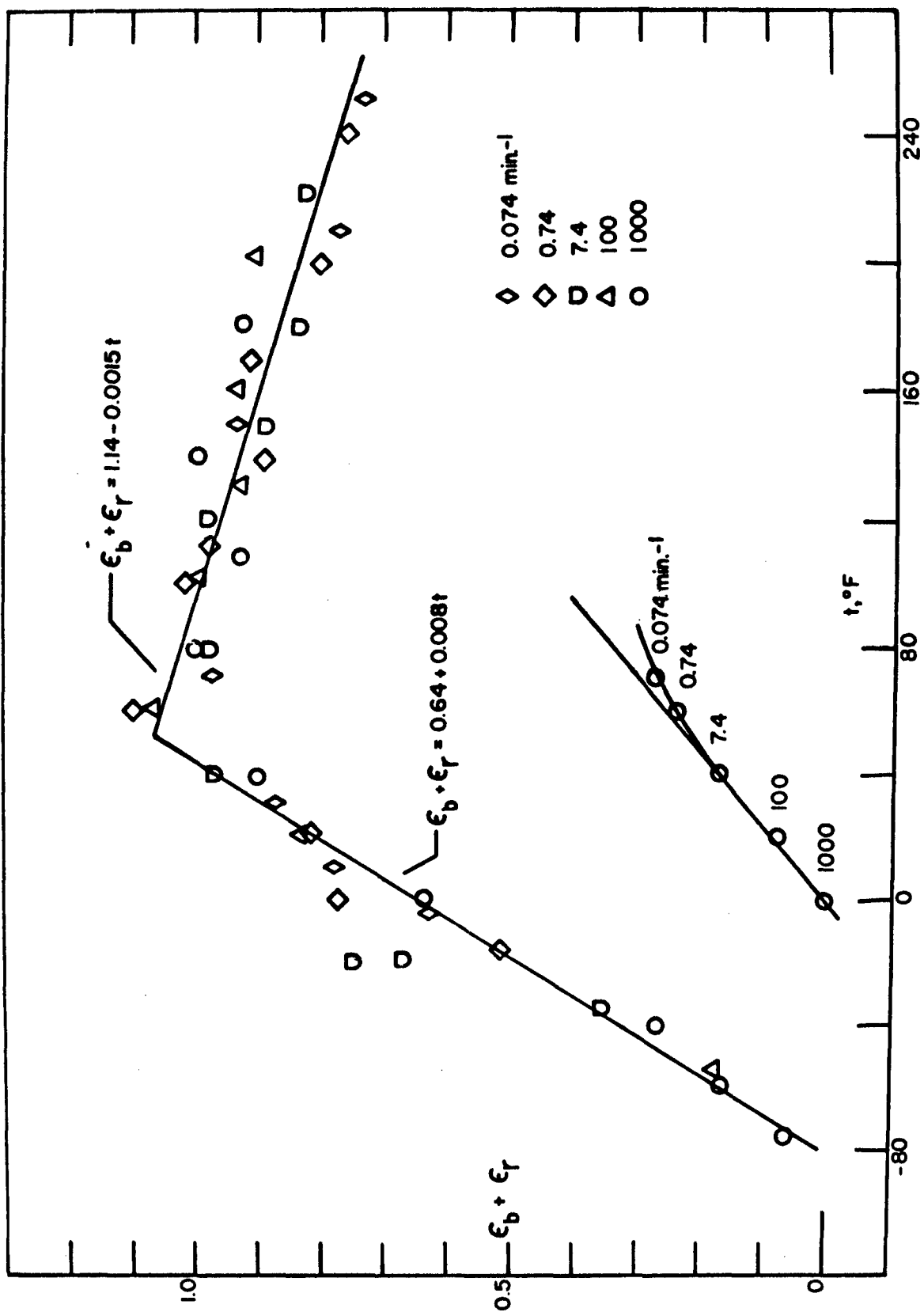SHIFT VALUES AND LINEARIZED SHIFT FUNCTION

FIGURE 8.
FAILURE STRAIN OF A POLYURETHANE PROPELLANT
WITH TEMPERATURE, USING THE RATE SHIFT FACTOR

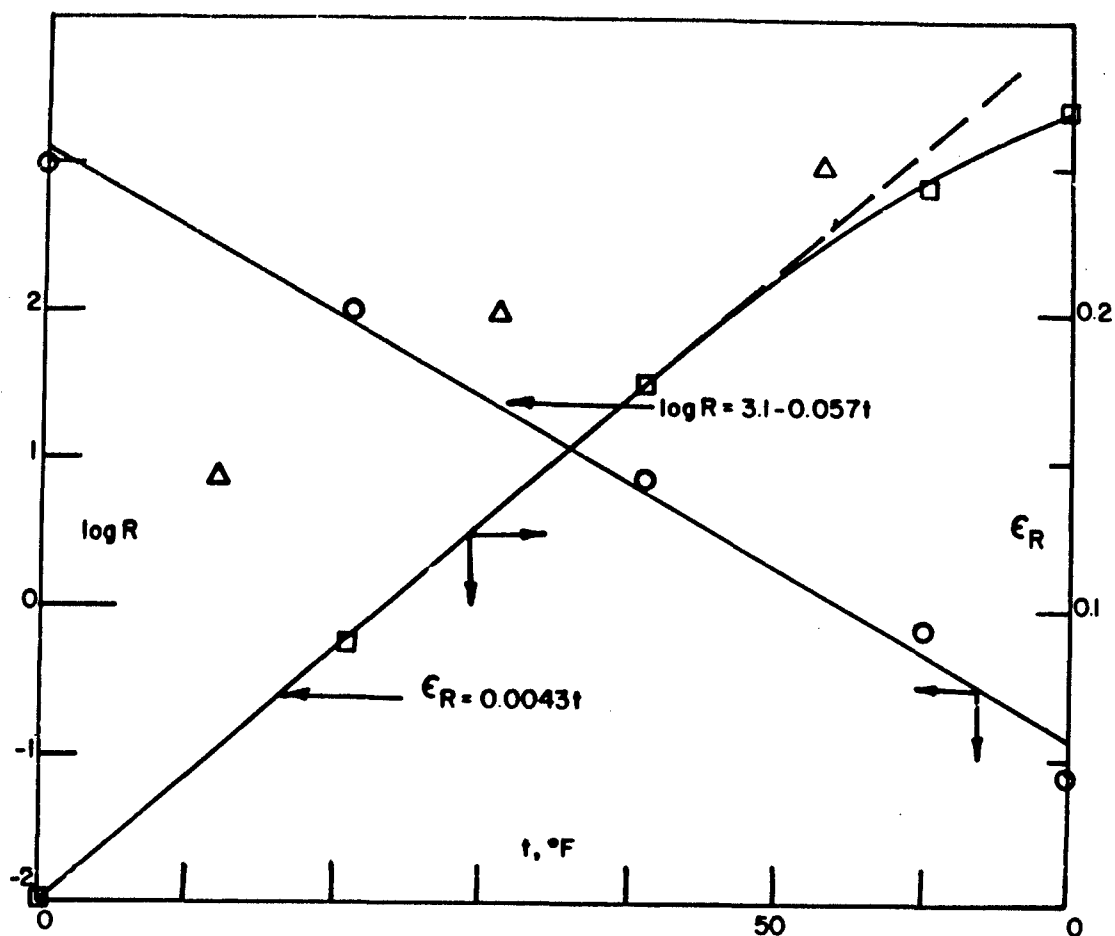FIGURE 9. RELATION OF LOG RATE AND RATE SHIFT FACTOR, ϵ_R, TO TEMPERATURE
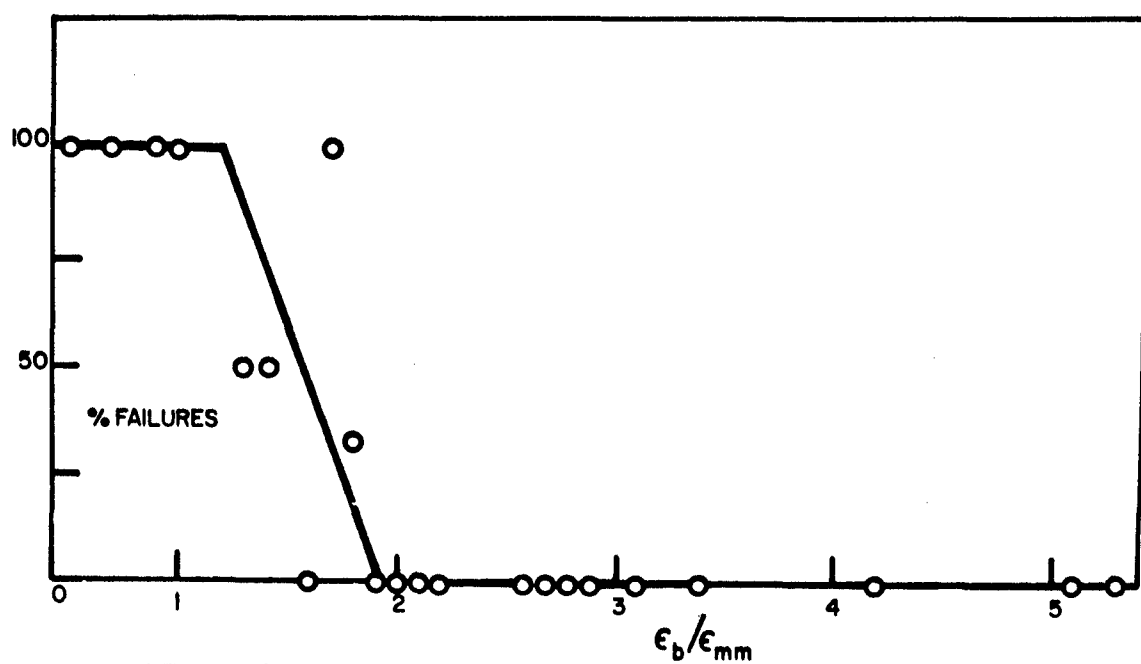
$$\log R = 3.1 - 0.057 t$$

$$\epsilon_R = 0.0043 t$$

FIGURE 10.
RELATION OF FAILURE STRAIN IN TENSILE SPECIMENS TO
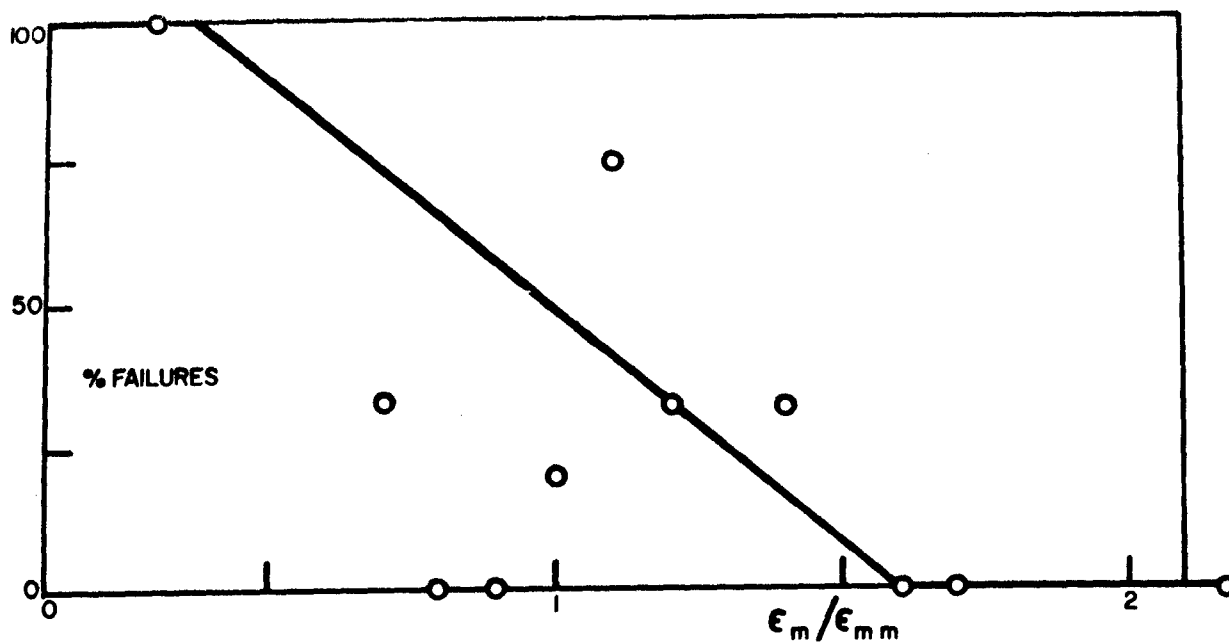CRACKING OF SUBSCALE TUBULAR CASE-BONDED GRAINS AT -75°F

FIGURE 11.
RELATION OF STRAIN AT MAXIMUM STRESS IN TENSILE SPECIMENS TO
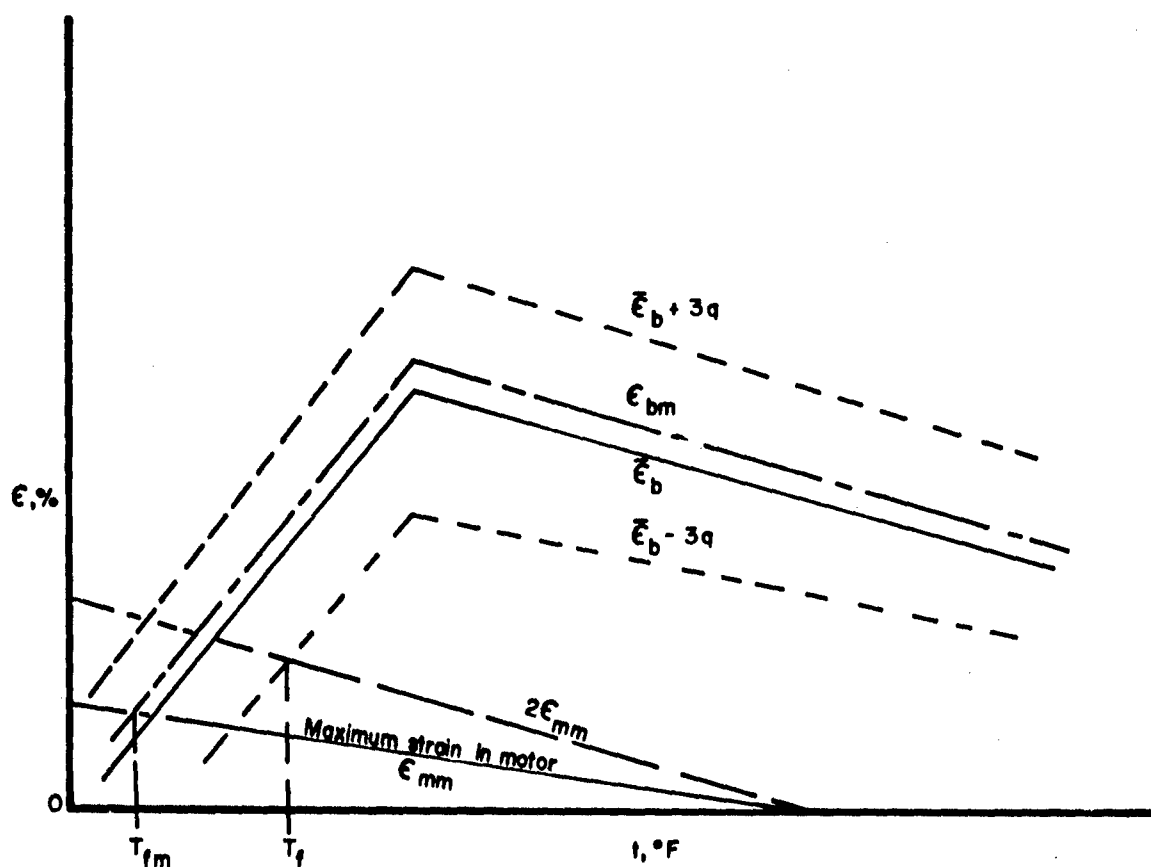CRACKING OF SUBSCALE TUBULAR CASE-BONDED GRAINS AT -75°F

FIGURE 12.   HYPOTHETICAL PROPELLANT PROPERTIES RELATED TO MOTOR STRAIN

THE EFFECT OF HYDROSTATIC PRESSURE ON THE UNIAXIAL
TENSILE PROPERTIES OF SOLID PROPELLANTS

C. C. Surland, J. R. Boyden, G. R. Givan

Aerojet-General Corporation

ABSTRACT

A method for determining the stress-strain behavior of binders and composites in the presence of hydrostatic pressure is discussed with a description of the remotely controlled test apparatus. Test results on binders and various propellants are given which support a modified strain-energy criterion for predicting the large effect of confining pressure on the tensile behavior of composites.

INTRODUCTION

The field of multiaxial propellant testing is more than adequately surveyed by J. H. C. Vernon (1), particularly for tensile tests with superimposed hydrostatic pressure. P. J. Blatz (2) indicates the need for multiaxial response behavior data to rectify various contemporary theories of failure for composites such as solid propellants.

This report discusses one method for obtaining the simple tensile behavior of composites prepressurized up to 1000 psi. The suppression of void formation in tensile tests of composites by the superimposed pressure is emphasized. Response data at various pressures are reported for polyurethane rubber and various polyurethane propellants. Calculations are presented which suggest that a total strain energy criterion may be useful for predicting the failure behavior of propellants in this type of stress field.

Additional data are presented which substantially verify the analysis of Milloway (3) which requires that the Young's Modulus of propellants be independent of the superimposed pressure.

TEST METHOD AND APPARATUS

Figure 1 describes schematically the essential details of the apparatus for obtaining uniaxial tensile tests with superimposed pressure. The complicated auxiliary features of the apparatus required for remote operation as dictated by safety considerations are not indicated.

The essentials of the strain gage — spring clip used to continuously monitor one lateral dimension of a tensile specimen during extension are shown in Figure 2. This device is described in more detail by Milloway and Surland (4).

Several procedures were used in the pressurized tensile testing. Tensile data were taken with pressure applied to the specimen prior to the application of tensile stresses and maintained constant throughout extension to

failure. In other cases, step changes in pressure were made during the course of extension. All testing was done at 75°F. Tensile force, specimen width, and jaw separation were all measured simultaneously for each specimen tested. The pressure level in the test chamber was monitored continuously with a strain gage pressure transducer. Some PV measurements were made on runs where the pressure level was changed during tensile tests. This was done to examine the feasibility of measuring PV energy exchanges for comparison with the FdL energy differences measured at the two pressure levels.

Lateral strain was calculated from X-Y records of the calibrated linear clip gage response and based on the initial dimensions of the specimen at atmospheric pressure. Longitudinal strains and FdL energy to break were assessed from X-Y records of the jaw separation of the tensile grips and the tensile load. Stresses are based on the original cross section of the specimen. An empirical relation suggested by Blatz (5)

$$e^{\frac{i.s.}{k}} - 1 = \epsilon \qquad (1)$$

gave a straight line fit for plots of ln $(1 + \epsilon)$ versus jaw separation, of slope 3.3. λ was obtained from photographic strain measurements coordinated with jaw separation values. $k = 3.3$ was found to hold satisfactorily for all composites tested. Above 47 percent strain, a nominal gage length of 2.70 inches was assumed for the standard JANAF shaped tensile specimen. These were machined in the manner described by Farris (6).

Specimen specific volumes were calculated from the relationship

$$(\lambda \text{ lateral})^2 \times (\lambda \text{ longitudinal}) = \lambda \text{ Volume} \qquad (2)$$

assuming a uniform straining throughout the specimen.

Various methods for direct measurement of the actual longitudinal extension in the gage section of the specimen were investigated. Some of these showed promise but could not be adapted to the prototype pressurized-tensile tester described in Figure 1, because of limited access to the specimen within the 2.0 inch diameter base of the pressure chamber. An improved pressure-tensile tester design based on the principles of Figure 1, but featuring a much larger test chamber, will permit more precise investigation of the longitudinal strain in the future. The energy contributions to failure concerned with volume changes in the specimen upon extension under pressure are very sensitive to accurate volume measurements. Both the single point assessment of lateral width and the exigency of using 2.70 as a nominal gage length for the JANAF tensile specimen at elevated pressures are recognized as sources of considerable error. Volumetric methods of assessing volume change are being studied, especially in view of the striation of propellants upon extension as observed by Bills (7).

All tensile results are reported for an initial nominal jaw separation rate of 2.0 inches per minute. No provision was made in the equipment to maintain the jaw separation rate constant in the instances where chamber pressure was changed during an extension cycle. However, for the cases discussed below, where this is important, pressure changes of 500 psig in

the chamber pressure resulted in changes of 10% or less in the jaw separation rate. These changes were determined to be negligible in the shape and energy content of the stress-strain curves for the materials tested.

THEORY AND RESULTS
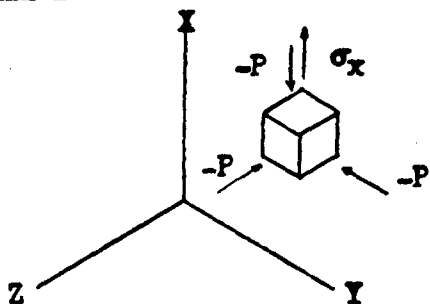
Effect of Pressure on Young's Modulus

FIGURE 3.
STRESS CONDITIONS FOR PRESSURIZED
UNIAXIAL TENSILE TEST

The anticipated strain behavior of the pressurized strain specimen can be assessed from the application of elastic theory to the unit specimen subjected to the stresses indicated in Figure 3.

The equation

$$\epsilon_3 = \frac{1}{E} (\sigma_3 - \nu \sigma_y - \nu \sigma_z) \qquad (3)$$

gives the relation between Young's Modulus (E), the stress (σ) and strain (ϵ) in the X direction, and Poisson's Ratio (ν). In this case σ_3, the combined tensile and hydrostatic stress in the X direction is $\sigma_3 = \sigma_x - P$, and the lateral stresses due to the pressure are $\sigma_y = \sigma_z = -P$.

Then
$$\epsilon_3 = \frac{1}{E} (\sigma_x - P + 2 \nu P) \qquad (4)$$

or
$$\epsilon_3 = \frac{\sigma_x}{E} - \frac{3 P(1 - 2\nu)}{3 E} \qquad (5)$$

$$\epsilon_3 = \frac{\sigma_x}{E} - \frac{P}{3K} \quad \text{where } K = \text{the bulk modulus} \qquad (6)$$

and
$$\epsilon_3 = \epsilon_x - \frac{1}{3} \cdot \frac{\Delta V}{V} \qquad (7)$$

then
$$E = \frac{d\sigma_3}{d\epsilon_3} \qquad (8)$$

independent of pressure, and $\frac{\Delta V}{V}$ is the unit volume strain.

The sketch of Figure 4 illustrates the anticipated stress-strain behavior of tensile tests at various pressures. It should be noted here that P=0 refers to absolute zero, which is not the ordinary condition for ambient tensile testing. Atmospheric pressure may have considerable effect on the observed stress strain behavior, especially for composites cured under vacuum. The dashed stress-strain curve for positive pressure has been displaced to the origin of the P=0 curve to show independence of the initial elastic modulus on the pressure. Note that $E = \sigma_3/\epsilon_3$ only when P=0.
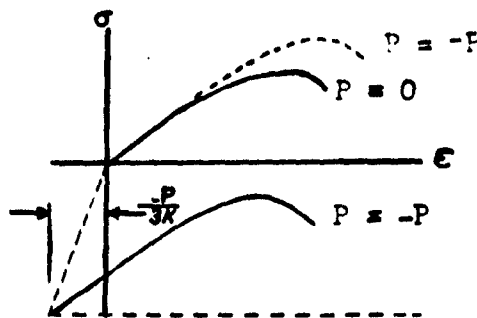

FIGURE 4.
STRESS-STRAIN CURVES
AT VARIOUS PRESSURES

Figure 5 compares stress-strain curves adjusted to common origins for tensile tests of polyurethane rubber at pressures of 15, 108, and 510 psia.

The coincidence of the curves at low strains shows little if any dependence of E on pressure level in accordance with (8). The effect of pressure on the breaking stress and strain cannot be assessed from this limited series. The results are averages for five specimens at each pressure with considerable variation in ultimate stress and elongation within each set.

Stress strain curves for a polyurethane propellant having 35% volume fraction binder and 65% volume fraction filler are shown in Figure 6. Average curves are shown for test chamber pressures of 36 psia and 512 psia. The spread in each set is shown by the lightly dashed curves. The origins are adjusted for comparison and show the initial moduli to be unaffected by pressure. It is interesting to note that failure occurred in the 512 psia specimens while the combined stress in the direction of extension was compressive.

ENERGY CONSIDERATIONS UPON EXTENSION TO FAILURE

Lateral contraction data for this series is presented in Figure 7. Both stress and lateral contraction were obtained by simultaneous X-Y recordings of these parameters as a function of jaw separation. The lightly dashed curves on either side of the average curve show the wide variability in both lateral contraction and ultimate elongation between individual specimens in a set.

Calculated volumes for the specimens as a function of elongation from the data of Figure 7 show that on the average significant volume changes occur upon extension even with superimposed pressures of 512 psia.

The work done by the pressurized gas of the chamber on the specimen may be equated to the work of volumetric expansion of the specimen caused by void formation upon extension. The thermoelastic expression

$$d\mathcal{E} = TdS - PdV + FdL \qquad (9)$$

relates the various forms of energy developed in the pressurized tensile dumbbell upon extension to the total energy $\mathcal{E}$.

> TdS is a measure of the energy changes
> associated with Temperature T and Entropy S.
> - PdV is the work of dilatation for pressure
> P and Volume V.
> FdL is the load-extension increment of work.

The thermoelastic properties of propellants are such that the TdS term in (9) contributes less than 1% to the total energy and is neglected in the gross energy discussions that follow for uniaxial extension of pressurized composites.

A total strain energy criterion for failure in the case of pressurized tensile tests would require that

$$d\mathcal{E}_{P_1} = FdL_{P_1} - PdV_{P_1} \quad \text{and} \quad d\mathcal{E}_{P_2} = FdL_{P_2} - PdV_{P_2} \qquad (10)$$

For data taken from the pressure tensile results shown in Figures 6 and 7,

$$\mathcal{E}_{36} = 52 \; \frac{\text{in-lb}}{\text{in}^3} \qquad\qquad \mathcal{E}_{512} = 103 \; \frac{\text{in-lb}}{\text{in}^3}$$

These results appear to be negative. However, the uncertainties of the volume measurements at high pressures preclude conclusions one way or another. Rearrangement of (10) to

$$PdV_{512} = FdL_{512} - (FdL_{36} - PdV_{36}) \qquad (11)$$

and calculation of the volume change at high pressure required to satisfy the strain energy hypothesis from the experimentally less critical terms on the right side of (11) results in a calculated volume increase of 20.4 percent at break. The heavy dashed curve shows the average lateral contraction and extension of the 5 specimens tested at 512 psia for 20.4 percent volume change at break. In any case, the unusual volumetric changes in composites upon extension warrant more careful measurements of their response to multiaxial stresses and further study of strain energy relationships, at least in the limited pressure ranges of interest in solid propellants.

Further experiments are planned to examine the effect of increasing pressure on the ultimate stress and elongation. Tensile behavior as a function of hydrostatic pressure level was obtained on six solid propellants representing considerable variation in composition, particularly in the amount and character of the oxidizers or fillers. The effect of pressure for one formulation, shown graphically in Figure 8, was generally characteristic of the behavior of all the composites tested. Maximum pressures of 600 psig have been used in testing to date. This range will be extended with improved equipment to at least 2000 psig.

TENSILE TESTS WITH STEP CHANGES IN PRESSURE

Figures 9 and 10 are tensile and lateral contraction curves (Specimen No. 22) representative of the behavior of propellant specimens subjected to rapid changes in the test pressure levels. The two extrapolated portions of this curve correspond quite well with the average behavior of this composite at similar pressure levels as shown in Figure 6. Some high degree of reversibility is indicated in the energy contribution of the dilatation in going from one pressure state to another. Specimens which are extended at high pressure beyond their ultimate elongation at low pressure failed immediately upon rapid reduction of pressure in the test chamber.

The difference in FdL energy between the low pressure and high pressure tensile curves at the extension for which the pressure shift applies was found to be 9.3 in-lb/in^3 by graphical integration for the example of Figures 9 and 10. Integration of the PV equation proposed by Milloway and Surland (4)

$$\frac{V^*}{V} = \left[\frac{1 - \delta}{1 - \delta e^{-3/4 \; P/\mu}} \right]^{4/3 \; \mu/\kappa} + 1 \qquad (12)$$

where: V^* = volume for material with voids
V = volume for void-free material (i.e., $\delta = 0$)
δ = volume fraction voids (17.5%)
P = hydrostatic pressure (40 - 505 psia)
μ = shear modulus (550 psi)
K = bulk modulus (void-free)(.70 x 10^6 psi)

for composities containing voids between the pressure limits of 40 to 505 psia gives a value of 11.7 in-lb/in³ for the energy of compression between these curves. The agreement in these results supports the suggestion of reversibility in the work of dilatation in the pressurized tensile test. The estimated properties of the material constants used in this calculation are given following the identification of the symbols.

Table I is a summary of the results of energy calculations on interrupted pressure tests such as for specimen No. 22 in Figures 9 and 10. Similar results are shown for the specimens of Figures 6 and 7. Such calculations for the interrupted tests required extrapolation of the low pressure portions of the stress-strain and lateral contraction records to failure on a best judgement basis-considering the average behavior for similar low pressure tests and symmetry with the high pressure portions of the records. Inspection of Table I shows considerable variation of the total energy to break, as before. However, on the average these data support a maximum strain energy criterion as a first approximation for a range of pressures of interest in applications of solid rocket propellant. At this stage in the development of a theory of failure for composites, even first approximations may have a place. Current objectives are to improve the procedures and equipment for obtaining pressurized tensile data. These data will be used to test various failure criteria.

REFERENCES

(1) Vernon, J. H. C., "The Effect of Confining Pressure on the Mechanical Properties of Solid Propellants," <u>Bulletin of the Joint Meeting of the JANAF Panels on Physical Properties and Surveillance of Solid Propellants</u>, SPIA, PP-13, pp. 1-23, August, 1960.

(2) Blatz, P. J., "The Yield Surface in Normal Stress or Normal Strain Space," <u>Bulletin of the Joint Meeting of the JANAF Panels on Physical Properties and Surveillance of Solid Propellants</u>, SPIA, PP-13, pp. 165-186, August, 1960.

(3) Milloway, W. T., Aerojet-General Corp. Memorandum, "Theoretical Elastic Analysis of Tensile Specimens Under Hydrostatic Pressure," MPR:575, August 8, 1961.

(4) Milloway, W. T., Surland, C. C., and Skulte, I., "The Effect of Initial Voids on the Bulk Modulus and Void Formation on Uniaxial Extension," <u>Bulletin of the JANAF-ARPA-NASA Panel on the Physical Properties of Solid Propellants</u>, November, 1961.

(5) Blatz, P. J., Guggenheim Aeronautical Laboratory, California Institute of Technology, Personal communications.

(6) Farris, R. J., Davidson, F. H., and Briar, H. P., "JANAF Tensile Specimen Preparation and Evaluation," <u>Bulletin of the JANAF-ARPA-NASA Panel on the Physical Properties of Solid Propellants</u>, November, 1961.

(7) Bills, K. W., "Study of Mechanical Properties of Solid Rocket Propellant," Report No. 0411-10Q-1, Contract AF 33(600)-40313 S.A. No. 1, pp. 33-41, 30 May 1961.

TABLE I

SUMMARY OF TENSILE AND LATERAL CONTRACTION DATA FOR INTERRUPTED AND UNINTERRUPTED PRESSURE LEVELS (~40 PSIA TO ~515 PSIA)

a. Specimens with change in pressure level during tensile test.

Specimen number	FdL Energy to break (in-lb/in³)		Extension at break (per cent)		Total energy to break (in-lb/in³)		Volume change at break (per cent)	
	~40	~515	~40	~515	~40	~515	~40	~515
19	63	133	83	103	53	67	.275	.120
20	61	117	83	95	49	25	.338	.176
21	68	134	93	114	59	114	.241	.147
22*	62	116	84	99	50	46	.305	.135
Average	64	125	86	103	53	63	.290	.144

b. Average values for five ~40 psia and five ~515 psia uninterrupted specimens.

	FdL Energy to break (in-lb/in³)		Extension at break (per cent)		Total energy to break (in-lb/in³)		Volume change at break (per cent)	
**	59	154	87	120	52	103	.200	.100

* Tensile and lateral contraction curves for this specimen are shown in Figures 9 and 10.

** Tensile and lateral contraction curves showing the average and range for these specimens are shown in Figures 6 and 7.
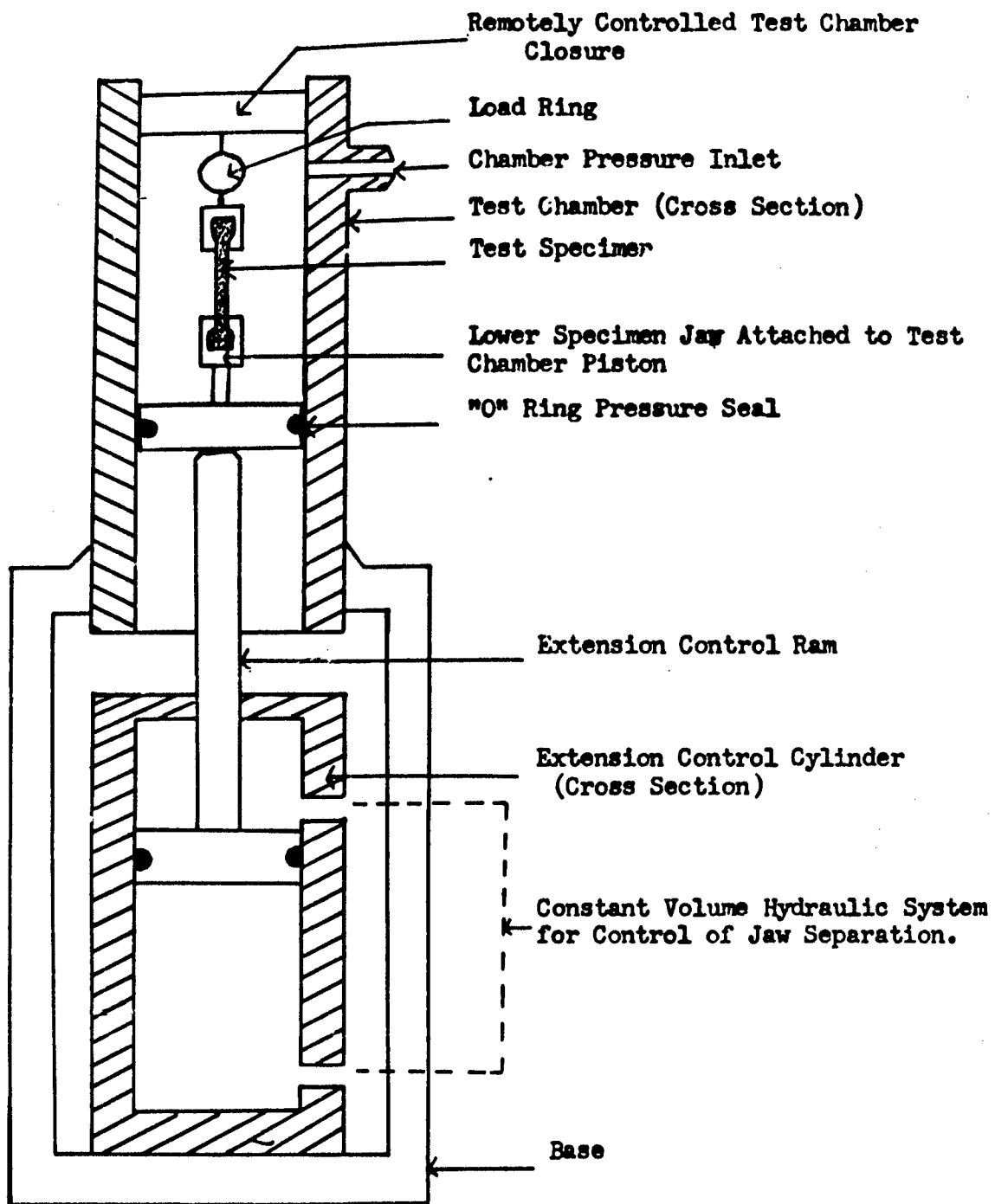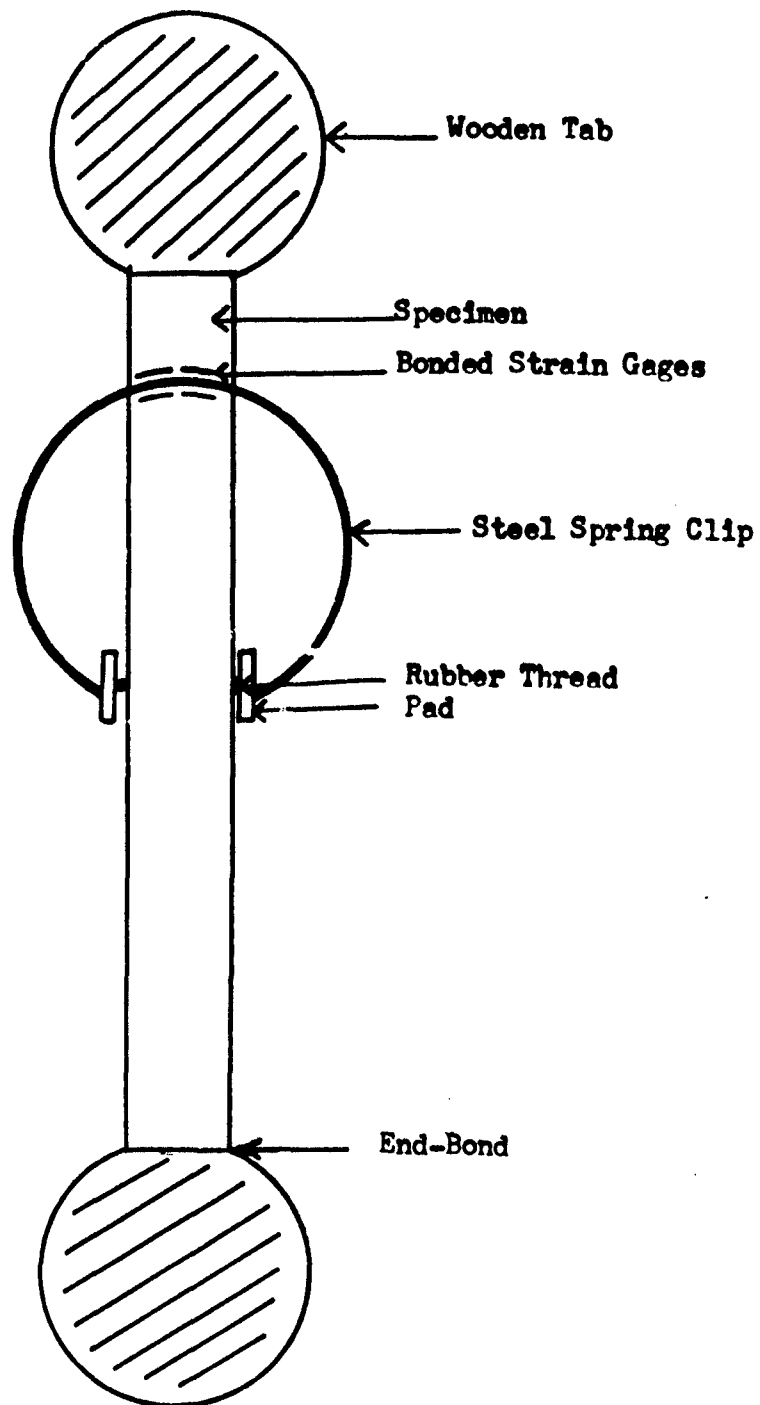
Remotely Controlled Test Chamber Closure

Load Ring

Chamber Pressure Inlet

Test Chamber (Cross Section)

Test Specimen

Lower Specimen Jaw Attached to Test Chamber Piston

"O" Ring Pressure Seal

Extension Control Ram

Extension Control Cylinder (Cross Section)

Constant Volume Hydraulic System for Control of Jaw Separation.

Base

FIGURE 1. PRESSURIZED TENSILE TEST

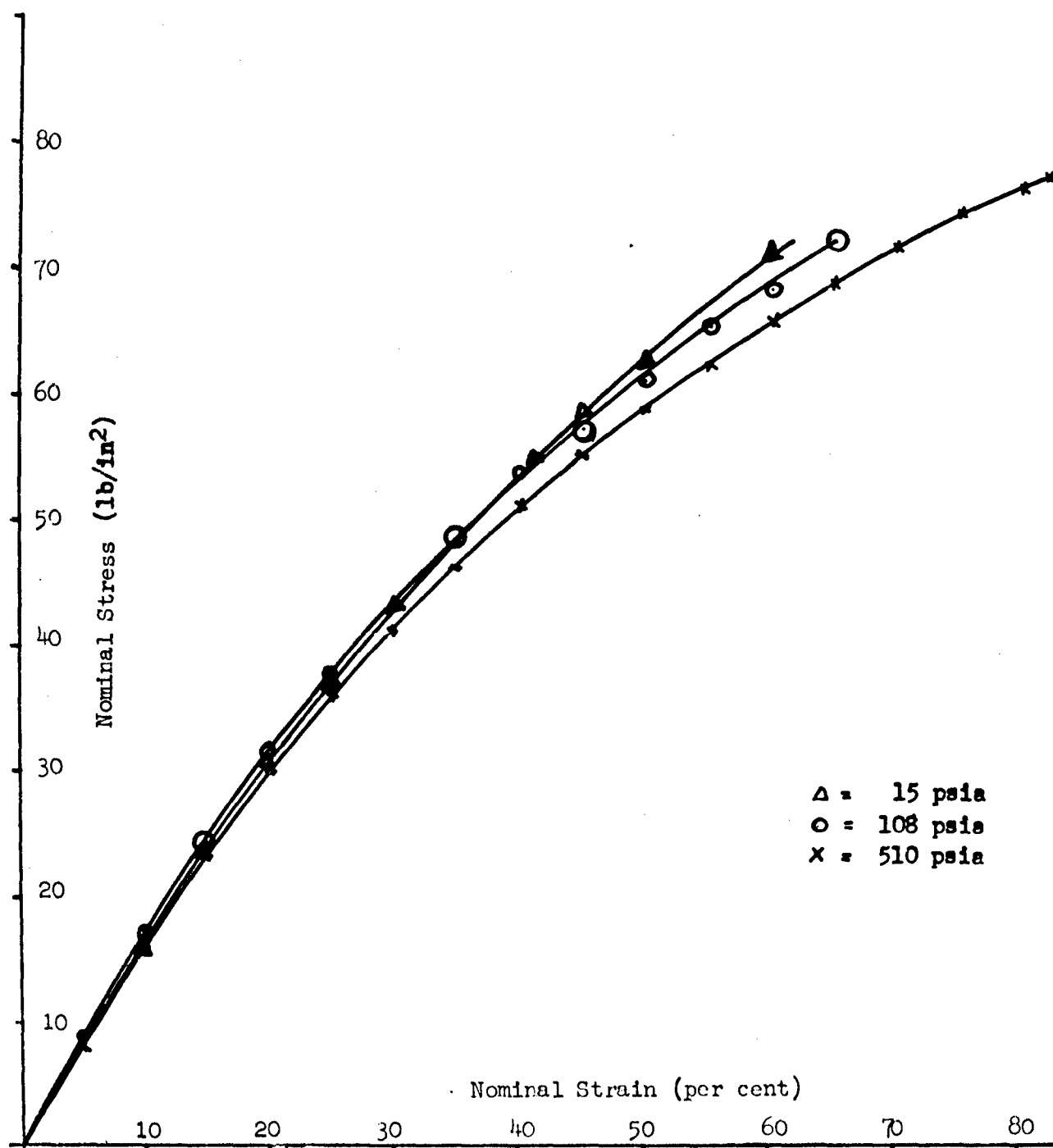FIGURE 2. LATERAL CLIP GAGE AND END-BONDED TENSILE SPECIMENS

FIGURE 5.
STRESS-STRAIN CURVES FOR POLYURETHANE RUBBER TESTED
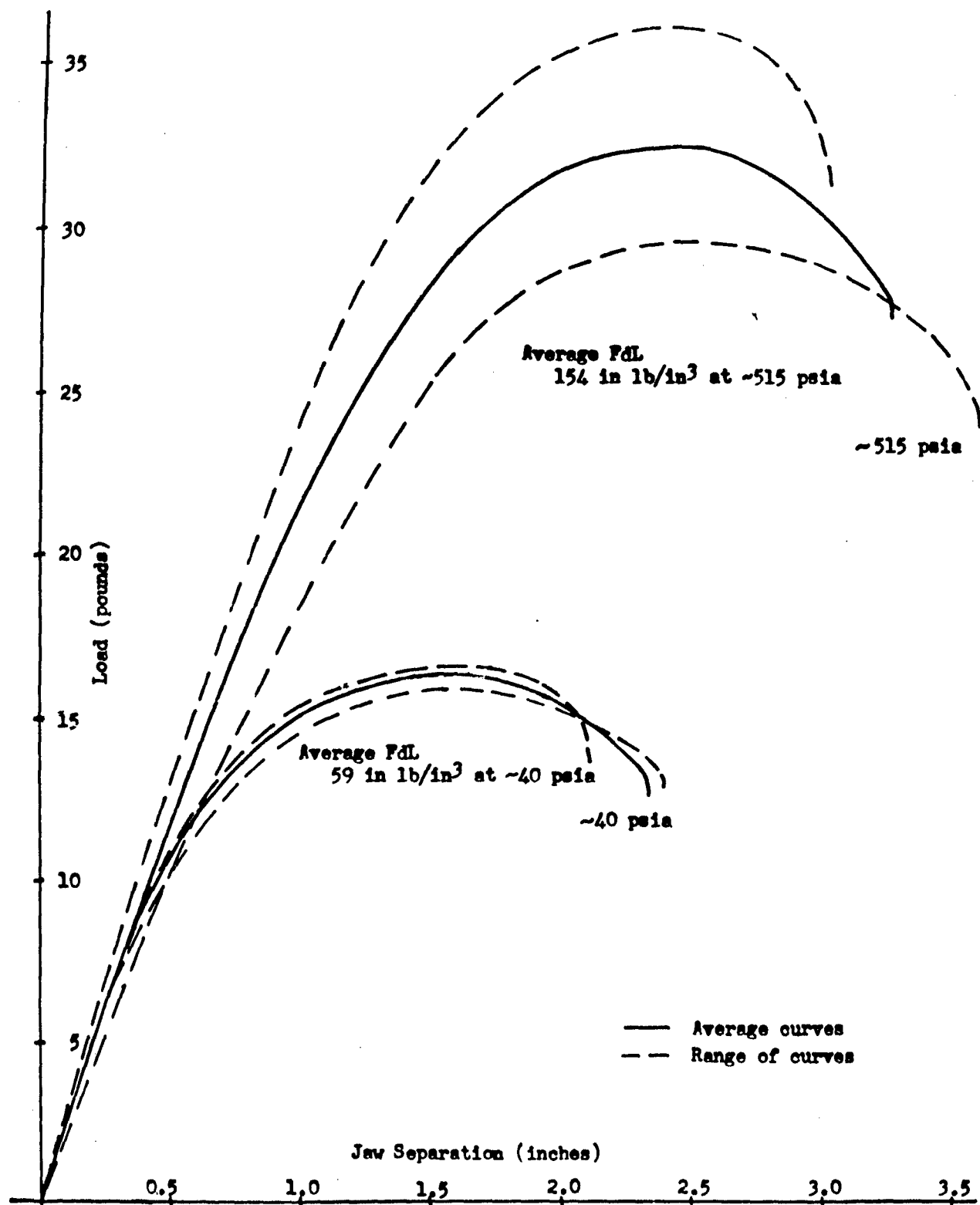AT CONSTANT PRESSURES OF 15, 108, AND 510 PSIA.

FIGURE 6.
STRESS-STRAIN CURVES FOR PROPELLANTS TESTED AT CONSTANT PRESSURES OF ~40
AND ~515 PSIA FOR WHICH LATERAL CONTRACTION DATA ARE SHOWN IN FIGURE 7

$w_0 =$ .375

Jaw Separation (inches)

~40 psia
—— Average curve
— — Range of curves

$w_0 =$ .375

~515 psia
Average curve
— — Range of curves
━ ━ Curve such that $d\mathcal{E}_{40} = d\mathcal{E}_{515}$
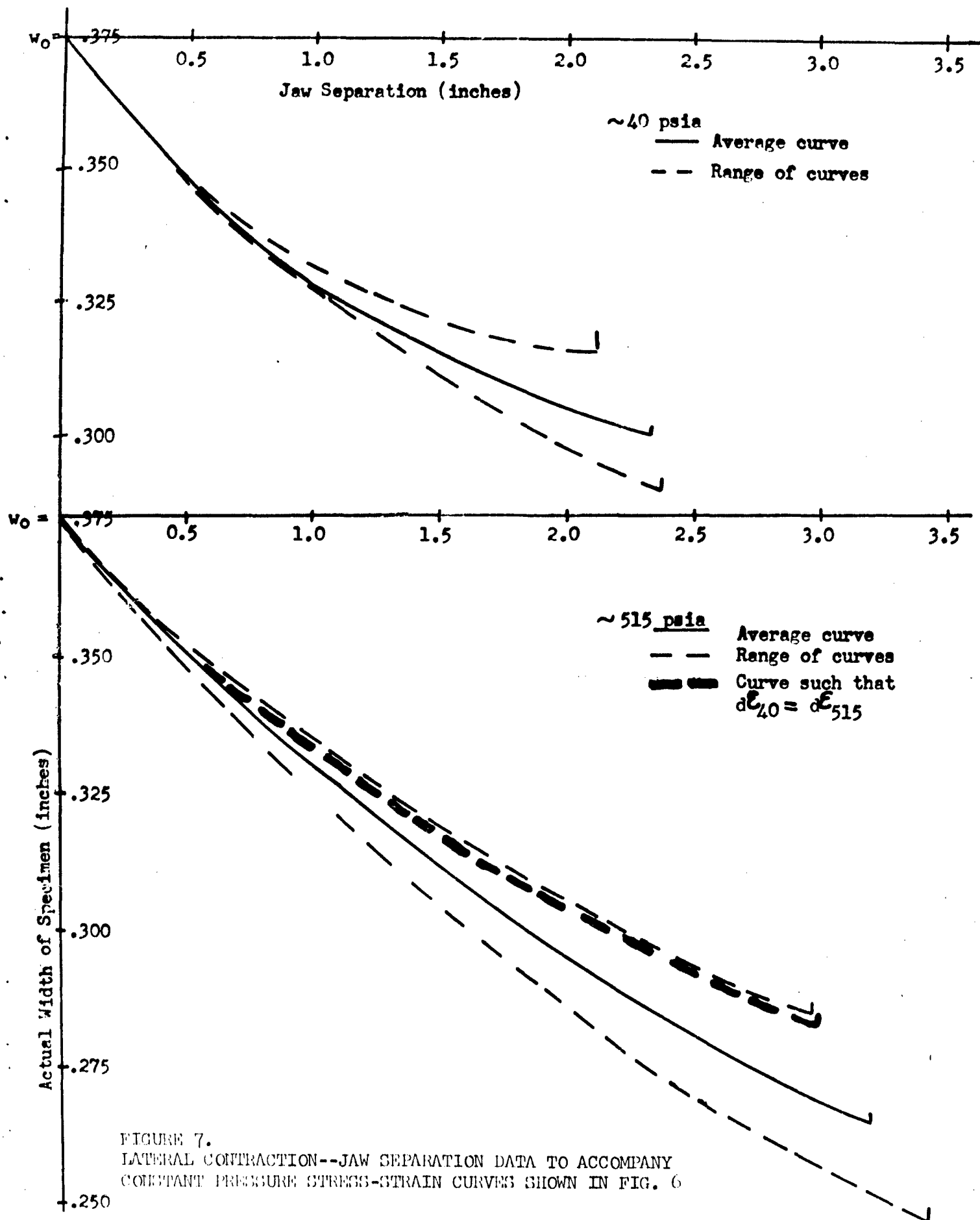
Actual Width of Specimen (inches)

FIGURE 7.
LATERAL CONTRACTION--JAW SEPARATION DATA TO ACCOMPANY
CONSTANT PRESSURE STRESS-STRAIN CURVES SHOWN IN FIG. 6

FIGURE 8.
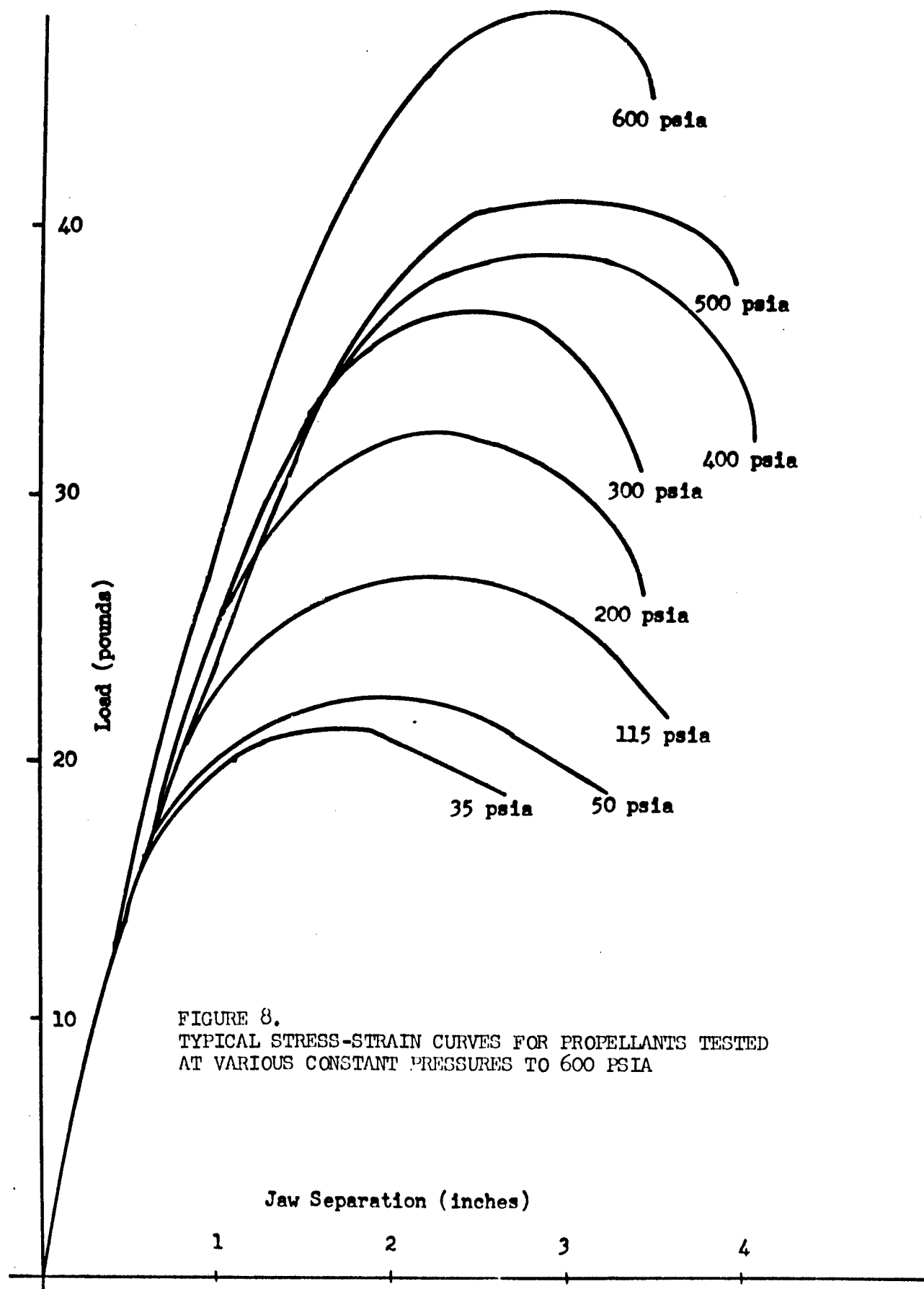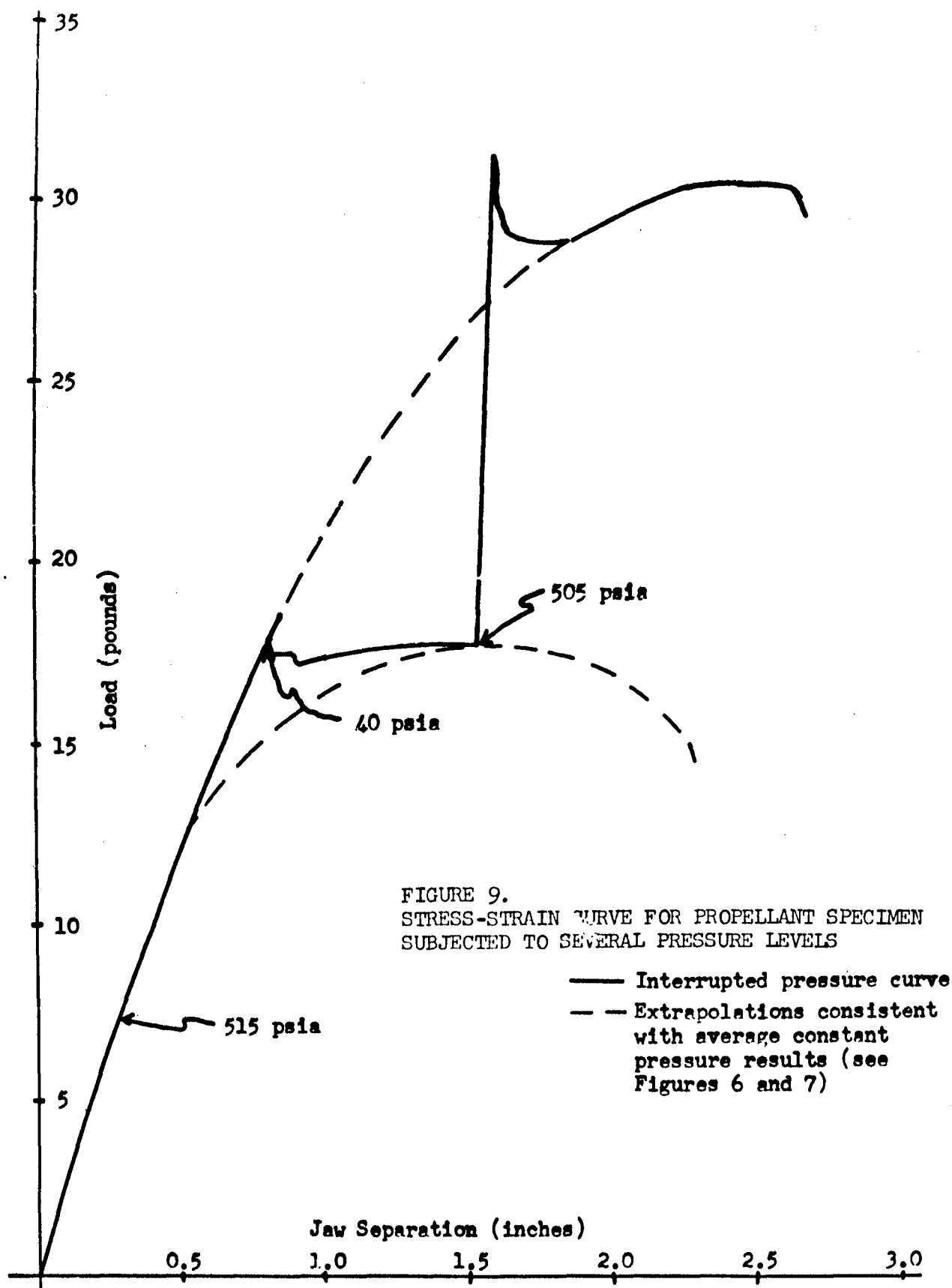TYPICAL STRESS-STRAIN CURVES FOR PROPELLANTS TESTED
AT VARIOUS CONSTANT PRESSURES TO 600 PSIA

FIGURE 9.
STRESS-STRAIN CURVE FOR PROPELLANT SPECIMEN
SUBJECTED TO SEVERAL PRESSURE LEVELS

——— Interrupted pressure curve

— — Extrapolations consistent
with average constant
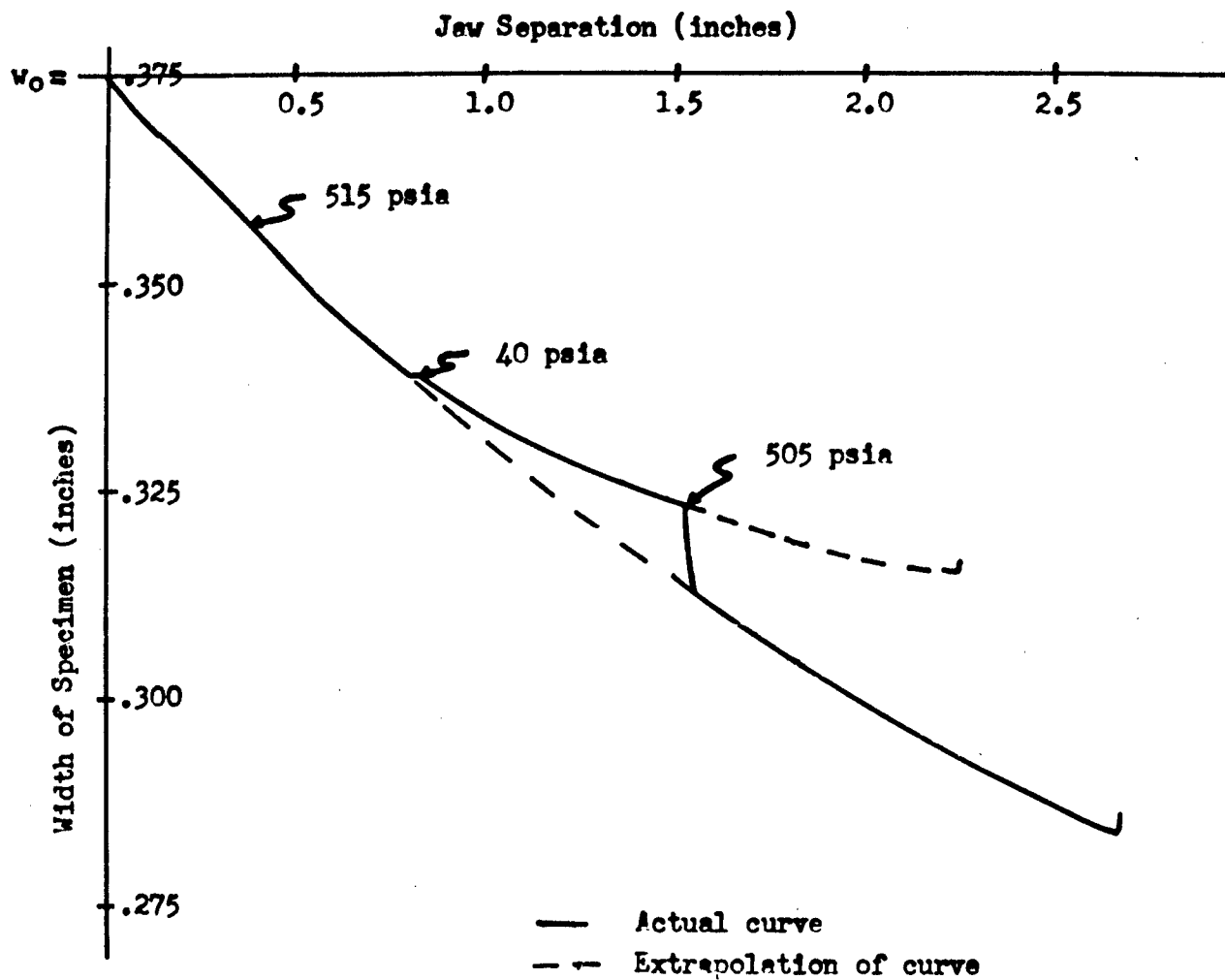pressure results (see
Figures 6 and 7)

FIGURE 10.
LATERAL CONTRACTION--JAW SEPARATION CURVE FOR PROPELLANT
SPECIMEN SUBJECTED TO SEVERAL PRESSURE LEVELS

THE TENSILE BEHAVIOR OF COMPOSITE PROPELLANTS[1]

Robert F. Landel

Jet Propulsion Laboratory
California Institute of Technology
Pasadena, California

ABSTRACT

The three-dimensional stress-strain-time surface generated in uniaxial tensile testing at constant strain rates is discussed. Implications for constant stress-rate, creep, and stress relaxation experiments are indicated. The generated failure surface and interrelations to be expected for failure under a given set of test conditions are discussed in qualitative terms.

INTRODUCTION

In this paper we shall represent the tensile behavior of a propellant as a three-dimensional plot of stress, strain, and time, and on this surface trace the course of experiments do..e at constant strain rate, constant strain (stress relaxation), constant stress (creep), and constant loading rate. In particular, we shall discuss creep and constant strain tests as a method of evaluating propellants; examine the failure surface portion of this total property surface, and compare the failure surface with the normal failure curves of tensile strength σ_m vs log time, or strain at maximum stress ϵ_m vs log time. Normal time-temperature superposition will be assumed and employed throughout. Failure will be defined as the set of properties associated with σ_m and ϵ_m; actual failure, or break properties, will be discussed in terms of a rupture curve or a rupture surface.

PREVIOUS REPRESENTATIONS OF DATA

In the past analysis of tensile data has lead to the construction of the failure curves: log σ_m vs log t, Fig. 1; ϵ_m vs log t, or log ϵ_m vs log t, Fig. 2, and the reduced stress-strain plot, Fig. 3. The time-dependence of the stress relaxation modulus can be derived from the slope of plots such as Fig. 3 (Ref. 1). However, it is very hard to see in Fig. 3 how the failure curves of Fig. 1 and 2 intersect the reduced stress-strain curve. The individual stress-strain curves have been divided by the strain rate and then shifted at a 45-deg angle to effect superposition--therefore, the curve shown in Fig. 3 is repetitively crossed by a failure line. More important than this difficulty of visualizing the interaction of the failure lines with the composite

---

stress-strain line is the fact that a more definitive failure plot has generally not been considered. Thus, one has also the possibility of a plot of σ_m vs ϵ_m. This failure curve is of especial importance because it is independent of time. Figure 4 shows such a stress-strain failure plot together with the individual stress-strain curves for 2 in./min data at various temperatures. Here the stress is based on the original cross sectional area, the measured quantity. Note that the scatter of the failure points seen in Fig. 2 is considerably reduced. Smith (2) found this to be true for SBR rubber and in fact obtained the same curve for constant strain rate and constant strain data, indicating that this failure curve is independent of the process by which the stress or strain is applied.

THREE-DIMENSIONAL PROPERTY SURFACES

Now let us replot the data isometrically as shown in Fig. 5 and sketch in the remainder of the surface. It is an ascending surface in the direction of increasing strain and decreasing time. A maximum in the stress is observed along any isochronal. The individual stress-strain curves of Fig. 4 are almost isochronal data when considered in terms of the log time scale. Actually, the projections of these curves on the ϵ-t plane are straight lines of unit slope. For the present scale, this means they are tilted slightly from a constant time axis. Projection of the maxima of these curves to the three planes, as shown in Fig. 5, gives the failure curves of Fig. 1, 2, and 4. Thus the failure surface is a vertical surface whose upper end, the failure line, describes a twisting ascent through space as indicated. The fracture surface follows a similar path. In performing tensile experiments, therefore, one can travel over any portion of the $\sigma - \epsilon - t$ surface to the left of the rupture cliff, but once reaching it, must inevitably fall over the brink to destruction.

Before turning to the various experimentally accessible paths which can be traced out on the surface, it should be pointed out that the constant strain rate data can be converted to isochronal data and tested for separation of time and strain as has been done for SBR (3). This work is now in progress and for a given propellant seems a feasible and promising approach.

The normal paths experimentally available are constant strain rate, stress relaxation, and creep. Constant loading rate is untried as yet, but offers some important advantages over constant strain rate. Therefore, we shall make a prediction as to the observed behavior. Finally we shall wish to consider the cumulative damage concept and to make a comment on the question of reduced variables and its meaning for this surface.

SOME EXPERIMENTALLY AVAILABLE PATHS

Constant strain rate. Constant strain rate data is shown in Fig. 4 and 5 and need not be considered again. The inclination of the constant strain-rate curves from isochronal lines is so slight as to be completely

masked in these projections, and can only be seen when looking directly down on the surface, see Fig. 2 for a projection of a 2-in./min test.

Stress Relaxation. Taking stress relaxation data means following the stress level along an isostrain, e.g., line ABC in Fig. 4. Thus the course of stress relaxation can be followed by computing the equivalent time for the intersection of a given strain line, e.g., 1% or 40%, with the constant rate data in Fig. 4 or 5. The very important point then to ask is, what is the course of the stress relaxation as the stress passes the failure line corresponding to σ_m? In some cases the answer can be, surprisingly, NOTHING. Figure 6 is an illustration for 40% strain for another propellant. The arrow indicates where in time the locus has passed over the failure line or the "hump" of the property surface. For this propellant no inflection shows. This points out a weakness of the constant strain tests. Unless there is a sharp drop in the stress beyond the maximum in the usual load-time or stress-time curve, there will be no indication of the failure point in the constant strain test, even when monitored with a load cell to measure stress relaxation. Furthermore, somewhere in the region of the failure line, the sample will actually undergo internal creep, and so the test is no longer being conducted at constant strain. Instead the strain is constantly diminishing with time and so the locus will tend to run parallel to the course of the failure line, though on the high-strain side. This will tend to prevent the sample from reaching the rupture surface.

Figure 6 also compares the stress relaxation modulus calculated at 1% strain with that calculated from the reduced stress-strain plot. The latter can be taken as an accurate small-strain modulus. The agreement at 1% is good, as it should be. The disagreement represents the inevitable error to be expected when trying to measure a modulus from an Instron curve at 1% strain. This inaccuracy is smoothed out in the curve calculated from reduced stress-strain plots such as Fig. 4, since here the modulus is derived from an average curve based on segments of the individual $\sigma - \epsilon$ curves. The disagreement at 40% strain simply reflects the nonlinearity of the $\sigma - \epsilon$ curve. Use of an appropriate strain function to convert the stress to a reduced stress as in Ref. 3, should alleviate much of this "discrepancy."

Creep. Taking creep data means following the strain level along an iso-stress, e.g., line DEF in Fig. 4. But, in contrast to stress relaxation experiments, there is a marked and characteristic change in the course of events after the failure line is passed. From E to F the strain increases rapidly in a short span of time. This gives rise to what has been termed the linear (D-E) and power law (E-F) portions of creep curves (1). Previously the critical time t_c at which the power law behavior begins had been associated with dewetting and σ_m of the constant strain rate tests.

Figure 7 shows a calculated creep curve for the same propellant as Fig. 6, illustrating the linear and power law portions, and compares these

values with the reciprocal modulus obtained from the slope of the reduced stress-strain plot. The agreement is very good except at small strains, where the same advantage of an averaged $\sigma - \epsilon$ curve is again in evidence, and at large strains where the failure line has been exceeded. The good agreement is possibly fortuitous and so must be checked by experiment. Such experiments have been performed, but the results were not available at the time this paper was written. For the moment we can only say that the shape of creep curves and the correlation of t_c with the time required to reach σ_m, t_m has been given a more rational foundation.

It is important to reiterate the greater utility of creep as opposed to stress relaxation experiments, i.e., the constant strain test. Failure and rupture are always well-defined experimental points in creep and do not depend on a practiced eye for their detection.

One of the reasons for initially trying the constant strain test was the supposition that in actual service the propellant might blanch (fail, under present definition), relieve itself, and thus prevent rupture. When the test is used in this sense, to test for rupture, and taking the appearance of microscopic tears as an end point, it can still be relatively good. However, when a subjective measure of internal flaws is used, the test is really a measure of the failure time, and the latter can be determined more readily and with more certainty by constant rate experiments (though at higher temperatures) or by creep.

Constant loading rate. Constant loading rate experiments are traced out by the projection of straight lines such as indicated in Fig. 1 onto the property surface. The results are omitted in the isometric figures for clarity there and are indicated schematically in Fig. 8. The stress-strain plot would be flatter than the constant strain rate curves, with a rather sharp inflection in the region where the strain rate data begins to be non-linear. On the other hand, the strain-time plot shows an abrupt change in slope at the failure stress, similar to that seen with creep. Note that as the constant strain-rate plot flattens out and it becomes more difficult to evaluate ϵ_m, the inflection in the strain-time plot for constant loading rate data is predicted to become more marked. This implies that we are over-looking an important test.

Cumulative strain damage. According to the cumulative strain damage concept, if one has progressed to some fraction of the total strain available at a given rate, then the same fraction of the strain available at any other rate is exhausted.

This can only be correct when the failure envelope varies linearly with time. Over short ranges of time scale this is approximately true, but Fig. 2 shows that the envelope is much better described as an exponential. Thus the approximation would be valid only when the strain rate range is not varied too widely. When the ϵ_m-t_m curve, plotted in linear coordinates, is

convex upward, the sample will have a greater life expectancy than predicted and conversely if the ϵ_m-t_m curve is concave.

Figure 9 shows in log-log coordinates the projection of the strain history for samples tested at two rates differing by a factor of 100, and for samples tested at one rate to 4% strain and then taken to failure at the second rate. Detailed analysis has shown that the cumulative damage theory gives the correct breaking time with failure envelope B, but underestimates the lifetime with envelope A.

Note that in the initial period after the change from low to high speeds, the sample is strained very rapidly, almost isochronally. This has an interesting effect in that, while working at low temperatures in the region where ϵ_m is just beginning its rapid rise, it might be possible to give a small elongation at a very low rate, switch to a high rate, and achieve a greater breaking elongation than would be possible with a straightforward test at the high rate alone.

In subsequent work we hope to examine a surface based on the total work expended on the sample during tensile testing. Then the cumulative work damage concept can be examined.

TIME-TEMPERATURE SUPERPOSITION

Time-temperature superposition has been explicitly assumed to be obeyed in deriving the σ - ϵ - t surface. This means that at any given temperature the Instron can scan about three decades of time. Figures 4 and 5 show that a large portion of the surface is portrayed by only a two-decade spread in testing speeds. If time-temperature superposition does not hold, then one may legitimately question the shape of the surface at either shorter or longer times. In particular, aging at higher temperatures could lead to a lowering of the stress-strain curves in Fig. 4. If the curves were mistakenly superposed, this would broaden the "maximum" of the σ_m - ϵ_m line. Predictions of lifetime, e.g., along line ABC, would thus be erroneously high.

CONCLUSIONS

It has been shown that examination of the three-dimensional tensile property surface consisting of stress, strain, and time gives additional insight into the behavior of composite propellants. The reason for the indistinct "end point" in constant strain tests; the correlation between the critical time t_c in creep and the time to maximum load t_m in constant strain rate tests; and the characteristic shape of creep curves are all explained. The shape of the constant rate of loading curve is deduced. A variation on the cumulative damage concept is proposed in which the rupture or failure curves are assumed to be characteristic of a specimen and all tests performed on

the sample trace out some locus on the σ - ϵ - t surface. Since time can never be reversed, the sample is inevitably made to approach failure.

REFERENCES

1. Landel, R. F., and Smith, T. L., "Viscoelastic Properties of Rubber-like Composite Propellants and Filled Elastomers, " ARS Journal, 31, 599 (1961); Smith, T. L., and Landel, R. F., Bulletin of the 17th meeting of the JANAF Physical Properties Panel, May 1958, p 133.

2. Smith, T. L., Private communications to be presented at the 140th meeting of the American Chemical Society, Sept. 1961, Chicago, Illinois. Note that this work is concerned with rupture properties of the rubber.

3. Landel, R. F., and Stedry, P. J., "Stress on a Reduced Variable: Stress Relaxation in SBR Rubber at Large Strains", J. Appl. Phys., 31, 1885 (1960).
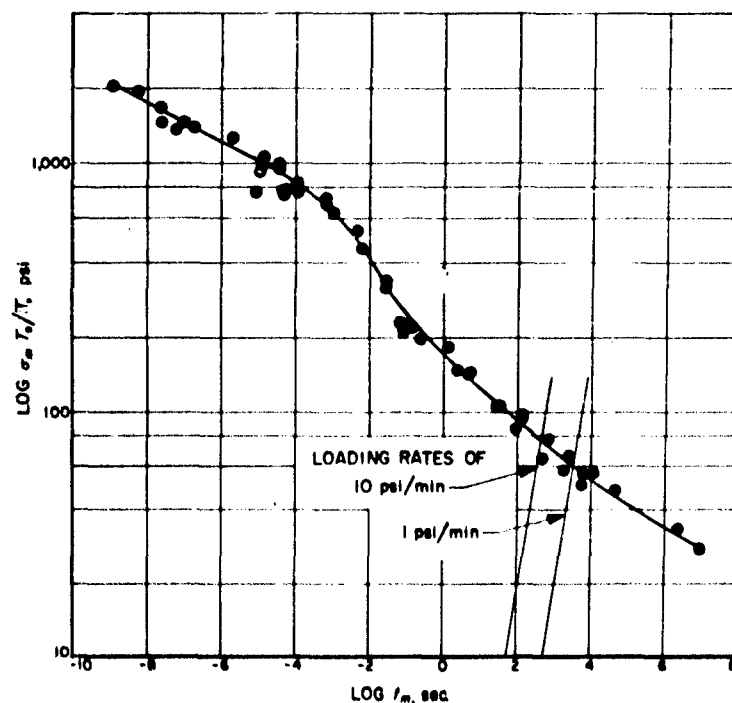
FIGURE 1. TYPICAL REDUCED TENSILE STRENGTH σ_m CURVE
Propellant 2531. T_0 = 263°K

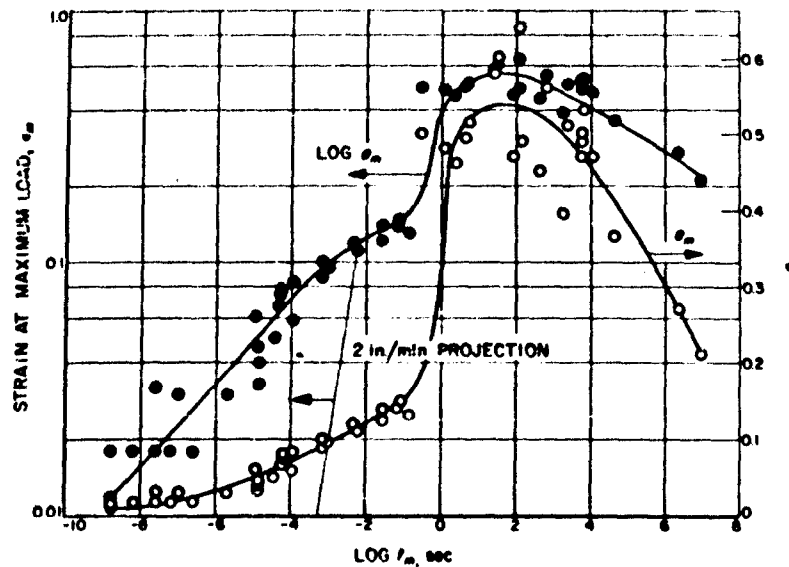FIGURE 2. STRAIN AT MAXIMUM ϵ_m vs REDUCED TIME

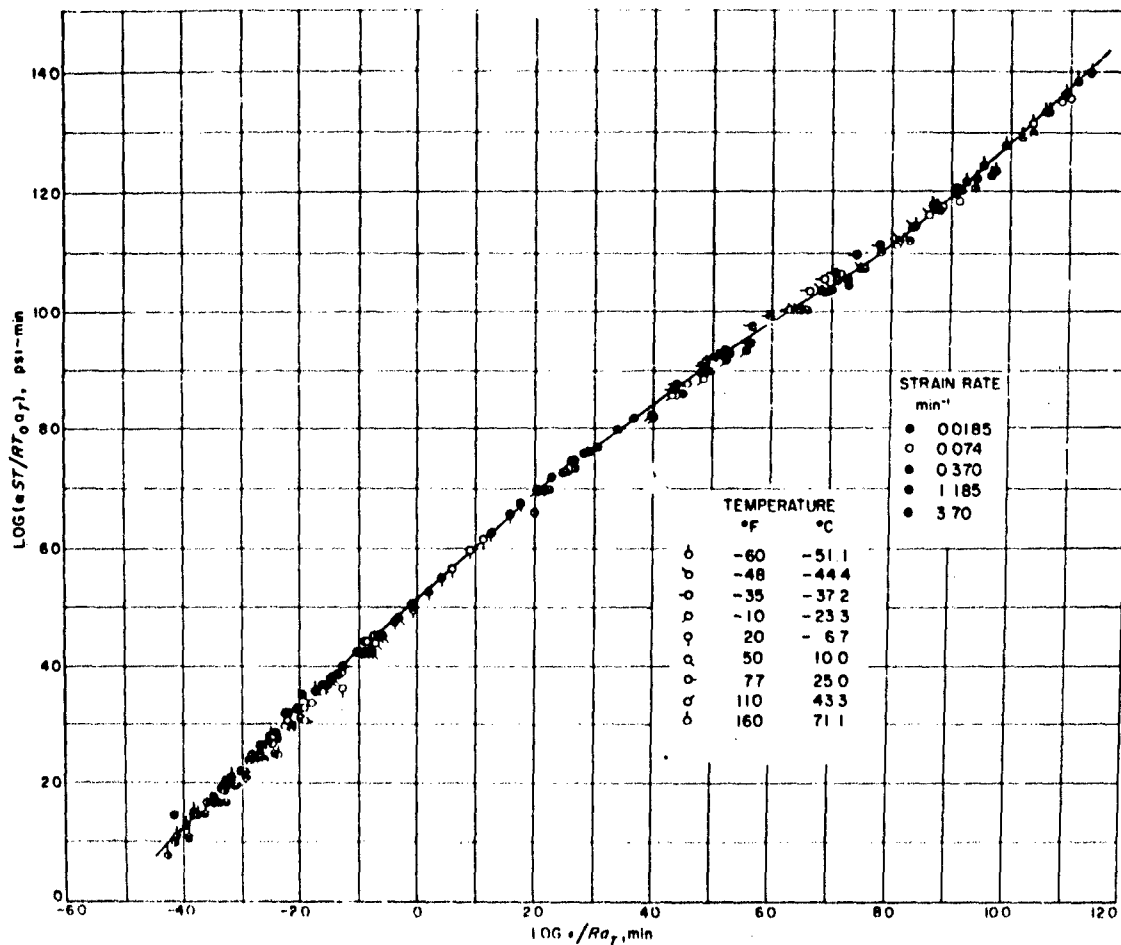Propellant 2531. Both semi-log and log-log repre-
sentation is shown. T_0 = 263°K

FIGURE 3. TYPICAL REDUCED STRESS-STRAIN PLOT
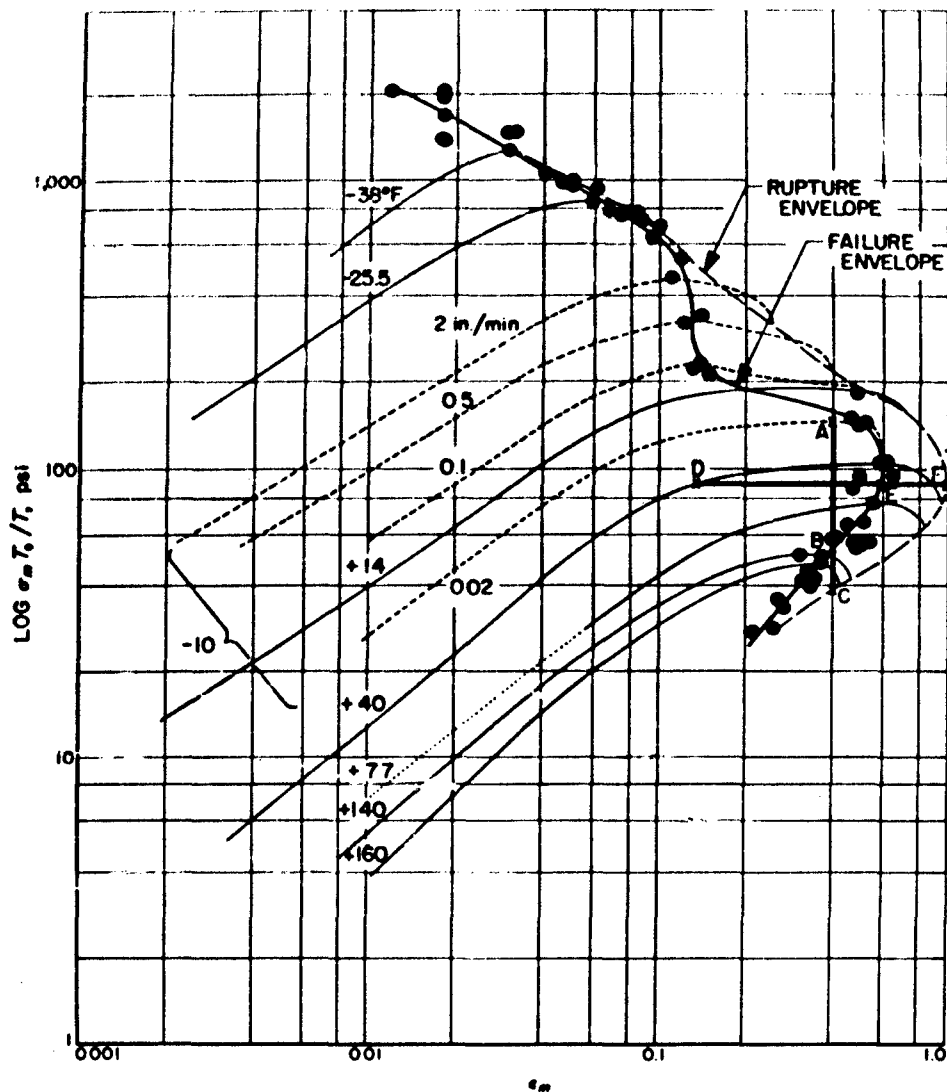Propellant is not that of Figures 1 and 2. T_0 = 266.5°K

FIGURE 4. THE FAILURE CURVE σ_m-ϵ_m and σ_b-ϵ_b.
Propellant 2531. Also shown are all the stress-
strain data at 2 in./min for the temperature
where that rate was used, and the -10°F data
at four different rates. Line ABC and DEF are
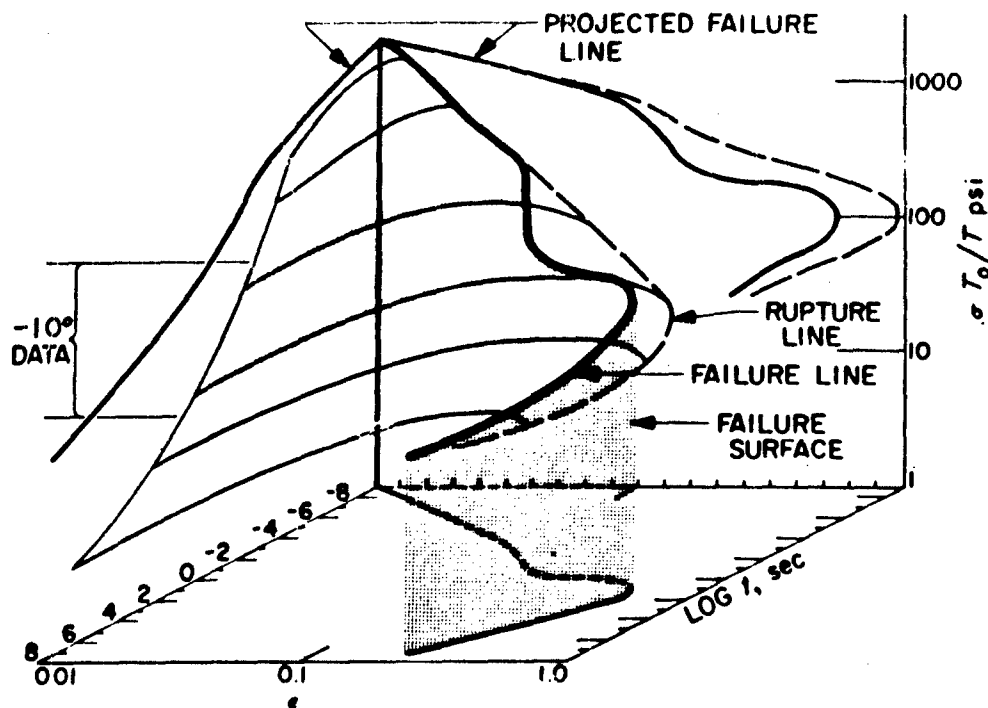explained in the text.

FIGURE 5.
TENSILE PROPERTY SURFACE. Propeller+ 2531. Failure curves are indicated by
heavy lines; rupture curves by dotted lines; and individual stress-strain
curves by light lines. The rupture surface is not sketched in because the
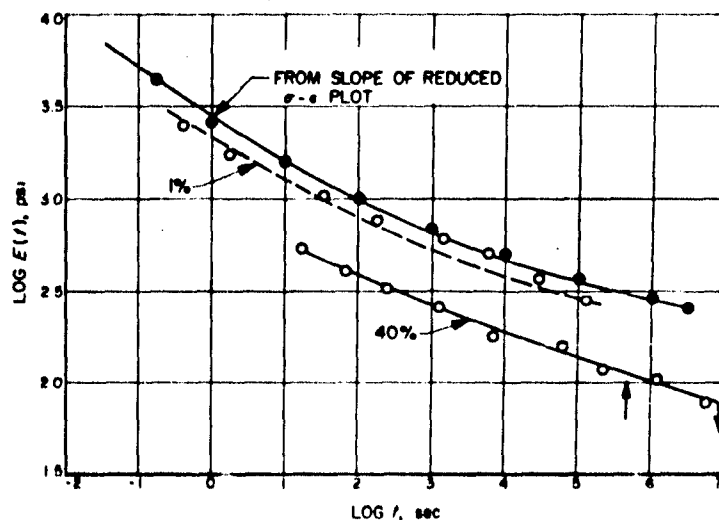failure surface lies behind it.

FIGURE 6.
STRESS RELAXATION MODULUS CALCULATED FROM A COMPOSITE STRESS-STRAIN CURVE,
FROM INDIVIDUAL STRESS-STRAIN CURVES AT 1% AND FROM INDIVIDUAL CURVES
AT 40% STRAIN. In the latter case there is no indication as to when the
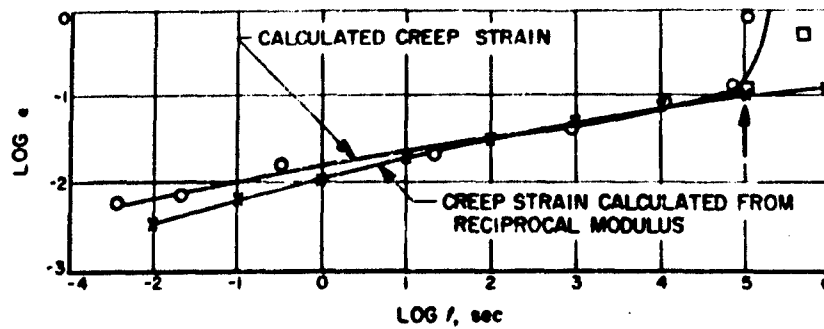test had passed beyond the failure envelope.

FIGURE 7.
CREEP STRAIN AT 50 psi FOR THE PROPELLANT OF FIGURE 6. Calculated from
constant strain rate data and compared with that calculated from the
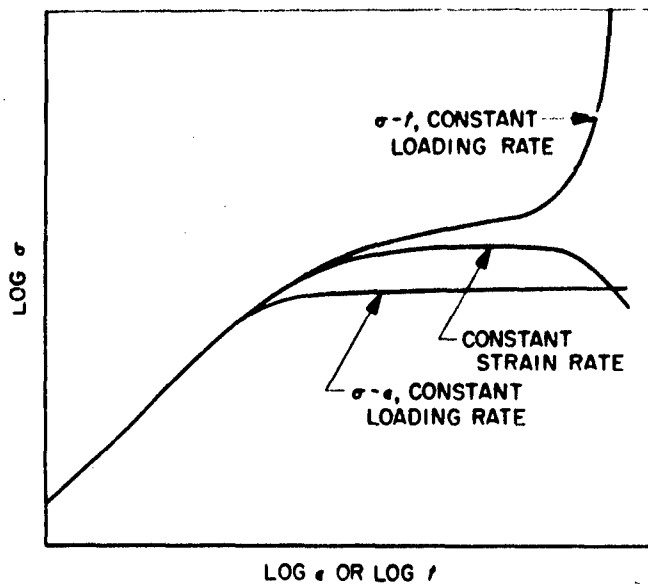modulus obtained from the reduced stress-strain curve.

FIGURE 8.
SCHEMATIC REPRESENTATION OF STRESS-
STRAIN AND STRESS-TIME DATA AT
CONSTANT RATES OF STRESS LOADING
AS COMPARED WITH THE STRESS-STRAIN
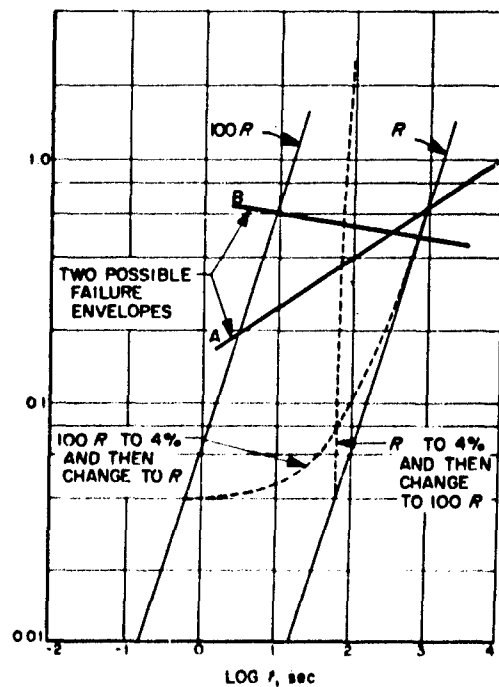OR STRESS-TIME CURVES SEEN IN
CONSTANT STRAIN RATE TESTS

FIGURE 9.
PROJECTION OF THE STRAIN HISTORY OF
SAMPLES TESTED AT DIFFERENT RATES

PHYSICO-CHEMICAL EFFECTS

R. F. Landel, Reporter

THE EFFECT OF INITIAL VOIDS ON THE BULK MODULUS AND VOID FORMATION ON UNIAXIAL EXTENSION

W. T. Milloway, C. C. Surland, I. Skulte

Aerojet-General Corporation

ABSTRACT

Methods and apparatus for measuring directly the lateral compliance of tensile specimens and the uniaxial compliance of small bars stressed hydrostatically are described and discussed. Test results on binders and composites are presented which relate to the change in volume of propellant specimens during uniaxial extension and their initial void content as assessed from the hydrostatic compliance data. Correlation between initial void content and subsequent void formation on extension of composites is demonstrated.

INTRODUCTION

Considerable effort has been devoted to devising reliable methods for measuring the bulk modulus of composites such as solid rocket propellants. Aside from its basic nature as a material property, intimately related to other elastic and thermoelastic properties, the bulk modulus shows great promise for assessing the nature of other important but difficult to measure properties of propellants in a nondestructive way.

Compressibility determinations on crystalline materials and metals are complicated by the extreme pressures required and the minute deformations that must be measured. P. W. Bridgman (1) has contributed the bulk of the contemporary published data in this field. Relatively little work or experimental hydrostatic compliance data is reported for polymers or plastics, aside from dynamic measurements.

Fortunately, propellants are quite compressible compared with metals, and small deformation measurements have become common in recent years. The hydrostatic compliance of composites can be readily determined with relatively low pressure equipment and various commercial low force deformation transducers (2). Even the dangerous nature of the closed bomb bulk modulus test for solid propellants can be offset by remote operation of the test equipment.

Hydrostatic compliance measurements are used in several ways to assess the degree of consolidation in composites. A surprising spatial variation of the amount of included voids is shown to exist within a gallon carton of cast solid propellant. Preliminary data illustrate the manner in which hydrostatic compliance measurements can be used as a screening test in choosing more nearly identical specimens for other highly variable mechanical property tests such as the tensile test. Or, when the effect of initial voids on the mechanical properties is known, the usual high variability may be accounted for by pretesting. The amount of void space in well-consolidated propellant is shown to be so small as to be impractical to assess by

common means such as density determinations. However, the compressibility of composites is decidedly affected by the amount of voids usually found in these materials. The amount of voids present in well-consolidated composites may be larger than the volume change in void free material at the usual range of pressures associated with the use and testing of these materials.

An equation for the hydrostatic compliance of composites with the volume fraction voids as a modifying parameter is presented and compared with measured behavior. As a working model, the composite was considered to be an otherwise homogeneous mass of known properties containing multitudinous minute voids. The compliance of each void and the material surrounding it were taken to be commensurate with that of an externally pressurized thick wall hollow sphere. For small void content, the proposed equation reduces to a simple useful form independently proposed by Bills (3). This simple form is adequate until the considered void content greatly exceeds that of well-consolidated propellants.

Unpublished data of the past two years indicates that composites are essentially isotropic in pure hydrostatic compression. The uniaxial compliance of hydrostatically stressed specimens then suffices to determine the bulk modulus. A detailed description of compliance measurements has been reported previously (2), and method descriptions here will be limited to important new details such as the specimen size and uniaxial treatment.

A device for measuring the lateral contraction of tensile dumbbells is described. However, it is limited to use with composites that do not exhibit striation or non-uniform void formation as described by Bills (4).

A correlation between void formation upon extension and initial void content is presented. The principle by which the extremely precise hydrostatic compliance measurements may be used to assess the effect of initial void content is indicated. The degree to which other properties may be affected by initial void content will require precise measures of the volume changes by means other than the clip gage since many composites striate upon extension. Volumetric measurements are being considered for further study (5).

METHODS AND EQUIPMENT

Bulk Modulus Tests

Figure 1 shows schematically the method for measuring the uniaxial hydrostatic compliance of composite specimens. These were nominally four inches by one-half inch by three-eighths inch, with corners sanded to fit the inside diameter of the pressure tube. Small metal tabs were cemented to the ends of the specimens. The differential transformer core was fixed to the top specimen tab, while the bottom tab supported the specimen in the pressure chamber. The body of the differential transformer was supported by the test stand coaxially about the pressure chamber, specimen, and core. Translation of the transformer was provided by a micrometer screw connection to the test stand for direct calibration of longitudinal deflection of the core with respect to the body of the transformer.

After enclosing the test specimen in the chamber, silicone fluid was introduced to a level above the core. This prevented heat transfer from the

pressurized gas to the specimen during pressurization. Pressure was introduced by throttling from a high pressure source to the chamber at a nominal rate of 100 psi per second.

An X-Y millivolt recorder was used to record longitudinal compliance as a function of chamber pressure. Such records show a remarkable linearity between pressure and compliance from 0 to 1500 psig for void free polyurethane rubber. Similar linear behavior is also obtained for composites with minimal void content beyond an initial region of high compliance at low pressures.

Two sets of compliance measurements are reported. A cylindrical gallon casting was divided into 17 equal spaced regions along the orthogonal diameters. A bulk modulus specimen was machined from each subsample at nominally the same elevation in the casting. The region of sampling and the results of bulk modulus tests and assessed void content are shown in Figure 2.

Lateral Contraction—Extension Measurements

A second set of specimens were obtained in a similar way. These were bonded to flats on wooden cylinders to prepare tensile specimens as indicated in Figure 3. Lateral contraction of one dimension was obtained on six specimens with the deflection clip gage and method described in the following section. Bulk modulus measurements were then taken on these specimens to compare the void formation—extension data for each specimen.

VOID FORMATION ON UNIAXIAL EXTENSION

The lateral contraction clip gage consists of a split spring steel ring fitted with four strain gage patches to form the usual Wheatstone Bridge transducer circuit. Plexiglas pads one-fourth inch square are fastened with flexible cement to the ends of the split ring. The flat surface of the pad is fitted with a tiny rubber thread on the surface that contacts the sides of the specimen. This thread is perpendicular to the direction of straining when the gage is installed and serves to maintain the clip at a fixed longitudinal position in conjunction with the light clamping action of the clip. (See Figure 3.)

The clip gage transducer output was calibrated against mechanical separation of the pads using a micrometer screw. The gage output versus separation curve was found to be linear within about one per cent over the range of the tensile specimens.

The end-bonded tensile specimens were then extended to failure while recording lateral contraction, extension, and load. These specimens all failed at the bonded ends below 15 per cent elongation. The results of volume change as a function of extension are shown in Figure 4. The bulk modulus and initial void content of each specimen is noted on the void formation curve. The preferred order of testing was reversed for this set, and the effect on the results is not known. Proper order of testing will be observed in further work.

The ability of the clip gage to measure lateral contraction was assessed as good on tests of polyurethane rubber. Logarithmic plots of the volume

ratio and extension ratio data for rubber were such that Poisson's ratio for the material was 0.502 by the method of Smith (6). This would indicate excellent performance of the gage on uniformly distorted specimens.

THEORY AND RESULTS

The bulk modulus values reported are based on direct compliance measurements of one dimension as illustrated in Figure 1. Two basic assumptions about the material are involved: (1) compression is uniform under hydrostatic pressure; and (2) dimensional changes are sufficiently small that second order volumetric terms can be neglected.

Tests on composites show that the orthogonal compliance of pressurized specimens of regular shape are not affected by uniaxial prestresses considerably greater than the body forces generated in four inch specimens. Thus the decided effects of prestress on the isotropy of binder materials (2) does not appear in composites in significant amounts, if at all.

The bulk modulus based on the definition

$$K = \left(\frac{\partial P}{\partial V}\right)_S \tag{1}$$

can be assessed for unit volume from the slope of the pressure compliance records. When a linear behavior between P and V exists, the calculated value for the modulus typifies the material over the range of pressure for which this is true. For isotropic materials and small strains the relation between the volumetric compliance J_V and the orthogonal compliances $J_x = J_y = J_z = J_L$ is approximately

$$J_V = 3 J_L \tag{2}$$

In all cases the time of pressurization was reasonably short compared with the thermal relaxation time of the specimen, so that the compliance behavior and calculated bulk modulus values are all for the adiabatic case.

DERIVATION OF THE PRESSURE-VOLUME RELATIONSHIP FOR COMPOSITES WITH VOIDS

Propellants or composites containing voids were presumed to behave as homogeneous externally pressurized thick wall hollow spheres. The expression for the radial displacement and stresses for the hollow sphere (7) is:

$$\frac{U}{r} = \frac{(P_b - P_a)\left(\frac{b^3}{b^3 - a^3}\right) - P_a}{3 K} + \frac{\left(\frac{P_b - P_a}{4\mu}\right)\left(\frac{a^3 b^3}{b^3 - a^3}\right)}{r^3} \tag{3}$$

where: U = radial displacement at radius r
a = internal radius
b = external radius
P = stress
μ = shear modulus
K = bulk modulus

If $P_b = P_a + dP$ and $P_a = 0$ then

$$\frac{U}{r} = \frac{dP\left(\frac{b^3}{b^3 - a^3}\right)}{3K} + \frac{dP}{4\mu}\frac{\left(\frac{a^3 b^3}{b^3 - a^3}\right)}{r^3} \tag{4}$$

This equation evaluated at the inner radius a and outer radius b gives the simultaneous equations

$$dP = \frac{\frac{da}{a}}{\left(\frac{1}{3K} + \frac{1}{4\mu}\right)\left(\frac{b^3}{b^3 - a^3}\right)} \tag{5}$$

$$dP = \frac{\frac{db}{b}}{\left(\frac{1}{3K} + \frac{a^3}{4\mu b^3}\right)\left(\frac{b^3}{b^3 - a^3}\right)} \tag{6}$$

The solution for (5) and (6) with $P_a = 0$ and evaluated from $P_b = 0$ to $P_b = P$ and from b_0 to b is

$$\frac{b^3}{b_0^3} = \frac{V}{V_0} = \frac{e^{-\frac{P}{K}}}{\left(\frac{1 - \delta e^{-\frac{3P}{4\mu}}}{1 - \delta}\right)^{\frac{4\mu}{3K} + 1}} \tag{7}$$

where $\delta = \frac{a_0^3}{b_0^3}$, the volume fraction voids.

Equation (7) can be simplified to the equation of Bills (3) when δ is small, and the ratio of shear modulus to bulk modulus is small, by neglecting second order terms in δ upon expansion of equation (7).

$$\frac{1}{K^*} = \frac{1}{K} + \frac{\delta}{P}\left(1 - e^{-\frac{3P}{4\mu}}\right) \tag{8}$$

where $K^* = \frac{\Delta P}{\frac{\Delta V}{V_0}}$

and K is the bulk modulus for void free material defined in equation (7) as

$$\frac{V}{V_0} = e^{-\frac{P}{K}} \quad \text{or} \quad K = V\left(\frac{\partial P}{\partial V}\right)_S \cong V_0\left(\frac{\partial P}{\partial V}\right)_S \tag{9}$$

Figure 5 compares theoretical compliance curves developed from equation (7) using various values for initial void content, with experimental data from the specimen set described in connection with Figure 2. Experimental values for the shear modulus were determined for the material in torsion. The theoretical bulk modulus of the void free composite was calculated from the measured bulk moduli of the constituents and volume fraction composition considerations. This theoretical value is in excellent agreement with the limiting slope of experimental data where the initial void content was small. The slope of the void free curve on Figure 5 is based on the bulk modulus equal to 0.60×10^6 psi. Experimental curves for five specimens that cover the estimated range of void content are plotted for comparison with the theoretical curves. In Figure 5, the initial void content for each specimen can be estimated from the experimental data as the separation of the limiting slope and the calculated slope for void free material. The shape of experimental and predicted compliance curves are in good agreement over the estimated total range of initial void content observed experimentally.

The experimental compliance curves of Figure 5 show good agreement with the curves derived from equation (7) for low initial void content and less exact correspondency for high initial void content. This might be expected in view of the simple premises on which the equation is based and the many complications which could occur with high initial void content. Void shape and size, distribution, instability of shape, and many other factors undoubtedly become more important with increasing void content. Further experimental compliance measurements to pressures of 5000 psig or higher will be required to properly evaluate the application of equation (7) to high void content behavior.

Precise specific gravity measurements are, at best, quite difficult to obtain for composite materials. Friability, temperature sensitivity, and solubility of the ingredients all contribute to errors in measuring the density of composites. However, the specific gravity of specimens numbered 4 and 14 in Figure 2 was very carefully measured and found to be 1.655 and 1.650, respectively, suggesting a difference of 0.30 per cent initial voids. An estimate of the maximum difference in initial voids for these specimens from the experimental data would be 0.20 per cent. Theoretical curves fitted to the experimental compliance data would predict an initial void content difference of only 0.10 to 0.12 per cent. Tests on a much larger sampling with statistical design and interpretation are indicated before more definite conclusions can be reached. This is experimentally practicable in the matter of compliance measurements, but may not be so for the specific gravity determinations.

A reasonable pattern of isolines can be drawn through the data of Figure 2a which illustrates the radial geometric distribution of voids in a gallon sample of carefully prepared cast composite. The isolines shown are for total volume change in the material at 1000 psig pressure. A similar pattern would be observed for isolines of bulk modulus because of its dependence at a given pressure level on the initial void content. Ordinary specific gravity determinations on the 17 specimens of this data set could indicate complete homogeneity in this sample.

Figure 4 illustrates the decided range of void formation upon extensions of 10 per cent or less for end bonded tensile specimens. Void formation was equated to the calculated increase of volume as determined from mensuration using the extension and lateral contraction records, except for the bottom curve of the figure. The latter was plotted from gravimetric measurements by Svob (5). Volume changes from clip gage measurements on given materials have been found to be consistently large compared with dilatometric data. This may explain the relatively low volume change for this material obtained dilatometrically.

However, to the extent that striation may be limited at low extensions, and that the precision of the clip gage data may be relied upon, an interesting negative correlation of volume change upon extension with initial void content is observed. The values for bulk modulus and initial void content shown on the body of the figure were obtained from the slope of the compliance curves between 600 and 900 psig and by fitting the experimental curves to plots of equation (7) as explained in connection with Figure 5. Comparing these data with the amount of void formation, it appears that specimens containing relatively small amounts of initial voids form voids on extension to a greater degree than those with relatively large amounts of initial voids. As mentioned before, the data of Figure 4 may be suspect because of the failings of the clip gage with striated behavior in the specimen. However, it serves to illustrate the manner in which compliance measurements may be useful in pretesting specimens for void content. The effect of initial void content on behavior or failure of composites has yet to be determined.

REMARKS

This paper outlines the progress in developing experimental methods for measuring initial void formation with hydrostatic compression. The question of the effect of initial void content, shown to be decidedly variable in otherwise presumably homogeneous composites, is raised. Few specific conclusions are drawn in view of the limited testing and variability in the prototype test equipment. Improved designs for remotely operated pressurized tensile and uniaxial hydrostatic compliance test equipment have been completed. Data taken with such equipment should be more amenable to analysis.

REFERENCES

(1) Bridgman, P. W., <u>The Physics of High Pressure</u>, G. Bell and Sons, Ltd., London, 1958.

(2) Surland, C. C., "Strain Measurements on Hydrostatically Stressed Materials Using Differential Transformer Transducers." (Oral Presentation.) To be Published in <u>Proceedings of the Society for Experimental Stress Analysis</u>, Spring Meeting, 1960.

(3) Bills, K. W., "Study of Mechanical Properties of Solid Rocket Propellant," Report No. 0411-10Q-1, Contract AF 33(600)-40313 S.A. No. 2, 31 August 1961.

(4) Bills, K. W., "Study of Mechanical Properties of Solid Rocket Propellant," Report No. 0411-10Q-1, Contract AF 33(600)-40313 S.A. No. 1, pp. 33-41, 30 May 1961.

(5) Svob, G. J., Colodny, P. C., Waddle, L. A., and Lefferdink, T. B., "Volume Changes in Polyurethane Propellants Subjected to Small Strains," <u>Bulletin of the JANAF-ARPA-NASA Panel on the Physical Properties of Solid Propellants</u>, 1961.

(6) Smith, Thor L., "Volume Changes and Dewetting in Glass Bead - Polyvinyl Chloride Elastomeric Composites Under Large Deformations," <u>Transactions of the Society of Rheology</u>, Volume III (1959) pp.113-136.

(7) Southwell, R. V., <u>An Introduction to the Theory of Elasticity for Engineers and Physicists</u>, Oxford University Press, London, 1941, page: 336ff.
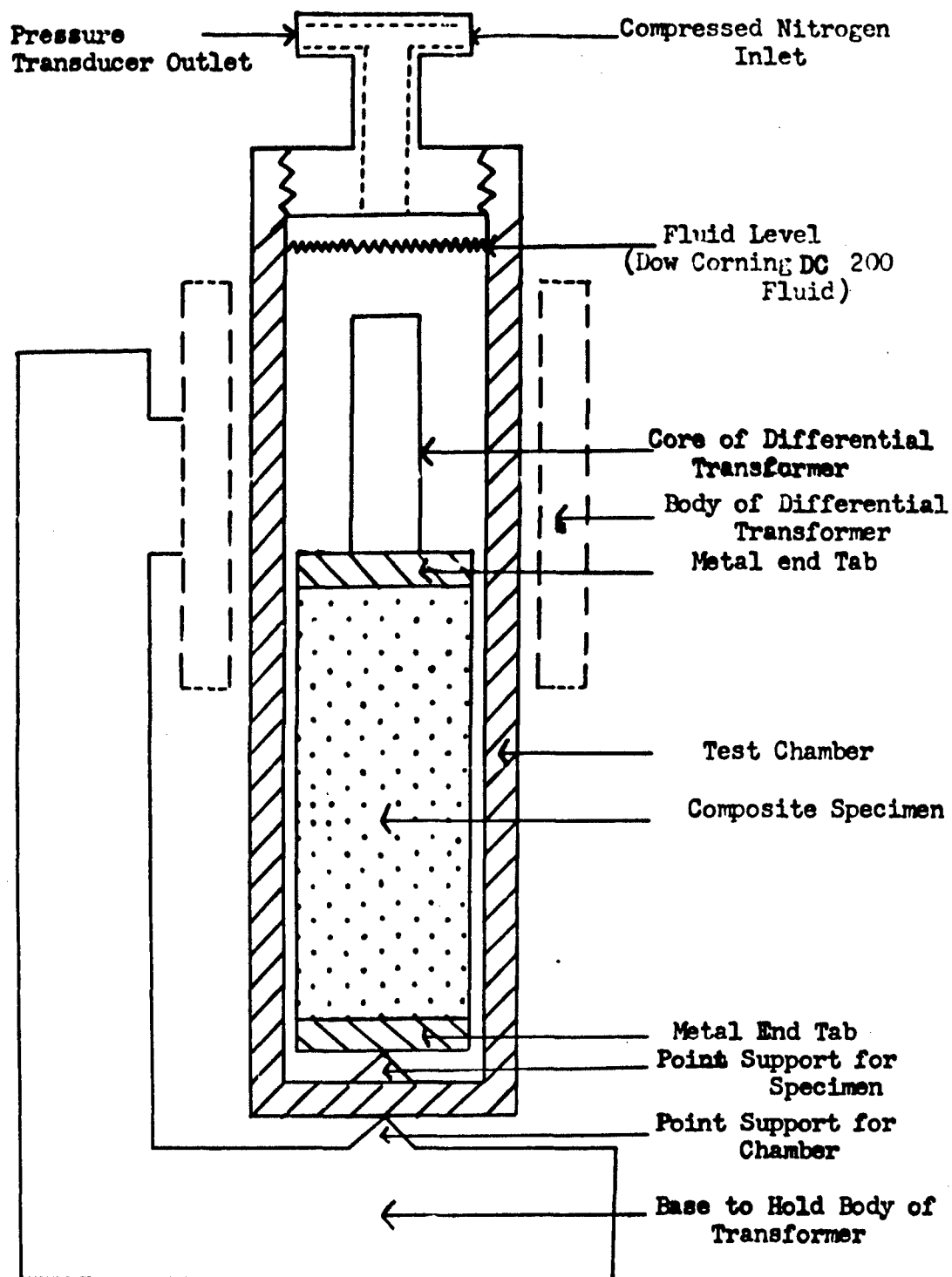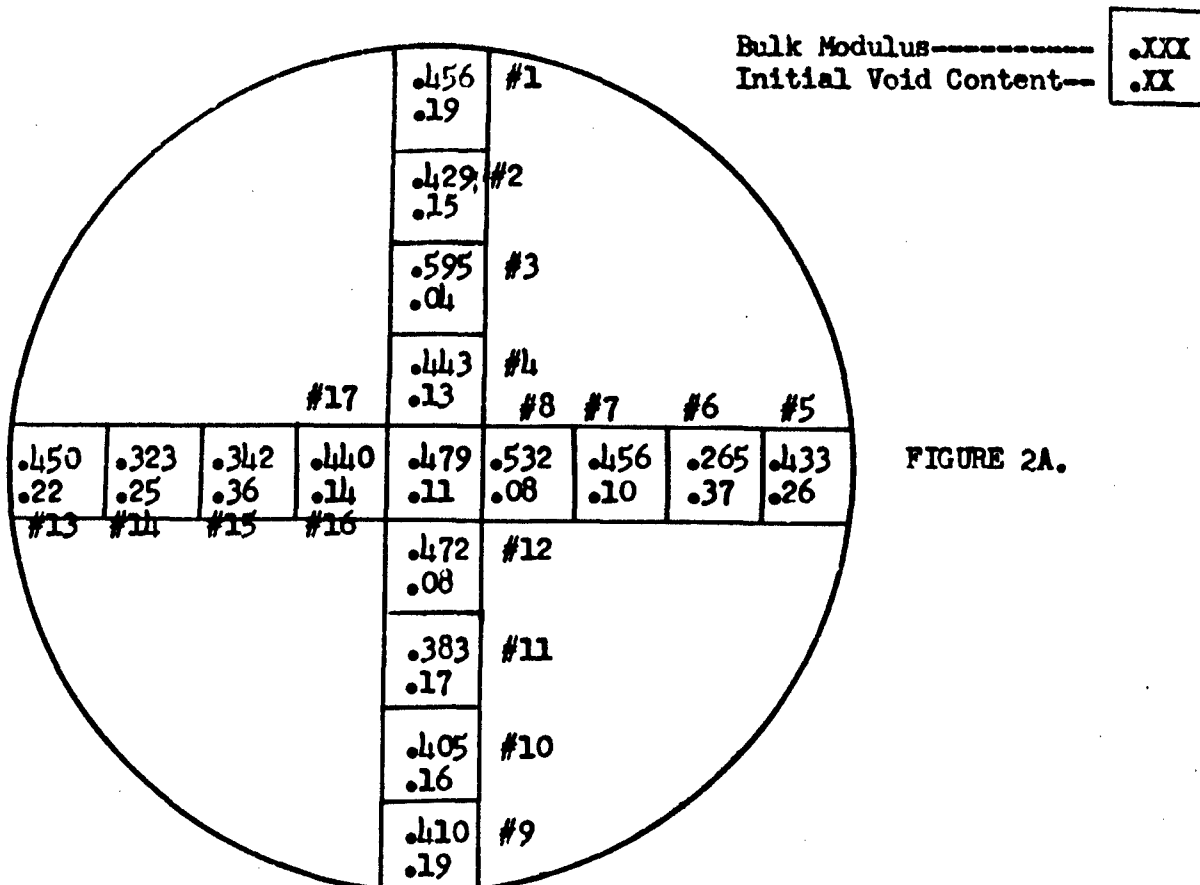
Pressure Transducer Outlet

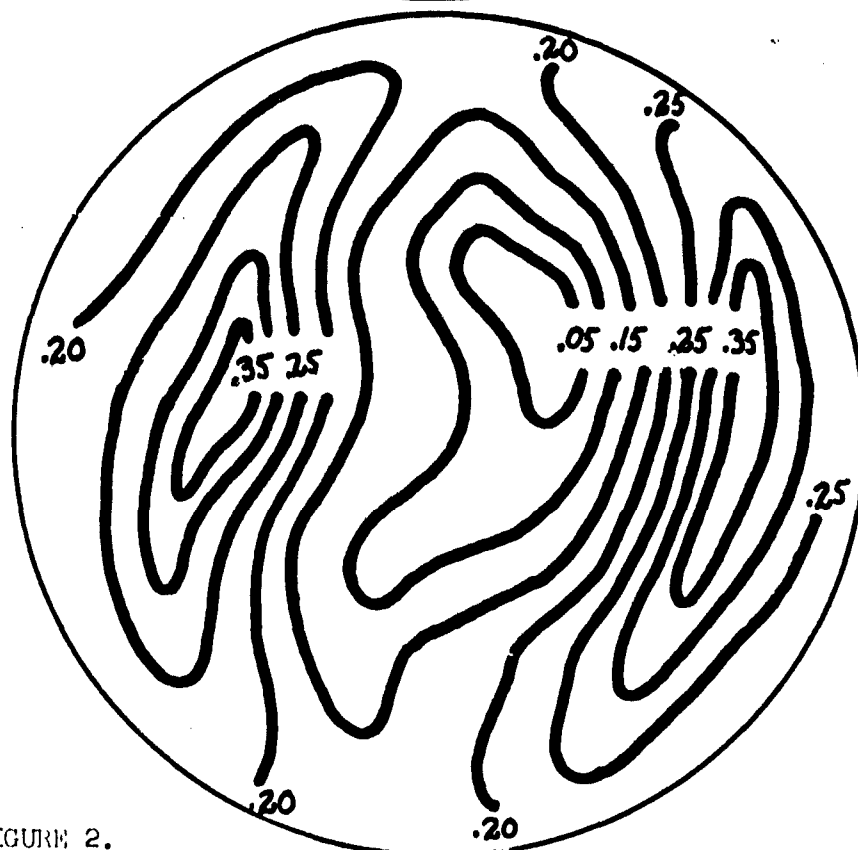Compressed Nitrogen Inlet

Fluid Level (Dow Corning DC 200 Fluid)

Core of Differential Transformer

Body of Differential Transformer

Metal end Tab

Test Chamber

Composite Specimen

Metal End Tab

Point Support for Specimen

Point Support for Chamber

Base to Hold Body of Transformer

FIGURE 1. BULK MODULUS TESTER

Bulk Modulus————— .XXX
Initial Void Content— .XX

FIGURE 2A.

FIGURE 2B.

FIGURE 2.
RADIAL LOCATION OF BULK MODULUS SPECIMENS FROM ONE GALLON CARTON
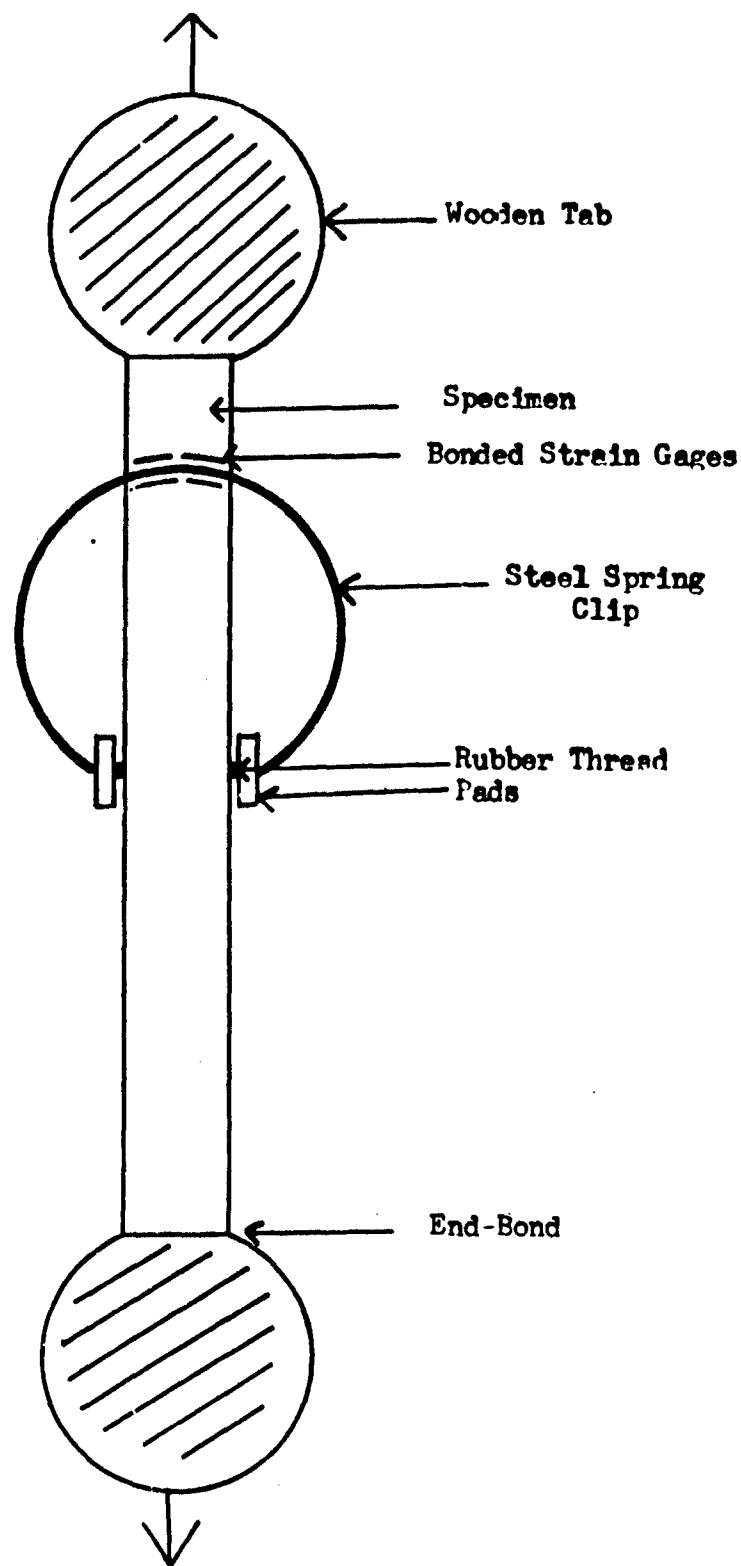CASTING WITH BULK MODULUS AND TOTAL COMPLIANCE AT 1000 PSI

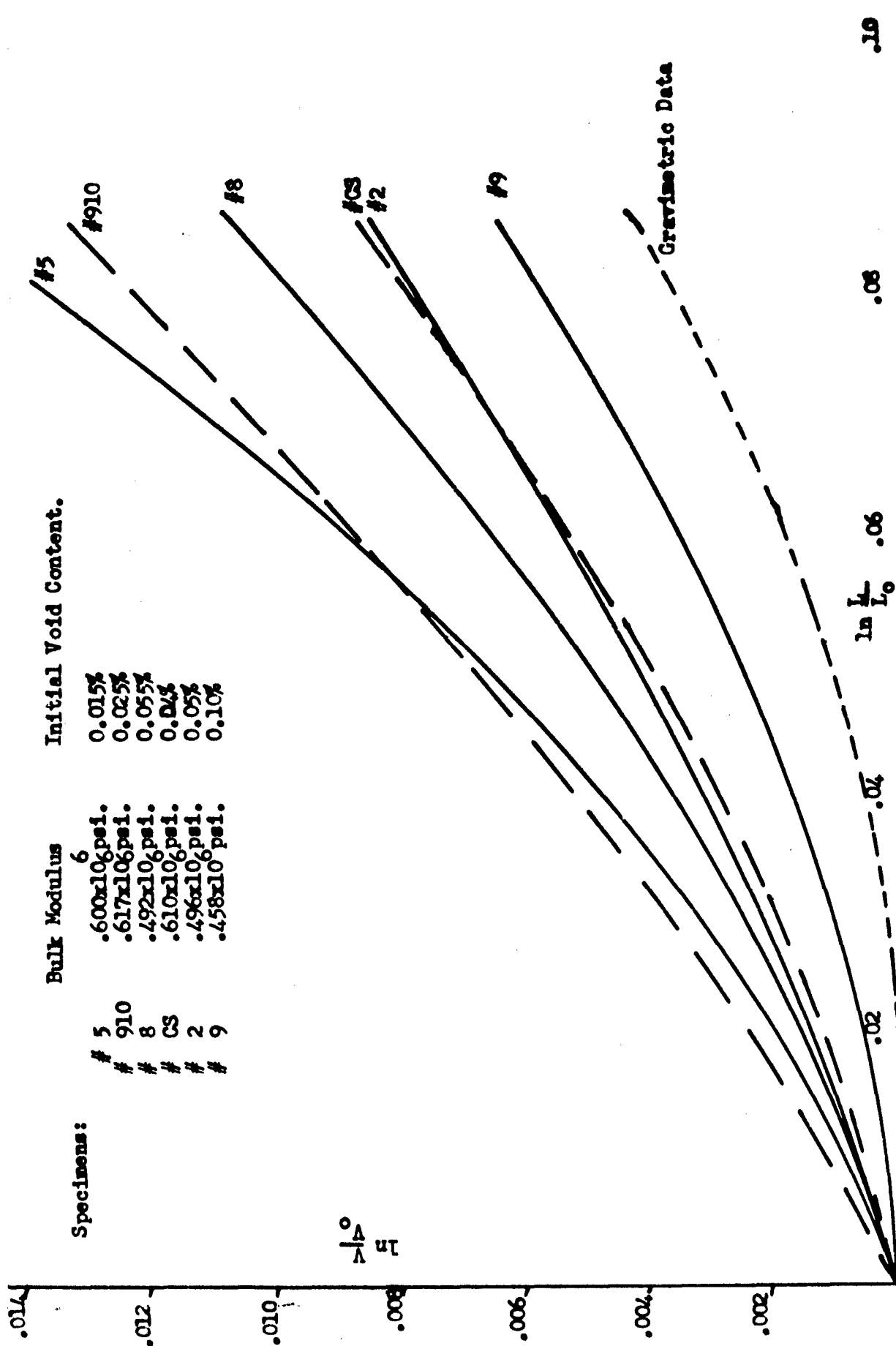FIGURE 3. LATERAL CLIP GAGE AND END-BONDED·TENSILE SPECIMEN

Labels in figure:
- Wooden Tab
- Specimen
- Bonded Strain Gages
- Steel Spring Clip
- Rubber Thread Pads
- End-Bond

Specimens:

	Bulk Modulus 6	Initial Void Content.
# 5	.600x10^6 psi.	0.015%
910	.617x10^6 psi.	0.025%
# 8	.492x10^6 psi.	0.055%
# CS	.610x10^6 psi.	0.045%
# 2	.496x10^6 psi.	0.05%
# 9	.458x10^6 psi.	0.10%

$\ln \dfrac{V}{V_o}$

$\ln \dfrac{L}{L_o}$

Gravimetric Data

FIGURE 4. VOLUME VS EXTENSION FOR END-BONDED SPECIMENS WITH BULK MODULUS AND INITIAL VOID CONTENT
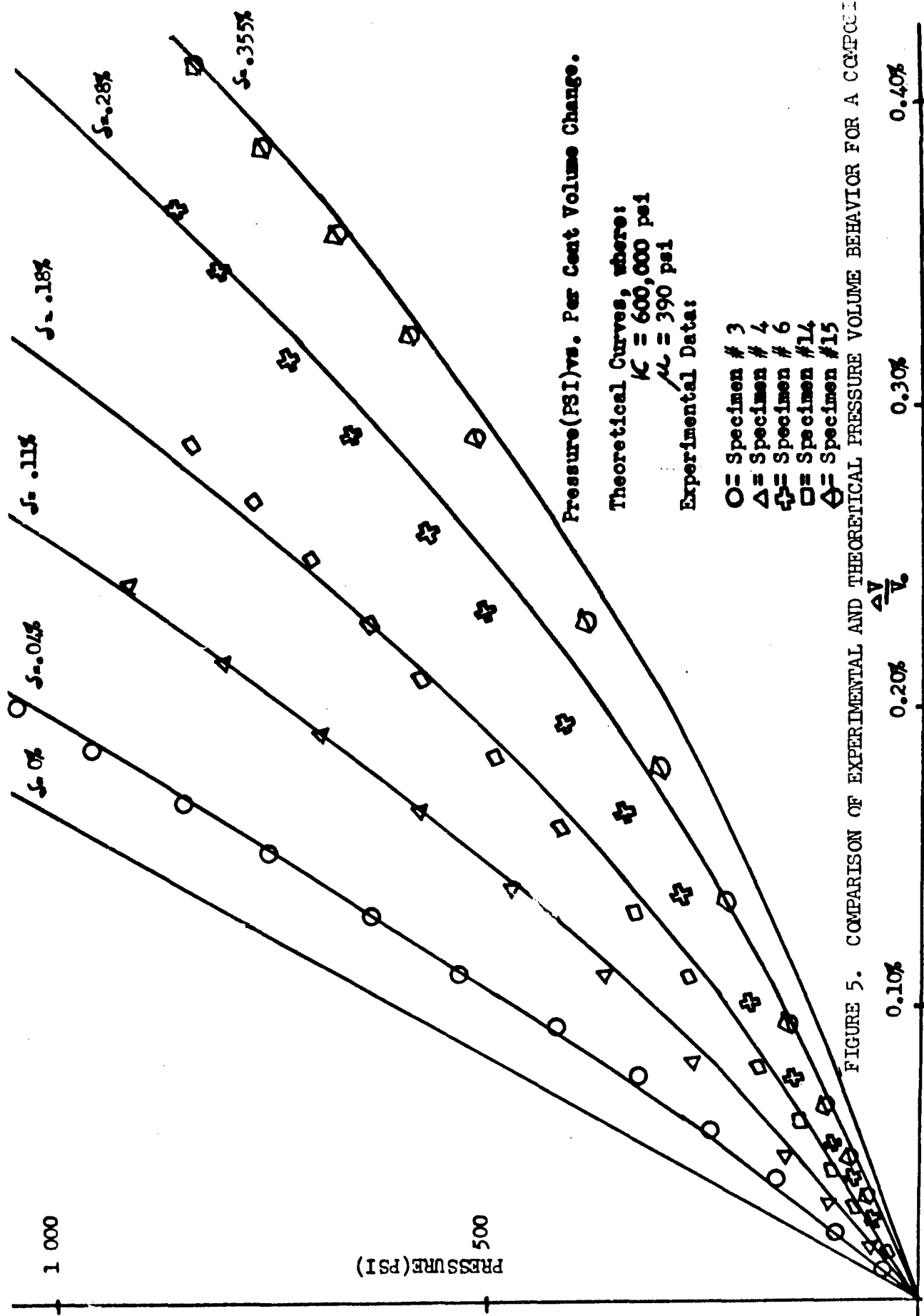
FIGURE 5.   COMPARISON OF EXPERIMENTAL AND THEORETICAL PRESSURE VOLUME BEHAVIOR FOR A COMPOSITE...

Pressure(PSI)vs. Per Cent Volume Change.

Theoretical Curves, where:
$K = 600,000$ psi
$\mu = 390$ psi

Experimental Data:

O = Specimen # 3
△ = Specimen # 4
⊕ = Specimen # 6
□ = Specimen #14
◇ = Specimen #15

Pages 380 to 394 inclusive

deleted by SPIA

THE ROLE OF BROAD-SPECTRUM MECHANICAL RESPONSE STUDIES IN PROPELLANT EVALUATION

R. B. Kruse, Thiokol Chemical Corporation,
Redstone Division, Huntsville, Alabama

ABSTRACT

Tensile tests of propellant carried out at various constant strain rates and temperatures have been superposed by use of shift factors calculated from the Williams-Landel-Ferry equation, into curves of tensile properties vs. reduced strain rate. The resulting curves are useful for direct comparisons of propellants using similar fuel-binder systems or propellants with differing solids content but the same fuel-binder system, the requirement for direct comparison being that the glass transition temperatures of the binders involved be the same.

In addition to superposition of tensile properties, some progress has been made toward a viscoelastic description of the propellants based upon superposed stress-strain curves. First approximations of the distribution spectra of relaxation times for three propellants have been obtained, and their relaxation moduli have been fitted with a modified power law.

INTRODUCTION

This paper describes the methods used by the Redstone Division of the Thiokol Chemical Corporation to compare the physical properties, mechanical response, and viscoelastic behaviour of a set of similar composite propellants. In it, propellants made with carboxyl-terminated polymers are compared with propellants made from older copolymers in which the carboxyl groups are randomly distributed, from the standpoint of tensile parameters, including modulus, tensile strength, strain at maximum stress, and strain at break.

The propellants compared here were made with Thiokol's HC polymer cured with an imine-type curing agent, Butarez CTL Type 2 cured with the same agent, and Thiokol's HA binder. These three propellants all had the same total solids loading, the same oxidizer loading, the same percentage of aluminum, and the same ratio of ground to unground oxidizer. In the remainder of this paper, TP-H8041 propellant will be referred to as HA propellant and the same formulation using HC polymer and corresponding curing agent will be termed HC analog.

EXPERIMENTAL PROCEDURE

The results of an early study of the application of the principle of time-temperature superposition to HA propellant were reported in a previous SPIA paper[1]. From the data generated by constant-strain-rate tests of HA propellant at four different rates of crosshead travel (0.02, 0.20, 2.00 and 20.0 inches per minute) and four different temperatures (-65°, 0°, +77°, and +140°F), it appeared initially that the WLF constants[2] did not apply exactly to HA propellant. Therefore the data were simply superposed, and the shift factors (a_T) necessary to effect this superposition were reported. When data were obtained on the HC analog at four different crosshead speeds (same as above) and six different temperatures (-70°, -60°, -40°, 0°, +77°, and +140°F), it was observed that the data could be superposed quite satisfactorily by using the WLF constants and a glass transition temperature of -80°C (193°K). This temperature was determined to be the glass transition temperature of both HA and HC polymers by thermal expansion measurements. Since the data obtained on the HC analog were considerably more precise and reliable than those originally obtained on HA propellant, it seemed probable that the lack of adequate superposition of the HA propellant data was due to lack of accuracy and precision in the data. All of the constant-strain-rate data which had been obtained on HA propellant were re-evaluated in the light of the more recent HC analog data. This included new determinations of strain rates and modulus values from the strain-time and stress-strain curves. A new reference temperature of 243°K (50° above the independently measured glass transition temperature) was used in place of the 298°K (room temperature) reference temperature which had previously been selected on a purely arbitrary basis.

Upon completion of this re-evaluation of the constant-strain-rate test data of HA propellant, it was found that the WLF constants superposed the data as satisfactorily as the shift factors which had previously been used. It was therefore possible to compare directly the broad-spectrum physical properties of TP-H8041 propellant and its HC analog.

The glass transition temperature of Butarez CTL also has been measured by thermal expansion methods and has been found to be approximately -80°C. It was found during the course of this study that the WLF constants superposed very satisfactorily the broad-spectrum properties of this propellant also. All three propellants could therefore be compared directly on the same broad-spectrum plot; this comparison would not have been possible had the glass transition temperatures been appreciably different.

All the data presented in this paper are based on photographic measurements of strain. In each case, the strain rate is obtained by plotting the photographically measured strains as a function of time. The best

straight-line plot is taken as the strain rate, which must be assumed to be constant throughout the test. Actually, some variation in strain rate is usually observed during a given test. This may be due either to an actual variation in strain rate due to non-uniform jaw flow or to errors in strain measurement from the photographs taken during the test. In any event, variations in strain rate are slight, and consequently error introduced by the assumption of a constant strain rate for a given test is small.

The stresses recorded on the Instron charts were corrected for the change in cross-sectional area undergone by the specimen as it was strained. This correction was based on the assumption that the volume of the specimen remains constant. Again, this assumption is not strictly correct. Recently a considerable effort has been made to measure the volume change with strain for propellant tensile specimens. The results of this program are reported in a separate paper presented at this meeting. However, the corrections based upon the constant-volume assumption result in considerably more realistic and useful data than would be obtained by leaving the stress uncorrected.

Plots of tensile properties as a function of reduced strain rate, such as those included in this paper, provide a complete graphic representation of propellant mechanical response to a wide range of environmental conditions and imposed strain rates. In general, low-strain-rate or high-temperature behaviour appears on the left side of the plot, and high-strain-rate or low-temperature behaviour appears on the right side. The whole plot may be roughly divided into five general areas: (1) the strain rates encountered on cool-down of a motor from the curing temperature to ambient, where $\log \dot{e}a_T < -9$, (2) the region of slump, long-time creep, and storage behaviour, where $-9 < \log \dot{e}a_T < -5$, (3) high-temperature ignition response, where $-5 < \log \dot{e}a_T < 0$, (4) low-temperature ignition response, where $0 < \log \dot{e}a_T < 4$, and (5) response to true shock loading, including very short-time creep and stress-relaxation response, and behaviour in the glassy region, where $\log \dot{e}a_T > 4$.

Where similarity of propellants permits a direct comparison on such plots, the technique of presenting tensile properties on a broad-spectrum basis has been found to be a very valuable aid in the description of propellant behaviour. The first four figures compare the broad-spectrum physical properties of HA propellant with those of HC analog. A comparison of the broad-spectrum modulus curves of these propellants is shown in Figure 1. Initial modulus, which is a small-deformation property, is the only parameter for which the principle of time-temperature superposition rests on firm theoretical grounds. In Figure 1 this initial modulus, referred to the reference temperature of 243°K, is plotted against the logarithm of the reduced strain rate. For both propellants, modulus increases considerably with an increased reduced strain rate up to the glassy region, where it would become constant. In addition to the constant

glassy modulus, a region of constant modulus would be expected on the extreme left of the curve, provided that the material is effectively cross-linked. If the material is not effectively crosslinked, the modulus would decay to zero rather than reach an equilibrium value on the lower left side of the graph. It can be seen from Figure 1 that the modulus of HA propellant changes more abruptly with reduced strain rate than does the modulus of the HC analog. Moreover, in the high-temperature or low-strain-rate regions, the HC analog retains a higher modulus value while the modulus of HA propellant is decreasing. The modulus values plotted here were calculated from the slopes of the initial straight-line portions of the stress-strain curves obtained as described previously.

Unlike modulus, tensile strength (that is, maximum stress) cannot be considered a small-strain property. Nevertheless, the principle of time-temperature superposition has been applied with considerable success to tensile values of both HA and HC propellants. The result is shown in Figure 2. In this graph, the logarithm of maximum stress (again referred to 243°K), is plotted versus the logarithm of the reduced strain rate. The maximum stress value increases with increasing reduced strain rate up to a nearly constant value in the glassy region. With respect to tensile strength, the HC analog displays a marked superiority to HA propellant. The shape of the tensile strength curves is quite similar, but the curve for HC analog remains consistently above that for HA propellant up to the glassy region.

The strain which propellant can withstand may be based upon either the strain at maximum stress or the strain at break. Again, these are ultimate rather than small-strain properties and, as such, the application of the time-temperature superposition principle to them rests upon an empirical basis. Considering that strain data are not inherently highly reproducible, the superposition principle works rather well for data gathered at various strain rates and temperatures. Figures 3 and 4 show the reduced strain rate plots of strain at maximum stress and strain at break, respectively. It is in the property of strain capacity more than any other tensile parameter reported in this paper that the superiority of HC analog to HA propellant becomes evident. Over almost the entire range of reduced strain rates measured, well into the region of glassy behaviour, the strain which can be sustained by HC analog is greatly in excess of that which can be sustained by HA propellant. The elongation of the HC analog is seen to be about twice that of HA propellant in the region $-7 < \log e a_T < -2$, the high-temperature-low strain rate region. Beyond this point, however, the elongation of HA propellant decreases while that of HC analog continues to increase, reaching a maximum near $\dot{e} a_T = 1$. As $\dot{e} a_T$ increases beyond 4, and the two propellants begin to exhibit glass-like behaviour, the elongations are not greatly different, as might be expected from an examination of the comparisons of moduli and stresses.

In general, then, at the 84 per cent solids loading level, HC propellant exhibits considerable improvement over the HA system from the standpoint of mechanical behaviour over the range of reduced strain rates studied. As a result of this investigation, it may be predicted that the solids loading level of the HC system might well be increased in order to improve ballistic performance while still retaining physical properties which are comparable with or superior to those of HA propellant at the 84 per cent solids level. Efforts in this direction have been initiated, and it seems highly desirable to undertake a thorough study of more highly loaded HC systems in order to determine whether the Williams-Landel-Ferry constants still apply at these higher loadings and to obtain some basis for prediction of the effects of increased loading upon the mechanical response of propellant.

Recent work has made possible a comparison of HA and HC propellants with the Butarez CTL analog based upon the TP-H8041 formulation. The Butarez CTL analog was studied in the same way as the HA propellant and HC analog already described.

Figures 5 through 8 show the broad-spectrum physical property curves for Butarez CTL analog. These include the data points for the Butarez CTL analog that were used to construct the curves. For comparison purposes, the broad-spectrum curves for HA and HC propellants, shown with their data points in the previous figures, are included in Figures 5 through 8, with data points omitted for clarity. The variation in modulus of the Butarez CTL analog with reduced strain rate is shown in Figure 5. The variation in modulus is greater than for either HA or HC based systems. The modulus of Butarez CTL analog near the equilibrium region is roughly comparable to that of the HA system. The modulus is low throughout the transition region, but becomes considerably higher than either HA or HC propellant in the glassy region. Some of this increase in glassy modulus might be accounted for by recent refinements in small strain measurements.

Figure 6 shows the variation of tensile strength of Butarez CTL analog with reduced strain rate. The tensile strength of Butarez CTL analog is very nearly the same as that of HA propellant over the entire range of reduced strain rates studied. The tensile strength of both of these propellants is considerably less than that of the HC analog.

Figures 7 and 8 show that the Butarez CTL analog does not exhibit a strain capacity, either at maximum stress or at break, that is quite equal to that of the HC analog, although in both of these properties it is clearly superior to the corresponding values for HA propellant.

As a consequence of the linearity of viscoelastic response which, according to presently available data, is exhibited by the propellants

included in this study, and of the principle of time-temperature equivalency, it is possible to make a start toward approximating from constant-strain-rate data the response of these propellant systems to conditions of dynamic stress and strain. As a start toward accomplishing this result, the distribution of Maxwellian relaxation times for the three propellants studied was determined. A discussion of how this approximation may be obtained is appropriate.

Just as tensile data from tests at various strain rates and temperatures may be superposed to form continuous physical property curves which are functions of the time-temperature complex, so the individual stress-strain curves obtained from constant-strain-rate tests may themselves be superposed, up to the point where yield of the material becomes apparent. If the stress and strain values used to obtain the tensile curves are each divided by the reduced strain rate, and the resulting reduced stress and strain values are all plotted on the same logarithmic scale, they will form a continuous master stress-strain curve. Such master stress-strain curves for HA propellant and for the HC and Butarez CTL analogs are shown in Figure 9.

The discussion of the derivation of stress relaxation curves representing the response of material to an instantaneously imposed strain from the master stress-strain curves of propellant has been presented by Smith[3]. His method has been followed in this study. Briefly summarized, it may be shown that:

$$\frac{\sigma}{e} \cdot \frac{d \log \tau}{d \log e}\bigg]_{e=\dot{e}t} = E_r$$

so that the slope of the master stress-strain curve would yield relaxation modulus (E_r) as a function of time. The relaxation modulus curves for HA propellant and for HC and Butarez CTL analogs that were obtained in this way are shown in Figure 10. These curves represent the stress relaxation behaviour of the three propellants at the reference temperature of 243°K. From the relaxation curves, an estimation of the distribution of the Maxwellian relaxation times may be obtained by using the Alfrey approximation[4]. The slope at each point on the relaxation curve is determined, and the negative of the slope is plotted versus log τ. The resulting graphical function is an approximation of the distribution function H (log τ). The relaxation spectra of the propellants made with the three types of binder are shown in Figure 11. It will be noted that the curves for propellants made with HA and Butarez CTL binders are considerably narrower and sharper than that of the HC analog, showing that the distribution function H (log τ) varies much more abruptly with relaxation time, τ, in the case of HA propellant than for the HC analog. The sharpness of the distribution curve is even more pronounced for the Butarez CTL analog than for HA propellant, and the peak occurs at about one decade smaller τ. From the relaxation spectra it is possible to calculate the response of the material to dynamic stress or strain conditions.

An alternative approach toward derivation of dynamic values from constant-strain-rate properties has been provided by fitting the relaxation curves of the three propellants studied to the modified power law suggested by Blatz[5]. The degree of fit to the relaxation modulus curves, which could be obtained by use of the modified power law, is shown in Figures 12, 13, and 14, in which the relaxation modulus curves obtained from the master stress-strain curves are compared directly with the curves described by the modified power law, with empirical constants inserted.

SUMMARY AND CONCLUSIONS

In summary, a study of propellant mechanical properties by the broad-spectrum method provides considerable data upon which to evaluate propellants for utilization in solid rocket systems. Provided that the propellants are of a sufficiently similar polymer structure to exhibit the same glass transition temperature, it is possible to compare them directly on the same scale of reduced strain rate in order to provide at a glance information concerning the mechanical response of the propellants to a wide variety of strain rate and temperature conditions. Once established, the technique does not require greatly increased time or manpower over that needed for the usual routine comparison of tensile properties at various temperatures, yet it provides a more meaningful and more widely applicable comparison than is generally possible with purely routine physical property tests. The broad-spectrum technique is now being used on a semi-routine basis at the Redstone Division. It provides the additional advantage that the viscoelastic treatment of the constant-strain-rate data makes possible engineering calculations of mechanical response of propellant to conditions which cannot be experimentally duplicated.

REFERENCES

1. R. B. Kruse, JANAF Publication No. PP-13/SPSP8, 25, August, 1960 (Confidential).

2. M. L. Williams, R. F. Landel, and J. D. Ferry, J. Am. Chem. Soc., 77, 3701 (1955).

3. T. L. Smith, SPIA 13th JANAF Solid Propellant Group Meeting Bulletin, Vol. III, p. 601 (Confidential).

4. Turner Alfrey, Jr., "Mechanical Behaviour of High Polymers," Interscience Publishers, Inc., New York, 1948.

5. M. L. Williams, P. J. Blatz, and R. A. Schapery: GALCIT SM61-5 (Final Report, GALCIT 101).
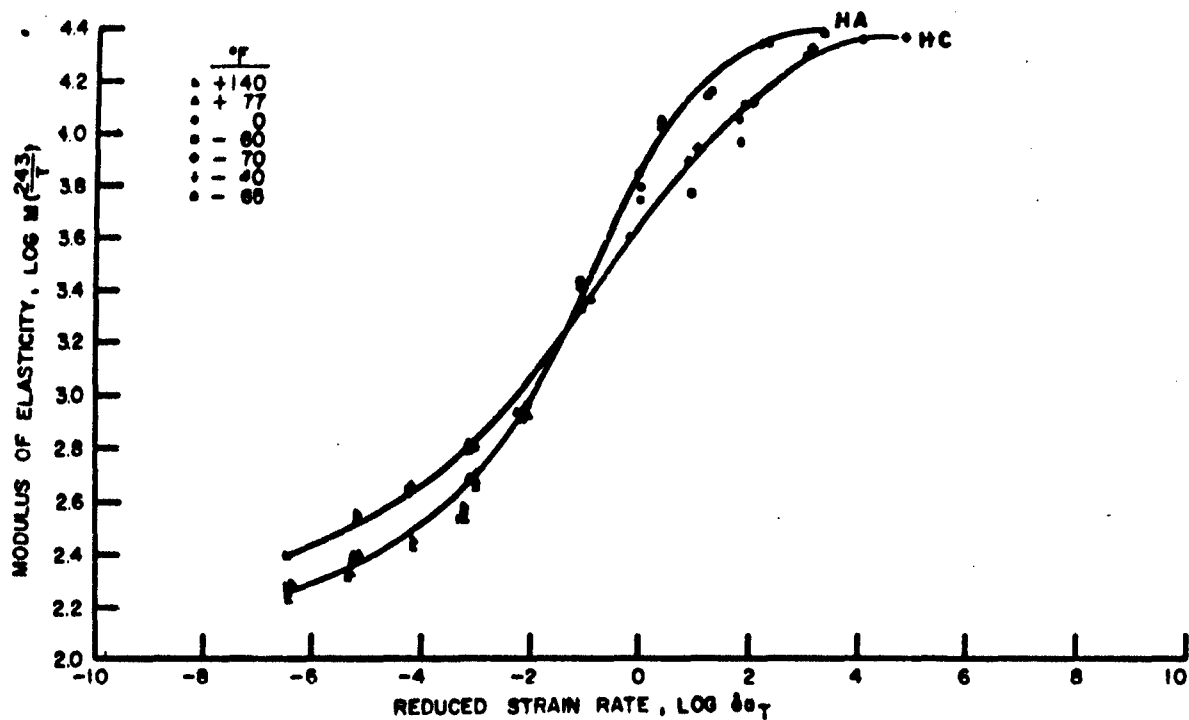
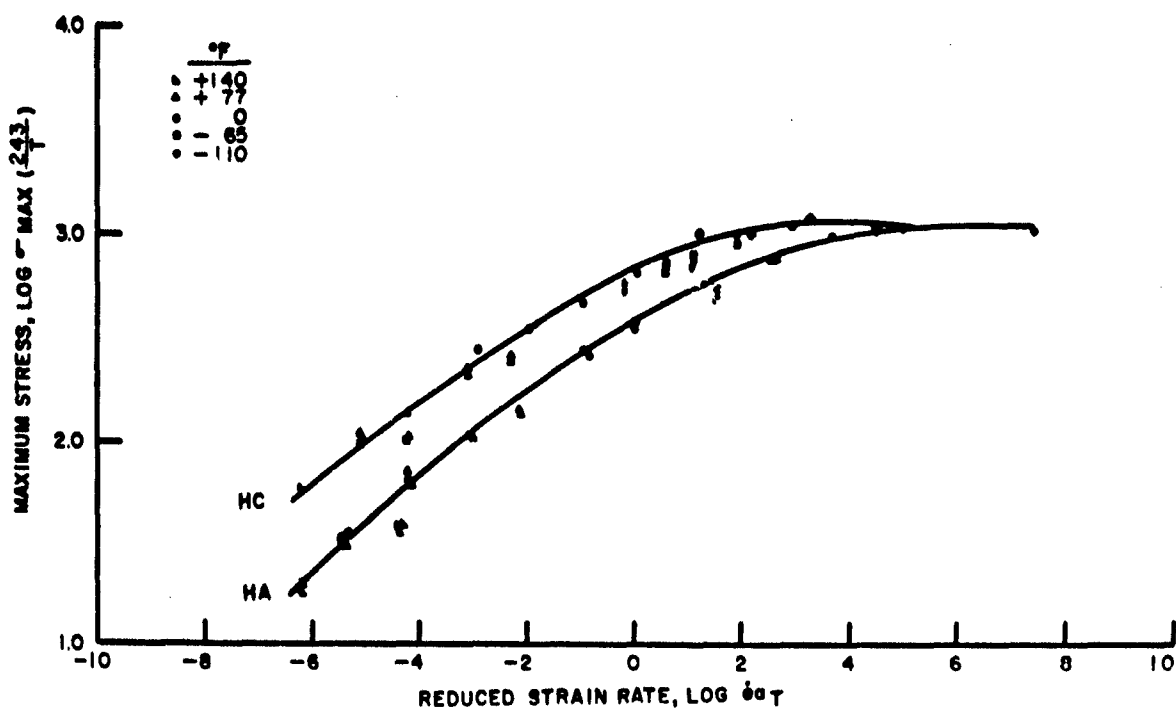FIGURE 1. VARIATION OF MODULUS WITH REDUCED STRAIN RATE

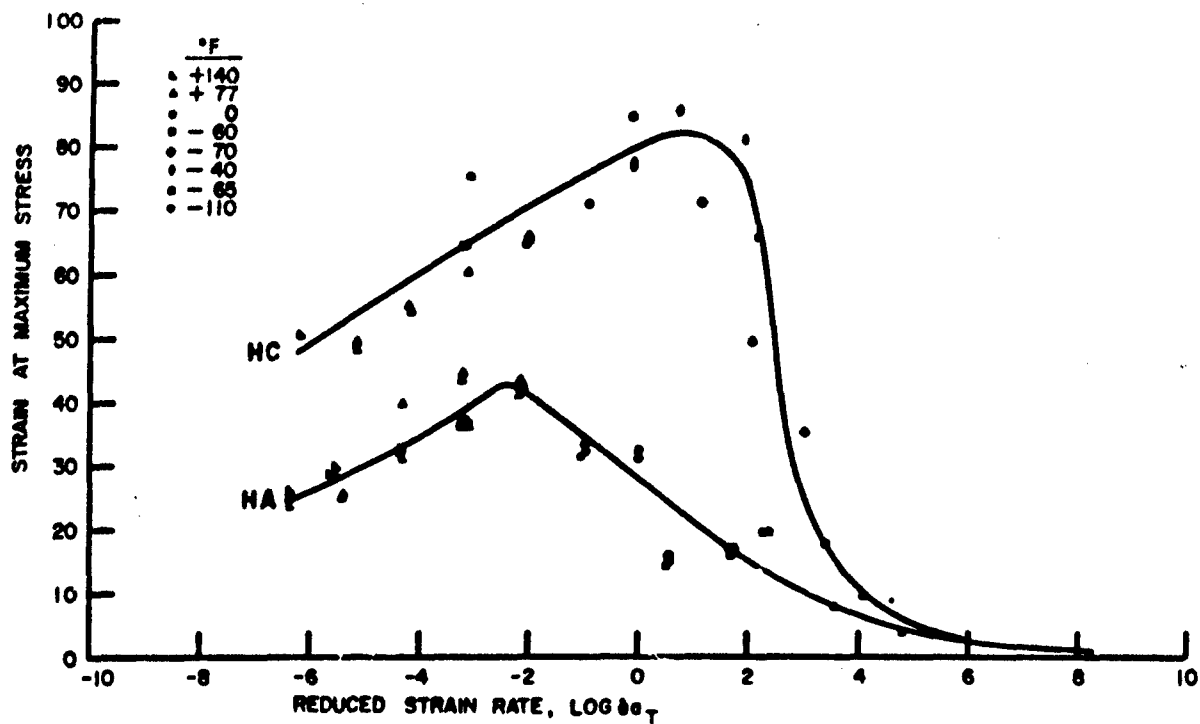FIGURE 2. VARIATION OF TENSILE STRENGTH WITH REDUCED STRAIN RATE

FIGURE 3. VARIATION OF STRAIN AT MAXIMUM STRESS WITH REDUCED STRAIN RATE
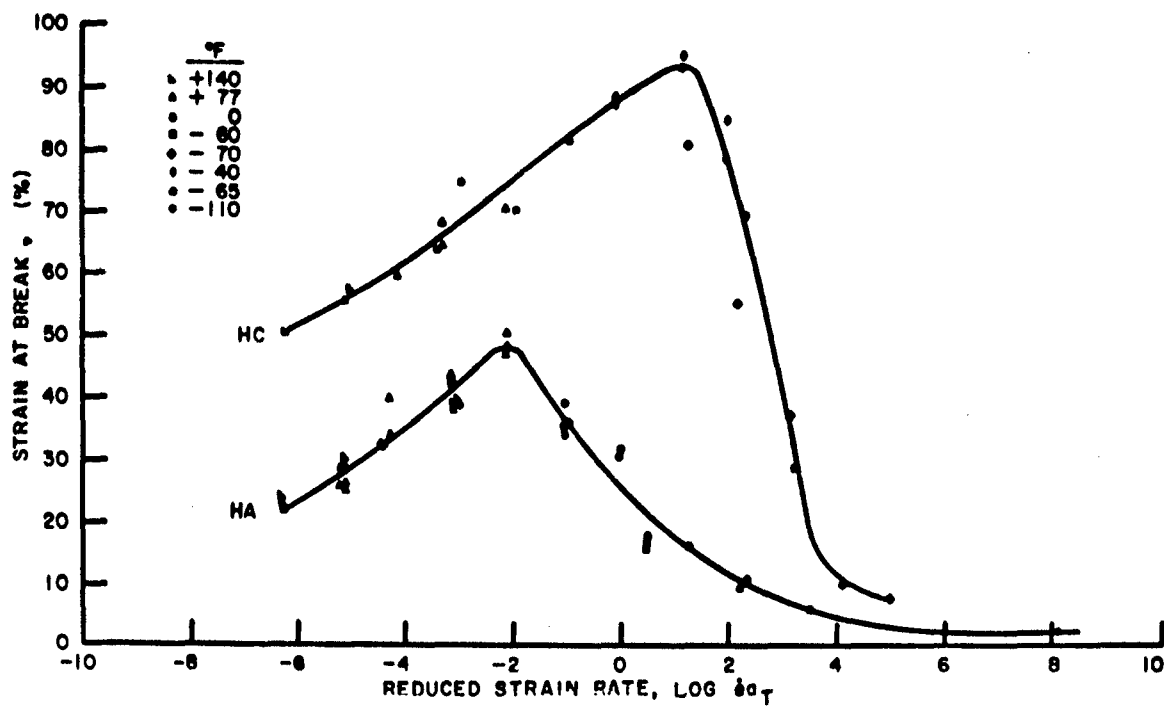

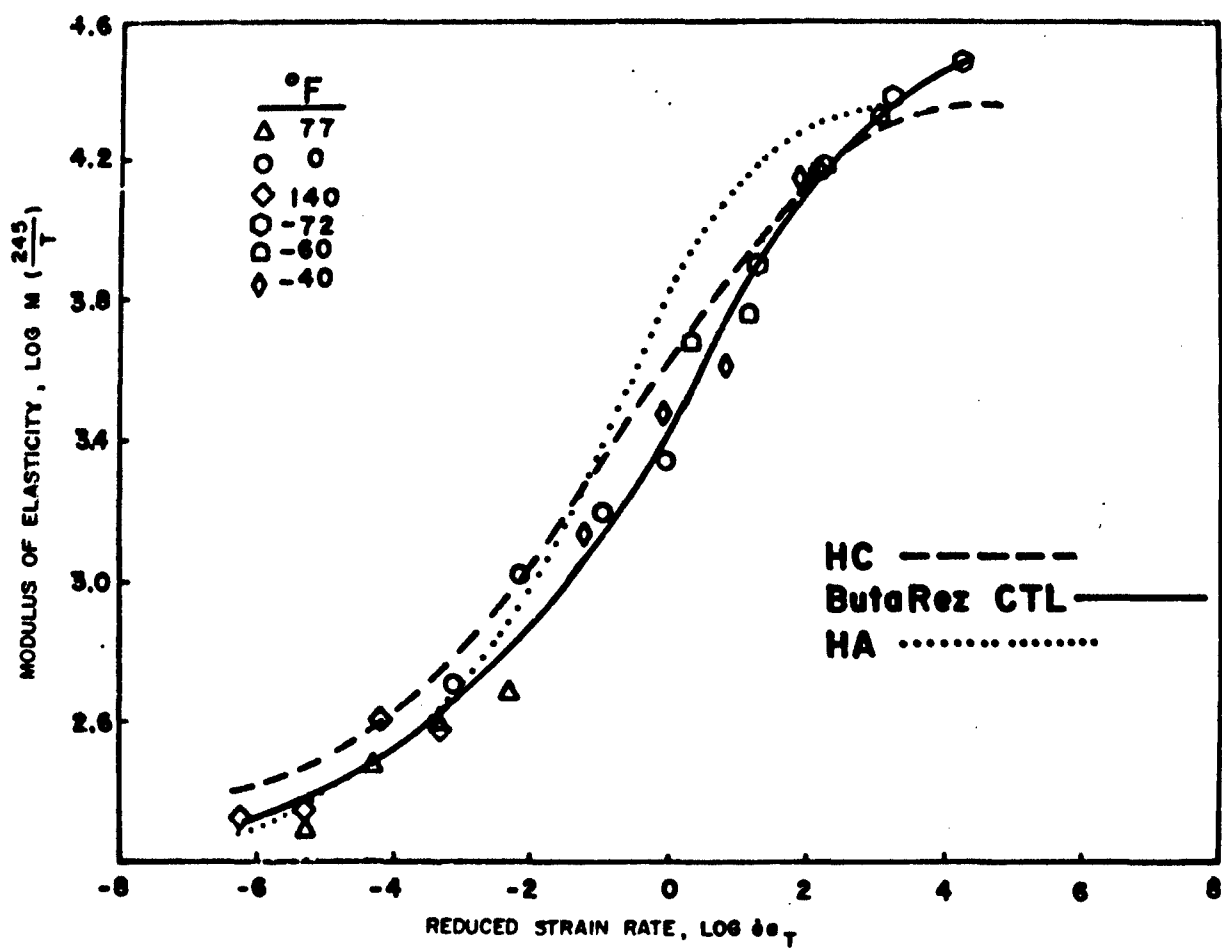FIGURE 4. VARIATION OF STRAIN AT BREAK WITH REDUCED STRAIN RATE

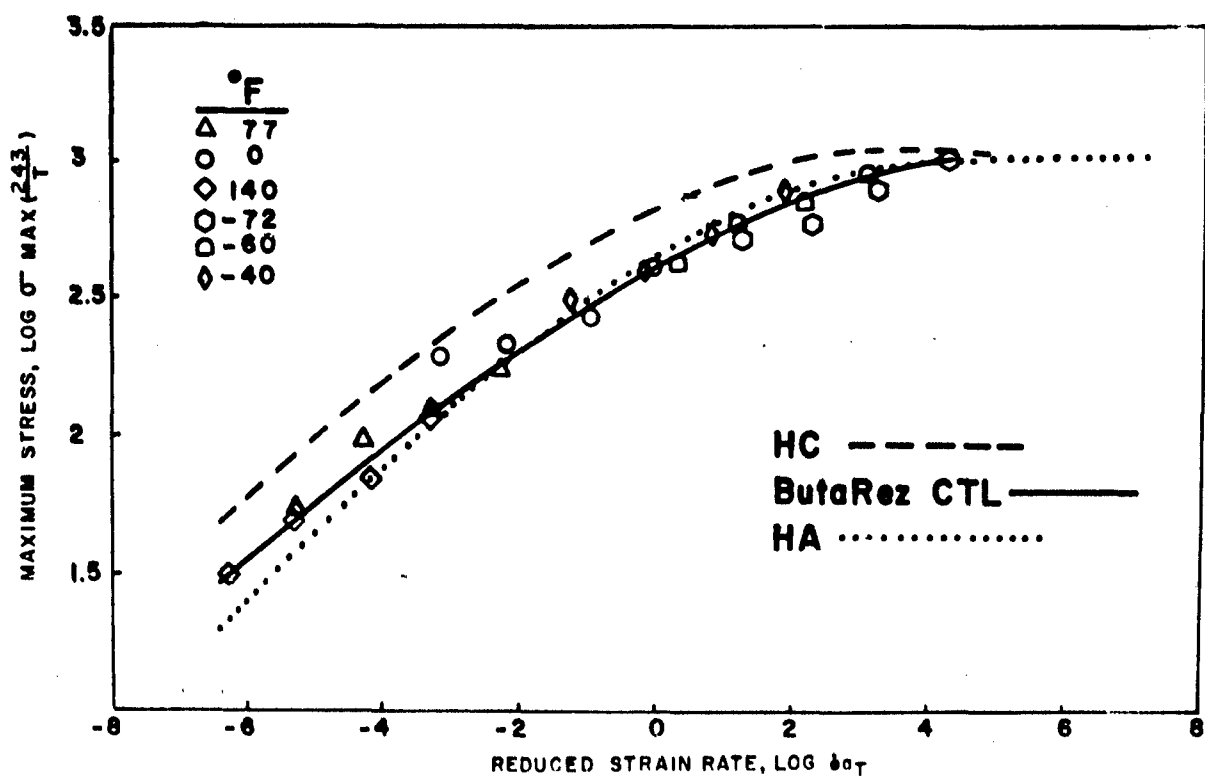FIGURE 5. COMPARISON OF BINDER SYSTEMS: MODULUS OF ELASTICITY

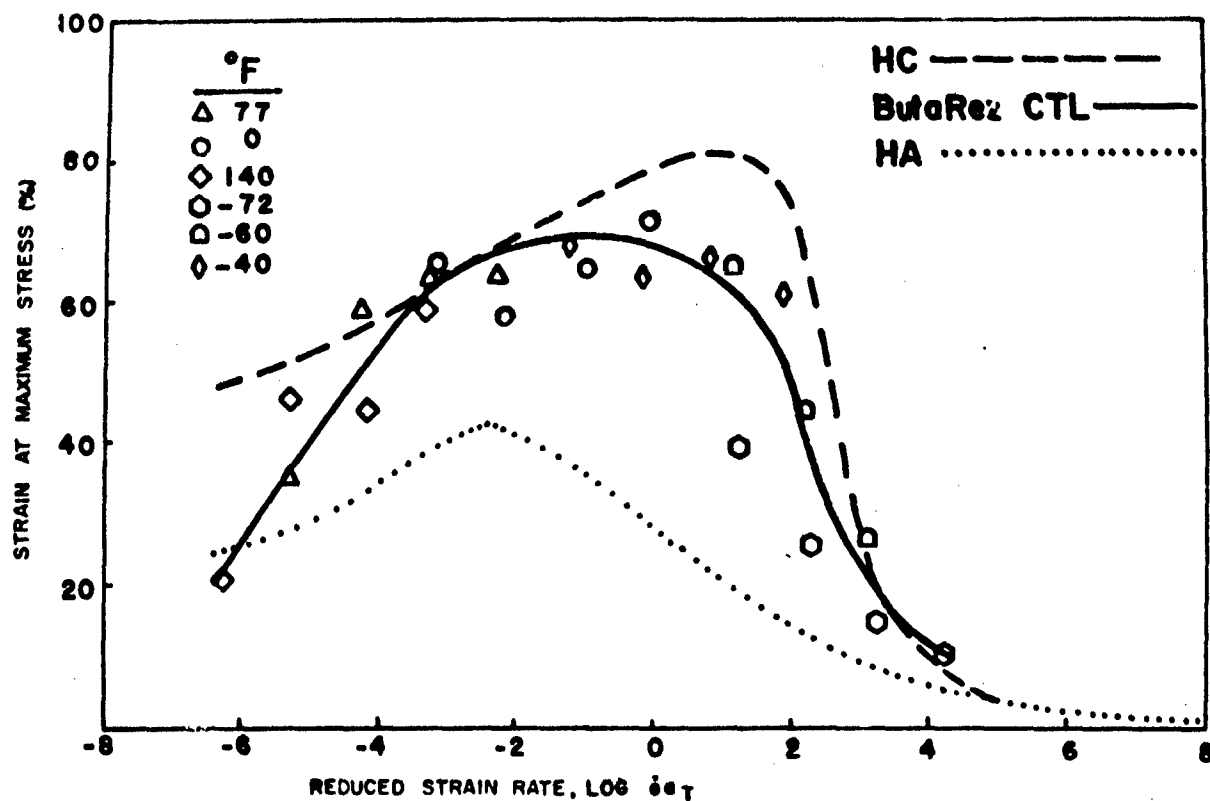FIGURE 6. COMPARISON OF BINDER SYSTEMS: TENSILE STRENGTH

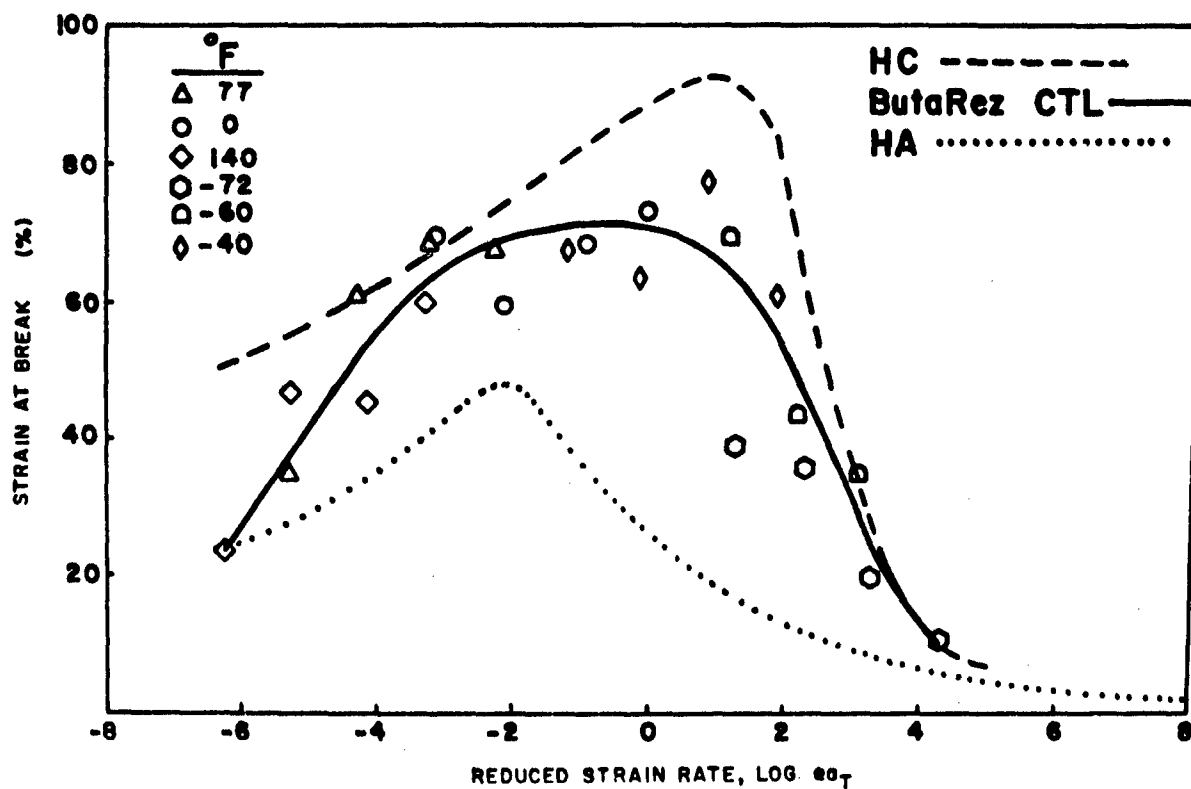FIGURE 7. COMPARISON OF BINDER SYSTEMS: STRAIN AT MAXIMUM STRESS

FIGURE 8. COMPARISON OF BINDER SYSTEMS: STRAIN AT BREAK
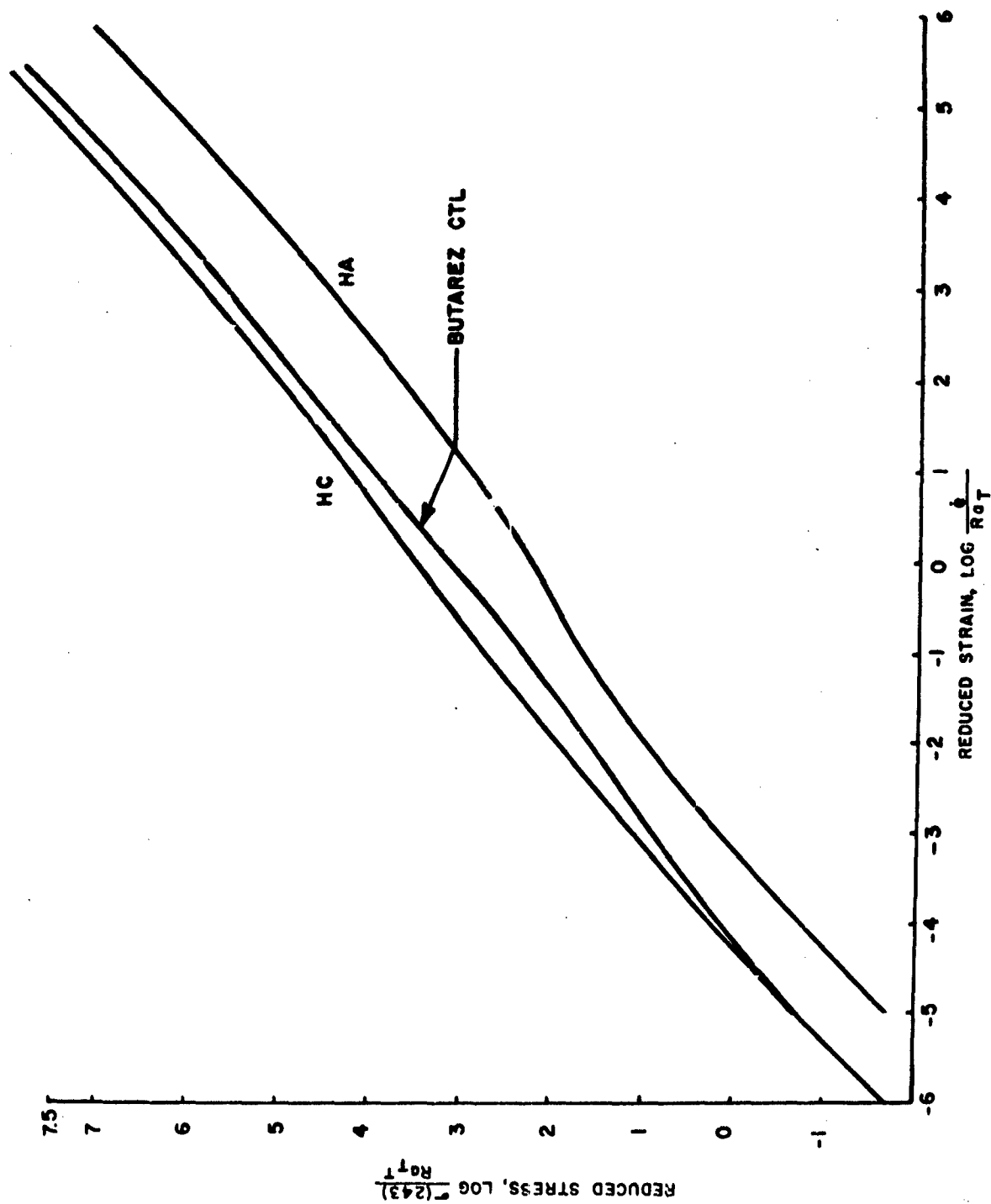
FIGURE 9. REDUCED STRESS-STRAIN

REDUCED STRAIN, LOG $\frac{\dot{\varepsilon}}{Ra_T}$

REDUCED STRESS, LOG $\frac{\tau_{(243)}}{Ra_T}$

HA

HC

BUTAREZ CTL
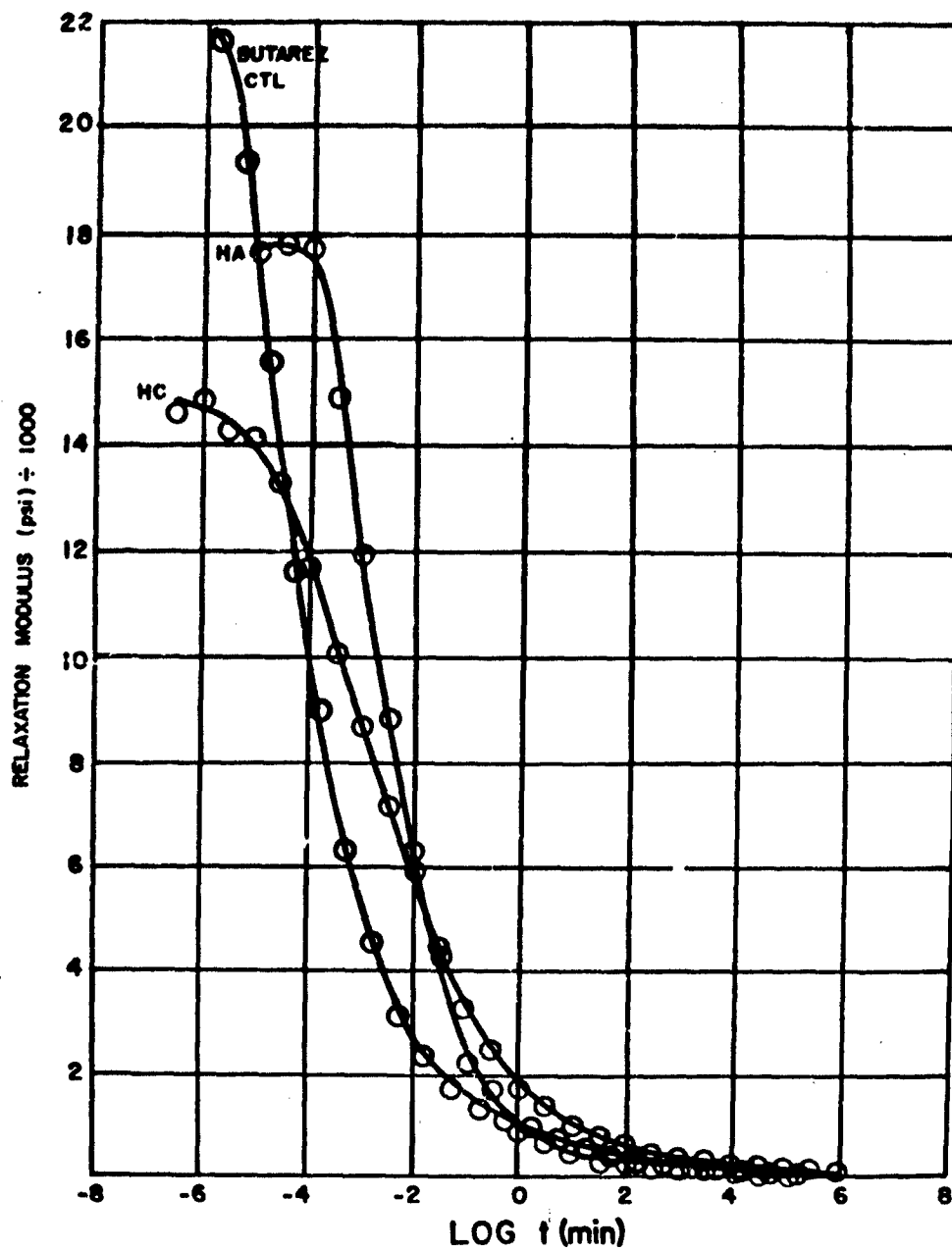
FIGURE 10.   STRESS RELAXATION CURVES
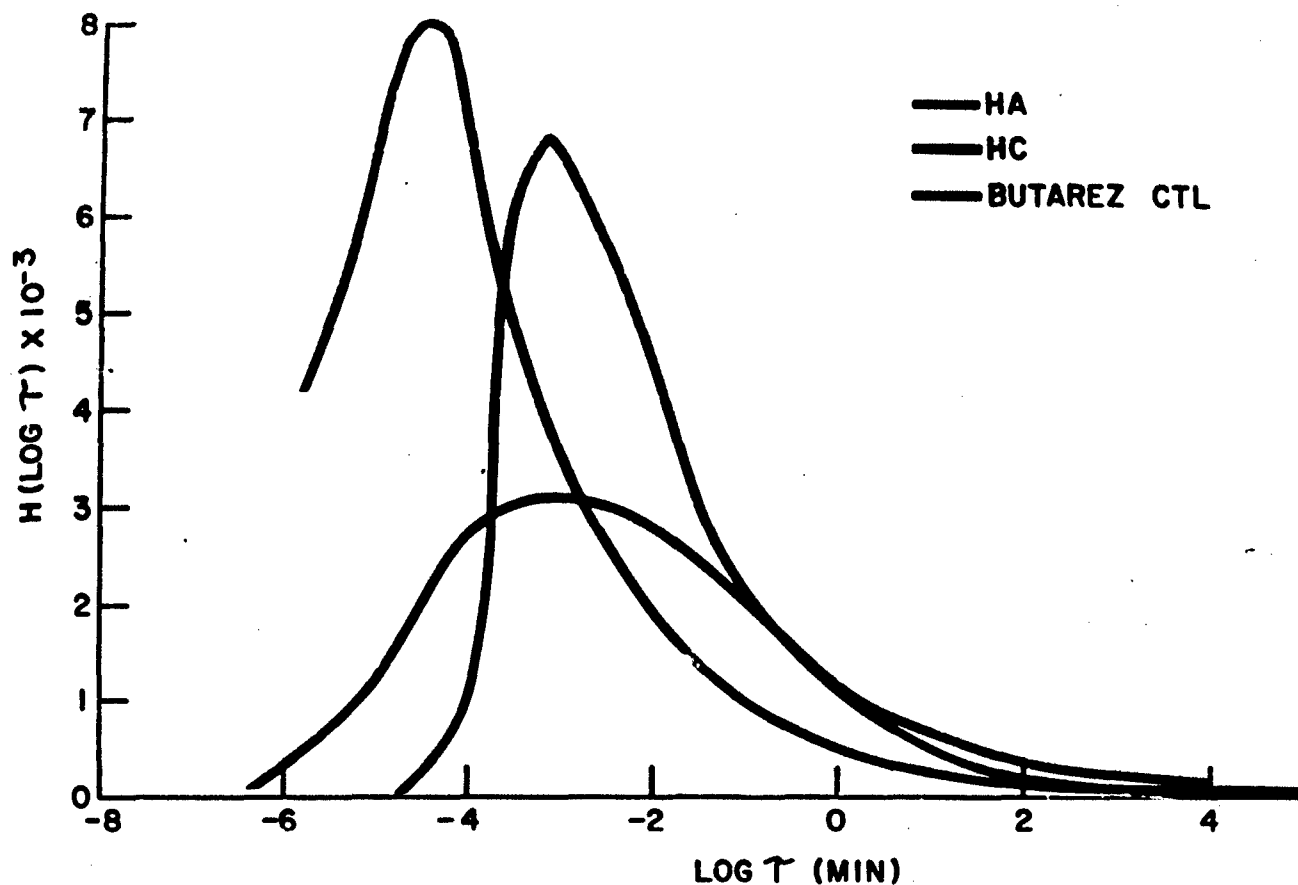
FIGURE 11. RELAXATION SPECTRA
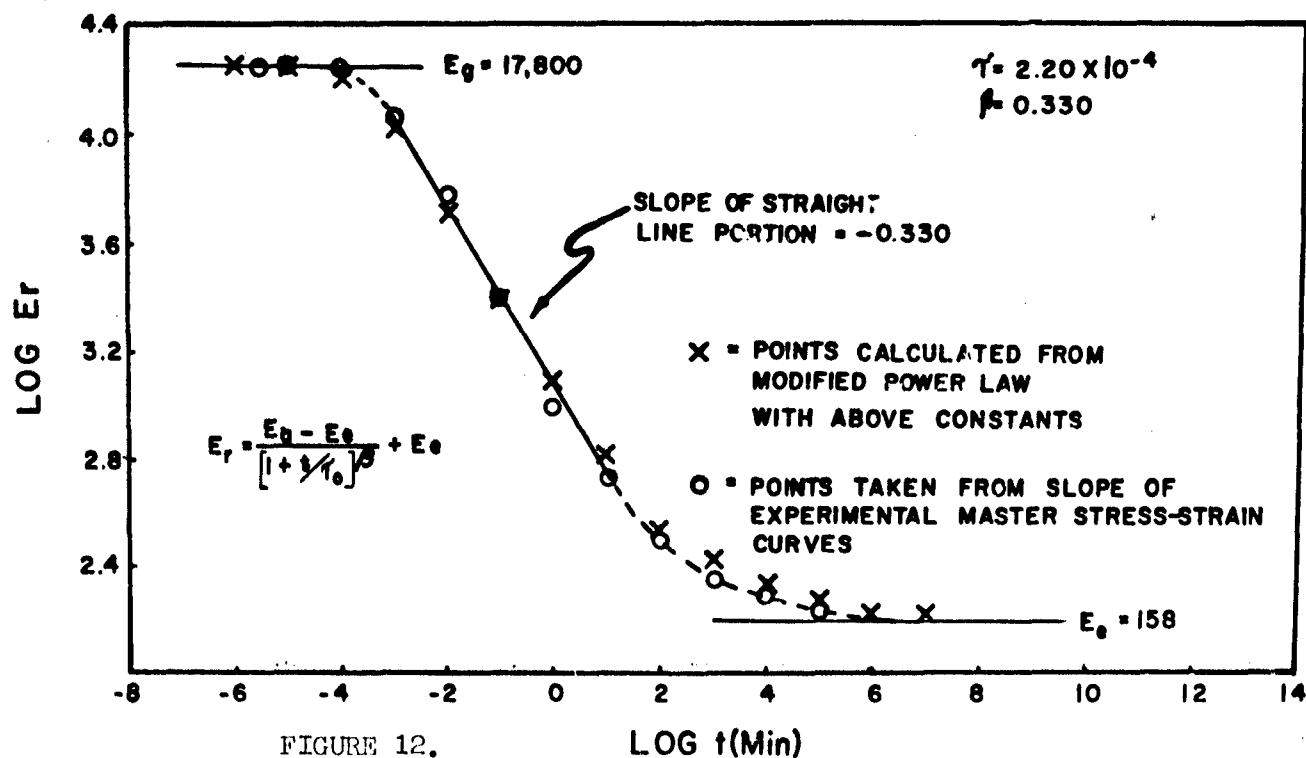
FIGURE 12.

RELAXATION MODULUS OF HA PROPELLANT: COMPARISON
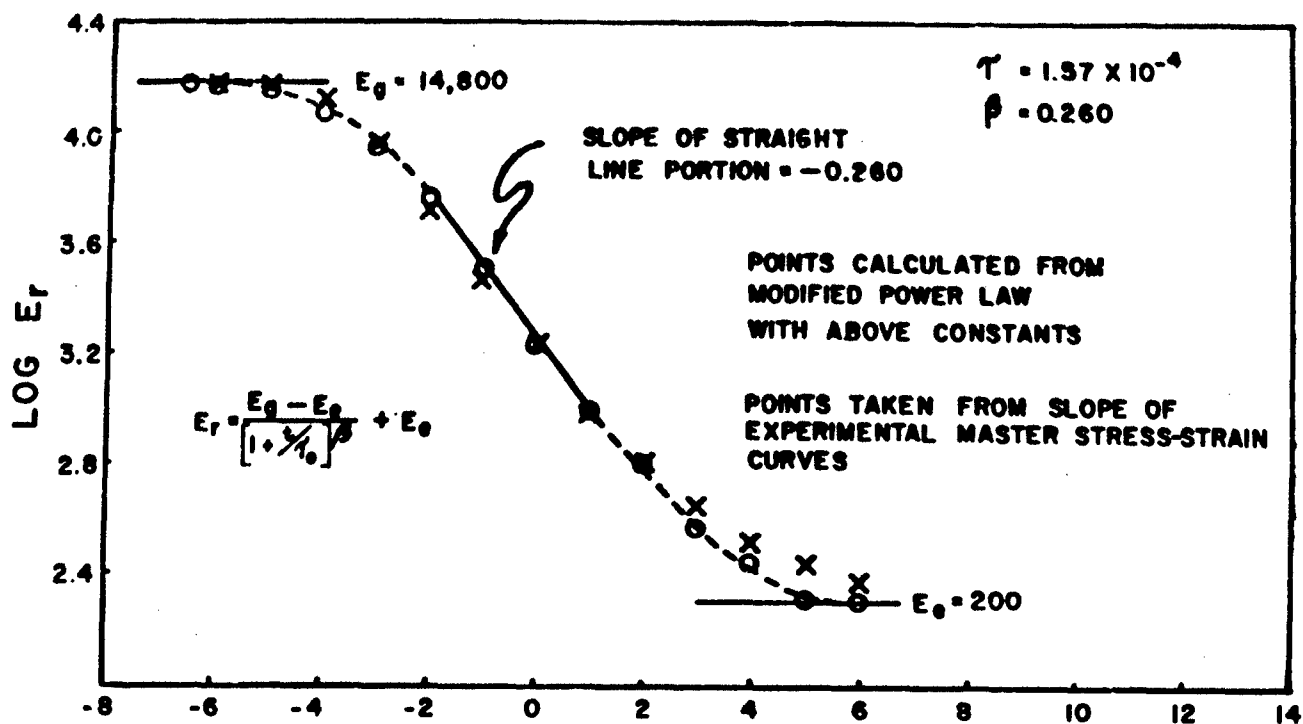OF EXPERIMENTAL DATA WITH MODIFIED POWER LAW

FIGURE 13.
RELAXATION MODULUS OF HC PROPELLANT: COMPARISON
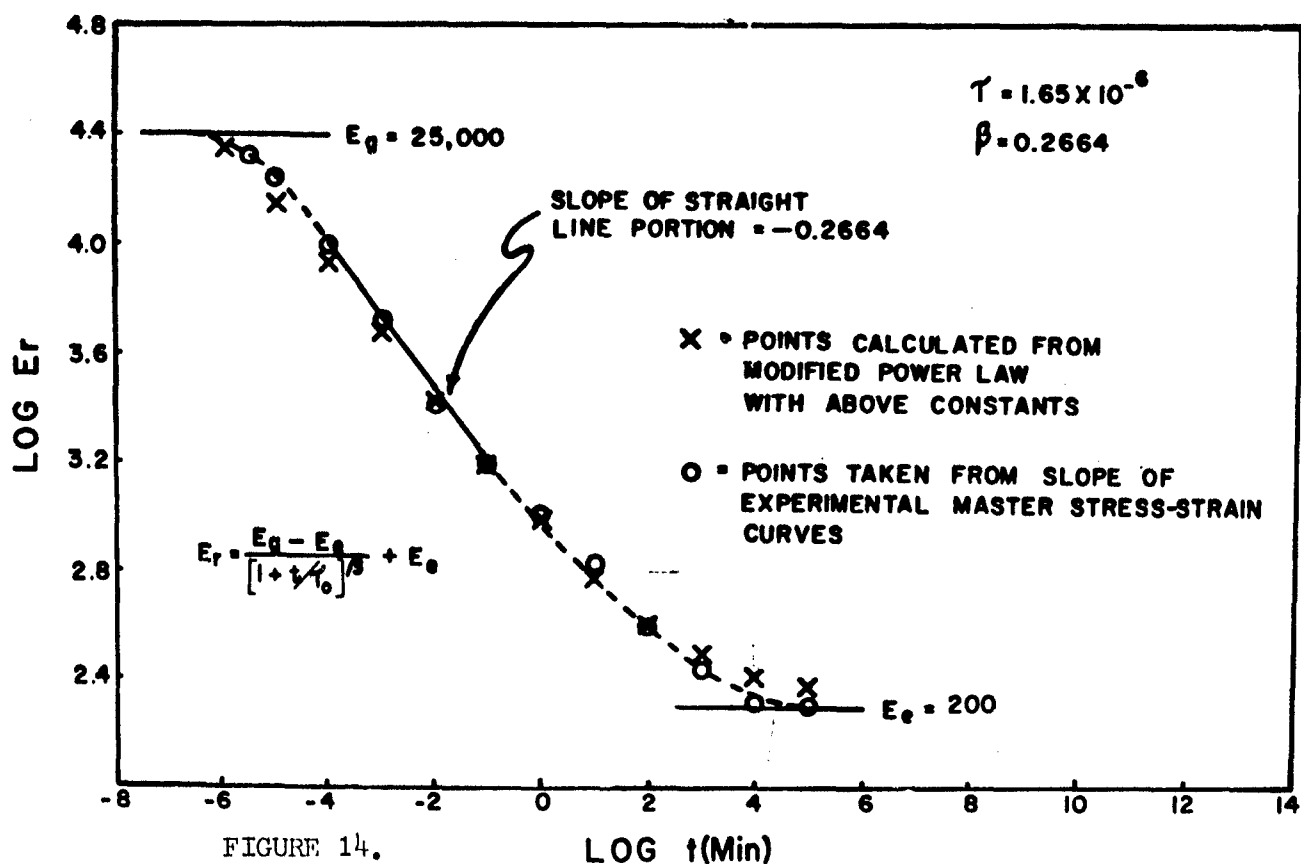OF EXPERIMENTAL DATA WITH MODIFIED POWER LAW

FIGURE 14.
RELAXATION MODULUS OF BUTAREZ CTL ANALOG: COMPARISON
OF EXPERIMENTAL DATA WITH MODIFIED POWER LAW